Volume 23 Number 1 December 1999

ISSN 0734–743X

ARO 39164.1-EG-CF

International Journal of

IMPACT ENGINEERING

Editor-in-Chief
Norman JONES

DISTRIBUTION STATEMENT A
Approved for Public Release
Distribution Unlimited

HYPERVELOCITY IMPACT

PROCEEDINGS OF THE 1998 SYMPOSIUM
PART II: PAGES 519–1024

Huntsville, Alabama, USA

17–19 November 1998

Guest Editor
CHARLES E. ANDERSON, JR

Indexed/abstracted in *Current Contents (Engineering, Technology & Applied Science), Engng Ind Monthly & Author Index, Appl Mech Rev, Cam Sci Abstr, Int Civil Eng Abstr, Metals Abstr, Materials Science Citation Index, Science Citation Index, Engineering Indr*

20000627 121
DTIC QUALITY INSPECTED

PERGAMON

INTERNATIONAL JOURNAL OF IMPACT ENGINEERING

Editor-in-Chief: Professor Norman Jones
Department of Engineering (Mechanical Engineering), The University of Liverpool,
Brownlow Hill, Liverpool L69 3GH, U.K. e-mail: njones@mechnet.liv.ac.uk

Associate Editor: Professor S. R. Reid
Applied Mechanics Division, Department of Mechanical Engineering, UMIST, Manchester
M60 1QD, U.K. e-mail: steve.reid@umist.ac.uk

Founder Editor-in-Chief (1983–1987): Professor W. Johnson
62 Beach Road, Carlyon Bay, St. Austell, Cornwall, PL25 3PJ, U.K.

EDITORIAL ADVISORY BOARD

W. Abramowicz
Polish Academy of Sciences
Institute of Fundamental Technological Research
Swietokrzyska 21
00-049 Warsaw, Poland

C. E. Anderson
Southwest Research Institute
San Antonio, TX 78284, U.S.A.

Y. L. Bai
Institute of Mechanics, Academia Sinica
Peking, People's Republic of China

S. R. Bodner
Faculty of Mechanical Engineering
Technion-Israel Institute of Technology
Haifa, Israel

W. Goldsmith
College of Engineering
Mechanical Engineering
University of California
Berkeley, CA 94720, U.S.A.

N. K. Gupta
Department of Applied Mechanics
Indian Institute of Technology
Delhi, Hauz Khas,
New Delhi-110029, India

J. F. Kalthoff
Ruhr-Universitat Bochum
Gebaude IA2/26
Universitatsstrasse 150
44780 Bochum
Germany
e-mail: kalthoff@tm.bi.ruhr-uni-bochum.de

V. N. Kukudzanov
Department of Mathematical Modelling in Solid Mechanics
The Institute for Problems in Mechanics
Academy of Sciences of Russia
Prospect Vernadskogo 101
Moscow 117526, Russia
e-mail: kukudz@ipmnet.ru

T. Kurokawa
Setsunan University
17-8 Ikeda-Nakamachi
Nayagawa, Osaka 572
Japan
e-mail: kurokawa@mec.setsunan.ac.jp

M. Langseth
Department of Structural Engineering
Norwegian University of Science and Technology
N-7491 Trondheim
Norway
e-mail: magnus.langseth@bygg.ntnu.no

O. Mahrenholtz
Technische Universität
Hamburg-Harburg, Eisendorfer Strasse 38
Technikan D-2100, Hamburg, Germany

J. B. Martin*
Department of Civil Engineering
University of Cape Town
Private Bag, Rondebosch
Cape Town, South Africa
e-mail: aesdrw@bremner.uct.ac.za

V. P. W. Shim
Mechanical and Production Engineering Department
National University of Singapore
10 Kent Ridge Crescent
Singapore 119260
e-mail: mpespwv@nsu.edu.sg

W. J. Stronge
University Engineering Department
University of Cambridge
Trumpington Street
Cambridge CB2 1PZ, U.K.
e-mail: wjs@eng.cam.ac.uk

Paul S. Symonds
Division of Engineering
Brown University
Providence RI 02912, U.S.A.

S. Tanimura
Department of Mechanical Systems Engineering
Osaka Prefecture University
1-1 Gakuen-cho, Sakai City, Osaka 593, Japan
e-mail: tanimura@center.osakafu-u.ac.jp

T. Wierzbicki
Department of Ocean Engineering
Massachusetts Institute of Technology
Cambridge MA 02139, U.S.A.
e-mail: wierz@mit.edu

R. L. Woodward*
Aeronautical and Maritime Research Laboratory
PO Box 4331, Melbourne
VIC 3001, Australia

T. X. Yu
Department of Mechanical Engineering
Hong Kong University of Science and Technology
Clearwater Bay
Kowloon, Hong Kong
e-mail: metxyu@usthk.ust.hk

J. A. Zukas
Computational Mechanics Consultants
P.O. Box 11314
5903 Wakehurst Way
Baltimore MD 21239-0314, U.S.A.

Publishing Office: Elsevier Science Ltd., The Boulevard, Langford Lane, Kidlington, Oxford OX5 1GB, U.K.

Advertising Information: Advertising orders and enquiries can be sent to: **USA, Canada and South America:** Mr Tino DeCarlo, The Advertising Department, Elsevier Science Inc., 655 Avenue of the Americas, New York, NY 10010-5107, USA; phone: (+1) (212) 633 3815; fax: (+1) (212) 633 3820; e-mail: t.decarlo@elsevier.com. **Japan:** The Advertising Department, Elsevier Science K.K., 9-15 Higashi-Azabu 1-chome, Minato-ku, Tokyo 106-0044, Japan; phone: (+81) (3) 5561 5033; fax: (+81) (3) 5561 5047. **Europe and ROW:** Rachel Leveson-Gower, The Advertising Department, Elsevier Science Ltd., The Boulevard, Langford Lane, Kidlington, Oxford OX5 1GB, UK; phone: (+44) (1865) 843565; fax: (+44) (1865) 843976; e-mail: r.leveson-gower@elsevier.co.uk.

Publication information: *International Journal of Impact Engineering* (ISSN 0734-743X). For 2000, volume 24 is scheduled for publication. Subscription prices are available upon request from the Publisher or from the Regional Sales Office nearest you or from this journal's website (http://www.elsevier.com/locate/ijimpeng). Further information is available on this journal and other Elsevier Science products through Elsevier's website: (http://www.elsevier.nl). Subscriptions are accepted on a prepaid basis only and are entered on a calendar year basis. Issues are sent by standard mail (surface within Europe, air delivery outside Europe). Priority rates are available upon request. Claims for missing issues should be made within six months of the date of dispatch.

Orders, Claims, and Product Enquiries: please contact the Customer Support Department at the Regional Sales Office nearest you:
New York: Elsevier Science, PO Box 945, New York, NY 10159-0945, USA; phone (+1) (212) 633 3730 [toll free number for North American customers: 1-888-4ES-INFO (437-4636)]; fax: (+1) (212) 633 3680; e-mail: usinfo-f@elsevier.com
Amsterdam: Elsevier Science, PO Box 211, 1000 AE Amsterdam, The Netherlands; phone (+31) 20 4853757; fax: (+31) 20 4853432; e-mail: nlinfo-f@elsevier.nl
Tokyo: Elsevier Science, 9-15 Higashi-Azabu 1-chome, Minato-ku, Tokyo 106-0044, Japan; phone (+81) (3) 5561 5033; fax: (+81) (3) 5561 5047; e-mail: info@elsevier.co.jp
Singapore: Elsevier Science, No. 1 Temasek Avenue, #17-01 Millenia Tower, Singapore 039192; phone: (+65) 434 3727; fax: (+65) 337 2230; e-mail: asiainfo@elsevier.com.sg
Rio de Janeiro: Elsevier Science, Rua Sete de Setembro 111/16 Andar, 20050-002 Centro, Rio de Janeiro - RJ, Brazil; phone: (+55) (21) 509 5340; fax: (+55) (21) 507 1991; e-mail: elsevier@campus.com.br [Note (Latin America): for orders, claims and help desk information, please contact the Regional Sales Office in New York as listed above].

Periodicals postage is paid at Rahway, NJ. *International Journal of Impact Engineering* (ISSN 0734-743X) is published 10 issues per year in January, February, March, April, May, July, August, September, October and November, by Elsevier Science Ltd., The Boulevard, Langford Lane, Kidlington, Oxford OX5 1GB, UK. The US subscription price is $1646 per year.
POSTMASTER: Send address corrections to: *International Journal of Impact Engineering*, Elsevier Science, Customer Support Department, PO Box 945, New York, NY 10159-0945.
Distributed in the USA by Mercury Airfreight International, 365 Blair Road, Avenel, NJ 07001.

Back Issues
Back issues of all previously published volumes are available direct from Elsevier Science offices.

Whilst every effort is made by the publishers and editorial board to see that no inaccurate or misleading data, opinion or statement appears in this journal, they wish to make it clear that the data and opinions appearing in the articles and advertisements herein are the sole responsibility of the contributor or advertiser concerned. Accordingly, the publishers, the editorial board and editors and their respective employees, officers and agents accept no responsibility or liability whatsoever for the consequences of any such inaccurate or misleading data, opinion or statement.

REPORT DOCUMENTATION PAGE

Form Approved
OMB NO. 0704-0188

Public Reporting burden for this collection of information is estimated to average 1 hour per response, including the time for reviewing instructions, searching existing data sources, gathering and maintaining the data needed, and completing and reviewing the collection of information. Send comment regarding this burden estimates or any other aspect of this collection of information, including suggestions for reducing this burden, to Washington Headquarters Services, Directorate for information Operations and Reports, 1215 Jefferson Davis Highway, Suite 1204, Arlington, VA 22202-4302, and to the Office of Management and Budget, Paperwork Reduction Project (0704-0188,) Washington, DC 20503.

1. AGENCY USE ONLY (Leave Blank)	2. REPORT DATE Jan 2000	3. REPORT TYPE AND DATES COVERED Final Report

4. TITLE AND SUBTITLE
HVIS98 Conference Grant

5. FUNDING NUMBERS
DAAG55-98-1-0492

6. AUTHOR(S)
William P. Schonberg, principal investigator

7. PERFORMING ORGANIZATION NAME(S) AND ADDRESS(ES)
University of Alabama in Huntsville
Huntsville, AL 35899

8. PERFORMING ORGANIZATION REPORT NUMBER

9. SPONSORING / MONITORING AGENCY NAME(S) AND ADDRESS(ES)
U. S. Army Research Office
P.O. Box 12211
Research Triangle Park, NC 27709-2211

10. SPONSORING / MONITORING AGENCY REPORT NUMBER
ARO 39164.1-EG-CF

11. SUPPLEMENTARY NOTES
The views, opinions and/or findings contained in this report are those of the author(s) and should not be construed as an official Department of the Army position, policy or decision, unless so designated by other documentation.

12 a. DISTRIBUTION / AVAILABILITY STATEMENT	12 b. DISTRIBUTION CODE
Approved for public release; distribution unlimited.	

13. ABSTRACT (Maximum 200 words)

NO ABSTRACT FURNISHED

14. SUBJECT TERMS	15. NUMBER OF PAGES
	16. PRICE CODE

17. SECURITY CLASSIFICATION OR REPORT	18. SECURITY CLASSIFICATION ON THIS PAGE	19. SECURITY CLASSIFICATION OF ABSTRACT	20. LIMITATION OF ABSTRACT
UNCLASSIFIED	UNCLASSIFIED	UNCLASSIFIED	UL

NSN 7540-01-280-5500

Standard Form 298 (Rev.2-89)
Prescribed by ANSI Std. 239-18
298-102

DTIC QUALITY INSPECTED 4

HYPERVELOCITY IMPACT

PROCEEDINGS OF THE 1998 SYMPOSIUM

Huntsville, Alabama, USA

17–19 November 1998

Guest Editor
CHARLES E. ANDERSON, JR

Published in two parts:
Part I comprises pages 1–518
Part II comprises pages 519–1024

PERGAMON

AIMS AND SCOPE

The *International Journal of Impact Engineering* exists for the publication of original research work concerned with the response of structures and bodies to dynamic loads arising from exposure to blast, collision or other impact events. The topics encompassed by the journal include the elastic and plastic response of structures and bodies to impact and blast loading, terminal ballistics, vehicle crashworthiness, containment and other processes and phenomena in which effects due to impact predominate, such as explosive welding. In addition, related matters such as research into fire hazards in association with impact loads will be included. Every paper accepted for publication is strictly refereed and assessed for its contribution to the understanding of impact phenomena or the insight gained for engineering design in areas of high rate loading.

Papers whose concerns are only in the fields of mathematics, materials science or computation are not requested. Similarly, papers whose contents are purely descriptive will not be accepted.

This journal should be of interest to engineers, designers and research workers in the fields of structural crashworthiness, energy-absorbing systems, structural failure, hazard assessments and safety calculations which involve impact loadings. Thus, papers in this journal will be of interest to aeronautical engineers, civil engineers, mechanical engineers, naval architects, nuclear engineers, ocean engineers, offshore engineers, transportation engineers and workers in other branches of engineering and science who are involved in impact loading of various kinds.

© 1999 Elsevier Science Ltd. All rights reserved.

This journal and the individual contributions contained in it are protected under copyright by Elsevier Science Ltd., and the following terms and conditions apply to their use:

Photocopying

Single photocopies of single articles may be made for personal use as allowed by national copyright laws. Permission of the publisher and payment of a fee is required for all other photocopying, including multiple or systematic copying, copying for advertising or promotional purposes, resale, and all forms of document delivery. Special rates are available for educational institutions that wish to make photocopies for non-profit educational classroom use.

Permissions may be sought directly from Elsevier Science Rights & Permissions Department, PO Box 800, Oxford OX5 IDX, UK; phone (+44) 1865 843830, fax: (+44) 1865 853333, e-mail: permissions@elsevier.co.uk. You may also contact Rights & Permissions directly through Elsevier's home page (http://www.elsevier.nl), selecting first 'Customer Support', then 'General Information', then 'Permissions Query Form'.

In the USA, users may clear permissions and make payments through the Copyright Clearance Center, Inc., 222 Rosewood Drive, Danvers, MA 01923, USA; phone: (978) 7508400, fax: (978) 7504744, and in the UK through the Copyright Licensing Agency Rapid Clearance Service (CLARCS), 90 Tottenham Court Road, London W1P 0LP, UK; phone: (+44) 171 631 5555; fax: (+44) 171 631 5500. Other countries may have a local reprographic rights agency for payments.

Derivative Works

Subscribers may reproduce tables of contents or prepare lists of articles including abstracts for internal circulation within their institutions. Permission of the publisher is required for resale or distribution outside the institution.

Permission of the publisher is required for all other derivative works, including compilations and translations.

Electronic Storage or Usage

Permission of the publisher is required to store or use electronically any material contained in this journal, including any article or part of an article.

Except as outlined above, no part of this publication may be reproduced, stored in a retrieval system or transmitted in any form or by any means, electronic, mechanical, photocopying, recording or otherwise, without prior written permission of the publisher.

Address permissions requests to: Elsevier Science Rights & Permissions Department, at the mail, fax and e-mail addresses noted above.

Notice

No responsibility is assumed by the publisher for any injury and/or damage to persons or property as a matter of products liability, negligence or otherwise, or from any use or operation of any methods, products, instructions or ideas contained in the material herein. Because of rapid advances in the medical sciences, in particular, independent verification of diagnoses and drug dosages should be made.

Although all advertising material is expected to conform to ethical (medical) standards, inclusion in this publication does not constitute a guarantee or endorsement of the quality or value of such product or of the claims made of it by its manufacturer.

♾ The paper used in this publication meets the requirements of ANSI/NISO Z39.48-1992 (Permanence of Paper).

PROCEEDINGS OF THE 1998 HYPERVELOCITY IMPACT SYMPOSIUM

Contents

N. Jones	ix	Editorial
C. E. Anderson, Jr. and W. P. Schonberg	xi	Preface
	xiii	HVIS 98 Symposium Chairmen
D. L. Orphal	xv	Tribute to Burton G. Cour-Palais
C. E. Anderson, Jr., J. S. Wilbeck and J. S. Elder	1	Long-rod penetration into highly oblique, water-filled targets
W. Arnold and F. K. Schäfer	13	Behind armor blast (BAB) caused by shaped charges
J. R. Asay, C. A. Hall, C. H. Konrad, W. M. Trott, G. A. Chandler, K. J. Fleming, K. G. Holland, L. C. Chhabildas, T. A. Mehlhorn, R. Vesey, T. G. Trucano, A. Hauer, R. Cauble and M. Foord	27	Use of *Z*-pinch sources for high-pressure equation-of-state studies
J. K. Baird and T. R. King	39	A Wien displacement law for impact radiation
O. S. Barnouin-Jha and P. H. Schultz	51	Interactions between an impact generated ejecta curtain and an atmosphere
G. V. Belov, E. P. Dyakin, S. A. Protasov, A. V. Petrushin and G. S. Smirnov	63	Penetration of compact steel projectiles into heterogeneous metal target of tied-wire fabric (TWF) type
S. R. Best and M. F. Rose	67	A plasma drag hypervelocity particle accelerator (HYPER)
S. J. Bless, S. Satapathy and M. J. Normandia	77	Transverse loads on a yawed projectile
R. Cauble, B. A. Remington and E. M. Campbell	87	Laboratory measurements of materials in extreme conditions: the use of high energy radiation sources for high pressure studies
L. C. Chhabildas, C. H. Konrad, D. A. Mosher, W. D. Reinhart, B. D. Duggins, T. G. Trucano, R. M. Summers and J. S. Peery	101	A methodology to validate 3D arbitrary Lagrangian Eulerian codes with applications to ALEGRA

E. L. Christiansen, B. G. Cour-Palais and L. J. Friesen	113	Extravehicular activity suit penetration resistance
E. L. Christiansen, J. H. Kerr, H. M. De La Fuente and W. C. Schneider	125	Flexible and deployable meteoroid/debris shielding for spacecraft
B. G. Cour-Palais	137	A career in applied physics: Apollo through space station
D. A. Crawford and P. H. Schultz	169	Electromagnetic properties of impact-generated plasma, vapor and debris
R. Destefanis, M. Faraud and M. Trucchi	181	Columbus debris shielding experiments and ballistic limit curves
D. L. Dickinson and L. T. Wilson	193	The impact of long rods into spaced-plate arrays
O. B. Drennov	205	About the state of two-metal contact boundary at a high-velocity oblique impact
B. D. Dvorak	215	Hypervelocity impact testing of the pressurized mating adapters for the international space station
H. J. Evans and J. Williamsen	225	Effects of uncertainty in hypervelocity impact performance equations and other parameters on variance in spacecraft vulnerability predictions
E. P. Fahrenthold and B. A. Horban	237	A hybrid particle-finite element method for hypervelocity impact simulation
M. Faraud, R. Destefanis, D. Palmieri and M. Marchetti	249	SPH simulations of debris impacts using two different computer codes
M. D. Furnish, L. C. Chhabildas and W. D. Reinhart	261	Time-resolved particle velocity measurements at impact velocities of 10 km/s
A. Geille	271	Numerical modeling of damage in various types of hypervelocity experiments
M. F. Gogulya, A. Yu. Dolgoborodov and M. A. Brazhnikov	283	Investigation of shock and detonation waves by optical pyrometry
F. I. Grace	295	Ballistic limit velocity for long rods from ordnance velocity through hypervelocity impact
D. Grady	307	Impact failure and fragmentation properties of tungsten carbide
G. A. Graham, A. T. Kearsley, M. M. Grady, I. P. Wright, M. K. Herbert and J. A. M. McDonnell	319	Natural and simulated hypervelocity impacts into solar cells

J. A. Grant	331	Evaluating the evolution of process specific degradation signatures around impact craters
C. A. Hall, L. C. Chhabildas and W. D. Reinhart	341	Shock Hugoniot and release in concrete with different aggregate sizes from 3 to 23 GPa
S. L. Hancock	353	Jet penetration for a class of cumulative mass profiles
C. J. Hayhurst, S. J. Hiermaier, R. A. Clegg, W. Riedel and M. Lambert	365	Development of material models for Nextel and Kevlar-epoxy for high pressures and strain rates
M. K. Herbert	377	Characterisation of rear incident hypervelocity impact phenomena on Hubble Space Telescope solar arrays
S. Hiermaier and F. Schäfer	391	Hypervelocity impact fragment clouds in high pressure gas numerical and experimental investigations
G. Jyoti, S. C. Gupta, T. J. Ahrens, D. Kossakovski and J. L. Beauchamp	401	Mass spectrometer calibration of high velocity impact ionization based cosmic dust analyzer
D. H. Kalantar, B. A. Remington, E. A. Chandler, J. D. Colvin, D. M. Gold, K. O. Mikaelain, S. V. Weber, L. G. Wiley, J. S. Wark, A. A. Hauer and M. A. Meyers	409	High pressure solid state experiments on the Nova laser
G. I. Kanel, J. R. Asay, K. Baumung, H. Bluhm, L. C. Chhabildas, V. E. Fortov, B. Goel, P. Hoppé, T. Mehlhorn, S. V. Razorenov, D. Rusch and A. V. Utkin	421	Applications of the ion beam technique for investigations of hypervelocity impacts
V. V. Kartuzov, B. A. Galanov and S. M. Ivanov	431	Concept of ultimate fracture velocity in the analysis of spherical cavity expansion in brittle materials: application to penetration problems
M. Katayama, A. Takeba, S. Toda and S. Kibe	443	Analysis of jet formation and penetration by conical shaped charge with the inhibitor
T. King and J. Shively	455	Shock-data constraints on interatomic potentials for condensed matter
A. A. Kozhushko, D. L. Orphal, A. B. Sinani and R. R. Franzen	467	Possible detection of failure wave velocity using hypervelocity penetration experiments
A. M. Krivtsov	477	Relation between spall strength and meso-particle velocity dispersion

G. R. Kruse, W. R. Mendes, W. J. Sommers, R. A. Weed, K. D. Nash and D. V. Mayo	489	Testing and simulation of microdebris from impacts with complex targets
P. V. Kryukov	501	Review of investigations under way on the large-scale TsNIIMASH ballistic facility
E. Lach, G. Koerber, M. Scharf and A. Bohmann	509	Comparison of nitrogen alloyed austenitic steels and high strength armor steels impacted at high velocity
C. G. Lamontage, G. N. Manuelpillai, E. A. Taylor and R. C. Tennyson	519	Normal and oblique hypervelocity impacts on carbon fibre/PEEK composites
J.-F. Legendre, M. Giraud and M. Henner	533	Ram-accelerator: a new hypervelocity launcher for ballistic studies
D. L. Littlefield, R. M. Garcia and S. J. Bless	547	The effect of offset on the performance of segmented penetrators
D. J. Liquornik, F. W. Yang, M. C. Zwiener and R. A. Hayami	561	Active attitude control of gun launched projectiles
N. J. Lynch	573	Constant kinetic energy impacts of scale size KE projectiles at ordnance and hypervelocity
M. Mayseless and R. Genussov	585	Jet penetration into low density targets
J. A. M. McDonnell	597	HVI phenomena: applications to space missions
M. R. McHenry, Y. Choo and D. L. Orphal	621	Numerical simulations of low L/D rod aluminum into aluminum impacts compared to the Tate cratering model
Yu. V. Milman and S. I. Chugunova	629	Mechanical properties, indentation and dynamic yield stress of ceramic targets
P. E. Nebolsine, N. D. Humer, N. F. Harmon and J. R. Baker	639	Statistical analysis of NRL 1964–1969 hypervelocity rod-plate impact data and comparison to recent data
I. V. Nemtchinov, V. V. Shuvalov, N. A. Artemieva, I. B. Kosarev and I. A. Trubetskaya	651	Expansion, radiation and condensation of vapor cloud, created by high-velocity impact onto a target in vacuum
M. J. Normandia	663	Eroded length model for yawed penetrators impacting finite thickness targets at normal and oblique incidence
M. J. Normandia and M. Lee	675	Penetration performance of multiple segmented rods at 2.6 km/s

D. L. Orphal	687	Highly oblique impact and penetration of thin targets by steel spheres
D. L. Orphal and C. E. Anderson, Jr.	699	Streamline reversal in hypervelocity penetration
A. J. Piekutowski	711	Holes produced in thin aluminum sheets by the hypervelocity impact of aluminum spheres
A. J. Piekutowski, M. J. Forrestal, K. L. Poormon and T. L. Warren	723	Penetration of 6061–T6511 aluminum targets by ogive-nose steel projectiles with striking velocities between 0.5 and 3.0 km/s
R. J. Rabb and E. P. Fahrenthold	735	Numerical simulation of oblique impact on orbital debris shielding
A. V. Radchenko, S. V. Kobenko, I. N. Marzenyuk, I. E. Khorev, G. I. Kanel and V. E. Fortov	745	Research on features of behaviour of isotropic and anisotropic materials under impact
M. N. Raftenberg and C. D. Krause	757	Metallographic observations of armor steel specimens from plates perforated by shaped charge jets
J. E. Reaugh, A. C. Holt, M. L. Wilkins, B. J. Cunningham, B. L. Hord and A. S. Kusubov	771	Impact studies of five ceramic materials and pyrex
J. H. Robinson	783	Orbital debris impact damage to reusable launch vehicles
Z. Rosenberg and E. Dekel	795	On the interaction between shaped charge jets and confined explosives at normal incidence
S. D. Rothman, A. M. Evans, R. T. Eagleton and L. B. Pearson	803	Material properties experiments using the AWE high power laser, HELEN
R. Roybal, P. Tlomak, C. Stein and H. Stokes	811	Simulated space debris impact experiments on toughened laminated thin solar cell cover glass
W. P. Schonberg and A. R. Ebrahim	823	Modelling oblique hypervelocity impact phenomena using elementary shock physics
W. P. Schonberg and E. Mohamed	835	Analytical hole diameter and crack length models for multi-wall systems under hypervelocity projectile impact
V. V. Shuvalov, N. A. Artem'Eva and I. B. Kosarev	847	3D hydrodynamic code SOVA for multimaterial flows, application to Shoemaker-Levy 9 Comet impact problem
V. V. Silvestrov, A. V. Plastinin, V. V. Pai and I. V. Yakovlev	859	An investigation of ceramic/aluminium composites as shields for hypervelocity impacts

L. L. Smalley and J. K. Woosley	869	Application of steady state maximum entropy methods to high kinetic energy impacts on ceramic targets
E. A. Taylor, M. K. Herbert, B. A. M. Vaughan and J. A. M. McDonnell	883	Hypervelocity impact on carbon fibre reinforced plastic/aluminium honeycomb: comparison with Whipple bumper shields
E. A. Taylor, K. Tsembelis, C. J. Hayhurst, L. Kay and M. J. Burchell	895	Hydrocode modelling of hypervelocity impact on brittle materials: depth of penetration and conchoidal diameter
I. Y. Telitchev, F. K. Schäfer, E. E. Schneider and M. Lambert	905	Analysis of the fracture of gas-filled pressure vessels under hypervelocity impact
A. V. Teterev	921	Cratering model of asteroid and comet impact on a planetary surface
R. E. Tokheim, D. R. Curran, L. Seaman, T. Cooper, A. T. Anderson, A. K. Burnham, J. M. Scott, J. Latkowski and D. Schirmann	933	Hypervelocity shrapnel damage assessment in the NIF target chamber
R. Vignjevic and J. Campbell	945	A penalty approach for contact in smoothed particle hydrodynamics
J. D. Walker	957	A model for penetration by very low aspect ratio projectiles
J. D. Yatteau, G. W. Recht and K. T. Edquist	967	Transverse loading and response of long rod penetrators during high velocity plate perforation
C. Yu, Y. Tong, C. Yang, F. Li, Y. Gui, M. Zhang, B. Wang, P. Xie and L. Li	981	Applied research of shaped charge technology
N. Zhou	989	A simple analysis model for the hypervelocity cratering of semi-infinite targets by projectile
E. L. Zilberbrand, A. S. Vlasov, J. U. Cazamias, S. J. Bless and A. A. Kozhushko	995	Failure wave effects in hypervelocity penetration
	1003	Attendees—HVIS Symposium
	1009	Author Index
	1013	Subject Index

PERGAMON

International Journal of Impact Engineering 23 (1999) ix

INTERNATIONAL JOURNAL OF IMPACT ENGINEERING

www.elsevier.com/locate/ijimpeng

EDITORIAL

This special issue of the International Journal of Impact Engineering contains the proceedings of the 1998 Hypervelocity Impact Symposium, which was held in Huntsville, Alabama, 17 - 19 October 1998.

I wish to take this opportunity to thank Charles E Anderson Jr for his considerable assistance in preparing this special issue of the International Journal of Impact Engineering. Many thanks are also due to the Organising Coimmittee of the Hypervelocity Impact Symposium

The proceedings of the 1986, 1989, 1992, 1994 and 1996 Hypervelocity Impact Symposia were also published as special issues of the International Journal of Impact Engineeering (Volume 5, Nos 1 - 4, Volume 10, Nos 1 - 4, Volume 14, Nos 1 - 4,Volume 17, Nos 1 - 6 and Volume 20, Nos 1 - 10). The next Hypervelocity Impact Symposium will be held in Galveston, Texas, USA, during 6 - 9 November 2000. Further announcements will be published in this journal as they become available.

Norman Jones

Editor-in-Chief

0734-743X/99/$ - see front matter © 1999 Elsevier Science Ltd. All rights reserved.
PII: S0734-743X(99)00159-1

PERGAMON International Journal of Impact Engineering 23 (1999) xi–xii

INTERNATIONAL JOURNAL OF IMPACT ENGINEERING

www.elsevier.com/locate/ijimpeng

PREFACE

This volume contains the papers presented at the *1998 Hypervelocity Impact Symposium* (*HVIS 98*) held in Huntsville, Alabama, on November 17-19, 1998. This was the sixth symposium since the re-initiation of the symposia in 1986, and the proceedings for the 1986, 1989, 1992, 1994, and 1996 *HVIS* are published as Volumes 5, 10, 14, 17, and 20, respectively, of the *International Journal of Impact Engineering*. The 85 papers in this volume address advancements in the basic understanding of hypervelocity impact physics, related phenomenology, and engineering applications.

Each paper in this volume has undergone peer review by experts in their respective fields of research. The authors are to be commended for keeping to the schedule for providing their draft manuscripts for review, making appropriate modifications and corrections, and preparing the final manuscript.

A listing of the various chairmen for *HVIS 98* is given on the following page; their time and dedication greatly assisted in making the symposium a technical success. A special note of thanks to Dr. William Schonberg, the Symposium Chair, and his Technical Co-Chairs, Drs. James Wilbeck and Joel Williamsen. These gentlemen worked tirelessly to ensure a technical and social program of distinction.

There were four special plenary presentations of distinction at this symposium. These were the Distinguished Scientist Award Keynote Presentation by the 1998 award recipient, Mr. Hallock (Hal) Swift, President of Physics Applications, Inc. Hal received the Distinguished Scientist Award for his sustained leadership, innovation, and technical excellence in hypervelocity research. Mr. Swift's paper should appear in the proceedings of the next *Hypervelocity Impact Symposium*. Mr. Dennis Orphal, President of International Research Associates, gave a plenary talk entitled "Effects of Strength on the Hydrodynamic Approximation," based on a paper by C. E. Anderson, Jr., D. L. Orphal, R. R. Franzen, and J. D. Walker, *Int. J. Impact Engng.*, **22**(1), 23-43, 1999. Robert C. Cauble, at the Lawrence Livermore National Laboratory, presented "Laboratory Measurements of Materials in Extreme Conditions: The Use of High Energy Lasers for High Pressure Studies." This presentation reviewed some of the work conducted at the NOVA facility, and provided a preview of the planned capabilities of the National Ignition Facility (NIF). Dr. Cauble's presentation starts on page 87 of this volume. Professor J. A. M. (Tony) McDonnell, from the University of Kent at Canterbury, gave the plenary presentation "Building a Bridge Between Microscale and Macroscale Hypervelocity Impact Phenomena with Applications to Space Design." Dr. McDonnell's presentation is contained in this volume, starting on page 597.

We are indebted to Ms. Janet Banda who worked diligently with us to assemble this volume. She has carefully reviewed formatting of the manuscripts, contacted authors where required to ensure consistency of the format, made minor corrections, and cleaned up smudges, etc.

On a sad note, several individuals who have played a major role in hypervelocity impact research and related areas passed away between the 1996 and 1998 symposia. Andrew (Andy) E. Williams (Naval Research Laboratory), who made substantial contributions in hypervelocity research using the two-stage light-gas guns at the Naval Research Laboratory, died suddenly of a heart attack in September 1997. Andy was 57. Some of Andy's work is documented in six articles in the 1986,

0734-743X/99/$ - see front matter © 1999 Published by Elsevier Science Ltd. All rights reserved.
PII: S0734-743X(99)00160-8

1992, and 1994 symposia proceedings. Daniel (Dan) J. Steinberg (retired from Lawrence Livermore National Laboratory) died in March 1997, at age 62, approximately a year and a half after diagnosed with pancreatic cancer. Although active in many areas, Dan was internationally known for his contributions to high-pressure, high-rate numerical constitutive modeling. A summary of the Steinberg-Guinan model is in *IJIE*, **5**, 603-611, 1997. Mr. Neil Blaylock (Southwest Research Institute) died in a freak automobile accident in October 1998, at age 52. Neil played a key role in the planning and organization of the *1986* and *1989 Hypervelocity Impact Symposia.* Neil helped in establishing the Constitution and By-Laws for the *Hypervelocity Impact Society*, and in the incorporation of the *Society* in October 1988. As these proceedings were being assembled, Dr. Alexander (Alex) C. Charters, the recipient of the first Distinguished Scientist Award from the *Hypervelocity Impact Society*, died after a short illness, May 1999. Up to his death at age 82, Alex remained vigorous and active, playing tennis almost daily. Alex's Distinguished Scientist keynote presentation is published in *IJIE*, **17**, 151-182, 1995. Alex also had articles in Volumes 5 and 10 of *Impact Engineering*. Andy, Dan, Neil, and Alex—we will all miss you, but are extremely grateful for your friendship and accomplishments.

We are deeply appreciative of Professor Norman Jones, the Editor-in-Chief of the *International Journal of Impact Engineering*, and his assistance in bringing these proceedings to publication. We also thank Mr. Ian Salusbury, Publishing Editor of Engineering and Technology for Elsevier Science, for his support and attention to details. Plans are to continue the Hypervelocity Impact Symposia, and we hope that the proceedings of future symposia can also become part of the archival literature.

HVIS 98 was supported by the generous contributions of the following organizations: Alabama Space Grant Consortium, Army Research Laboratory, Army Research Office, Ernst-Mach-Institut, European Research Office, Lawrence Livermore National Laboratory, NASA/Marshall Space Flight Center, Sandia National Laboratories, University of Alabama at Huntsville, and US Army Aviation and Missile Command. The views, opinions, and/or finds contained in this volume are those of the authors and should not be construed as an official Department of the Army or Department of Energy position, policy, or decision, unless so designated by other documentation.

Charles E. Anderson, Jr.
William P. Schonberg
July 1999

PERGAMON International Journal of Impact Engineering 23 (1999) xiii

INTERNATIONAL JOURNAL OF IMPACT ENGINEERING

www.elsevier.com/locate/ijimpeng

HVIS 98 SYMPOSIUM CHAIRMEN

ORGANIZING COMMITTEE

Lalit C. Chhabildas
Sandia National Laboratories

Andrew J. Piekutowski
University of Dayton Research Institute

William P. Schonberg
University of Alabama in Huntsville

Charles E. Anderson, Jr.
Southwest Research Institute

Jeanne L. Crews
NASA/Johnson Space Center

Dennis Grady
Applied Research Associates

Alois J. Stilp
Ernst-Mach-Institute

SYMPOSIUM CHAIRMAN

William P. Schonberg
University of Alabama in Huntsville

TECHNICAL CHAIRMEN

James S. Wilbeck
ITT Systems Corporation

Joel E. Williamsen
University of Denver Research Institute

Publications Editor
Charles E. Anderson, Jr.
Southwest Research Institute

Awards Committee Chairman
Jeanne L. Crews
NASA/Johnson Space Center

Educational Outreach
Gordon R. Johnson

Exhibition Co-Chairmen

Lanny P. Bell
AEDC/Sverdrup Technology, Inc.

Justin H. Kerr
NASA/Johnson Space Center

SESSION CHAIRMEN

Hypervelocity Impact Phenomenology
Hallock A. Swift
Physics Applications, Inc.

Alois J. Stilp
Ernst-Mach-Institute (ret.)

Penetration Mechanics
Scott A. Mullin
Southwest Research Institute

Bert Peskes
TNO-Prins Maurits Laboratory

Analytical Techniques
William A. Gooch
U.S. Army Research Laboratory

James D. Walker
Southwest Research Institute

Pulsed Power
James R. Asay
Sandia National Laboratories

Peter Thompson
Atomic Weapons Establishment

Experimental Techniques
Michelle Rucker
NASA/White Sands Test Facility

Don Berry
Institute for Advanced Technology

Shielding
Roberto Destefanis
Alenia Aerospazio

Eric P. Fahrenthold
University of Texas at Austin

SESSION CHAIRMEN (Cont'd)

Material Response
Leonard T. Wilson
Naval Surface Warfare Center

Tim Holmquist
Network Computing Services, Inc.

Planetary Impacts
David A. Crawford
Sandia National Laboratories

Olivier Barnouin-Jha
Johns Hopkins University

Fracture and Fragmentation
Dennis E. Grady
Applied Research Associates, Inc.

Donald R. Curran
SRI International

Numerical Modelling
Klaus Thoma
Ernst-Mach-Institut

Eugene S. Hertel, Jr.
Sandia National Laboratories

Spacecraft Studies
Jennifer Robinson
NASA/Marshall Space Flight Center

Kim Luu
U.S. Air Force Research Laboratory

Special Applications
Randolph S. Coates
U.S. Army Research Laboratory

James Pearson
U.S. Army ARDEC

Glenn W. Pomykal
Lawrence Livermore National Laboratory

0734-743X/99/$ - see front matter © 1999 Published by Elsevier Science Ltd. All rights reserved.

PERGAMON

International Journal of Impact Engineering 23 (1999) xv–xvi

INTERNATIONAL JOURNAL OF IMPACT ENGINEERING

www.elsevier.com/locate/ijimpeng

TRIBUTE TO BURTON G. COUR-PALAIS

DENNIS L. ORPHAL

International Research Associates, Inc., 4450 Black Ave, Suite E., Pleasanton, CA 94566

Editor's Note: The following was used to introduce Burton (Burt) Cour-Palais at the 1996 Hypervelocity Impact Symposium, held in Freiburg, Germany, 8-10 October 1996.

The Hypervelocity Impact Society is honored to present its Distinguished Scientist Award to Burton G. Cour-Palais.

All those familiar with the progressive development of spacecraft shielding against meteor and debris impact are well aware of Burt's work. For more than 30 years, beginning with Apollo, Burt has been at the forefront of designing meteor and debris protection systems. He was responsible for meteoroid environment definition and shielding design for the Apollo Command and Service Module as well as the Lunar module during the conceptual design phase. As part of this effort he laid the initial groundwork for meteoroid protection reliability calculations. He was ultimately responsible for specifying the meteor shielding requirements for the Apollo spacecraft and the astronaut's space suit.

Following Apollo, Burt continued to lead research to better define the meteor and debris threat environment, and to improve the effectiveness of shielding. As part of this effort, he analyzed data on impacts against the Apollo Command Module window as well as conducted a long series of fundamental hypervelocity impact experiments using two-stage light-gas guns.

A result of all this effort is a continually evolving set of engineering design equations for spacecraft meteor and debris shields. Burt developed the methodology, including the general form of the equations, over 30 years ago, and they are still in use today. He and others have continued to update the equations for new materials and alternative designs, based on that pioneering work. These equations are used worldwide for shield design.

Burt has played a leading role in the development of advanced concepts for spacecraft protection. Most recently he has been instrumental in conceiving and developing advanced, multi-material shields based on the concept of multi-shock effects on impacting meteors and debris. Tests and analyses of these concepts have led to engineering design equations and more effective shielding for Space Station Freedom. Burt and Jeanne Crews received a patent in 1992 for the multi-shock shield concept.

Burt was born a British citizen in India in 1925. He received his B. S. in mathematics, physics, and chemistry at St. Xavier College in Calcutta in 1945. He pursued post-graduate studies at both the College of Aeronautical Engineering in London and at the University of Houston at Clear Lake. He worked in England at Vickers-Armstrong and Bristol Aircraft from 1947 to 1957. He then went to Avro Aircraft in Canada until joining NASA in 1960. Burt became a U. S. citizen in 1966.

0734-743X/99/$ - see front matter © 1999 Elsevier Science Ltd. All rights reserved.
PII: S0734-743X(99)00161-X

Over the years Burt has published a very large number of papers and NASA reports. It is probably fair to say that if one wanted to get up to speed on meteor and debris shielding, both it's history and the current state of the art, one should start by going to "Burt's literature". Burt has received many awards for his work at NASA. These include the Superior Achievement Award in 1969 and Superior Performance Awards in 1976, 1980. Burt received NASA's Sustained Superior Performance Award in 1988. In addition, Burt's research group received 13 Group Achievement Awards, beginning in 1966.

For a lifetime of superior achievement, innovation, and contribution to the discipline of meteor and debris shielding of spacecraft, and his continuing contributions to the science of hypervelocity impact in general, the *Hypervelocity Impact Society* is pleased to present the 1996 HVIS Distinguished Scientist Award to Burton G. Cour-Palais.

Editor's Note: Mr. Cour-Palais' Distinguished Scientist keynote presentation begins on page 137 of this volume.

PERGAMON

International Journal of Impact Engineering 23 (1999) 519–532

INTERNATIONAL JOURNAL OF IMPACT ENGINEERING

www.elsevier.com/locate/ijimpeng

NORMAL AND OBLIQUE HYPERVELOCITY IMPACTS ON CARBON FIBRE/PEEK COMPOSITES

CHANTEL G. LAMONTAGE*, GERALD N. MANUELPILLAI*, EMMA A. TAYLOR, and RODERICK C. TENNYSON***

* University of Toronto Institute for Aerospace Studies, 4925 Dufferin Street, Downsview, Ontario, Canada, M3H 5T6; ** Unit for Space Sciences and Astrophysics, School of Physical Sciences, University of Kent at Canterbury, Canterbury, Kent, CT2 7NR, U.K.

Summary—A series of normal and oblique hypervelocity impact tests were performed on carbon fibre/PEEK composite specimens using the Light Gas Gun facilities at the University of Kent at Canterbury. The tests were conducted on 16 ply and 24 ply targets, using 1 mm and 2 mm aluminum projectiles, at velocities of approximately 5 km/s, and at impact angles of 0, 30 and 45 degrees. The primary objective of this investigation was to add oblique impact data to the University of Toronto Institute for Aerospace Studies (UTIAS) database on hypervelocity impact damage to composites. The parameters investigated in this study were debris cloud (primary and secondary) dispersion cone angles, (equivalent) entry and exit crater diameters, and front and rear surface delamination damage zones. The results of the analysis showed that the cone angles were not symmetric about the projectile velocity vector, maxima for both angles occurring at a normalized energy of approximately 55 J, followed by an asymptotic decrease. The results obtained for the entry crater diameter and equivalent entry damage diameter were found to be in good agreement with the existing UTIAS database. For a given impact energy, the damage area in the 24 ply targets was found to be nearly twice that of the damage in the 16 ply targets. Results were found to be in good agreement when compared, using an empirical equation, to predictions of impact damage of Al projectiles on aluminum targets (when a scaling factor of 0.9 was applied to the PEEK data to account for the greater damage in composites). © 1999 Elsevier Science Ltd. All rights reserved.

NOTATION

A	= Area (mm^2)
D_p	= projectile diameter (mm)
D_c	= crater diameter (mm)
E	= impact energy (J)
t	= target thickness (mm)
V	= impact velocity (km/s)
α	= primary damage cone angle (deg)
β	= secondary damage cone angle (deg)
ϵ	= turning angle (deg)
θ_i	= impact angle (deg)

INTRODUCTION

In the design of spacecraft structures and components, polymer matrix composites offer significant advantages over metals due to their high specific strength, high stiffness and low coefficient of thermal expansion. Carbon fibre/PEEK (PolyEtherEtherKetone) composite is the material of choice for the structural components of the Space Station Remote Manipulator System

0734-743X/99/$ - see front matter © 1999 Elsevier Science Ltd. All rights reserved.
PII: S0734-743X(99)00101-3

(SSRMS). The SSRMS is being built by Spar Aerospace Ltd. and is Canada's contribution to the International Space Station. The SSRMS is constructed from four long composite booms, each approximately 4 meters in length and 33 cm in diameter. The booms are made of 19-ply (2.7 mm) IM7/PEEK lamina, which is produced by Fiberite Inc.

In low earth orbit, the SSRMS will be exposed to impacts from micrometeoroids and orbital debris with velocities typically ranging from 5 to 20 km/s. To improve the survivability of the SSRMS, the potential damage caused by micrometeoroid and orbital debris impacts must be assessed, by means of ground-based testing, so that enhanced protection schemes can be considered if necessary.

Unlike ductile materials, which have been extensively tested since the 1960s, relatively few hypervelocity impact (HVI) studies have been conducted on composites [1-3]. Since 1991, the University of Toronto Institute for Aerospace Studies (UTIAS) has been compiling an extensive database of hypervelocity impacts on composites [4-8], with the aim of creating comprehensive damage models for characterization of HVI damage to composites. A recent UTIAS impact study on the 33 cm circular SSRMS boom [9-12] has shown that a large, high energy ejecta cloud forms behind the impact site which impinges on the inside rear wall and significantly degrades the structural integrity of the SSRMS. In addition, it was shown that the debris cloud could seriously damage any wiring or components housed within the boom. The extent of the damage to the rear or inside wall can be characterized by studying the spread of the debris cloud, defined by the cone angle. The dependence of the debris cloud cone angle on the impact angle for PEEK is an unknown factor; all 143 hypervelocity impact tests in the database existing prior to this study were for normal incidence impacts only.

Another characteristic of impacts on composites is the surface delamination zones caused by the peeling of surface plies surrounding the impact and exit craters, due to the reflection of stress waves from the front and back free surfaces. This in turn causes tensile forces between the plies, leading to inter-ply delamination and spall. Characterization of these delamination zones is important even if the structural strength of the composite is not significantly affected by surface damage. This is due to the fact that composites employed in the space environment are vulnerable to erosion by atomic oxygen [13,14] and therefore may have protective coatings, which can be compromised by hypervelocity impact damage. Surface delamination in composites creates a larger damage zone, stripping off the protective coating along with the surface ply, whereas the damage caused by just an impact crater (as would happen in metals), while still compromising the coating, is limited to the dimensions of the hole itself.

The motivation for the current study is to garner oblique incidence hypervelocity impact data on PEEK and to extend the existing UTIAS HVI composite damage database. Even though most meteoroid and orbital debris impacts will be at angles between 30 and 50 degrees to the surface normal, most existing hypervelocity impact data relate to normal impacts. To this end, hypervelocity impact tests were performed on a series of carbon fibre/PEEK composite plates at impact angles of 0, 30 and 45 degrees. The tests were carried out using the Light Gas Gun (LGG) facilities at the University of Kent at Canterbury. This database can then be used to ultimately improve the design of the SSRMS with a view to enhancing its HVI survivability.

EXPERIMENTAL PROGRAMME

The hypervelocity impact tests were performed on a series of nominally 10 cm square 16 ply (1.8 mm) and 24 ply (2.6 mm) AS4 carbon fibre/PEEK (61% fibre volume) composite targets, with a laminate lay-up of $(0,\pm45,90)_s$. AS4 fibre-based prepreg (see Table 1) was used in the composite specimens instead of IM7 (due to the unavailability of IM7). The composite target specimens were cut from 12 inch square plates, manufactured in the hydraulic/thermal press of the Aerospace Materials Group at UTIAS.

Table 1. Physical Properties of APC-2 (PEEK)/AS-4 (Fibre) Composite

Mechanical properties	*0° Tensile*	*0° Compressive*	*90° Tensile*	*In-plane Shear*
Strength (MPa)	2070	1360	86	186
Modulus (GPa)	138	124	10.2	5.7
Failure strain (%)	1.45	-	0.88	-
Poisson's ratio	0.30	-	-	-

The average density of orbital debris less than 10 mm in diameter is approximately 2.8 g/cm^3 [15], therefore aluminum was used as the impactor in this investigation. Spherical Al-2017 projectiles, 1 mm and 2 mm in diameter, were accelerated at velocities ranging between 4.50-5.45 km/s to impact the target at incidence angles of 0, 30 and 45 degrees (measured from the surface normal). The ejecta damage was recorded by 1 mm thick Al-2024 witness plates, at a stand-off distance of 100 mm parallel to the rear surface of the targets. The target configuration and geometry are shown in Figure 1.

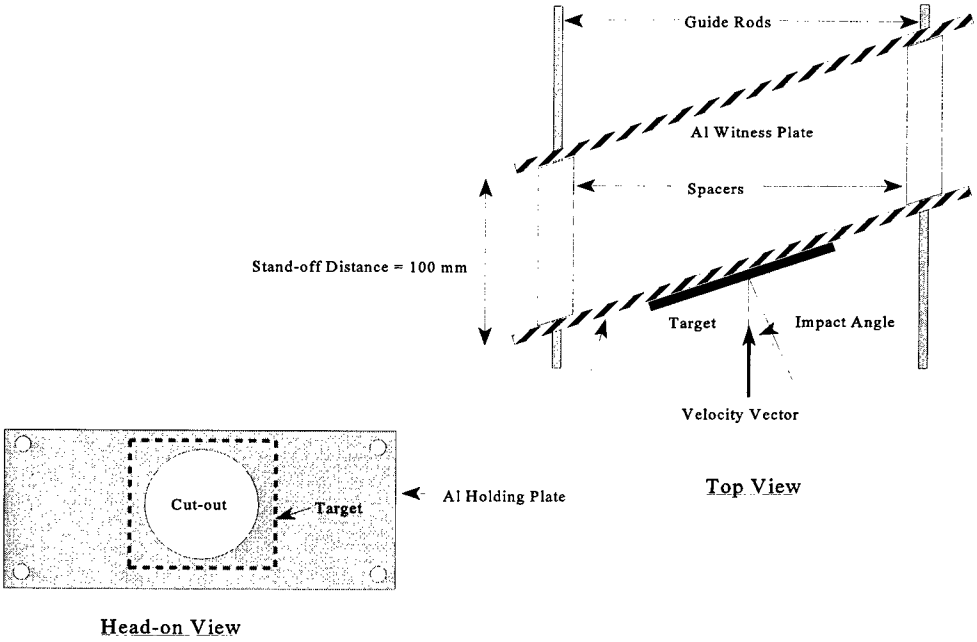

Figure 1. Target configuration and geometry

The target specimens were mounted in the test chamber by clamping them to an aluminum holder plate that contained a circular cutout, as shown in the head-on view in Figure 1. Rubber spacers on the guide rods were used to offset the target from the aluminum witness plate. Due to the size limitations of the test chamber, instead of angling the whole test fixture (including guide rods) with respect to the velocity vector, only the target and witness plates were angled. This was done by cutting rubber spacers at the appropriate oblique angle and mounting them on the guide rods, as seen in the top view of Figure 1. The tests were performed using the LGG facilities at the University of Kent at Canterbury, described in detail in Baron [16]. The complete test programme is summarized in Table 2.

Table 2. Hypervelocity impact test parameters

Shot ID	*Target ID*	*Number of plies*	*Thickness (mm)*	*Projectile diameter (mm)*	*Angle of impact (degrees)*	*Projectile velocity (km/s)*
16P001-1	0-1	16	1.68	1	0	5.01
16P301-15	30-15	16	1.72	1	30	5.17
16P451-18	45-18	16	1.86	1	45	5.19
16P002-11	0-11	16	1.83	2	0	4.66
16P302-16	30-16	16	1.75	2	30	4.79
16P452-8	45-8	16	1.81	2	45	4.82
24P301-20**	30-20	24	2.55	1	30	5.26
4P451-19**	45-19	24	2.46	1	45	5.39
24P002-10	0-10	24	2.52	2	0	4.51
24P302-6	30-6	24	2.68	2	3	4.55
24P452-9	45-9	24	2.63	2	45	4.88

** multiple impacts on target (from sabot or gun debris fragments)

The targets were first visually inspected to determine the characteristics of the impact crater. The impact areas on the front and rear surfaces of the composite plates, as well as the damage on the witness plates, were then photographed. Entry and rear (spall) delamination damage areas and equivalent crater diameters [$D_c = \sqrt{(4\text{Area}/\pi)}$] were obtained by digitizing the contours on these photographs and integrating over the surface. The debris cloud dispersion cone angles and the turning angles (see following section) were determined by measuring the extent of the damage areas directly off the witness plates, similar to Schonberg *et al.* [17] and Schonberg and Taylor [18].

RESULTS AND DATA ANALYSIS

Analysis of the debris cloud impacts on the witness plates showed two classes of impact damage, a primary damage area containing higher energy impact craters most likely caused by projectile fragments, and a secondary damage area consisting of a large number of fine craters and long carbon fibres embedded in the aluminum plate, similar to the debris characterization in Taylor *et al.* [19]. Photographs of the debris cloud damage on the aluminum witness plates for the 24 ply targets, impacted with a 2 mm projectile, at angles of 0, 30 and 45, are shown in Figure 2. Figures 3 and 4 illustrate the primary (α) and secondary (β) damage cone angles for typical 0 degree and 30 degree impact target configurations. The turning angle, ϵ, is defined as the angle between the initial projectile vector and the estimated center of mass of the primary damage - or the location where the highest energy impact(s) of the primary damage occur (i.e., where the projectile debris was deflected upon fragmentation). The cone angle and turning angle results are listed in Table 3.

Table 3. Debris cloud cone angle data from hypervelocity impacts

Target ID	*α (degrees)*	*β (degrees)*	*ϵ (degrees)*
0-1	19	59	-
30-15	-	67	-
45-18	-	58	-
0-11	33	69	0
30-16	43	75	2
45-8	54	85	10
0-10	37	66	0
30-6	35	71	1
45-9	53	75	12

For oblique incidence impacts, the debris cloud exiting from the rear of the target plate did not follow the line of flight of the projectile, as expected. As shown in Figures 2(b) and (c), both the primary and secondary cone angles are not symmetric about the projectile impact velocity vector. For normal incident impacts, angles γ and δ are approximately equal to half of α and β, respectively, due to symmetry. Figure 5 shows both cone angles, α and β, plotted against the impact angle, θ_i. For the 16 ply, 1 mm diameter oblique impacts, no evidence of primary debris was found on the witness plates. Figure 6 shows both cone angles plotted against normalized impact energy (impact velocity is multiplied by the cosine of the impact angle). Both angles exhibit a gradual rise, and then decline towards an asymptote, with a maximum occurring at a normalized energy of approximately 55 J. This is probably due to the higher energy imparted to the debris plume at higher impact energies, resulting in less debris scatter, causing much narrower damage cones. Figure 7 shows the turning angle (ϵ) versus impact angle. The turning angle seems independent of the thickness of the target, instead showing an exponential relationship with the impact angle, although more data is needed to further explore this phenomenon.

The damage to the target surface area was typical of hypervelocity impacts on a composite material. For all impacts, the entrance and exit craters were roughly circular, though frayed, and surrounded by large areas of surface delamination, with the peel direction oriented in the fibre direction in the surface laminae. The impact and exit craters for the 2 mm aluminum projectile onto the 24 ply targets at 0, 30 and 45 degrees are shown in Figure 8. The figure clearly reveals severe fracturing of the fibre and matrix materials in the vicinity of the crater.

The entry crater diameter was measured to be approximately 2.5 times larger than the projectile diameter, and was not found to be significantly affected by either the number of plies in the laminate (i.e., the thickness of the target) or the impact angle. This is clearly shown in the plot of entry crater diameter versus impact angle in Figure 9. Since the composite target plate is thin compared to the projectile diameter, the hole in the plate is most likely generated by the impact and the initial passage of the shock waves [1], regardless of the angle of impact. The results obtained for the entry crater diameter, as a function of both projectile diameter and the Christiansen energy parameter[1], $(E \cdot t/D_p)^{1/3}$ defined in [8,20], are in good agreement with the existing UTIAS database results. Figure 10 compares earlier UTIAS test results [9-12] with data from the current experimental programme as a function of the Christiansen parameter, using normalized impact energy. The normalized impact energy, E`, considers only the normal component of the impact velocity vector, and is given as:

$$E` = E \cdot \cos^2(\theta_i) \tag{1}$$

The complete front and rear (spall) surface ply delamination zones are shown in Figure 11 for the 2 mm projectile, impacting 24 ply targets at angles of 0, 30 and 45. As a first order approximation, a linear relationship can be inferred between the entry damage area and the normalized impact energy (see Figure 12). For a given impact energy, the damage area in the 24 ply targets was found to be nearly twice that of the damage in the 16 ply targets. Results were inconclusive in trying to obtain a relationship between spall damage and impact angle, target thickness and impact energy. This is possibly due to the manner in which the targets were clamped onto the aluminum holder plate. Since the composite target overlapped the edges of the circular cutout in the holder plate, the clamped edges prevented the delamination from propagating further. Furthermore, some targets were not large enough to capture the entire delamination area. Excellent agreement (regression results within 1%) was also obtained between the UKC data and previous UTIAS data for equivalent entry damage diameter as a function of the Christiansen energy parameter (see Figure 13).

[1]The Christiansen energy parameter was developed in the late 1980s, for analysis of HVI on composite Space Station truss tubes (since replaced by aluminum), and has been used in previous analyses of UTIAS HVI composites data.

An understanding of the hypervelocity impact cratering process (as a function of target thickness) can be gained by comparing the carbon fibre/PEEK impact data to that predicted by an empirically-determined hypervelocity impact damage equation. The previously published GMC equation [21] covers the full range of target thicknesses, from thin foils (projectile diameter/target thickness $D_p/t >> 1$) to semi-infinite targets ($D_p/t \sim 0.1$), and has been validated over a wide range of impact velocities. The crater diameter D_c in a composite target is larger than that predicted by the GMC equation for an equivalent thickness of aluminum. Figure 14 shows the GMC-derived crater diameter D_c, normalised by the target thickness, t, for impacts by spherical aluminum projectiles onto aluminum targets, at a velocity of 5 km/s. The carbon fibre/PEEK data, scaled to an equivalent thickness of aluminum, are also plotted. An arbitrary scaling factor was applied to the carbon fibre/PEEK data (k=0.9) in Figure 14; the data show good agreement with the 5 km/s GMC curve.

As the impact processes in composites and metals are different, such a simple scaling factor applied to the GMC equation can be used only to obtain a guideline to the target damage. The UTIAS database will be compared to the GMC equation to determine whether this scaling can be applied over a wide range of target thicknesses.

CONCLUSIONS

This investigation was successful in its primary objective of adding oblique hypervelocity impact data on PEEK composite plates to the UTIAS database. The primary and secondary cone angles were found to not be symmetric about the projectile velocity vector for oblique incidence impacts. The cone angles reach a maximum at a normalized energy of approximately 55 J, and then decrease asymptotically, most likely due to the higher energy imparted to the debris plume at higher impact energies which results in less debris scatter, causing much narrower damage cones.

The results obtained for the entry crater diameter, as a function of both projectile diameter and the Christiansen energy parameter (normalized with respect to impact angle), were found to be in good agreement with the existing UTIAS database. Excellent agreement (within 1%) was also obtained between the UTIAS database and the equivalent entry damage diameter as a function of the Christiansen parameter. For a given impact energy, the damage area in the 24 ply targets was found to be nearly twice that of the damage in the 16 ply targets. The entry crater diameter was not found to be significantly affected by either the number of plies in the laminate (i.e., the thickness of the target) or the impact angle.

The turning angle seems independent of the thickness of the target, although more data is needed to further explore this phenomenon. Results were also inconclusive in trying to obtain a relationship between spall damage and impact angle, target thickness, and impact energy. Spall results may have been affected by the limitations of the target chamber and test fixture.

The carbon fibre/PEEK data was compared, using the empirical GMC equation, to predictions of impact damage of Al projectiles on aluminum targets. Results were found to be in good agreement when compared to impacts at 5 km/s, when a scaling factor of 0.9 was applied to the PEEK data to account for the greater damage in composites.

Work is currently underway at UTIAS to determine a comprehensive hypervelocity impact damage model for PEEK composites. This includes experimental determination of the ballistic limit of PEEK, as well as ultrasonic scans (C-scan) of damaged composites to determine the extent of internal damage. Further tests are also planned to characterize the debris cloud variations in this composite with target thickness, angle of impact, projectile density and impact energy.

Acknowledgement—The authors are grateful to Professor J.A.M. McDonnell for access to the hypervelocity impact facilities of the University of Kent at Canterbury, and Mr. M. Cole for his assistance in the experiments. The authors would also like to acknowledge the assistance of Dr. W.D. Morison in the manufacturing of the composite specimens.

REFERENCES

1. Yew, Ching H., and Kendrick, Rodney B., "A study of damage in composite panels produced by hypervelocity impact", *Int. J. of Impact Engineering*, **5**, 729-738 (1987).
2. Cour-Palais, Burton G., "Hypervelocity impact in metals, glass and composites", *Int. J. of Impact Engineering*, **5**, 221-237 (1987).
3. Schonberg, William P., "Hypervelocity impact response of spaced composite material structures", *Int. J. of Impact Engineering*, **10**, 509-523 (1990).
4. Tennyson, R.C., "Debris and micrometeoroid impact damage on spacecraft materials and structures", Final report submitted to the Canadian Space Agency, March 31 (1994).
5. Yew, C.H., Yang, C.Y., Crews, J., "A phenomenological study of the effects of hypervelocity impacts on graphite-epoxy plates", The University of Texas at Austin (1986).
6. Grosch, D.J., "Impact testing of advanced metal matrix composites and reinforced plastic materials", Southwest Research Institute, June (1993).
7. Tullos, R.J., Mullin, S.A., Graef, R.C., "Evaluation of the response of advanced structural materials to hypervelocity impact", Technology Application Program Management (TAPM), Department of the Air Force, San Antonio Air Logistics Center, Kelly Air Force Base, Texas. Prepared under contract by the Southwest Research Institute (Report #: 06-1974-206), June (1993).
8. Christiansen, E.L., "Investigation of hypervelocity impact damage to space station truss tubes", Final report submitted by Eagle Engineering Inc. for NASA JSC, February (1988).
9. Tennyson, R.C., Shortliffe, G.D., "Hypervelocity impact tests on composite boom structures for space robot applications", *Canadian Aeronautics and Space Journal*, **43**(3), 195-202 (1997).
10. Friesen, L.J., "Initial hypervelocity impact tests of Canadian Space Agency Space Station Remote Manipulator System components", JSC 27256, September (1996).
11. Tennyson, R.C., Shortliffe, G.D., "A computer model for micrometeoroid and orbital debris damage assessment on spacecraft structures", *NATO Proc.* (1996).
12. Tennyson, R.C., Shortliffe, G.D., "Hypervelocity impact damage to composite structures", *Proc. of Conference on Composite Engineering*, South Africa, (1996).
13. De Groh, K.K., and Banks, B.A., "Atomic oxygen undercutting of LDEF aluminized-Kapton multi-layer insulation", *Proc. of LDEF - 69 Months in Space, 1st Post Retrieval Symp.*, NASA CP 3134, June (1991).
14. Tennyson, R.C., "Atomic oxygen and its effects on materials in space", **160**, *Progress in Astronautics and Aeronautics*, AIAA, Washington, DC (1993).
15. Kessler, Donald J., Reynolds, Robert C., Anz-Meador, Phillip D., "Orbital debris environment for spacecraft designed to operate in low Earth orbit", NASA TM-100471, September 1 (1988).
16. Baron, J. M., "Microparticle hypervelocity impacts on satellites in low Earth orbit", Ph.D. Thesis, University of Kent at Canterbury (1996).
17. Schonberg, W.P., Taylor, R.A., Horn, J.R., "An analysis of penetration and ricochet phenomena in oblique hypervelocity impact", NASA TM-100319, February (1988).
18. Schonberg, W.P., Taylor, R.A., "Penetration and ricochet phenomena in oblique hypervelocity impact", *AIAA Journal*, **27**(5), 639-646, May (1989).
19. Taylor, E.A., Herbert, M.K., Gardner, D.J., Kay, L., Thomson, R., Burchell, M.J., "Hypervelocity impact on carbon fibre reinforced plastic/aluminum honeycomb", *Proc. of the Institution of Mech. Engineers*, **211** (G), 355-363, (1997).
20. Christiansen, E.L., "Investigation of hypervelocity impact damage to space station truss tubes", *Int. J. of Impact Engineering*, **10**, (1990).
21. Gardner, D.J., McDonnell, J.A.M., Collier, I., "Hole growth characterisation for hypervelocity impacts in thin targets", *Int. J. of Impact Engineering*, **19**, 589-602, (1997).

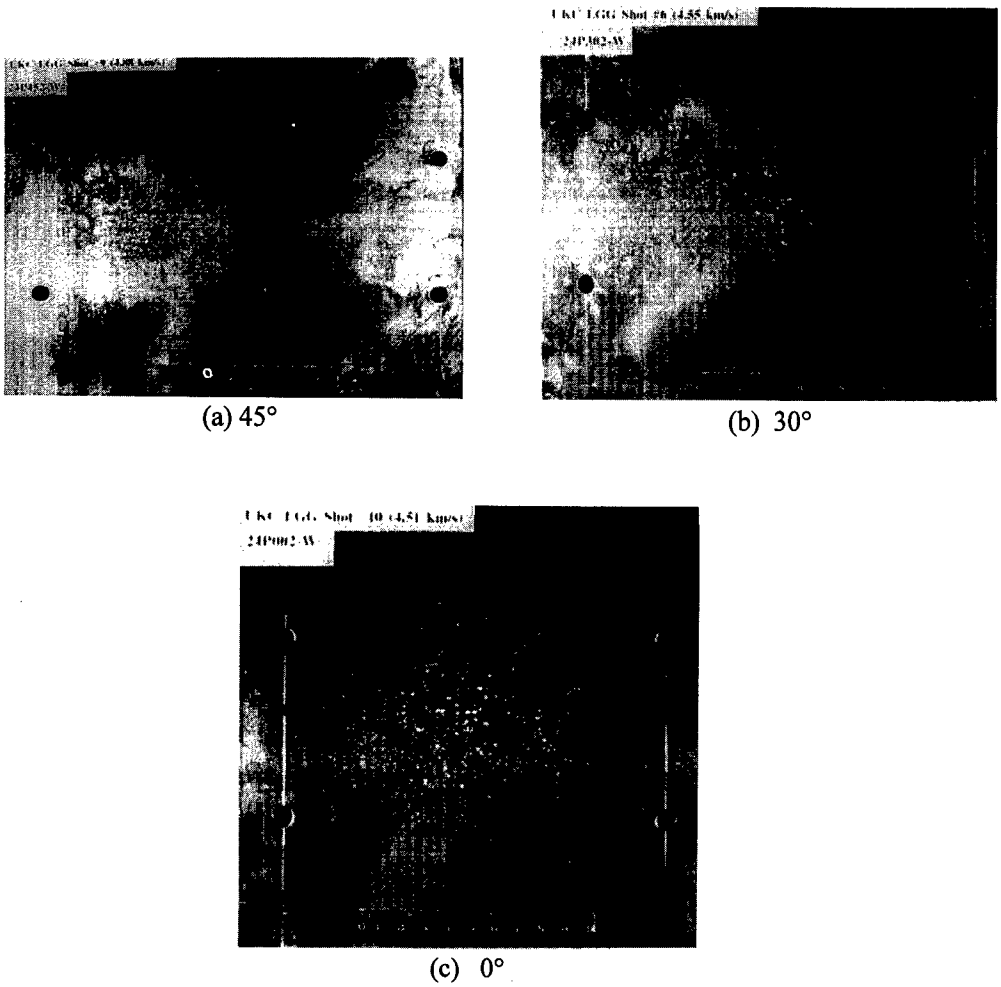

(a) 45° (b) 30°

(c) 0°

Figure 2. Witness plate debris cloud damage for 24 ply PEEK, 2mm Al projectile

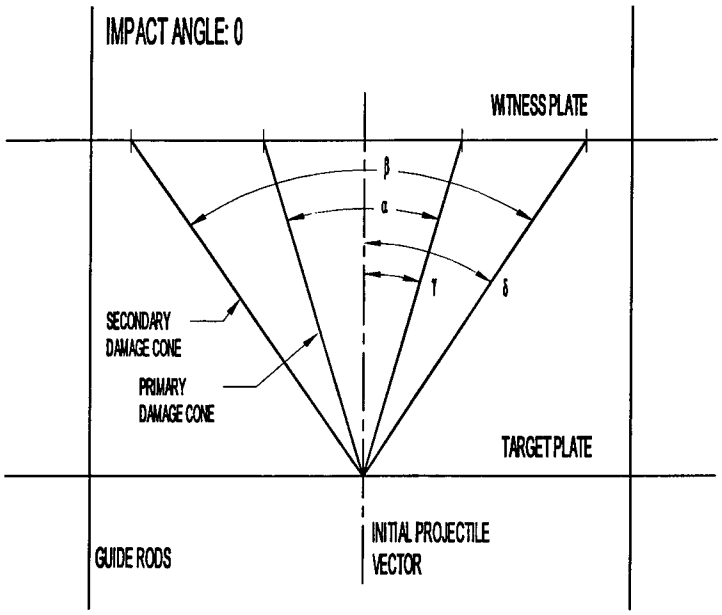

Figure 3. Damage cones for 0 degree target configuration

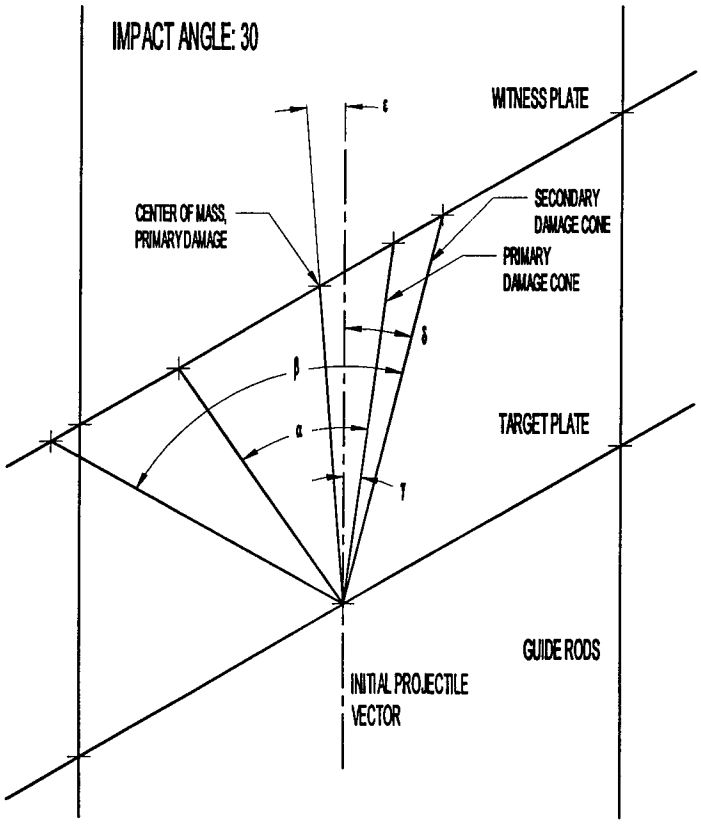

Figure 4. Damage cones for 30 degree target configuration

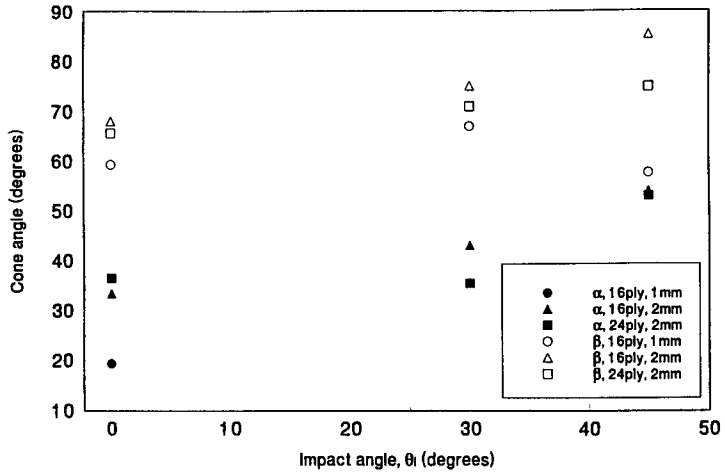

Figure 5. Cone angles vs impact angle

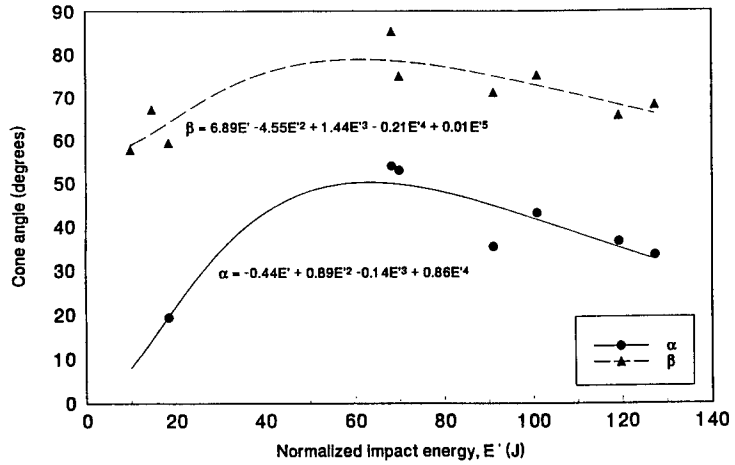

Figure 6. Cone angles vs normalized impact energy

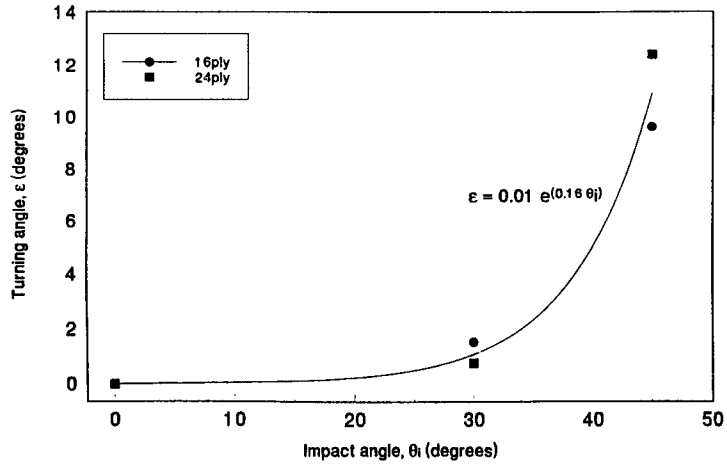

Figure 7. Primary turning angle vs impact angle

Figure 8. Impact and exit craters for 24 ply, 2mm Al projectile

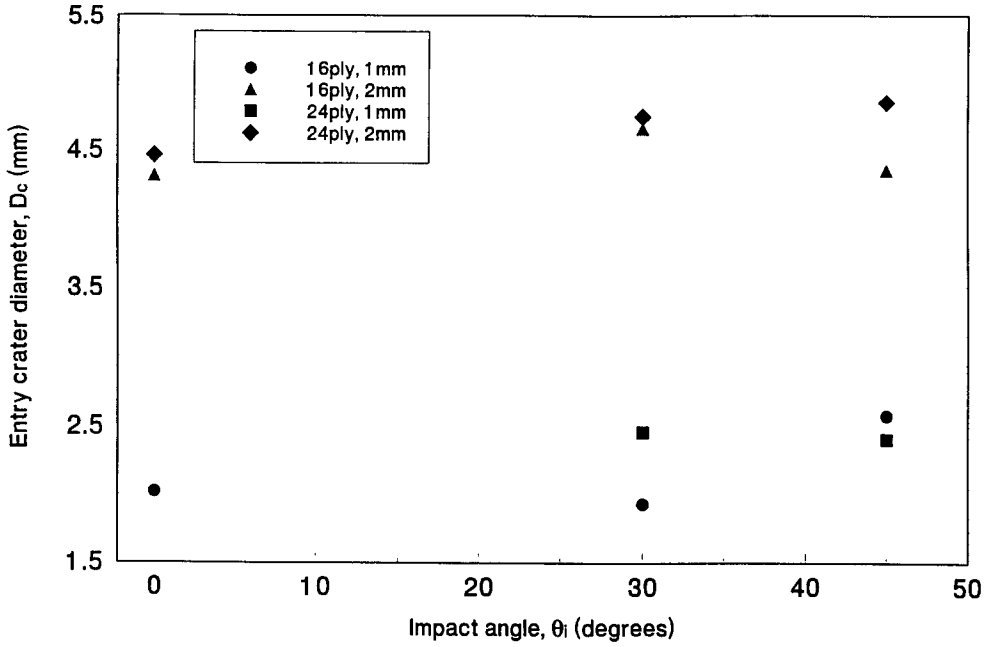

Figure 9. Entry crater diameter vs impact angle

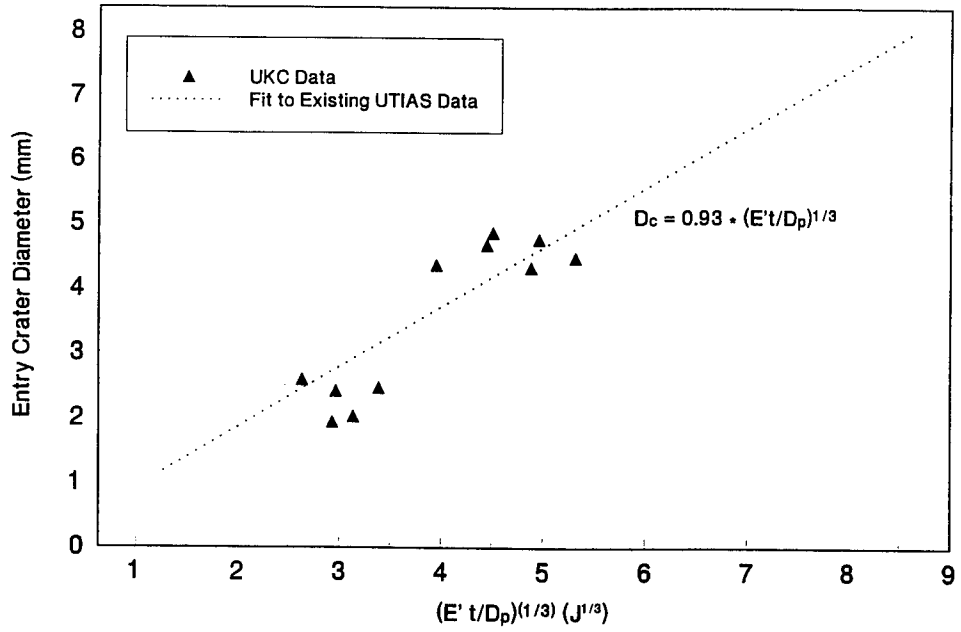

Figure 10. Entry crater diameter vs normalized Christiansen parameter

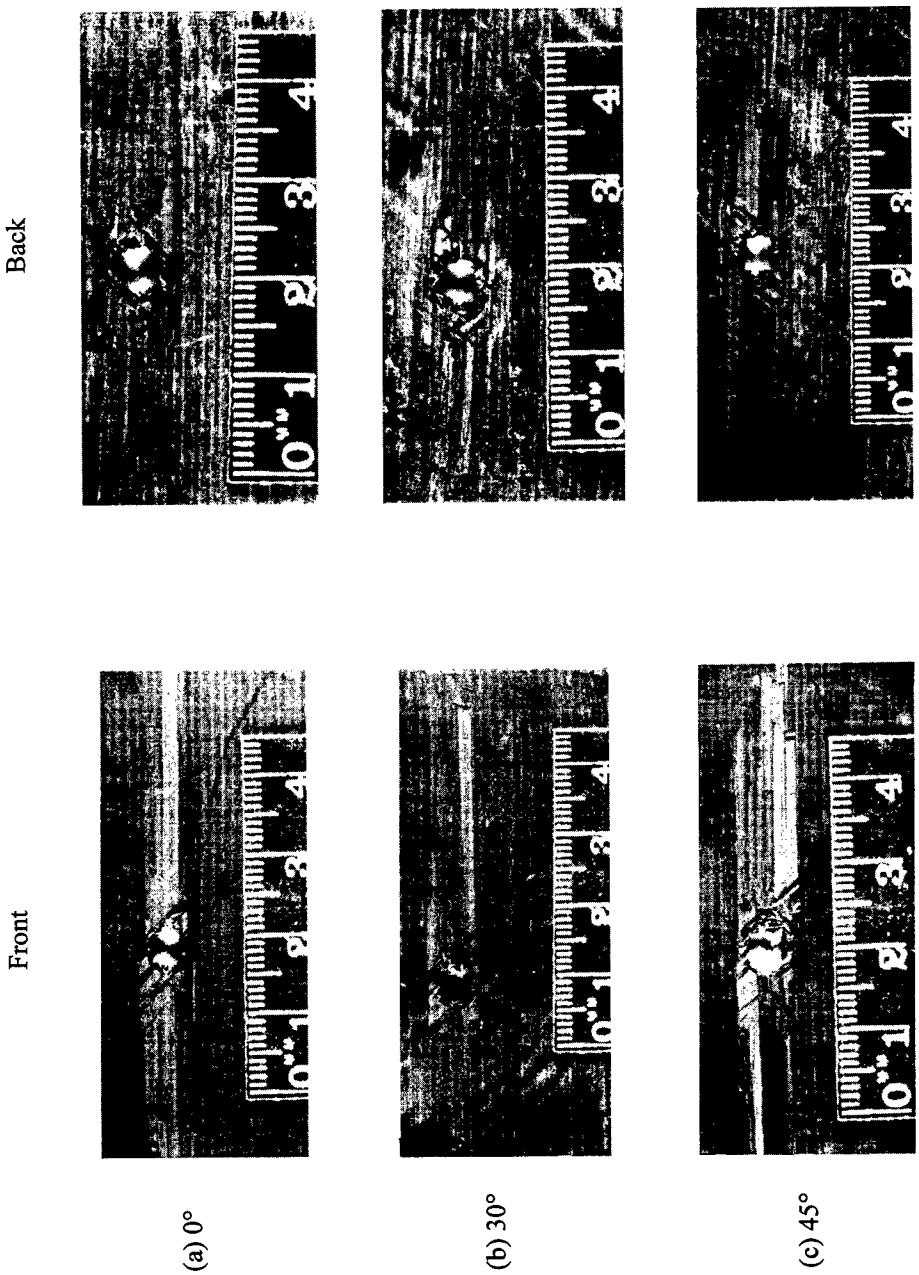

Figure 11. Front and rear (spall) surface ply delamination zones in 24 ply PEEK, 2mm Al projectile

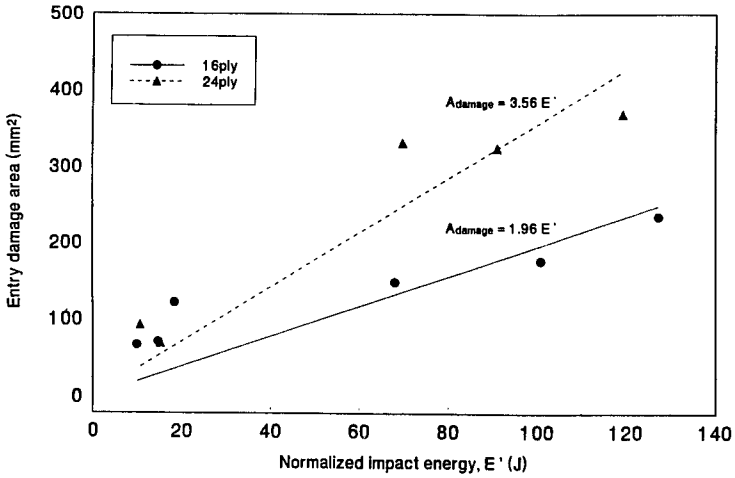

Figure 12. Entry damage area vs normalized energy

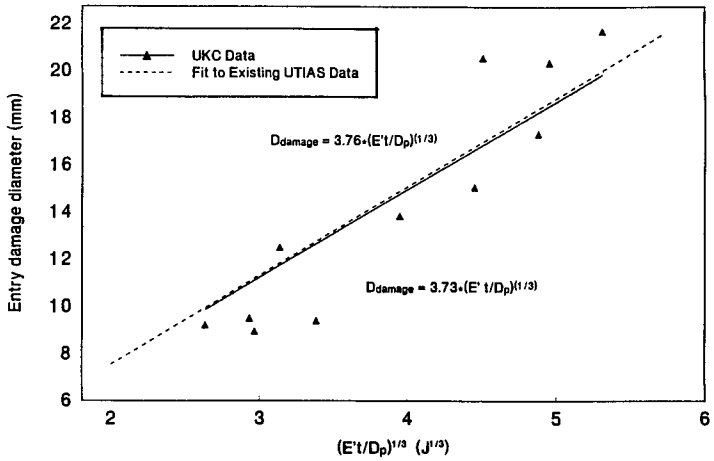

Figure 13. Entry damage diameter vs normalized Christiansen parameter

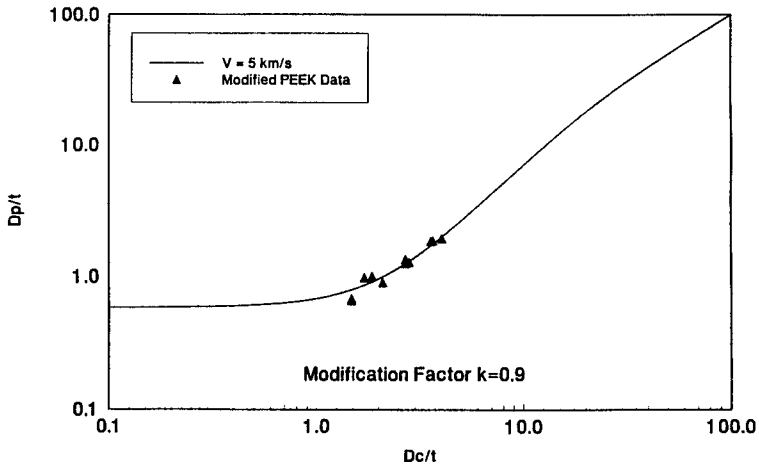

Figure 14. Comparison to GMC equation

PERGAMON International Journal of Impact Engineering 23 (1999) 533–545

INTERNATIONAL JOURNAL OF IMPACT ENGINEERING

www.elsevier.com/locate/ijimpeng

RAM-ACCELERATOR : A NEW HYPERVELOCITY LAUNCHER FOR BALLISTIC STUDIES

J-F. LEGENDRE, M. GIRAUD and M. HENNER

ISL, French-German Research Institute of Saint-Louis
BP 34, F-68301 Saint-Louis Cedex, France

Summary—Investigations are conducted at ISL on new hypervelocity launchers to fulfill requirements in different fields of ballistics such as launching dynamics, aeroballistics, terminal ballistics, aerothermodynamics, and supersonic combustion studies.

One objective considered is to determine the operational conditions to accelerate a 90mm-caliber projectile with a mass of ~1.5kg to a velocity of 3km/s while keeping the acceleration level below 40,000g. This moderate level of acceleration is required to investigate at high velocities models that are fragile because of their design and/or their onboard opto-electronical equipments. A means to fulfill these velocity and acceleration requirements is ram-accelerator technology.

This paper presents research conducted at ISL with smooth-bore ram-accelerators in the thermally choked propulsion mode. Therefore, two accelerators in calibers 30 and 90mm respectively, operated within the launch room of the aeroballistic range facility are described. Experimental results are presented describing the two-fold strategy followed to achieve the maximum performance, i.e., optimization of the projectile configuration and optimization of the combustible gas mixtures.

To date a maximum velocity of about 1985m/s has been achieved with the 90mm accelerator (projectile mass = 1.34kg, ram-section length 16.2m, injection velocity in the ram-section 1330m/s) and 2380m/s with the 30mm accelerator (projectile mass 68.6g, ram-section length 9m, injection velocity in the ram-section = 1380m/s).

Potential applications of ram-accelerators for ballistic studies are discussed and performances compared to those of conventional launchers that are currently used at ISL for ballistic studies.

Finally, very first preliminary experiments are presented describing the acceleration of high l/d rods using a ram-accelerator. © 1999 Elsevier Science Ltd. All rights reserved.

INTRODUCTION

Investigations are conducted at ISL on new hypervelocity launchers to fulfill requirements in different fields of ballistics such as launching dynamics, aeroballistics, terminal ballistics, aerothermodynamics, and supersonic combustion studies.

Among numerous research conducted worldwide on the development of hypervelocity launchers, an accelerator based on the principle of the airborne ramjet engine has been designed in 1983 at the University of Washington (Seattle, WA-USA) [1]. The feasibility of accelerating a projectile by this means has been experimentally demonstrated there in 1986 in a 38mm accelerator [2], in 90mm in 1992 at ISL [3] and in 120mm at the US Army Research Laboratory in 1993 [4]. This type of launcher is called a ram-accelerator and denoted in its condensed form of RAMAC. The projectile to be launched behaves as the centerbody of a conventional ramjet which moves at a supersonic velocity down a tube filled with a dense premixed explosive gaseous mixture. The bi-conical projectile centerbody, smaller than launch-tube diameter, is coaxially centered in this tube by means of guiding fins in the case of a smooth-bore. An alternative configuration is also investigated at ISL [5] in which the tube itself is fitted with rails and the projectile is a fin-less body. The projectile centerbody being undersized, whichever guiding means is used, a flow has to be established around it and combustion initiated and

0734-743X/99/$ - see front matter © 1999 Elsevier Science Ltd. All rights reserved.
PII: S0734-743X(99)00102-5

stabilized on or at the vicinity of the afterbody situated downstream of the throat. This combustion zone results in an increase of pressure on the afterbody, producing a forward thrust. In order to produce a positive acceleration, this thrust must be greater than the sum of the resisting forces acting on the projectile, i.e. friction drag on the tube surface and aerodynamic drag in the dense gaseous medium. The existence of this combustion zone attached to the projectile and generating continuously a forward thrust represents the major difference between a RAMAC and a conventional powder gun (Fig.1).

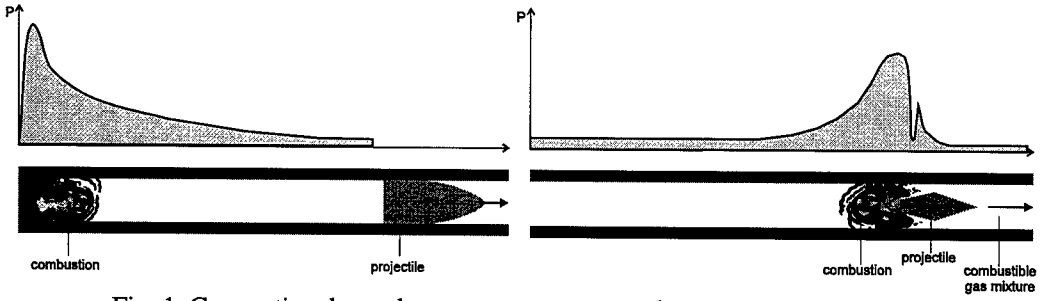

Fig. 1. Conventional powder-gun versus ram-accelerator pressure distribution

Three basic propulsion modes have been described based on the ratio of the local projectile velocity over the Chapman-Jouguet detonation velocity (denoted Dcj) [6]. This detonation velocity is calculated using the initial conditions of the combustible gaseous mixture at rest upstream the projectile.

The thermally choked or subdetonative propulsion mode, is encountered for projectile velocities lower than the computed Chapman-Jouguet detonation velocity. In this mode, the flow is compressed via the conical shock waves attached to the nose cone and then decelerated to subsonic velocity through a normal shock wave situated on the projectile conical afterbody (Fig. 2). Auto-ignition of the gaseous mixture occurs and the combustion zone is stabilized by thermal choking in the subsonic recirculation zone at the base of the projectile [3],[7-10].

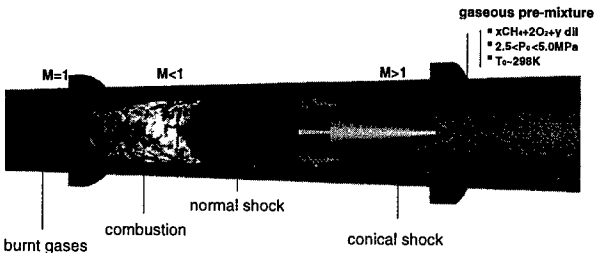

Fig. 2. Thermally choked propulsion mode

When the projectile velocity reaches the range 0.9 to 1.1Dcj, the propulsion mode is denoted transdetonative and is characterized by an unsteady combustion zone moving slowly upstream on the projectile afterbody [11-12].

Finally for velocities above approximately 1.1Dcj the propulsion mode is denoted super-detonative with the ignition and stabilization of a detonation wave in the annular region situated just downstream the projectile throat [5],[13-15].

The potential performances expected with such technology in terms both of high muzzle velocity and tailored acceleration level have motivated the study of this type of accelerator at ISL dating back to 1988. In order to conduct research on hypervelocity projectiles in the areas of interior ballistics, aeroballistics, terminal ballistics, and aerothermodynamics and in order to demonstrate the scalability of the principle, the caliber 90mm and smooth-bore tubes have been chosen for the main accelerator [3],[16]. In order to study the basic physical phenomena of the different combustion modes, two 30mm ram-accelerators have also been developed at ISL.

The first one, denoted RAMAC 30, has been designed to study the superdetonative combustion mode, either with a fin-guided projectile in a smooth bore [17] or with a tube fitted with rails launching a fin-less projectile [15],[18].
In order to get comparison data for the study of the scaling laws in the thermally choked propulsion mode, a second 30mm accelerator fitted with smooth bore has been realized and denoted RAMAC 30-II. It furthermore facilitates, at limited costs, studies of new geometries, new materials, or new gaseous mixtures to be developed for the main 90mm launcher in the thermally choked propulsion mode.
The validation of scaling laws as well as determining the limiting operational parameters of the principle are required in order to predict the feasibility of large scale launchers up to the size of an accelerator usable for the future application of direct launching of payloads into space [19-20].

Experiments conducted at ISL, exploring the potential of a ram-accelerator as a launcher for ballistic studies are aimed at determining the experimental conditions required to accelerate a 90mm caliber projectile having a mass of about 1.5kg to a velocity of 3km/s with a maximum acceleration not exceeding 40,000g [21]. To achieve this goal, an hybrid propulsion mode will probably be required, i.e. initially subdetonative then transitioning to superdetonative propulsion mode.

The experimental results presented in this paper concern investigations on the maximum performance that can be achieved with smooth-bore tube in the thermally choked propulsion mode and their applicability to ballistics studies.

EXPERIMENTAL FACILITIES

Two smooth-bore ram-accelerators, 30mm and 90mm respectively, are operated within the launch room of the aeroballistic range facility. Both launchers share the same security monitoring, gas handling and data acquisition systems. The basic elements of these launchers have been extensively presented elsewhere [10],[12] and only the latest enhancements will be described in this paper.

The newest configuration of the 90mm ram-accelerator has an overall length of 33.6m (373 calibers) in which 24m (267 calibers) can contain the dense combustible gas mixtures (Fig. 3). These 24m are composed of 7 ram-tubes connected to each other which can be filled with any required gas mixture composition at an initial pressure limited for safety reasons to 5.0MPa. With the gas handling device available, a maximum of 4 different mixtures can be used simultaneously along these 7 tubes. A total of 58 instrument cross-sections are situated along the tubes which allow the use of up to 174 probes in order to measure the time-position history of the projectile, shock waves, and combustion fronts [22]. The latest improvement of this facility is the installation of an evacuated safety vessel (volume $30m^3$) situated at the muzzle of the launcher and which contains the blast effect and the expansion of the combustion gas at the muzzle. A flash x-ray station, situated after the accelerator muzzle, allows the visualization of the projectile and the control of its integrity. The projectile finally impacts and is destroyed in a projectile catcher moving along rails.

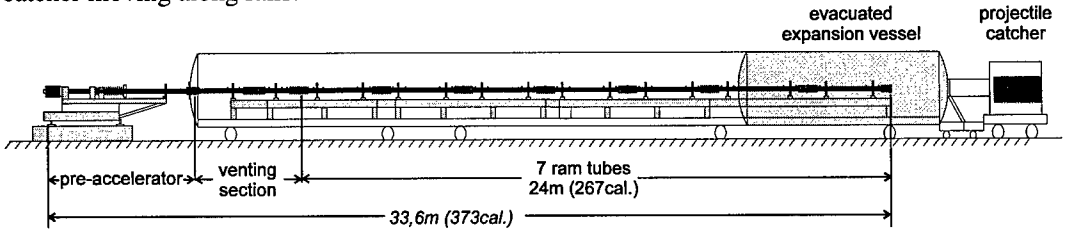

Fig. 3. RAMAC 90 experimental setup

The second facility is 30mm-caliber which allows convenient study of scale effects. It is also used to evaluate the feasibility and to optimize new configurations of both projectile and gas mixture. The newest set-up of the RAMAC 30-II facility, has an overall length of 14.25m (475 calibers) in which 9m (300 calibers) contain the combustible gas mixtures (Fig. 4). This 9m ram-section is composed of three 3m-long tubes which allow the use of up to 3 different combustible mixtures.

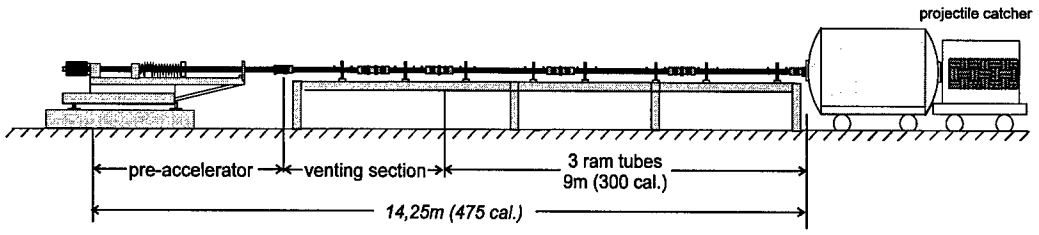

Fig. 4. RAMAC 30-II experimental setup

Numerous investigations have been carried out on projectile configurations adaptable to the 90mm accelerator. Basically, it has been decided to use 90mm projectiles having a mass of 1.3 to 2kg depending on the material used. The corresponding centerbody volume is ~660cm^3 which allows insertion of test models of significant size for possible future use of this launcher as a tool for ballistic studies. In order to investigate the scaling laws ruling the subdetonative propulsion mode, a standard outer geometry of the projectile (Fig. 5) has been designed [9] which has been used in both 90 and 30mm experiments.

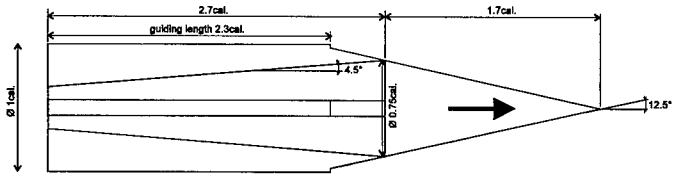

Fig. 5. Fin-guided standard RAMAC projectile

Parametric studies have been carried out both numerically [23] and experimentally [10],[24] for the two calibers, investigating the effect of the number and geometry of the fins on the overall performance. Fin numbers have been varied from 3 to 5, thickness (e) from e=0.08 to 0.156cal. and chamfer (θ_{CF}) on the leading edge of the fins varied from 90° (no chamfer) to 1.5° (Fig. 6).

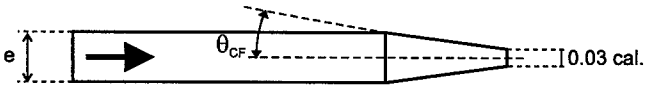

Fig. 6. Profile of the fins

EXPERIMENTAL RESULTS

A two-fold strategy has been followed in order to obtain the highest forward thrust so that the highest velocity in the thermally choked propulsion mode could be achieved :

(i) optimization of the projectile in terms of geometry (cone angles, rear base area, design of the fins) and material (density, mechanical and thermal properties) [24], [25],
(ii) optimization of the combustible gas mixture staging in terms of sensitivity to detonation, specific heat release, sound velocity [26-29].

To date maximum muzzle velocity achieved with the 90mm accelerator remains about 1985m/s (Mach number 5.8 in ambient air) for a 1.34kg projectile with afterbody machined from magnesium alloy [10]. The injection velocity at the entrance of the ram section filled with the combustible mixture was 1330m/s. The ram section was composed of 5 tubes representing a total length of 16.2m (180cal.) filled with a single mixture of $3CH_4+2O_2+10N_2$ at an initial pressure of 4.5MPa (Fig. 7). In first approximation, an averaged acceleration ($\Gamma_{average}$) has been estimated by the classical relation : $\Gamma_{average} = \frac{1}{2L}(V_{out}^2 - V_{in}^2)$, where L is the ram-section length filled with the combustible gas mixture, V_{out} and V_{in} the experimental velocities at the exit and entrance of the ram-section respectively. Accordingly, along the L=16.2m ram-section, the average acceleration has been determined at 6,830g. Further increase in velocity could not have been obtained even with a longer ram-section for a projectile afterbody machined of Magnesium alloy. Ablation and erosion of both the fins and afterbody of the projectile were very important and combustion could not be further stabilized at the base after a travel of 16.2m. This corresponds to a time spent in ram section of about 10ms.

In order to develop a projectile which could withstand a longer time length in the ram section, aluminum alloy was chosen for the afterbody. The minimum mass of such a projectile, while still maintaining the standard outer geometry, could only be reduced down to 1.57kg by hollowing to a maximum the centerbody. This aluminum alloy projectile has been launched in the latest upgraded facility along a 24m-long ram-section. Injection velocity was 1360m/s and exit velocity achieved was 1730m/s with a mixture $3CH_4+2O_2+10N_2$ at an initial pressure of 4.0MPa (Fig. 8). Average acceleration along the 24m-long ram-section was 2,430g. Although the muzzle velocity and average acceleration are less than that achieved with a magnesium afterbody, this experiment demonstrates the enhanced survivability of an aluminum projectile during a time length of at least 15.5ms and for an increasing Mach number in the ram-section varying from 3.75 to 4.78.

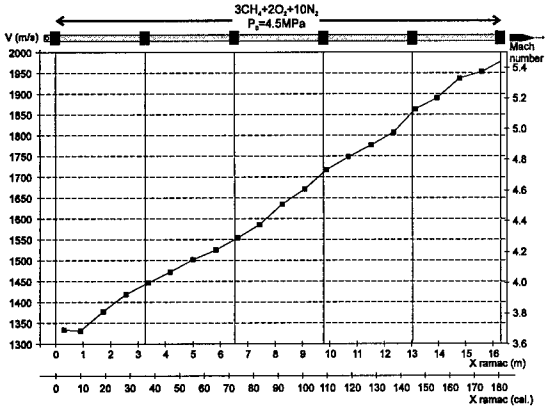

Fig. 7. RAMAC 90 velocity performance, Magnesium alloy afterbody, 4 fins, e=0.1cal., θ_{CF}=90°, mass=1.34kg

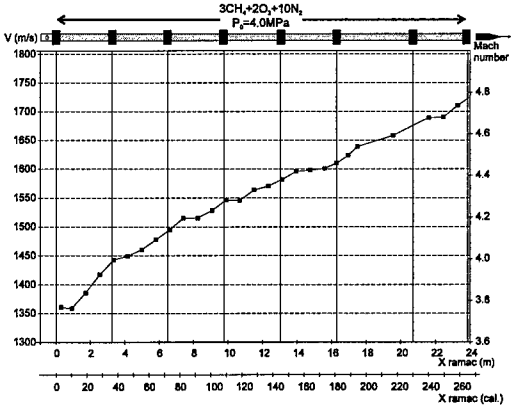

Fig. 8. RAMAC 90 velocity performance, Aluminum alloy afterbody, 4 fins, e=0.1cal., θ_{CF}=90°, mass=1.57kg

The latest results concern the increase of the forward thrust through the optimization of the gas mixtures. According to the one-dimensional model that has been determined to fairly accurately predict the performance in the thermally choked propulsion mode [8], [30], it appears that among the parameters to vary in order to increase the thrust are the following :

(i) decrease projectile mass : limited for a given outer geometry by mechanical construction and material,
(ii) increase heat release of the combustible mixture : limited by the sensitivity to detonation and stabilization in the subsonic combustion zone at the base of the projectile,
(iii) decrease the local Mach number : the lowest Mach number is limited by the aerodynamic choking of the flow at the throat.

Major efforts have been aimed at reducing the range of projectile Mach number variation due to the velocity increase along the ram section [10],[25],[28]. Therefore, staging of the mixtures had been experimentally studied in both calibers. This staging involves the use of successive gaseous mixture compositions adapted to the increasing velocity of the projectile. In order to keep the local Mach number of the projectile in an optimized limited range, successive mixtures must exhibit increasing sound velocities but also heat release and sensitivity to detonation compatible with the operating parameters [27],[29].

This limited range of Mach number variation allows to :

(i) optimize the non-dimensional thrust,
(ii) prevent the aerodynamic choking of the flow at the throat,
(iii) prevent aerothermodynamic choking of the flow near the throat caused by thermal ablation effects,
(iv) prevent too rapid ablation and erosion of the fins and their leading edge which cause canting of the projectile, resulting in choking of the flow.

Feasibility of mixture staging has been first demonstrated in 90mm for a 13.2m-long ram section [9] for two different compositions. The first mixture $3.55CH_4+2O_2+7.45N_2$ was filled at an initial pressure of 3.5MPa in the first 6.6m, the remaining 6.6m being filled with $3.1CH_4+2O_2+10.35N_2$ also at an initial pressure of 3.5MPa. In that case, a successful transition at a Mach number of 4.45 between these two mixtures of similar sound velocities has been achieved for an magnesium alloy projectile afterbody.

Next experiments in 90mm staging have demonstrated a smooth and undisturbed transition between two successive mixtures having a relative sound velocity increase of 10% and a relative heat release increase of 20%. The corresponding facility setup involved 5 ram-tubes, i.e., a 16.2-m-long ram-section. The first mixture was the standard ISL Nitrogen heavy diluted mixture ($\sim 3CH_4+2O_2+10N_2$), which provides repeatable successful starting conditions, at an initial pressure of 3.5MPa and having a sound velocity of 360m/s. The second mixture used was $\sim 7.5CH_4+2O_2+1.5N_2$ also at an initial pressure of 3.5MPa and having a sound velocity of 400m/s. Successful transition between the two stages have been demonstrated for three different Mach numbers at the exit of the first mixture, i.e. 4.2, 4.5 and 4.75 [10].

Finally, the feasibility of achieving a successful transition between two mixtures with a sound velocity increase of 22% and heat release increase of 25% has been demonstrated in 30mm with the RAMAC 30-II facility. In that case, the first section (3m-long, i.e. 100 cal.) was filled with $3.2CH_4+2O_2+7.7N_2$ at an initial pressure of 4.5MPa which corresponds to a sound velocity of 364m/s. The remaining 6m-long section is filled with $5CH_4+2O_2+2.2He$ at an initial pressure of 4.9MPa with a sound velocity of 452m/s. A new projectile afterbody [28] was used, machined of both magnesium and aluminum alloy and total initial mass of projectile was 68.6g. Figure 9 presents the velocity profile for these conditions with an injection velocity of 1380m/s and a muzzle velocity of 2380m/s (Mach number about 7 in ambient air), whereas Figure 10 represents the Mach number variation profile in the ram-section. Average acceleration along the entire 9m-long ram-section was 21,300g.

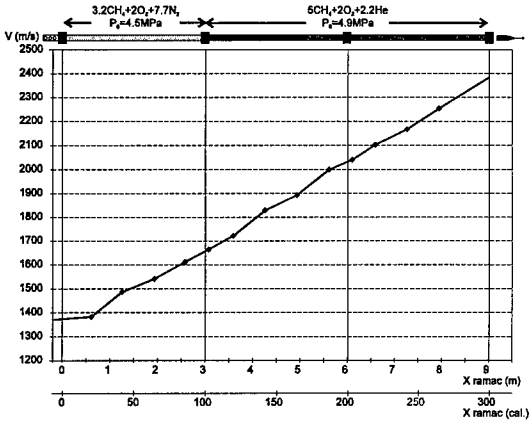

Fig. 9. RAMAC 30-II
velocity performance, 4 fins,
e=0.156cal., θ_{CF}=1.5°, mass=68.6g

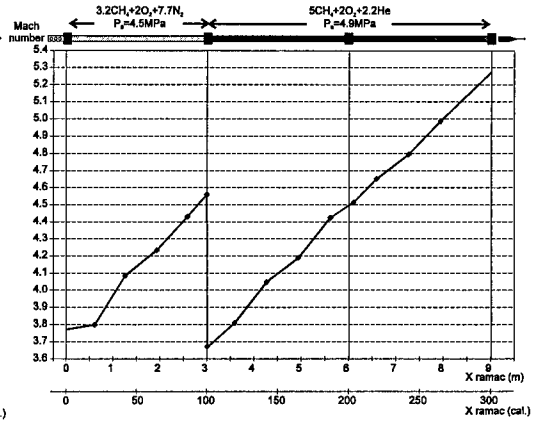

Fig. 10. RAMAC 30-II
Mach number variation, 4 fins,
e=0.156cal., θ_{CF}=1.5°, mass=68.6g

Experimental results achieved so far in the thermally choked propulsion mode allow to foresee the feasibility of achieving in the short term a velocity of 2.5km/s for both 30mm and 90mm calibers using a 300-caliber-long ram section.

APPLICATION OF RAM-ACCELERATOR TO BALLISTICS STUDIES.

According to the experimental results achieved so far on both 30mm and 90mm caliber ram-accelerators, and on the basis of a better knowledge of the scale effects in the thermally choked propulsion mode, the use of a ram-accelerator as a laboratory launcher can now be realistically considered.
Different laboratory applications have been taken into consideration among which are :

(i) aeroballistics : free-flight studies of hypervelocity projectiles characterized by fragile structures or equipped with on-board opto-electronics,
(ii) terminal ballistics : hypervelocity impact studies of high l/d ratio long rod penetrators,
(iii) aerothermodynamics : simulation along a pressurized ram-section developing within a few milliseconds the thermal stress encountered by projectile wall in air at sea level during a few seconds of flight,
(iv) material studies : characterization of material resistance to high aero-thermal stresses,
(v) propulsion : basic studies for the parametric design involved in supersonic combustion ram-jet engine (scramjet).

At present, potential uses of a ram-accelerator are primarily focused on ballistics applications. Therefore the relative performances of ram-accelerators and laboratory powder guns for increasing Mach numbers are compared.
The first comparison is the total mass launched. This maximum launched-mass capacity has been considered for accelerators up to 90mm currently used at ISL for ballistic studies. Figure 11 represents the total mass launched (sabot and test-model) versus the maximum muzzle velocity (or Mach number in ambient air) for high-performance powder guns denoted by their caliber in mm and tube length in calibers and two-stage light gas gun. Powder guns available are in the caliber range 25 to 90mm [31] whereas the light gas gun caliber shown here is 30mm. Also plotted are the two ISL's smooth-bore RAMAC performances that have been repeatedly achieved (continuous line) as well as the expected further increase in performance (broken line).

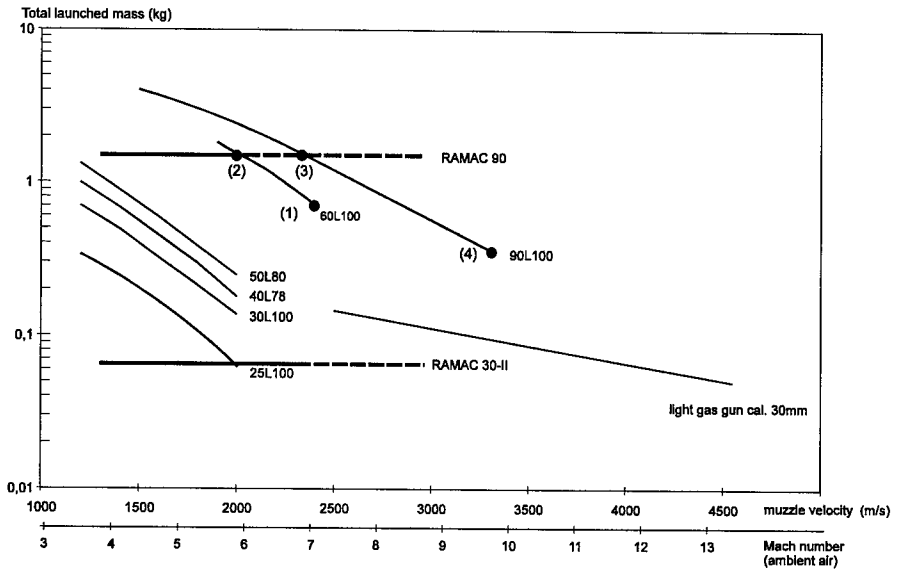

Fig. 11. Performances of launchers used in the ballistic facilities at ISL, launched-mass versus muzzle velocity.

It can be obviously pointed out that, speaking strictly of launched-mass, the RAMAC 90 technology would overtake the 90L100 (90mm-caliber, 100-caliber-long tube) performances only for velocities above 2.4km/s or (Mach number about 7 in ambient air). For similar performances in terms of muzzle velocity and launched-mass, an advantage of the ram-accelerator concerns the lower barrel erosion. In case of high performance powder guns, extreme erosion is encountered in the chamber and in the gun tube due to the high pressure required in the combustion chamber and very high calorific content of the powder. Typically a maximum pressure of 700MPa in the chamber of the 60L100 is required to reach 2.5km/s for a 0.7kg projectile (point denoted (1) on Figure 11) . In case of the RAMAC 90, the maximum pressure that the tubes have to withstand is 120MPa in the pre-accelerator chamber (required to pre-accelerate the projectile up to an injection velocity of about 1.35km/s in the ram-section) and around 100MPa in the ram-section filled with combustible gas mixtures. In the RAMAC 90, after more than 160 experiments with combustible gas mixtures and more than 115 with inert gas, no more than a few 1/100 of a millimeter erosion of the tubes can be detected.

A second comparison concerns the shape and size of the models to be launched to high velocities. The parameter considered is therefore the Reynolds number (R_{eL}) based on the total length of the projectile. This allows us to better illustrate the major advantage of ram-accelerator technology for the launching of long and fragile projectiles to hypervelocities. Figure 12 presents the relative performance of conventional powder guns and ram-accelerators in the coordinates of Reynolds number as a function of Mach number. The area denoted as "Powder guns capabilities" represents the domain experimentally covered in the aeroballistic range facility at ISL with powder guns for calibers up to 90mm [31-32]. The RAMAC domain corresponding to the potential capabilities anticipated at ISL is defined by ram-projectile lengths between 5 and 60cm and Mach numbers from 3.5 (performance of the pre-accelerator alone) up to an expected Mach number of about 9. In the case of an increased size of the facility (caliber and length), this domain could be further enlarged for both higher Mach and Reynolds numbers. The up-to-date smooth-bore RAMAC performances are also represented in this domain (continuous line being experimental and broken line being anticipated results).

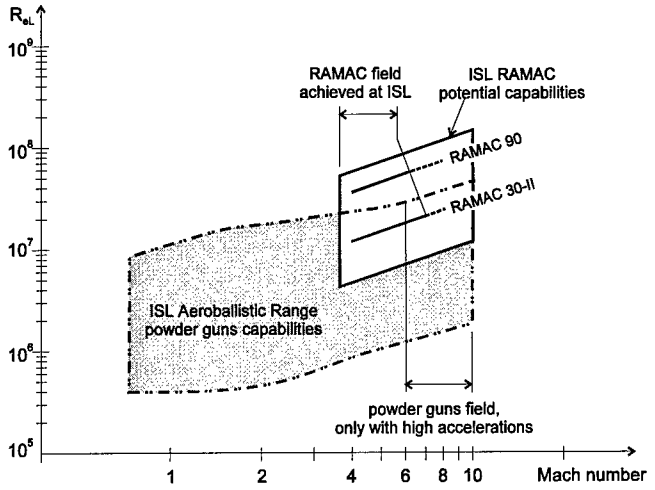

Fig. 12. Performances of launchers used in the ballistic facilities at ISL, Reynolds number R_{eL} versus Mach number

Figure 12 highlights an intersection of both domains for projectile lengths typically between 5 and 15cm. In this common region, for high Mach numbers (6 to 10 for example) the acceleration levels encountered with powder guns are so high that only massive projectiles (low l/d ratios) could be accelerated without structural damage. On the contrary, for RAMAC technology, the peak acceleration levels remain moderate and easily tailored. Basically, the acceleration profile that is encountered in a ram-accelerator is composed of two main regions.

The first is the classical acceleration profile that is found in the pre-accelerator which, at ISL, is composed of a powder gun. According to the type of powder used, measured acceleration levels reached by a 90mm, 1.5kg ram projectile accelerated to an injection velocity of 1.3 to 1.4km/s remains below 40,000g.

The second acceleration that is achieved in the ram-section itself while the projectile is "surfing on the combustion waves" in case of the thermally choked propulsion mode. Depending on the operating parameters, a maximum acceleration of 10,000g has been experimentally observed in 90mm. It is not expected that, even with the optimization of every single operating parameter, the maximum acceleration in the ram-section will exceed the 40,000g, at least at our operating scale and in the thermally choked propulsion mode. This means that, whatever the required muzzle velocity, the maximum acceleration should never exceed the peak value obtained in the pre-accelerator. The muzzle velocity then depends on the proper ram-section length, gas mixture staging (composition and initial pressure) and thermo-mechanical resistance of the projectile. Choosing which portion of the available length of the ram-section should be filled with combustible gas mixture will allow us easily to obtain any required velocities between the injection velocity and the maximum performance available, with peak acceleration always remaining at the same level.

The importance of acceleration levels can be further illustrated regarding some experimental points highlighted on Figure 11.

As a matter of example, we can consider the point denoted as (2) on Figure 11, which corresponds to a launched mass of about 1.5kg at a muzzle velocity of 2km/s. In case of the 60L100 powder gun the peak acceleration level reached for that point is 77,000g whereas for the RAMAC 90 the experimental maximum acceleration is the 38,000g obtained in the pre-accelerator. This shows that, for this launch condition, the acceleration level in the 60L100 powder gun maximal is twice that found in the RAMAC 90. If the muzzle velocity can be further increased for the RAMAC 90, the benefit of this type of launcher will be enhanced compared to high performance powder gun. In case of the 90L100 high performance powder gun, the

maximum performance for a 1.5kg projectile is 2.4km/s. At that point, denoted (3) on Figure 11, the maximum acceleration is 57,000g and the peak pressure in the chamber is 250MPa. For the same launcher, a maximum muzzle velocity of 3.3km/s has been obtained for a 0.40kg projectile (point denoted (4) on Figure 11) but with a peak acceleration of 115,000g and a maximum chamber pressure of 400MPa.
These examples show that for the Reynolds /Mach regions that can be covered both by conventional powder guns and ram-accelerators, the latter technology provides an important launch-capability for structurally fragile projectiles.
Furthermore, in case of increasing Reynolds numbers, the RAMAC covers a domain that could not be reached with conventional powder guns. In that case the RAMAC technology enables a new range of experiments for fragile geometries (high l/d ratios, finned projectiles, detailed scale-down models or projectiles equipped with sensitive on-board opto-electronics) and therefore represents a decisive step forward for ballistic studies.

PRELIMINARY EXPERIMENTS FOR HIGH L/D PROJECTILE LAUNCHING.

In case of smooth-bore ram-accelerator technology, the characteristic caliber-dimension that should be considered when comparing to other launchers is the centerbody maximal diameter. In the case of ISL main accelerator (90mm), the centerbody presents a throat diameter of 68mm which corresponds to a little less than a ½ scale of the future tank gun caliber of 140mm. This makes the RAMAC 90 a valuable candidate for subscale experiments concerning this future ammunition.
Considering a long rod penetrator, Figure 13 shows the principle shape of the sabot in the case of a conventional full-caliber powder gun compared to that of a ram-accelerator respectively.

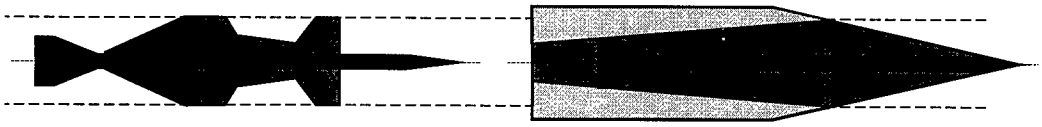

Fig. 13. Sabot designs : conventional powder gun / ram-accelerator

Preliminary experiments on the acceleration of long rods using a ram-accelerator have been carried out in caliber 30mm with the RAMAC 30-II smooth-bore facility.
The feasibility of accelerating a RAMAC 30 projectile fitted with a 15g steel rod (diameter=5mm, length/diameter ratio =21) has been successfully demonstrated .
Figure 14a) shows a flash-X-rays picture taken at rest of this 30mm RAMAC projectile fitted with such steel long rod. Figure 14b) presents the same projectile in free-flight taken 20cm after the RAMAC 30-II muzzle. In this experiment, the projectile has been successfully accelerated to a velocity of 1415m/s without structural damage.
Further investigations with different rod-penetrator designs and masses are currently underway with the corresponding optimization of the different gas mixture compositions to be used for staging.

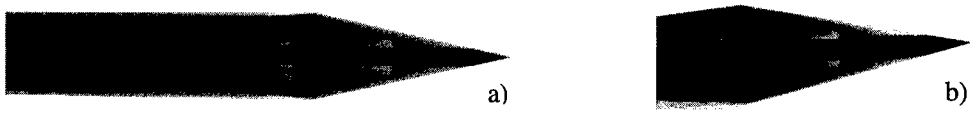

Fig. 14. RAMAC 30-II long rod penetrator projectiles a) x-rays at rest, b) x-rays in free flight

This first series of experiments have been undertaken with the long rod rigidly attached inside the ram projectile centerbody. Further investigations are underway as well on the design of

new projectile configurations which will allow the separation of the on-board test model from fin-guided bi-conical sabots required for the ram acceleration principle.

PERSPECTIVES

Ram-accelerator studies are aimed at enhancing the performance in terms of muzzle velocity, total launched mass, Reynolds number, and also developing projectile designs compatible with ballistics studies.

First, the increase in muzzle velocity relies on the optimization of thrust through the optimization of the projectile design in terms of both geometry and material and on the optimization of the gas mixture staging.

The second action is to increase the ram-section length up to 300 calibers for the RAMAC 90 facility. This addition of an extra 3m-long ram-tube is due to be operational for the last trimester 1998. With these two upgraded facilities, based on the experimental results already achieved and on validated performance predictions, a muzzle velocity of 2.5km/s for both calibers is expected in the thermally choked propulsion mode. The projectile configuration will remain with a mass of 1.5kg and 70g in calibers 90 and 30mm respectively.

CONCLUSION

This paper has presented the state of the researches carried out at ISL on smooth-bore ram-accelerators. Two accelerators 30mm and 90mm respectively, are involved in the investigation of the maximum performance that can be reached in the thermally choked propulsion mode. The strategy followed is based on optimizing the thrust and enhancing the projectile survivability in very dense gaseous mixtures. Previously published results with magnesium alloy projectile afterbodies are reviewed. New results concerning the staging of the mixtures aimed at reducing the local Mach number of the projectile thus increasing the thrust have been presented for both magnesium and aluminum alloy projectile afterbodies. Increased survivability of 90mm projectiles has been demonstrated along the upgraded RAMAC 90 facility with an aluminum alloy afterbody. Feasibility of increasing both thrust and survivability has been demonstrated with the RAMAC 30-II facility by using a new material combination for projectile afterbody. Perspectives on the performance that should be achieved with the next facility upgrades, corresponding to a 300-caliber-long ram-section for both 30 and 90mm calibers, have been presented.

Based on the experimental results already achieved, the applicability of a ram-accelerator as a hypervelocity laboratory launcher for ballistics application is discussed. Present ram-accelerator performances are compared to those of other operational laboratory launchers available at ISL. For given values of launched mass and muzzle velocity, the advantages of RAMAC technology are highlighted versus other launchers in terms of both lower acceleration and lower gun-barrel erosion.

Finally preliminary experiments have been described concerning the design of 30-mm-caliber RAMAC projectile fitted with simulated long rod penetrators.

REFERENCES

1. Hertzberg A., Bruckner A.P. and Bogdanoff D.W., An exploratory study of ram accelerator principles, AFATL-TR-88-94 AD-A202-85, Eglin Air Force Base, FL-USA (1988)
2. Hertzberg A., Bruckner A.P.and Bogdanoff D.W., The ram accelerator : a new chemical method of achieving ultrahigh velocities, *37th meeting of the Aeroballistic Range Association*, Québec, Canada (1986)

3. Giraud M., Legendre J-F, Simon G. and Catoire L., Ram-accelerator in 90-mm-caliber : first results concerning the scale effect in the thermally choked propulsion mode, presented not published at the *13th Int. Symp. Ballistics*, Stockholm, Sweden (1992), ISL report CO210/92
4. Kruczynski D., Analysis of firings in a 120-mm ram accelerator at high pressures, *1st Int. workshop on ram-accelerators*, Saint-Louis, France (1993)
5. Smeets G., Seiler F., Patz G. and Srulijes J., First results obtained in a 30-mm-caliber scram accelerator using a rail tube for cylindrical projectiles, *Proc. 25th Int. Symp. on Combustion*, Irvine, CA-USA, The Combustion Institute, Pittsburgh, PA-USA (1994), ISL report PU327/94
6. Hertzberg A., Bruckner A.P. and Knowlen C., Experimental investigation of the Ram accelerator propulsion modes, *Shock Waves: Proc. 18th Int. Symp. Shock Waves*, July 1991, Sendai, Japan, (edited by Takayama K.), **1**, 17-25, Springer, Germany (1992)
7. Bruckner A.P., Knowlen C., Hertzberg A. and Bogdanoff D.W, "Operational characteristics of the thermally choked Ram Accelerator", *Journal of Propulsion and Power*, **7**, 828-836 (1991)
8. Knowlen C., Theoretical and experimental investigation of the thermodynamics of the thermally choked Ram Accelerator, Ph. D Thesis, University of Washington, Seattle, WA-USA (1991)
9. Giraud M. Legendre J-F, Simon G., Henner M. and Voisin D., RAMAC in 90mm caliber : starting process, control of the ignition location and performances in the thermally choked propulsion mode, *2nd Int. Workshop on Ram Accelerators*, Seattle, WA-USA (1995), ISL report PU349/95
10. Giraud M., Legendre J-F and Henner M., RAMAC in subdetonative propulsion mode. State of ISL studies, *Ram-Accelerators, Proceedings of the 3rd Int. Symp. on Ram-Accelerators held in Sendai, Japan, 16-18 July 1997* (edited by K. Takayama and A. Sasoh) , pp. 39-52, Springer, Germany, (1998), ISL report PU312/98
11. Burnham E.A., Kull A.E., Knowlen C., Bruckner A.P. and Hertzberg A., Operation of the Ram Accelerator in the transdetonative velocity regime, AIAA 90-1985 (1990)
12. Giraud M., Legendre J-F and Simon G., Ram-accelerator in 90-mm-caliber or RAMAC 90 : experimental results concerning the transdetonative combustion mode, *Proc. 14th Int. Symp.Ballistics*, pp. 95-104, Québec, Canada (1993), ISL report PU363/93
13. Kull A.E., Burnham E.A., Knowlen C., Bruckner A.P. and Hertzberg A., Experimental studies of superdetonative ram-accelerator modes, AIAA89-2682 (1989)
14. Knowlen C., Higgins A.J., Bruckner A.P. and Bauer P., Ram-accelerator operation in the superdetonative velocity regime, AIAA96-0098 (1996)
15. Seiler F., Patz G., Smeets G. and Srulijes J., Influence of projectile material and gas composition on superdetonative combustion in ISL's RAMAC 30, AIAA 98-3445 (1998)
16. Giraud M. and Simon G., Premier accélérateur par effet stato de l'ISL : choix du pré-accélérateur, ISL report RT507/88 (1988)
17. Patz G., Seiler F., Smeets G. and Srulijes J., The behavior of fin-guided projectiles superdetonative accelerated in ISL's RAMAC 30, *Ram-Accelerators, Proceedings of the 3rd Int. Symp. on Ram-Accelerators held in Sendai, Japan, 16-18 July 1997* (edited by K. Takayama and A. Sasoh), pp. 89-95, Springer, Germany, (1998)
18. Seiler F., Patz G., Smeets G. and Srulijes J., The 30-mm-caliber Scram accelerator RAMAC 30 of ISL, *Proc. IUTAM Symposium on Combustion in Supersonic Flows*, October 1995, Poitiers, France, (edited by Champion M. and Deshaies B.), pp. 263-272, Kluwer Academic Pub., Dordrecht, The Netherlands (1997), ISL report PU372/95
19. Bruckner A.P. and Hertzberg A., Ram Accelerator direct launch system for space cargo, *38th Congress of International Astronautical Federation*, Brighton, United Kingdom, Paper IAF-87-211 (1987)
20. Bogdanoff D., Ram-accelerator direct space launch system : new concept, *Journal of Propulsion and Power*, **8**, p. 481 (1992)
21. Giraud M., Legendre J-F and Simon G., RAMAC90 : experimental studies and results in 90mm caliber, length 108calibers, *1st Int. Workshop on Ram Accelerators*, Saint-Louis, France (1993), ISL report PU360/93
22. Giraud M., Legendre J-F, Simon G., Mangold J-P, Simon H. and Kauffmann H., RAMAC90 : facility and diagnostic methods, *44th meeting of the Aeroballistic Range Association*, Munich, Germany (1993), ISL report PU362/93
23. Henner M., Giraud M., Legendre J-F and Berner C., CFD computations of steady and non-reactive flow around fin-guided ram projectiles, *Ram-Accelerators, Proceedings of the 3rd Int. Symp. on Ram-Accelerators held in Sendai, Japan, 16-18 July 1997* (edited by K. Takayama and A. Sasoh), pp. 325-332, Springer, Germany, (1998), ISL report PU311/98
24. Henner M., Contribution to the design of a new RAMAC projectile : modelisation and experiments, *47th meeting of the Aeroballistic Range Association*, Saint-Louis, France (1996), ISL report PU361/96
25. Giraud M., Legendre J-F and Henner M., RAMAC in subdetonative propulsion mode, *Proc. 17th Int. Symp. Ballistics*, pp. 2_17-2_24, Midrand , South-Africa (1998), ISL report PU319/98
26. Legendre J-F, Contribution à l'étude de la sensibilité et des caractéristiques de détonation de mélanges explosifs gazeux denses à base de méthane utilisés pour la propulsion dans les accélérateurs à effet stato, Ph.D dissertation, University of Poitiers, Poitiers, France (1996), ISL report R101/97

27. Legendre J-F, Bauer P. and Giraud M., RAMAC 90 : detonation initiation of insensitive dense methane-based mixtures by normal shock waves, *Ram-Accelerators, Proceedings of the 3rd Int. Symp. on Ram-Accelerators held in Sendai, Japan, 16-18 July 1997* (edited by K. Takayama and A. Sasoh), pp. 223-231, Springer, Germany, (1998), ISL report PU310/98
28. Legendre J-F, Giraud M. and Henner M., Velocity performance in RAMAC 90 multistage experiments, AIAA 98-3447 (1998), ISL report PU353/98
29. Legendre J-F, Giraud M. and Bauer P., Detonation properties of dense methane-oxygen-diluent mixtures : application to ram-accelerators, *Shock Waves,* **8**, 267-273 (1998), ISL report PU303/99
30. Henner M., Legendre J-F, Giraud M. and Bauer P., Thrust prediction of a ram accelerator projectile in the subdetonative propulsion mode, AIAA 98-3149 (1998), ISL report PU354/98
31. Giraud M., Sur les études d'aérobalistiques menées au tunnel de tir classique de l'ISL, ISL report R111/76 (1976)
32. Giraud M., Sur le programme RAMAC à l'ISL, ISL report R103/92 (1992)

PERGAMON International Journal of Impact Engineering 23 (1999) 547–560

INTERNATIONAL JOURNAL OF IMPACT ENGINEERING

www.elsevier.com/locate/ijimpeng

THE EFFECT OF OFFSET ON THE PERFORMANCE OF SEGMENTED PENETRATORS

DAVID L. LITTLEFIELD, RICHARD M. GARCIA, AND STEPHAN J. BLESS

Institute for Advanced Technology, The University of Texas at Austin, 4030-2 W. Braker Lane, Austin, TX 78759

Summary—The purpose of this investigation is to study the effect of offset on the performance of segmented penetrators. The Eulerian wave propagation code CTH is used for this purpose. The veracity of the code in predicting the penetration depth of short *L/D* projectiles where channel sidewall interference is present is examined by comparing to a few experiments involving penetration of tungsten alloy cylinders into pre-configured cavities in monolithic armor steel. Having established the validity of the code in predicting this behavior, a series of calculations using four and eight *L/D* = 1 tungsten alloy segment trains at varying degrees of offset is performed, impacting semi-infinite armor steel targets. It is demonstrated that the alignment of the segments can have a considerable impact on the performance of the penetrator.
© 1999 Elsevier Science Ltd. All rights reserved.

INTRODUCTION

It is well known that the penetration depth P of cylindrical penetrators, when normalized by the length L, increases as the aspect ratio L/D decreases. This is particularly true of $L/D < 1$ penetrators at hypervelocities. The phenomenon suggests that the penetration depth of large aspect ratio penetrators can be increased if the penetrator is subdivided into a large number of short L/D segments. Because of their great potential for increased penetration efficiency, segmented rods have been investigated by a number of researchers (e.g., see [1] - [3]). In general, the penetration efficiency of the segmented rod will always be greater than its *parent rod*; that is, the rod that is formed from removing all of the space between each of the segments.

In practice, however, there are several practical difficulties associated with the implementation of segmented penetrators that can limit their performance. For example, the spacing S between each of the penetrators in the segment train must be sufficient to insure the penetration of preceding segments has ceased. In this way, the segments that preceded it into the cavity do not impede the penetration of any particular segment. Another difficulty is associated with offset between the segments in the segment train; it is essential that the segments remain highly aligned during penetration. Slight offsets in the alignment of the segments can result in interference with the sidewalls of the penetration channel and degrade the performance.

A possible source of segment misalignment is associated with the deployment of a segmented penetrator. For example, one way to produce a segmented penetrator might be to launch it in a collapsed (parent) configuration and separate the segments during flight. As the parent rod flies, it is subject to a cyclic damped pitching motion that is a natural consequence of launching long rods. Thus, when the segments are deployed it is likely that the segment train will have pitch associated with it, as is shown in Fig. 1. Naturally, the cyclic pitching must stop after the seg-

0734-743X/99/$ - see front matter © 1999 Elsevier Science Ltd. All rights reserved.
PII: S0734-743X(99)00103-7

ments are deployed since it is elastic bending down the length of the rod that causes the pitching motion. After separation, the center-to-center offset of the segments, δ, is related to the segment geometry and the pitch α of the parent rod at the time of deployment as $\delta = (S + L) \tan \alpha$.

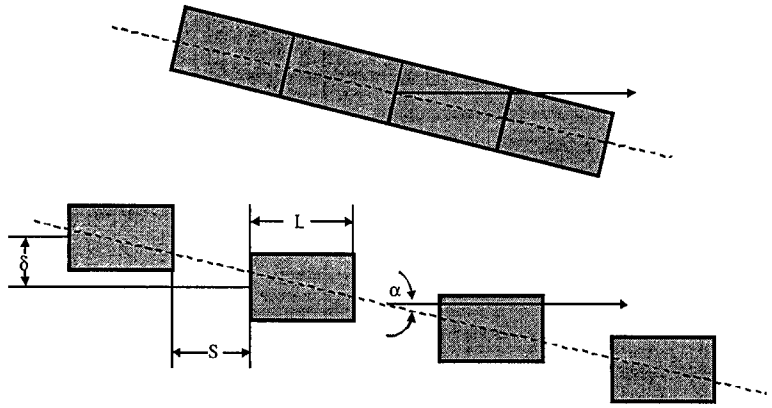

Figure 1. Deployment of a segment train.

In this study, the effect of offset on the performance of segmented penetrators is studied. The Eulerian wave propagation code CTH is used for this purpose. An experimental study was first performed to verify predicted penetration depths of short aspect ratio projectiles, when subjected to cavity sidewall interference. In the tests, L/D = 1 tungsten alloy cylinders were fired into semi-infinite armor steel blocks containing pre-drilled holes. The aim point of the cylinders was varied from shot to shot to produce various degrees of interference between the sidewall of the hole and the cylinder. In the second part of this investigation, the effect of offset on the performance of multiple segment trains was studied parametrically, by performing computations of four and eight L/D = 1 segment trains for a range of offsets.

EXPERIMENTS

The purpose of the experimental portion of this study was to verify the veracity of the code in predicting the penetration channel details when a semi-infinite target is impacted by pitched multiple segment trains. In practice, however, achieving pitch for a multiple segment train in a repeatable, controlled manner is somewhat difficult; to simplify the experimental procedure it was decided to impact single L/D = 1 penetrators into a semi-infinite target containing a pre-drilled hole, at various degrees of offset. The hole in the target was intended to represent the penetration channel created by three previous segments, each of which did not result in any channel sidewall interference.

The experimental geometry is illustrated in Fig. 2. The targets were 4030 steel with a hardness of BHN 277; the targets were 125 mm thick by 155 mm square. The hole diameter, D_h, was maintained at 28 mm; the hole was 79 mm deep. The included angle at the bottom of the hole was 118°. The 22 g L/D = 1 tungsten alloy penetrators, with a length and nominal diameter of 11.9 and 12 mm, respectively, were impacted onto the target with a velocity of 2.5 km/s. For these conditions, the normalized hole diameter D_h/D for the target is about 2.3, which is close to the value reported experimentally (e.g., see [4]) for the impact of L/D = 1 segments at this velocity. The offset δ is the distance measured between the centerlines of the pre-drilled hole and target, respectively, and ε is the amount of overlap between edges of the penetrator and pre-drilled hole [i.e., $\varepsilon = \delta - (D_h - D)/2$].

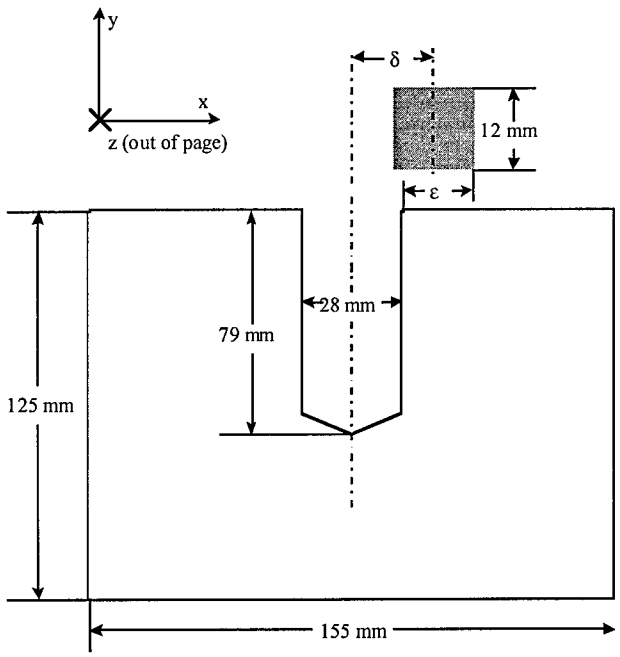

Figure 2. Test configuration.

Results from the tests are given in Table 1. Shots 313 and 322 had the same offset δ of 17 mm; Shot 296 had an offset of 10 mm. These two offsets represent near limiting cases of sidewall interference, producing either complete or no additional penetration from the segment when it impacts the base of the pre-drilled hole. For δ = 10 mm and 17 mm the normalized overlaps ε/D are 0.16 and 0.75, respectively. The change in penetration depth ΔP is 25 mm in Shot 296; the penetration efficiency $\Delta P/L$ associated with this change is 2.08. This value is close to the penetration efficiency reported in the literature (e.g., see [4]) for L/D = 1 cylinders, which is about 2.17 at 2.5 km/s, suggesting that there was little or no degradation in penetration associated with interference of the channel sidewall. A side view of the crater from this test is shown in Fig. 4. On the other hand, in Shots 313 and 322 the change in hole depth ΔP is near zero, indicating that channel sidewall interference is significant at this offset. Views of the crater from Shot 313 are shown in Fig. 3.

Table 1. Test data

Shot	*Velocity (km/s)*	*Offset δ (mm)*	*ΔP (mm)*
296	2.50	10	25
313	2.45	17	1
322	2.39	17	0

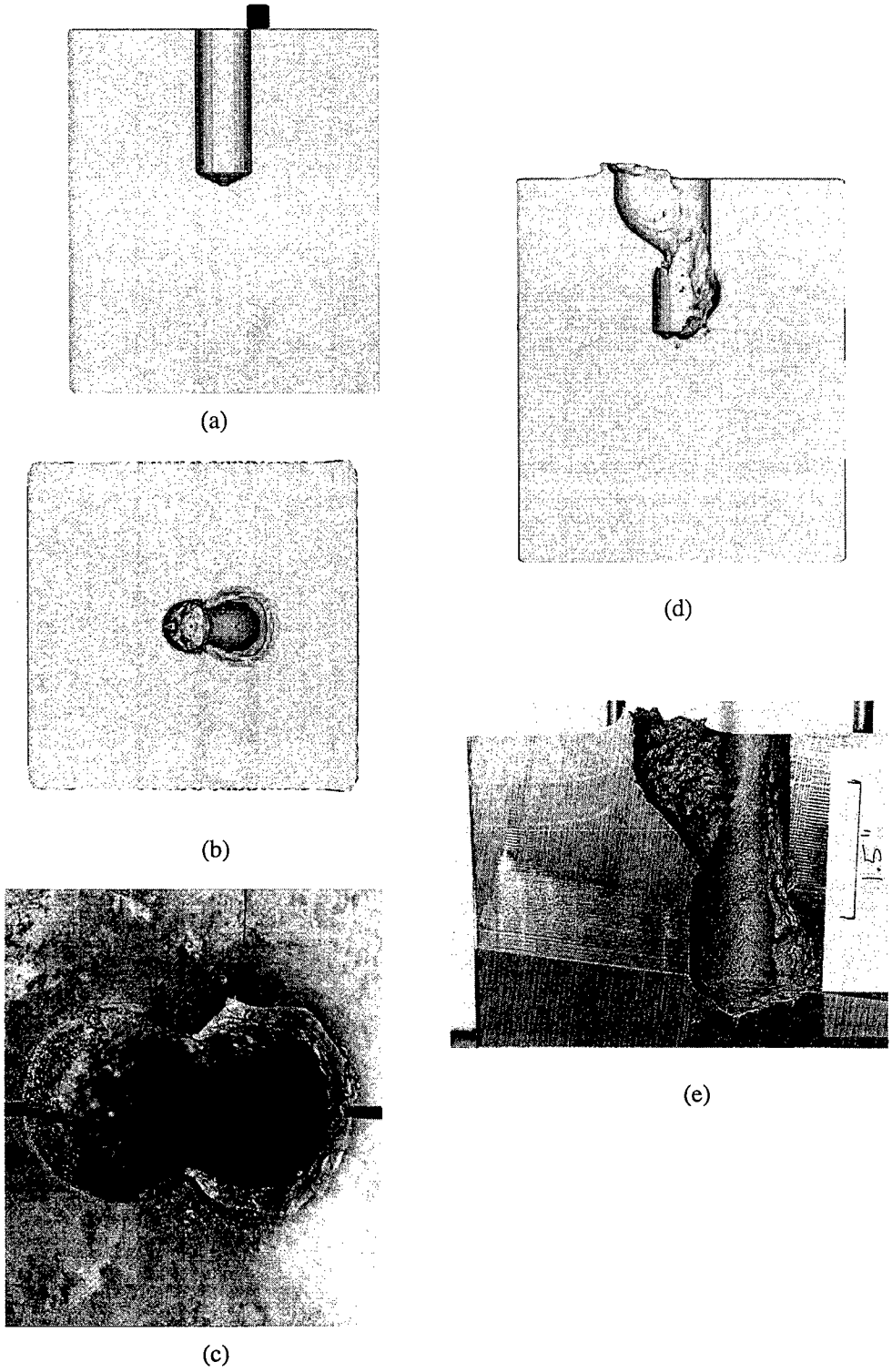

Figure 3. Test and simulation results from Test 313: (a) initial configuration, (b) face view at 80 μs from simulation, (c) face view from test, (d) cross section at 80 μs from simulation, and (e) cross section from test.

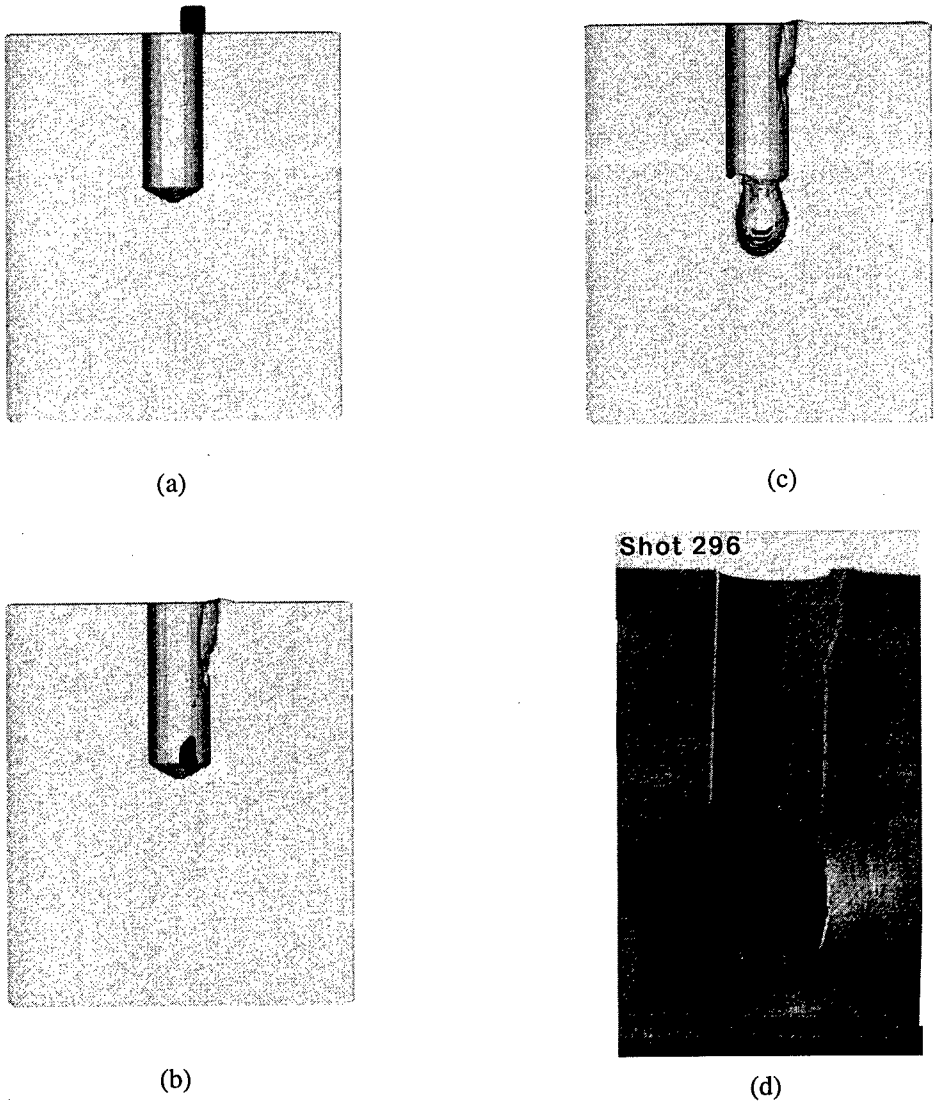

Figure 4. Test and simulation results from Test 296: (a) initial configuration, (b) cross section at 30 μs from simulation, (c) cross section at 80 μs from simulation, and (d) cross section from test.

CODE VALIDATION

Numerical simulations were carried out using the June 1996 version of the three-dimensional, multi-material Eulerian hydrocode CTH [5]. CTH uses the van Leer algorithm for second-order advection that has been generalized to account for a non-uniform and finite grid, and multiple materials; CTH also has an advanced material interface algorithm for the treatment of mixed cells [6]. Several advanced equation-of-state and constitutive models are available in the code [7].

The target and penetrator geometry used in the simulations was identical to those presented in Fig. 2, except the width of the target was increased to 180 mm to insure semi-infinite behavior (in the tests, the target plate was backed up with a steel witness block for the same reason). The symmetry of the impact scenario at $z = 0$ was exploited in the simulations and only half of the problem was run (refer to Fig. 2 for the location of the z - axis). A total of eight zones were used across the diameter of the penetrator. The zoning was maintained cubical in regions of the grid where strong interactions were expected, estimated to be one penetrator diameter beyond furthest lateral extent of the target hole and penetrator, and one diameter beyond the expected penetration depth. A zoning sensitivity study was not performed, but previous studies for long rods have shown that this zoning is adequate to provide reasonable numerical convergence [8].

Penetrator and target material properties used in the simulations are given in Table 2. The Mie-Grüneisen equation of state and the Johnson-Cook viscoplastic model [9] were used to describe the constitutive response. A tensile-void insertion model was used to model material failure, wherein the void is introduced into a cell whenever the mean stress exceeds a predefined value of $-p_{fail}$. Parameters required in the Mie-Grüneisen model are the reference density ρ_{ref}, the bulk sound speed c_b, slope of the U_s - U_p curve s, and the specific heat at constant volume c_v, and are given in Table 2. Likewise, the empirical constants a, b, c, m, and n in the Johnson-Cook viscoplastic model are listed in Table 2. The melt temperature, T_{melt}, is also used in the Johnson-Cook model to insure hydrodynamic behavior at temperatures above the melt temperature. Poisson's ratio ν is required for modeling elastic deformations, and is also listed in Table 2.

Table 2. Penetrator and target material properties

	Material	
Property	*Tungsten Alloy*	*RHA*
ρ_{ref} (g/cm^3)	17.3	7.85
c_s (m/s)	3850	4500
s	1.44	1.49
Γ_{ref}	1.58	2.17
c_v (J/kg K)	135	450
ν	0.3	0.29
a (GPa)	1.35	0.744
b (GPa)	0.0	0.503
c	0.0600	0.0147
m	1.00	1.02
n	--	0.265
T_{melt} (K)	1498	1783
p_{fail} (GPa)	-2.00	-2.00

The penetrator material was assumed to be a generic ballistic tungsten alloy, and the target material rolled homogeneous armor (RHA) of hardness BHN 277. Target material properties given in the table are interpolated values taken from historical data that has been generated for armor steels with hardnesses from BHN 286 to 467 [10].

Results from the simulations are compared with the test data in Figs. 3 - 4. In Figs. 3b and d, the face views and cross sections of the target from a simulation of Shot 313 are shown at 80 μs after impact. The corresponding views from the test are shown in Figs. 3c and e, respectively. Figure 3a shows the initial impact geometry. Agreement between the calculations and test results is quite good; both predict that at this offset the penetrator does not significantly contribute to the depth of the penetration channel. The channel diameter and overall shape are captured very well in the simulation. In Fig. 4c, a cross section of the target from a simulation of Shot 296 is shown 80 μs after impact; Fig. 4d shows the corresponding test result. Figure 4a shows the initial impact geometry. The calculation predicts the change in penetration depth ΔP associated with impact of the segment; the calculated value is 26 mm, which is in good agreement with 25 mm from the test given in Table 1. The penetration efficiency associated with this change $\Delta P/L$ is 2.17. However, good agreement in the final penetration depth does not imply that the transient details of the impact are modeled correctly. For example, in Fig. 4b, the penetration channel geometry is shown at 30 μs after impact; a time just before the segment impacts the base of the pre-drilled hole. Comparing the penetrator shape with its initial configuration shown in Fig. 4a, it is evident that the segment has lengthened as a result of interaction with the sidewall. Without this length enhancement, the penetration depth of the segment changes a small amount (a calculation of the same segment striking along the centerline of the hole results in a ΔP of 23 mm). It is unknown whether the length enhancement occurred in the tests, but more than likely the edge of the segment simply sheared off when it contacted the edge of the hole. The failure model used in the simulations, on the other hand, is rather simplistic and is intended primarily to model spall failure, and will not capture this shear failure.

PARAMETER STUDIES

Having established a reasonable agreement between the tests and computations, a series of calculations was performed to investigate the effect of offset on the penetration of multiple segment trains into semi-infinite targets. The setup for the computations is shown in Figure 5. A total of six simulations were performed with four-segment trains of $L/D = 1$ cylindrical penetrators at offsets δ varying from 0 to $2D$. The initial spacing S between the segments was maintained at $2.5D$. Two additional calculations were performed with eight-segment trains, having a segment spacing of $2.5D$ and offsets of 0 and $0.25D$. The impact velocity in all the simulations was 3.0 km/s.

In Table 3, specifics of the geometry for each of the computations are described. Here, n is the number of penetrators in the segment train. The equivalent pitch angle α is also given for each condition. Note that the pitch angles listed are quite large compared to the value that might be anticipated from the deployment of a segment train. However, longer segment trains at more realistic pitch angles will still result in channel sidewall interactions during the later stages of penetration; the short segment trains considered here simply start their interactions earlier, and can be run with considerably less computer time. The target dimensions were kept large enough to insure semi-infinite behavior in all the calculations. Thus, the lateral dimensions of the target increased as the offset increased. The zoning and material properties used on the simulations were identical to those given in Table 2 and described in the previous section.

Four Segment Trains

Results from the simulations of the four segment train are summarized in Fig. 6, where two measures of penetration efficiency (the penetration depth, normalized by both L and nL, where n is the number of segments), are shown versus the normalized offset δ/D. At zero offset, P/nL approaches a limit close to its value for a $L/D = 1$ cylindrical penetrator, suggesting that for this spacing the interference between the segments is minimal. That is, the total penetration depth is the sum of the penetration depths for each of the individual segments. Likewise, at two diameters

of offset *P/L* approaches its limiting value for an *L/D* = 1 segment, indicating that at this offset each of the projectiles in the segment train penetrate the target in an independent manner. There is a slight increase in penetration efficiency at 0.25 diameters of offset, which is probably somewhat anomalous since it is caused by an elongation of the fourth segment in the train, similar to the behavior illustrated in Fig. 4b. In all likelihood, the penetration efficiency does not increase at this offset.

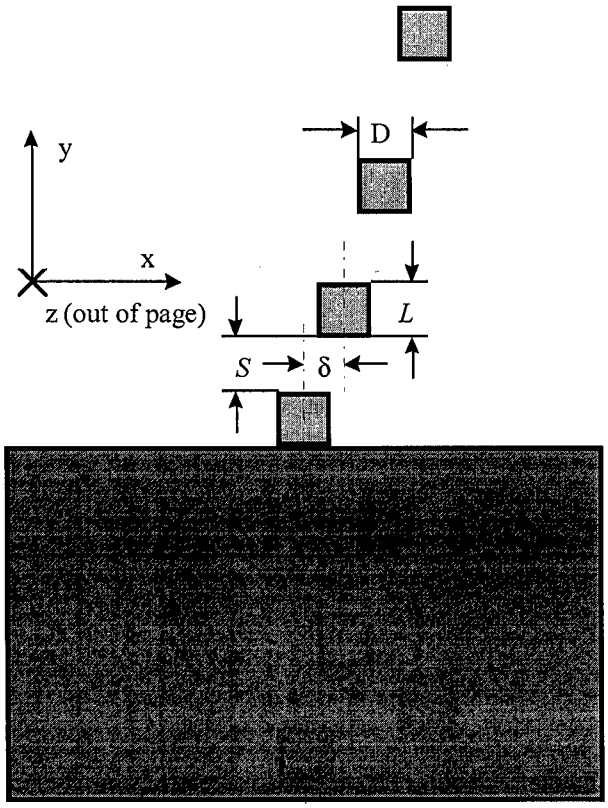

Figure 5. Setup for computations.

Table 3. Segment train dimensions

n	*L (cm)*	*D (cm)*	*S (cm)*	*δ (cm)*	*L/D*	*S/D*	*δ/D*	*α (deg)*
4	1.2	1.2	3.0	0	1.0	2.5	0	0
4	1.2	1.2	3.0	0.3	1.0	2.5	0.25	4.1
4	1.2	1.2	3.0	0.6	1.0	2.5	0.5	8.1
4	1.2	1.2	3.0	1.2	1.0	2.5	1.0	15.9
4	1.2	1.2	3.0	1.8	1.0	2.5	1.5	23.2
4	1.2	1.2	3.0	2.4	1.0	2.5	2.0	29.7
8	1.2	1.2	3.0	0	1.0	2.5	0	0
8	1.2	1.2	3.0	0.3	21.0	2.5	0.25	4.1

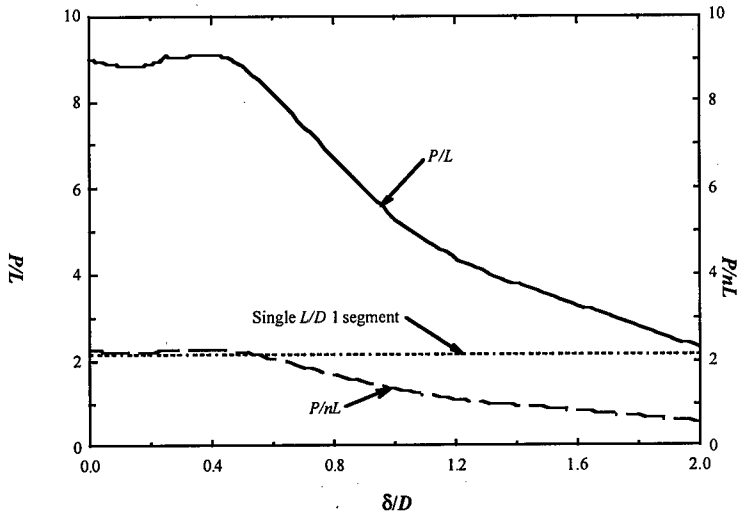

Figure 6. Penetration efficiency versus normalized offset for impact of a four segment train on a semi-infinite target.

Details of the penetration behavior are illustrated in Figs. 7 – 8, where material plots are shown at various times for offsets of $0.5D$ and $1.0D$, respectively. For $\delta/D = 0.5$, Fig. 7 shows that by 15 μs the second segment in the train enters the penetration channel and does not interfere with the sidewall. Further, the first segment appears to have ceased penetration by this time, and will not significantly interfere with the penetration of the second segment when it reaches the base of the cavity. By 40 μs, the third segment has entered the penetration channel and is somewhat elongated from its interaction with the sidewall. The fourth segment is subjected to significant interference with the crater sidewall, resulting in substantial elongation and lateral displacement. As a result, the penetration channel is skewed and has a narrow diameter near its base at 100 μs, when the penetration has ceased. For $\delta/D = 1.0$, Fig. 8 shows that by 15 μs the second segment in the train begins to penetrate the target and interferes with the sidewall of the penetration channel. By 40 μs, the second segment has resulted in a narrow penetration channel at the base of the crater, but the third segment has penetrated primarily from the original target face and does not contribute to the penetration depth at the base of the original channel. The fourth segment, on the other hand, gets elongated after impact and acquires a significant lateral displacement; as a result it contributes somewhat the depth of penetration at the base of the original crater. It is clear from these results that the interactions between segments can be quite complex and variable as the offset changes.

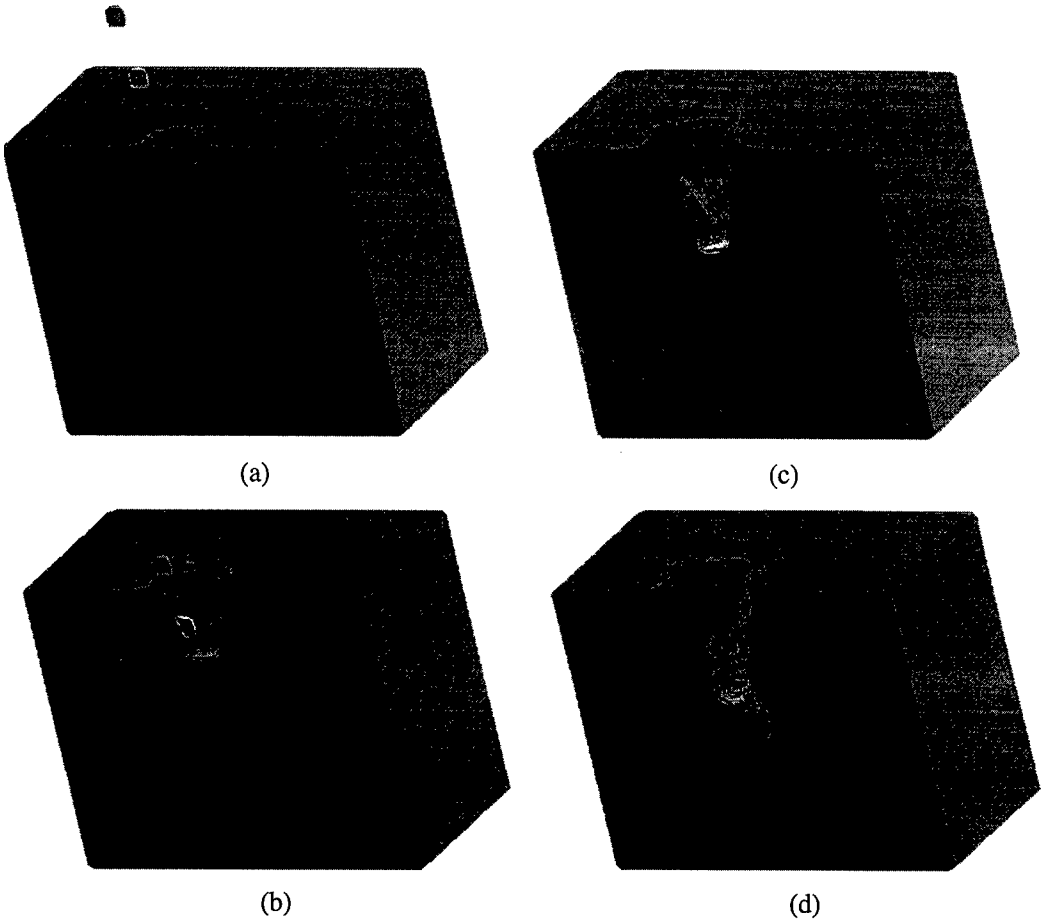

Figure 7. Penetration channel geometry from the impact of a four $L/D = 1$ segment train with $\delta/D = 0.5$ at various times after impact: (a) 15 μs, (b) 40 μs, (c) 60 μs, and (d) 100 μs.

Eight Segment Trains

Two simulations were performed with eight segment trains, one with zero offset and one with 0.25 diameters of offset. Results from the simulations are illustrated in Figs. 9 and 10. In Fig. 9, material plots are shown for the penetration of the last four segments when the offset is zero. The results show that no channel sidewall interference occurs for any of the segments, and that the spacing of each segment allows the penetration to occur in a fairly independent manner; that is, the segments are not impeded by the ones preceding them in the penetration cavity. The penetration efficiency based on the collapsed length nL is 2.21, which is reasonably close to the values given in Fig. 6 for the single $L/D = 1$ segment and the four segment train at zero offset. In Fig. 10, material plots are shown at various times when the offset is $0.25D$. The first three segments enter the penetration channel without any interference with the cavity sidewall, but by 60 μs the fourth segment has entered the channel and is somewhat elongated from its contact with the sidewall. Likewise, the fifth and sixth segments are elongated from sidewall interference. By 110 μs, however, the seventh segment has entered the penetration channel and penetrates primarily the sloped sidewall of the crater a few diameters down from the original target face. As a result, it acquires a significant lateral displacement, causing it to gouge the opposite sidewall of the cavity instead of contributing to the depth of the cavity. Likewise, the eighth segment gets trapped in the

sidewall and does not contribute appreciably to the depth of the channel. The penetration efficiency based on the collapsed length is 1.77, which is lower than the value for the four segment train at this offset, which exhibited no degradation in penetration efficiency. However, a more realistic value for the penetration efficiency is probably somewhat lower than this since the depth of this cavity was enhanced by elongation of the fourth, fifth and sixth segments. Moreover, results for penetration of the seventh and eighth segments are questionable since they rely so strongly on the topology of the penetration channel created from the six segments that preceded them into the cavity. Nevertheless, at the minimum the results do suggest that when offset is present, increasing the number of segments in the train results in diminishing performance for the segments added to the train.

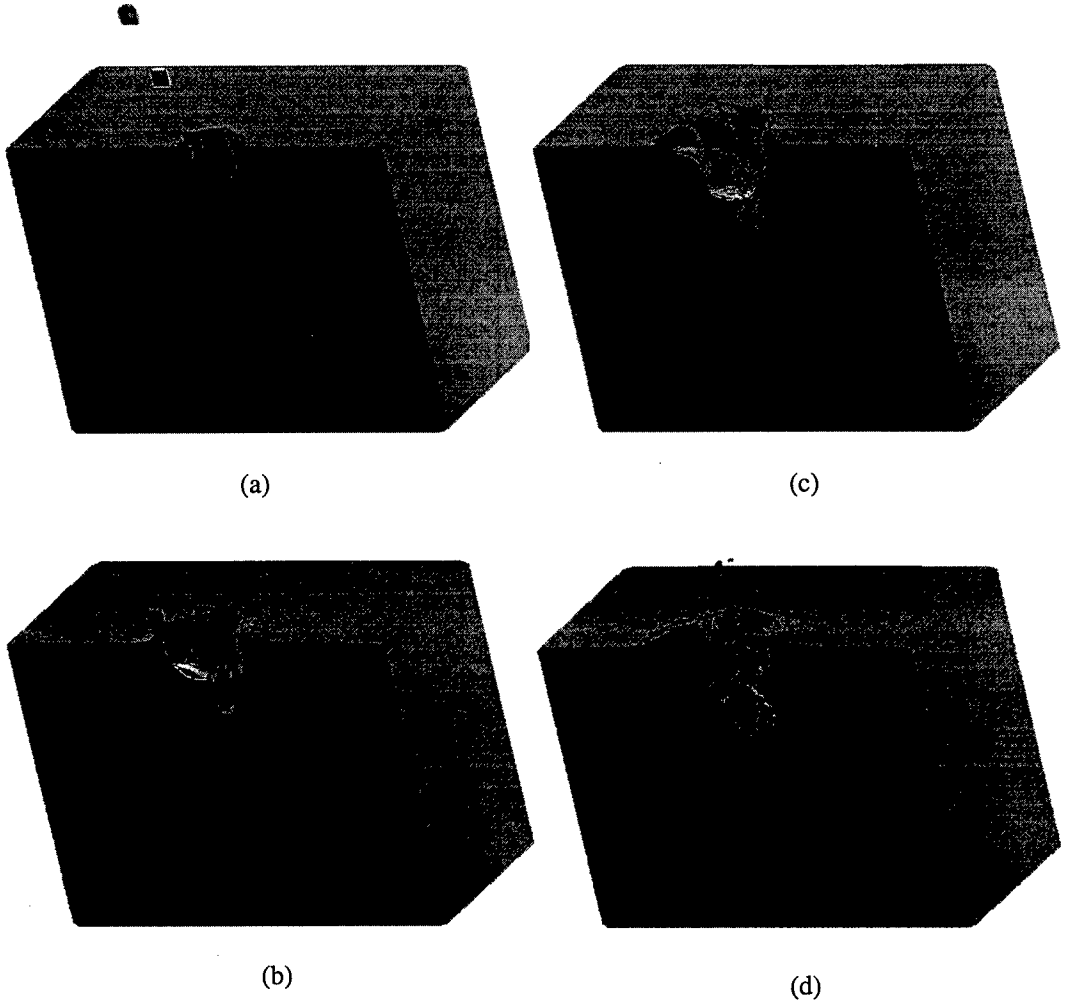

Figure 8. Penetration channel geometry from the impact of a four L/D = 1 segment train with δ/D = 1.0 at various times after impact: (a) 15 μs, (b) 40 μs, (c) 50 μs, and (d) 100 μs.

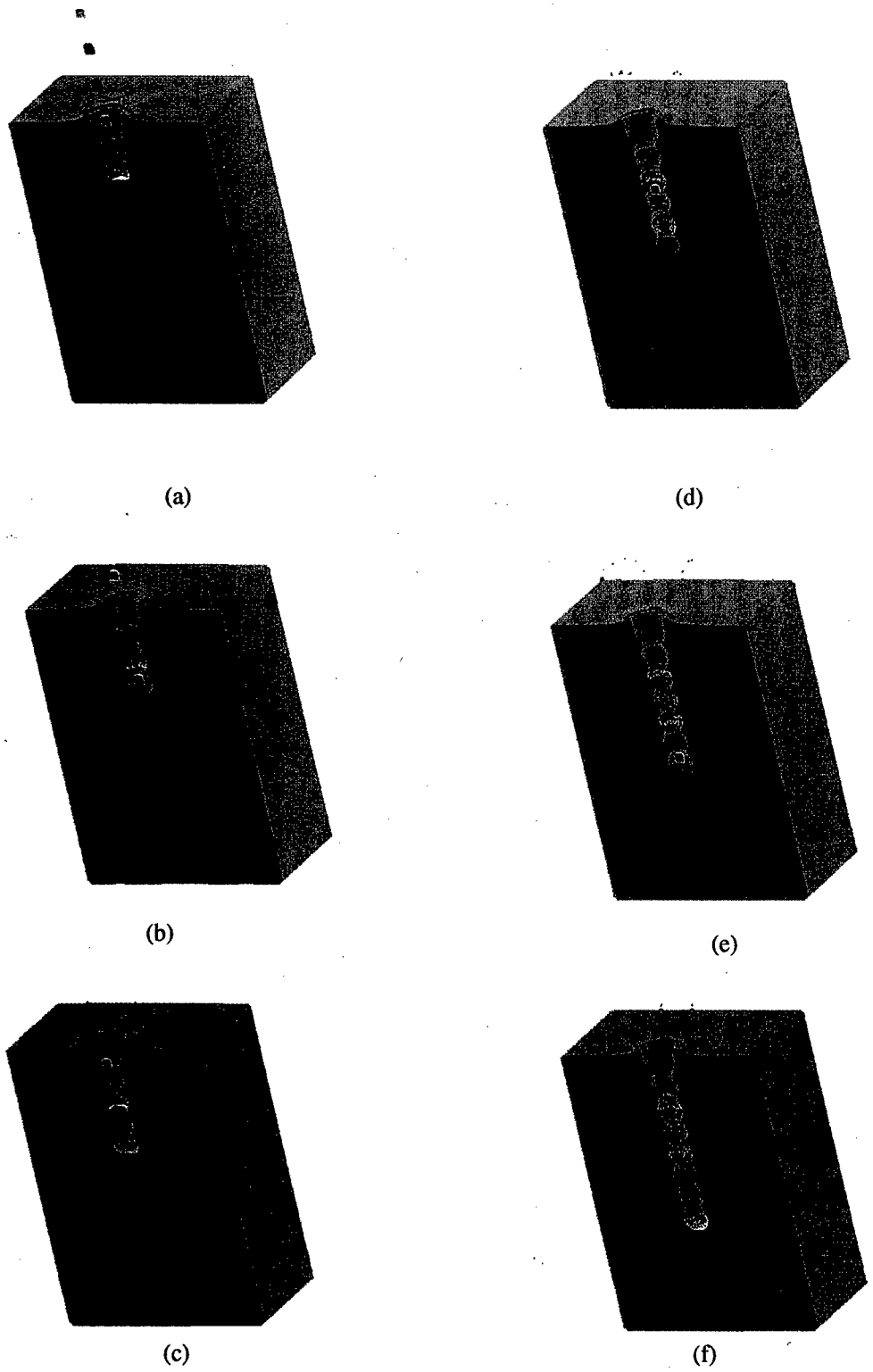

Figure 9. Penetration channel geometry from the impact of a eight L/D = 1 segment train with δ/D = 0 at various times after impact: (a) 60 μs, (b) 90 μs, (c) 110 μs, (d) 130 μs, (e) 160 μs, and (f) 200 μs.

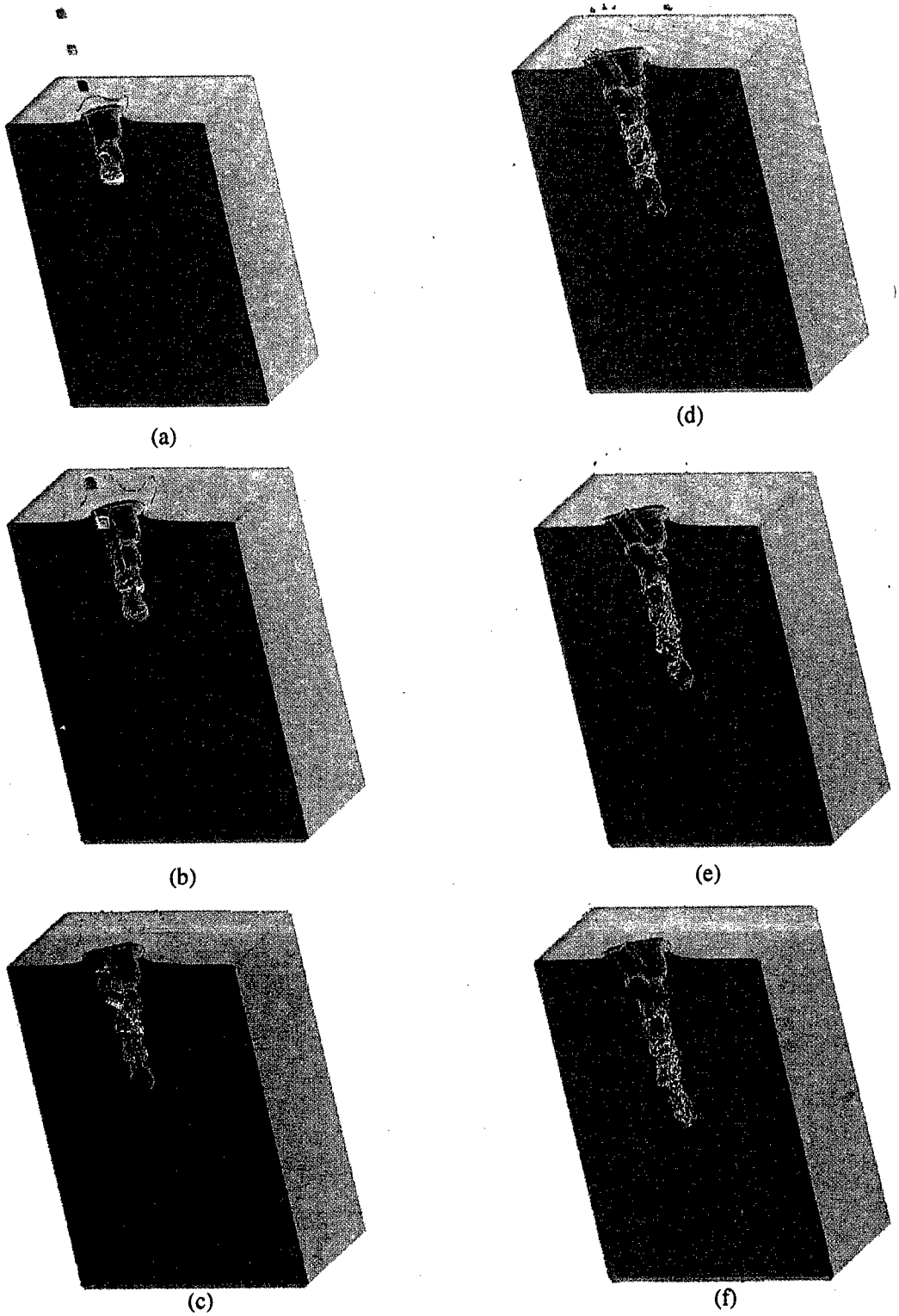

Figure 10. Penetration channel geometry from the impact of an eight *L/D* 1 segment train with $\delta/D = 0.25$ at various times after impact: (a) 60 μs, (b) 90 μs, (c) 110 μs, (d) 130 μs, (e) 160 μs, and (f) 200 μs.

CONCLUSIONS

The effect of offset on the performance of segmented penetrators was investigated in this study. The results show that when the offset is enough to produce interference between the trailing segments and the sidewall of the penetration cavity, the degradation in penetration can be significant.

Acknowledgments—This work was supported by the U.S. Army Research Laboratory (ARL) under contract DAAA21-93-C-0101. The authors also wish to acknowledge computational resources provided by the Texas Advanced Computation Center at the University of Texas at Austin.

REFERENCES

1. D. L. Orphal and R. R. Franzen, Penetration mechanics and performance of segmented rods against metal targets. *Int. J. Impact Engng.*, **10**, 427 – 438 (1990).
2. P. Naz and H. F. Lehr, The crater formation due to segmented rod penetrators. *Int. J. Impact Engng.*, **10**, pp. 413 – 425 (1990).
3. V. Hohler and A. J. Stilp, Penetration performance of segmented rods at different spacing – comparison with homogeneous rods at 2.5 – 3.5 km/s. *Proc. 12th Int. Symp. On Ballistics*, **3**, pp. 178 – 187 (1990).
4. C. E. Anderson, Jr., B. L. Morris, and D. L. Littlefield, A penetration mechanics database. SwRI Report No. 3593/001, January (1992).
5. J. M McGlaun, S. L. Thompson and M. G. Elrick, CTH: A three dimensional shock wave physics code. *Int. J. Impact Engng.*, **10**, pp. 351 – 360 (1990).
6. R. L. Bell, An improved material interface reconstruction algorithm for eulerian codes. Sandia National Laboratories Report No. SAND 92-1716, September (1992).
7. S. A. Silling, Stability and accuracy of differencing methods for viscoplastic models in wavecodes. *J. Comp. Phys.*, **104**(1), pp. 30 – 40 (1993).
8. D. L. Littlefield and C. E. Anderson, Jr., A study of zoning requirements for 2-D and 3-D long-rod penetration. Proceedings of the 1995 APS Topical Conference on Shock Compression of Condensed Matter, Seattle, WA, August 13 – 18 (1995).
9. G. R. Johnson and W. H. Cook, Fracture characteristics of three metals subjected to various strains, strain rates, temperatures and pressures. *Engng. Fract. Mech.*, **21**(1), pp. 31 – 48 (1985).
10. G. C. Bessette, Modification of Johnson-Cook parameters for RHA. Institute for Advanced Technology Technical Memorandum No. IAT.TM 0019, April (1998).

PERGAMON

International Journal of Impact Engineering 23 (1999) 561–572

INTERNATIONAL JOURNAL OF IMPACT ENGINEERING

www.elsevier.com/locate/ijimpeng

ACTIVE ATTITUDE CONTROL OF GUN LAUNCHED PROJECTILES

DAVID J. LIQUORNIK*, FENG WEI YANG**, MARK C. ZWIENER*, and RICHARD A. HAYAMI*

*Aerophysics Research Center of the University of Alabama in Huntsville; **Morgan Research Corporation

Summary - This paper describes a novel technique for controlling the attitude of a projectile launched by a light gas gun operated by the University of Alabama in Huntsville (UAH). This capability is required to evaluate the effects of the relative attitude orientations of the interceptor and target in hit-to-kill engagements since this affects the footprint of the projected area of the interceptor on the target. In a ground based experiment, the attitude of the target can be readily set at any arbitrary orientation relative to the shot-line by adjusting the target support system. The projectile (Interceptor) attitude at impact without attitude control would normally be at zero pitch and yaw angles except for gun or flight induced variations. Since the interceptor is expected to impact the target at angle of attack at various angles other than zero, there is a need for capability to control the attitude of the projectile after launch to hit the target at specified angles of attack. © 1999 Elsevier Science Ltd. All rights reserved.

INTRODUCTION

In order to provide a ground based test capability to obtain hypervelocity impact data of missile interceptor engagements, a number of requirements need to be met. These include capability to launch projectile configurations that are at least one quarter scale of the full scale vehicle, match the scaled mass, reasonable match in mass distribution to that of the full-scale vehicle, match the closing velocities of the actual intercept engagement conditions vehicle, and match the footprint of the intercepting vehicle on the target.

The use of light gas guns is needed to meet the test velocity requirements. The size and projectile fidelity requirements could be met with some gun system modifications. The requirements for matching the footprint of the interceptor vehicle on the target were more challenging. The orientation of the target relative to interceptor shot line can be readily adjusted to various pitch and yaw angles as well as in the vertical and lateral displacement of the interceptor center of gravity (Cg) from that of the target Cg by adjusting the target suspension system in the impact chamber. Without active attitude control of the interceptor vehicle model, however, its normal flight would be at nominal zero pitch and yaw angle, with its cross sectional projected frontal area as the footprint on the target. Since this represents only one of the possible engagement conditions for a full-scale interceptor with attitude control, the need for attitude control in the gas gun launch tests becomes clear.

In order to meet these ground test capability requirements, Hayami proposed a novel concept for active attitude control of gun launched projectiles (1). Active injection of gases and fluids into the wake and boundary layer of light gas gun launched vehicles have been performed previously (2,3)

0734-743X/99/$ - see front matter © 1999 Elsevier Science Ltd. All rights reserved.
PII: S0734-743X(99)00104-9

for modification of the flow properties, however, this technique had not been applied to the active attitude control of light gas gun launched projectiles to the authors' knowledge. The results obtained from concept validation tests performed under internal funds were reported previously (4). Refinements and analytical efforts continued under development efforts funded by the US Army Space and Strategic Defense Command (now Space and Missile Defense command (5, 6, 7) as well as with internal UAH funds.

Other options for attitude control were considered. These include flight through high ambient pressure atmosphere with a vehicle with a nose shaped to cause predictable pitch angle change as developed for sled track tests at Sandia National Labs (8) and use of bow shock reflected from a surface near the flight trajectory to a location on the vehicle behind its center of gravity as tried recently by AEDC (9). We decided to use the reaction jet control method due to its predictable behavior and prior experience with gas injection techniques in ballistic range projectiles.

The principles for the operation of the attitude control system selected are described with the governing equations in the next two sections. The experimental features for the validation effort, including the facilities, instrumentation, the initial vehicle design used for concept validation and the vehicle configurations used in three subsequent test series, are described next. The attitude control results obtained in the three test series for a total of 28 tests are then presented followed by a discussion of the results. The paper concludes with a summary.

ATTITUDE CONTROL METHOD

Reaction Jet Attitude Control

The method selected to achieve attitude control of a gun launched projectile relies on the use of reaction jet(s) releasing compressed gas through nozzle(s) oriented normal to the projectile flight axis. This method relies solely on the reactive forces of the stored gas released through the nozzle(s) for generating the rotational motion required to achieve the desired pitch angle attitude at target impact. In fact, ideally, flight of the projectile prior to impact should be through the lowest possible density atmosphere to avoid aerodynamic force effects.

For attitude control by rotational motion of the vehicle in the pitch plane, the angular acceleration can be induced by acting with a force normal to the vehicle axis, but in the plane of rotation, at some distance from the center of gravity (C_g) of the vehicle. If only one reaction jet nozzle located at the nose is used, the component of the pitch forces normal to the flight axis will cause a drift of the trajectory of the C_g of the vehicle from the nominal flight axis in the pitch plane. This drift in the C_g of the vehicle from the nominal trajectory can be avoided if another reactive jet nozzle located at other end of the vehicle but pointing in the opposite direction to provide an equal and opposite force.

Candidate gases that might be used for the attitude control must be non-reactive with hydrogen used as the projectile driver gas. Readily available candidate gases include nitrogen, argon and helium. Argon is the most efficient of the three gases for attitude control in terms of lowest initial reservoir pressure and pressure decay rate for a given attitude control force. However, we found that nitrogen gas could adequately meet the test requirements, and since nitrogen gas is readily available in our range operations, we decided to use nitrogen as the candidate attitude control gas.

The design of the valve used to load and release the gas stored in the vehicle was kept very simple for reliable operation. This, however, resulted in not being able to easily reduce the reservoir pressure if the desired value was inadvertently slightly exceeded during the gas loading process. Since the pressure overshoot is typically quite small, say less than 20 torr, this does not cause a significant problem. The actual reservoir pressure can be obtained from the measured mass of the stored gas. This pressure together with the actual vehicle velocity measured in the test is then used to calculate a corrected predictive dependence of pitch angle with flight distance. The deviations in the actual measured pitch angle from those predicted were then determined.

Since we recognized that projectile roll must be eliminated for predictable controlled attitude at the target, we developed launch tube honing and polishing procedures to eliminate roll caused by residual hone scoring of launch tube surface. Once these procedure were implemented, we did not experience undesired projectile roll in subsequent tests.

THEORY OF OPERATION

Approach

The following conditions are assumed when approaching a solution to this problem. The model has zero induced pitch or yaw at the muzzle. Aerodynamic effects are assumed negligible due to the low flight chamber pressure. The models velocity remains constant throughout free-flight. The back pressure, (i.e. flight chamber pressure), is less than half of the internal pressure of the model ensuring choked flow at the throat. The throat, smallest diameter, is located at the exit of the nozzle. The direction of force from the gas jet is normal to the longitudinal axis of the model. The change in the models center of gravity and moment of inertia due to gas loss is assumed negligible. Real gas effects are assumed insignificant relative to other sources of error.

Equations describing pitch

Fundamental equation describing rotational motion about a fixed center of gravity,

$$\sum M_{cg} = I\alpha = Fd \tag{1}$$

$$\frac{d^2\theta}{dt^2} = \alpha = \frac{Fd}{I} \tag{2}$$

where θ is the pitch angle, α is the angular acceleration, F is the force, d is the length of the moment arm, and I is the moment of inertia.

Equations for force. The force is proportional to the change in momentum over time.

$$F = \frac{d[mu]}{dt} = m\frac{du}{dt} + u\frac{dm}{dt} = PA + u\rho Au \tag{3}$$

where P is the pressure, A is the cross-sectional area of the orifice, u is the gas velocity, and ρ is the gas density.

Time-varying parameters. Given that the cross-sectional area of the orifice and the gas exit velocity are taken as constant, determine how the force, pressure, and density change with time. Using the following relations, two differential equations are developed to describe the density and pressure variations over time.

$$\frac{dm}{dt} = c_2\rho Au = V\frac{d\rho}{dt} \tag{4}$$

$$\frac{dP}{dt} = u^2\frac{d\rho}{dt} \tag{5}$$

$$P = \rho u^2 \tag{6}$$

$$\frac{d\rho}{dt} = \left(\frac{c_2 Au}{V}\right)\rho \tag{7}$$

$$\frac{dP}{dt} = \left(\frac{c_2\rho Au}{V}\right)u^2 = \left(\frac{c_2 Au}{V}\right)P \tag{8}$$

Equation (7) and (8) illustrate how the density and pressure vary with time. The coefficient, c_2, is used to account for density variations at the throat of the choked nozzle with gas exit velocity of Mach one.

Substituting the solutions for pressure and density results in the following time-varying force eqtn.

$$F(t) = c_1 P_o e^{\left(-\frac{c_2 Au}{V}t\right)} A + c_2 \rho_o e^{\left(-\frac{c_2 Au}{V}t\right)} Au^2 \tag{9}$$

where, P_o is the initial reservoir pressure, ρ_o is the initial reservoir density, and c_1 is the coefficient used to account for pressure variation at the throat.

Time-varying Equation of Motion. Substituting the force eqtn., (9), into the equation of motion, (2), and modifying the time parameter to account for gas loss in the launch tube

$$\frac{d^2\theta}{dt^2} = \frac{d}{I}\left[c_1 P_o A + c_2 \rho_o A u^2\right] e^{\left(-\frac{c_2 Au}{V}(t_1+t)\right)} \tag{10}$$

where t_1 is the time in the launch tube. Integrating twice, the expanded solution for the pitch angle at time t is:

$$\theta(t) = \frac{d}{I}\left[c_1 P_o A + c_2 \rho_o A u^2\right] e^{\left(-\left(\frac{c_2 Au}{V}\right)t_1\right)} \left[\frac{e^{-\left(\frac{c_2 Au}{V}\right)t} - 1}{\left(\frac{c_2 Au}{V}\right)^2} + \frac{t}{\left(\frac{c_2 Au}{V}\right)}\right] \tag{11}$$

Equations Describing Drift

Two forces considered for determining drift are the vertical component of the force exerted by the gas jet and the drop due to gravity.

$$F_y(t) = F(t)\cos(\theta) - m(t)g \tag{12}$$

$F_y(t)$ is the net vertical component of drift and m(t) is the time-varying mass of the projectile. However, the typical effect of gravity on displacement is on the order of 0.1 to 0.2 cm. and may be disregarded. So, consider displacement due to the gas jet and change in mass,

$$\frac{d^2 y}{dt^2} = \frac{F(t)\cos(\theta)}{m(t)} \tag{13}$$

$$m(t) = m_m + m_g(t) \tag{14}$$

where m_m is the model mass and $m_g(t)$ is the mass of the remaining gas. Replacing force in eqn. (13) with eqn. (9) and modifying $m_g(t)$ to account for density changes, results in

$$\frac{d^2 y}{dt^2} = \frac{\left[c_1 P_o A + c_2 \rho_o A u^2\right] e^{\left(-\frac{c_2 Au}{V}(t_1+t)\right)} \cos(\theta)}{m(t)} \tag{15}$$

$$m(t) = m_m(t) + V\rho_o e^{\left(-\frac{c_2 Au}{V}(t_1+t)\right)} \tag{16}$$

Solving eqn.(15) for displacement and substituting eqn (16) for mass loss results in the expanded solution for drift.

$$y(t) = \frac{\left[c_1 P_o A + c_2 \rho_o A u^2\right]\cos(\theta)}{\left[m_m + V\rho_o e^{\left(-\frac{c_2 Au}{V}(t_1+t)\right)}\right]} e^{\left(-\left(\frac{c_2 Au}{V}\right)t_1\right)} \left[\frac{e^{-\left(\frac{c_2 Au}{V}\right)t} - 1}{\left(\frac{c_2 Au}{V}\right)^2} + \frac{t}{\left(\frac{c_2 Au}{V}\right)}\right] \tag{17}$$

EXPERIMENTAL FEATURES

Test Facility

The concept validation test were conducted at the UAH Aerophysics Research Center located on Redstone Arsenal. This facility has three light gas gun systems, each operating on the same principles, but with different kinetic energy / size / mass /velocity capabilities. The gun systems are characterized by their pump tube diameter which is invariant for a given gun system, while different size launch tubes can be used with the three gun systems.

The launcher used for the concept validation tests was the large, or 254 mm diameter pump tube gun system due the requirements for large projectile sizes and closing velocities above 2 km/s. For the initial tests the launch tube used was 100 mm (4") bore diameter. Later tests were performed with the 152 mm (6") and 86.4 mm (3.4") bore diameter launch tubes.

The flight chambers and impact test chamber are normally pumped down to below 1 torr pressure and then filled with Helium at various pressures depending on whether the projectile is saboted or bore fitting. For non-saboted projectiles, a nominal helium pressure of 20 to 50 torr is typically used as buffer to dilute and isolate the hot hydrogen gun gases from any significant amount of oxygen. For projectiles that will have active attitude control reaction jets, the flight chamber gases should be kept at as low a pressure as possible to minimize any effects due to aerodynamic forces.

Diagnostic instrumentation for determining the functioning of the attitude control system include the following:

- flash X-ray with a top down view of the projectile after it exits from the muzzle-shows model integrity, indication of roll, initial tip-off yaw
- flash X-ray (orthogonal) - pre-impact set #1 ~4 m from the target
- flash X-ray (orthogonal) - pre-impact set #2 ~1.8 m from the target
- orthogonal shadowgraph stations ~17 m downrange from muzzle
- high speed camera (Hycam) operating at ~9300 frames per second

Flight Vehicle Design

Concept Validation The initial concept validation design, model EX-1, is shown in Figure 1. This vehicle was 10 cm in diameter and 28 cm long, with reaction jet nozzles at the front and rear of the vehicle. The second concept validation design, EX-2, is shown in Figure 2. This second vehicle design had a conical nose to be more representative shape than the near cylinder geometry of the first design. Yaw stabilizing nozzles were also used in this design, but were eliminated in later designs for simplicity. The EX-2 vehicle was 34.93 cm (13.75") long and 10 cm (4") diameter.

Subscale Test Vehicle Design Series #1 Vehicle Design - Photographs of the assembled vehicle and components are shown in Figures 3 and 4 respectively. This vehicle has an open, cylindrical tube tail with clearance between the outer diameter and the launch tube bore which was 152 mm (6"). There were four 5/8" diameter vents holes at the forward end of the tail to help equalize the pressure between the inner and outer wall of the tail section during the launch cycle. The launch gas pushes the vehicle at the bulkhead between the tail section and the forebody. A nylon sleeve over the vehicle midsection provided the seal for the launch gases and acted as bore-rider for the vehicle. A valve located at the nose of the vehicle was used both for the loading of the gas into the vehicle reservoir and for release of the stored gas on launch acceleration.

This vehicle used only one reaction jet nozzle that is located at the nose. This results in a translational offset drift from the nominal flight trajectory in the pitch plane. This translational drift was taken into account in positioning the target for the correct anticipated hit point. A typical prediction for the pitch angle and translational drift is shown in Figure 5 versus flight distance for this vehicle. The nominal distance of the target from the muzzle for this test series was 50 meters. Flash X-ray photographs taken in the impact chamber about 4 meters uprange of the target are shown in Figure 6.

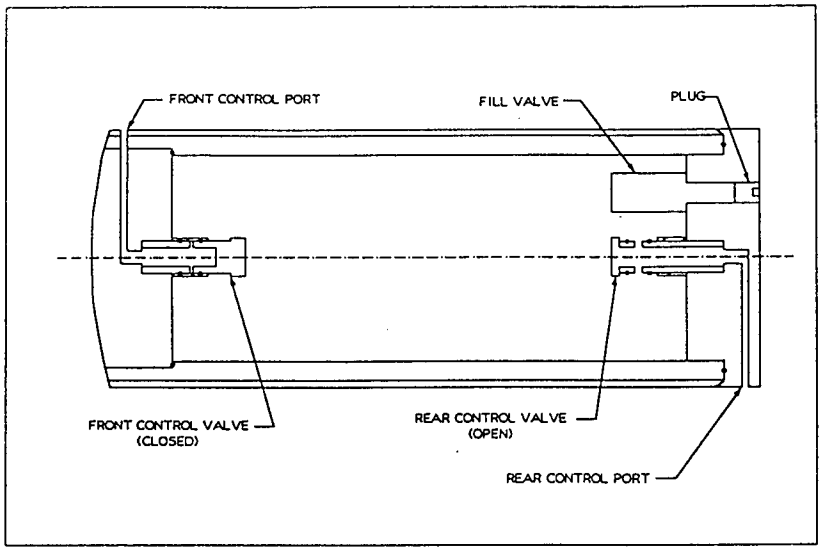

Figure 1. Line Drawing of EX-1 Concept Validation Design Vehicle

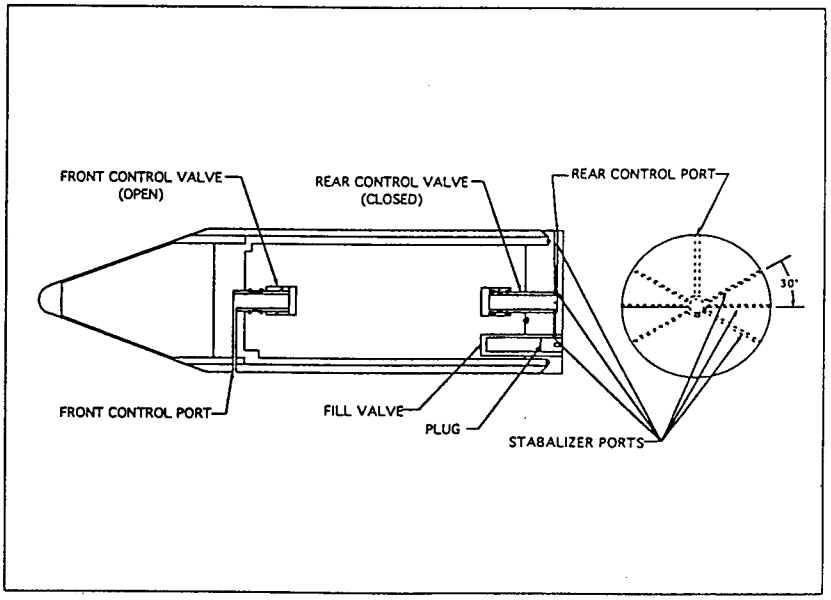

Figure 2. Line Drawing of EX-2 Concept Validation Design Vehicle

Figure 3 Photograph of the Assembled Vehicle for Test Series 1 Design

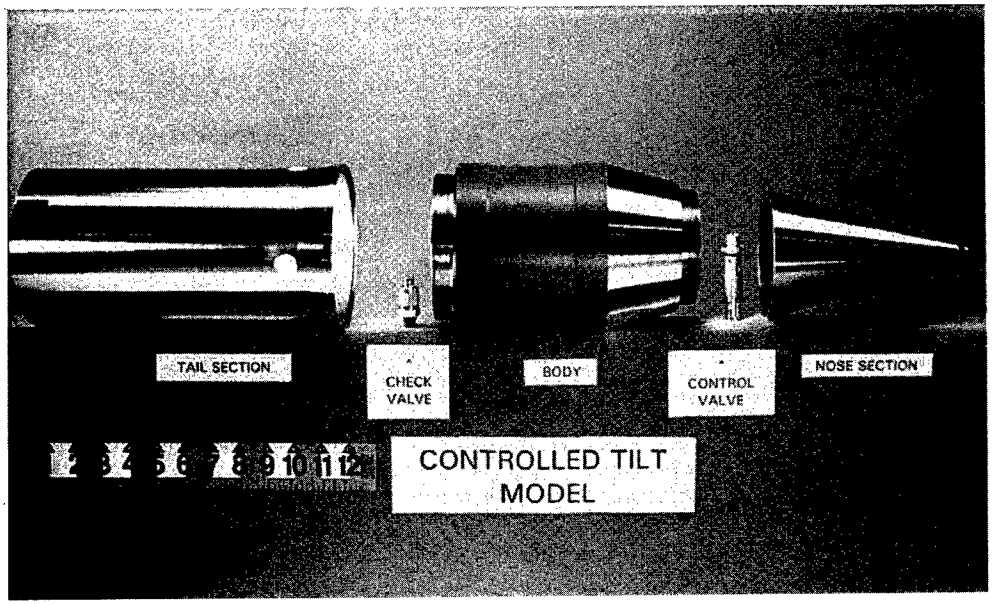

Figure 4 Photograph of the Components of Test Series 1 Vehicle Design

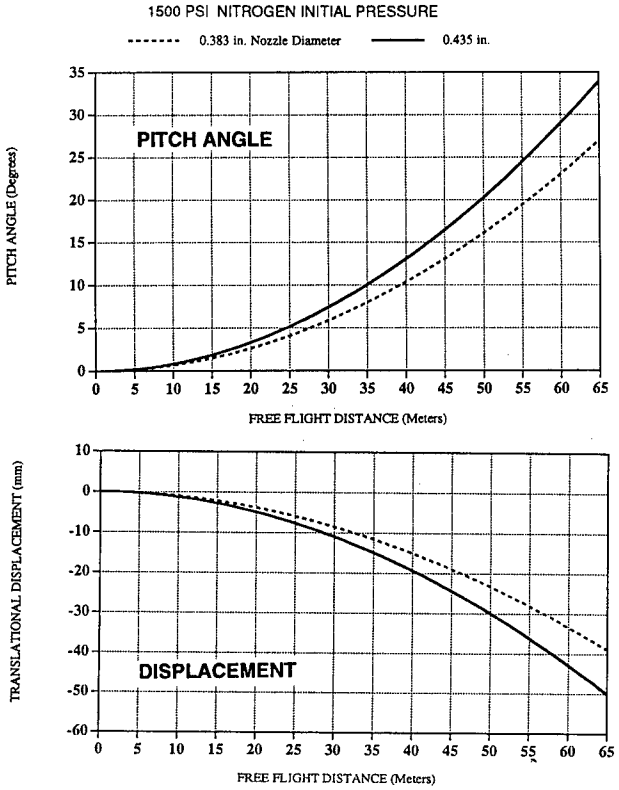

Figure 5 Typical Pre-test Predictions of Pitch Angle and Drift

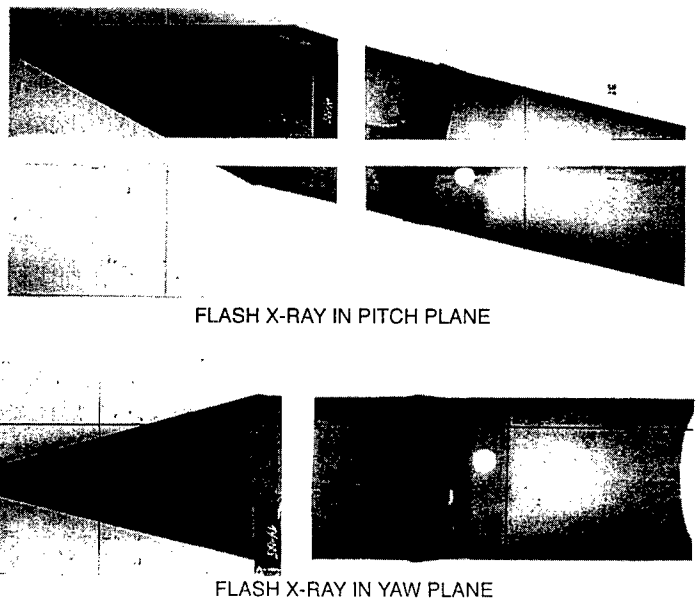

Figure 6 Flash X-ray Photographs of Series 1 Vehicle Taken in the Impact Chamber Up-range of the Target

Series #2 Vehicle Design - A photograph of this vehicle as assembled is shown in Figure 7. This vehicle differs considerably from that in Series 1 tests in that the mid-body is conical, separate bore-riders are used at the nose and at the bulkhead location and the tail is fully vented since the tail structure consists of a short cylindrical ring attached to the fore-body with thick spokes. The bore-riders for this vehicle had outer diameter of 152 mm (6"). The nose was a mass simulator for an ideally conical configuration.

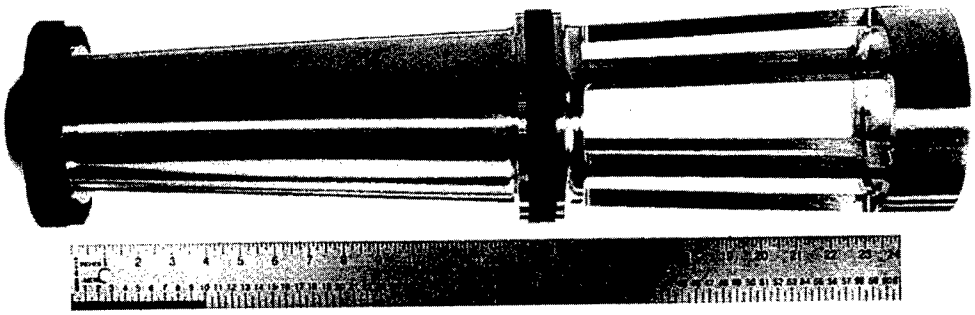

Figure 7. Photograph of Assembled of Test Series 2 Vehicle Design

Series #3 Vehicle Design - A photograph of the assembled vehicle is shown in Figures 8. This vehicle has an open, cylindrical tube tail with clearance between the outer diameter and the launch tube bore which was 86.4 mm (3.4"). There were six 1/2" diameter vents holes at the forward end of the tail to help equalize the pressure between the inner and outer wall of the tail section during the launch cycle.

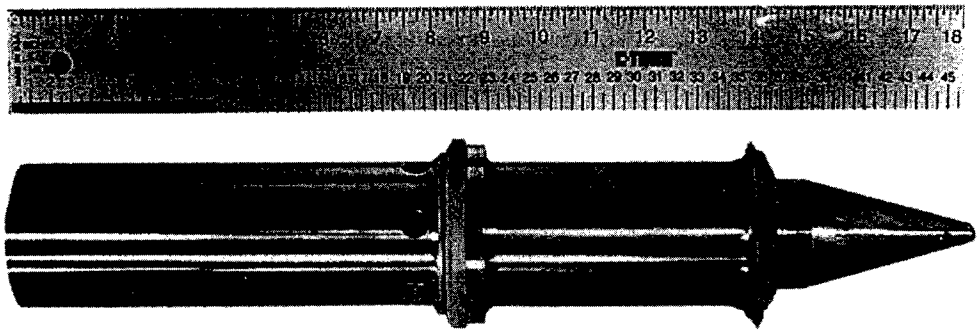

Figure 8. Photograph of Assembled of Test Series 3 Vehicle Design

RESULTS

Concept Validation Tests

The vehicle models used in the concept validation tests were shown previously in Figures 1 and 2 for Tests EX-1 and EX-2 respectively. Launch muzzle pressure for these tests was ~4000 psi. The range flight chamber pressure was less than 1 torr helium atmosphere.

The X-ray photographs of the pitch and yaw angles taken at a station about 5 meters up-range of the target for test EX-2 are shown in Figure 7 with the plot of the actual versus predicted pitch angles for tests EX-1 and EX-2. The vehicle velocity for these tests was 3 km/s, range pressure was < 1 torr He, and launch gas pressure at the muzzle was ~4000 psi. The results show good agreement between the actual versus predicted pitch angles, and therefore validating the attitude control concept.

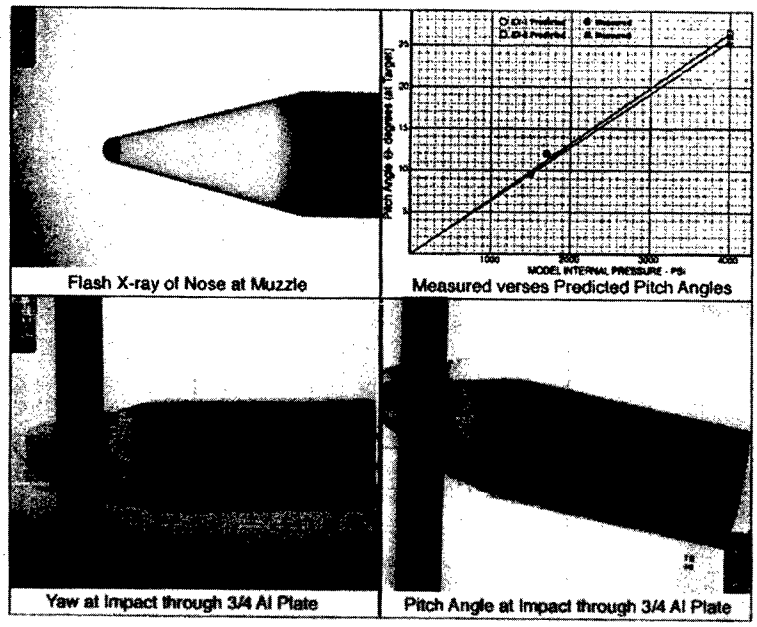

Figure 9 Flash X-ray Photograph of EX-2 Test & Comparison of Pitch Data with Predictions

Subscale Vehicle Tests

The Subscale Vehicle tests consisted of three separate series with somewhat different vehicle configurations for each of the series. The test series will be identified as Series 1, 2 and 3. In Series 1, results were obtained for twelve tests with vehicles that were 152 cm (6") diameter. In Series 2, results were obtained for six tests on vehicles that were 152 cm (6") diameter. In series 3, results were obtained for ten tests with vehicles 86.4 cm (3.4") in diameter. The primary differences in configuration among the vehicles used in the three series were the cylindrical shell tails in Series 1 and 3, and the open, spoke like tail structure for the vehicles used in Series 2.

The differences in the magnitudes of the pitch angles are plotted versus the magnitudes of the yaw angles for the same rounds in the three test series in Figure 10. This data shows least differences between the theoretical and experimental results in test series 2. The standard deviations in the magnitude of pitch angle error was 3.74 for Test Series 1, 0.86 for Test Series 2, and 4.30

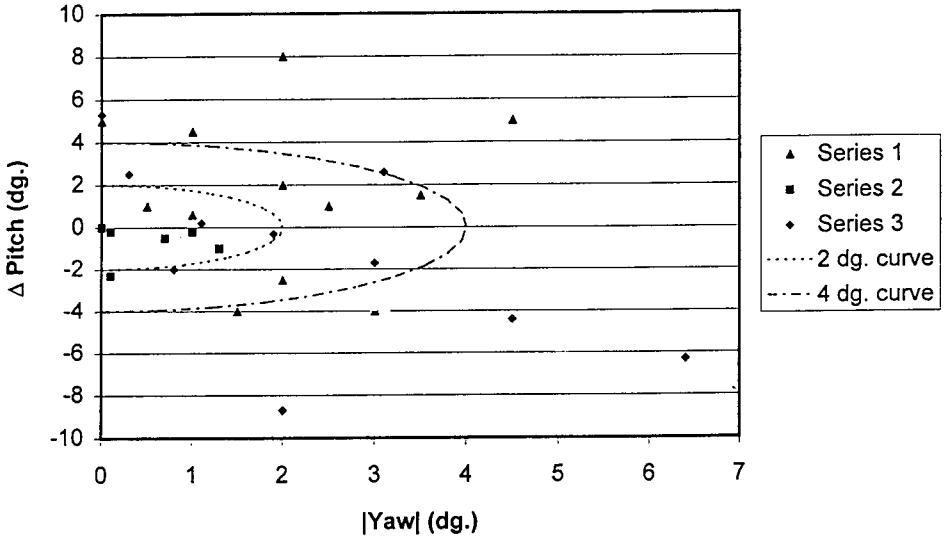

Figure 10. Differences in Pitch Angles versus Magnitude of Yaw Angles

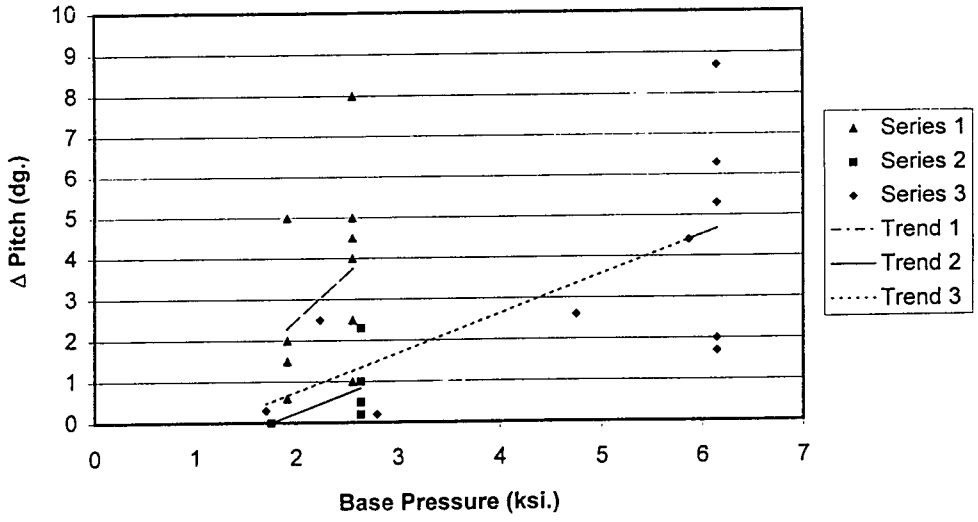

Figure 11. Differences in Pitch Angle versus Base Pressure at the Muzzle

for Test Series 3. In an attempt to determine whether the cause of the relatively large deviations from predicted pitch angles in series 3 might be due to high muzzle pressures, we plotted the pitch angle errors versus the launch gas pressure at the muzzle for the three test series in Figure 11. The trend lines showing the sum of least squares linear data fit to the results for the three series indicate some correlation of the pitch angle errors with muzzle pressure.

DISCUSSION OF RESULTS

Good agreement between predicted and actual pitch angles was obtained for the concept validation tests. Of note is the modest muzzle pressure of ~<3000 psi in these tests. The relatively large errors attitude control angle in series 1 is somewhat puzzling since the launch pressures were not excessive (<3000 psi). A factor for the errors may be the less than ideal gun cycle used in the launch of the vehicles in this series due to the large mass (~5.6 kg) and velocity requirements (3 km/s).

A recent design validation shot prior to commencement of test series 4 using a Series 3 design vehicle, a, may provide a clue to a more definitive answer for the principal error source. The vehicle in this test was launched with a reduced muzzle pressure (~3400 psi) and resulted in less than 1 degree error in pitch angle and ~2 degree error in yaw angle. While this result may be a statistical anomaly, this may indicate that the principal cause of the deviations / errors in the attitude control is due to excessive muzzle blast pressure effects.

We will be performing a planned 8 shot test series 4 this summer with series 3 design vehicles. Since we will be launching these vehicles with reduced muzzle pressures of 3700 psi or less compared to >6000 psi for a number of the shots in test series 3, we should be able to resolve the primary attitude control error source from these tests.

SUMMARY

The principles of reaction jets for attitude control of missiles have been well established. What is novel is the application of this technique to light gas gun launched projectiles. We have demonstrated that good agreement between predicted and experimental pitch angle can be achieved where launch conditions permit. Launch and flight conditions that are less than ideal can result in undesired errors in the actual versus predicted attitude control angle. While there are a number of factors which can contribute to errors in actual versus predicted pitch angle, recent data point to excessive muzzle gas pressure as the primary cause of control angle errors. Further data from forthcoming tests should resolve whether this is, in fact, the case. At any rate, active attitude control using reaction jets for gas gun launched projectiles provides a new and useful capability for hypervelocity lethality testing.

REFERENCES

1. R. I. Primich et al, Radar Observables- Re-entry Experiments of Bell Spheres Fired in a Free-Flight Range, *GM Defense Research Labs, Santa Barbara CA, Report*, TR 66-01-E, (1966)
2. R. A. Hayami, et al, Fluid Injection Experiments with Cones Launched in a Free-Flight Range *AC Electronics Defense Research Labs, Santa Barbara CA, Report* TR 69-26 (1969).
3. R. A. Hayami, Technology Development for 1/2 Scale HTK Testing," *Presentation at the Theater Missile Defense Quarterly Review at Teledyne Brown Engineering*, (1993).
4. R. A. Hayami Sub-Scale HTK Test Capability - UAH Facility, *Presentation at the BMDO Annual Lethality Review Meeting held at Lawrence Livermore National Labs*, (1994)
5. R. A. Hayami & D. J. Liquornik, TMD Lethality Test Program-Final Technical Report, *University of Alabama in Huntsville Technical Report UAH/ARC TR94-06*, (1994).
6. D. J. Liquornik & R. A. Hayami, Subscale Medium Mass Interceptor Kill Vehicle Lethality Test Program *University of Alabama in Huntsville Technical Report UAH/ARC 96-02*, (1996)
7. D. J. Liquornik & R. A. Hayami, Medium Mass Interceptor II, FY96 Development & Test Program*University of Alabama in Huntsville Technical Report UAH/ARC 97-01*, (1997).8.)
8. Eric W. Reece, Sandia National Labs, *private communications*, 1993.

PERGAMON

International Journal of Impact Engineering 23 (1999) 573–584

INTERNATIONAL JOURNAL OF IMPACT ENGINEERING

www.elsevier.com/locate/ijimpeng

CONSTANT KINETIC ENERGY IMPACTS OF SCALE SIZE KE PROJECTILES AT ORDNANCE AND HYPERVELOCITY

N. J. LYNCH

DERA Fort Halstead, Sevenoaks, Kent, TN14 7BP, UK

Summary—This paper presents scale size firings of tungsten alloy KE penetrators into RHA and ceramic targets at constant impact energy. Experiments were carried out mainly at 1.55 and 2.15 km/s but additional data and hydrocode simulations cover a wider velocity range. Semi-infinite RHA and 100 mm thick RHA targets at normal incidence were used, in addition to 40 mm thick RHA at 60 degrees obliquity. The Al_2O_3 ceramic target was at normal incidence and used a thick lateral confinement, and an RHA backing to measure residual depth of penetration. Behind armour effects (BAE) measurements were made using the finite thickness targets. The semi-infinite RHA experiments show the expected peak in performance at about 2200 m/s and an analytical equation was in good agreement to experiment. The hypervelocity penetrator eroded slightly less than the ordnance velocity case against finite thickness RHA. The mass efficiency of the ceramic target increased from 1.65 at 1.55 km/s to 1.93 at 2.15 km/s but there was still an improvement of 25 % in penetration at the higher velocity. Simulations of the experiments used the GRIM2D and 3D hydrocode and an Armstrong-Zerilli material model and generally gave good agreement. Penetration simulations with a simplified Johnson-Holmquist ceramic model compare well with experiments at the two velocities. Further simulations indicate an optimum velocity at 2500 m/s. The higher velocity impacts produced more behind armour debris, with the fragment number approximately in proportion to the square of the impact velocity. © Crown Copyright 1999, Defence Evaluation and Research Agency. Published by Elsevier Science Ltd.

INTRODUCTION

In the design of future ordnance systems where velocities in excess of 1800 m/s are feasible, it becomes important to establish the optimum use of the available energy. On the assumption that the muzzle energy available from an EM (Electro-Magnetic) gun, for example, will not be significantly different from that available from conventional ordnance (but the velocities achievable will be significantly higher), the question is therefore whether the performance of projectiles which are slow and heavy is better than those which are light and fast.

The accepted optimum strike velocity for unitary tungsten KE projectiles up to length to diameter ratio (L/D) 20 against semi-infinite RHA at normal obliquity is in the region of 2200 m/s [1]. For constant impact energy projectiles, a change in velocity from 1600 m/s to 2200 m/s increases penetration by 25-30 %. Against other target types the performance increase and the optimum velocity are likely to change, depending on the geometry and materials used.

The aim of this work was to examine performance gains against ceramic and oblique RHA targets, and to see how much they differed from zero obliquity semi-infinite RHA at close to the optimum velocity. There was also a need to assess the differences in behind armour debris at ordnance and hypervelocity. The experiments could also be used to assess the capability of the GRIM hydrocode and material constitutive models. The improving accuracy of such codes gives more confidence in using them to extrapolate trends where only minimal experimental data exists.

0734-743X/99/$ - see front matter © Crown Copyright 1999, Defence Evaluation and Research Agency. Published by Elsevier Science Ltd.
PII: S0734-743X(99)00105-0

EXPERIMENTS

Projectiles

Experimentally, the constant kinetic energy assessment requires a different projectile design for each velocity being considered, and hence it was not feasible to obtain a full performance curve across the velocity range. The exception was where semi infinite penetration was available for a range of penetrator designs at various impact velocities. Data were therefore obtained at two discreet velocity points. The two velocities chosen were 1550 m/s and 2150 m/s. The lower velocity is representative of the impact velocities of current cannon calibre KE projectile designs, and the higher velocity is close to the optimum impact velocity against RHA. Tungsten-nickel-iron alloy projectiles with conical noses and length to diameter (L/D) ratios of 20 were used. The higher velocity projectile has the same proportions as the lower velocity design, but 80% of its linear dimensions. Details of the projectiles are given below. All the projectiles were launched using a 10 metre long, 40 mm calibre smooth bore cannon.

Table 1. Projectile details

Type	*Diameter* (mm)	*Length* (mm)	*Mass* (g)	*Velocity* (m/s)	*Impact Energy* (kJ)
S26	8.6	177	161.2	1550	193.6
S46	6.88	142	83.2	2157	193.6

Target Details

The following targets were used: a) 200 mm square semi-infinite RHA at 0° obliquity, b) a ceramic laminate at 0° obliquity with a semi-infinite RHA backing plate, c) 100 mm RHA at 0° and d) 40 mm RHA at 60° obliquity. The finite thickness targets were additionally used to measure behind armour debris at the two velocities. The geometry of the ceramic target is given in Figure 1.

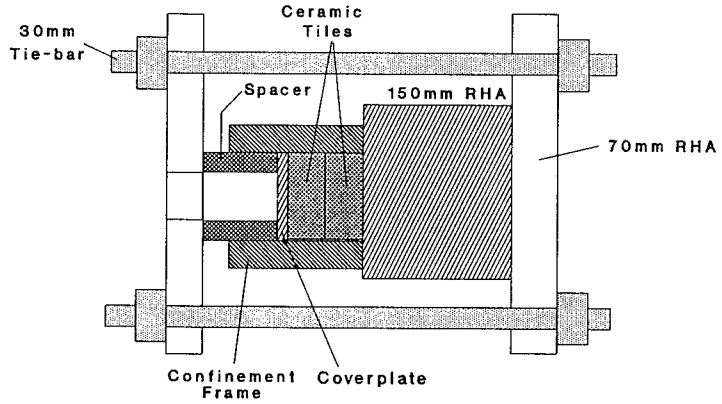

Fig. 1. Design of the ceramic target.

The target consists of a heavily confined Al_2O_3 (Morgan-Matroc Deranox 975) tile, 200 mm square by 80 mm thick. Deranox 975 has a density of 3.78 g/cc, a hardness of 80 (R45N) and an elastic modulus of 340 GPa. The 80 mm thickness was built up using two 40 mm tiles epoxied together. Shimming into the 75 mm thick confinement was by steel and brass strips with a transition grade of fit. A 9 mm thick RHA plate covered the ceramic and a 150 mm thick backing

RHA was used to measure depth of penetration. The cover plate was clamped to the ceramic using a pressure collar and tie bars. The RHA used was to UK DEFSTAN 95/13-1, with average Brinell hardnesses of 290, 299, and 330 for the 100 mm, 40 mm, and 9 mm thick plates respectively.

EXPERIMENTAL RESULTS

Semi-infinite RHA

The velocities achieved in the experiments were 20-30m/s slower than the intended 1550m/s, and hence the hypervelocity firings were adjusted where possible so that there was a match of impact energies at the two velocities. Semi-infinite RHA performance for the two penetrator designs is shown in Table 2.

Table 2. Results of the semi-infinite and ceramic firings

Impact Velocity (m/s)	*Target Type*	*Yaw at Target (degrees)*	*DoP (mm)*	*KE at Target (KJ)*	*P/L*	*Em*
1521	Semi-inf. RHA	0.35	137.5	186.5	.776	
1523	Semi-inf. RHA	1.05	131.8	187.1	.744	
2114	Semi-inf. RHA	0.3	177.5	188.4	1.25	
2102	Semi-inf. RHA	2.0	169.5	186.2	1.193	
2112	Semi-inf. RHA	1.8	166	188.0	1.169	
2147	Semi-inf. RHA	1.0	175	194.3	1.232	
1525	9RHA/80ceramic/150RHA	1.55	60.5	187.5		1.61
1531	9RHA/80ceramic/150RHA	0.8	64	189.0		1.53
2120	9RHA/80ceramic/150RHA	1.4	93	186.9		1.89
2130	9RHA/80ceramic/150RHA	1.4	91.5	188.7		1.95

The data are plotted in Fig. 2 with additional data points from selected L/D=20 projectiles having the same impact energy from 1289 m/s to 2550 m/s. Details of the additional penetrators and their semi-infinite RHA performance is given in Table 3.

Table 3. Additional projectile details

Type	*Diameter (mm)*	*Length (mm)*	*Mass (g)*	*Velocity (m/s)*	*Penetration (mm)*
S23	9.8	197	233	1289	110
S28	7.5	147	90.5	2087	172[1]
S20	6.5	132	59.5	2550	180

[1] Based on a result at 2100 m/s

The maximum penetration is observed between 2200-2300 m/s as noted by Frank & Zook and others. For comparison, the solid line is an equal impact energy penetration prediction derived from an analytical fit for L/D 20 rods given by Anderson and Walker [2] where

$$P/L = \frac{a V^c}{b^c + V^c} \quad (1)$$

and $a = 1.606$, $b = 1.542$ and $c = 4.273$. The prediction is applicable for impact velocities between $0.5 < V < 4.5$ km/s. The S26 penetrator dimensions were then multiplied through by $V_0/V^{2/3}$ as outlined in Ref. [3] to obtain a constant energy curve, where V_0 is the reference velocity, taken here as 1550 m/s. The experimental results are slightly below the prediction at

2150 m/s but other points are in good agreement. The gain in penetration from 1550 m/s to 2250 m/s is 30%. Aerodynamic drag has not been allowed for. Drag effects would favour heavier, slower projectiles so this gain would reduce if flight distances were included.

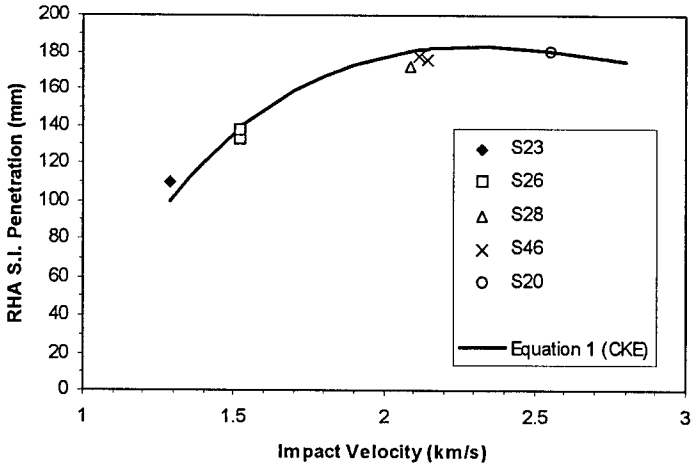

Fig. 2. Penetration vs velocity for 188 KJ constant energy rods.

Ceramic Target

Firings were carried out at nominal velocities of 1530 m/s and 2130 m/s, the results also being shown in Table 2. The semi-infinite results discussed above were used to calculate mass efficiency (E_m) values, based on:

$$E_m = \frac{(RHA_{DoP} - T_{cp} - DoP) \times \rho_{RHA}}{(T_{cer} \times \rho_{cer})} \quad (2)$$

Where RHA_{DoP} = performance into semi-infinite RHA at the appropriate velocity; T_{cp} = coverplate thickness; T_{cer} = ceramic thickness, DoP is the depth of penetration into the RHA backing, and ρ_{cer}, ρ_{RHA} are the ceramic and steel densities respectively.

Therefore, at 1530 m/s an average of the results gives :

$$E_m = \frac{(135 - 9.2 - 62.2) \times 7830}{(80 \times 3770)} = 1.65$$

and similarly at 2130 m/s the E_m averages 1.93. The E_m value at ordnance velocity is typical for this type of ceramic and confinement method, as given for example in Ref. [4]. E_m values of 1.8 to 2.2 have been observed using a purer alumina (99.7%) and impact velocities of 2.5 km/s, so 1.9 is not atypical [5]. As the E_m ratings indicate, the target is more efficient at higher velocities, but the hypervelocity rod still shows a 25% improvement in penetration performance compared to the lower velocity projectile.

Finite Thickness target at normal and obliquity

The results of the finite thickness target firings are shown in Table 4. X rays behind the target were used to measure penetrator residual length and velocity, and most of the residual penetrators were recovered to confirm their mass. Against 100 mm thick RHA at normal, the same percentage of the original length was eroded at both velocities (42%). Measurements of the crater section from a low and high velocity firing show the crater shape up to half thickness to be very similar. The crater profile on entry echoes the tapered penetrator nose shape in reverse. In the middle of the 100 mm thick block the diameter was 14.5 mm at 2150 m/s and 16 mm at

1550 m/s. Both exit holes are a similar diameter, but at the lower velocity the target material has more axial displacement before fracture occurs, reflecting the lower strain rate. For the 40 mm target at 60° the projectile erosion was less at hypervelocity (45-46%) than at ordnance (41-42%). This may be due to the ability of the higher velocity rod to establish symmetric flow quicker and thus it loses less rod material in frontal spall. X-rays of the residual projectile and surrounding debris at 1550 and 2150 m/s are shown in Figures 3 and 4.

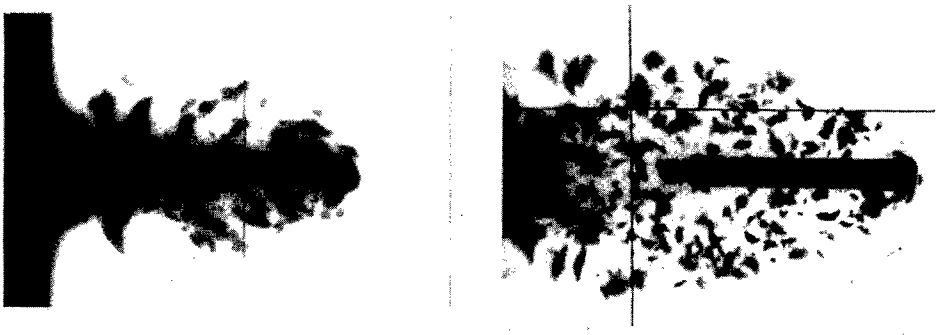

Fig. 3. 100 mm RHA at normal. 1550 m/s (left) and 2150 m/s (right).

Fig. 4. 40 mm RHA at 60°. 1550 m/s (left) and 2150 m/s (right).

BEHIND ARMOUR EFFECTS

Packs of 'strawboard'(a compressed paper board) were placed behind the finite thickness targets to recover fragments of the target and penetrator. The target was also weighed before and after firing to allow a mass balance to be calculated. The masses of the fragments were weighed using a digital balance (+/-0.005g) and average dimensions taken, from which it was possible to divide the fragments into RHA and tungsten.

Number of fragments produced

Figure 5 shows the fragment distributions from the 100 mm thick targets at the two velocities. The average number of fragments increased from 75 at 1561 m/s to 160 at 2136 m/s. For the 40 mm oblique target there were 100 fragments at 1565 m/s and 198 at 2145 m/s. Thus for both targets there were approximately twice as many fragments produced at the higher velocity as there were at the lower velocity. The firings at obliquity produced more fragments than at normal by between 23% and 33%. The ratio of the number of fragments produced is approximately the same as the square of the ratio of velocities; ie $N_f \propto V^2$.

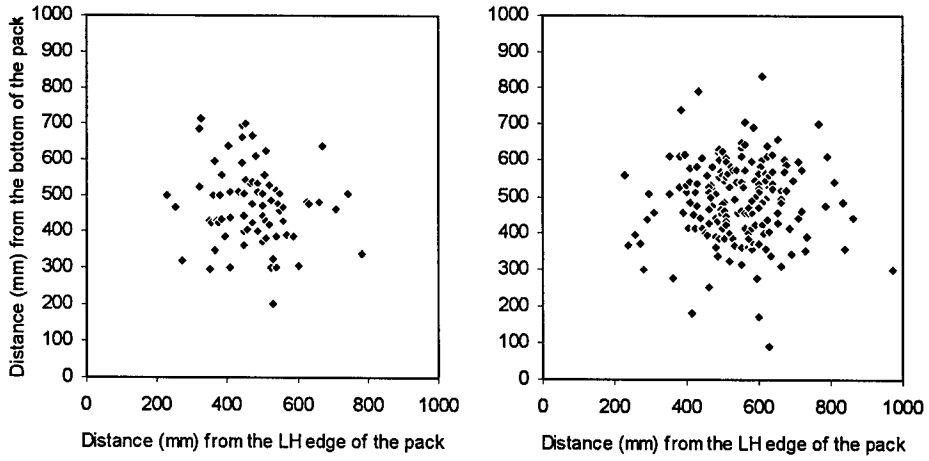

Fig. 5. Plots of fragment positions on the first strawboard layer. 0° obliquity. 1561 m/s (left) and 2150 m/s (right).

Anderson and Bless [6] reported debris results at impact velocities of 1.75 km/s and 2.55 km/s, where the ratio of the square of velocities is 2.1. They also found the number of fragments to be approximately double at the higher velocity, so the relationship appears valid. Work by Grady, Kipp and Swegle [7] indicated three regimes under which the average fragment dimension varies. Taking the most applicable regime (that the solid spall is flow stress rather than fracture toughness dominated), Grady indicated that the average fragment dimension, S could be described by:

$$S = \left(\frac{1.2\ Y}{\rho\ \dot{\varepsilon}^{2}} \right)^{1/2} \tag{3}$$

The strain rate, $\dot{\varepsilon}$, will vary with position in the target bulge, but as a first approximation it is reasonable to assume that the strain rate is proportional to impact velocity. The fragment area, A_m will also be proportional to S^2, and hence the fragment area is proportional to $1/\varepsilon^2$ and $1/V^2$. DERA has used algorithms for fragment numbers where: $N_f = k\ (t \sec\theta)^a\ (P_{max} - t \sec\theta)^b$, where k has dimensions of 1/area, θ is the target angle of obliquity, t is the target thickness, P_{max} is the semi-infinite penetration capability of the penetrator and a and b are constants. If the constant, k, is directly proportional to the inverse of the mean fragment area predicted by Grady, then it follows that $k \propto V^2$ which corresponds to the earlier observation of $N_f \propto V^2$. However it should be noted that this does not validate the flow stress description. It is possible that the rod fragments follow the predicted average dimension suggested by the liquid spall expression, whereas the target fragments could follow the flow stress prediction. Additional work is required to confirm this hypothesis.

Mass Distributions

The mass distributions of the fragments were quantified using a Mott like distribution. A plot of $\log_e[\log_e(N_0/N_f)]$ should be a straight line if the fragments obey this distribution. Figure 6 shows plots for the lowest yaw, zero obliquity firings at 1550 and 2150 m/s. It was found that the plots were not always linear throughout the mass range. Also, the values for α (intercept) and λ (slope) do not appear to correlate with the differing conditions in the firings. Values found for α and λ are given in Table 4.

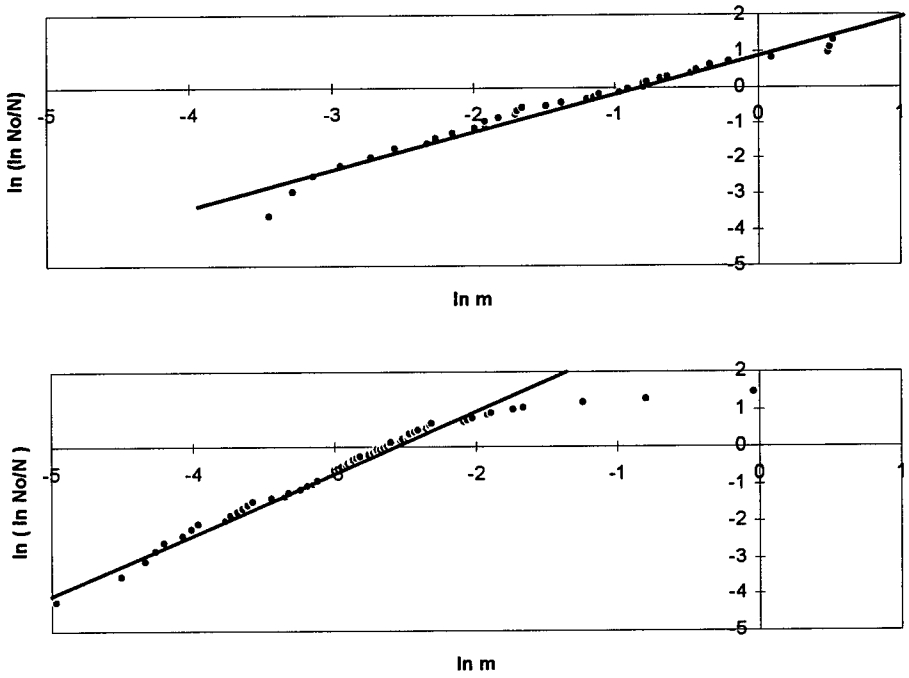

Fig. 6. Mass distributions from 100 mm thick RHA firings.
1540 m/s (top) and 2136 m/s (bottom).

The conclusions from Ref. [8] were that the parameter values were velocity dependant, with α increasing and λ decreasing with impact velocity. For constant impact energy the parameter change is relatively weak. It is possible that penetrator diameter has an influence, since in this work the diameter of the projectile reduces with increasing velocity. To assess the effect of incomplete fragment recovery on α and λ, three studies of the effect of synthetic removal of fragments showed that the slope of the graph is not substantially altered when parts of the distribution are removed, but the intercept parameter tends to decrease when more of the distribution is missing.

HYDROCODE ANALYSIS

General

The DERA Eulerian code GRIM was used in two dimensional (2D) and 3D form to assess how well the experimental results could be simulated, to provide timing information for trial instrumentation, and to study of the way the rod and target debris start to form during penetration.

Semi-infinite penetration

For impact velocities > 1600 m/s the use of material constitutive models without strain and strain rate terms has been shown to give good agreement with experiment though there is some divergence in the comparison over a range of velocities. As this work needed a comparison over a 600 m/s velocity range, a modified Armstrong-Zerilli material model was used for RHA and an elastic-plastic model for tungsten. The resulting comparison of penetration depth and crater diameter (Table 5) show a good comparison with experimental results.

Table 5. Comparison of GRIM2D and experiments for 0° semi-infinite RHA

	Penetration Depth (mm)		*Crater Diameter (mm)*	
Velocity (m/s)	*GRIM*	*Experiment*	*GRIM*	*Experiment*
1550	139	132-137	16.0	16.0
2150	172	176	14.7	14.5

Finite thickness target at zero obliquity

The computational cell size plays an important part in resolving the breakout at the rear of the target. Comparisons for 0.6 mm cell size are shown in Table 6. If the cell size is changed from 0.6 mm to 0.8 mm, (i.e. from 13 to 10 cells across the diameter of the penetrator), the residual velocity of the low velocity penetrator is reduced by 30 m/s (2 % change in V_r). Although smaller cell sizes than 0.6 mm were not examined, it would appear that the simulations are converging away from the experimental results. The simulated X rays from the code at the two velocities are shown in Fig. 7. These can be compared to the experiments in Fig 3, which are to the same scale.

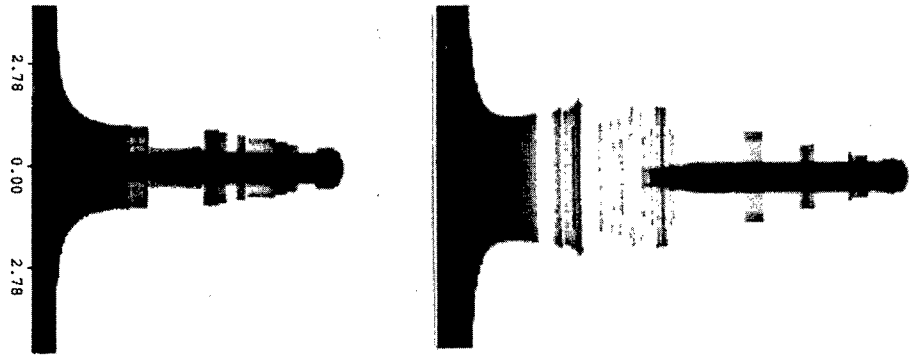

Fig.7. Simulated X rays from GRIM2D. (left) 1550 m/s, (right) 2150 m/s.

The 2D axisymmetry produces fragment 'rings' rather than discrete fragments and hence it is to be expected that the radial displacement of the debris field in the simulation is less than seen in the experiment.

Table 6.Comparison of GRIM2D and experiments for 100mm thick RHA at 0°

	Residual Velocity (m/s)		*Residual Length (mm)*	
Velocity (m/s)	*GRIM*	*Experiment*	*GRIM*	*Experiment*
1550	1360	1312	68-69	73
2150	2030	2019	57	57.6

Oblique (60°) finite thickness target

GRIM3D was used to model the 1550 and 2150 m/s oblique impacts, with 0.75 mm cells in the impact region and cell expansions of 1.06 out to the mesh edges. The simulated X rays from the code are shown in Figure 8. Both the simulations and experiment (Fig. 4) show a greater quantity of penetrator and target debris at 2150 m/s than at 1550 m/s. In the oblique cases it is difficult to accurately state and compare the residual lengths since in the experiment the tip of the rod

fractures whereas it bends in the simulation. However, as can be seen in Table 7 below, the residual velocities and lengths compare quite well.

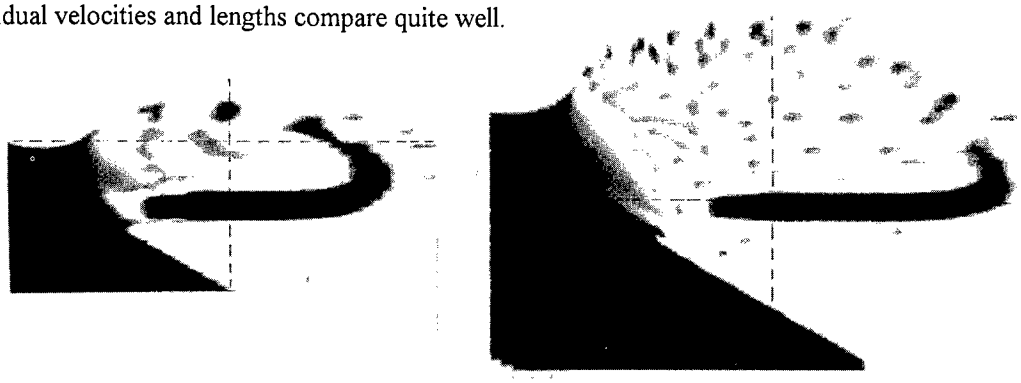

Fig. 8. Simulated X rays from GRIM3D. (left) 1550 m/s, (right) 2150 m/s.

Table 7. Comparison of GRIM3D and experiments for 40 mm thick RHA at 60°

	Residual Velocity (m/s)		*Residual Length (mm)*	
Velocity (m/s)	*GRIM*	*Experiment*	*GRIM*	*Experiment*
1550	1410	1386-1417	67	68.5-72
2150	2070	2057-2074	67	60.3-62.5

Figure 9 compares the crater shape of the code and experiment for the two impact velocities. At 1550 m/s the code erodes more of the open face of the entry crater. On exit the lack of a failure model leads to a more stretched lower 'lip'; in the experiment, fracture of the RHA causes a blunter profile. At 2150 m/s only the failed lips of the entry and exit faces differ between code and experiment. Total yaw for this case was approximately 0.5°.

Fig. 9. Comparison of crater profiles - GRIM3D and experiment.
1550 m/s (left), 2150 m/s (right). Entry is from the right.

Ceramic target

A simplified Johnson-Holmquist type ceramic model was used to simulate the experiments [9]. The yield strength-pressure relationships used in the model are given in Table 8 below. The change from intact to fractured material is assumed to be instantaneous, i.e. there is no damage accumulation.

Table 8. Johnson-Holmquist model parameters

	Yield Strength (GPa)	*Pressure (GPa)*
Fracture surface for intact material	0	-0.3
	1.75 (Y_0)	0
	$4.457*Y_0 = 7.8$	25
	7.8	35
Yield surface for fractured material	0	0
	$1.66*Y_0 = 2.9$	2.5
	2.9	35

The simulated total depth of penetration (i.e. coverplate plus ceramic plus backing) was 149 mm at 1550 m/s and 182 mm at 2157 m/s, compared to averages of 151 mm and 181 mm for the experiments. Agreement was therefore very good at both velocities, encouraging further simulations over a wider velocity range to estimate the optimum velocity. The four additional simulations from 1289 m/s to 2900 m/s are shown in Figure 10 together with the RHA trend from Figure 2. The cell size was reduced in stages from 1 mm at 1289 m/s to 0.7 mm at 2900 m/s to maintain the number of cells across the radius of the projectile. The maximum penetration for the ceramic target is obtained at 2500 m/s, and the trend with velocity appears to have a flatter profile than that for RHA.

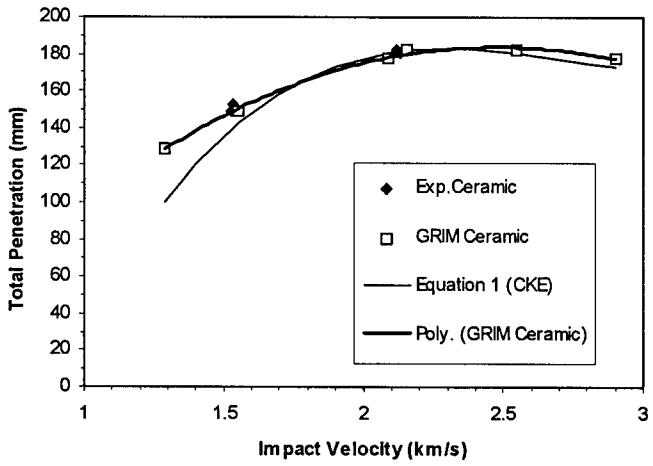

Fig. 10. Total penetration into the ceramic target. Experiment and hydrocode prediction compared with the trends into RHA.

CONCLUSIONS

Two similarly proportioned, L/D 20 penetrators were launched with the same impact energy against armour steel and ceramic targets at nominal velocities of 1550 and 2150 m/s. The gain in penetration at the higher velocity against semi-infinite RHA was 30%. A predictive equation for RHA compared well with experimental values, and indicated an optimum velocity of ~2250 m/s. Against finite thickness RHA the residual KE for both the normal and oblique impacts was higher at 2150 m/s than at 1550 m/s, by between 5 and 9 %. Against a confined Al_2O_3 target, the greater penetration efficiency of the higher velocity penetrator gave a 27 % increase in penetration depth, even though the mass effectiveness (E_m) of the ceramic increased. Hydrocode simulations using a simplified Johnson-Holmquist brittle material model compared very well with experimental data, and indicated an optimum velocity of 2500 m/s.

The BAE (behind armour effects) experiments show a greatly increased number of fragments at higher velocity. This applies to both normal and oblique target angles.

Acknowledgement—The author acknowledges the work of Mr H V Embling of CARDINAL CONSULTANTS in the analysis of the witness pack data.

© British Crown Copyright 1998

REFERENCES

1. K. Frank and J. Zook, Energy efficient penetration and perforation of targets in the hypervelocity regime. *Intnl. Jnl. Impact Engng.* Vol 5, pp 277-284. (1987).
2. C. E. Anderson and J. D. Walker, An analytical model for P/L for WA long rods into armour steel. *Shock Compression in Condensed Matter,* pp1135-1138 (1995).
3. S. J. Bless and C. E. Anderson, Penetration of hard layers by hypervelocity projectiles. *Intnl. Jnl. Impact Engng.* Vol 14, pp 85-93. (1993).
4. J. Cagnoux, M. Cauret, W. Carson, I. Cullis, Penetration of alumina ceramics by tungsten rod penetrators. *Proc. 14th Int. Symp. Ballistics*, TB36, pp 545-554, September 26-29, Quebec, Canada (1993).
5. B. Lundberg, L. Westerling, B Lundberg, E_m values calculated from: Influence of Scale on the penetration of tungsten rods into steel backed alumina targets. *Intnl. Jnl. Impact Engng.* Vol 18, pp 403-416. (1996).
6. C. E. Anderson, S. J. Bless, T. R. Sharron, R. Subramanian, Analysis of behind armor debris at two impact velocities *Proc. 15th Int. Symp. Ballistics*, V5, pp 463-470, May 21-24, Jerusalem, Israel (1995).
7. D.E.Grady and M.E. Kipp, Fragmentation of solids under dynamic loading. In: *Structural Failure* (edited by T Wierzbicki and N Jones), pp.1-38, J Wiley (1989).
8. V. Hohler, K. Kleinschnitger, E. Schmolinske, A. Stilp, K. Weber, M. Maysless, N. Sela, Debris cloud expansion around a residual rod behind a perforated plate target. *Proc. 13th Int. Symp. Ballistics*, TB48, pp.327-334, June 1-3, Stockholm, Sweden (1992).
9. G. R. Johnson and T. J. Holmquist, A computational model for brittle materials subject to large strains, high strain rates and high pressures. *Shock Wave and High Strain Rates Phenomena in Materials.* pp 1075-1081, (1992).

Table 4. Results of the finite thickness RHA firings

V_s (m/s)	Target Type	Total Yaw at Target (deg.)	KE at Target (KJ)	L_r (mm)	V_r (m/s)	M_r (g)	L_r/L -	V_r/V_s -	% KE lost	Target Mass (kg)	Target Mass Change (kg)	α	λ
1561	100 RHA @ 0	0.15	196.5	72.9	n/r	68.7 estd.	0.423	-	-	31.550	0.022	2.78	0.94
1541	100 RHA @ 0	1.2	191.3	73	1312	68.8	0.424	0.852	69	31.523	0.027	4.01	0.85
2139	100 RHA @ 0	3.6	190.3	(36) 3 PIECES	2074	18.2	-	0.969	79	31.50	0.103	3.71	0.76
2136	100 RHA @ 0	0.9	189.8	57.6	2019	36.2	0.426	0.945	60	31.493	0.055	83.51	1.68
1552	40 RHA @ 60°	1.3 @ 190°	194.3	68.5-70	1386	70.4	0.407	0.893	65	39.727	0.025	1.74	0.97
1545	40 RHA @ 60°	0.25 @ 320°	192.5	72	1417	58.6	0.418	0.917	69	39.624	0.021	2.25	0.59
2153	40 RHA @ 60°	~0.5	191.4	62.5	2074	36.0 estd.	0.462	0.963	59	39.75	0.063	3.97	0.66
2166	40 RHA @ 60°	~0.8	197.7	60.3	2057	34.7 estd.	0.446	0.949	62	39.687	0.058	3.77	0.82

V_s = Strike Velocity; L_r = Residual Length of Penetrator; V_r = Residual Velocity of largest fragment; M_r = Residual Mass of recovered fragment

PERGAMON

International Journal of Impact Engineering 23 (1999) 585–595

INTERNATIONAL JOURNAL OF IMPACT ENGINEERING

www.elsevier.com/locate/ijimpeng

JET PENETRATION INTO LOW DENSITY TARGETS

M. MAYSELESS and R. GENUSSOV

RAFAEL, Ballistics Center, Haifa, Israel

Summary — It is well known that the penetration depth of high velocity rods is inversely proportional to the square root of the target density. Hence, it is expected that low density targets are more effective than high density targets in defeating shaped charge jets. However, careful analysis of real jets - with velocity gradients, penetrating targets constrained by fixed areal weight, shows that this is not always the case. Moreover, it was found that there is an optimum value of target density (ρ_{opt}) for maximizing jet erosion. This effect was also verified experimentally. © 1999 Elsevier Science Ltd. All rights reserved.

INTRODUCTION

Consider a short segment of a shaped charge jet of length L and density ρ_j, moving with a constant high velocity, and penetrating a monolithic target of density ρ_t. Neglecting strength effects and assuming a steady-state penetration process the depth of penetration P of this segment is:

$$P = L\left(\frac{\rho_j}{\rho_t}\right)^{1/2} \equiv \frac{L}{\gamma} \tag{1}$$

The mass per unit area of the target necessary to stop this segment is therefore:

$$m = P\,\rho_t = L\,(\rho_j \rho_t)^{1/2} \tag{2}$$

Hence, the lower the density of the target the lower the weight needed to erode the jet. For example, reducing the density of the target material by a factor of four reduces the mass needed to erode the jet by a factor of 2. The penalty for using low density materials is the low volume efficiency.

This outcome is correct assuming no velocity gradient along the jet, and it is therefore applicable for calculating the penetration depth of very fast long rod projectiles. In reality, shaped charge jets are characterized by the velocities of the tip - V_0 and of the tail - V_{tail}. Real jets are stretching while penetrating a target and their length is therefore not constant in time. The erosion rate and the final stretched length of a jet depend on jet velocity and target characteristics. The penetration of real jets should be described in a way which takes into account the stretching process of the jets.

The spatial distribution of the velocity of most of the jets is almost linear, hence one can assume the existence of a virtual origin (in space and time) from which the jet emerges [1]. Based on these assumptions Allison and Vitali [1] derived the penetration equation for a continuous jet (Case I) as:

0734-743X/99/$ - see front matter © 1999 Elsevier Science Ltd. All rights reserved.
PII: S0734-743X(99)00106-2

$$P_I = S\left[\left(\frac{V_0}{V_{min}}\right)^{1/\gamma} - 1\right] \qquad \text{Case I} \qquad (3)$$

S is the standoff measured from the virtual origin to the target, and γ is the square root of the target to jet densities, as defined by Eq. (1). V_{min} is the lowest jet velocity that contributes to penetration. The continuously stretching jet breaks into short segments (droplets) at a given time T_b (T breakup). The penetration of a jet that starts penetration as a continuos jet but breaks up before completion of penetration (Case II) can be expressed as:

$$P_{II} = \frac{(1+\gamma)(V_0 T_b)^{1/(\gamma+1)} S^{\gamma/(\gamma+1)} - V_{min} T_b}{\gamma} - S \qquad \text{Case II} \qquad (4)$$

The penetration of a fully particulated jet can be expressed as:

$$P_{III} = \frac{(V_0 - V_{min})T_b}{\gamma} \qquad \text{Case III} \qquad (5)$$

Assuming that the jet particulates all over at the same time - T_b.

The velocity of the tip of the jet V_{out} that emerges from the back of the target with a finite thickness D, can be expressed as (see for example references [2 or 3]):

$$V_{outI} = \frac{V_0}{\left(\frac{D}{S}+1\right)^{\gamma}} \qquad \text{Case I} \qquad (6)$$

$$V_{outII} = \frac{(1+\gamma)(V_0 T_b)^{1/(\gamma+1)} S^{\gamma/(\gamma+1)} - \gamma(S+D)}{T_b} \qquad \text{Case II} \qquad (7)$$

$$V_{outIII} = V_0 - \frac{\gamma D}{T_b} \qquad \text{Case III} \qquad (8)$$

Ignoring all edge effects that might affect these velocities.

Real targets are constrained by a given weight or volume. These constraints should be added to Eq. (4) and solved together. In the following sections we shall analyze the erosion process of a jet penetrating into targets of different areal masses and densities.

WEIGHT CONSTRAINT

Case I

Let us assume that the target has a given mass per unit area - m:

$$m = D\,\rho_t = Const. \qquad (9)$$

Substituting m in Eq. (6) we derive:

$$V_{outI} = \frac{V_0}{\left[\frac{m}{S\rho_t}+1\right]^{\gamma}} \tag{10}$$

Assuming that the jet tail velocity is lower than the minimum velocity necessary for penetrating the target. Plotting V_{outI}/V_0 vs. target density, as shown in Fig. 1, one can see that by reducing the density of the target the velocity of the emerging tip decreases too, up to a certain point, below which the velocity starts to increase with further decreasing of the target density.

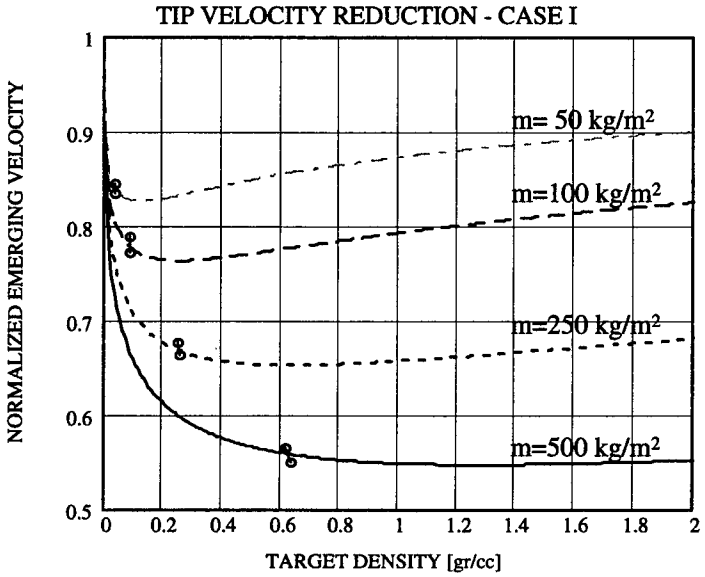

Fig. 1. Relative final jet tip velocity of a continuos copper jet vs. target density, after penetrating a finite thickness target with an areal mass of "m", S=100mm.

The optimal target density is the density of the target at the point where the final jet tip velocity is minimal. For constant mass targets, the lower the density the thicker the target, hence at a certain point the jet will emerge from the back side of the target particulated. To set a limit to the lowest density relevant for Case I, one should note that by considering the target thickness penetrated up to the breakup moment a permissible region for the out coming velocity can be obtained:

$$\frac{S+m/\rho_t}{T_b} < V_{outI} \tag{11}$$

The lines presenting this bound are shown in Fig. 1 for $V_0 = 8$ km/s and $T_b = 200$ μs by the two circles.

In order to find the exact value of the optimal target density - ρ_{opt} as a function of target mass, we need to equate the derivation of V_{out} given by Eq. (10), to zero. ρ_{opt} will be derived by solving the following equation:

$$(x+1)^{[(x+1)/2\,x]} = e \tag{12}$$

where:

$$x = \frac{m}{S\rho_{opt}} \tag{13}$$

The approximate solution for Eq. (12) is: $a \equiv x \approx 3.92$, and the optimal target density is:

$$\rho_{opt} = \frac{m}{a\,S} \tag{14}$$

Hence, the optimal target density is directly proportional to the target areal weight, and inversely proportional to the stand-off as shown in Fig. 2. The heavier the target the greater the optimal density for defeating the jet. S is usually proportional to the diameter of the charge, consequently the greater the charge the lower the optimal density, for the same target mass.

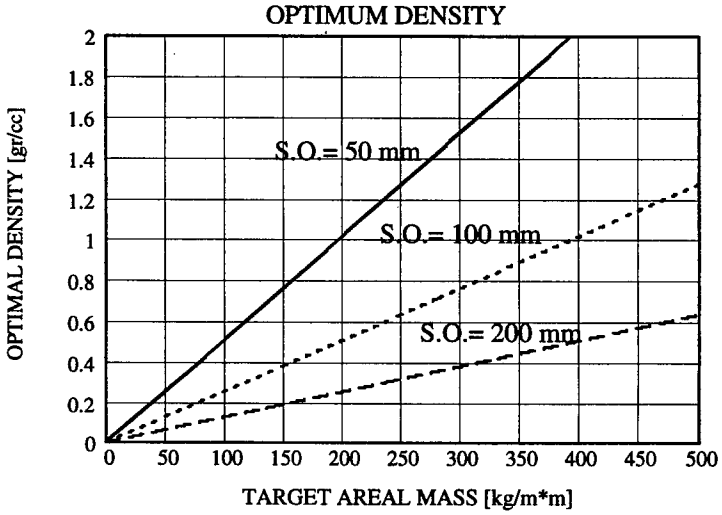

Fig. 2. The optimal target density as a function of target areal mass.

The velocity of the tip of the out coming jet decreases as target mass increases, and may get to a point where all the jet will be fully consumed. Since additional mass will reduce target efficiency, it is important to find the minimum mass required to stop a given charge. The minimum target weight needed to erode this jet - m_{min} - will be found by substituting ρ_{opt} into Eq. (10), and solving it. By doing so we get:

$$m_{min} = \left[\left(\frac{V_0}{V_{min}}\right)^{1/\gamma} - 1\right] S\,\rho_{opt} \tag{15}$$

By substituting the optimal value of the target density from Eq. (14) we get:

$$\rho_{opt} = \rho_j \left[\frac{Ln(V_0 / V_{min})}{Ln(a+1)} \right]^2 \tag{16}$$

The optimal target density needed to erode a continuous jet is shown in Fig. 3. It should be noted that in reality V_{min}, (designated as the cutoff velocity) depends mainly on the yield point and the density of the target and on the alignment and diameter of the jet. The optimal target density needed to erode real jets, with a velocity ratio between 2.5 and 3 is about 3 gr/cc to 4.25 gr/cc. RHA targets are best for eroding jets with tip to cutoff velocity ratio of 4.5, like copper jets with tip velocity of about 13 km/s for example (if it exists). For eroding jets with higher densities higher targets densities should be used in accordance with Eq. (16).

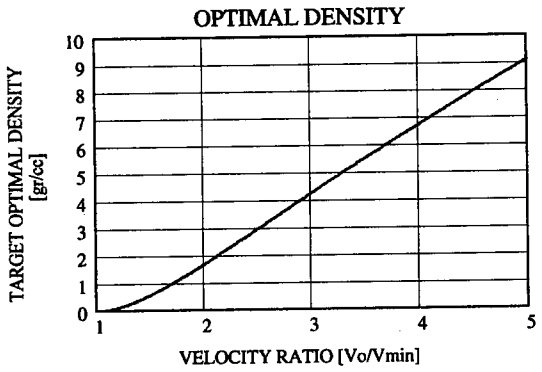

Fig. 3. Optimal target density needed to erode a copper jet.

Using Figs. 2 and 3 one can find out the characteristics of the best target to stop a given jet. Assume, for example, that the jet velocity ratio needed to be stopped is 2, the standoff is 100 mm and that the jet tip velocity is 8 km/s. Hence the target optimal density should be about 1.7 gr/cc, and the target areal mass should be about 660 kg/m^2. This argument is valid for Case I penetration for which the breakup time is longer than 120 μs. If the breakup time is shorter the jet will penetrate this target and emerge particulated.

The dependency of V_{out} on the standoff, after penetrating 100 mm thick targets of various areal masses, is plotted in Fig. 4. It is clearly seen that a target positioned at a very close standoff is very efficient. Scaled up charges operate at longer standoffs, and their penetration capability increase proportionally to the increase in their diameter. Hence, to obtain the same defeating efficiency, the target mass should be increased proportionally, without change in the target density, as can be seen from Eq. (13).

The densities of the targets in four of the curves in Fig. 4 are calculated assuming constant target thickness. In the fifth bottom curve the velocity reduction was calculated differently by assuming optimal density for the target weighing 500 kg/m^2. It is interesting to note that the emerging velocity of the last curve is always lower than that of the constant thickness curve. In addition, according to Eq. (14) the density of the target with constant thickness is higher than the optimal density for long standoffs, but is lower for the short ones.

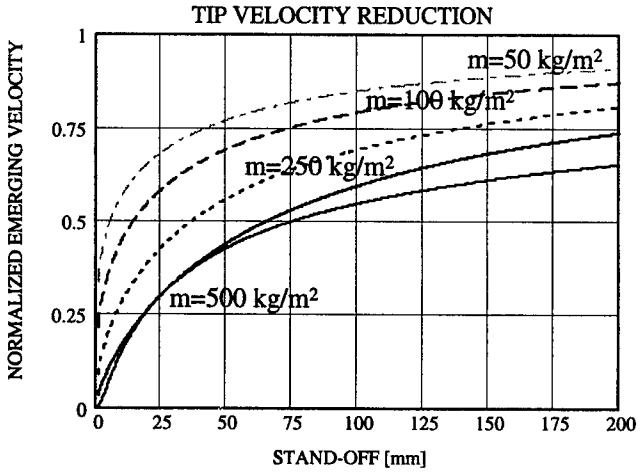

Fig. 4: Relative final jet tip velocity, of a continuous copper jet, vs. stand-off, after penetrating 100 mm thick targets of various areal mass.

Case II

The analysis of Case II can be done in the same way it was done for Case I. Using Eq. (7) the calculated jet tip velocity is plotted as a function of target density, as shown in Fig. 5, for S=300 mm.

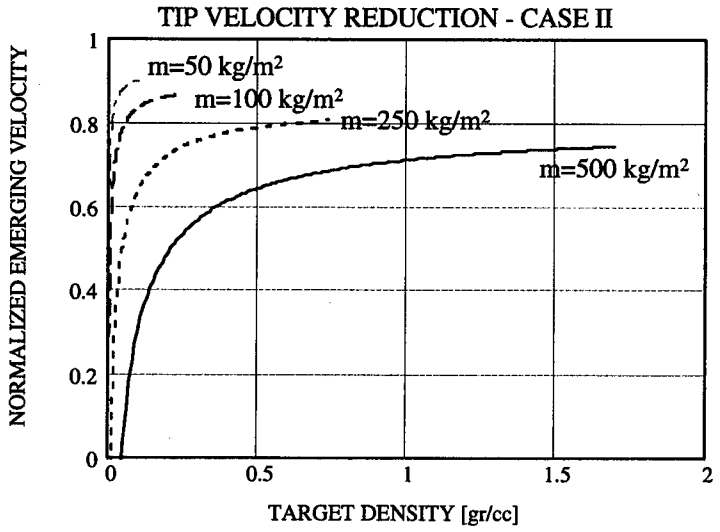

Fig. 5. Relative final jet tip velocity vs. target density for Case II, Vo=8 km/s, T_b = 100 μs.

The curves in Fig. 5 are valid only for density ranges in which the target is thick enough to ensure jet particulation while penetrating - Case II.

To summarize this case, it is clear that for a given target mass, the lower the density of the target the lower the velocity of the tip of the jet that will emerge from the back side of the target.

Case III

Examining Eq. (8), one can see that the velocity of the tip of a fully particulated jet, emerging from the back of a target of areal mass m is:

$$V_{outIII} = V_0 - \frac{m / T_b}{(\rho_j \rho_t)^{1/2}} \tag{17}$$

Hence, using a lower target density the out coming jet tip velocity will decrease too. Therefore, for this case, targets made of low density materials are more effective. The reason for this result is the assumption that each particle is moving with a constant velocity and the penetration depth can be calculated using Eq. (1). No bounds on the density of the target are imposed in this case since it is assumed that the jet hits the target after being fully particulated. The final jet tip velocity as a function of target density, for various targets areal mass is shown in Fig. 6.

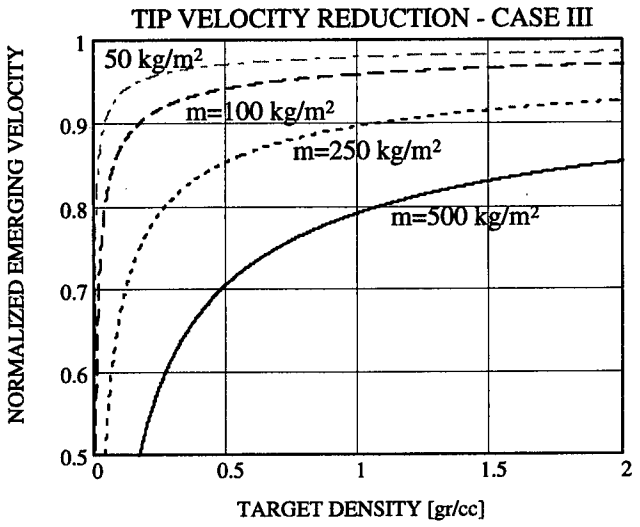

Fig. 6. Relative final velocity vs. target density for Case III, Vo=8 km/s, T_b= 100 μs.

Since the total jet penetration is a function of the lowest effective jet velocity V_{min} that depends on target strength, it is recommended to use low density materials with high yield strength (like ceramics and titanium).

VOLUME CONSTRAINT

If the volume of the target has to be kept constant, then the velocity of tip of the jet that will emerge after penetrating the target will decrease with increasing target density for all three cases, as can be seen from Eqs. (6)-(8).

EXPERIMENTAL SETUP AND RESULTS

The experimental setup is shown in Fig. 7. A precision shaped charge (SC) (84 mm diameter, 60°, point initiated), was used in most of the tests. Different targets were placed 200 mm ahead of the SC. The targets were made of various types of materials and had different thicknesses. The jet emerging from the target was examined using two flashes of X-ray and the residual penetration in RHA witness plates was measured.

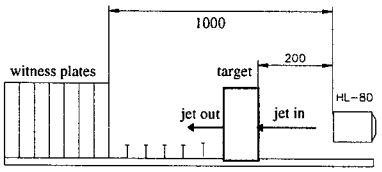

Fig. 7. Experimental Setup

The first test was performed without a target in order to characterize the jet. It was found that the velocity of the tip of the jet is V_0 = 6.95±0.05 km/s, and the tail velocity is V_{tail} =1.97±0.07 km/s. The position of the virtual origin was calculated to be 30 mm away from the charge cone base, towards the cone apex. Eleven additional tests were performed using various targets, as presented in Table 1.

Table 1. Experimental results

Test	*Target*		*Density [gr/cc]*	*Thickness [mm]*	*Emerging Jet Velocity & Time [km/s] V_{out}*	*[μs] T_{out}*
1	RHA	(+)	7.82	40	6.02	47
2	RHA	(+)	7.82	80	5.20	62
3	RHA	(+)	7.82	203	3.65	113
4	RHA	(+)	7.82	320	2.53	195
5	Mild Steel	(o)	7.83	80.5	5.22	63
6	Mild Steel	(o)	7.83	206	3.63	110
7	Aluminum	(◊)	2.75	232	4.75	98
8	Aluminum	(◊)	2.75	232	4.65	96
8	Aluminum	(◊)	2.75	115	5.57	65
10	Polyethylene	(□)	0.945	494	4.62	156
11	Water	(x)	1	573	4.44	181

RHA stands for rolled homogeneous armor steel and the aluminum used was 6061T6Al. The copper jet density is: ρ_j =8.94 gr/cc. The two X-Ray exposures enable us to measure the new tip velocity V_{out}, and the time the jet emerged from the back of the target (measured from the virtual time).

In addition we were able to examine whether this jet is still continuos or particulated.

DISCUSSION

Direct validation of the relation between target mass efficiency and target density is somewhat complicated. The penetration of a jet into a semi-infinite target usually involves penetration of continuous and particulated jet (Case II). The breakup time and the cut-off velocity are not well defined parameters, and they may vary from one charge to another. Hence, many parameters may have to be adjusted to fit the theoretical curve to the experimental data. To avoid these kind of difficulties we chose to validate our observation indirectly by measuring the out-coming velocity of a well defined jet after penetrating a given target and comparing the results with the theoretical values.

Numerical simulations of the penetration process of fast rods and stretching jets into various targets show [5] that the penetration velocity is very close to the one expected by the simple steady-state theory. The initial penetration velocity is higher than expected, in accordance with the planar shock loading of the target at this stage. Soon after the rarefactions from the free boundary reach the axis of symmetry, typically less than one microsecond, the penetration velocity drops down, fluctuates somewhat and, as the penetration proceeds, the rate of penetration slowly approaches the steady-state value.

The comparison between the measured velocities of the jets, that emerge from the back side of the targets, and the calculated values, (Eqs. (6) and (7)) are shown in Fig. 8. The calculated lines are for three materials: steel (bottom), aluminum (center), and water (top). For each material we have plotted two lines: one for the continuous jet - Case I (solid line), and one for the mixed mode of penetration- Case II (dashed line).

In all the experiments in which the jets penetrated the targets unbroken, the velocities of the emerging jets measured experimentally are in excellent agreement with those calculated by Eq. (6). In some cases there is a small deviation between the two values. The main reason for this deviation is the break-up process of the jet.

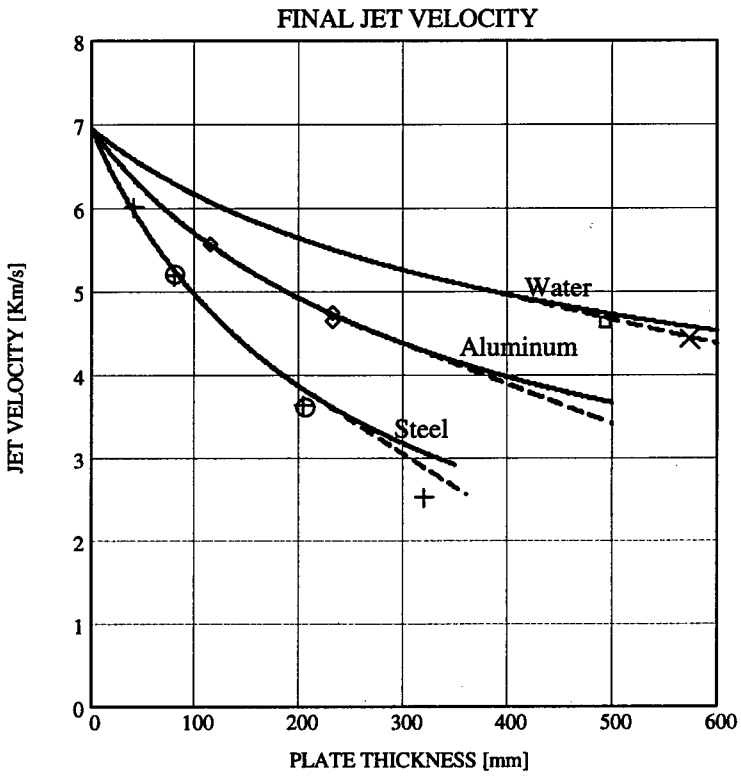

Fig. 8. Jet tip velocity after perforating a finite thickness target.
Experimental (symbols: presented in Table 1) vs. calculated results

Although it is commonly assumed that the jet breaks up all over at the same time, this is not exactly true in reality. Some parts of the jet break earlier, as seen for example in ref.[4]. In addition we have to take into consideration that the jet is ductile and the break-up, a necking process, is not instantaneous. Breaking can occur over a period of ten to twenty microseconds (or even more), depending on the jet diameter, local strain rate and material properties.

The breakup time of the jet examined varies along the jet and is about 115 μs at the middle of the jet, as measured from the virtual time. Hence the jets that emerge from the back side of the water and polyethylene targets in tests number 10 and 11, were expected to be particulated, as indeed was observed in the X-Ray radiographs. These experimental data points in Fig. 8 should therefore be compared with the Case II dashed line, and the agreement is indeed very good.

In three tests, using steel targets, the measured velocities are lower than expected. In one of tests the jet is particulated - test number 4 (RHA), and in the other two the emerging jet is continuous - tests number 3 (RHA) & 6 (MS), as seen in Fig. 9. A possible explanation for this phenomena is the strength of the steel, that decelerate the penetration rate. Another explanation for this discrepancy is an early break-up of jet.

Break-up is usually defined as the time the jet starts to particulate but it should be defined as the time the accumulated length of the jet segments ceases to increase. This time is earlier than the actual break-up time based on the old classical definition. This topic will be studied in detail in the near future.

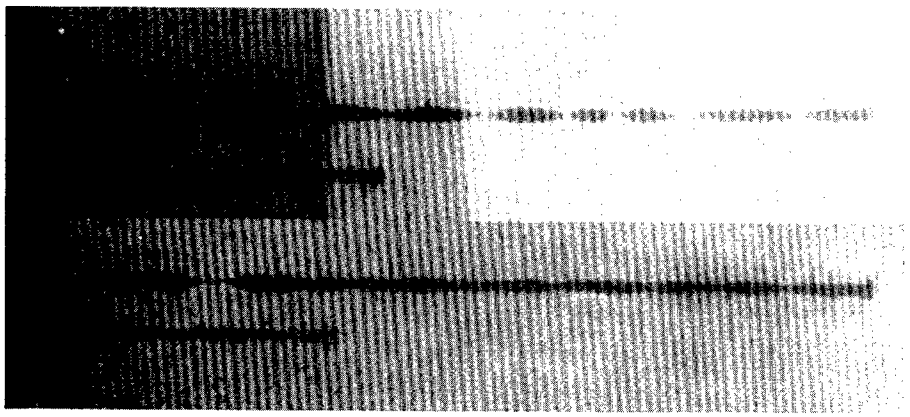

Fig. 9. X-Ray radiographs of the jets emerging from the back side of a 203 mm RHA target (top) and 206 mm mild steel target (bottom), at 140 μs and 170 μs.

To examine experimentally the efficiency of very low density targets (lower than the optimal one), we considered the penetration of jets into air. According to Backofen [6], the tip of jet is slowed and eroded while moving in air. Taking into account the compressibility of air, the erosion length should be about 30% smaller compared with the incompressible model (Eq. (1)). It is noted that this theoretical model is based on the assumption of steady flow. This assumption seems well justified for air, but does not hold for the jet tip erosion flow unless the ratio between the eroded length and jet diameter is considerably larger than unity. The reasoning behind this argument is that the steady flow established about the jet-air interface is a two-dimensional one (like a fountainhead). The time to establish such steady flow is proportional to its characteristic lateral dimension, i.e., the jet diameter. It would therefore take a run of a large distance before the jet tip erosion would be given in terms of the steady flow (one-dimensional) theory. Therefore, to test erosion in air small charges should be used.

Using small charges, we found that over a distance of about one meter in air (about 1.3 kg/m^2) the missing length of jet particles along the jet path (some of which are eroded) should be about 12 mm, in accordance with Eq. (1). As can be seen in Fig. 10, the tip of the jet after one meter distance of flight is spread into many small particles (circled) that amount to about 4 mm jet length. Hence the exact eroded length is not well defined in this case, and it is not clear if this experiment validates the incompressible theory. It should be noted that only particles in the front section of the jet were eroded, as was also observed by Held [7].

By neglecting the front spread out particles, the experimental observation confirms the conclusions presented in this paper: targets made of very low density materials are less efficient compared with those made of materials with the optimal density. The compressibility of air (and of other low density targets) changes somewhat the value of the optimal density (especially for jets with small diameters), in favour of lower density materials.

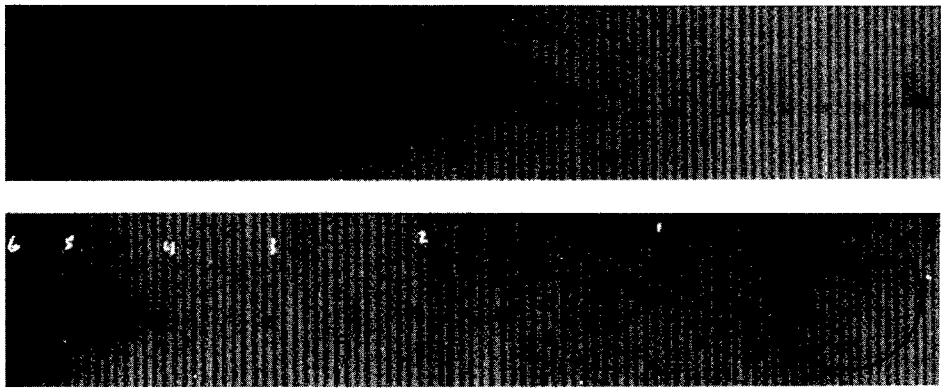

Fig. 10. X-Ray radiograph of the front part of a jet at two standoffs in air: top - 300 mm, bottom - 1300 mm.

CONCLUSIONS

Analyzing the penetration process of a shaped charge jet into targets of constant weight and various densities it was found that there is an optimal target density for eroding continuous jets.

This new concept is complementary to the classical view that low density targets are more effective in defeating shaped charge jets, a view which was found to be true only for particulated jets.

The analysis is based on the assumption that penetration is a steady-state phenomenon. The velocity of the out coming jet was measured and was found to be in a very good agreement with the classical penetration model.

Different values of the optimal density were derived and plotted as a function of various constraints, such as the areal mass and the standoff, and the characteristics of the jet.

REFERENCES

1. F.E. Allison and R. Vitali, A new method of computing penetration variables for shaped charge jets, BRL Report No. 1184, 1963.
2. R. DiPersio and J. Simon, The penetration relation for idealized shaped-charge jets, BRL Report No. 1542, 1964.
3. M. Held, Characterizing shape charge performance by stand-off behavior, *7th Int. Symp. on Ballistics*, The Netherlands, 1983.
4. M. Held, Particulation of shaped-charge jets, *11th Int. Symp. on Ballistics*, Belgium, 1989.
5. M. Mayseless, Penetration of fast rods and jets into finite thickness targets of various densities, *27th Israel Conference on Mechanical Engineering*, 1998
6. J.E. Backofen, Shaped charge jet aerodynamics, particulation and blast field modeling, *10th Int. Symp. on Ballistics*, California, 1987.
7. M. Held, The orthogonal syncho-streak technique as a diagnostic tool, particularly for shaped charge jets, *Propellants, Explosives, Pyrotechnics*, **11**, pp 170-175, 1986.

PERGAMON International Journal of Impact Engineering 23 (1999) 597–619

INTERNATIONAL JOURNAL OF IMPACT ENGINEERING

www.elsevier.com/locate/ijimpeng

HVI PHENOMENA: APPLICATIONS TO SPACE MISSIONS

J.A.M. McDONNELL

Unit for Space Sciences & Astrophysics, University of Kent, Canterbury Kent CT2 7NR, UK

Summary—Space Missions, by virtue of the energy required for geocentric or heliocentric orbits, generally explore and hence encounter objects at velocities in excess of terrestrial values for macroscopic objects. Their demand, to quantify impact relationships, extends from penetration to momentum exchange; from ionisation to plasma diagnostics. Response to the "need to know" in space and defence has led to the development of laboratory facilities and of hydrocodes; but because the parameter space of velocity and dimension in space cannot be replicated in full, the scaling of velocity and dimension is a vital element in establishing quantitative formula to decode space impact features. Such scaling - vital to generalised formula for both astrophysical and engineering aspects of space research - is reviewed; hypervelocity impact products generated for cratering, marginal penetration, hole growth, impact momentum and ionisation charge and current in the space environment are presented.
© 1999 Elsevier Science Ltd. All rights reserved.

SPACE MISSIONS AND THE HVI POTENTIAL

The task, demanded for both the development of missions and the analysis of data, is both the understanding and the quantitative formulation of hypervelocity impact phenomena; unless the encounter speed with solid objects is low (as in a rendezvous mission such as Rosetta[1]) or in co-orbiting geo-stationary space, then a velocity of greater than some 3 kms^{-1} is necessarily involved. For geo-centric space debris, the average impact velocity is 9.5 kms^{-1} and for meteoroids some 20 kms^{-1} [2]. Demands are placed from different disciplines, namely the understanding and quantitative formulation of hypervelocity impact Phenomena:

Engineering : Design, Reliability and Post Flight Analysis (PFA) of Spacecraft

Physics : Instrument Design; Calibration (of in-situ detectors); PFA of impacts

Astrophysics : Meteoroids, Comets, Interplanetary Dust, Interstellar Dust

The quantitative characterisation of HVI phenomena leads to a product which can be the kernel of other disciplines; the formula may be embodied in spacecraft design or software utilised in application programmes such as ESABASE [3] or ORDEM 96[4] to predict likely impact damage. The intrinsic physics involved can be prosecuted to any depth in its own right but we focus here on quantitative first order parametric equations: impact effects characterised by the detector bulk material properties and by the impactor velocity, size and density.

Space missions are the end product of an "organic" process of advocacy and assessment within or between the Agencies or nations; a process of consultation and assessment balancing objectives against feasibility and cost. Figure 1 shows factors in such a process; the cycle

0734-743X/99/$ - see front matter © 1999 Elsevier Science Ltd. All rights reserved.
PII: S0734-743X(99)00107-4

though to data acquisition ("results") is minimally 5 years often 15 to 20. Essential inputs are HVI relationships, both at the sensor or instrument characteristics and to also assess mission reliability. In the GIOTTO and VEGA Halley Missions [5,6] and in the Stardust Mission ahead [7], the extremely high velocity of particulates needed to be encountered for the in-situ measurements places high demands on impact survivability. Miss-distances of some several hundred kilometres may involve collision with particulates having the energy of a domestic motor car but a mass of only one gramme! The 'carousel' of space mission development, where HVI performance cririically governs the mis-distance, is ridden once more after the actual mission using the tools used for mission planning. Facilities for HVI characterisation must remain open for post flight analysis (PFA); actual results rarely conform to expectations.

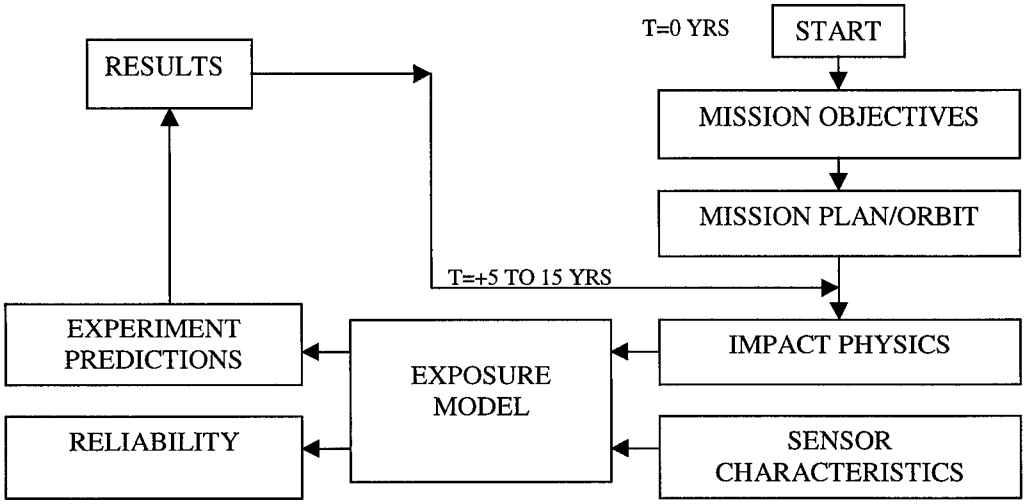

Fig. 1. The Carousel of Cometary Space Mission development; providing an opportunity for HVI exploitation and demands in terms of mission planning, the software and routines used for reliability and impact damage in planning get exercised later when real post flight impact data is analysed.

We look first at the parameters which are demanded in space missions and then the extent to which we can replicate these parameters.

SPACE IMPACTORS AND FACILITY PERFORMANCE

In geo-centric space the velocity of any bound orbits of satellites, or space debris exceeds 7.6 kms^{-1} for circular LEO orbits increasing to 10.8 $km.s^{-1}$ for the highest eccentricities. The average satellite-satellite collision velocity gives a value of 9.5 kms^{-1} [8]. Meteoroids have a higher geocentric range, namely from 10.8 to 72.0 kms^{-1} but, yet, a mean value of some 21.4kms^{-1} relative to a satellite [9]; the effective mean depends on the weighting of parameters relative to a particular impact process, the "detector". This is a factor which must be incorporated to compare data on the same objects but from different sensing techniques. Encounter velocities of satellites, space debris and meteoroids are parameters which can be well-reproduced in the laboratory but not at the same scale.

The dimension of interest may vary from femtogram scale for the Comet Halley grains detected on the PIA/Puma experiment [10] to the largest particle likely encountered with a spacecraft. In Earth orbit, critical attention currently focuses on space debris particles of some centimetre in diameter, which cannot be tracked so as to employ avoidance maneuvers. This

scale can be well reproduced in the Light Gas Gun and mimicked in hydrocodes; for astrophysical matter, we may not be able to replicate fragile agglomerates but at high velocities this is a second order effect. The velocity of centimetre scale impactors in the laboratory could not approach the 68 kms^{-1} of GIOTTO or 78 kms^{-1} of the VEGA duo; for this velocity we must access electrostatic microparticle accelerator facilities which can well exceed this velocity, albeit at smaller scale. The smaller particles of interplanetary dust, cometary coma or stardust are well replicated in electrostatic facilities in both velocity and size, hence being vital for the development of space sensors. Figure 2 shows the parameter range of space impactors.

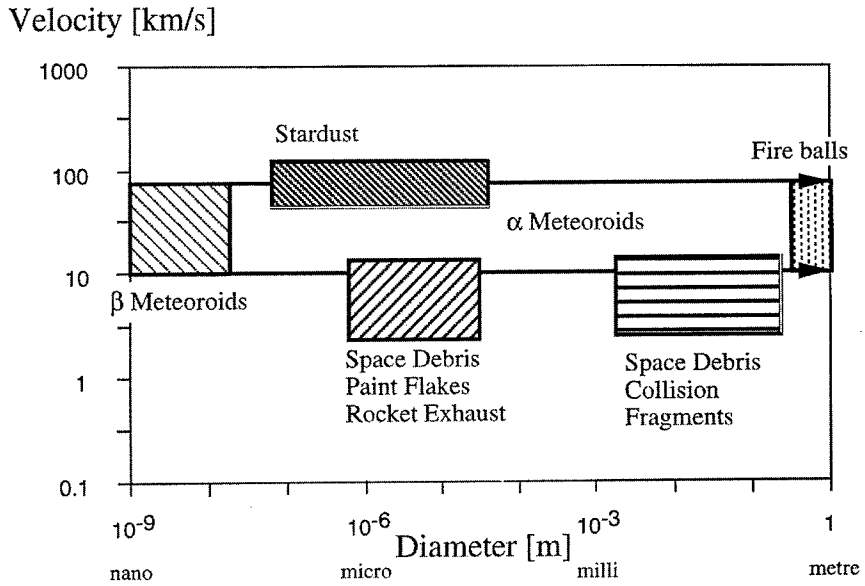

Fig. 2. Space impactors encountered in Earth orbit and interplanetary space. The range extends from nanometres to centimetres - the velocity from some 3 to 80 kms^{-1} relative to a spacecraft.

Facility parameters, shown in Figure 4 on the same scale, thus overlap at higher speeds for small particles and - for space debris - are not far from reality in terms of engineering space debris bumpers. To apply laboratory data to astrophysical particles we must, therefor, learn to scale up and down the axis of velocity and along the axis of dimension.

Scaling of an effect, quantified at one mass and velocity, to another point on the same mass velocity plane is closely coupled to the phenomenon being considered. In establishing that a stimulus to a sensor, giving a signal which is a function of momentum, for example, a functionality of signal proportional to $(\text{mass})^{\alpha}.(\text{velocity})^{\beta}$ may be established where α = say 1.0 and β= 1.0 to 2.0; but for an impact plasma with a relationship of very similar form we might find $\beta = 4$.

To find, therefore, a facility appropriate to calibrating a momentum sensor for cometary grain impacts we would scale the mass inversely as $1/V^{1.5}$ but for a plasma detector as $1/V^4$. These lines of constant signal level labeled "isophenomena" are shown as overlays to the facility parameter space in Figure 4 for velocity dependence indices of 1, 2 and 4.

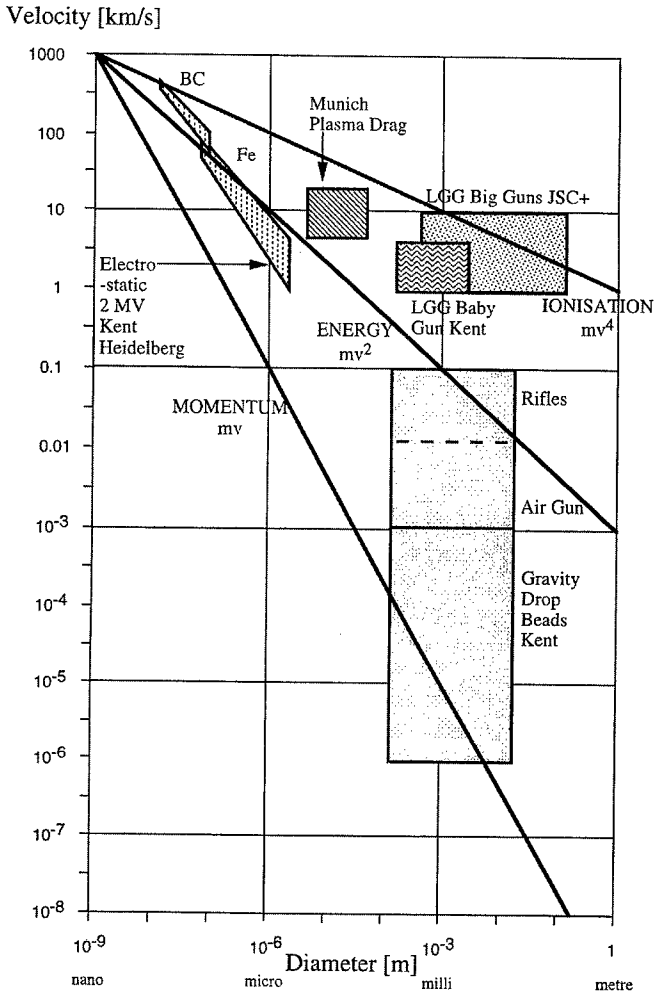

Fig. 3 Performance limits for major electrostatic and macroscale facilities; the correspondence with space demands (Fig. 2) which displays only the range 0.1 to 1000 kms^{-1}) is fair, but not fortuitous. Where specifications have a known functional dependence the appropriate calibration facility can be sought for the impactors in mind using "isophenomena". .These lines of constant product mv, mv^2 , mv^4 typify e.g. functional dependences of impact momentum (mv), cratering (mv^2) and ionisation (mv^4). They can be used to ascertain which facilities could be used with scaling to provide calibration for space impactors. Momentum measurements on microparticulates in space e.g. if dependent on mv, may demand relatively simple facilities such as bead dropping to establish sensor response. Light gas guns may be needed to investigate the momentum enhancement which depends on crater volume (mv^2).

The implication is vital to the choice of facilities to calibrate sensors; for momentum sensing of cometary grains we need to quantify not only the momentum exchange and ejecta at hypervelocities, but would follow the "isophenomenon" of index 1 on the mass-velocity plot to calibrate the sensor momentum response; minute glass beads so called for and impacting at the low velocities induced by gravity drops extend our "facility" mass velocity regime by four

decades. The Light Gas Gun misses the momentum isophenomenon by a wide margin but, yet, may be quite appropriate for impact plasma studies of cometary grains in the laboratory.
Major facility attributes are sketched in Table 1; bead dropping (not included) is not considered a facility, although the techniques for quantitative calibration have proved vital to sensor calibration and attracted attention in their own right[11].

Table 1 . Comparative properties of Electrostatic Accelerator Light Gas Gun and plasma drag facilities [12,13].

	ELECTROSTATIC	LIGHT GAS GUN	PLASMA DRAG
Cost	Mid	Mid-Major	Major
Rate	1 per second	1 per 2 hours	2 per day
Projectile characterisation	± 1% mass velocity (no shape)	Good 5%	Difficult but acceptable
Enviroment	Perfect No gas No blast No discharge	Dirty unless effort spent	Dirty and electrically noisy
Analysis	Re-usable	Non-Resuseable	Not Re-usable
Analysis	Electronic or SEM	Electronic or Visual	Electronic? or microscope
Flight calibration	Yes	No	No

Where dimension cannot be scaled (such as multiple plate perforation or more complex shields) Light Gas Guns are the workhorse complemented by plasma drag facilities [12] and other electromagnetic techniques: the electrostatic facilities provide, though, an abundance of data without target destruction and, if the results can be 'grabbed' electronically, several hundred data points per hour can be acquired. A sample of 124 Fe particle parameters accelerated on a 2MV Van de Graaff accelerator [13] is shown in Fig. 4, with velocities ranging from some 3 to 90 kms^{-1}. The facility may be gated by a velocity window but (to utilise the high data rate) experiments are best designed to "grab" data from all impacts.

We see the interest, for space missions and satellite design, covering a wide range of dimensions: some 15 decades of mass and 5 in linear dimension. For planetary impacts this range is, however, minute; although the latter have not been calibrated, the end morphology is grossly comparable. Figure 5 identifies parameters we must consider in scaling when navigating the mass-velocity regime. Because the impact velocity determines the specific energy of both the projectile and target, impact compression crosses the same barriers of yield strength and traverses the same phase charges at all dimensions; scaling with size is, consequentially, weak and often has to be sought to be identified and characterised. Comparison of micro-dimension impact cratering (ES facilities) and centimetre scale impacts leads to a scaling dependence proportional to particle $(\text{dimension})^{.056}$ [14,15]; for the impact plasma, normalised to particle mass, a mass scaling of plasma yield independent of mass or perhaps $(\text{mass})^{.02}$ is typical; this figure is equivalent to a dimensional scaling exponent of .06; scaling of the ion yield with mass is compatible with the slight increase of crater excavation volume with dimension. We are then left, in dimensional scaling, only with a search for non volumetric effects of which surface radiation, viscosity and conductivity are key physical effects. None of these parameters are modeled in hydrocodes but, to be fair, they are not usually dominant in cratering, and certainly not at centimetre scale; they may, however, (e.g. viscosity, radiation cooling) determine this

weak scaling with dimension. In ionisation studies, surface radiation is essential to HVI expansion processes and may dominate energy loss of ejecta.

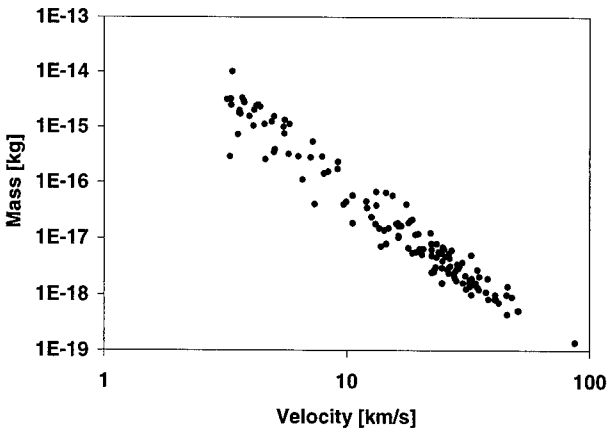

Fig. 4 Parameters of projectiles accelerated by an electroststic accelerator facility (courtesy M. J. Burchell); a high data rate (1/second) and high velocities provides ready calibration and, with weak dimensional scaling pemits the exploration of velocities extending knowledge gained from the limited performance of macroscale facilities.

SCALING OF VELOCITY AND DIMENSION

We see the interest, for space missions and satellite design, covering a wide range of dimensions: some 15 decades of mass and 5 in linear dimension. For planetary impacts this range is, however, minute; although the latter have not been calibrated, the end morphology is grossly comparable. Figure 5 identifies parameters we must consider in scaling when navigating the mass-velocity regime. Because the impact velocity determines the specific energy of both the projectile and target, impact compression crosses the same barriers of yield strength and traverses the same phase charges at all dimensions; scaling with size is, consequentially, weak and often has to be sought to be identified and characterised. Comparison of micro-dimension impact cratering (ES facilities) and centimetre scale impacts leads to a scaling dependence [15,16] proportional to particle (dimension)$^{.056}$; for the impact plasma, normalised to particle mass, a mass scaling of plasma yield independent of mass or perhaps (mass)$^{.02}$ is typical; this figure is equivalent to a dimensional scaling exponent of .06; scaling of the ion yield with mass is compatible with the slight increase of crater excavation volume with dimension. We are then left, in dimensional scaling, only with a search for non volumetric effects of which surface radiation, viscosity and conductivity are key physical effects. None of these parameters are modeled in hydrocodes but, to be fair, they are not usually dominant in cratering, and certainly not at centimetre scale; they may, however, (e.g. viscosity, radiation cooling) determine this weak scaling with dimension. In ionisation studies, surface radiation is essential to HVI expansion processes and may dominate energy loss of ejecta.

In velocity scaling, therefore, the scene is very different. Impact velocities, necessary to exceed the weakest at physical threshold (yield strength) are low. For bulk yield strengths of typical engineering materials only some hundred metres per second is sufficient. Space velocities thus well exceed strength of the target and projectile but the next threshold of impact melting might require some 2 kms^{-1} and vapourisation some 5 kms^{-1}. The question of ionisation is less clear and the mechanisms more complex. In addition to these specific thresholds for

phase change under compression, increasing velocity takes matter further up the shock Hugoniot and subsequent relaxation (because of the difference in energy between the shock compression and release adiabat) leaves the expanded target/impactor material in a state "elevated" above the pre-impact conditions. Facilities must, therefore, either singly or in concert reproduce the actual velocity; this "vertical" scaling of the facility mass-velocity plot is the critical issue and a costly one to solve at large dimensions. If this cannot take place at the same dimension, we can first traverse the horizontal axis, which involves only weak scaling, and the climb the vertical axis at small dimensions.

Table 2 . Characteristic timescales for impactors at microscale and centimetre scale for the extreme velocity range of all facilities. Even the shortest time (at 200 kms^{-1} for a 0.1 micron particle) is still short compared to electronic processes, and dimensional scaling is consequently weak.

Dimension	Velocity	τ
0.1 μm	200 km s^{-1}	$5\text{-}10^{-15}$ s
1 cm	10 km s^{-1}	10^{-6} s

Dimensional scaling has also been related to time dependent effects such as strain rate hardening [16] and is incorporated in hydrocodes as elements of e.g. Johnson Cook models [17]. The characteristic time (considered equal to the value for an impacting particle to traverse its own length) varies from some 5.10^{-15} s for a 0.1 micron particle at 200 kms^{-1} to 1.10^{-6} s for a centimetre scale Light Gas Gun projectile at 10 kms^{-1}. This range, of 8 decades, could well be considered a factor in the several phase changes involved and of consequence relative to the dislocation propagation times in crystal lattices; but impact effects have been studied at these extreme mass-velocity limits and the effect is fairly minor!

IMPACT AND PERFORATION

Regimes where we need formulae vary from cratering (in a target thick compared to the final crater depth) to thin foil or plate perforation (where the projectile may pass through only lightly shocked); its signature in the witness foil may reveal its geometric profile and other clues may testify to its velocity.

A critical region delineating the two regimes is the ballistic limit of penetration when a projectile **just** leads to a small perforation; equations generally follow this divide, comprising

1. Crater diameter/depth formulation in semi-infinite targets
2. Ballistic limit equations, and
3. Hole growth equations.

A further class of damage equation would apply to more complex studies such as debris shields, honeycomb and Solar Array structures.

Impact Cratering

Being less sensitive to scale, numerous equations from microscale to centimetres describe the resulting crater diameter (D_c) or depth (T_c) at velocity V for a projectile of mass m. The general form is

$$D_c = Am^{\alpha}v^{\beta} \quad (1)$$

where $\alpha \approx 1.02$ and $\beta \approx 0.7$. Crater volume per impactor energy is a key basis for these formulae, but the difference between observed effects and this exact relationship (where we would have $\alpha = 1$ and $\beta = 2/3$) result largely from velocity scaling at a given impactor mass; the energy, increasingly invested in higher energy phases at early times during cratering is clearly made available for crater excavation in the later stages (e.g. vapour under pressure) since $\beta > 2/3$ in experiment. A failing of many hydrocodes, in trying to replicate this, is the throwing away of "failed material" in such a state because of difficulties in modelling; in reality, vapour phases are trapped inertially within high pressure regions and, on release, contribute effectively to crater expansion. We see in the next section that thick target cratering formula are complemented by equations of very similar form as for the ballistic limit. This is because the ballistic limit of hemispherical craters is some 1.5 times the thick target crater depth T_c in metallic targets.

Ballistic Limit Equations

Representative equations [14,15,18,19,20], applicable to metallic targets, show a dependence on parameters fairly close to projectile energy but differences are significant. Although the velocity exponent varies in degree, an exponent higher than 2/3 is universal and 0.8 is typical: this is explained partly be by increased ductility for larger crater size as velocity increases although size scaling of the entire ratio f_{max}/d_p at constant velocity is incorporated independently. Effect such as viscosity and conductivity identified in Figure 5 can account for this factor. An exception to this weak dimensional scaling is shown in the formula of Pailer & Grün [19], which is a parametric fit to their data sources incorporated; this anomaly results from comparing "small apples" to "large oranges" in the mass-velocity database and should be used with caution outside that mixed dataset. All the empirical ballistic limit formula fit their respective source data; several formulae do, however, extend to projectile and target parameters such as density and strength. Their range is, strictly, limited to the sources data used but, where a wide range of target densities and strengths for metals has been explored, their validity may well be generalised for that class of material e.g. ductile metals; less confidently it can be used for "any materials" if a wide range of projectile/target strengths and densities has been explored.

Table 3 . Ballistic limit equations in terms of various selection of projectile and target dependence A particle size dependence having an exponent of .056 characterises most relationships. Some include more properties but generally agree where common arguments are inserted. McDonnell & Sullivan is based on impact experiments to above 16 kms^{-1} and hence readily applied to space impacts on metal surfaces.

Fish and Summers:

$$\frac{f_{\max}}{d_p} = 0.57 d_p^{0.056} \varepsilon^{-0.056} \left(\frac{\rho_p}{\rho_t}\right)^{0.5} V^{0.875}$$

Pailer and Grün 1980:

$$\frac{f_{\max}}{d_p} = 0.772 d_p^{0.2} \varepsilon^{-0.056} \rho_p^{0.73} \rho_t^{-0.5} (V \cos\alpha)^{0.806}$$

McDonnell and Sullivan 1992 – 'Equation C':

$$\frac{f_{\max}}{d_p} = 1.272 d_p^{0.056} \left(\frac{\rho_p \rho_{Al}}{\rho_{Fe} \rho_t}\right)^{0.476} \left(\frac{\sigma_{Al}}{\sigma_t}\right)^{0.134} V^{0.806}$$

Cour Palais:

$$\frac{f_{\max}}{d_p} = 0.65 d^{0.056} \rho_p^{0.52} V^{0.875}$$

Gardner 1995 et al:

$$\frac{F_{\max}}{d_p} = 0.129 \left(\frac{V \rho_p}{\sqrt{\sigma_t \rho_t}}\right)^{0.763} \left(\frac{\sigma_t}{\sigma_{Al}}\right)^{0.229} d_p^{0.0}$$

Table IV . Equations for hole growth for spheres on plane finite targets. Applicable to single plate space impacts, the GMC formulae incorporates the same ballistic limit (Table III) and beyond. This has been derived from perforations to above 16 kms^{-1} at microscale and, with the dimensioinal scaling, conforms with centimetre scale data (Fig.6).

Sawle 1969:

$$\frac{D_t}{d_p} = 2.6\left[\left(\frac{\rho_p}{\rho_t}\right)\left(\frac{V}{c}\right)\right]^{-0.2}\left(\frac{f}{d_p}\right)^{2/3} + 1$$

Maiden et al 1963:

$$\frac{D_h}{d_p} = 0.45\left(\frac{f}{d_p}\right)^{2/3} + 0.9$$

Nysmith and Denardo 1969:

$$\frac{D_h}{d_p} = 0.88\rho_p^{0.5}\left(\frac{f}{d}\right)^{0.45} V^{0.5}$$

Carey, McDonnell and Dixon 1985:

$$\frac{D_h}{d_p} = 1 + 2.9\left(\frac{\rho_t}{\rho_p}\right)^{0.6}\left(\frac{f}{d_p}\right)V + \left[\frac{1}{1 + 2.9\left(\frac{\rho_t}{\rho_p}\right)^{0.6}\left(\frac{f}{d_p}\right)^2 V^{-n}}\right]$$

Where n is defined as:

$1.02 - 4\exp(-0.9V^{0.9}) - 0.003(20 - V)$ For $2<V<20$ km/s

1.02 For $V>20$ km/s

The New Formula:

Gardener, McDonnell and Collier 1996 (GMC):

$$d'_p = A\left(\frac{10}{9 + \exp\left(\frac{D'_h}{B}\right)}\right) + D'_h\left(1 - \exp\left(-\frac{D'_h}{B}\right)\right)$$

$$d'_p = \frac{d_p}{f} \text{ and } D'_h = \frac{D_h}{f}$$

$$A = 6.97\left(\frac{V\rho_p}{\sqrt{\sigma_t \rho_t}}\right)^{-0.723}\left(\frac{\sigma_t}{\sigma_{Al}}\right)^{-0.217} f^{-0.053}$$

$$\frac{f_{max}}{d_p} = 1.272 d_p^{0.056}\left(\frac{\rho_p \rho_{Al}}{\rho_{Fe}\rho_t}\right)^{0.476}\left(\frac{\sigma_{Al}}{\sigma_t}\right)^{0.134} V^{0.806}$$

The equations of McDonnell & Sullivan [15] and (incorporating the same data for metal targets) that of Gardner et al.[20] are widely applicable to meteoroids and debris impacting foil detectors or spacecraft (single thickness) skins; they include projectile density relationships appropriate for meteoroids or e.g. space debris projectiles. They have been vital to analysing the results of

numerous threshold detectors in space. For larger particles (or thinner targets) we review some hole growth formulae.

Hole Growth

Above the ballistic limit, the hole increases rapidly for only modest marginal projectile energy. The non-linear relationship has attracted fewer modellers than has impact cratering or the ballistic limit. but several formulae are now offered. Different formulae incorporate different parameters; Sawle et al.[21], refer to the front hole diameter which is independent of any perforation. Carey, McDonnell & Dixon [22] provide a formula for the perforation diameter used to decode space impactor dimensions but in a restricted form, thus defining hole growth only above a perforation limit corresponding to $D_h = 0.6f$. Other classic formulae are shown [23,24] lacking either appropriate dynamic range or the characterisation of both target and impactor parameters.

These difficulties are removed in the GMC equation, which derives the particle diameter from a given perforation and removes this problem; it is based on a ballistic limit formulation and models the onset of progressive growth at the ballistic limit and perforation thereafter. The source data, as per that of the CMD equation, is identical to that used for the McDonnell and Sullivan ballistic limit, namely thin foil penetration measurements performed at velocities of up to 16 kms^{-1} during 1966 and 1967 [25] at the NASA GSFC 2MV electrostatic facility. The type of facility, first developed at TRW Redondo Beach Ca. by Becker et al [26], was used by Friichtenicht [27] to detect impact ionisation; his pioneering initiative led to facilities now at Heidelberg and Kent employing almost identical techniques and the development of numerous space sensors.

A test of the GMC equation in which is derived at scales down to 0.1 micron particle diameter but extending to beyond 16 kms^{-1} is provided in Figure 6 where aluminium plate perforation by glass spheres performed by Horz et al [28] was explored in a carefully executed series of accurate measurements in the millimetre to centimetre scale. It will be valuable to test the equations or more recent hole growth experimental data [29]. The agreement is reassuring but attention is drawn to an typographical erratum in the first publication [20] of the GMC equation; the equation and summary parameters appropriate to its application to spacecraft are presented

Definition of GMC

For a hole of diameter D_h μm in a foil f μm thick, the particle diameter is given by

$$d'_p = A\left(\frac{10}{9+\exp(D'_h/B)}\right)+D'_h\left(1-\exp(-D'_h/B)\right)$$

where

$$d'_p = \frac{d_p}{f} \text{ and } D'_h = \frac{D_h}{f}$$

and A is given by

$$A = 6.97\left(\frac{V\rho_p}{\sqrt{\sigma_t\rho_t}}\right)^{-0.723}\left(\frac{\sigma_t}{\sigma_{Al}}\right)^{-0.217} f^{-0.053}$$

where all units in the brackets are in either SI or cgs except for d_p, D_h and the dimensional scaling factor f, which can be in any units providing they are the same; for parameter A, V is in km s^{-1}; B is given by

$$B = B_1 + B_2 V$$

B_1 and B_2 are given by Table 4 (below) and V is in km s^{-1} (not m s^{-1} as for parameter A!).

Table 4. Parameters for the GMC equation for common metallic targets. r^2 is the linear regression coefficient.

Material		Velocity (km s^{-1})	Density (kg m^{-3})	Yield stress (Pa)	B_1	B_2	r^2
Al	Aluminium	1.2-6.0	2780	6.90×10^7	-0.004	1.85	
Al	Aluminium	6.0-10.7	2780	6.90×10^7	6.66	0.74	0.933
Ag	Silver	2.9-5.6	10500	1.50×10^8	7.92	3.14	0.26
Au	Gold	2.1-7.5	19300	1.20×10^8	6.65	2.77	0.85
BeCu	Beryllium copper	3.7-6.4	8240	8.28×10^8	-26.3	10.3	0.82
Cu	Copper	2.0-6.9	8950	2.20×10^8	3.20	2.62	0.744
SS	Stainless steel	2.2-3.7	7840	7.59×10^8	0.11	2.34	0.902
Ti	Titanium	2.3-6.6	4720	9.86×10^8	0.618	2.26	0.958

Ballistic limit equation is derived from McDonnell and Sullivan (1992C) and is the solution for f when the hole size tends to zero.

$$f'_{\max} = 0.129 \left(\frac{V \rho_p}{\sqrt{\sigma_t \rho_t}} \right)^{0.763} \left(\frac{\sigma_t}{\sigma_{Al}} \right)^{0.229} d_p^{\,0.056}$$

where

$$f'_{\max} = \frac{f_{\max}}{d_p}$$

and as before, the units in the brackets are in either SI or cgs, V is in m s^{-1} and the dimensional scaling factor d_p is in microns.

Table 5: Example of the velocities of meteoroids and space debris, together with application of GMC hole growth formula for aluminium 6061 T6.

Density of target	ρ_t (kg m^{-3})	2780
Yield stress of target	σ_t (Pa)	6.90×10^7
Yield stress of aluminium	σ_{Al} (Pa)	6.90×10^7

Particle populations / spacecraft surface orientation

		LEO			Sun pointing		LEO RTP Mean V
		RAM	WAKE	ZENITH	Meteoroids	Debris	Meteoroids
Normal component of Velocity	V (km s^{-1})	21.4	15.3	16	17.6	10	17.9
	V (m s^{-1})	21400	15300	16000	17600	10000	17900
Density of projectile	ρ_n (kg m^{-3})	2500	2500	2500	2500	4000	2500

Ballistic limit

Particle diameter*	d_p (μm)	1	1	1	1	1	1
Ballistic limit / particle diameter	f_{max}'	5.05	3.91	4.04	4.35	4.04	4.40
McD & S f_{max}'	McD&S	5.19	4.01	4.15	4.47	3.59	4.53

Hole growth

Foil thickness†	f (μm)	5	5	5	5	5	5
Parameter A	A	0.20	0.25	0.24	0.23	0.24	0.23
From lookup table	$B1$	-0.004	-0.004	-0.004	-0.004	-0.004	-0.004
	$B2$	0.74	0.74	0.74	0.74	0.74	0.74
Parameter B	B	15.83	11.32	11.84	13.02	7.40	13.24
	D_h'	d_p'					
	0.5	0.26	0.34	0.33	0.31	0.34	0.30
	1	0.31	0.40	0.39	0.36	0.44	0.36
	5	1.61	2.13	2.05	1.90	2.80	1.87
	10	4.96	6.25	6.07	5.69	7.89	5.63
	50	47.74	49.36	49.23	48.86	49.94	48.79
	100	99.82	99.99	99.98	99.95	100.00	99.95
	500	500.00	500.00	500.00	500.00	500.00	500.00

*f'_{max} scales as $d_p^{0.056}$
†d_p' scales as $f^{0.053}$

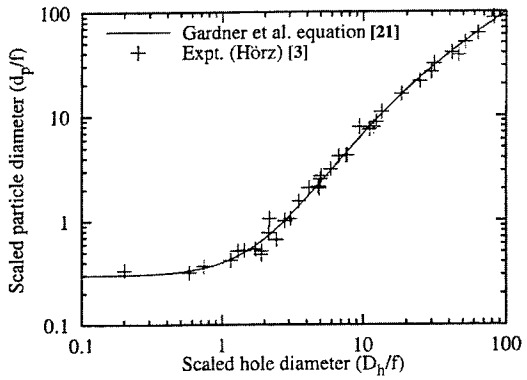

Fig. 6 Test of the GMC hole growth equation [20] with perforation data of Horz[28] on aluminium plates by glass projectiles at 4.9 kms^{-1}. The correspondence is comforting; since the GMC equation is derived from data to 16 kms-1 it has been applied to space data with confidence.

Application of Impact Equations to Space Data

We look at an application of the McDonnell & Sullivan equation firstly to the body of spacecraft threshold sensors accumulated since the beginning of space research. Early thrust for measurements in space was the threat of meteoroid damage and many early experiments carried high area-time products thus yielding high flux and, critically, extended to relatively large masses. We note the "Beercan" satellites (Explorers XVI and XXIII); the Pegasus series (I, II and III), which unfolded giant wings of detector panels. Launched by the Apollo I rockets, they were well visible in the evening sky. Valuable now is the assessment of these experiments by a unified penetration equation. Baron [30 31] has carefully evaluated the properties of the differing detector materials and applied the McDonnell & Sullivan equation, together with Earth Shielding factors. The result (Table 6) provides a valuable base for LEO assessment in an era prior to the advent of space debris.

Table 6. Meteoroid properties in the low Earth Environment deduced from the application of thick target cratering formulae [12], and the GMC thin foil hole growth equation [18]. A characteristic density of 1.5 gcm^{-3} results for foil perforations - skewed from a real density distribution with an unweighted mean of 2.5 gcm^{-3} by the non-linearities of the cratering relationships.

Mean/characteristic density	2.0-2.4 g cm^{-3} / 1.5 g cm^{-3}
Velocity distribution	Taylor (1996) (Reanalyzed HRMP)
Mean impact velocity – Impact (penetration formula) weighted for all angles	16 km/s
Source	Isotropic in LEO exposures but Earth-apex direction biased in heliocentric space
Shape	Irregular
Aspect ratio	1.0-1.5

Data from different detectors (Figure 2) but referred now to an equivalent thickness of Aluminium, is compared with the meteoroid impact penetration modelling for LEO satellites at

comparable altitudes using ESABASE. Earliest exposures are consistent with domination by meteoroids, but when folded with more recent data, we find the meteoroid flux dominates only in the mid mass range; orbital debris, depending on attitude and altitude, is now found to dominate at micron dimensions and above 1 millimetre.

Using comprehensive flux modelling programmes, McBride [2,9] has taken the modelling of the meteoroid population to a more sophisticated level, including the velocity distribution of meteoroids, directionality in the heliocentric and geocentric space, Earth shielding and gravitational enhancement; plus the full spacecraft attitude and orbit history. Summary results of the modelling of a modified Grün meteoroid flux distribution [32] for LDEF's space face (to which only meteoroids have access) is shown in Figure 8; with this test of accuracy for the model and penetration formulae, this model is then applied to the other periphal faces of the same satellite using the vast Meteoroid & Debris Special Investigation Group Database [33]. The flux enhancements (i.e. above the meteoroid distribution) yield the non orbital component, presumed space debris from flux arguments and to some extent confirmed by residue studies [34,35]. Shown in Figure 9 is the flux distribution we derive for the RAM (E) direction and trailing direction of LDEF (W).

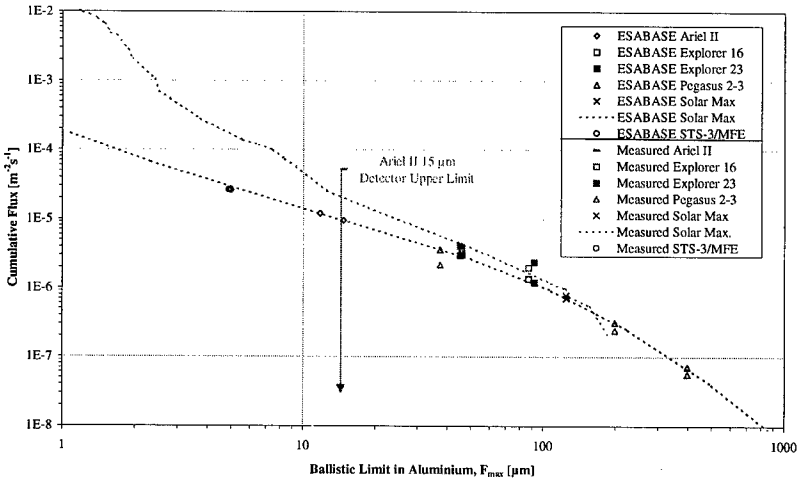

Fig.7 Application of ballistic limit equations of McDonnell & Sullivan to early space missions metallic target threshold penetration sensors [30]. Incorporating sensor material properties, it yields a flux distribution compatible with the Grun meteoroid environment modelled in ESABASE. This may be compared to more recent data (below) demonstrating additional fluxes of space debris at microscale and millimetre dimensions.

We see quite distinctive space debris signatures for the two directions, showing the two orbital populations of "micro" and "milli" space debris. The two populations may be compatible with: 1) a low inclination, low eccentricity population dominating the Ram directions (compatible with GTO launche activity and 2) a more eccentric higher inclination population related to e.g. Molnya type orbits. These space debris fluxes, derived to update environmental models, were derived an a study supported by the European Space Agency [36].

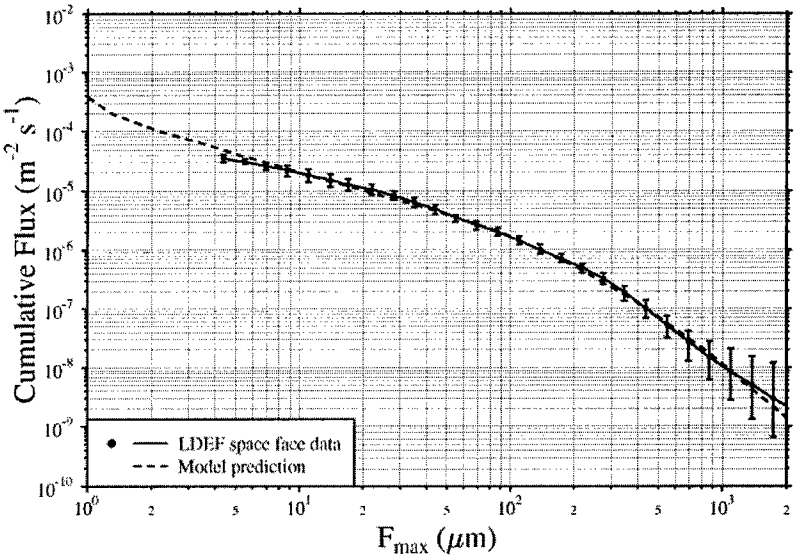

Fig. 8 Application of a flux modelling programme by McBride to the meteoroid flux impacting LDEF's space pointing face in terms of the ballistic limit in aluminium, F_{max}. Space debris has insignificant access to the space face. The programme, used of the average meteoroid distribution, as validation is then applied to other faces to which space debris does have access. It demonstrates an excess flux in some directions due to space data due to space debris (Fig.9).

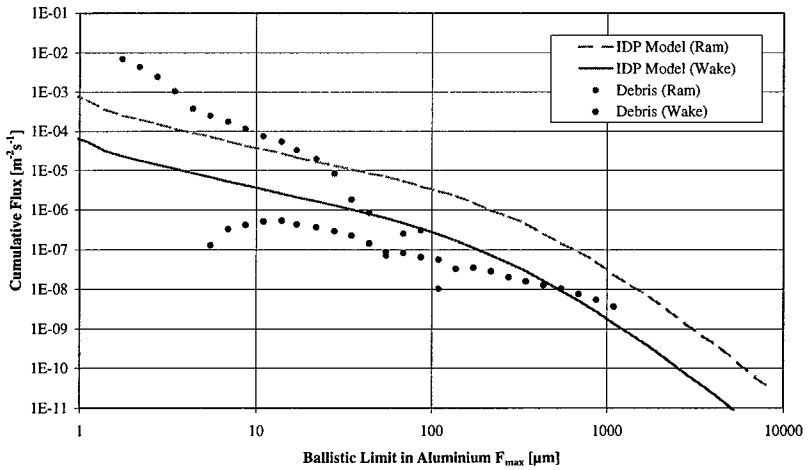

Fig. 9. Excess fluxes above the modelled meteoroid distributions from LDEF's RAM(E) and WAKE(W) directions. Attributed to space debris, the debris fluxes have quite different different signatures in terms of their size distribution reflecting two different populations.

Armed with a space impact ballistic limit equation, honed on LDEF's actual impact exposure records, and also a hole growth formula tested at space velocities, we have applied the two self-consistent formulae together in an interesting manner. This is based on the two premises:

1. crater dimensions in thick targets are dependent on projectile mass and only weakly dependent on particle density (at a given velocity we can estimate a particle's *mass*);
2. in thin targets particle diameter determines the hole size, and we can therefore, at the same velocity, estimate a particle's effective *diameter*.

Hence, if we know the functional relationships for a crater in a thick target and the same particle's perforation through a thin foil, we can eliminate the velocity to yield particle mass, aspect ratio and, significantly, particle density. On LDEF's space faces we have a well measured crater size distribution for the meteoroid population on thick aluminium (Love & Brownlee [37]) and on foils at 5μm thickness (McDonnell et al [38]). Although we never have truly the same particle causing both affects, the sheer number of impacts in both sets - and for identical mission exposure factors - provides ready opportunity for a statistical comparison. The results, supported by complex modelling to test for errors and uncertainties in the formulae and models are shown in Table 4.

Impact Damage of Solar Arrays also deserves attention because of the common deployment of these elements but also because of the opportunity to use their large area-time product on retrieved systems for space debris and meteoroid assessment [39,40]. A programme of laboratory calibration on Eureca and Hubble arrays was conducted at Kent, UK and at EMI, Germany, using the Light Gas Gun. The programme stepped through projectile size using at the small size regime finely graded powders and, for the larger regime, discrete spheres. At the upper limit of size, the unsplit 4.3mm Nylon sabot provided measurements where the HST solar array (900 μm thickness) is essentially thin. Scaling of the damage equations to meteoroid velocities was performed and damage equations derived for the characteristic feature: the conchoidal diameter of the cover glass.

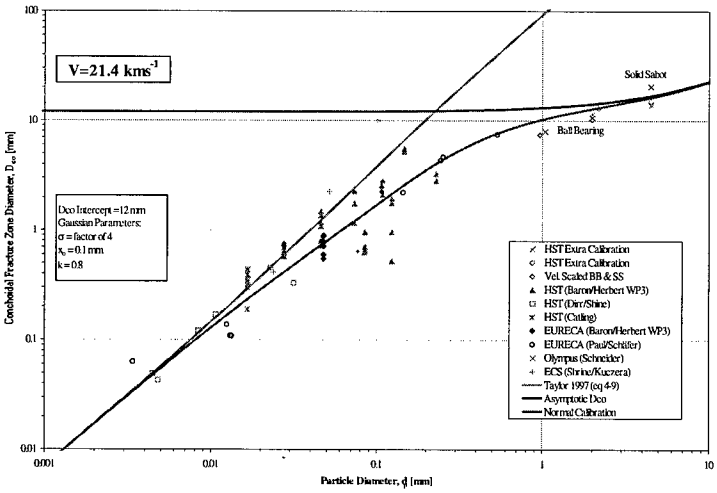

Fig.10 Damage equations developed for the Hubble Space Telescope Solar Array impacts on the front surface [39]. The (conchoidal) cover cell damage diameter D_{co} is related to the particle diameter; the combined equation is asymptotic to a thick target cratering equation [41], for small particles and a thin plate perforation limit for large particulates. Laboratory data assists the traversal between the two regimes.

The damage composite equation encompasses plotted on Figure 10 uses the thick target penetration equation on glass by Taylor [41] for the smaller impactors on the cover glass perforation; at the other extreme, where the target is thin, an asymptotic approach is made to a damage diameter approaching the particle size plus a factor for hole growth and for conchoidal fracture beyond the perforation hole diameter. The asymptotes, supported by laboratory impact

data in the transition regions, are critical because of the varying damage growth relationship at values comparable to the laminates in the complex target. "Resonance" effects are seen at one velocity which are compatible with penetration thresholds or shock wave reflections in the target but these are, in practice, smoothed out by the velocity distribution and density distribution of the meteoroid or space debris populations.

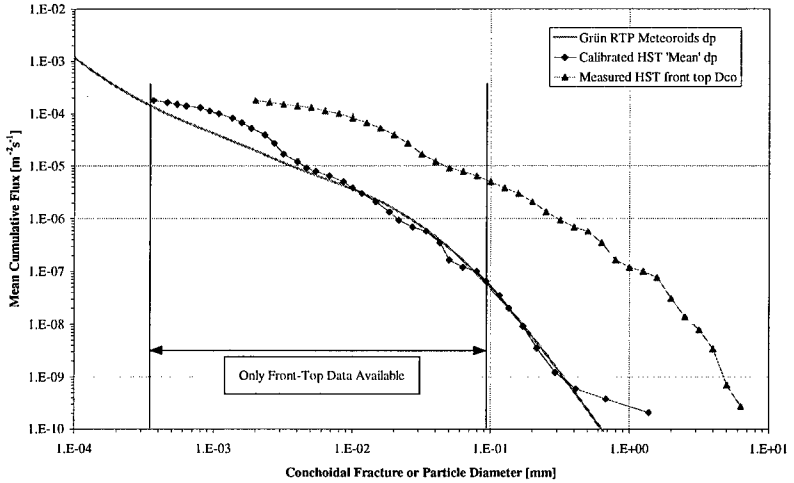

Fig. 11. Using the damage equation developed for the Hubble Solar array and measurements taken in terms of the conchoidal diameter (D_{co}) the impactor size distribution is derived and compared to the Grün meteoroid predictions. Good agreement is shown except at large sizes (> .4mm) where an excess, also supported by the LDEF data, is seen. Compatiblity with space debris is noted.

From the damage equation and the damage distributions, the incident particle size distribution was derived; comparison with the Grün model - now well tested on the LDEF space face shows the impactor flux-size distribution; it shows good agreement at mid sizes with the Grün distribution but also seen in Figure 11 is a significant increase in the flux of larger particles (greater than 0.5mm particle diameter. LDEF's exposure from 1986 to 1990 is supported by the HST data (1990 to 1994) at small and large and sizes; it is compatible with the existence of space debris but does not show significant growth over this period.

MOMENTUM EXCHANGE

Momentum is conserved during all phases of any impact, but what is not conserved is the mass coupled to the target. A sensor on the target may detect the target displacement caused by the impactor momentum but this may be enhanced (for a thick target) by the ejecta splashed "backwards". Contrarily for perforations, momentum may be carried away by ejecta emerging behind the target and for thin targets little of the momontem coupled to the detector.

Demands for space detectors have shown momentum detection to be a valuable asset. Piezo-electric crystals, first used in V2 rocket flights in the US by Bohn and Nadig [42] were shown to be susceptible to interference by Nilsson [43] but are effective with adequate control and can be placed strategically to form a position sensitive system [44]; this permits derivation not only of the impact position but also the initial amplitude. The piezo electric elements have been shown to respond to the bending wave and yield a voltage proportional to the initial momentum exchange; thus the characterisation of this parameter in the physical process of cratering is vital. For planetary defence studies also, momentum exchange plays a vital role in the effectiveness of

surface explosions in deviating the target body. For the Giotto mission a series of measurements on various calibration facilities stusied the momentum enhancement as a function of velocity [45,46]. Giotto's encounter of 68.4 kms^{-1} necessarily demanded extrapolation since momentum from impacts to only 7 kms^{-1} could be measured; an enhancement of $\varepsilon = 11$ was used at 68 kms^{-1}, but the precision not satisfactorily evaluated; it was based on a signal proportional to m.velocity$^{1.5}$. Figure 12 sketches the arrangements on Giotto for momentum detection for small and large impactors.

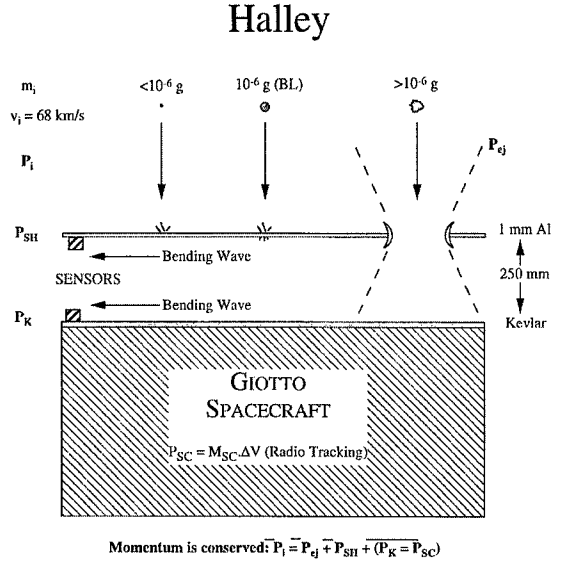

Fig. 12. Schematic of Giotto's momentum detection system [45,38], and momentum relationships for momentum in the spacecraft at large. The integrated spacecraft deceleration (measured by the GRE radio science experiment [36] proved vital to momentum de-rating for large particles perforating the 1 mm Whipple bumper shield.

This velocity dependence used is compatible with an enhancement over the incident momentum proportional to (velocity)$^{.5}$ and less strong than an enhancement proportional to crater volume which gives an enhancement proportional to velocity.

Whereas the enhancement ε was not satisfactorily defined at actual impact velocity by laboratory experiments, space encounter with Comet Halley provided further opportunities for scrutiny of the relationships. For large particles the de-rating of the (enhanced) momentum on perforations above the ballistic limit was able to be tested by comparison to the total momentum transferred to the target (the 2 tonne spacecraft) because this deceleration was measured to high accuracy by the Radio Science Experiment (GRE) [47].

Thus the integrated momentum detected by the piezo electric Dust Impact Detection System could be compared - together with assumed enhancement and de-ratings - with the results of the spacecraft deceleration. An enhancement factor for de-rating for particles above the ballistic limit proportional to (particle mass/ballistic limit)$^{\gamma}$ was applied; a value of γ=2/3 provided the best fit. Examples of the choice of the de-rating mass exponent, γ=1, 2/3 or 3/3 are shown in Figure 13. The effect on the mass distribution inferred is critical for the estimation of the total mass intercepted; together with a measure of the total gas intercepted this astrophysically critical "gas/dust ratio" was revised from values in the region of 0.5 in pre-encounter estimates to some 2.0 after DIDSY's shield enhancements and de-rating had been reconciled with the total

momentum. The value of the maximum mass of particle intercepted increased from 100 mg to 1 gramme.

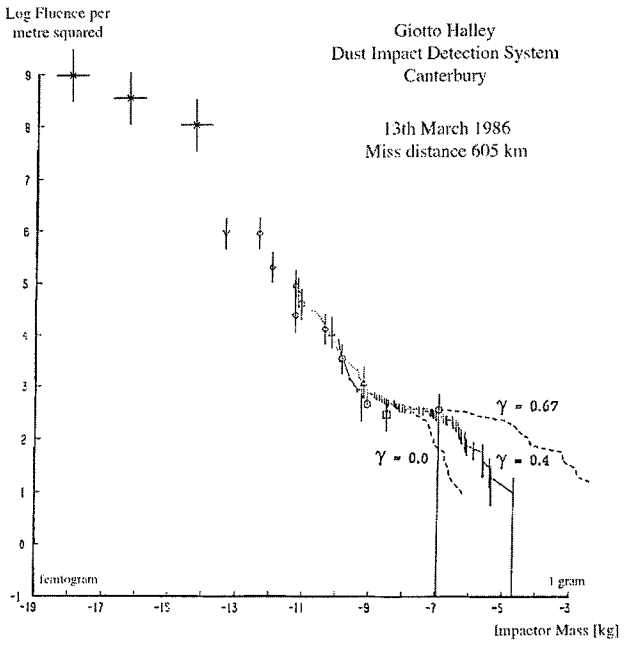

Fig. 13 Signals from piezo-electric detectors from impactors on Giotto's shield during the close encounter with Comet Halley. The signal amplitudes reflect momentum enhancement for small particles but are also moderated (above the shield perforation limit) by de-rating. An enhancement of E = 11 was used. A value of $\gamma = 0.67$ for the exponent of the mass sensitive de-rating for large particles was found yield compatibility with the integrated spacecraft deceleration. This choice of γ led to an increase in the mass of particulates deduced by some 2 decades above the uncorrected values and a significant increase in the dust to gas ratio inferred for comet Halley.

Impact Plasma

The ready availability of ionised projectile and target above several kilometres per second has provided opportunity for detection in a wide range of sophisticated detectors, dominantly in deep space missions such as Ulysses, Galileo and Cassini [48,49,50]. Low resource flux counters have been developed in lunar orbit and near Earth regions [51,52] respectively; Muses [53] has explored cis-lunar space and Planet A is on its way to Mars. Plasma detection is reliable and carries decodable information of the impactor.

The total impact charge, extracted by an applied electric field, is simply characterised. We take one such formulation [54]:

$$Q \alpha m^{1.02} v^{3.45}$$

The current depends on the rise time of this charge integral and in space, the dependence on impact speed has been utilised to derive the projectile velocity. The Ulysses/Galileo/Cassini

detectors employ this principle, following earlier application of the concept on HEOS II [55]. The current is hence dependent on a higher power of velocity [56] and can take the form:

$$I \alpha m^{1.02} v^{4.45}$$

The characterisation of these relationships falls well within the remit of the electrostatic accelerators and their use applied to the potential damage to spacecraft by the Perseid and the Leonid meteoroid streams. Not only the impact penetration, but also the impact plasma can be predicted. McBride et al. [9] have analysed the effect of impact penetration and impact charge and current for all known significant showers; based on averaged yearly expectations, the results are shown in Figure 14.

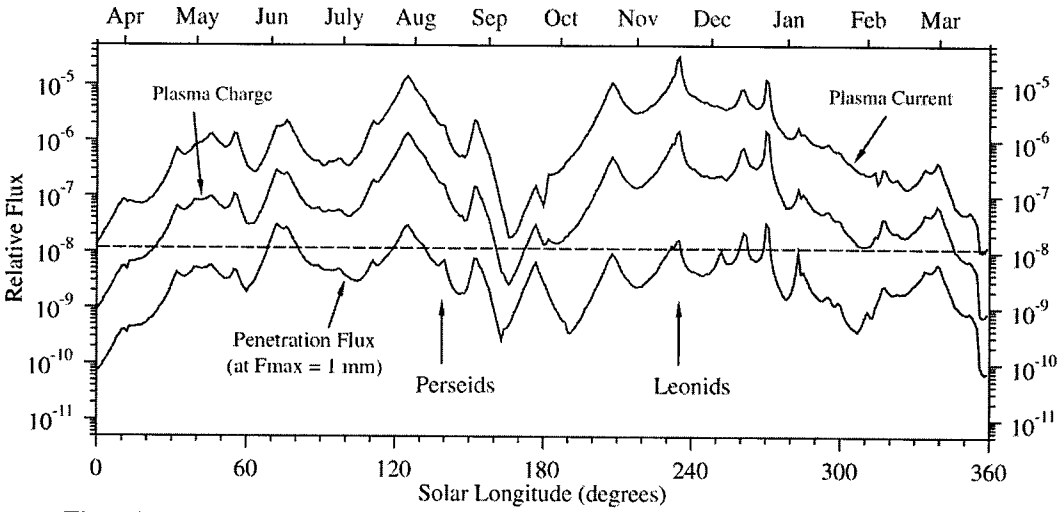

Fig. 14. Impact ionisation charge and current shown for the annual meteoroid shower complex (scale arbitrary). The high velocity of the Leonids enhances their effect in terms of ionisation but not significantly for penetration flux (shown below calculated for LEO exposures). Under enhanced conditions the rate could increase by several decades (1998 and 1999); impact ionisation is considered potentially the most damaging aspect of the Leonids and Perseids.

The scales are arbitrary for the available plasma charge and current, demonstrating more the relative contribution from different streams; for penetration they are shown in actual flux values which can be applied to any spacecraft. Based on the average yearly performance the Leonids are modest regarding penetration. Because of the high velocity of 71 kms^{-1}, we see the Leonids dominating all other showers in terms of instantaneous intensity in terms of plasma effects; in enhanced Leonid stream activity, such as 1998 and 1999, concern for the unexpected effect of induced current on spacecraft has been emphasised [9,56]. Currents can exceed 100A at impactor masses of only 10^{-6} grammes; in addition to the integrated current, the radio frequency noise generation has been identified by Foschini [57]. Though large effects are common, such as fireballs in the Leonids, it is fair to point out that the Leonids are visually active only because of this very high velocity and their masses are in reality shifted towards smaller values. Peak 1998 shower rates were in the ZHR=500, and lower by a factor of 30 than a peak of 15,000 used in the estimation of satellite damage effects predictions. We await 17 November 1999 for another manifestation; certainly 1966 was very intense following a mediocre display in 1965.

SUMMARY

Space missions have set a new scene where exposure to hypervelocities is intrinsic. They have opened new vistas for hypervelocity impact - a need to know and an opportunity to test understanding and parametric relationships generally at velocities higher than in defence or terrestrial applications. In responding to demands in space, ground facilities are seen to be even more valuable to exploit data and to further understanding of the physics and engineering. The cost, albeit modest compared to the mission itself, is however an important figure and coming hard against the walls of increasing cost as we approach the limits of performance. **Scaling** is seen to be the key to traversing the velocity-size parameter space of differing facilities. With the ability to bridge between the facility "islands", we have provided effective scaling laws to interpret most basic space phenomena relevant to detection. In contrast, the detailed understanding of the physics and hydrocode performance over the range is currently very much in a lag situation; the scaling laws established to date do, however, constrain wild extremes of behaviour which might otherwise be conjectured and set targets for their calibration.

Acknowledgements - Research products from the Canterbury Electrostatic Accelerator and Light Gas Gun Facilities, from Space Missions, testify to a close collaboration over 30 years between the author and a number of talented colleagues, researchers and support staff.
The presentation and publication acknowledges very significant support from Margaret Fowler in manuscript preparation and especially Andrew Griffiths, Nick Shrine and David Catling in technical advice and discussion. Financial support from PPARC, UK and the European Space Agency is acknowledged.

REFERENCES

1. McDonnell. J.A.M. (Ed), 1986. Proc. of Rosetta Comet-Nucleus Sample Return Mission Workshop, ESA SP-249., European Space Agency.
2. McBride, N., McDonnell, J.A.M. and Green, S.F., 1998. Meteoroids and small sized debris in Low Earth Orbit and at 1 AU: Results of recent modelling. *Adv. Space Res.* (in press).
3. Drolshagen, G. and Borde, J., 1992. ESABASE Debris-Meteoroid/Debris Impact Analysis Technical Description. ESA ESTEC, Noordwijk, the Netherlands.
4. Kessler, D.J., Zhang, J., Matney, M.J., Eichler, P., Reynolds, R.C., Anz-Meador, P.D. and Stansbery, E.G., 1996. A computer based orbital debris environment model for spacecraft design and observations in low Earth orbit. NASA Technical Memorandum 104825.
5. Reinhard, R. and Battrick, B., 1986. The Giotto mission - its scientific investigations. ESA SP-1077.
6. Grün, E. (Ed.), 1986. Chapter 3 - VEGA 1 and 2. *Adv. Space Res.*, **5** (12) 95-186
7. McDonnell, J.A.M., Burchell, M.J., Green, S.F, McBride, N., Vaughan, B.A., Zarnecki, J.C., Tsou, P., Hanner, M.S., Tuzzolino, A.J., DiDonna, F. and Brownlee, D.E., 1998. The Stardust dust flux monitor. *Adv. Space Res.* (in press).
8. Kessler, D.J., Reynolds, R.C., Anz-Meador, P.D., 1989. Orbital Debris Environment for Spacecraft Designed to Operate in Low Earth Orbit. NASA TM-100-471.
9. McBride, N. and McDonnell, J.A.M., 1998. Meteoroid impacts on spacecraft: sporadics, streams and the Leonid meteoroid storm. *Planet. Space Sci.* review.
10. Kissel, J.and Krueger, F.R., 1987. Die Physik der massenspektrometrischen Staubanalysebeim Kometen Halley, *Phys. Bl.* **43**, **45**, 277-281
11. McDonnell, J.A.M., 1969. Calibration studies on a piezoelectric sensing diaphragm for the detection of micrometeoroids in space. Sci. Instruments (J. Phys. E), Series 2, **2** 1026-1030.
12. Stilp, A. 1987. Review of Modern Hypervelocity Impact Facilities. Int J of Impact Engineering, **5**, 613-621.
13. Burchell, M.J., Cole M.C., McDonnell J.A.M., Zarnecki J.C., 1999. Hypervelocity impact studies using the 2MV Van de Graaff accelerator and the two-stage light gas gun of the University of Kent at Canterbury. Measurement Science Technology **10**, 41-50
14. Paul, K.G., Rott, M. and Dirr, B., 1995. Post-flight particle impacts on HST solar cells. Proc. HST Solar Array Workshop, ESTEC, Noordwijk, The Netherlands, 30-31 May 1995, ESA WPP-77, 493-500.
15. Cour-Palais, B.G., 1979. Space vehicle shielding design. In *Proc. comet Halley micrometeoroid hazard workshop* ESA SP-153, 85-92.

16. McDonnell, J.A.M., and Sullivan, K., 1992. Hypervelocity impacts on space detectors: decoding the projectile parameters. In *Hypervelocity Impacts In Space*, (ed. J.A.M. McDonnell). Unit for Space Sciences, University of Kent at Canterbury, Canterbury, 1992, 39-47.
17. Walsh, J.M., Stradling, G.L., Idzorek G.C., Schafer, B.P. and Curling, H.L. 1992. On size scaling in shock hydrodynamics and the stress-strain behaviour of copper at exceedingly high strain rates. In *Hypervelocity Impacts In Space*, (ed. J.A.M. McDonnell). Unit for Space Sciences, University of Kent at Canterbury, Canterbury, 84-91.
18. Tanner, W.G., 1997. Meteoroids and space debris hypervelocity impact penetrations: the role of hydrocodes. *Ph.D. Thesis*, University of Kent at Canterbury, UK.
19. Fish, R.H. & Summers, J.L., 1965. The Effect of Material Properties on Threshold Perforation, Proc. Hypervelocity Impact Symposium 7th, Vol VI.
20. Pailer, N., & Grün, E. 1980. The Penetration Limit Of Thin Films, Planet. Space Sci. **28**, 321-331.
21. Gardner, D.J., McDonnell, J.A.M. and Collier, I., 1996. Hole growth characterisation for hypervelocity impacts in thin targets. *Int. J. Impact Engng.* **19** (7) 598-602 (Note erratum, referenced this paper).
22. Sawle, D.R., 1969. Hypervelocity Impact in Thin Sheets and Semi-infinite Targets at 15 kmk/sec. In Proc. AIAA, Hypervelocity Impact Conf., Cincinnati, Ohio.
23. Carey, W.C., McDonnell, J.A.M. and Dixon,D.G., 1984. An Empirical Penetration Equation for Thin Metallic Films used in Capture Cell Techniques, in: *Properties and Interactions of Interplanetary Dust.* eds, R.H. Giese and P. Lamy, D.Reidel, 291-295.
24. Maiden, C.J., Gehring, J.W. and McMillan, A.R., 1963. Investigation of Fundamental Mechanism of Damage to Thin Targets by Hypervelocity Projectiles. NASA TR 63-225.
25. Nysmith, C.R. and Denardo, B.P., 1969. Experimental Investigation of the Momentum Transfer Associated with Impact into Thin Aluminium Targets, NASA TND 5492.
26. McDonnell, J.A.M. 1970, Factors affecting the choice of foils for penetration experiments in space. *Space Research,* **10**, 314–325.
27. Shelton, H., Hendricks, C.D. and Wuerker, R.F., 1960. Electrostatic acceleration of microparticles in hypervelocity, *J. Appl. Phys.* **31**, 1243-6
28. Friichtenicht, J. F., 1964, "Micrometeoroid Simulation Using Nuclear Accelerator Techniques', Nuclear Inst. and Methods, **28**, 70.
29. Piekutowski, A.J. Holes produced in thin aluminium sheets by the hypervelocity impact of aluminium spheres. IM J Impact Engineering 23, 1999
30. Hörz, F., Cintala, M.J., Bernhard, R.P., See, T.H., 1994. Dimensionally scaled penetration experiments: aluminium targets and glass projectiles 50 μm to 3.2 mm in diameter. *Int. J. Impact Engng.*, **15**, 257-280.
31. Baron, J.M., 1996. Microparticle hypervelocity impact on satellites in low-Earth orbit. *Ph.D. Thesis*, University of Kent at Canterbury, UK.
32. McDonnell, J.A.M., and Baron, J.M., 1993. Penetration rates over 30 years in the space age. In *Proc. Third LDEF Post-retrieval Symp.*, NASA CP-3275, 337-351.
33. Grün, E., Zook, H.A., Fechtig, H., and Giese, R.H., 1985. Collisional balance in the meteoritic complex. *Icarus*, **62**, 244-272.
34. See, T., Allbrooks, M., Atkinson, D., Simon, C., and Zolensky, M., 1990, Meteoroid and debris impact features on the Long Duration Exposure Facility: A preliminary report. NASA Lyndon B. Johnson Space Center (JSC #24608).
35. Bernhard, R.P., See, T.H. & Hörz, F., Projectile Compositions and Modal Frequencies on the "Chemistry of Micrometeoroids" LDEF Experiment, 1993. Proc. Second Post-Retrieval Symposium, June 1992, Publication 3194 Part 2, 551-574.
36. Graham G.A., Kearsley A., Grady M.M., Wright, I.P. & McDonnell J.A.M. The collection of micrometeoroid remnants from low Earth orbit, Abstract submittted to COSPAR, Nagoya, Japan, 12-19 July 1998.
37. ESA Contract 11887, 1996/1998, Meteoroids and Debris Flux and Ejecta Modelling. Unisapce Kent, Final Report.
38. Love, S.G. *et al,* 1995. Morphology of meteoroid and debris impact craters formed in soft metal targets on the LDEF satellite. *Int. J. Impact Eng.*, **16**, 405–418.
39. McDonnell, J.A.M., Deshpande, S.P., Niblett, D.H., Neish, M.J. and Newman, P.J., 1993. The near Earth space impact environment - an LDEF overview. *Adv. Space Res.*, **13**, (8), 87-101.
40. Unispace Kent, 1998. Solar Array Impact Calibration Studies, Technical Note 2 for ESA Contract 11887/96/NL/JG.
41. Space Applications Services, Mare Crisium, CERT-ONERA-DERTS, Unispace Kent, 1995. Hubble Space Telescope micrometeoroid and space debris post-flight analysis – Final report. ESA contract number 10830/94/NL/JG.

42. Taylor E.A., Shrine, N.R.G., McBride, N., Green, S.F., McDonnell, J.A.M. and Drolshagen, G. (1998), "Impacts on HST and EURECA solar arrays compared with LDEF using a new glass to aluminium conversion", *Adv. Space Res.*, (in press).
43. Bohn, J.L. and Nadig, F.H., 1950. Acoustical studies with V-2 rockets, Res. Inst. Temple Univ., rept. No. 8, 1-26.
44. Nilsson, C., 1966, "Some doubts about the Earth's dust cloud", Science, **153**, 1242-1246.
45. McDonnell J.A.M. and Abellanas, C., 1972, A Technique for Position Sensing and Improved Momentum Evaluation of Microparticle Impacts in Space, The Review of Scientific Instruments, **43**(8), 1214-1216.
46. McDonnell, J.A.M., and 24 authors, 1986. ESA SP 1077, 85-107.
47. McDonnell, J.A.M. and Alexander, W.M., 1983. Hypervelocity impact on the Giotto Halley mission dust shield: Momentum exchange and measurement. Adv. Space Res. **2** (12) 185-187.
48. Patzöld, M., Edenhofer, P., Bird, M.K. and Volland, H., 1993. The Giotto encounter with comet P/Grigg-Skjellerup: first results of from the Giotto radio-science experiment. A&A, **268** L13-L16.
49. Grün, E., Fechtig, H., Giese, R.H., Kissel, J., Linkert, D., Mass, D., McDonnell, J.A.M., Morfill, G.E., Schwehm, G. and Zook, H.A., 1992b. The Ulysses dust detector. *Astron. Astrophys. Suppl.*, **92**, 411-423.
50. 47) Grün, E., Fechtig, H., Giese, R.H., Hanner, M.S., Kissel, J., Lindbald, B.A., Linkert, D., Mass, D., Morfill, G.E., Schwehm, G. and Zook, H.A., 1992a. The Galileo dust detector. *Space Sci. Reviews*, **60**, 317-340.
51. Srama R., Grün, E., Linkert, D. and Reber, M. 1996. The dust detector for Cassini.*Adv. Space Res,*
52. Iglseder, H., Uesugi, K. and Svedhem, H., 1995. Cosmic Dust Measurements in Lunar Orbit. Adv. Space Res., **17** (12) 177-182
53. Leese, M.R., McDonnell, J.A.M., Burchell, M.J., Green, S.F., Jolly, H.S., Ratcliff, P.R. and Shaw, H.A., 1996. Debie: A low resource dust environment monitor. Space Station Utilisation Symposium, Darmstadt, Germany 30 Sep-2 Oct 1996. ESA SP-385, 417-420.
54. Igenbergs, E., Hüdepohl, A., Uesugi, K.T., Svedhem, H., Iglseder, H., Grün, E., Mizutani, H., Yamamoto, T., Fujimura, A. and Araki, H., 1991. The Munich Dust Counter Cosmic Dust Experiment: Results of the First Year of Operation. IAF 42nd Congress, 470-?
55. Burchell, M.J., Cole, M.J., McDonnell, J.A.M., 1998. Role of Particle Charge in Impact Ionization by Charged Microparticles, Nucl. Instr. and Meth. in Phys. Res. **B 143**, 311-318.
56. Hoffmann, H.-J., Fechtig, H., Grün, E. and Kissel, J. 1975. Temporal Fluctuations and Anisotropy of the Micrometeoroid Flux in the Earth-Moon System Measured by HEOS-2. Planet. Space Sci. **23**, 981.
57. McDonnell, J.A.M., McBride, N. and Gardner, D.J., 1997. The Leonid Meteoroid Stream: Spacecraft Interactions and Effects, Proc. of the Second European conf. on Space Debris, ESOC, Darmstadt, Germany, ESA SP-393.
58. Foshchini, L., 1998. Electromagnetic interference from plasmas generated in meteoroids impacts, *Europhys. Lett.*, **43** (2), pp 226-229.

PERGAMON

International Journal of Impact Engineering 23 (1999) 621–628

INTERNATIONAL JOURNAL OF IMPACT ENGINEERING

www.elsevier.com/locate/ijimpeng

NUMERICAL SIMULATIONS OF LOW L/D ROD ALUMINUM INTO ALUMINUM IMPACTS COMPARED TO THE TATE CRATERING MODEL

MICHAEL R. MCHENRY*, Y. CHOO*, and D. L. ORPHAL**

* Lockheed Martin Missiles & Space, Sunnyvale, CA 94089, U.S.A.;** International Research Associates, Pleasanton, CA 94566, U.S.A.

Summary – Hydrocode numerical simulations have been made for 1100-0 aluminum rods into thick plates of the same material with parametric variations in the penetrator length to diameter ratio (L/D from ½ - 10) and impact velocity (1 - 6 km/s). The normalized penetration depth (P/L), primary penetration (P_p/L), after-flow penetration (P_a/L) and crater diameter (D_c/D) were determined and compared with the results of the Tate penetration model and available test data. It was found that the hydrocode results agreed very well with the test data, but there was a trend for the Tate model to over-predict the after-flow penetration and crater diameter for low L/D values and high velocities. Correction factors that are a function of L/D and velocity have been found that, when applied to the Tate model penetration and diameter results, greatly improve the agreement with the test data and hydrocode calculations. © 1999 Elsevier Science Ltd. All rights reserved.

INTRODUCTION

Tate [1,2] developed a model for long rod penetration. Recently, for a number of applications, the Tate model has been used to calculate penetration and crater diameters for penetrators with low to moderate length to diameter ratios (L/D) in the range of ½ to 10. The efficacy of Tate's model for penetrators with such L/D ratios is unclear. The objective of this paper is to determine the accuracy of the Tate model when applied to low to moderate L/D ratio rods impacting a thick plate. We have compared penetration depth and crater diameter predictions of the Tate model with those of the CTH hydrocode for L/D ratios of ½ , 1, 2, 3, 6, and 10 and velocities of 1, 2, 3, 4, 5, and 6 km/s for aluminum 1100-0 rods into plates of like material. Soft aluminum was selected for this study because we were interested in impacts of relatively weak materials. In addition, there are experimental data for this material (Christman and Gehring data compiled in Anderson, et al [3]) which allows the results of these calculations to be compared with data for L/D = 1 and 3 impacts at velocities up to greater than 7 km/s.

Eichelberger and Gehring [4] suggested that target penetration by a long rod could be viewed as a four phase process as indicated in Fig. 1. Assuming hydrodynamic behavior for like-material impacts, no secondary penetration of the target by eroded projectile material is expected according to Allen and Rogers [5]. Therefore, Phase 3 of the penetration process is expected to be entirely due to after-flow. After-flow penetration occurs after the impacting projectile has stopped eroding and is due to the momentum remaining in the target at that time. As will be shown below, after-flow is a significant component of the total penetration for low L/D projectiles. After-flow penetration is poorly understood because, to the best of the knowledge of the authors, there are no experimental data directly measuring after-flow. Hydrocode numerical simulations are considered to be the best approach for understanding the velocity and L/D dependence of after-flow penetration.

0734-743X/99/$ - see front matter © 1999 Elsevier Science Ltd. All rights reserved.
PII: S0734-743X(99)00108-6

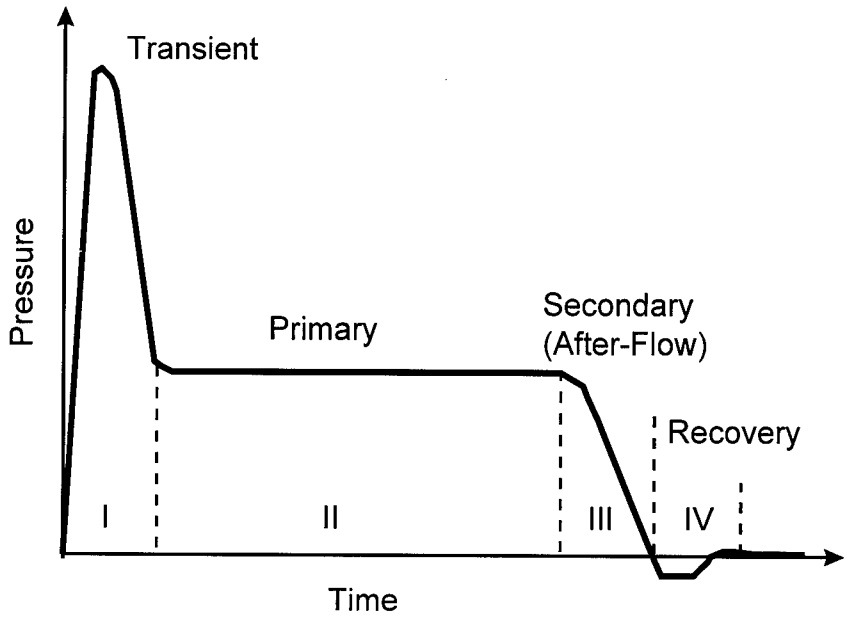

Fig. 1. Four phases of penetration.

COMPARISON OF NUMERICAL SIMULATIONS WITH TEST DATA

The numerical simulations were performed using the CTH hydrocode (McGlaun, et al. [6]). The Johnson-Cook model [7] was used for 1100-0 aluminum, including strain hardening. Table 1 summarizes the properties used for this analysis. The results of the CTH analysis are summarized in Table 2.

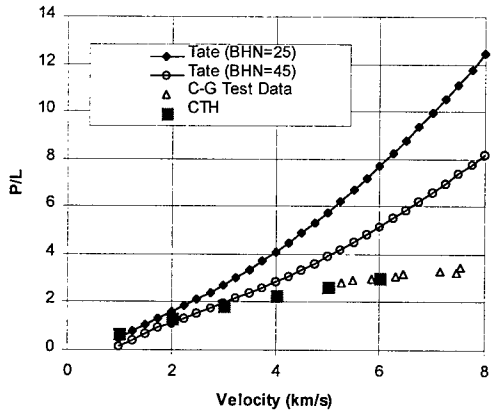

Fig. 2. Comparison of L/D=1 test data [3] with Tate model and CTH analysis of P/L.

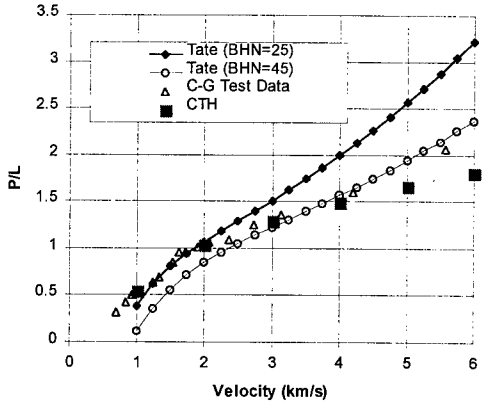

Fig. 3. Comparison of L/D=3 test data [3] with Tate model and CTH analysis of P/L.

Figure 2 shows total penetration depth, P, normalized by the projectile length (P/L) versus impact velocity for the L/D = 1 projectiles. Shown in Fig. 2 are the results of the CTH numerical

simulations for velocities between 1 and 6 km/s and the Tate model results using both the handbook value of the Brinell hardness number (BHN) for 1100-0 aluminum (25 kg/mm^2) and the strain hardened value of 45 kg/mm^2 reported by Christman and Gehring [8]. In the range between 5 and 6 km/s where we have both data and CTH calculations, there is very good agreement between the two. In contrast, for both values of BHN, the Tate model greatly over-predicts the penetration at high velocities (5 to 7.5 km/s) where data are available. At low velocity (1 - 3 km/s) the Tate model, using the higher BHN value, agrees reasonably well with the CTH analysis.

For the L/D = 3 projectiles, the agreement between the CTH calculations and experimental data is good between 1 and 4 km/s, as shown in Fig. 3, but the data point at 5.7 km/s is about 20 percent higher than the CTH result. The low velocity data was found to agree well with the Tate model calculations if BHN=25 is used, but above 2 km/s better agreement is found using BHN=45 for the target hardness.

The crater diameter normalized by the rod diameter (D_c/D) predicted by CTH for the L/D=1 case (measured in the plane of the original surface level) is compared with the test data and the Tate model in Fig. 4. Again, relatively good agreement is found between CTH and the test data at high velocities, and the agreement with the Tate model and CTH is satisfactory for the higher BHN value between 1 and 3 km/s velocity. At higher velocities, the Tate model over-predicts the crater diameter for both hardness values.

Figure 5 makes a similar comparison of D_c/D for the L/D=3 case. Very good agreement between the test data and the CTH results are found over the full range of velocities (1-6 km/s). Good agreement is also found for the Tate model using the lower BHN value. However, the higher BHN value, which gave good agreement with the penetration depth, under-predicts the crater diameter.

Overall, the CTH results agree very well with the limited available data for penetration depth and crater diameter for both L/D=1 and 3. This gives some degree of confidence in using the

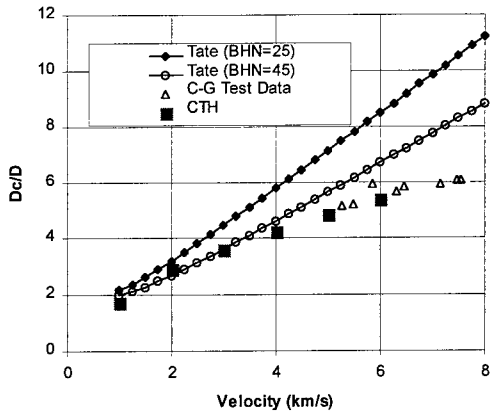

Fig. 4. Comparison of L/D=1 test data [3] with Tate model and CTH analysis of D_c/D.

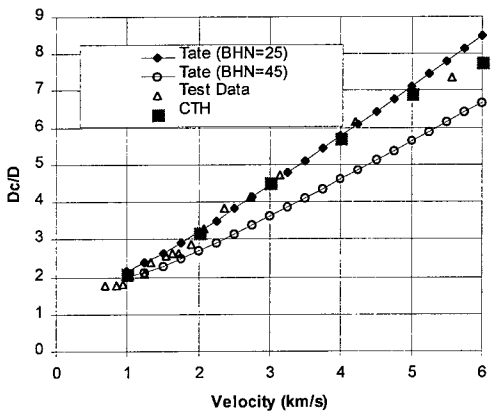

Fig. 5. Comparison of L/D=3 test data [3] with Tate model and CTH analysis of D_c/D.

CTH results to assess the accuracy of the Tate model over a range of L/D values and velocities. It is not clear from the above comparisons which value of BHN should be used in the Tate model. The lower handbook value (BHN=25) agrees best with the L/D=3 test data and the CTH analysis of D_c/D at all velocities and for the P/L at low velocity. The Tate model does not agree well with the L/D=1 data or CTH analysis for either hardness value. In the remainder of this paper we will use the handbook value of BHN (25) for comparison of the Tate model with the CTH hydrocode.

Table 1. Properties for 1100-0 aluminum used for the CTH calculations

Johnson-Cook Strength Model [8]

$$\sigma = \left[A + B\varepsilon^{n}\right]\left[1 + C\ln\dot{\varepsilon}\right]\left[1 - T^{*m}\right]$$

$A = 1.158 \times 10^{9}$ dyne / cm^2

$B = 6.895 \times 10^{8}$ dyne / cm^2

$n = 0.58$

$C = 0.016$

$m = 1.13$

Gruneisen Equation-of-State

$$P = P_H + \Gamma\left(E - E_H\right)$$

$$P_H = \frac{\rho_0 c_0^2\left(1 - \frac{\rho_0}{\rho}\right)}{\left[1 - s\left(1 - \frac{\rho_0}{\rho}\right)\right]^2}$$

$$E_H = \frac{P_H}{2}\left(\frac{1}{\rho_0} - \frac{1}{\rho}\right)$$

$\rho_0 = 2.72$ gm / cm^3

$c_0 = 5.376 \times 10^{5}$ cm / s

$s = 1.55$

$\Gamma = 2.10$

Table 2. Summary of results from CTH calculations

L/D	Velocity (km/s)	P/L	P_p/L	P_a/L	D_c/D
0.5	1	0.853	0.606	0.247	1.595
1	1	0.703	0.531	0.172	1.727
2	1	0.569	0.564	0.005	2.073
3	1	0.539	0.525	0.014	2.073
6	1	0.429	0.429	0.000	2.073
10	1	0.351	0.351	0.000	2.073
0.5	2	1.671	0.769	0.902	2.245
1	2	1.346	0.746	0.600	2.936
2	2	1.119	0.803	0.316	3.109
3	2	1.034	0.835	0.199	3.190
6	2	0.922	0.846	0.076	3.190
10	2	0.875	0.849	0.026	3.282
0.5	3	2.460	0.877	1.583	2.764
1	3	1.859	0.835	1.072	3.627
2	3	1.450	0.867	0.583	4.328
3	3	1.285	0.882	0.403	4.501
6	3	1.106	0.901	0.205	4.501
10	3	1.034	0.922	0.112	4.501
0.5	4	3.125	0.878	2.247	3.190
1	4	2.303	0.861	1.492	4.237
2	4	1.715	0.915	0.800	5.364
3	4	1.494	0.905	0.589	5.710
6	4	1.240	0.922	0.318	5.740
10	4	1.123	0.926	0.197	5.791
0.5	5	3.766	0.950	2.927	3.637
1	5	2.683	0.916	1.767	4.846
2	5	1.956	0.913	1.043	6.228
3	5	1.661	0.906	0.755	6.919
6	5	1.349	0.927	0.422	7.092
10	5	1.201	0.939	0.262	7.092
0.5	6	4.301	0.970	3.331	3.983
1	6	3.020	0.971	2.049	5.385
2	6	2.153	0.914	1.239	6.919
3	6	1.814	0.936	0.878	7.783
6	6	1.448	0.933	0.515	8.219
10	6	1.263	0.937	0.326	8.128

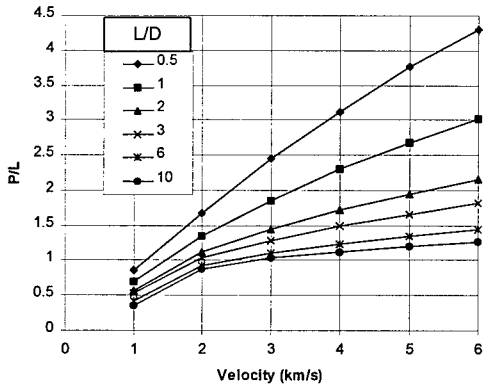

Fig. 6. CTH calculations of total penetration (P/L) variations with velocity and L/D.

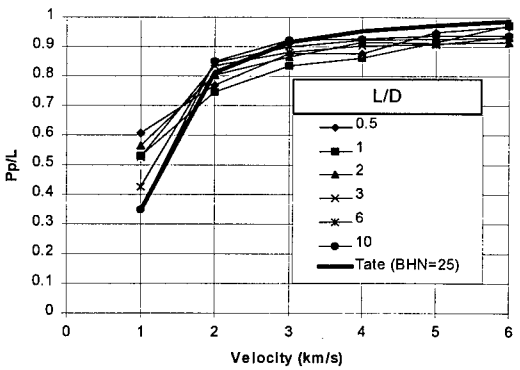

Fig. 7. CTH calculations of primary penetration (P_p/L) variations with velocity and L/D.

The total penetration (P/L) was determined by measuring the depth of the crater relative to the initial surface after the elastic recovery phase of penetration. The primary penetration (P_p) was estimated by determining the penetration depth at the time the penetrator had stopped eroding (i.e., phases 1 and 2 in Fig. 1). This time was estimated by dividing the penetrator eroded length by the erosion velocity (approximately ½V for this case). The after-flow penetration (P_a) was determined by P_a=P-P_p. The crater diameter D_c was measured at the level of the original target surface. Figures 6 through 9 are plots of P/L, P_p/L, P_a/L and D_c/D, respectively, as a function of velocity and parametric in L/D. Figure 6 shows that the total penetration efficiency (P/L) increases nearly linearly with velocity for L/D= ½ and increases much more slowly for higher L/D ratios. The primary penetration efficiency (P_p/L) is shown in Fig. 7 along with the Tate model prediction (which is L/D independent). The Tate model agrees best with the L/D=10 case, as might be expected since the model was originally developed for long rods. Subtracting P_p/L from P/L gives the values of P_a/L shown in Fig. 8. The after-flow penetration efficiency is found to increase rapidly with velocity for low values of L/D and much more gradually for large L/D. The crater diameter is found to increase nearly linearly with velocity for the higher L/D values and more gradually with the smaller L/D values as shown in Fig. 9.

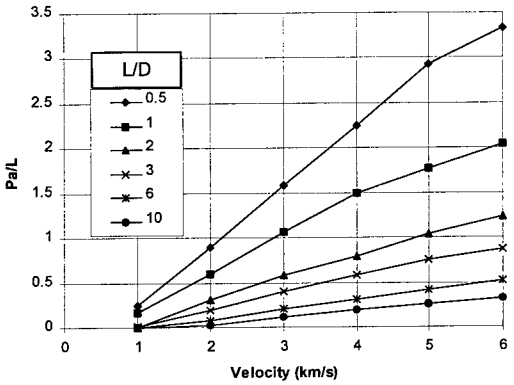

Fig. 8. CTH calculations of after-flow penetration (P_a/L) variations with velocity and L/D.

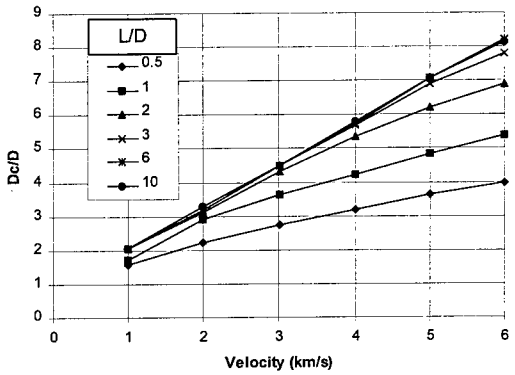

Fig. 9. CTH calculations of crater diameter (D_c/D) variations with velocity and L/D.

COMPARISON OF TATE MODEL RESULTS WITH CTH

The Tate model was used to calculate the penetration and crater diameter for the same cases as the CTH analysis for a BHN value of 25. The ratio of the Tate model total penetration, P(Tate), prediction to the CTH calculation, P(CTH), for velocities between 2 and 6 km/s is plotted in Fig. 10. It was found that the Tate model penetration was always greater than the CTH value, with increasing ratio values for decreasing L/D and increasing velocity. A similar result was found for the ratio of the crater diameters as shown in Fig. 11. The discrepancy between the Tate model and CTH is primarily due to the after-flow penetration being over-predicted by the Tate model as shown in Fig. 12.

At this time the reason for the apparent deficiency of the Tate after-flow model is unclear. It may be related to the fact that as projectile L/D is reduced the penetration process becomes increasingly influenced by the initial impact transient and a quasi-steady state approximation becomes increasingly poor. Further research is required. However, as noted earlier, regardless of this apparent deficiency, the Tate model is being actively used to predict results for low to

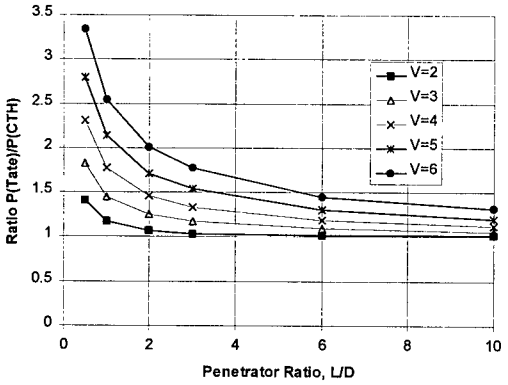

Fig. 10. Ratio of Tate model to CTH penetration versus L/D for velocities between 2 and 6 km/s.

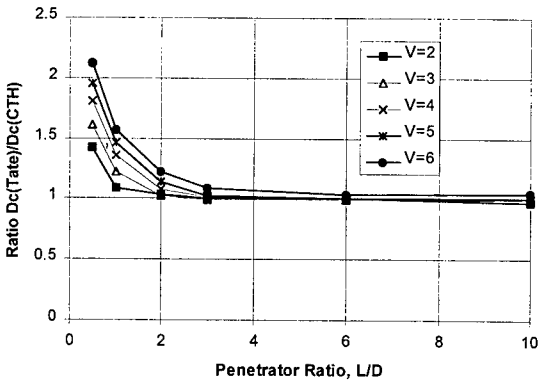

Fig. 11. Ratio of Tate model to CTH crater diameter versus L/D for velocities between 2 and 6 km/s.

moderate L/D projectile impacts. Therefore, it is of practical interest to develop "correction factors" which, when applied to the results from the Tate model, will produce much better agreement with the limited experimental data and CTH results.

Shown in Fig. 12 are fits of the P_a(Tate)/P_a(CTH) ratio to a power law function for velocities between 3 and 6 km/s. It was found that the ratio could be approximately described by the following function:

$$f_1 = \frac{P_a(\text{Tate})}{P_a(\text{CTH})} = (0.304 + 0.493V)\left(\frac{L}{D}\right)^{-0.2} \tag{1}$$

Applying this correction factor to the Tate after-flow penetration greatly improved agreement between the Tate model predictions and the CTH results for total penetration as shown in Fig. 13. These results were achieved by computing the modified Tate model penetration from the relationship:

$$\frac{P}{L}(\text{Mod Tate}) = \frac{P_p}{L}(\text{Tate}) + \frac{1}{f_1}\frac{P_a}{L}(\text{Tate}) \tag{2}$$

The agreement between the modified Tate model and the CTH results is very good except for a slight over-prediction of the L/D= ½ case for velocities between 2 and 6 km/s and under-prediction of the L/D= ½ and 1 cases for velocity of 1 km/s. A similar analysis was done for the crater diameter. Figure 14 shows the results of power law fits to (D_c(Tate)/D_c(CTH)-0.97) versus L/D for velocities between 2 and 6 km/s. The resulting modified Tate model crater diameter is given by the relationship:

$$\frac{D_c}{D}(\text{Mod Tate}) = \frac{1}{f_2}\frac{D_c}{D}(\text{Tate}) \tag{3}$$

Where

$$f_2 = \left(0.128 - 0.0151V + 0.0139V^2\right)\left(\frac{L}{D}\right)^{-1.2397} + 1.0 \tag{4}$$

Note that to avoid negative numbers in the power law fit, 0.97 was subtracted from the diameter ratio rather than 1.0. In Eqn. (4) this was rounded to 1.0.

The results of the modified Tate model crater diameter are compared with the CTH results in Fig. 15. The results are found to be in very good agreement with CTH over the full range of velocities and L/D values studied.

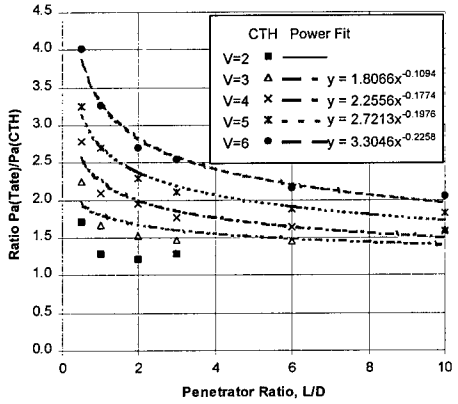

Fig. 12. Fit of after-flow penetration ratio of Tate model to CTH to a power function of L/D.

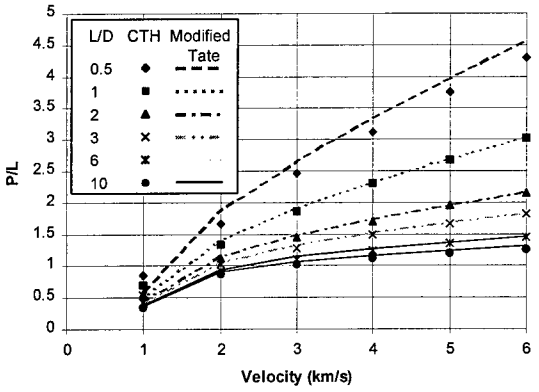

Fig. 13. Total penetration (P/L) calculated with the modified Tate model compared with the CTH results.

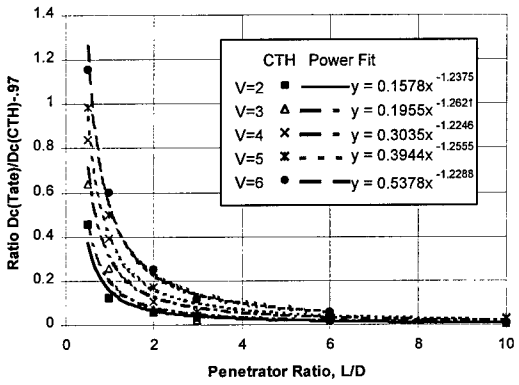

Fig. 14. Power law fits to ratio of Tate model and CTH crater diameter.

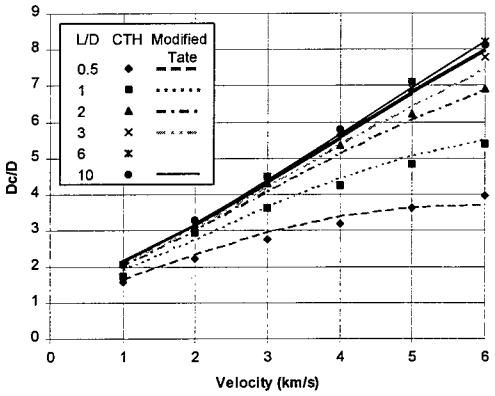

Fig. 15. Crater diameter (D_c/D) calculated with the modified Tate model compared with the CTH results.

CONCLUSIONS

A detailed comparison of limited experimental data and CTH calculations was made with predictions using the Tate model for 1100-0 aluminum projectiles with $\frac{1}{2} \leq L/D \leq 10$ impacting 1100-0 aluminum targets at velocities $1 \leq V \leq 6$ km/s. The CTH calculations generally agree well with the experimental data; the Tate model does not. The deficiency in the Tate model appears to be in the after-flow model. The reason for this deficiency is not clear at this time, but may have to do with the increasingly transient nature of the penetration process as projectile L/D is reduced.

The Tate model is being actively used to calculate penetration for low to moderate L/D projectiles. Therefore, it is encouraging that a relatively minor modification to the Tate after-flow and crater diameter models can be made to greatly improve the accuracy of the Tate model predictions for low to moderate L/D values. The "correction" or modification for the Tate model developed here only applies to 1100-0 aluminum rod impacts into 1100-0 aluminum targets. However this analysis suggests a methodology that could be extended to other projectiles and targets of interest. In particular, a similar series of CTH calculations could be performed for other material combinations of interest. Determining the L/D and velocity dependence of the "Tate correction factors" for penetration and crater diameter could allow the development of an empirically modified Tate cratering model that would eliminate the over-prediction of crater size for low L/D projectiles and high velocity demonstrated in this paper.

Acknowledgement –This work was funded by Lockheed Martin Missiles & Space internal research and development.

REFERENCES

1. A. Tate, "Long Rod Penetration Models-Part II. Extensions to the Hydrodynamic Theory of Penetration", *Int. J. Mech. Sci.* **28**, No. 9, pp. 599-612 (1986).
2. A. Tate, "A Theory for the Deceleration of Long Rods After Impact", *J. Mech. Phys. Solids* **15**, pp. 387 - 399 (1967).
3. C. E. Anderson et al, "A Penetration Mechanics Database", SwRi Report 3593/001, Southwest Research Institute, San Antonio, TX (1992).
4. R. J. Eichelberger and J. W. Gehring, "Effects of Meteoroid Impacts on Space Vehicles", *Am. Rocket Soc. J.* **32**, 1583-1591 (1962).
5. W. A. Allen and J. W. Rogers, *J. Franklin Inst.* **272**, 275-284 (1961)
6. J. M. McGlaun, S. L. Thompson, and M. G. Elrick, "CTH: A Three-Dimensional Shock Wave Physics Code", *Int. J. Impact Eng.* **10**, pp. 351-360 (1990)
7. G. R. Johnson and W. H. Cook, "Fracture Characteristics of Three Metals Subjected to Various Strains, Strain Rates, Temperatures and Pressures," *Engineering Fracture Mechanics*, **21**, pp. 31-48 (1985).
8. D. R. Christman and J. W. Gehring, "Analysis of High-Velocity Projectile Penetration Mechanics", *J. Appl. Phys.* **37**, 1579-1587 (1966)

PERGAMON

International Journal of Impact Engineering 23 (1999) 629–638

INTERNATIONAL JOURNAL OF IMPACT ENGINEERING

www.elsevier.com/locate/ijimpeng

MECHANICAL PROPERTIES, INDENTATION AND DYNAMIC YIELD STRESS OF CERAMIC TARGETS

YU. V. MILMAN and S. I. CHUGUNOVA

Institute for Problems of Materials Science
(3, Krzhizhanovsky Str. 252180 Kiev, Ukraine)

Summary — The dynamic yield Y_D (which is determined usually in dynamic experiments from Hugoniot elastic limit) can be calculated for ceramic targets from static indentation experiments using Vickers hardness and plasticity characteristic δ_H. The magnitude of Y_D approximately equals to the static yield stress σ_s calculated by Marsh equation. The employment of a set of diamond indenters with different angles of sharpening makes possible to construct stress-strain curves for ceramic materials and to determine yield stress at different deformation degrees.
© 1999 Elsevier Science Ltd. All rights reserved.

INTRODUCTION

Many ceramics provide a combination of extreme hardness and low density thereby they can be used as a light armour against kinetic energy projectiles. However, while the mechanism of penetration in metal targets has been extensively studied, and there is a fundamental understanding of this process, the link between dynamic strength of ceramic targets and their static mechanical properties as well as fundamental understanding of penetration process are in the early stage of investigation [1-4].

In connection with brittle fracture static mechanical tests of ceramics give very limited data (elastic constants, fracture stress and fracture toughness). It is impossible to obtain the value of yield stress Y.

For this reason the indentation tests of ceramics are of great interest. It was shown by Tabor [5, 6] that for metals

$$H = CY \tag{1}$$

where H is the hardness (determined by a rigid indenter) and $C \approx 3$. It is very important that Y in this equation corresponds to the yield stress at deformation ε during indentation. This deformation depends on the indenter shape and as an example for Vickers indenter $\varepsilon \approx 8\%$ [5-7]. At the same time, as it was shown in [1], the cavity expansion during dynamic penetration into metals and ceramics and static indentation are closely related. Consequently, it could be possible to use laboratory measurements of hardness for determination of the magnitude of the dynamic yield for ceramics. Important results in this direction were obtained in [1]. Now it is possible to use for this purpose plasticity characteristic δ_H that can be determined during hardness measurements [7, 8].

δ_H is determined as the part of plastic deformation in total deformation while penetration of the indenter into a specimen

0734-743X/99/$ - see front matter © 1999 Elsevier Science Ltd. All rights reserved.
PII: S0734-743X(99)00109-8

$$\delta_H = \frac{\varepsilon_p}{\varepsilon_t} = 1 - \frac{\varepsilon_e}{\varepsilon_t} \tag{2}$$

where ε_p is the plastic deformation, ε_e is the elastic deformation and ε_t is the total deformation. Eqn. (2) shows that δ_H is dimensionless parameter which changes from zero (for purely elastic deformation) to 1 in the case when elastic deformation is negligibly small. Parameter δ_H is the material plasticity characteristic, and it shows the ability of the material to change its shape when fracture is absent. δ_H is generalized characteristic of plasticity, and to a certain extent it characterizes also the plastic deformation to fracture or ductility.

In the work [8] these concepts were developed further which allowed to take into account the influence of the compressibility of the core of deformation under the indenter on the values of plastic deformation. In this approach

$$\varepsilon_p = ln\ sin\gamma_2 \tag{3}$$

where γ_2 is the angle between the facet of the pyramid of hardness print and the line of the action of the load. At that $\gamma_2 > \gamma_1$ (γ_1 is the angle of indenter grinding). The γ_2 angle for pyramid indenters can be determined [8, 9] from the relationship

$$ctg\gamma_2 = ctg\gamma_1 - 1.77\frac{HM}{E_{ef}} \tag{4}$$

where E_{ef} is the effective Young's modulus of the contact pair indenter - specimen, HM is Meier hardness,

$$\frac{1}{E_{ef}} = \frac{1-\nu_1^2}{E_1} + \frac{1-\nu_2^2}{E_2} \tag{5}$$

where E_2 and ν_2 are Young's modulus and Poisson's ratio for the material of the indenter, E_1 and ν_1 are the same characteristics for the material of the specimen.

The value of the elastic deformation ε_e is determined from the relation

$$\varepsilon_e = (1 - \nu_1 - 2\nu_1^2)\frac{HM}{E_1}, \tag{6}$$

and the total deformation is calculated as

$$\varepsilon_t = \varepsilon_e + \varepsilon_p \tag{7}$$

The consideration of the compressibility of deformation core and elastic properties of the indenter itself is very significant for the investigation of hard and superhard ceramic materials and refractory compounds.

In Table 1 δ_H parameters for metals, covalent crystals and ceramics [7, 8] are given.

Table 1. Plasticity characteristic δ_H for metals, covalent crystals and ceramics [7, 9]

Metals			*Covalent crystals and ceramics*	
Crystal structure	*Material*	δ_H	*Material*	δ_H
b.c.c.	W	0.924	C*	0.048
- " -	Mo	0.952	Si*	0.374
- " -	Fe	0.969	Ge*	0.461
- " -	Ta	0.970	SiC*	0.347
f.c.c.	Ni	0.978	SiC**	0.368
- " -	Cu	0.978	Al_2O_3*	0.428
- " -	Al	0.982	LaB_6*	0.498
- " -	Au	0.989	TiB_2**	0.437
h.c.p.	Mg	0.949	NbC*	0.543
- " -	Ti	0.973	TiC*	0.463
- " -	Re	0.946	TiN**	0.570
- " -	Co	0.945	Si_3N_4**	0.646
			WC**	0.794

* - single crystal,
** - polycrystal

It can be seen from this table that the lowest δ_H value close to zero are inherent to diamond. Indeed, plastic indentation is usually expressed very weakly when measuring hardness in diamond, mainly along the indenter diagonals, where the local stress concentrations is high. For other covalent crystals (silicon and germanium) δ_H is also low. The same is true for SiC and Al_2O_3 where covalent component of interatomic bond is high. Further, with the growth of δ_H borides, carbides and nitrides of transition metals are situated in Table 1. In carbides of IV-A group metals (TiC, ZrC), as well as in carbide NbC and borides $\delta_H \approx 0.5$, i.e. plastic deformation is about 50% from total deformation under the indenter. At the same time tungsten carbide has a considerably higher value $\delta_H \approx 0.8$ which is a great advantage in comparison with other refractory compounds.

For nitrides the $\delta_H \approx 0.6$, i.e. somewhat higher than for borides and carbides (excluding tungsten carbide).

For all pure metals $0.9 < \delta_H < 1.0$. The δ_H value is higher for metals with f.c.c. lattice (Ni, Al, Cu, Au) than for metals with b.c.c. lattice (Mo, Cr, Fe, etc.) and h.c.p. lattice (Co, Re, Mg, Ti). The δ_H values given in Table 1 are consistent with the concept of relative plasticity of materials as determined by the type of interatomic bonds and by measurements of other mechanical properties. However, the measurement of the δ_H parameter is probably the only way for direct comparison of plasticity for a number of materials which are usually considered to be brittle, but during indentation elastoplastic deformation without substantial macroscopic fracture takes place in them.

For our purpose the parameter δ_H gives possibility to establish the quantitative difference between deformation mechanisms during indentation of metals and ceramics.

One of the purposes of this paper is to use both hardness and δ_H parameter to calculate dynamic yield stress Y_D which as it is known can be obtained from the measurement in dynamic experiments after values of Hugoniot elastic limit (*HEL*) by the Eqn.

$$Y_D = HEL\frac{(1-2\nu)}{1-\nu}. \tag{8}$$

Another point of interest of this paper is the analysis of fracture mechanism of ceramic targets. Tate [10] represented the pressure p on the axis at the interface between a long rod penetrator and the target as

$$p = \frac{1}{2}\rho_t U^2 + R_t \tag{9}$$

where U is the rate at which the interface is penetrating into the target, R_t is the dynamic strength term of the target and ρ_t is the density of target. R_t was determined for a number of ceramic targets and it has been shown that the ratio $R_t/H \sim \gamma^{1/3}$, where γ is the specific fracture surface energy [1]. It is important that all investigated ceramics had higher values of R_t than 4340 steel and the value of R_t was closed to Y_D.

MECHANICAL PROPERTIES OF CERAMIC MATERIALS

Mechanical properties for four standard ceramic materials were investigated in this work (Table 2).

Table 2. Mechanical properties of ceramic materials

	AD-995 (Al_2O_3)	*PAD SiC-B*	*PAD* TiB_2	*PAD WC*
Hardness, HV (P = 2 N) (GPa)	18.0	26.0	26.4	24.0
Young's modulus, E (GPa)	383	455	556	690
Poisson's ratio, ν	0.23	0.14	0.11	0.20
δ_H	0.55	0.39	0.45	0.62
Fracture toughness, K_{Ic} (MPa·m$^{1/2}$)	5.2	5.2	6.95	7.6
Ratio, HV/E	0.043	0.057	0.047	0.034
Yield stress calculated by Marsh Eqn. (10), σ_s (GPa)	6.5	11.4	10.8	8.9
Compressive strength, σ_{comp} (GPa)	2.8	3.4	4.8	4.5
Ratio σ_{comp}/σ_s	0.43	0.30	0.44	0.50
Bending strength, σ_{bend} (GPa)	0.41	0.66	0.28	1.10
Ratio σ_{bend}/σ_s	0.061	0.057	0.025	0.123
Ratio $\frac{Y_D}{HV}$	0.33	0.37	0.36	0.31
Y_D, calculated (GPa)	5.9	9.6	9.5	7.4

In experiments there were determined Vickers microhardness HV (at the load P = 2 N when cracking is not essential), Young's modulus E, Poisson's ratio ν, fracture toughness K_{Ic}, compressive strength σ_{comp} and bending strength σ_{bend}. Plasticity parameter δ_H was calculated by the technique given above using Eqns. (2-7). Static yield stress σ_s was calculated from the Marsh Eqn. [11]

$$\frac{HV}{\sigma_s} = 0.28 + 0.60 \cdot ln\left(\frac{3}{4+\nu}\right)\frac{E}{\sigma_s} \tag{10}$$

There are also presented the ratios of the strength in bending σ_{bend} to σ_s (σ_{bend}/σ_s) and of the strength in compression σ_{comp} to σ_s (σ_{comp}/σ_s). Brittle materials are known to fracture at the stresses much lower than σ_s. The given ratios are also the characteristics of material plasticity and are of practical importance.

Among investigated ceramic materials the highest δ_H value is in the ceramics PAD WC, then AD-995 (Al_2O_3) and PAD TiB_2 follow, and the lowest δ_H is in PAD SiC ceramics. Approximately in the same sequence the fracture toughness K_{1c} is changed. However, as it was shown earlier [7], a precise correlation between K_{1c} and δ_H shall be observed only at temperatures higher than the ductile-brittle transition temperature T_b. At temperatures lower than T_b, K_{1c} does not practically depend on temperature, whereas δ_H lowers with the decrease of temperature.

In the ceramic PAD WC the ratios σ_{bend}/σ_s and σ_{comp}/σ_s are also the highest (Table 2) which again confirms the larger plasticity of this material in comparison to other ceramics. If the value of σ_{comp}/σ_s weakly differs for various ceramics and is in the interval $0.3 \div 0.5$, the value of σ_{bend}/σ_s is changing much more significantly because the increase of brittleness (the lowering of plasticity) makes ceramics more sensitive to tensile stresses which define the strength in bending test.

There exist several other theories which relate the Meier hardness *HM*, flow stress σ_s and Young modulus *E*. So, according to Johnson [12].

$$\frac{HM}{\sigma_s} = \frac{2}{3}\left(1 + ln\frac{E_{ef}\, ctg\gamma_1}{3\sigma_s}\right) \tag{11}$$

In this theory $HM/\sigma_s = 1$ for elastic deformation and $HM/\sigma_s = 3$ for completely plastic deformation. The condition of complete plasticity is achieved at $\frac{E_{ef}\, ctg\gamma_1}{\sigma_s} = 40$ [12].

In the theory [13] the compressibility of deformation core under the indenter is taken into account which makes it more preferable.

In accordance to [13]

$$\frac{HM}{\sigma_s} = \frac{2}{3}\left[1 + \frac{3}{2}f + ln\left(\frac{E\sqrt{\pi}\, ctg\gamma_1}{12(1-\nu)\sigma_s}\right)\right] \tag{12}$$

where $f = 1$ for metals and $f \approx 1/3$ for ceramics. Unfortunately the more precise choose of parameter f for ceramics has not been given.

It is seen from above said that the ratio $\frac{HV}{\sigma_s}$ should be lower for elastic deformation (that is close to ceramics) and larger for metals where the share of plastic deformation during indentation is larger than 0.9 ($\delta_H > 0.9$).

CORRELATION BETWEEN HARDNESS *HV*, PLASTICITY PARAMETER δ_H AND DYNAMIC YIELD Y_D

Eqns. (10-12) are written for the static values of H and σ_s. The increasing of deformation rate should increase HV and σ_s. For metals (Al, Cu, Pb and soft steel) dynamic hardness is approximately 20-50% larger than static one [14]. For both metals and covalent crystals the dependence of flow stress (and hardness) on the strain rate $\dot{\varepsilon}$ is strong at the temperatures close to characteristic deformation temperature T^* and higher ones [15]. T^* is defined as the temperature at which the crystal lattice resistance to dislocations motion is essential and causes a sharp growth of flow stress when the temperature drops below T^* [16]. For covalent crystals the dependence $\sigma_s(\dot{\varepsilon})$ is even more strong than for metals. But the temperature T^* is very high for these crystals.

For ceramics under investigation $T^* \geq 1000^\circ$C. With decreasing the temperature the dependence $\sigma_s(\dot{\varepsilon})$ becomes weaker and at $T = 0$ K σ_s does not depend on $\dot{\varepsilon}$. For this reason we can suppose that σ_s and H depend on $\dot{\varepsilon}$ very weakly at room temperature.

From the above discussion we can suppose that

$$H = c\, Y_D \tag{13}$$

where c depends on the share of plastic deformation during indentation, i.e. $c = f(\delta_H)$. From above discussion it is possible to write

$$Y_D = \frac{H}{\alpha}\delta_H + \frac{H}{\beta}(1-\delta_H) \tag{14}$$

If $\delta_H = 0$ (pure elastic deformation), $H = \beta\, Y_D$, i.e. $c = \beta$. And if $\delta = 1$ (pure plastic deformation), $H = \alpha Y_D$ and $c = \alpha$. In the common case $\beta \leq c \leq \alpha$.

We obtain from (14)

$$\frac{Y_D}{H} = \frac{1}{\beta} - \left(\frac{1}{\beta} - \frac{1}{\alpha}\right)\delta_H \tag{14a}$$

The experimental results that were calculated from the data [1] (see Table 3) indeed give the linear dependence of Y_D / HV versus δ_H (Fig.1). Only the results for BeO do not correspond to this dependence, that may be connected with phase transformation during indentation or with other factors. From Fig. (1) and Eqn. (14a) we have $\alpha = 4.9$ and $\beta = 2.1$.

This concept may be used for the estimation of Y_D by indentation method.

For materials investigated in this work (Table 2) we have calculated Y_D/HV from Eqn. (14a). The obtained results are given in Table 2 and in Fig. (1). We could wait that calculated values of Y_D will be somewhat greater than calculated magnitudes of σ_s. Actually Y_D is close to σ_s, but $Y_D < \sigma_s$. It may be the result of some inaccuracy of Eqn. (10). But it's more probable that Marsh Eqn. (10) gives the yield stress σ_s that corresponds to the deformation during indentation by Vickers indenter ($\varepsilon_t \approx 8\%$ and $\varepsilon_p = 3$-5% for different ceramics). And σ_s exceeds yield stress at the beginning of deformation, e.g. $\sigma_{0.2}$, by the magnitude of strain hardening. It is important that both Y_D and σ_s decrease in the same row SiC-B, TiB_2, WC and Al_2O_3 (see Table 2).

From obtained results it is seen that the ratio $\frac{HV}{Y_D}$ is some larger than one predicted by theories [11-13]. But we must remember that we have used Vickers hardness when deformation during indentation is close to 8% whereas Y_D is determined at the beginning of plastic flow.

Table 3. Mechanical properties for ceramic materials [1], plasticity parameter δ_H was calculated by Eqns. (2-7)

Materials	*E (GPa)*	*H (GPa)*	*HEL (kbars)*	Y_D *(kbars)*	$\frac{H}{Y_D}$	δ_H
KT SiC	365	18.6	80±30	65±24	2.86	0.473
TiB_2	482	23.0	86±30	76±25	3.03	0.470
Al_2O_3 (high density)	399	19.6	92	65	3.01	0.542
B_4C	457	27.4	137±4	101	2.71	0.440
MgO	314	9.2	35	26	2.45	0.707

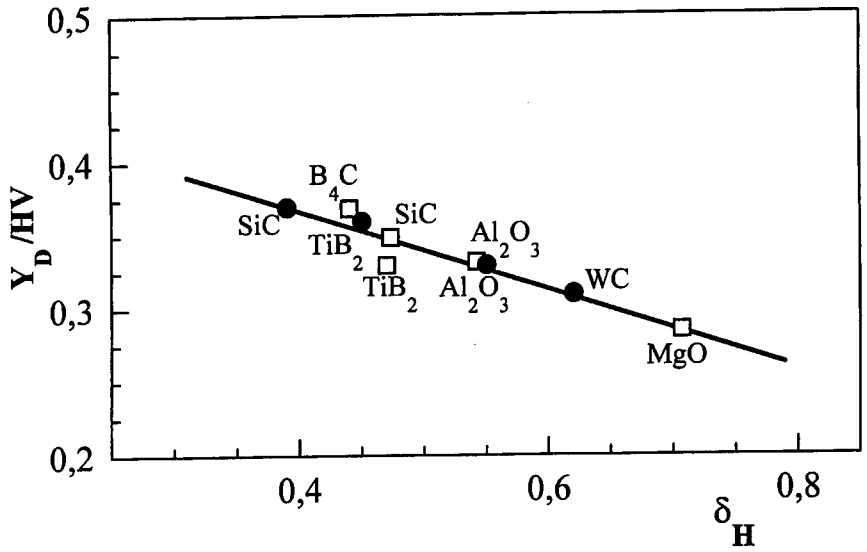

Fig 1. The dependence of the ratio of dynamic yield Y_D to Vickers hardness HV versus plasticity parameter δ_H: □ - Y_D/HV are data of [1], δ_H was calculated by data [1] (Table 3); ● - data of present work; δ_H from Table 2, Y_D/HV was calculated by Eqn. (14a).

STRESS-STRAIN CURVES OBTAINED BY INDENTATION METHOD

In the present work the stress-strain curves were constructed by indentation technique for investigated ceramics.

The main idea of the method is in the employment of the set of pyramid indenters with various angles of sharpening [8, 9, 17]. For each indenter the Meier hardness HM equal to the average contact pressure is determined, and deformation under the indenter is calculated. Eqns. (3-7) given earlier are used for this purpose.

Each indenter gives one point in the stress-strain curve. For the investigation 9 diamond trihedral pyramid indenters with the angles between pyramid axis and side γ_1 = 45, 50, 55, 60,

65, 70, 75, 80 and 85 degrees were manufactured. The results of measuring hardness with the indenters pointed above and of calculating deformation are given in Table 4.

Table 4. The angles at the tip of the indenter γ_1 and of hardness print γ_2, Meier hardness HM, plastic ε_p, elastic ε_e and total ε_t deformations for ceramic materials

γ_1 (deg.)	γ_2 (deg.)	HM (GPa)	ε_p (%)	ε_e (%)	ε_t (%)
		"PAD" WC			
45	48.5	29.70	28.8	3.2	32.0
55	58.8	25.30	15.6	2.6	18.2
60	64.9	28.00	9.9	3.0	12.9
65	69.4	24.18	6.5	2.5	9.0
70	74.5	23.16	3.7	2.4	6.1
75	78.8	19.18	1.9	2.0	3.9
80	82.4	11.44	0.8	1.2	2.0
85	87.4	11.32	0.1	1.2	1.3
		"PAD" SiC-B			
55	60.5	25.31	13.0	4.6	17.6
60	66.2	25.00	8.9	4.0	12.9
65	71.8	25.77	5.1	4.6	9.6
70	76.9	24.73	2.6	4.4	7.0
75	80.3	18.19	1.4	3.2	4.6
80	83.8	12.65	0.6	2.2	2.8
		"PAD" TiB_2			
45	47.6	19.61	30.0	3.0	33.0
55	59.2	23.07	15.9	3.6	19.5
60	65.5	27.30	9.3	4.2	13.5
65	70.0	22.90	6.2	3.2	9.4
70	75.5	23.88	3.2	3.7	6.9
75	79.9	20.11	1.6	3.1	4.7
80	82.8	11.13	0.8	1.7	2.5
		AD - 995 (Al_2O_3)			
60	63.8	14.80	8.2	2.6	10.8
65	70.1	17.88	6.1	3.1	9.2
70	74.5	14.91	3.6	2.6	6.2
75	78.6	12.74	2.0	1.9	3.9
80	84.2	12.82	0.5	2.2	2.7

In Fig.(2) there are shown the deformation curve $HM(\varepsilon)$ for investigated ceramic materials.

It is pertinent to note that for ceramic materials not all of above - mentioned indenters can be used because under sharp indenters (high degrees of deformation) intensive failure of print takes place.

It is seen from Table 4 that for ceramic materials the angle γ_2 is essentially higher than γ_1, and the part of elastic deformation under the indenter is very large, especially for indenters with big angle γ_1. Everyone can see from Table 4 and Fig.2 that hardness at big γ_1 where the plastic deformation is low is approximately two times lower than the hardness at angles $\gamma_1 \approx 68°$ (as for Vickers indenter). Consequently, the ratio H/Y_D approaches to 1 for pure elastic deformation (parameter β in Eqn. (14) will be two times lower and approximately equal to 1) in conformity with above mentioned theories.

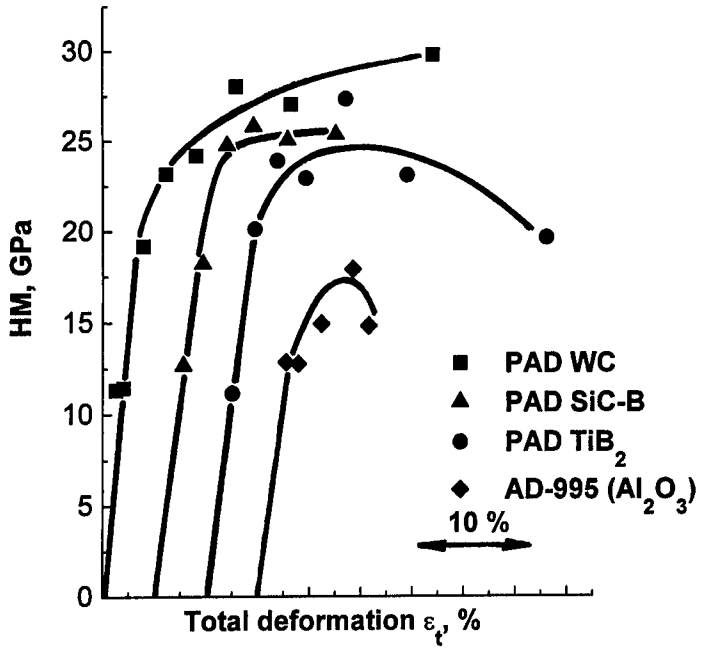

Fig.2. Stress-strain curves as Meier hardness *HM* versus total deformation under the indenter ε_t for ceramic materials.

CONCLUSION

The plasticity characteristic δ_H introduced early for the characterization of ductility of ceramics and other brittle materials by indentation method can be used for the description of behaviour of ceramic targets at impact loading because the dependence of yield stress (and hardness) on strain rate is weak for ceramic materials at room temperature. Determination of Vickers hardness *HV* with simultaneous determination of plasticity characteristic δ_H makes possible to estimate dynamic yield Y_D from the relation $\frac{Y_D}{HV} = A - B\,\delta_H$. Experimental results give $A \approx 0.48$ and $B \approx 0.27$. For purely elastic deformation ($\delta_H = 0$) $\frac{Y_D}{HV} = A$ and for completely plastic deformation ($\delta_H = 1$) $\frac{Y_D}{HV} = A - B$. In common case the ratio HV/Y_D decreases with the diminution of δ_H, i.e. with increasing the share of elastic deformation, and $HV/Y_D \approx 2$ for purely elastic deformation. The stress-strain curves in coordinates Meier hardness-deformation were constructed by employment of a set of diamond indenters with various angles of sharpening for four investigated ceramic materials. It has been shown that if to use a blunt indenter that corresponds to the small plastic deformation degree $\varepsilon_p \to 0$, the ratio $\frac{H}{Y_D} \to 1$ for elastic deformation in conformity with indentation theories. The dynamic yield Y_D calculated in the present work for four investigated ceramic materials approximately coincides with the static flow stress σ_s calculated by Marsh Eqn., if to take into account that σ_s exceeds yield stress at the beginning of deformation, e.g. $\sigma_{0.2}$, by the magnitude of strain hardening.

Acknowledgement — This work was supported, in part, by the International Soros Science Education Program through grant No SPU 072038 and by contract DA AL 01-96-M-146.

REFERENCES

1. J.Strenberg, Material properties determining the resistance of ceramics to high velocity penetration. J.Appl. Phys. **65** (9), 1 May, 3417-3424, (1989).
2. R.M.Contiliano, T.B.Donough, C.V.Swanson, Aeronautical Research Assotiates of Princeton (ARAP) Rep 368, (1978).
3. C.P.Donaldson, R.Contiliano, C.V.Swanson, ARAP Rep. 295, (Dec.1976).
4. Z.Rozenberg, E.Dekel, Y.Yeshurun, E.Bar-On Int. J.Impact Engng. **17,** 697-706, (1995).
5. D.Tabor. Indentation hardness: fifty years on. A personal view, Phil. Mag. **A74**, 1207-1212, (1996).
6. D.Tabor. The Hardness of Metals, Clarendon Press, Oxford, 130p. (1951).
7. Yu.V.Milman, B.A.Galanov, S.I.Chugunova. Plasticity characteristic obtained through hardness measurement. Acta Met.Mater. **41** (9), overview (107), 2523-2532, (1993).
8. Yu.V.Milman, B.A.Galanov, S.I.Chugunova, I.V.Goncharova. Determination of the mechanical properties of low-ductile materials by indentation method, Polish Ceramic Bulletin **12** (50), 95-102, (1996).
9. B.A.Galanov, Yu.V.Milman, S.I.Chugunova, I.V.Goncharova. Investigation of high-hard materials mechanical properties by indentation. Sverkhtverdye Materialy (English translation: Journal of Superhard Materials) in press.
10. A.Tate, J.Mech. Phys Solids **15**, 387-394, (1967).
11. D.M.Marsh. Plastic flow in glass. Proc.Phys.Soc., **A279**, 420-434, (1964).
12. K.J.Johnson. Contact Mechanics, Cambrige University Press, 510p. (1985).
13. K.Tanaka. Elastic/plastic indentation hardness and intentation fracture toughness: the inclusion core model. J.of Mater.Science, **22**, 1501-1511, (1987).
14. L.V.Beljakov, F.F.Vitman, N.A.Zlatin, Journal of technical physics, **33** (8), 990-995, (1963) in Russian.
15. V.I.Trefilov, Yu.V.Milman, O.N.Grigoriev, Progr. Crystal Growth and Charact., **16**, 225-277, (1988).
16. V.I.Trefilov, Yu.V.Milman, I.V.Gridneva, Crystal Res. Technol., **19** (3), 413-421, (1984).
17. Yu.V.Milman, S.I.Chugunova, I.V.Goncharova and S.Luyckx. Determination of Ductility and Stress Strain Curve of WC Based Hard Metals by Indentation Method. Science of Sintering, **29** (Sep.-Dec.), 155-161, (1997).

PERGAMON International Journal of Impact Engineering 23 (1999) 639–649

INTERNATIONAL JOURNAL OF IMPACT ENGINEERING

www.elsevier.com/locate/ijimpeng

STATISTICAL ANALYSIS OF NRL 1964-1969 HYPERVELOCITY ROD-PLATE IMPACT DATA AND COMPARISON TO RECENT DATA

P.E. NEBOLSINE*, N.D. HUMER*, N.F. HARMON*, and J.R. BAKER**

*Physical Sciences Inc., 20 New England Business Center, Andover, MA 01810-1077, USA;
**U.S. Naval Research Laboratory, Washington, DC 20375, USA

Summary — The previously reported Naval Research Laboratory hypervelocity rod-plate impact database was studied to derive the statistical variation that could be assigned to measurements of rod erosion for various impact conditions and impacting materials. The database covers impacts of 3.175 mm diameter rods having diameter-to-length ratios of 10 at velocities between 2.6 and 6.1 km/s upon targets whose thickness varied from 0.0355 to 6.5 rod diameters. Seven different projectile materials and 10 different target materials as well as alloys of aluminum and steel were tested. Of the 275 individual impacts reported, 157 were selected for statistical analysis. It was found that all of the data were normally distributed with a mean of 0.966 and standard deviation of 7.6% of the mean when the individual experimental measurements of rod erosion were normalized to predicted values calculated for the same impact conditions using the semi-empirical equation reported by Baker. Using this normalization, recent data from a multiple plate impact experiment was found to lie well within the uncertainty band. Subsets of the data are discussed.
© 1999 Elsevier Science Ltd. All rights reserved.

INTRODUCTION

In engineering studies on the lethal effectiveness of hypervelocity rod attack on complex structures the damage created by the rod is defined in terms of its ability to penetrate into or through its target. For many targets this penetrating ability is conveniently stated in terms of the rod shortening, i.e., erosion, experienced during the penetration and perforation processes. In order to perform meaningful systems engineering weapons effectiveness studies a rapid method of calculating the erosion under different engagement and impact conditions is required along with the uncertainties in the calculated results. Such a rapid computational technique can be applied to a wide variety of engagements and knowledge of the uncertainties in the results are necessary to define quantitatively the statistical characteristics of the weaponry under study. The speed requirement obviates the use of detailed numerical calculations, e.g., hydrocodes, and argues for the use of an analytic calculation based upon the results of both detailed computations and experimental data. This was the approach undertaken at the Naval Research Laboratory (NRL) using a large experimental data base generated over several years [1-3] and the results of two dimensional hydrodynamic calculations simulating the impact processes for certain impact conditions. A fortuitous consequence of the large data base available is that many repeat conditions and a range of impact conditions are available from the same experimental apparatus and analysts. This allows a statistical analysis of the data which is the purpose of this paper.

0734-743X/99/$ - see front matter © 1999 Elsevier Science Ltd. All rights reserved.
PII: S0734-743X(99)00110-4

BACKGROUND

Baker [3,4] reported a simple, semi-empirical equation (henceforth called the Baker equation) for rod loss , $\Delta\ell$, as a function of the rod impact parameters for hypervelocity perforation of a plate of the same material. This equation is:

$$\frac{\Delta\ell}{d} = \frac{t}{d} + \frac{\Delta t}{d} + \frac{v\tau}{d}\left\{1 - \exp\left[-\left(\frac{\Delta\ell/d + t/d + \Delta t/d}{f\, v\, \tau/d}\right)\right]\right\} \quad (1)$$

where all lengths have been normalized by the rod diameter, d. t is the target thickness, v is the impact velocity, and f, τ, and $\Delta t/d$ are empirical constants. Note that Eqn. (1) must be solved iteratively since the unknown parameter $\Delta\ell/d$ appears on both sides of the equation.

The first term in Eqn. (1), t/d, is simply the length loss commonly associated with steady-state hydrodynamic erosion. The second term, $\Delta t/d$, is a small additional loss due to a non-steady-state process that is possibly associated with the initial shock phase of the impact process. For most cases of practical interest ($t/d > 0.05$), this term can be taken as a constant; however, as noted below, this is not strictly true. The third term, involving $v\tau/d$, is the primary non-steady state loss associated with the final breakout phase of the perforation process. The value of $v\tau/d$ can be computed from the equation:

$$\frac{v\tau}{d} = \frac{1.98\ v}{\sqrt{[c^2 - (u_s - v/2)^2]}} \quad (2)$$

where c is the sound speed in the shocked rod material, and u_s is the shock velocity. These quantities can be obtained using either published equation-of-state data or coefficients for the approximation that the shock velocity is a linear function of the particle velocity.

It should be noted that for thick target plates ($t/d > 2$) the rod loss approaches a linear dependence on t/d given by

$$\frac{\Delta\ell}{d} = \frac{t}{d} + \frac{\Delta t}{d} + \frac{v\tau}{d}$$

with constant transient erosion terms of $\Delta t/d + v\tau/d$. For very thin target plates ($t/d < 0.1$), the term $\Delta t/d$ in Eqn. (1) should be replaced by the expression $(\Delta t/d)\ [1 - \exp(-\xi t/d)]$ so that the rod loss approaches zero as t/d approaches zero. The effect of this modification is however negligible for $t/d > 0.05$.

Equation (1) was generated by adding the empirical constants cited to a theoretical model describing the impact process such that the resultant equation fit both the computer generated results for hole depth and the experimental data for rod erosion in the case of aluminum on aluminum impacts (Baker [3]).

For an impact configuration in which the projectile and target plate are of different materials, the rod loss can still be computed using a modification of Eqn. (1). By analogy with the theory of steady state, incompressible hydrodynamic penetration modeling which predicts that for unlike fluids, the penetration varies as the square root of the density ratio of the two fluids, so too did Baker [3] find the normalized rod erosion depend on the rod and target material densities, i.e.,

$$\left(\frac{\Delta\ell}{d}\right)_{1\to 2} = \sqrt{\left(\frac{\rho_2}{\rho_1}\right)}\left(\frac{\Delta\ell}{d}\right)_{1\to 1} \tag{3}$$

where 1→2 signifies rod material of density, ρ_1, impacting target material, ρ_2. This paper will examine the NRL experimental database in the light of the Baker equation in order to generate the statistical parameters associated with rod loss predictions made with the equation.

The main focus of the NRL experiments was centered on using 2024-T86 aluminum rods 0.3175 mm (1/8 in.) in diameter with a length to diameter ratio (l/d) of ~10, impacting 2024-T3 plates at 90 deg (normal impact) and a nominal 4.6 km/s impact velocity. This data was used in determining the dependence of rod loss on impact conditions and target thickness. In addition, a substantial amount of data was generated to study the effect of changing the various impact conditions, e.g., target and rod material, rod diameter, impact velocity and impact angle. Table 1 lists the various combinations and the number of data points attempted. Of the of the 275 individual impacts listed in this table, 54% were aluminum rod-aluminum plate impacts , about 18% were steel rod-steel plate impacts with the remaining 36% unevenly distributed among seven different projectile materials and eight different target materials.

ANALYSIS

This analysis will examine the aluminum rod-aluminum plate impacts in two steps: 1) examine the rod erosion dependence on target thickness for the experimental data taken at impact velocities of (4.65 ± 0.233)km/s, and 2) expand the analysis to data taken at other impact velocities. This will be followed by a discussion of the distribution of this data about its mean. The analysis will then be expanded to include the other rod-target material pairs though application of the square root of the density ratio scaling of Eqn. (3).

For the analysis highly yawed rods (greater than 10 deg), oblique impacts, impact velocities less than 2.3 km/s, and experimental points for which the pre-impact rod length were unspecified were excluded. In addition those experiments using tool steel rods were excluded since there was experimental evidence that rod loss continued after plate perforation rendering the quoted values suspect [2]. These exclusions left 165 impacts for analysis. For the aluminum on aluminum impacts, this left 79 experimental data points spanning the velocity range from 2.3 to 6.1 km/s while the target thickness varied from 0.035 to 6.5 rod diameters. Of the 79, 9 were 2024-T86 rods and 1100 F targets, 7 were 2024-T3 rods and 2024-T3 targets the rest being 2024-T86 rods and 2024-T3 targets. Forty-seven of these data points are for impacts in the (4.65 ± 0.233) km/s range.

Nearly Constant Velocity Aluminum Rod-Aluminum Plate Impacts

Figure 1 shows the measured erosion for a the subset of the aluminum on aluminum data taken at impacts in the nearly constant (4.65 ± 0.233) km/s range plotted versus target thickness each being normalized to the rod diameter, a convention that will be followed throughout this paper. The sloping line in the figure is the prediction from Eqn. (1) of the erosion for the indicated thickness at an impact velocity of 4.65 km/s. This curve appears to give a good fit to the data. The triangles centered near the scaled erosion of 1.0 mark are the experimental erosion normalized to that predicted by the Baker equation for the same impact conditions. The large amount of scatter for thickness less than about 0.5 rod diameters is the result of the small erosion and the appearance of

Table 1. Summary of NRL rod impact conditions

Projectile Material	Plate Material	t/d	Impact Velocity (km/s)	Shots	Plate Angle
2024 Aluminum	2024 Aluminum	0.16 - 5.5	4.6, 6.1	83	90 deg
↓	↓	1.0	0.5 - 6.3	37	90 deg
		0.25 - 2.0	4.1 - 4.6	18	10 - 60 deg
	1100F Aluminum	0.03 - 2.0	4.4 - 4.7	11	90 deg
	4340 Steel	0.4 - 2.0	4.6	9	
	Copper	0.5 - 2.0	4.6	8	
	Lead	1.0 - 1.5	4.6	5	
	Zinc	1.0 - 2.0	4.6	3	
	Uranium	0.25, 1.0	4.6	3	
	1020 Steel	0.9	1.3	2	
	Cold Rolled Steel	1.0	4.5	1	
	6061 Aluminum	0.1	4.6	1	
	Titanium	0.5	4.7	1	
	Magnesium	3.0	4.1	1	
	Phenolic Refrasil	2.2	4.6	1	
4340 Steel	4340 Steel	1.0	1.3 - 5.9	17	
↓	↓	0.16 - 2.0	4.5	4	↓
		0.25, 1.0	4.6	3	10 - 20 deg
	2024 Aluminum	0.25 - 8.0	4.0 - 4.5	6	90 deg
	Cold Rolled Steel	0.22	4.7	3	10 - 20 deg
	Uranium	1.0	4.6	1	90 deg
	Magnesium	3.2, 3.5	5.3 - 5.6	2	
Tool Steel	2024 Aluminum	0.25 - 2.0	4.2 - 4.6	15	
Nickel	Nickel	0.25 - 1.0	4.0	5	
↓	2024 Aluminum	1.0	4.4	2	
	Copper	0.75 - 2.0	4.2 - 4.4	6	
Uranium	Uranium	1.0	1.4 - 3.7	5	
↓	2024 Aluminum	0.75 - 3.5	3.1, 3.8	4	
	Uranium	0.3 - 1.5	3.1	3	
	Titanium	1.1 - 2.4	3.1	3	
Tungsten	Tungsten	1.0	4.0	1	
↓	2024 Aluminum	0.5 - 1.0	3.9 - 4.4	3	
Titanium	Titanium	0.5 - 1.0	4.5	5	
↓	↓	0.23	3.2, 4.0		
	Uranium	0.5 - 1.0	4.6	3	↓

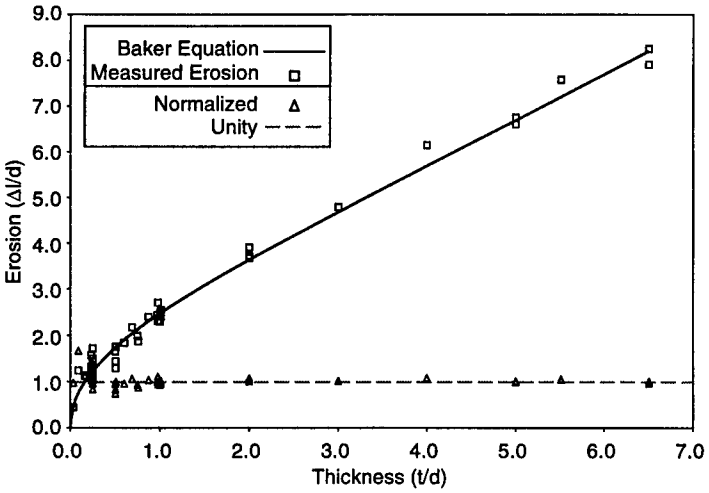

Fig. 1. NRL Al on Al data (4.412 < v < 4.883 km/s).

the front of the rods in the flash x-ray images. The rod tip is jagged rather than smooth as in the case for thick target impacts. Both of these effects lead to the increased data scatter [1] for the thin plate data. As is clear from the figure for aluminum rods impacting aluminum plates, there are target thicknesses for which several data points are available. Table 2 lists these target thickness ratios (A) along with the average of the measured erosion, (B), the root mean square (rms) deviation about the average (C), the fractional deviation (D) (the rms value ÷ Δℓ/d (column C ÷ column B)), the erosion calculated using the Baker equation (E), the ratio of the averages of the measured erosions to calculated (Baker) erosion (F) (equivalent to B ÷ E), and the rms deviation of these ratios (G), along with its fractional deviation

Table 2. Comparison of measured to calculated erosion for aluminum rods impacting aluminum plates.

A	*B*	*C*	*D*	*E*	*F*	*G*	*H*
Target thickness ratio (t/d)	*Average erosion* $\left(\frac{\Delta\ell}{d}\right)$	*rms deviation* $\left(\frac{\Delta\ell}{d}\right)$	*Fractional deviation*	*Cacluated erosion* $\left(\frac{\Delta\ell}{d}\right)$	*Measured ÷ calculated erosion*	*rms deviation* $\left(\frac{\Delta\ell}{d}\right)$	*Fractional deviation*
0.233	1.379	0.139	0.10	1.200	1.150	0.114	0.10
0.250	1.360	0.215	0.16	1.238	1.099	0.173	0.16
0.50	1.536	0.180	0.12	1.741	0.880	0.102	0.12
1.0	2.442	0.131	0.054	2.477	0.987	0.054	0.053
2.0	3.743	0.084	0.02	3.638	1.028	0.023	0.02
5.0	6.686			6.700	1.000		
5.5	7.585			7.200	1.050		
6.5	8.080			8.200	0.984		

(H). All dimensions are normalized to the rod diameter. Although the Baker equation was not fit at these points, the agreement between experiment and calculation is good. Column F for the measured divided by the calculated erosion gives a measure of the agreement between the two. In general, the agreement is quite good particularly for the thicker targets although there are too few

data points available for meaningful rms deviation calculations at the three largest thicknesses. The fractional deviation in this ratio is the fractional deviation in the experimental data as shown by comparing the fourth and last columns in the table. The use of this ratio affords a means of comparing all of the data and generating a standard deviation that applies to the entire data set.

For the data shown in Fig. 1 by the triangle centered near the scaled erosion of 1.0 line, the measured/calculated erosion has an average value of 1.037 with an rms deviation of 0.15. Thus the Baker equation, on average, under-predicts the experimental results but not to a significant degree. Excluding the experimental data for plate thickness less than 0.6 rod diameters the average measured/calculated erosion for the remaining 31 data points is 1.003 with a rms deviation of 0.05. This success of the Baker equation in predicting the experimental result is encouraging since it represents a semi-empirical rather than an empirical fit to the data.

All Aluminum Rod-Aluminum Plate Impacts

Figure 2 shows the measured normalized erosion scaled by Eqn. (1) to 4.65 km/s for the full velocity range of the NRL aluminum on aluminum data plotted versus the target thickness rate. Note that the additional data are for target thicknesses of 3.0 rod diameters and less. As expected for the range of impact conditions represented, the apparent data scatter is increased. As in Fig. 1 the points marked with triangles near the horizontal line at a scaled erosion of 1.0 on the plot are the experimental erosion normalized to the Baker equation result at the same experimental condition. In this case the average of the measured/calculated erosion is 1.027 with an rms deviation of 0.13. Thus, even with this expansion in experimental conditions beyond those for which the Baker equation was intended, it still predicts, on average, the experimental erosion. Excluding target thicknesses less than 0.6 rod diameters yields an average measured/calculated erosion of 1.011 with an rms deviation of 0.06, a striking agreement of calculation with measurement.

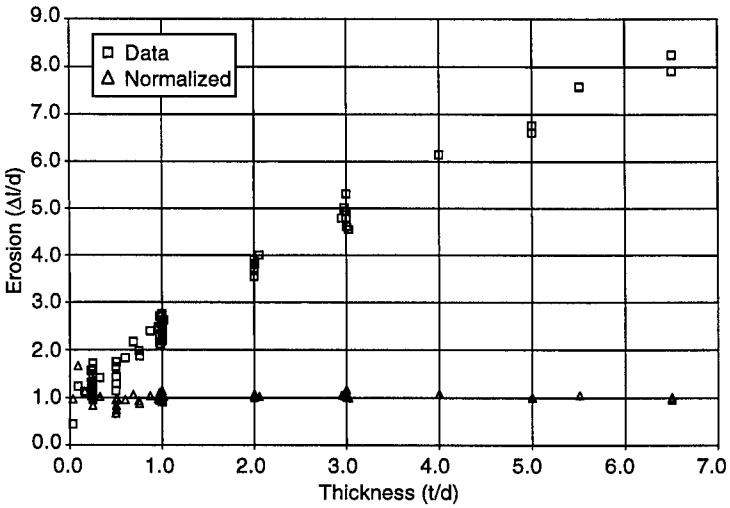

Fig. 2. Velocity scaled NRL Al on Al data (all impact velocities).

The experimental data for the thinner targets represents a different class of data from that for the thicker targets as a result of the difficulty in making the measurements. For the 24 data points available, for normalized target thickness less than 0.6 rod diameters the average measured/calculated erosion is 1.06 with an rms deviation of 0.22. Thus, on average, the Baker equation is in good agreement with the experimental data even though the data scatter is large.

Distributions

Figure 3 shows a more graphic illustration of this scatter. In this figure, the experimental data normalized to the Baker equation result for the same experimental conditions and the experimental

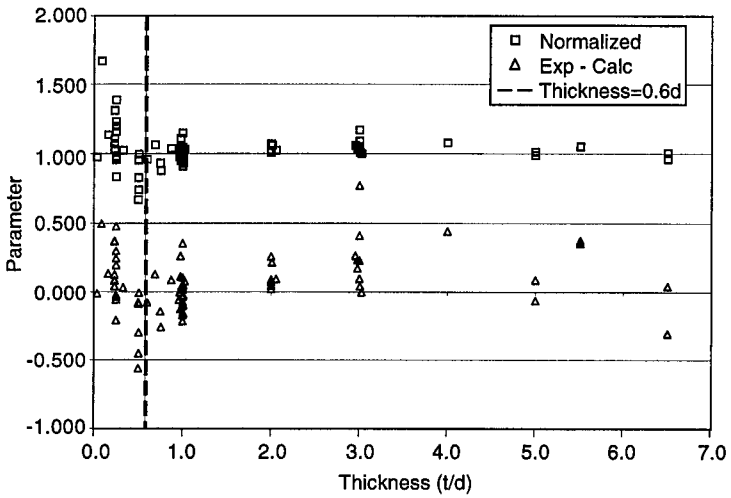

Fig. 3. Scaled NRL Al on Al data.

data minus the calculated result (exp-cal) are displayed as a function of thickness. The exp-calc points show a tendency for the calculations to underestimate the experimental data at thicknesses greater than two rod diameters however the fractional deviation is not large as is evident by the scatter in the points of the normalized data. At the lesser thicknesses the large scatter in the deviations is almost evenly distributed and the fractional deviations are large as is reflected in the scatter in the normalized points. Considering the points to the right and left of the vertical line at just under 0.6 rod diameters illustrates the makeup of the data whose averages were presented previously.

Figure 4 shows the distribution of the normalized data and compares it to two normal distributions having the same mean but different rms deviations. The distribution of the data is slightly skew, by about 3% toward higher values than the average as expected from Fig. 3. This distribution is symmetric about its mean. Comparing Fig. 4 with Fig. 3 shows that the outliers are mainly from the thinner plate data where the scatter is greater. The Normal 1 curve is a normal distribution having the same mean and rms deviation as the data. This curve appears to overestimate the rms deviation exhibited by the data in this plot. The Normal 2 curve is a normal distribution having the same mean as the data but with an rms deviation calculated from the average amplitude of the data at its peak, 5.8, yielding an rms deviation of 0.069 as shown on the plot. This distribution gives a better fit at the peak but increase the number of outliers. Figure 5 shows the cumulative distributions derived from the plots of Fig. 4. The very steep rise in the data near its average is not mirrored in either of the normal distributions. The Cumulative 1 curve, with same mean and rms deviation as the data, doesn't match the data. On the other hand, the Cumulative 2 curve, with the same mean and rms deviation as derived from the data peak, is a good match to the data except at its extremes. In the case of the former distribution 16% of the data points lie outside the rms deviation while for the latter distribution 36% do.

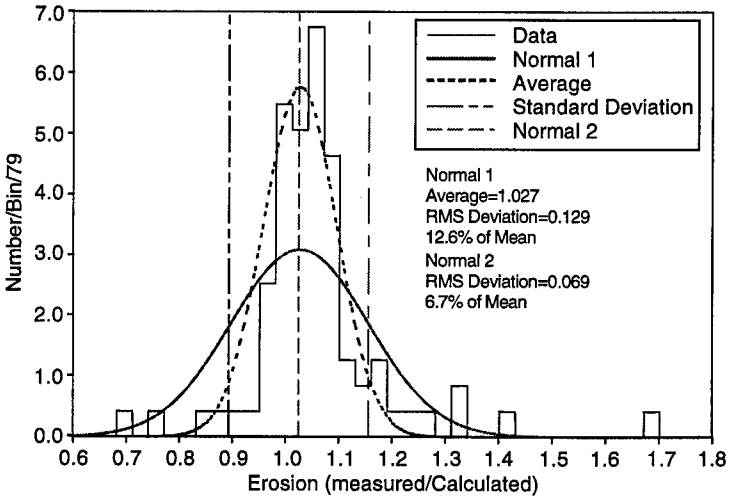

Fig. 4. Scaled NRL Al data histogram distributions.

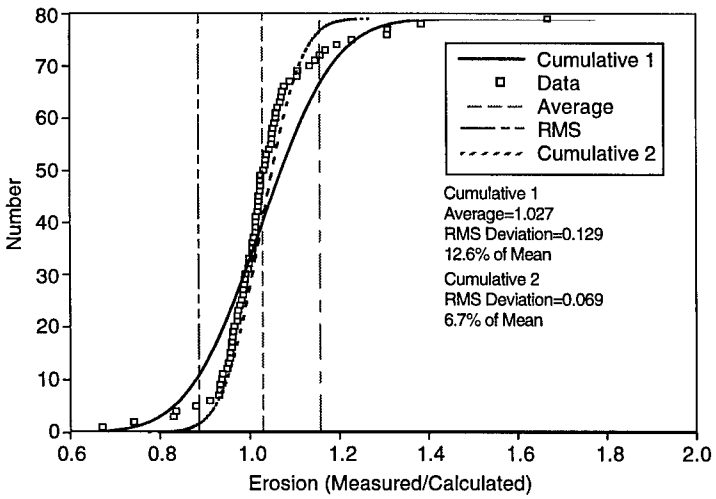

Fig. 5. Scaled NRL Al data, cumulative distribution.

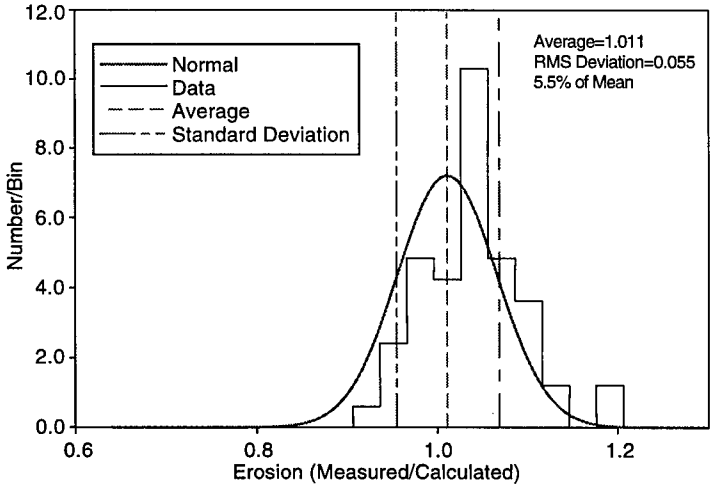

Fig. 6. Scaled NRL Al data histogram distributions (t/d > 0.6).

Figure 6 shows the distribution resulting from excluding the data for plate thickness less than 0.6 rod diameters compared with a normal distribution having the same mean and rms deviation as the data. The distribution is a good match to the data. As expected, the distribution of the data is much narrower with fewer outliers. It maintains the slight skewness and concentration of data near and just above the average. Figure 7 shows the cumulative distribution of this data and illustrates both the good fit of the normal distribution and the slight peakiness of the data near its upper rms deviation. These plots show that the NRL aluminum data normalized to the value calculated by the Baker equation is well represented as a normal distribution.

Density Scaling

Extending the analysis to the entire database includes unlike rod and target material impacts. To provide for comparison of data taken at different conditions, the Baker equation provides a common condition of v = 4.65 km/s and t/d = 1. Then all the data for each projectile and target material pair has been averaged. Scaling for density is accomplished by applying Eqn. (3), the square root of density ratio scaling (hydrodynamic limit scaling), to all of the rod projectile-target combinations. Figure 8 is a plot for each projectile and target material combination of the scaled averaged data versus the square root of the ratio of target density to projectile density. The solid line on this plot is the Baker prediction for the scaled erosion given its value for like material impacts. Note that for like material impacts the mean scaled erosion is nearly material independent. This scaling is expected to apply to the steady-state erosion associated with penetration [5], but not necessarily to the non-steady-state part of the process. Figure 8 indicates that it applies to both processes. Figure 9 shows the scaled measured erosion versus target thickness for all of the data scaled through the Baker equation to an aluminum on aluminum impact at a velocity of 4.65 km/s to examine only t/d dependence. This scaling is accomplished by multiplying the experimental data by the Baker

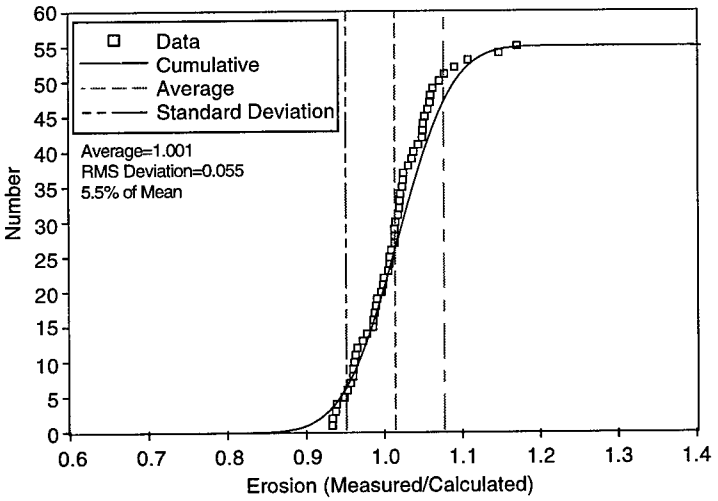

Fig. 7. Scaled NRL Al data, cumulative distribution (t/d > 0.6).

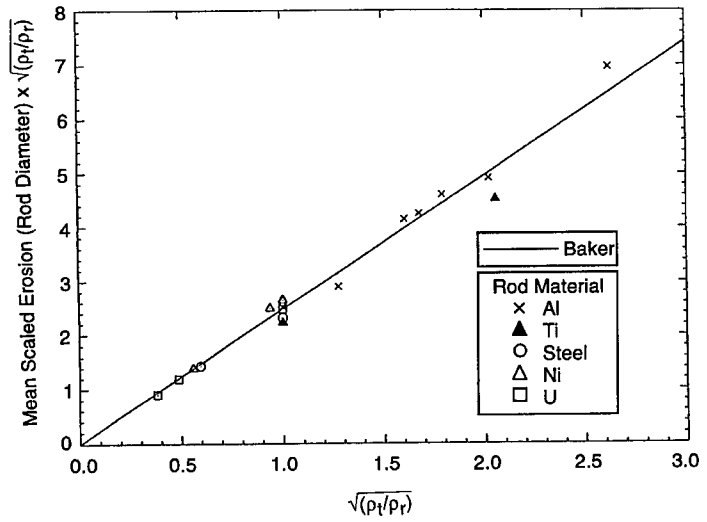

Fig. 8. Scaled mean erosion versus square root of target/rod density ratio (Baker 1969 data).

equation predicted erosion for an aluminum rod impacting an aluminum plate at a velocity of 4.65 km/s and the square root of the density ratio and dividing this product by the Baker equation prediction for impact conditions corresponding to the experimental data. The solid line on this plot is the Baker equation prediction for these conditions. Comparing Fig. 9 with Fig. 2 shows that the additional 86 data points tend to increase the scatter in the data. Figure 10 shows the distributions for the experimental erosion minus the calculated erosion and the measured/calculated erosion for the experimental data shown in Fig. 9 excluding the aluminum on aluminum data for thicknesses less than 0.6 rod diameters. Here the normalized data and the experimental minus the calculated erosion are plotted versus a number that identifies the rod-plate material combinations. Only the rod material is indicated in the figure. The preponderance of aluminum rods among the 141 points in the data set is clear from this figure. The left portion of this plot, the experimental data minus the calculated value, show that for the aluminum and nickel rods the calculated values tend to underestimate the experimental results more often than not while for the steel and titanium rods the opposite seems to be the case. The normalized erosion shown on the right side of the plot has a mean value of 0.996 with an rms deviation of 0.076, 7.6% of the mean. The points near the 140 marker show a tendency for the calculated values to always overestimate the experimental results. That is a result of the observation that the titanium rods used in those experiments were always eroded less than the other rod materials under the same experimental conditions. Figure 11 shows the cumulative distribution of the data and compares it to a normal distribution having the same mean and rms deviation. Unlike the aluminum data alone shown in Fig. 4, this expanded data set follows fairly closely the normal cumulative distribution much as the subset of aluminum on aluminum data shown in Fig. 6. Once again this close agreement suggests that the data conforms to a normal distribution.

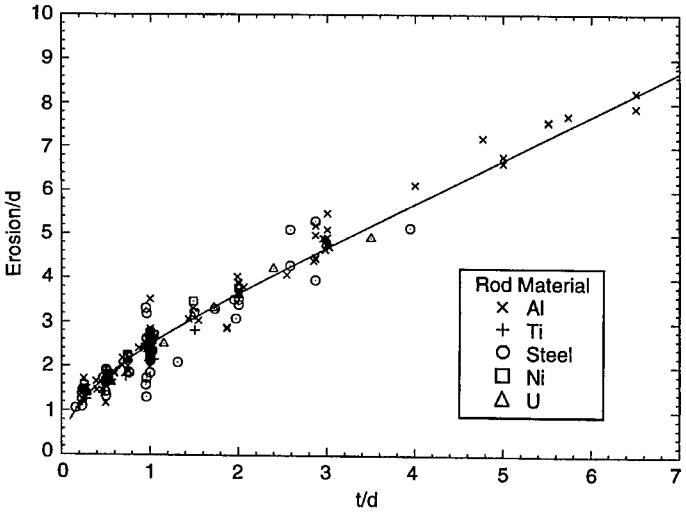

Fig. 9. Normalized NRL rod erosion data for Al, Ti, Fe, Ni, and U rods (1969 data: Baker data, scaled to Al → Al at v = 4.65 km/s).

Recent Experimental Data

Figure 11 also includes recent experimental data from a multi-plate experiment performed in 1996. In that experiment a tungsten-nickel-cobalt alloy rod of 0.42 cm diameter and 5.9 cm length traveling at 3.37 km/s impacted a stack of 0.635 cm (¼ in, t/d = 1.5) thick steel plates separated by approximately 5 cm. The angle of attack was less than 2 deg. Seven plates were perforated and a very modest amount of pitting occurred on the eighth plate. The rod was totally consumed. The Δ on the plot labeled UAH Data, (arbitrarily

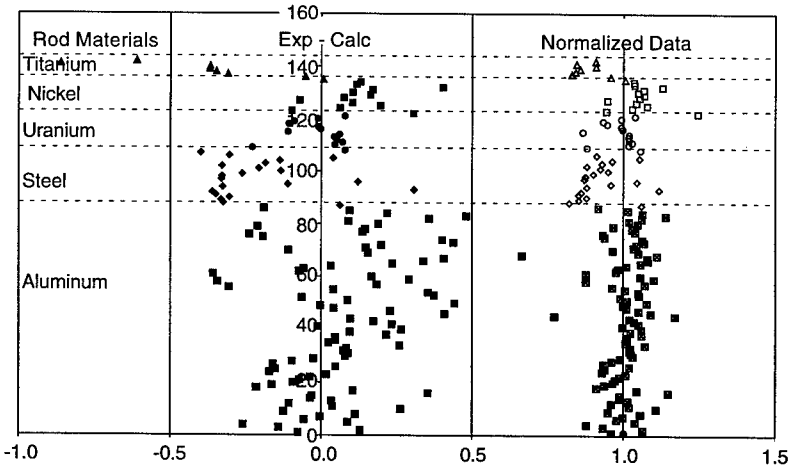

Fig. 10. Scaled NRL data, distributions versus rod material.

vertically positioned), is the experimental data normalized to its Baker equation prediction assuming that perforation of the seventh plate occurred by the rod remnant being above the ballistic limit for that plate. The erosion was calculated for each plate individually and then summed to obtain the final result as suggested in Baker 1987. The agreement with the 30 year old NRL results is striking. We have also examined by what factor the erosion would need to be enhanced or diminished in order to have a total of six or eight plates be penetrated. Those points are also shown in Fig. 11.

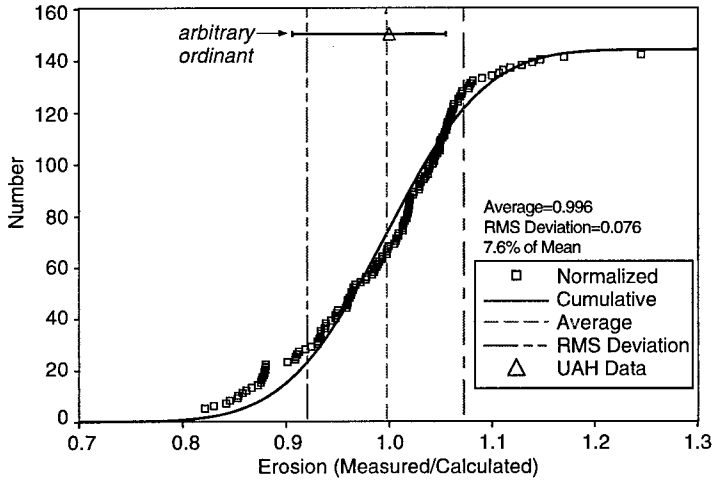

Fig. 11. Scaled NRL data, cumulative distribution.

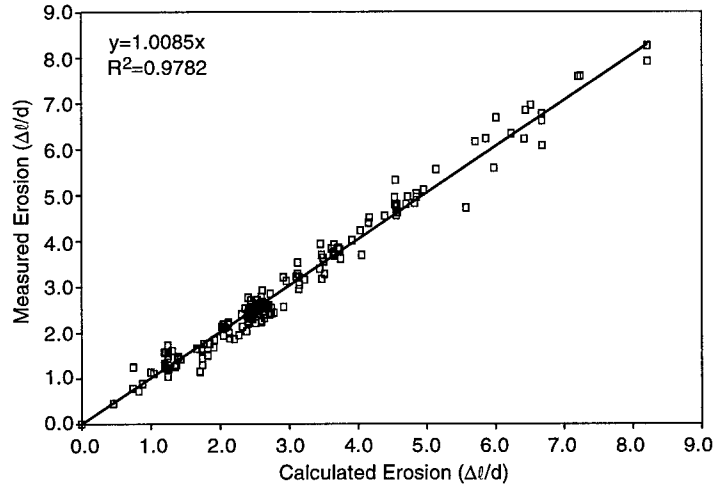

Fig. 12. NRL data, experiment-theory comparison.

Discussion

The preceding analysis has shown not only that the Baker equation is an excellent fit to all of the NRL experimental data but also that the data is distributed approximately normally about the mean with small standard deviation, 7.6% of the mean. Thus one more measurement within the bounds of the data set when normalized with its Baker equation prediction has a 68% chance of lying within the range 0.92 to 1.072. Figure 12 shows the comparison between the experimental and calculated erosion in a slightly different form. Here the calculated erosion is plotted versus the measured erosion for all of the NRL data considered here. The straight line in this plot is a least squares fit to the points shown assuming that the calculated erosion is the independent variable and that the line passes through the origin. This line might prove a convenient "bench mark" for new computations aimed at describing more complex impact conditions.

Acknowledgment—The data for the 5.9 cm tungsten alloy rod impact was provided by the Aerophysics Research Center, University of Alabama in Huntsville.

REFERENCES

1. J.J. Condon, "Rod Lethality Studies," NRL Report ALT-TR-65-18, Naval Research Laboratory, Washington, D.C., March 1965.
2. J. J. Condon and J.R. Baker, "Annual Technical Progress Report on Rod Lethality Studies," NRL Memorandum Report 18092, Naval Research Laboratory, Washington, D.C., September 1967.
3. J.R. Baker, "Rod Lethality Studies," NRL Report 6920, Naval Research Laboratory, Washington, D.C., July 1969.
4. J.R. Baker and A. Williams, "Hypervelocity penetration of plate targets by rod and rod-like projectiles," *Int. J. Impact Engr.* **Vol. 5**, pp.101-110, 1987.
5. Zukas J.A., HIGH VELOCITY IMPACT DYNAMICS, Chapter 5, John Wiley and Sons, Inc., New York, 1990.

PERGAMON International Journal of Impact Engineering 23 (1999) 651–662

INTERNATIONAL JOURNAL OF IMPACT ENGINEERING

www.elsevier.com/locate/ijimpeng

EXPANSION, RADIATION AND CONDENSATION OF VAPOR CLOUD, CREATED BY HIGH-VELOCITY IMPACT ONTO A TARGET IN VACUUM

I.V.NEMTCHINOV, V.V.SHUVALOV, N.A.ARTEMIEVA, I.B.KOSAREV, and I.A.TRUBETSKAYA

Russian Academy of Sciences, Institute for Dynamics of Geospheres, 38 Leninsky Prosp. (bldg.6), Moscow, 117979, Russia
e-mail: ivvan@idg.chph.ras.ru

Summary–The results of numerical simulations of small meteoroid impacts against the rocky lunar surface are presented which give an estimate of impact luminous efficiency. The obtained values of luminosity can considerably differ from the real ones because of the influence of regolith. Specific features of impacts into the regolith are discussed and a simple model discribing the shock wave structure in the porous target is proposed. © 1999 Elsevier Science Ltd. All rights reserved.

INTRODUCTION

One of the consequences of meteoroid impacts on airless cosmic bodies (asteroids, comets, Moon), apart from cratering and fragmentation of a target, is a formation of luminous vapor plumes. In case of asteroid-sized impactors these plumes may expand over the surface, forming an atmosphere, escape the planet, form a cosmic dust, etc. Light flashes and their observations are important for studies the small bodies impacts. Though the coefficient of the kinetic energy conversion into the radiation impulse is rather small (in comparison to the impacts onto planets having atmospheres), it may be sufficient for detection of such impacts. Radiation efficiency is determined by many factors: mechanical and chemical composition of the target and projectile, optical properties of the ejecta material, impact parameters (velocity, trajectory inclination, event scale, etc.).

An estimate of the light impulse created by a 1m-in-radius silica body impacting the lunar surface with the velocity of 50 km/s has been made by Melosh et al. [1]. In view of some impending experimental work [2] it appeared important to review and refine the estimates of luminous efficiencies and other characteristics of impact originated light flashes, e.g., shape, duration, spectra for various velocities, sizes, compositions, etc. Some results of numerical simulations of the impact of chondritic projectiles with radius 1-100 cm and velocity 20-50 km/s have been presented in [3]. Some experimental data, including spectra of radiation, have been given and discussed by Schultz [4] and Sugita and Schultz [5]. Aluminium, pyrex and nylon projectiles with the diameter of 7 mm and velocity up to 6.2 km/s impacted dry ice, dolomite, carbonate, calcite, silica sand and liquid water at different angles of impact in the vacuum chamber at air pressures of 6 Torr and larger.

0734-743X/99/$ - see front matter © 1999 Elsevier Science Ltd. All rights reserved.
PII: S0734-743X(99)00111-6

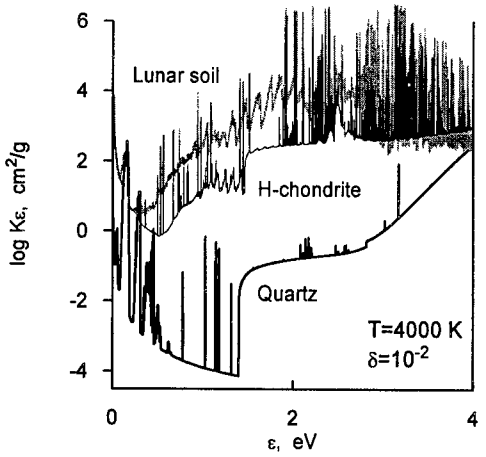

Fig.1. Mass absorption coefficients versus photon energy for H-chondrite (thin black line), pure quartz (thick black line) and a lunar soil (thick gray line).

We have tested various equations of state [6, 7] and opacity coefficients [8] for pure quartz, water, H-chondrite, cometary type vapor and lunar soil with initial chemical composition from [9]. To determine luminous efficiencies for impacts we have performed 2D and 3D numerical simulations of these impacts, using a multimaterial Eulerian SOVA code [10] similar in many respect to the CTH code [11]. Radiation fluxes and spectra at different moments of time were determined by direct solution of transfer equation for various photon energies along a great number of rays.

In reality the target is porous, e.g. the lunar surface is covered by a regolith. This causes specific features of the impact: the porous substance heated and compressed by shock wave may remain nonuniform, and the temperature and velocity of the vapor filling the pores may substantially differ from that of the unevaporated grains. A simple model describing this differences and the shock wave structure is proposed in this paper (section three). This model is compared with the results of laboratory experiments [12], demonstrating formation of high-velocity and high-temperature jets at the moment of shock arrival to the boundary of the target with vacuum.

NUMERICAL SIMULATIONS OF IMPACTS

Thermodynamical and Optical Properties in Use

Equation of state is critical for temperature determination, especially at the late stage of vapor release. We considered the impactor and target to consist of similar materials. We tried ANEOS for quartz [7], equation of state for granite [6] and tabular equation of state for H-chondrite vapor [8]. The most difficult is a consideration of condensation process. The theory of condensation has not been developed enough yet, and different assumptions give conflicting results. If equilibrium is established, the plume temperature remains constant for a long time due to release of evaporation energy. This leads to prolongation of radiative impulse. If there is no condensation at all, vapor temperature drops very fast due to adiabatic cooling. Our estimations of condensation have shown, that condensation degree at the moment of freezing does not exceed 0.3 for a wide range of impactor sizes (from 1 cm to 1 km) and impact velocity of 25 km/s, while the droplet radius increases linearly with increase of the impactor. In the range of projectile radii from 1 cm to 100 cm the luminous efficiency is approximately proportional to the square root of the size.

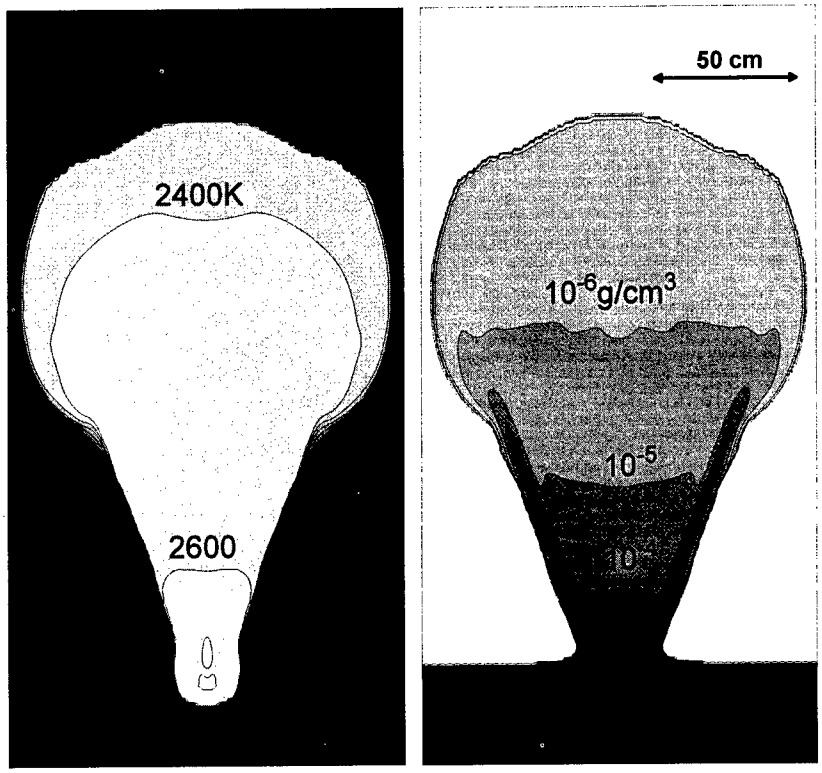

Fig.2. Temperature (left-hand image) and density (right-hand image) distributions at 250 s after 1 cm-in-radius body impact with the velocity of 20 km/s.

Opacities of the vapor are much more sensitive to chemical composition than thermodynamical properties. Even small impurities can significantly change the absorption coefficients. For this reason we have used calculated optical properties of H-chondrite [8], which is more representative for meteoroid composition than pure silica and lunar soil. Fig.1 demonstrates absorption coefficients for typical parameters of a vapor cloud : $T = 3000$ K and $\delta = 0.01$, where T is the temperature and δ is the relative density (with respect to normal density $1.09 \cdot 10^{-3}$ g/cm^3). The difference between pure SiO_2 and H-chondrite is clearly seen, for the visible range of the wavelengths this difference reaches 5–8 orders of magnitude.

Our theoretical data on thermodynamical and optical properties of H-chondrite vapor have been tested by comparison of radiation intensity and spectra with observations for the case of the Benešov bolide impact into the Earth's atmosphere [13, 14]. All the numerous lines detected in observations were presented in the predicted spectra. The intensities in different parts of the spectra in theory and observations correlate rather well.

Results of 2D and 3D Gasdynamic Simulations

To determine luminous efficiencies for impacts we have performed 2D and 3D numerical simulations, using a multimaterial Eulerian code [10]. Simple estimates and the results of numerical simulations show that radiated energy is much less than the thermal energy of the plume for the entire period of interest. So radiative cooling does not change the plume temperature, and the influence of radiation on gasdynamic flow need not be taken into account. Fig.2 demonstrates typical temperature and density distributions for a vertical impact. The plume has a conical shape with rarefied inner core and dense envelope formed due to ejection of partially evaporated matter. In the case of equilibrium condensation it

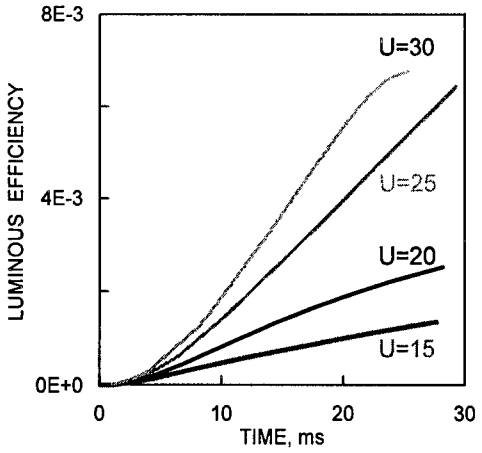

Fig.3. Luminous efficiencies versus time for the runs equilibrium condensation. The values of impact velocity are indicated near the curves. Projectile radius equals 1 cm.

is this envelope that radiates the main portion of energy. Fig.3 presents luminous efficiencies (the ratio of emitted energy to kinetic energy of a projectile) for different velocities in assumption of equilibrium condensation. Most of the energy is radiated at the late stage of the plume evolution, when vapor temperatures are almost constant due to energy release in the process of condensation. It follows from our simulations that a difference in luminous efficiency between runs with condensation and without reaches an order of magnitude. And this difference appears about 100 μs after the collision. As it was expected, luminous efficiency considerably increases with the increase of velocity.

Analysis of spectra obtained in the course of simulations shows that in the case of equilibrium condensation only 10-20% of radiation is emitted in the visible. So, for better detection IR sensors should be used. Luminous efficiency depends on the impactor size as well. An increase of projectile radius from 1 to 10 cm leads to increase in luminous efficiency by a factor of 1.5-3.0.

For an oblique impact (which is more probable) density and temperature under shock loading are defined by the vertical component of the impact velocity (and are smaller than those in the case of vertical impact). Fig.4 demonstrates the density and temperature distributions for an oblique impact with an angle of 30° to the horizon and a velocity of 25 km/s. For small angles the projectile does not penetrate deep into the target, it slides over the surface, forming a high-velocity jet. Some part of this jet may be decelerated by different natural obstacles (crater rims, boulders, walls of the ramparts, etc.). This effect may substantially increase luminous efficiency. Shock waves created due to reflection of the jet are close to critical ones [15] at angles exceeding 30^0. This results in very high radiation energy over a wide range of wavelengths (up to 10% of the impactor energy). Most part of the radiation is emitted in the UV region. So, the problem of impact induced radiation is closely related with the target surface profile.

IMPACT ONTO A REGOLITH LAYER

Numerical simulations demonstrating the formation of the jet have been conducted for a rocky surface, and thus in reality are applicable only for meter-sized or larger bodies or for impacts into the specific localities of lunar surface where thickness of regolith layer is small. Influence of the regolith may be manifested by two factors: first, the density of regolith is lower than the density of rocks; second, the regolith is a porous substance. Let us consider these two factors thoroughly.

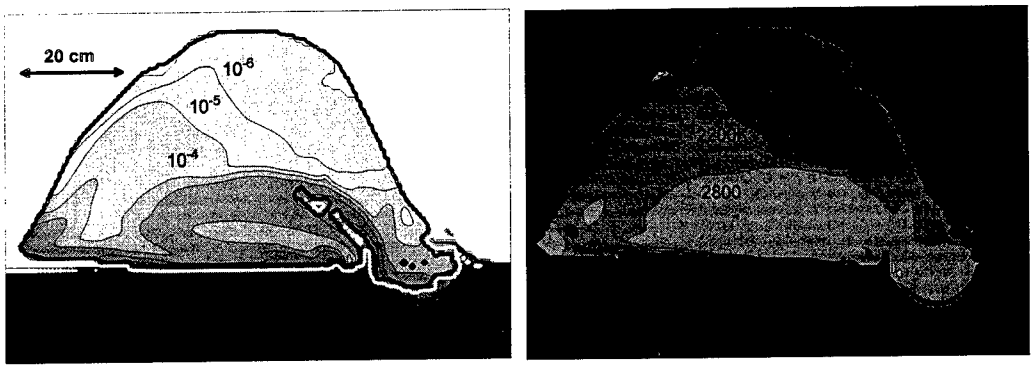

Fig.4. Density (left-hand image) and temperature (right-hand image) distributions at 10μs after oblique (30° to horizon) 1cm-in-body impact with the velocity of 25 km/s.

Impact on a Low Density Layer

One can easily understand an influence of the first factor – target density. If a projectile is hitting the very high density layer it does not penetrate below the surface but is totally (or partially) evaporated due to the action of the shock wave originated in the point of contact. The degree of evaporation and vapor temperature depend on the value of vertical velocity component. The smaller is the angle of incidence (to horizon), the less is the vapor temperature and vapor fraction. For a typical velocity of 15 km/s and angle of about 30° (i.e. for a vertical velocity component of 7.5 km/s) the projectile becomes partially evaporated. Formation of a high velocity jet moving along the surface of a target and substantial increase of the vapor mass due to ablation and erosion for the oblique impacts have been demonstrated in laboratory experiments [4, 5].

For very low density of the lunar soil the projectile may not be even not evaporated and remain in a liquid or solid state. It will easily penetrate the ground similar to the process of a meteoroid atmospheric entry. A quasistationary shock wave will be formed at the blunt nose of the projectile. The pressure behind this shock wave is very high and the lateral gradient of pressure will be established – maximum at the center and falling down to the sides. Under the action of aerodynamic loading the projectile substance becomes fragmented and dispersed.

For a typical density of the upper regolith layer of about 1.4 g/cm^3 and a typical velocity of 15 km/s the maximum pressure is 3 Mbar and that is larger than the bulk modulus of the meteoroid substance. On the other hand, the low density substance of the target will become heated to a rather high temperature. This substance will flow back through the expanding hole in the target, and the pressure will decrease. The substance will evaporate, as it crosses the phase boundary below the critical point. The plume, expanded and ejected along the trajectory in the backward direction, will emit some radiation. The projectile decelerates in a time proportional to $L\rho_b/\rho_a V$, where L is the diameter of the projectile, V is its velocity, ρ_b is its density and ρ_a is the target density. This is also the characteristic time of jet expansion.

One should keep in mind an additional factor, i.e. the instabilities at the projectile-target interface and turbulent mixing of those substances. The additional loss of mass due to this process is an analogue of ablation or liquid layer entrainment from the meteoroid surface due to aerodynamic loading. Such effect has been demonstrated in modelling experiments [4, 5].

The density of the regolith gradually increases with depth. Assuming it increases to the normal density of rocks at a sharp boundary one can find that large meteoroids will penetrate the layer to this boundary and the further process will somehow resemble an underground

explosion with a channel along the trajectory. The difference is due to the horizontal velocity component leading to motion of debris along the contact boundary of the regolith with rock. The projectile will not only be buried below the regolith layer but will dig a hole in a horizontal direction. The regolith may be thrown away by the underground explosion and hot plasma or vapor mixed with droplets will appear from beneath and leak through the fragments of regolith. This complicated process has not been theoretically studied in detail.

Nonequilibrium Effects in the Porous Regolith

Compression of porous media by the shock waves is a complicated process. In the assumption of the thermodynamic and mechanic equilibrium it has been described by Zel'dovitch and Raizer [15], but the question arises if this assumption is valid. It is clear that the answer to this question depends on the size of the grains. The conditions of thermal and mechanical equilibrium may become violated, especially for small projectiles with sizes comparable to that of the grains and the pores. The high-velocity and high temperature jets may be formed due to leakage of the hot vapor through the pores, while grains may remain cold and unevaporated. Experimental results obtained by Russian scientists are described below. A simple theoretical quasi-2D model for description of such processes is suggested.

Shock Waves in Porous Matter – Experiments. Experiments [12] have been conducted to model rapid deformation of porous media. Compression of aluminum, magnesium and graphite powder with grain sizes of 0.2 mm and porosity $m = 2$ have shown that for the time interval of 0.1 μs the sample surface in the vacuum chamber is very bright. Brightness temperature as large as 10^4 K has been measured for aluminum and $5 \cdot 10^3$ K for graphite. The thermodynamically equilibrium temperature at $p = 50$ kbar is only 1500 K. This means that the shock loaded porous substance remains in nonequilibrium condition for some time. Estimates show that for the grains with characteristic scale r of about $2 \cdot 10^{-2}$ cm (200 μm) the characteristic hydrodynamic time r/V is 0.1 μs (for the velocity $V = 2$ km/s behind the shock wave), while the thermal conductivity time is about 400 μs. Thus the characteristic size of the grains should be much less than about 1 μm to obtain thermal equilibrium in the surface layers of the sample.

In the experiments [12] samples of magnesium powder with the initial density of 1 g/cm^3 and grain sizes of 1–5 μm were loaded by the shock waves with pressure in the range of 65 to 186 kbar. The velocity behind the shock wave changed from 1.5 km/s to 3.0 km/s and the density from 1.63 to 2.17 g/cm^3 correspondingly. The vapor streams appeared from the free surface of the sample with substantially higher velocities – from 9.5 to 14.4 km/s. If the radius of the grains is increased to 100 μm the velocity of the stream also increases: from 15.1 to 17.7 km/sec for the same pressure range. Brightness temperature at the moment of shock wave reaching the free surface is 6700–8000 K. These values are substantially higher than estimates of the average temperature obtained using Hugoniot adiabat and some simplified magnesium EOS, i.e. 1000–3000 K.

Very interesting data were obtained for the velocity of about 7.6 km/s, created by detonation of the high explosive surrounding the glass tube filled with the magnium powder with the initial density of 1 g/cm^3 (porosity 0.7) and with the diameter of spherical particles of about 500 μm. After the shock wave reached the boundary of the porous sample with vacuum (more precisely air pressure was 10^{-5} torr), the brightness temperature was about $1.7 \cdot 10^4$ K. Products (vapor and unvaporized material) continued to move along the empty tube for another 11 cm. Brightness temperature substantially decreased after about 0.6 μs. The velocity of the vapor reached 29 km/s. After the stream hit the glass obstacle (in about 3 μs), the brightness temperature reached very high values, of about 29,000 K. At minimum intensity the temperature was rather low, and cannot be measured as it was below the sensitivity limit (of about 2000 K). Assuming radiation emitted before the reflection of

the jet, in the stage of the free flight of the vapor stream, as a blackbody source with the temperature of 1.5 eV we obtain the radiation flux 0.5 MW/cm^2, and for the duration of 0.5 μs the radiated energy is about 0.25 J/cm^2, while the energy of the sample is about 250 kJ/cm^2. Thus the luminous efficiency is about 10^{-6}. If we decrease the thickness of the porous target (or the length of the tube) to about 1 cm we'll obtain the same duration and energy of the radiation pulse, while due to decrease in the target energy the luminous efficiency will increase to about 10^{-5}.

Thus, experiments demonstrate a high degree of thermodynamic and mechanical nonequilibrium in the outer layers, adjacent to the free surface: the higher the velocity of the shock wave, the larger the temperature of the vapor and the velocity of the jet. In the last example this velocity exceeds the velocity of the shock wave by about 4 times. But the mass of this extremely nonequilibrium layer is very small, on the order of the mass of the grain sized layer. In the deep layers the excess temperature decreases in time due to thermal conductivity. The total duration of the compressed substance being at high pressures is about r/V, where r is the projectile radius, e.g. for $r = 3$ mm it is about 1 μsec. It is still small in comparison to the time necessary for thermal conductivity to equalize temperature in the grain. The vaporized substance will escape between the unevaporized grains. The small amount of hot vapor will give the main input into the radiation.

It was assumed in [12] that heating of the outer layer is due to plastic deformation of the boundary of the grains and friction. The amount of heat released is proportional to the shear strength of the grains. Temperature achieved in this process is limited due to heat conduction. The amount of energy released at the contact areas of the grains in the unit time is estimated as GV, where G is the shear strength, V is the velocity of the particle behind the shock wave. It is assumed that energy is dissipated in the layer with the thickness $\delta = \sqrt{a^2 t}$, where a is the thermal conductivity, and t is the time of contact. If we define the characteristic time t as the time interval necessary to move one grain along the surface of another to the distance Δ, where Δ is the grain size ($t = \Delta/V$), one obtains:

$$\delta_T = \sqrt{a^2 \Delta / V} \tag{1}$$

and the specific energy is

$$e = \frac{G\sqrt{\Delta V}}{\rho_0 a} \tag{2}$$

According to this relation, the larger is the size of the grains Δ and the velocity V, the larger is the specific energy and temperature. This agrees with the experimental data.

Shock Waves in Porous Matter – Physical Model. We assume that some way a portion of the solid material has been transformed into vapor at the initial stage of shock wave propagation, e.g. at the distances on the order of about ten grain sizes (10^{-1} cm for 100 μm grains). At the distances of 100-1,000 grain sizes (1 cm to 10 cm), the exact amount of the initial vapor and its temperature are not very important factors. A new, quasistationary regime of shock wave propagation is established. It is represented schematically in Fig.5. The grains move with velocity equal to the velocity of the piston (projectile) generating the shock wave. Some amount of vapor leaking through the gaps between grains and reflected at the next row of grains is forming the gas puff, through which the shock wave moves and heats the gas. Temperature is easily determined by using the Hugoniot relations and gaseous EOS, as vapor is formed in the previous stages of shock wave propagation. Vapor temperature is about 0.5 eV for a 5 km/s-velocity piston, and 1 eV for 7 km/s. The temperature rapidly increases with the velocity of the shock wave and reaches 3–5 eV for the velocity of about 20 km/s (temperature slightly depends on the vapor density as the degree of dissociation and ionization and the specific energy weakly change with the density). Let us assume for simplicity that the structure of the porous target is a periodic structure of loosely packed

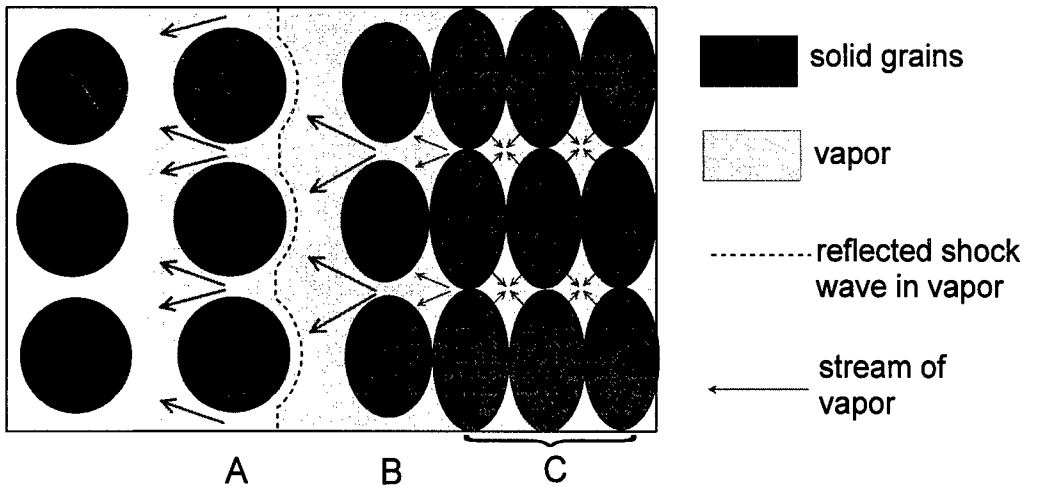

Fig. 5. Propogation of the shock wave in porous matter. **A)** Motionless "fence" of grains. **B)** Row of grains begining to move. **C)** Rows of grains behind the shock wave in solid matrix.

grains and we can speak about parallel rows of the grains perpendicular to the direction of shock wave propagation. There are gaps between the grains in each row through which the vapor may leak into the gap between the first moving row and the next row in front of the shock wave. We shall distinguish one row, which acts like a piston on the vapor appearing in front of it, and the next one which acts like a "fence" for the vapor, causing reflection of the shock wave in the gas and compression of the gas. The grains constitute a solid matrix. If the pressure is rather low, i.e. much less than the bulk modulus of the compression of the material with the periodic structure under consideration, we may assume that the solid grains are incompressible, and their density remains constant. That does not mean that the porous substance is incompressible as a whole. Volume of the pores may substantially decrease, leading to increase of the average density.

Pores between grains constitute volume into which vaporized material from the grains may escape, raising the pressure and density inside the pores. Motion of the grains is caused by elastic forces in the grains. As the grains are loosely packed the contact area is small in comparison to the cross-sectional area of the grains, and the modulus of compression is much less than the modulus of the solid (or liquid) subsystem, hence the shock wave is rather strong even at the velocity of 3–5 km/s. The subsystems of vapor and of the solid (or liquid) grains weakly interact through vapor compression by the shock wave and vaporization of the grains. The shock wave being reflected from the next, still motionless row (the "fence") moves back and reaches the moving row of grains, forming a piston, and reflects once more and so on. Multiple reflections increase the pressure (and temperature), but the maximum values of pressure and temperature are limited, as the fence row begins to move under the action of the increasing pressure and the velocity of this row of grains eventually reaches the steady velocity.

In the quasistationary regime of the shock wave propagation through the porous target the amount of vapor flowing through the gaps between grains from one row to another is constant in time and is equal to amount of vapor formed on the side surface of the grains due to heat transfer from the hot vapor to the cold grains, solid or liquid. The heat transfer is realized by electron or radiation thermal conductivity.

The estimate of the radiation flux q_r is

$$q_r = \frac{16}{3}\frac{l_R}{\Delta}\sigma T^4 \tag{3}$$

where T is the temperature, l_R is the Rosseland mean free path, σ is the Stefan-Boltzmann constant, Δ is the characteristic size of the pores. We shall assume for simplicity that evaporation is going intensively only between the first row of grains (immobile) which serves as a trap for the vapor, and the second one, which serves as a piston compressing the vapor.

Mass losses from the side walls of the grains due to evaporation are:

$$\dot{m} = q_r/H, \qquad H = Q + h(T_\nu) \tag{4}$$

where Q is the vaporization energy, $h(T_\nu)$ is the vapor enthalpy and H is the effective enthalpy. The temperature of the vapor T_ν is no less than the vaporization temperature, but it may be even higher due to the screening effect, i.e. absorption of the infalling radiation in the newly formed vapor.

Combining equation (3) and (4) we obtain

$$\dot{m} = \frac{16}{3}\frac{\sigma T^4}{\Delta H} l_R \tag{5}$$

On the other hand, due to assumption of quasistationarity, mass losses equal:

$$\dot{m} = \eta \rho u, u = \sqrt{e(\gamma - 1)} \tag{6}$$

where u is the velocity of vapor through the gaps between grains, γ is adiabatic exponent, ρ is the density of vapor in the pores and η is the ratio of the gaps cross-section to the total area:

$$\eta = \frac{r_0^2}{\Delta^2} \tag{7}$$

where r_0 is the characteristic size of the gaps. We have assumed that the velocity of the gas injected through the gap in front of the shock wave is of the order of the speed of sound. Combining (6) and (7) we obtain

$$\frac{16}{3}\frac{\sigma T^4 l_R}{\Delta H} = \eta \rho \sqrt{e(\gamma - 1)} \tag{8}$$

In the temperature range of 1–3 eV the Rosseland mean free path in the various substances usually weakly depends on the temperature, but rather strongly depends on the density, e.g. in the aluminum vapor $l_R = 5 \cdot 10^{-3}$ cm for $\rho = 3 \cdot 10^{-3}$ g/cm^3. Increase of the vapor density in the pores decreases the coefficient of heat transfer and mass rate evaporation.

The following set of self-consistent parameters is: $T = 2$ eV, $\sigma T^4 = 1600$ kW/cm^2, $l_R = 5 \cdot 10^{-3}$ cm, $\rho = 3 \cdot 10^{-3}$ g/cm^3, $Q = 10$ kJ/g, $e = 50$ kJ/g, $H = 60$ kJ/g, $\gamma = 1.2$, $\eta = 10^{-1}$. From the relation (8) one obtains $\dot{m} = 60$ g/cm^2 s. The velocity of vapor leaking through gaps between grains equals to the sound speed $u = \sqrt{e(\gamma - 1)} = 2.2$ km/s and $\rho = \dot{m}/u = 3 \cdot 10^{-3}$ g/cm^3. The velocity V of the shock wave heating the vapor to the specific energy e is $V = \sqrt{2e} = 10$ km/s. Thus a very high temperature (about 2 eV) is reached in the vapor while simple estimates show that in the uniform solid temperature would be only about 0.2 eV. Calculating pressure from the usual gaseous EOS we obtain $p = 300$ bar.

As the vapor density is low, pressure is much lower than the dynamic pressure in the shock wave, i.e. $p = \rho_0 V^2 = 300$ kbar. The existence of the gas in the pores can not influence a propagation of the shock wave and can not stop compression of the pores. If the pressure in the solid matrix is about 200–300 kbars, compression of solid is very small and we assume solid matrix is incompressible. As to the compression of the gas in the pores it is first of all determined by the shock wave, i.e. the vapor density is increased in about 6–10 times. Later the density additionally increases due to multiple shock waves reflections (quasiadiabatic

compression) and due to additional injection of vapor into the pores. Gas pressure in the gas also increases until it becomes comparable to the pressure in the solid or liquid. Initially the mass of vapor is very small in comparison to the total mass of the porous sample, as the vapor density is by two or three orders of magnitude lower than the solid density. The characteristic time t_Δ of the shock wave propagation through a single pore volume is Δ/V, where Δ is the characteristic size. For $\Delta = 10^{-2}$ cm, $V = 10$ km/s we have $t_\Delta = 10^{-8}$ s. The amount of vaporized material is very low, i.e. $6 \cdot 10^{-7}$ g/cm^2, while the specific mass of the grain $\rho_0\Delta$ is $3 \cdot 10^{-2}$ g/cm^2. Thus, the grains will not be immediately evaporated.

Let us establish the scaling laws. In the temperature range 1–3 eV the Rosseland mean free path may be described by a power law:

$$l_R = AT^a\rho^{-b} \tag{9}$$

Also using the power approximation for the specific energy of unit mass $e = ET^\alpha$ we finally obtain

$$\rho^{1+b} = \frac{A\sigma T^{4+a-\alpha/2}}{\Delta Q\sqrt{E}}$$

Typical values of constants are $a = 0$, $b = 2$ and $\alpha = 3/2$. Thus

$$\rho^3 = \frac{A\sigma}{\sqrt{E}}\frac{T^{5/2}}{Q\Delta}$$

or

$$\rho = \frac{A^{1/3}\sigma^{1/3}}{E^{1/6}}\frac{T^{5/6}}{Q^{1/3}\Delta^{1/3}} \tag{10}$$

In the strong shock wave $e \sim V^2/2$, thus $T \sim V^{4/3}$. The density $\rho \sim V^{20/18}$ is almost linearly proportional to the velocity, strongly depends on the temperature and is inversely proportional to the cube root of the pore sizes. One may assume that density and pressure do not change further on, as all the rows move with the same velocity (the velocity at the shock wave front) until the moment when the shock wave reaches the boundary with vacuum. But the vaporization goes on not only in the gap between the first and second rows. The Rosseland mean free path strongly depends on the density, and increase of density decelerates the vaporization process. Nevertheless, vaporization continues for a long time, much longer than t_Δ.

Due to compression, temperature in the pores increases which partially compensates for the increase in the density. Using (4) and (9), assuming adiabatic law $T \sim \rho^{(\gamma-1)/a}$ and assuming $\Delta \sim 1/\rho$ the ablation mass rate may be determined as:

$$\dot{m} = \frac{16}{3}\frac{\sigma T^4 l_R}{\Delta H} \sim \frac{\rho^{\frac{4(\gamma-1)}{a}+1-b}}{\rho\Delta H}$$

For $\gamma = 1.2$, $a = 3/2$, $b = 2$ we obtain $\dot{m} \sim \rho^{-0.47}$. So the increase of the density due to compression of 10 times decreases ablation mass rate by about 50 times. Pressure p is proportional to ρ^γ, and increase of the density of 100 times increases the pressure by 150 times, up to 50 kbar. On the other hand, the total duration of the ablation is three orders of magnitude longer than the characteristic time of the shock wave crossing the pore t_Δ, e.g. for the target thickness $L = 10$ cm it is about 10 μs. For the ablation rate $\dot{m} = 6$ g/cm^2/s and $t = 10^{-5}$ s, this gives the total vaporized mass $m_v = 0.6 \cdot 10^{-4}$ g/cm^2, still much less than the total mass of the grains. So, the temperature and density distribution remains substantially nonuniform.

When the shock wave reaches the boundary with vacuum vapor trapped in the first row rapidly expands between the gaps. Vapor from the deep layers goes out much more slowly,

but we should keep in mind that the process of expansion is not one-dimensional. We assume the process of vapor expansion to be an adiabatic one. During the compression of the vapor in the pores temperature increases, but then falls down to the shock temperature, i.e. about 1–2 eV. Main luminosity is reached much later, when the gas substantially expands and the Rosseland mean free path increases to the value of the projectile size. In this stage the expansion is two or even three-dimensional.

The grains are flying inertially, as the mass and energy of the vapor are rather small, and expanding vapor can not substantially accelerate the grains. Increased area of the gaps facilitate the escape of the vapor. The phenomenon resembles the flight of the fragments of the fragmentation bomb, while vapor serves as the products of high explosive leaking between fragments.

The escape of radiation is most efficient when the Rosseland mean free path reaches the size of the target, i.e. in the example under consideration $l_R = 2$ cm for $\rho = 3 \cdot 10^{-5}$ g/cm^3. During adiabatic process the specific energy falls down in about 2.5–3 times (to about 1 eV), density – in 100 times and the size increases in about 5 times, e.g. from 0.4 cm to 2 cm. Duration of this process is about 2 μs. Energy emitted during this time interval is 0.2 J/cm^2, while the mass of the target is 1 g/cm^2 and the total energy of the target is 50 kJ/cm^2. Thus the luminous efficiency in the first peak is very low, only about $2 \cdot 10^{-6}$. But the energy continues to be emitted, especially when the temperature falls down to about 0.2 eV and condensation begins.

The total initial amount of vapor is estimated as $0.6 \cdot 10^{-4}$ g/cm^2, the total energy of the vapor is 3 J/cm^2, while the total energy of the target is 50 kJ/cm^2. That gives maximum luminous efficiency of about $6 \cdot 10^{-5}$ (due to the onset of condensation). The larger is the size of the grains, the higher is the degree of nonuniformity.

This model is not valid for the case of very high velocities and small sizes of the grains where the grains become totally vaporized and the radiation heat transfer helps to establish rather uniform temperature and density distribution within the target.

DISCUSSION AND CONCLUSIONS

The results of numerical simulations without taking porosity into account show that a lower limit of luminous efficiencies is $10^{-6} - 10^{-5}$ (depending on impactor velocity). The results depend on equation of state in use and especially on equilibrium or nonequilibrium of condensation process. The lower limit is determined by radiation of hot noncondensed material. The energy emitted during this stage is small because of fast adiabatic cooling. The assumption of equilibrium condensation gives an upper limit of luminous efficiency (up to 10^{-3}). Although in many cases the real value may be considerably greater due to the specific geometry of the target. The value of luminous efficiency of about $10^{-5} - 10^{-4}$ is believed to be rather feasible and may be used to forecast a lunar impacts detection probability.

Porosity of the target (lunar soil) can considerably change the value of luminous efficiency, especially in the case of small (1–10 cm in radius) impactors. This problem should be theoretically investigated further. As a first step of such investigations a new physical model has been proposed to describe the nonequilibrium compression of a porous substance. The model explains a high degree of nonuniformity in the porous target, the existence of hot spots and high-temperature, high-velocity mini-jets emerging through the gaps between grains. Simple estimates of the characteristic values of temperature and density of the vapor in the pores should be checked by numerical hydrodynamic simulations. The relevant code is now being developed.

We are looking forward to continue these theoretical investigations on basis of actual impact observations and laboratory experiments.

Acknowledgments. We are very grateful to prof. Peter Franken and prof. Igor Sobelman for valuable remarks and discussions. The work is partially supported by the USA Department of Defense.

REFERENCES

1. H.J.Melosh , N.A.Artemjeva, A.P.Golub', I.V.Nemtchinov, V.V.Shuvalov, and I.A.Trubetskaya, Detection of the Thermal Radiation Pulse Caused by Impact of Small Meteorites on Moon's Surface. *LPSC XXIV, Houston*, 975-976(1993).
2. D.Crowe, P.Franken, T.Hunter and J.McGaha, Optical Detection of Asteroidal Impacts on the Moon. *XXVI Microsimposium on Comparative Planetology, Moscow*, 28(1997).
3. I.V.Nemtchinov , V.V.Shuvalov , N.A.Artemieva , B.A.Ivanov, I.B.Kosarev, and I.A.Trubetskaya, Light flashes caused by meteoroid impacts on the lunar surface. *Solar System research.* **32**(2), 116–132(1997).
4. P.H.Schultz, Effect of impact angle on vaporization. *JGR* **101**(E9), 21,117–21,136 (1996).
5. S.Sugita, P.H.Schultz, Spectroscopic observation of atmospheric interaction of impact vapor clouds. *LPSC XXIX* (1998).
6. B.V.Zamyshliaev and L.S.Yevterev, *Models of dynamic deforming and failure for Ground Media.* Nauka, Moscow(1990).
7. S.L.Thompson and H.S.Lauson, Improvements in the Chart D radiation hydrodynamic CODE III: Revised analytical equations of state. *Sandia National Laboratories Report SC-RR-71 07-14*,(1972).
8. I.B.Kosarev, T.V.Loseva and I.V.Nemtchinov, Optical properties of vapor and ablation of large chondritic and icy bodies in the Earth's atmosphere. *Solar System Research*, **30**(4), 265-278(1996).
9. J.J.Papike and D.T.Vaniman, Mare Crisium. *The view from Luna 24.* (edited by R.R.Merrill and J.J.Papike). Lunar and Planet. Inst., Houston, Tex., 281-289(1978).
10. V.V.Shuvalov, 3D hydrodynamic code SOVA for interfacial flows, application to thermal layer effect. *Shock Waves.* (1998), submitted.
11. J.M.McGlaun , S.L.Thompson and M.G.Elrick, CTH: a three-dimensional shock wave physics code. *Int.J.Impact.Engng.*, **10**, 351-360(1990).
12. G.V.Belyakov, V.N.Rodionov and Samosadny, On the heating of the porous substance by the shock wave compression. *Fizika gorenia i vzryva (Physics of combustion and explosion).* **13**(4), 614-619 (1977) (in Russian).
13. J.Borovička, O.P.Popova, I.V.Nemtchinov, P.Spurny, and Z.Ceplecha, Bolides produced by impacts of large meteoroids into the Earth's atmosphere: comparison of theory and observations. I. Benešov bolide dynamics and fragmentation. *Astr.Astrophys.*. **334**, 713–728 (1998).
14. J.Borovička, O.P.Popova, A.P.Golub, I.B.Kosarev, and I.V.Nemtchinov, Bolides produced by impacts of large meteoroids into the Earth's atmosphere: comparison of theory with observations. II. Benešov bolide spectra. *Astr.Astrophys.*. **337**, 591–602 (1998).
15. Zel'dovitch, Ya.B. and Yu.P.Raizer *Physics of Shock Waves and High-temperature Hydrodynamic Phenomena.* Academic press, New York (1967).

PERGAMON

International Journal of Impact Engineering 23 (1999) 663–674

INTERNATIONAL JOURNAL OF IMPACT ENGINEERING

www.elsevier.com/locate/ijimpeng

ERODED LENGTH MODEL FOR YAWED PENETRATORS IMPACTING FINITE THICKNESS TARGETS AT NORMAL AND OBLIQUE INCIDENCE

MICHAEL J. NORMANDIA

The Institute for Advanced Technology, The University of Texas at Austin, 4030-2 W. Braker Lane, Austin, TX 78759

Summary—A simple expression is derived to estimate the residual length of a yawed, long-rod penetrator impacting finite thickness targets at both normal and oblique incidence. The unique feature of this model is a determination of the different penetration path through the plate which is not simply a line-of-sight thickness. The presence of yaw results in a penetration path which is determined by the magnitude and direction of the penetration velocity vector which is dependent upon the penetrator velocity component along that path. Hence, the material thickness penetrated through the finite target is an explicit, and variable, function of the impact geometry, (obliquity and yaw), impact velocity, and relative penetrator and target properties (densities and strengths). The eroded penetrator length is also dependent on both the penetration path angle and on the velocity component along that path and thus becomes an explicit function of these variables. Two simple expressions are derived to determine the eroded penetrator length and implications for deep target penetration degradation due to yaw are discussed. © 1999 Elsevier Science Ltd. All rights reserved.

INTRODUCTION

The literature contains numerous approximations for the penetration (or interface) path of a yawed penetrator which shows that it is inclined in somewhat of a mirror image of the penetrator at impact, distorted in both length (depth) and diameter, as seen in Fig. 1 extracted from Bjerke, et al. [1]. An approximate empirical relation between the interface path and the yaw angle was also reported in [1] and derived by Silsby, et al. [2]:

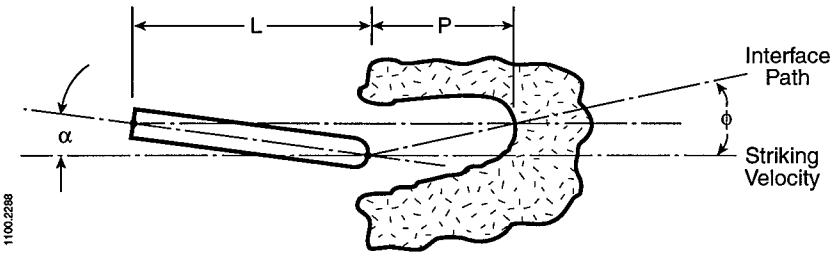

Fig. 1. Suggested empirical relationship between penetration (interface) path angle and impact yaw angle, from Bjerke [1] and Silsby [2].

$$\phi = \sin^{-1}[\alpha(\pi/180)/(P/L)] \tag{1}$$

A general relationship is derived between the interface path angle and incident yaw angle for oblique impacts. The empirical relation, Eqn. (1) is the first term in a small yaw angle expansion.

The influence of the target properties on the penetration path manifests itself in determination of the penetration velocity, and hence the penetrator erosion rate. Normandia, et al. [3] and Satapathy [4] have shown that this erosion rate changes when the elastic zone reaches a finite boundary

0734-743X/99/$ - see front matter © 1999 Elsevier Science Ltd. All rights reserved.
PII: S0734-743X(99)00112-8

and hence is a function of the distance that the penetrator is from a finite rear surface. The introduction of target obliquity complicates the situation even further. Assuming that the penetration rate is known, however, yields a surprisingly simple analytic expression for the residual penetrator length—of value in systems level codes which require rapid estimation of eroded lengths. Hypervelocity experiments have also been conducted [5] using long rods impacting finite thickness oblique plates at impact velocities between 2.2 and 2.9 km/s with significant yaw (5 to 10 degrees). Traditional analyses of this data was unable to capture the trends in eroded length, but the simple expression derived here agreed remarkably well with all of the data.

The derived relation between the penetration path and the yaw angle is implicit and hence is the expression for eroded length. Some additional, but not necessary, simplifying approximations are used to develop a simple explicit relation between eroded length and yaw angle. This simplified relation can be depicted geometrically. This approach also provides significant insight into deep target penetration. If the penetration path is regarded as constant, an upper bound for penetration into very thick targets is estimated. In deep target penetration, the penetration path eventually changes for impacts above the critical yaw value due to tail swiping of the crater wall, subsequent breaking and/or gouging of the crater walls [1]. A more comprehensive, time-based model that accounts for these complexities is required [6, 7]. Until this tail swiping occurs, the relations derived here follow closely the empirical yaw degradation relations which appear in [1].

The penetrator diameter to target thickness ratio also affects the eroded lengths and an approximation to account for these effects has been included in this model but details are omitted until it is validated. Also presented at this conference by Bless, Satapathy, and Normandia [8] is a more comprehensive time-based model SLOTPEN which includes the effects of diameter embedding and slot cutting to describe the resulting penetrator shape. In that model, the simplified (approximate) treatment for penetrator erosion presented here is used.

PENETRATION PATH

Consider the yawed impact of a long-rod penetrator of length L impacting a target at obliquity θ_s to the target normal at velocity v_s with a yaw angle α in the plane of the target as shown in Fig. 2. A more general representation of this impact with compound obliquity and compound yaw angles has been derived but is not included here. The target thickness is assumed to be finite so that the penetration path, along z with penetration velocity u, can be assumed to remain linear, that is the local yaw angle remains constant and that tail swiping has not affected the erosion rate.

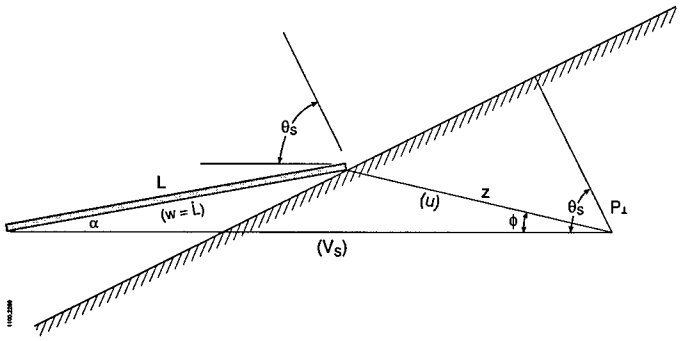

Fig. 2. Impact geometry of yawed penetrator striking oblique target at velocity v_s. For finite thickness plates, $P_\perp$ represents the thickness of the plate (T) and L represents the eroded length (ΔL).

The geometry of the impact situation pictured in Fig. 2 suggests that the final penetration depth normal to the oblique target surface is given by $P_\perp$:

$$P_{\perp} = z \cos(\theta_s - \phi) \tag{2}$$

where the angle ϕ is defined by the angle between the penetration path z and the original velocity vector v_s. The unknown penetration path z is related to the unknown penetration angle ϕ by:

$$\frac{z}{\sin\alpha} = \frac{L}{\sin\phi}, \tag{3}$$

using the Law of Sines. Eliminating z in Eq. (2) results in an expression for $P_{\perp}$ in terms of ϕ:

$$P_{\perp} = \frac{L\sin\alpha\cos(\theta_s - \phi)}{\sin\phi} = L\cos\theta_s\sin\alpha(\tan\theta_s + \cot\phi). \tag{4}$$

As expected, the penetrator length projected on the velocity vector, $L\cos(\theta_s)$ is the dominant term, modified by yaw, obliquity, and path angle. Eqn. (4) is only valid for finite thickness targets, where $P_{\perp}$ is replaced by the target thickness, T, and L is replaced by the eroded length, ΔL, to obtain

$$\Delta L = \frac{T\sin\phi}{\sin\alpha\cos(\theta_s - \phi)} = \frac{T\sec\theta_s}{\sin\alpha(\cot\phi + \tan\theta_s)} \tag{5}$$

illustrating the deviation from the line-of-sight thickness $T\sec\theta_s$ due to impact yaw which is compounded further by target obliquity. For normal plate impacts ($\theta_s = 0$) Eqn. (4) reduces to

$$P_{\perp}(\alpha;\theta_s{=}0) = \frac{L\sin\alpha}{\tan\phi}. \tag{6}$$

To determine a relation between the penetration path angle ϕ and the yaw angle α, the velocity vector components shown in Fig. 2 are used to obtain:

$$v_s = w\cos\alpha + u\cos\phi \tag{7}$$

and by using the Law of Sines, analogous to Eqn. (3):

$$\frac{u}{\sin\alpha} = \frac{w}{\sin\phi}. \tag{8}$$

This equation is used to eliminate the erosion rate w (= v-u) in Eqn. (6), which results in an expression for the penetration velocity u in terms of the penetration path angle ϕ,

$$u = \frac{v_s}{\sin\phi\cot\alpha + \cos\phi} = \frac{v_s\cos\phi}{1 + \tan\phi\cot\alpha}, \tag{9}$$

which has the form $u = u(v_s\cos\phi)$. This suggests that the component of the velocity vector along the penetration path z, namely, $v_s\cos\phi$, is the relevant quantity to be used to calculate the penetration velocity u. Eqn. (9) provides an implicit relation between the penetration path angle ϕ and the yaw angle α, which is further complicated by the fact that u is a function of the path angle ϕ:

$$\alpha = \tan^{-1}\left[\frac{\sin\phi}{\frac{v_s}{u} - \cos\phi}\right]. \tag{10}$$

Since u depends on ϕ, it is not possible to write an explicit function to determine ϕ given α. However, Eqn. (10) is used to determine a table of α values for a wide range of ϕ values. For a given impact situation, where α is known, the value of ϕ can be determined from this table, provided we can determine (or use a model for) the penetration velocity u. This is the assumption that is the nemesis of most penetration models and unfortunately cannot be eliminated, except in the hydrodynamic limit (HDL), a reasonable approximation for hypervelocity impacts. Once Eqn. (10) is used to determine the value of ϕ, Eqn. (5) is then used to determine the eroded penetrator length, ΔL. To determine u, typical penetration models or empirical relations can be used, such as the Tate-Aleskeevski [9] modified Bernoulli relation or the Lanz-Odermatt [10] curve fits.

Thus far, no simplifying assumptions have been made, other than a constant penetration path (equivalent to the plate thickness being less than that required to have tail swipe affect the penetration). To proceed further, a variety of possible assumptions are examined and the resulting simplifying expressions are compared with hypervelocity impact data for residual lengths. It is useful to relate these assumptions to deep target yawed penetration, realizing they only apply to finite thickness targets. Then, Eqn. (4) provides an upper bound on $P_\perp$ ($\theta_s = 0$) namely

$$\frac{P(\alpha;\theta_s=0)}{L} \le \frac{\sin\alpha}{\tan\phi}. \tag{11}$$

Using typical nomenclature to represent the P/L function for zero yaw, namely:

$$\frac{P(\alpha = 0;\theta_s=0)}{L} = \frac{u}{v-u} \equiv g(v_s) \tag{12}$$

yields an expression for the normalized degraded penetration due to yaw,

$$\frac{P(\alpha;\theta_s=0)}{P(0)} \le \frac{\sin\alpha}{g(v_s)\tan\phi}. \tag{13}$$

PENETRATION VELOCITY

The penetration velocity u along the unknown penetration path z is computed by using the component of v_s in the unknown penetration direction, or $u = f(v_s\cos\phi)$. Using a Tate-Aleskeevski modified Bernoulli relation, as an expample, this yields

$$u = kv_s\cos\phi \tag{14}$$

similar to the form given in Eqn. (9) with the quantity k being a function of $v_s\cos\phi$, namely

$$k(v_s\cos\phi) \equiv \frac{1-\mu\sqrt{1+\dfrac{(R_t - Y_p)(1-\mu^2)}{k_t\rho_t v_s^2\cos^2\phi}}}{1-\mu^2}, \tag{15}$$

where R_t and Y_p denote the target resistance and penetration strength and $\mu \equiv \sqrt{k_t\rho_t/k_p\rho_p}$, with the shape factors k_t and k_p typically having values of 0.5. Note that this expression contains the

unknown penetration path angle ϕ so it cannot be used directly. For high velocity applications, however, the HDL ($v_s \to \infty$) has $k \to \frac{1}{1+\mu}$, so that the penetration velocity becomes independent of the path angle ϕ , and hence the yaw angle. For like material impacts, $\mu = 1$ and in the HDL limit , $k \to 1/2$. In the general case, it is preferable to eliminate u in favor of k and ϕ to obtain:

$$\alpha = \tan^{-1}\left[\frac{k\sin 2\phi}{2(1-k\cos^2\phi)}\right]. \tag{16}$$

Shown in Fig. 3 are curves using Eqns. (15) and (16) relating the penetration interface path angle to the yaw angle as a function of impact velocity for tungsten sintered metal penetrators and RHA steel targets for which $\rho_p = 17.45$ g/cc; $Y_p = 2$GPa and $\rho_t = 7.85$ g/cc; $R_t = 5.2$ GPa yielding $k \cong 0.6$. Expanding Eqn. (16) for small yaw angles α yields an approximate ***explicit*** relation between the path angle ϕ and the yaw angle α, $\phi = \alpha\left(\frac{1}{k}-1\right) + O(\alpha^2)$; for small α,

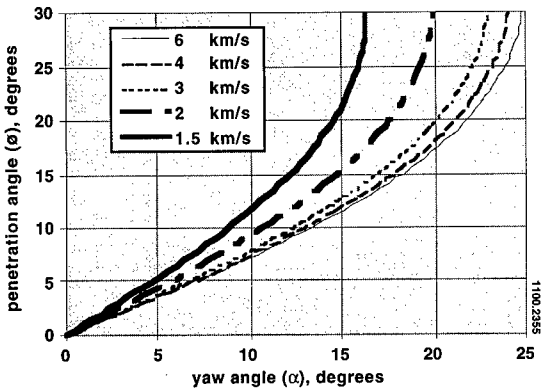

Fig. 3. Penetration path (interface) angle vs. impact yaw angle for tungsten sintered metal penetrators impacting RHA steel targets.

This small yaw angle approximation shows a linear relationship between the penetration path angle and the yaw angle for yaw angles up to (and greater than) 10 degrees. Note that ϕ is approximately equal to α for typical values for k. For $k = 1/2$, $\phi \cong 4/3\alpha$ and for $k = 0.6$, $\phi \cong 25/24\alpha$. In the HDL, this simplifies further to $\phi \to \mu\alpha$, or for like-on-like materials, $\phi \to \alpha$. ***Thus, the penetration path is an exact mirror image for high velocity, like-on-like impacts.*** Deviations from this path are due to penetration velocity strength effects. Further noting that $g(v_s) = \frac{P}{L} = \frac{u}{v-u} = \frac{k}{1-k}$, this small angle relation becomes $\phi = \alpha/(P/L) + 0(\alpha^2)$ similar to the leading term of the empirical approximation used by Silsby [1, 2] expressed as Eq. (1).

Insights into deep target, yawed penetration degradation can also be obtained by using the relation (16) in Eqn. (11) and expanding for small yaw angles, α, to obtain:

$$\frac{P(\alpha;\theta_s=0)}{L} \approx \frac{k}{(1-k)} - \alpha^2\left[\frac{1-k}{3k} + \frac{k}{6(1-k)}\right], \text{ for small } \alpha. \tag{17}$$

This results in a surprisingly simple expression for the determination of the absolute penetration degradation rate as a function of yaw, namely,

$$\frac{\partial}{\partial\alpha}P(\alpha;\theta_s=0) \approx -2\alpha\left[\frac{1-k}{3k}+\frac{k}{6(1-k)}\right].$$

Penetration normalized by penetration without yaw is given by the relative penetration relation:

$$\frac{P(\alpha;\theta_s=0)}{P(0)} \approx 1-\frac{\alpha^2}{3}\left[1+\frac{k^2}{2}\right]+0(\alpha^3), \tag{18}$$

which also results in a simple expression for normalized yaw degradation rate:

$$\frac{\partial}{\partial\alpha}\left(\frac{P(\alpha)}{P(0)}\right) \approx \frac{-2\alpha}{3}\left[1+\frac{k^2}{2}\right]. \tag{19}$$

For high impact velocities, the limiting expressions for k in the HDL are used to obtain the high velocity yaw degradation approximations:

$$\left.\frac{P(\alpha;\theta_s=0)}{L}\right|_{HDL} \approx \frac{1}{\mu}-\alpha^2\left[\frac{\mu}{3}+\frac{1}{6\mu}\right]. \tag{20}$$

or perhaps written in a more revealing manner: $$\left.\frac{\mu P(\alpha;\theta_s=0)}{L}\right|_{HDL} \approx 1-\frac{\alpha^2}{6}[1+2\mu^2],$$

so that the degradation rate in terms of yaw angle becomes:

$$\left.\frac{\partial\frac{P}{L}}{\partial\alpha}\right|_{HDL} \sim -2\alpha\left[\frac{\mu}{3}+\frac{1}{6\mu}\right].$$

In Fig. 4 the predicted penetration degradation with incident yaw angle is shown for tungsten penetrating armor steel at 1.5 km/s for L/D = 10 penetrators. Also shown are the Bjerke empirical curve fit approximation [1] and the small angle approximation, Eqn. (18).

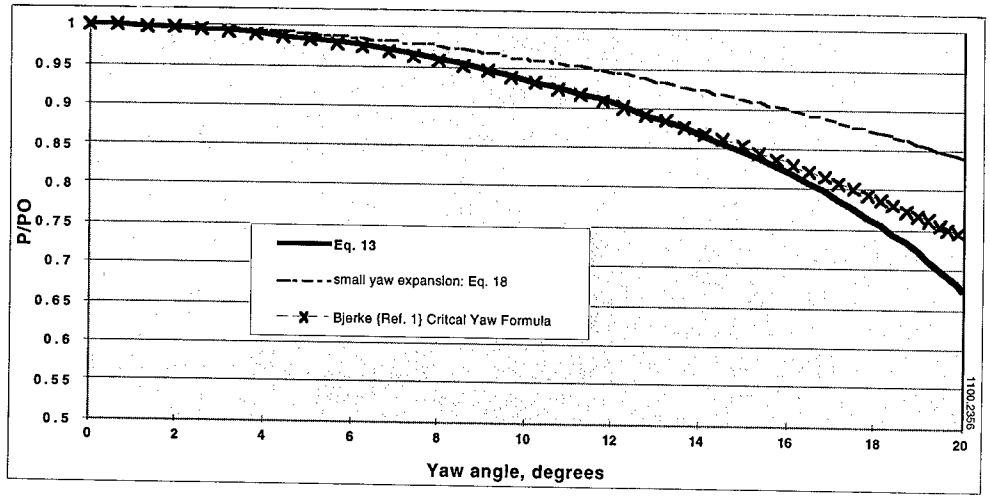

Fig. 4. Normalized penetration with yaw for L/D 10 tungsten rods impacting RHA steel @ 1.5 km/s.

ALTERNATIVE SIMPLIFIED APPROXIMATION

An alternative to using the implicit relation between yaw and path angle is to use the components of the penetration velocity v_s along and normal to the penetrator axis to approximate the penetration path, as depicted in Fig. 5a. A simple geometric formulation is used to determine residual penetrator length as a function of impact yaw angle. The component along the rod axis is used to compute u; that is $u = f(v_s\cos\alpha)$. The penetration during a time Δt is given by $u\Delta t$. During this time, the penetrator has moved $v_s\Delta t\sin\alpha$ due to the normal component of v_s. An angle γ is defined as the angle between the penetration path z and the rod axis (as opposed to the velocity vector). Thus, referring to Fig. 5a, or triangle I(ΔI)

$$\gamma = \tan^{-1}\left[\frac{(v_s\sin\alpha)\Delta t}{u\Delta t}\right] = \tan^{-1}\left[\frac{v_s\sin\alpha}{u}\right] \tag{21}$$

where u is computed using Eqn. (15) using α instead of ϕ so that $u = kv_s\cos\alpha$, where k is itself a function of $v_s\cos\alpha$, rather than $v_s\cos\phi$ as used earlier. Substituting this form for u suggests that

$$\gamma = \tan^{-1}\left(\frac{\tan\alpha}{k}\right). \tag{22}$$

This in an explicit relation between the penetration angle γ, relative to the penetrator axis, and the yaw angle, unlike Eqn. (10), which was an implicit relation between the penetration path angle ϕ and the velocity vector v_s. Having defined this angle in ΔI, we use triangle II(ΔII) as shown in Fig. 5b to relate the penetration path z to the finite target thickness T by the relation

$$T = z\cos(\theta_s+\alpha-\gamma) \tag{23}$$

revealing that the penetration path deviates from the path length along the penetrator line-of-sight, $\theta_s + \alpha$ by the angle γ suggesting that the path length is a function of γ, hence of u and v_s. Finally, examine triangle III(ΔIII) in Fig. 5c which relates the path length z to the eroded length ΔL or,

$$\Delta L\sin\alpha = z\sin(\gamma-\alpha). \tag{24}$$

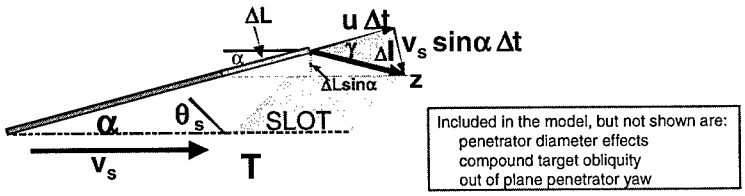

Fig. 5 (a): $\Delta l,\ \gamma = \tan^{-1}\{v_s\sin\alpha\,\Delta t/u\Delta t\}$

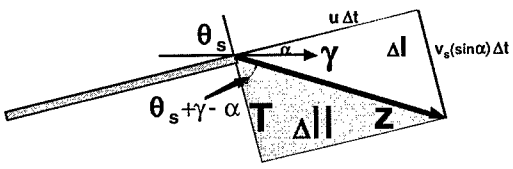

Fig. 5 (b): $\Delta II,\ z = T\sec(\theta_s+\alpha-\gamma)$

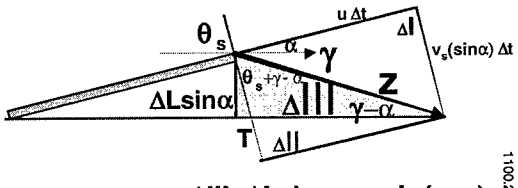

Fig. 5 (c): $\Delta III,\ \Delta L\sin\alpha = z\sin(\gamma-\alpha)$

1100.2357

Fig. 5. Schematic illustrating three triangles which define the relationships between the penetration path angle (approximated), impact yaw angle, and eroded penetrator length for yawed impact of oblique target plates of finite thickness.

Combining Eqns. (23) and (24) results in a simple expression for the eroded length ΔL penetrating a finite target of thickness T and obliquity θ_s for a rod with impact velocity v_s and yaw α as

$$\Delta L \cong \frac{T\sin(\gamma-\alpha)}{\sin\alpha\cos(\theta_s+\alpha-\gamma)}, \tag{25}$$

where Eqns. (21) or (22) are used to determine γ. Note again that this is an approximation to the penetration path due to the assumption that the component of v_s along the rod axis is used. In practice, however, the computed eroded lengths are similar to the more exact relation, Eqn. (5), but expressions (25), (23) and (15) are extremely easy to use. *However, these approximations fail to produce the penetration degradation shown in Fig. 4 when applied to semi-infinite targets.*

DIAMETER EFFECTS (APPROXIMATIONS)

Finite penetrator diameters change the path length z as the interface sweeps from the part of the penetrator initially in contact with the plate to the oppostite side of the penetrator upon exiting the plate. The additional eroded length due to this effect, ΔL′ is approximated using the penetration path based on γ instead of ϕ (using velocity components along and normal to the penetrator axis). The modified penetation path length is used instead of z to estimate ΔL = ΔL(z) + ΔL′. The problem is further complicated by continued erosion upon exiting the plate but should be bounded by the assumption that erosion continues until the entire penetrator has exited the plate, or

$$\Delta L'(diameter) \le -D\sin\alpha + D\cos\alpha\left[\frac{\cos\alpha\tan\theta_s-\left(\frac{T}{D}\right)\sec(\theta_s+\alpha-\gamma)\cos(\gamma-\alpha)}{\cos\alpha+\left(\frac{T}{D}\right)\sec(\theta_s+\alpha-\gamma)\sin(\gamma-\alpha)}\right]. \tag{26}$$

For small T/D ratios this is approximated by $D\tan\theta_s[\cos\alpha - \sin\alpha]$ illustrating that $xD\tan\theta_s$ is an appropriate oblique erosion effect, but the factor x is a variable function of the penetration velocity u and the incident pitch angle. The time for the penetrator top to impact the target relative to the time the penetrator bottom hits the target is $\Delta t_1 = \frac{(\sin\alpha+\cos\alpha\tan\theta_s)}{v_s}$ as illustrated in Fig. 6. In this time, the lower portion of the rod has penetrated along the penetration path z a depth $u_1\Delta t_1$, so that the erosion front has changed to be at an angle ε as shown in the figure. The erosion continues through the plate until the lower portion of the penetrator exits the plate. During the additional time, Δt_3 it takes for the penetrator top to reach the rear surface, the lower part of the rod continues to erode for a portion of, or perhaps all of, this time. This additional erosion is at most $(v-u)\Delta t_3$ where $v = v_s\cos\alpha$ and $\Delta t_3 = \frac{T\sec(\theta_s+\alpha-\gamma)-u_1\Delta t_1}{u_3}$ yielding $\Delta L' \le (1-k)$ $D\cos\alpha(\cos\alpha + \sin\alpha\tan\theta_s)$. Note this reduces to $(1-k)$ D $\tan\theta_s$ for the situation with zero yaw. Typical values of k range between 1/2 to 2/3 so that depending on k, this effect is approximated by

$$L' \approx \frac{D}{2}\tan\theta_s \text{ or } \frac{D}{3}\tan\theta_s. \tag{27}$$

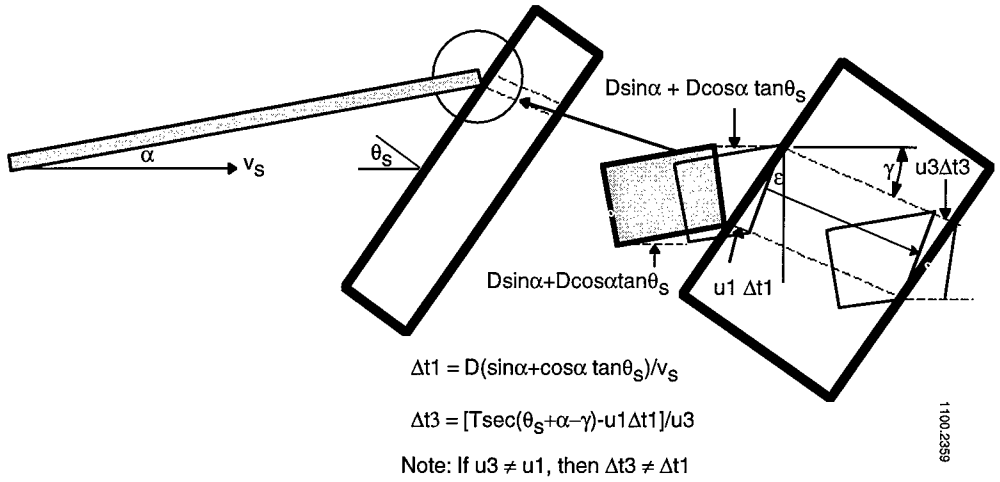

Fig. 6. Diameter effect for oblique plate, yawed impact penetration.

Additional insight is provided by examination of a typical velocity profile through a finite target as illustrated in Fig. 7, a CTH computation at 2.6 km/s. The initial impact phase consists of a rapid deceleration from v to u_{ss} during a time Δt_1, and after the steady state phase of duration Δt_2 in which u_{ss} is nearly constant, u begins to increase in the exit phase of duration Δt_3 attempting to equilibrate with v. This profile is approximated as shown in Fig. 7 using average values for u in each phase.

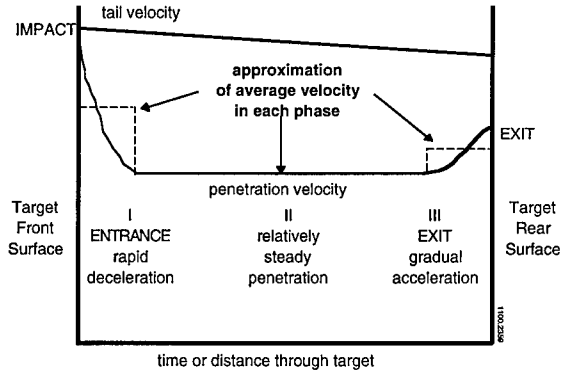

Fig. 7. Typical velocity profile through a finite thickness target from a CTH computation of an l/d 30, tungsten sintered metal LRP at 2.6 km/s impacting a relatively thick, but finite RHA target at normal incidence (Anderson, et al. [11]).

In the first phase, $u_I \sim u_{ss} + a_1(v-u)$, where $0 < a_1 < 1$ and a1 is approximately 1/2. During phase II, $u_{II} \sim u_{ss}$ and during the third exit phase $u_{III} \sim u_{ss} + a_3(v-u)$, where $0 < a_3 < 1$ and a_3 is approximately 1/4 (as an illustrative example).

Thus the amount of penetrator eroded during each phase is different. The erosion on the rod bottom is

$$\Delta L_{bottom} = \Delta L_I + \Delta L_{II} = (v - u_I)\Delta t_I + (v - u_{ss})\Delta t_{II} = (1-k)v_s[(1-a_1)\Delta t_I + \Delta t_{II}] \quad (28)$$

while on the top of the rod, the erosion is

$$\Delta L_{top} = \Delta L_{II} + \Delta L_{III} = (v - u_{III})\Delta t_{III} + (v - u_{ss})\Delta t_{II} = (1-k)v_s[(1-a_3)\Delta t_{III} + \Delta t_{II}] \quad (29)$$

The different penetration velocities imply that the times Δt_1 and Δt_3 are not equal. To note the size of this effect, if these times were equal, a minimum difference would be:

$$\Delta L_{bottom} - \Delta L_{top} \cong (1-k)(a_1 - a_3)V_s\Delta t_1 \cong \frac{1-k}{4}[\cos\alpha + \sin\alpha\tan\theta_s]D. \quad (30)$$

For $k = 1/2$ and no yaw, this value is $\frac{D}{8}\tan\theta_s$. Any incident yaw would increase this value. The important points are that obliquity compounds this effect, the effect is velocity dependent (changes k), and therefore there is no simple approximation.

OBLIQUE PLATE EXPERIMENTS

The model was compared with a set of hypervelocity impact experimental data generated at the IAT. A baseline L/D = 10 long-rod, tungsten sintered metal penetrator with a mass of 65 g, length of 80 mm and diameter of 7.8 mm with a hemispherical nose was used to impact finite thickness oblique plates at impact velocities between 2.2 and 3.0 km/s. Variations from this baseline included tests with a 9.3 mm diameter rods to examine T/D effects. The tests consisted of different tungsten alloy variants: Plansee HF, Plansee FNC, Teledyne X27C or Osram-Sylvania (formerly GTE) WN108F. The tungstens are all conventional W-Ni-Fe, 91% tungsten, with densities of 17.45 g/cm^3, except for the Plansee FNC, which is a cobalt alloy having a relatively high value of fracture toughness. Although the fracture behavior was affected by the particular tungsten alloy, erosion behavior seemed to be independent of the tungsten alloy used. Thus, this particular data set provides quite a good test of the current model. These different penetrator material properties are discussed in Ref. [5] and dimensions, material and shot number are listed in Table 1. A schematic of an oblique plate test with radiographs of the penetrator before and after impact can be seen in Fig. 8.

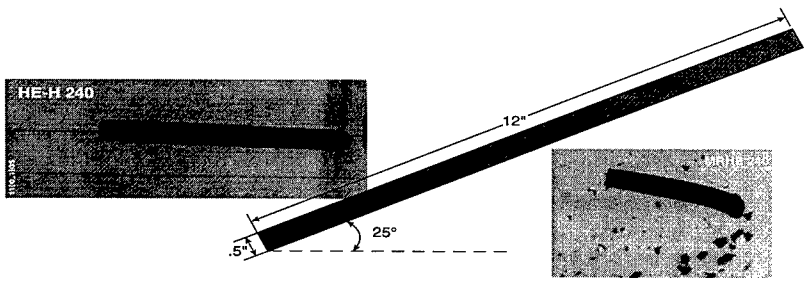

Fig. 8. A schematic of an oblique plate experiment and typical radiographs from IAT test 240 (Bless, et al. [5]).

Table 1. Test Summary for 65 Degree Obliquity Impact Experiments

IAT Test Number	Rod Length, mm	Rod Diameter, mm	Total Plate Thickness, mm	Yaw at Target, deg.	Pitch at Target, deg.	Impact Velocity, km/s	Average Residual Length, mm	Average Residual Velocity, km/s
233†	80.5	7.9	12.8	-8.36	4.35	2.62	49.4	2.49
240	81.0	8.1	12.8	-5.7	-1.41	2.61	51.6	2.51
243	78.4	7.9	12.8	-1.2	-0.21	2.63	53.7	2.54
268	93.0	9.3	12.8	-0.48	-0.02	2.64	55.6	2.47
269	93.0	9.3	6.4	-10.23	10.59	2.62	69.1	2.58
270	70.0	4.6	12.8	-4.69	-4.53	2.66	38.2	2.58
272	98.0	9.8	12.8	1.73	-0.85	2.20	68.1	N/A
273	78.8	7.8	12.8	-8.11	8.7	2.56	49.8	2.48
277	98.0	9.8	12.8	N/A	N/A	2.19	62.2	N/A

† Target obliquity was 60 degrees for this test

The eroded lengths (ΔL) were calculated using the original rod length and subtracting the residual lengths measured from the radiographs, or $\Delta L = L_0 - L_r$. The residual length was measured on the radiograph image along each side of the residual penetrator and an average of the two values was used in the analysis. If the rod was not straight, the length along its arc was measured. The ambiguity associated with residual length measurement definition was estimated as ±1/4 D. Table 1 lists the penetrator residual lengths and velocities.

The data were examined extensively in [5] for systemic dependence of the eroded length on the typical impact parameters, used for nonyawed impacts. The authors in [5] concluded that "*the eroded length did not correlate well with either target thickness or rod diameter, from which it would appear that the mass loss mechanics involves a combination of these parameters.*"

This particular data set was interrogated using the analytic expression in Eqs. (5) and (26) to calculate eroded lengths. The results are tabulated in Table 2 and plotted in Fig. 9.

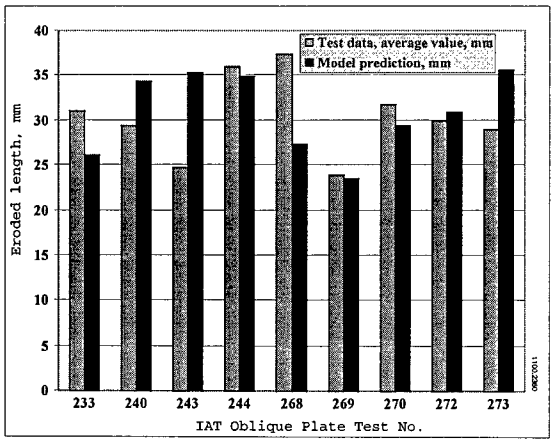

Fig. 9. Predicted eroded lengths using Eqs. (5) and (26) vs. hypervelocity experimental data with l/d tungsten alloy penetrators impacting steel targets at 60 and 65 degrees obliquity.

Table 2. Data Comparison for Oblique, Yawed Impact Experiments

IAT Test Number	Yaw at Target, deg.	Pitch at Target, deg.	Average Eroded Length, mm	Computed Eroded Length, Eqs. (5) and (26), mm
233†	-8.36	4.35	31.1	26.1
240	-5.7	-1.41	29.5	34.4
243	-1.2	-0.21	24.7	35.4
268	-0.48	-0.02	36.0	34.9
269	-10.23	10.59	37.3	27.3
270	-4.69	-4.53	23.9	23.6
272	1.73	-0.85	31.8	29.5
273	-8.11	8.7	30.0	30.9
277	N/A	N/A	29.0	35.6

CONCLUSIONS

This effort determined the initial penetration path through a target at normal or oblique incidence for penetrators impacting with yaw. For finite thickness plates, this results in a direct computation of the eroded length, which agrees with residual lengths from high velocity experiments conducted at the IAT. A larger data set is being interrogated at this time.

Implications for the degradation due to yaw on normal impact conditions were discussed, which formalizes, in a more rigorous manner, the effect of penetration path change, at least initially. Approximate degradation formulas for small yaw angles were derived, which agree with empirical models widely used in the community.

Acknowledgment—This work was supported by the U.S. Army Research Laboratory (ARL) under contract DAAA21-93-C-0101. Special recognition is given to Ravi Subramanian who assisted the author in checking the assumptions and relations used in this analysis and casting them in a more general vectorial format.

REFERENCES

1. T. W. Bjerke, G. F. Silsby, D. R. Scheffler and R. M. Mudd, "Yawed long-rod armor penetration," *Int'l. J. Impact Engng.*, **12**(2), 281-292 (1992).
2. G. F. Silsby, R. J. Roszak and L. Giglio-Tos, "BRL's 50-mm high pressure powder gun for terminal ballistic testing—the first year's experience," BRL-MR-03326 (January 1983).
3. M. J. Normandia, S. Satapathy, D. L. Littlefield, J. D. Walker and C. E. Anderson, Jr., "Modified cavity expansion analysis for modeling finite target penetration," presented at 16th International Symposium on Ballistics, San Francisco, CA (September 1996).
4. S. Satapathy, M. J. Normandia and S. J. Bless, "Cavity expansion analysis modified to account for finite rear surface," IAT.R 0122, Institute for Advanced Technology (1996).
5. S. Bless, B. Pedersen, J. Campos, M. Normandia and R. Subramanian, "Penetration of oblique plates," IAT.R 0149, Institute for Advanced Technology (December 1997).
6. S. Bless and S. Satapathy, "Penetration of thick targets by yawed long rods," Proc. 1997 Conference Shock Compression of Condensed Matter, Am. Phys. Soc., Amherst, MA (1998).
7. Y. I. Bukharev and V. I. Zhukov, "Model of the penetration of a metal barrier by a rod projectile with an angle of attack," *Fizika Goreniya Ivzryva* 31, 104-109 (1995).
8. S. J. Bless, S. Satapathy and M. Normandia, "Transverse loads on a yawed projectile," 1998 Hypervelocity Impact Symp., Huntsville, AL (November 1998).
9. A.Tate, "A theory for the deceleration of long rods after impact," *J. Mech. Phys. Solids*, **15**, 387 (1967).
10. W. Lanz and W. Odermatt, "Penetration limits of conventional large caliber antitank guns kinetic energy projectiles," Proc. of the 13th International Symposium on Ballistics, Stockholm, Sweden (1992).
11. C. Anderson, Jr., S. Bless, D. Littlefield and R. Subramanian, "Prediction of large-scale impact experiments on steel targets," Proc. of the 14th International Symposium on Ballistics, Quebec, Canada (September 1993).

PERGAMON

International Journal of Impact Engineering 23 (1999) 675–686

INTERNATIONAL JOURNAL OF IMPACT ENGINEERING

www.elsevier.com/locate/ijimpeng

PENETRATION PERFORMANCE OF MULTIPLE SEGMENTED RODS AT 2.6 KM/S

MICHAEL J. NORMANDIA and MINHYUNG LEE

The Institute of Advanced Technology, The University of Texas at Austin, 4030-2 W. Braker Lane, Austin, TX 78759

Summary—We investigated the penetration capabilities of segmented penetrators consisting of small aspect ratio segments, ($1/8 \leq L/D \leq 1$) using axisymmetric numerical simulations for constant mass, diameter, and collapsed length, tungsten alloy, long-rod penetrators impacting semi-infinite thick rolled homogeneous armor steel (RHA) at 2.6 km/s. The specific technical issues investigated were whether the total penetration of multiple segments is a constant multiple of the penetration of a single segment (not necessarily the first segment); whether the primary cause of any penetration degradation was due to entrance effects or to material remaining at the crater bottom; and whether the cumulative degradation effects for multiple segment impacts changed the optimum aspect ratio based upon single segment penetration. © 1999 Elsevier Science Ltd. All rights reserved.

INTRODUCTION/LITERATURE REVIEW

The dramatic improvement in potential penetration performance of individual segments as compared to long rods is well documented and this history is summarized in an extensive IAT technical report [1]. Under investigation here is the capability of multiple, very low aspect ratio segments ($L/D \leq 1$) to penetrate as a multiple of a single segment as discussed by Charters [2], Orphal and Franzen [3], and others [4-6]. Increased penetration depth per unit of collapsed length, P/L_{coll}, is well documented (refer to [1] for an historical perspective and for summaries of the work of Eichelberger et al.).

Between 2 and 3 km/s, single segment data and calculations show that segments with aspect ratios of 1/8th are optimal near 2 km/s, Bjerke et al. [7]. The optimal aspect ratio decreases with increasing velocities to approximately 1/16th at 3 km/s, and decreases further as the impact velocity is increased, Orphal et al. [8]. The penetration of segments exhibited large scatter, but $L/D = 1/8$ segments demonstrate a performance increase of approximately 81% versus $L/D = 1$ segments (P/L of 4.35 vs. 2.4), which themselves are about 65% more effective on a per mass, per unit collapsed length basis than $L/D \geq 30$, long-rod penetrators (P/L of 2.4 vs. 1.44). Thus, overall performance increases of over 300% are possible for $L/D = 1/8$ segments as compared to long rods, if they can be realized and engineered. Naz and Lehr [9] investigated very small segments at high impact velocities, 2 to 5 km/s, illustrating that the secondary penetration after each segment impact is responsible for this performance enhancement. Tate [10] attempts to optimize the segment spacing based on this principle.

Attempts to exploit this enhancement using multiple segments have been reported with mixed results. There is a multitude of existing data and simulations that are divided into those investigations that demonstrate no or little penetration performance degradation and those that suggest that residual material remaining interferes with the penetration of successive segments. The material remaining issue is definitely important for low aspect ratio segments, $L/D < 1$ and at lower impact velocities as shown in Bjerke [7] at 2 km/s. However, it is generally believed that this effect is much less of a factor as either the velocity or segment aspect ratio is increased, particularly to 5 km/s as demonstrated by Naz and Lehr [9].

0734-743X/99/$ - see front matter © 1999 Elsevier Science Ltd. All rights reserved.
PII: S0734-743X(99)00113-X

The observed increase in P/L_{coll} is achieved at the expense of crater width. Orphal et al. [11] and Reinecke [12] examined the ratio of impact kinetic energy (KE) to target crater volume (V_c). This ratio is approximately constant for long rods > L/D = 1, and then increases as the segment aspect ratio is further reduced. This increase is quite dramatic for L/D ≤ 1/8 and appears to be a function of impact velocity. Our calculations at 2.6 km/s show a crater diameter-to- penetration diameter ratio of 1.6 for the first L/D = 1/8 segment, as compared to 2.50 for an L/D = 1 segment, a difference of over 55%. Both values are consistent with experimental data reported in the literature [11, 13] although crater diameters are slightly smaller. Our calculations also show that the crater diameter is largest for the first segment and decreases for successive segments as reported by Hohler and Stilp [13] in their experiments using L/D = 1 segments.

Many potential factors limit terminal performance of multiple segment penetrators. Other than the engineering issues and associated parasitic mass necessary to launch and deploy the segment train, performance has been demonstrated to be a strong function of segment spacing (Scheffler [4], Zukas [5], Franzen [14], Naz and Lehr [9] and Cline [15]), segment alignment and reduced crater diameter (Hohler and Stilp [13]), and residual penetrator material remaining at the bottom of the crater (Hauver [16]). Despite all of these challenges and issues, the segmented penetrator performance on a penetration depth criterion is still significantly more effective on a per unit collapsed length, mass, or energy basis.

Attempts to examine multiple segment penetrators using L/D = 1 segments showed little or no apparent degradation. Hohler and Stilp [13] conducted experiments at 2.5 km/s and measured only 90% of the penetration depth obtained by multiplying single segment depth times the number of segments. They attributed performance reduction to impact of the crater wall with a decreasing crater volume for successive segments. Experiments were also conducted by Frank et al. [17] at 1.85 km/s in which single L/D = 1 segments were fired into RHA, and after the target was recovered, it was impacted successively so that five segments impacted the same penetration channel. They measured *very little change* in unit penetration depth for all five segments, although the crater diameter was decreasing. In addition, they also fired L/D = 1 segments into predrilled cylindrical holes of the same depth as the first segment penetration depth within the target in the velocity range between 1.65 km/s and 1.8 km/s. This investigation examined the effect of penetrator material in the cavity bottom on the performance of the successive segments. The measured penetrations were slightly greater than that measured for a single segment impacting a flat target without predrilled holes.

On the other hand, numerical simulations using CTH were reported by de Rosset and Sherrick [18] for a fixed segment spacing at 1.7 and 2.6 km/s against RHA and they observed penetration degradation attributed to successive segments impacting the rear of previous segments. This effect was more pronounced at low velocities. Hauver et al. [16] also found that successive segments contribute progressively less to the total penetration due to interaction with residue.

NUMERICAL SIMULATIONS

Numerical simulations of tungsten segmented rods (L/D = 1/8, 1/4, 1/2, and 1) impacting semi-infinite RHA steel targets were conducted using the AUTODYN wave-propagation finite-difference code assuming axial symmetry. The diameter of each individual segment was kept constant at 16 mm as was the impact velocity at 2.6 km/s. A transmissive boundary condition was used on the rear surface (120 mm) to emulate a semi-infinite thick target. The matrix of computer simulations consisted of two segments for L/D = 1 and L/D = 1/2, four segments for L/D = 1/4 and eight segments for L/D = 1/8. The target diameter used was 300 mm for L/D = 1, 280 mm for L/D = 1/2, 260 mm for L/D = 1/4 and 240 mm for L/D = 1/8. A constant subgrid was used with ten cells across the *length* of the interacting region (2.5 times the segment radius) for L/D = 1/8 segments; 16 cells for L/D = 1/4; 20 cells for L/D = 1/2; and 30 cells for L/D = 1. The

Mie-Gruniesen equation of state was used with values identical to those used in [19]. For the armor steel target these are: ρ_0= 7.86 g/cc, c = 3.57 km/s, s = 1.92, Γ_0 = 1.7, and P_{min} = -2. For the tungsten penetrator these are: ρ_0= 17.4 g/cc, c = 4.03 km/s, s = 1.26, Γ_0 = 1.7, and P_{min} = -2.

A constant shear modulus, G (140 GPa) was used with a von Mises yield surface with a yield strength, Y (2 GPa) for tungsten segmented rods. Two levels of failure models are used, both of which are based on the effective plastic strain [8]. When the first failure level of strain is reached, the element behaves like a fluid and can only support hydrodynamic compression. The element is completely removed from the calculation when the second failure level of strain, set at 250%, is reached. The constitutive response for RHA was represented by the Johnson-Cook model:

$$\sigma = \left[960 + 1330\left(\varepsilon^{p}\right)^{0.85}\right]\left[1 + 0.06875\ \ln\dot{\varepsilon}^{*}\right]\left[1 - T^{*1.15}\right] \quad \text{MPa}, \tag{1}$$

where σ is the von Mises effective flow stress, ε^p the equivalent plastic strain, $\dot{\varepsilon}^*$ the dimensionless plastic strain rate, and T^* the homologous temperature.

The spacing parameter between each segment was eliminated by performing the calculations of successive segments one at a time into the recovered target after the individual segment penetration processes came to a complete stop (but before elastic rebound). Numerical time history data were collected and consisted of penetration velocity, depth of penetration and crater diameter.

NUMERICAL RESULTS

Penetration Phases

Figure 1 depicts the penetration and tail velocities along the centerline as a function of time, for the impact of a single L/D = 1/8 segment. At this aspect ratio, a condition of steady flow is established after several rarefaction waves have traversed between the rear of the projectile and the impact interface, but before the side rarefaction wave arrives at the centerline. For segments with greater aspect ratios, the ratio of the longitudinal to radial wave traversal times increases, becoming approximately equal for L/D = 1/4 to 1/2, and much larger for longer segments and for long rods (Bjerke et al. [7]).

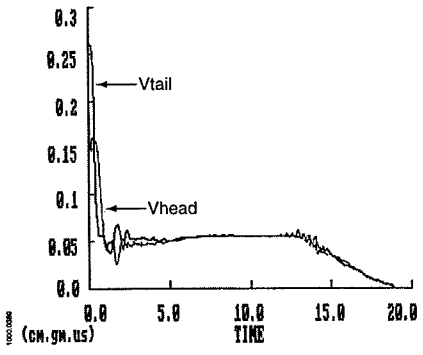

Fig. 1. Penetration and tail velocities for L/D = 1/8 segments.

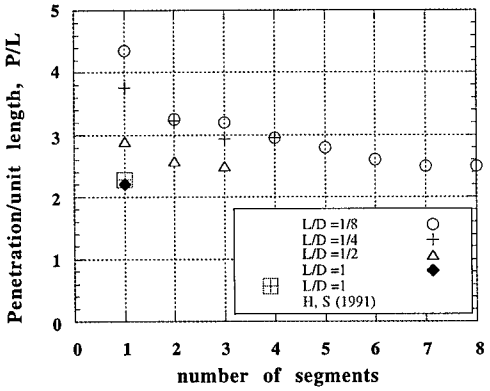

Fig. 2. P/L versus number of segments at 2.6 km/s. Experimental data from Hohler and Stilp [13].

Segment Penetration Data

The penetration depth, P, from the calculations was determined by measuring the distance from the undisturbed target surface to the *deepest* location of the crater bottom at the *interface* between the penetrator and target material. Infinite segment spacing was modeled by conducting simulations until the penetration velocities become less than 1% of the impact velocity. Figure 2 shows the normalized penetration, P/L, versus number of successive segments for L/D = 1/8, 1/4, 1/2, and 1 impacting at 2.6 km/s showing that P/L increases with decreasing penetrator L/D over the range $1/8 < L/D < 1$. Experimental data for L/D = 1 (Hohler and Stilp, [13]) is also shown for comparison. The penetration of the second segment is always smaller than the first segment with the possible exception of L/D = 1, consistent with the experiments of Frank et al. [17] which show a nearly constant penetration for each L/D = 1 segment for 5 segments at lower impact velocities. Those experiments resulted in almost no material residue at the cavity bottom which is consistent with our calculational results (not plotted in figure).

For $L/D < 1$ segments, the penetration continued to degrade for each successive segment, with the ratio of penetration of segment i to the penetration of the first segment continuing to decrease. The calculational results in Fig. 2 show degradation for the L/D = 1/4 and 1/2 segments as well, but to a lesser degree than the L/D = 1/8 segments. For the L/D = 1/8 segments the details of the calculations are listed in Table 1. There is a reduction of 25% for the second segment as compared to the first segment, a 26% reduction for the third, and a 32% for the fourth segment. We investigated the unexpected leveling of the penetration efficiency in a second set of calculations by increasing the target dimensions to remove any possibility that boundary effects may have affected the results. While the absolute number values were different, the same leveling trend was observed in this second set of computations.

Table 1. Penetration Degradation for L/D = 1/8 Segment i Versus First Segment

Segment	Penetration (mm)	P/L	P_i/P_1	Max. Diameter (mm)	D_i/D
1	8.7	4.35	1.0	25.6	1.6
2	6.5	3.25	0.75	21.6	1.35
3	6.4	3.2	0.74	22.0	1.38
4	5.9	2.95	0.68	22.2	1.39
5	5.6	2.8	0.64	22.2	1.39
6	5.2	2.6	0.60	22.0	1.38
7	5.0	2.5	0.57	22.0	1.38
8	5.0	2.5	0.57	22.0	1.38

The calculations reveal that each segment impacts a successively larger amount of residual penetrator material, and after several impacts, the bottom of the cavity is covered with a significant amount of tungsten residue, which the remaining projectile segments must deal with. Figure 9 depicts this continual buildup. To estimate a possible lower bound for P/L of successive L/D = 1/8 segments, a calculation representative of a continual increase in penetrator residue at the crater bottom was performed of a single tungsten alloy segment impacting a tungsten alloy target. In this case, the segment P/L is found to be 2.15, considerably lower than the penetration of the eighth segment, suggesting a potential for a further decrease in penetration for the following segments above and beyond the eighth segment.

Using the L/D = 1/8 tungsten into steel, and tungsten into tungsten first segment penetration values, P/L scales as $(\rho_p/\rho_t)^{0.93}$, where ρ_p and ρ_t are the projectile and target material densities, respectively. Several researchers have estimated that penetration should scale as $(\rho_p/\rho_t)^{1/3}$, $(\rho_p/\rho_t)^{1/2}$, or $(\rho_p/\rho_t)^{2/3}$ for L/D = 1 projectiles [20]. From the experimental data in the work of Hohler and Stilp [13], using D17 tungsten alloy impacting German Armor Steel, the value of P/L is 2.276 at 2.602 km/s, and for C110W2 steel impacting German Armor Steel is P/L = 1.141 at 2.593 km/s. These results for penetration scale as $(\rho_p/\rho_t)^{0.87}$, closer to what we observed computationally.

In an additional set of calculations, we artificially removed (numerically) the residual tungsten from cells at the bottom of the crater before we calculated the impact of the second segment. Some small amount of tungsten remained along the crater wall because of mixed cells, a computational artifact of multi-material Eulerian calculations. We did this for a total of four successive L/D = 1/8 segment impacts and for two successive L/D = 1/4 segments, that is we removed any remaining material after each segment. These simulations are similar to those with a predrilled hole performed computationally by de Rosset et al. [18] and experimentally by Frank et al. [17], except that we retained the actual crater shape in our calculations. The computational results are displayed in Table 2. Each successive rod segment contributes an equal amount of penetration, which is consistent with the results of the predrilled hole test for L/D = 1 segments [17].

Table 2. Penetration Results for L/D = 1/8 Segments with and without Residual Tungsten

L/D = 1/8	With Residue			Without Residue		
Segment #	P	P/L	P_t/L_t	P	P/L	P_t/L_t
First	8.7	4.35	4.35	8.7	4.35	4.35
Second	6.5	3.25	3.80	8.5	4.25	4.30
Third	6.4	3.20	3.43	8.6	4.30	4.30
Fourth	5.9	2.95	3.31	8.5	4.25	4.29

From these results we conclude that the penetration degradation of the successive segments is solely due to the penetrator material remaining in the cavity bottom. These effects become significant for low values of L/D. The performance of segmented rods could be enhanced if somehow the material remaining in the crater bottom can be removed, especially for L/D << 1. The situation is similar for the L/D = 1/4 segments, for which the data are summarized in Table 3. Listed are the penetration data for L/D = 1/4 segments, both with and without residual crater material removed.

Table 3. Penetration Results for L/D = 1/4 Segments with and without Residual Tungsten

L/D = 1/4	With Residue			Without Residue		
Segment #	P	P/L	P_t/L_t	P	P/L	P_t/L_t
First	15	3.75	3.75	15	3.75	3.75
Second	12.9	3.23	3.49	14.8	3.75	3.73
Third	11.7	2.93	3.3			
Fourth	11.8	2.95	3.21			

In Fig. 3, the calculated results of the L/D = 1/8 and L/D = 1/4 segments are shown both with and without the residual penetrator material removed. Note that the penetration is approximately constant when the material is removed, and approaches the penetration behavior of the L/D = 1 segments, which showed very little degradation. In Table 4, the remaining numerical calculations are summarized for the L/D = 1/2 and L/D = 1 segments.

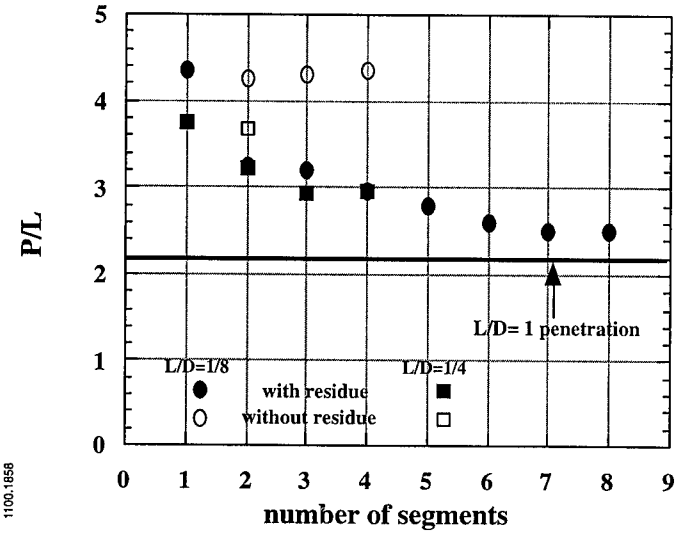

Fig. 3. P/L versus number of L/D = 1/8 and L/D = 1/4 segments both with and without residue.

Table 4. Penetration Results for L/D = 1/2 and L/D = 1 Segments

L/D	Segment #	P	P/L	P_t/L_t
1/2	1	23.2	2.9	2.9
1/2	2	20.6	2.58	2.74
1/2	3	20.0	2.5	2.66
1	1	35.2	2.2	2.2
1	2			

In Fig. 4, we examine the effectiveness of the various segment aspect ratios by depicting the total penetration (P_t) normalized by the total collapsed segment length (L_t) as a function of the total length normalized by the length of an individual L/D = 1/8 segment. A constant value of P_t/L_t would imply that penetration depth of n segments is n times this value. Clearly, the error in estimating total penetration depth from that of the first segment penetration and multiplying by the number of segments would continually increase for L/D < 1/2. For L/D = 1/2 and L/D = 1, the error would be minimal. The results show almost identical absolute penetration for the L/D = 1/8 and 1/4 segments for up to eight segments.

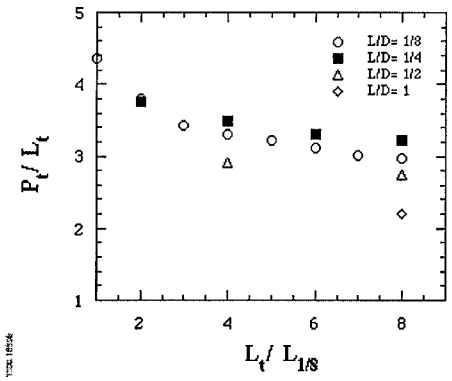

Fig. 4. P_t/L_t versus $L_t/L_{1/8}$ at 2.6 km/s.

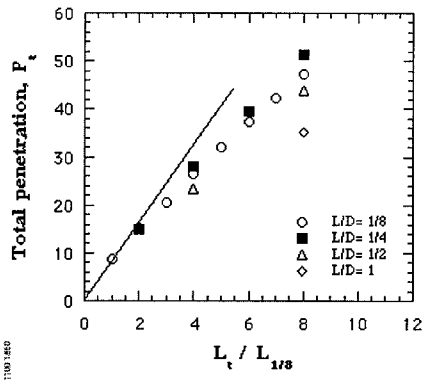

Fig. 5. Total penetration versus normalized total length at 2.6 km/s.

In Fig. 5, we depict the total penetration versus total collapsed penetrator length, normalized by the length of an L/D = 1/8 segment. For L/D = 1/8 segments, the total penetration for eight segmented rods is 47.3 mm, (P_t/L_t = 2.96) as compared to 69.6 mm using the penetration of the first segment 8.7 mm x 8 segments (P_t/L_t = 4.35). Thus, the actual penetration performance of an 8-segment rod consisting of L/D = 1/8 segments is only 68% that obtained by the multiplication scheme. Even if the second segment penetration of 6.5 mm was used, the estimated penetration would be 8.7 mm + 6.5 mm x 7 segments, or 54.2 mm, still 15% greater than the actual penetration.

Despite this noticeable decrease in penetration, the value of P/L for the eighth segment of L/D = 1/8 is 2.5, which is still significantly larger than P/L = 1.45 for a long rod (L/D ≥ 30) at an impact velocity of 2.6 km/s. In addition, compared to a single L/D = 1 segment penetration, eight L/D = 1/8 segments still penetrate 36% more RHA at 2.6 km/s. Our calculations simply suggest that the performance *gain* of small segments decreases progressively as the number of segments is increased. The absolute gain in penetration is still present and is still very significant.

Crater Diameter, Crater Shape and Efficiency (KE/V_c)

Crater diameter was also measured slightly below the cavity entrance for the first segment and at the largest size for the successive segments. Figure 6 shows the computed normalized crater diameter, D_c/D_p, versus number of segments for an impact velocity of 2.6 km/s. The data from the experiments of Hohler and Stilp [13] are also displayed. It is shown that a constant channel shape approaching long rod behavior is formed from the second segment. With the exception of L/D = 1, the ratio of the crater diameter to projectile diameter decreases with decreasing L/D. A least squares fit to the results of D_c/D_p versus L/D is linear using a log-log scale with $D_c/D_p = (L/D)^s$, giving the following values for s:

Table 5. D_c/D_p, Normalized Crater Diameter Ratio Behavior with $(L/D)^s$

Impact Velocity, km/s	s	Correlation Coefficient
1.5 (Ref. [11])	0.14	0.97
2.6	0.225	0.977
3.0 (Ref. [11])	0.25	0.99

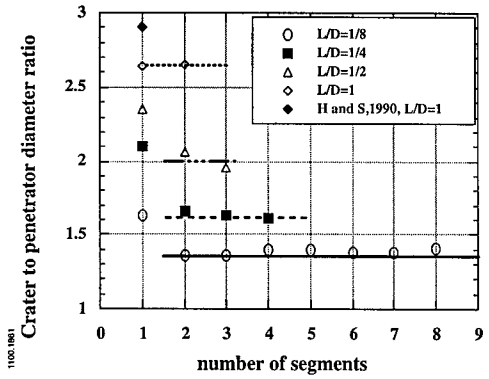

Fig. 6. Normalized crater diameter versus number of segments. Experimental data given by Hohler and Stilp [13].

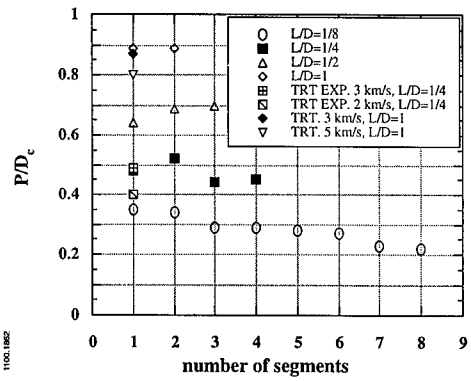

Fig. 7. Penetration to crater diameter ratio versus number of segments. (Note in Fig. 8 that the crater shape for L/D = 1/8 segments, while approaching a cylinder, is quite scalloped. The minimum diameter is less than those indicated in the preceding figures and discussion.)

The ratio of the penetration depth to crater diameter, P/D_c, is a measure of crater shape and is shown in Fig. 7 versus number of segment impacts at 2.6 km/s. Experiments performed by Titan Research & Technology are denoted by TRT [21] and computational results from [11] are also displayed. A number of studies have found that the crater shape for L/D = 1 segments is not an ideal hemispherical shape, that is $P/D_c > 1/2$. The calculated value of $P/D_c = 0.88$ is close to that reported in [11] and this is also true for the L/D = 1/4 segment calculations. The ratio P/D_c decreases with decreasing segment aspect ratio. For each successive L/D = 1/8 segment impact, the crater shape becomes more like a shallow disk. This is a consequence of a decrease in the penetration while the crater diameter remains nearly constant. Thus, the cratering efficiency (the ratio of impact kinetic energy to crater volume, V_c) becomes progressively worse. On the other hand, P/D_c increases for the successive L/D = 1/4 segment impacts due to less decrease in penetration depth.

It was found by Murphy [22] that the ratio of impact kinetic energy (KE) to crater volume did not vary greatly for a given material. However, it was also found that there are variations in the parameter KE/V_c with projectile L/D for $L/D < 1$, increasing with decreasing projectile L/D [11]. We estimated the *actual crater volume from the numerical simulations* using AUTOCAD software not by assuming a cylindrical-like shape. The craters generated by the impact and penetration of the first L/D = 1/8, 1/4, 1/2 and 1 projectiles are displayed in Fig. 8, showing that L/D = 1 projectile produces a non-cylindrical crater. Figure 9 shows the craters generated by the impact of eight segments of L/D = 1/8 and four segments of L/D = 1/4. In Fig. 10, the estimated values for KE/V_c, including the results given by Orphal et al. [11] are shown. The present results compare well with other data and for segments up to L/D = 1/8, also suggest that KE/V_c increases with decreasing projectile L/D. Thus the small L/D segments are less efficient in terms of kinetic energy required per unit crater volume.

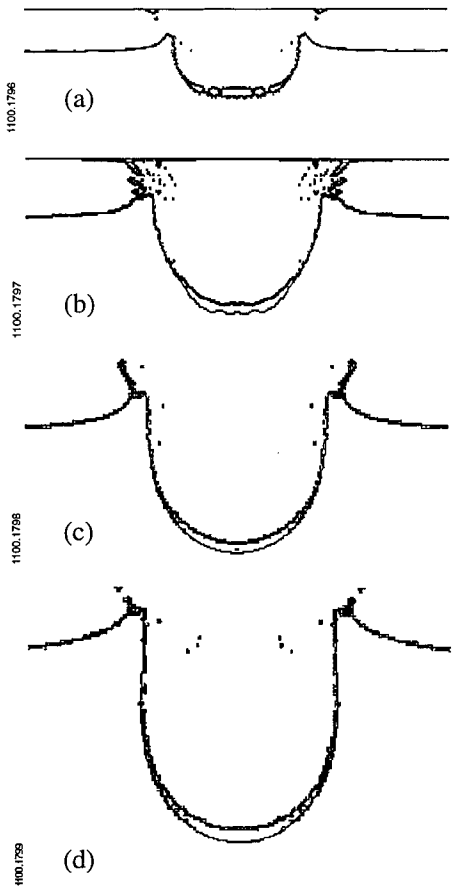

Fig. 8. Craters created by the first segment impacts for L/D = 1/8 (a), 1/4 (b), 1/2 (c) and 1 (d) segments.

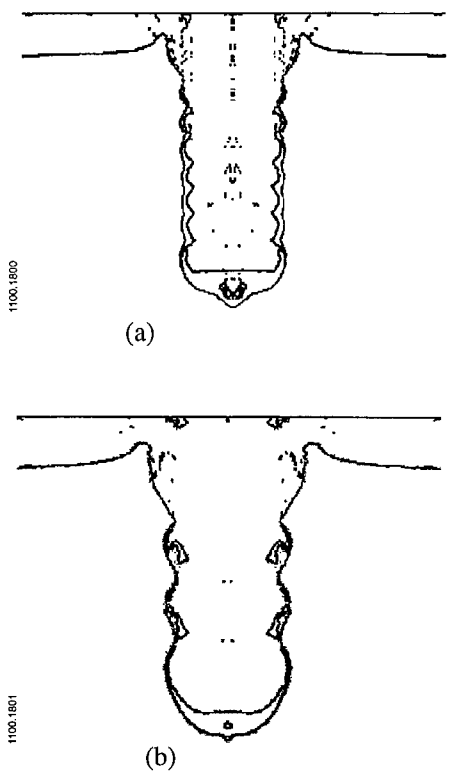

Fig. 9. Crater shape, (a) eight-segment impacts of L/D = 1/8 and (b) four-segment impacts of L/D = 1/4.

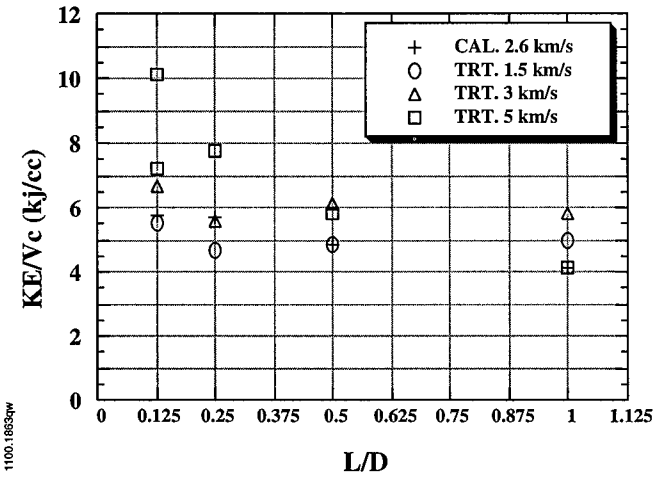

Fig. 10. Kinetic energy per unit crater volume versus segment L/D.

CRITICAL COLUMN ANGLE-OF-ATTACK (CAOA)

The calculations reveal that the relative advantage of smaller segments (L/D = 1/8 and L/D = 1/4) decreases with respect to larger segments (L/D = 1/2 and 1) for each subsequent segment impact. However, despite a considerable degradation in penetration performance for low aspect ratio segments, they still penetrate significantly deeper than larger L/D = 1 segment aspect ratios.

Deep penetration of a large number of small aspect ratio segments, ($1/8 \leq L/D \leq 1$) are effected by: (1) the degraded penetration depth of each successive segment which increases the number of segments required to penetrate a specified depth; (2) a corresponding increase in expanded segment train length; and (3) a decrease in cavity diameter for successive segments as compared to the first. The optimal spacing(s) between segments is determined using the numerically computed penetration times, as opposed to an estimate based on penetration velocity or crater growth rate. The critical CAOA is defined as the value of impact yaw produced by the equivalent extended segment train, which just encounters the crater entrance wall, approximated by [23] as:

$$\gamma_c = \sin^{-1}\left[\frac{(D_c/D)-1}{(L/D)}\right] \tag{2}$$

For each segment, the numerical results to be used in Eqn. (2) are summarized in Table 6. The L/D = 1 equivalent column is the cumulative P/L for the same length as an L/D = 1 segment.

Table 6. Penetration Results for Each Segment

L/D	single (P/L)	L/D = 1 equivalent (P/L)	P/L segment (n)	D_{c1}/D (seg 1)	D_{cn}/D (seg n)	s_∞/D	$s_{0.9}/D$
1/8	4.35	2.96	2.5 (8)	1.61	1.38	2.37	1.9
1/4	3.75	3.21	2.95 (4)	1.98	1.60	3.1	2.1
1/2	2.90	2.74	2.58 (3)	2.33	1.95	3.6	2.0
1	2.20	2.20	2.20 (1)	2.50	2.34	3.4	1.9

For each L/D ratio, the critical CAOA angle and the total number of segments is estimated for a total penetration depth of 500 mm using two approaches. The traditional method is based on single segment performance and the *entrance* diameter, without consideration for any subsequent degradation in either. For L/D = 1/8, the total number of segments based on single segment results (n) is 500 mm/(4.35x2 mm) = 58. The total length based on a spacing s = 2.37D and the individual segment length L is 2277 mm for 5ъ L/D = 1 segments. The CAOA is $\gamma_c = \sin^{-1}(0.61D_{cl}/2L_{ext}) \cong 0.12°$. A more realistic spacing using the time to penetrate 90% of the final depth is s = 1.9D yields a total length of 1849 mm and critical angle of 0.15°.

We recompute the CAOA using the more practical method based on multiple segments, using the behavior of the first eight segments, and *then* assuming no *further* degradation. For the eighth segment and all subsequent segments, P/L = 2.5 and D_c/D = 1.4. The total number of segments is now 99 and the total length increases to 3914 mm with the critical CAOA decreasing to just 0.045°, also due to a smaller crater diameter. Again, based on the 90% timed spacing of s = 1.9D, the total extended length is 3177 mm and the critical angle becomes 0.055°.

Similar calculations are conducted for L/D = 1/4, 1/2 and 1 and the results are shown in Table 7 with L_{coll} denoting the collapsed length. For comparison, we utilize a long rod (P/L = 1.44) and compute an L/D equal to 21.7 to penetrate 500-mm RHA (denoted by M_{LR} in Table 7).

Based on this analysis, it is evident that the same mass of L/D = 1/2 and 1/8 segments penetrate approximately the same amount of RHA but segments of L/D = 1/2 have a significantly larger critical CAOA angle due to considerably shorter extended length and larger crater diameters. L/D = 1/4 appears to be a more optimal segment size requiring the least mass to penetrate 500-mm RHA according to this estimation procedure.

Table 7. Critical Angles for L/D = 1/8, 1/4, 1/2 and 1

L/D	n (P = 500 mm)	L_{coll}/D	M/M_{LR}	L_{ext}*	$\gamma_c(^\circ)$
1/8	99	12.375	0.57	3177	0.055
1/4	43	10.75	0.50	1583	0.174
1/2	25	12.50	0.58	956	0.465
1	16	16	0.74	707	0.570
Long rod (LR)	1	21.70	1	347	2.64

* Spacing is based on a time equal to 90% of the final penetration depth of first segment ($s_{0.9}/D$ in Table 6).

SUMMARY

Our calculations for L/D = 1 segments agree with observations in the literature showing little or no performance degradation (on the order of 10%) for multiple segment impacts and therefore the multiplicative formula of calculating final penetration depth based on the performance of the first segment is a reasonable approximation, disregarding the effects of segment spacing.

For L/D < 1 most of the experiments and calculations reported in the literature used single segments while multiple segment performance investigations concentrated on segment spacing. Our numerical investigation revealed an increasing amount of degradation as the segment aspect ratio was reduced due to reduced crater diameter (hence reduced crater volume per unit of penetrator impact energy). The calculations show a clear delineation between L/D = 1 segments and L/D = 1/8 segments as well a transitional behavior for L/D = 1/4 and 1/2 segments.

A set of calculations was conducted in which the remaining residue material was artificially removed (numerically) from the crater bottom before performing each subsequent calculation. These results clearly revealed that residual penetrator material is the primary cause of degradation. Additional calculations using tungsten segments impacting tungsten targets to represent a limiting case of a cumulation of residue revealed that a further degradation in P/L is possible as tungsten accumulates on the crater bottom. Entrance effects did not affect the penetration depth, but did significantly affect the crater diameter. We estimated the effects on a large number of segments required to penetrate 500-mm RHA by examining column angle-of-attack (similar to critical yaw). A train of L/D = 1/4 segments resulted in a minimal mass, 50% of the monolithic L/D = 21.7 long rod required, while both the L/D = 1/8 and L/D = 1/2 segments required approximately 57%. However, the critical CAOA is significantly larger for L/D = 1/2 (.465°) than for L/D = 1/8 (.055°), both of which are far less than the 2.64° critical angle-of-attack for the rod.

Despite all of these challenges and issues, the segmented penetrator performance for very small segments is still significantly more effective than long-rod penetrators. This is true for penetration depth with a criterion being either per unit collapsed length, mass, or energy. Significant implications of this numerical investigation are (1) the optimum segment aspect ratio shifts toward higher aspect ratios for multiple segments and may shift further still for very deep penetration; (2) the multiplicative penetration depth formula of Charters [2] does *not* apply to segments of very small L/D aspect ratio (< 1/2); (3) material remaining at the crater bottom is a critical

issue for very small segment penetration; (4) the crater diameter for subsequent segments is less than that of the first segment; and (5) engineering measures for deep penetration applications should be considered, and on a critical column angle-of-attack measure, smaller segments require extraordinary alignment to achieve their performance advantage. This suggests that, in practical deep penetration applications, larger L/D segments may perform better than smaller L/D segments.

Acknowledgment—This work was supported by the U. S. Army Research Laboratory (ARL) under contract DAAA21-93-C-0101.

REFERENCES

1. T. M. Kiehne, D. Orphal, M. J. Normandia, S. J. Bless and E. Stroebel, "Review of research on segmented rods, focusing on DARPA efforts," Institute for Advanced Technology, IAT.R0062 (November 1994).
2. A. C. Charters, "The penetration of rolled homogeneous armor by continuous and segmented rods at high velocity: theory and experiments," Report No. CR-87-1008, General Research Corporation, Santa Barbara, CA (December 1986).
3. D. Orphal and R. R. Franzen, "Penetration mechanics and performance of segmented rods against metal targets," *Int. J. Impact Engng.*, **10**, 427-438 (1990).
4. D. R. Scheffler, "Two-dimensional computer simulations of segmented penetrators," Report No. BRL-TR-3013, Army Ballistic Research Lab, Aberdeen Proving Ground, MD (July 1989).
5. J. A. Zukas, "Numerical simulation of semi-infinite target penetration by continuous and segmented rods," Report No. BRL-TR-3081, Army Ballistic Research Lab, Aberdeen Proving Ground, MD (February 1990).
6. R. Hunkler, "Numerical optimization of segmented rods," Report No. ISL-CO-242/90, Institut Franco-Allemand de Recherches, Saint-Louis, France (November 1990).
7. T. W. Bjerke, J. A. Zukas and K. D. Kimsey, "Penetration performance of disk shaped penetrators," *Int. J. Impact Engng.*, **12**(2) 263-280 (1992).
8. D. L. Orphal, C. E. Anderson, R. R. Franzen, J. D. Walker, P. N. Schneidewind and M. E. Majerus, "Impact and penetration by L/D ≤ 1 projectiles," *Int. J. Impact Engng.*, **14**, 551-560 (1993).
9. P. Naz, and H. F. Lehr, "The crater formation due to segmented penetrators," *Int. J. Impact Engng.*, **10**, 413-425 (1990).
10. A. Tate, "Engineering modelling of some aspects of segmented rod penetration," *Int. J. Impact. Engng.*, **9**(3) 327-341 (1990).
11. D. L. Orphal, C. E. Anderson, R. R. Franzen and S. M. Babcock, "Variation of crater geometry with projectile L/D for L/D ≤ 1," *Int. J. Impact Engng.*, **17**(2) 595-604 (1995).
12. W. R. Reinecke, "A comparison of RHA penetration and critical angle of attack among monolithic, segmenting, and extending tungsten rods at 2.5 km/s," 17th International Symposium on Ballistics, Midrand, South Africa (March 1998).
13. V. Hohler and A. Stilp, "Penetration performance of segmented rods at different spacing: comparison with homogeneous rods at 2.5-3.5 km/s," Proceedings of the 12th International Ballistic Symposium, San Antonio, TX (November 1990).
14. R. R. Franzen, J. D. Walker, D. L. Orphal, and C. E. Anderson, Jr., "An upper limit for the penetration performance of segmented rods with segment-L/D ≤ 1," *Int. J. Impact Engng.*, **15**(5) 661-668 (1994).
15. C. F. Cline, R. P. Gogolewski, J. E. Reaugh, A. S. Kubusov, B. L. Ford, G. D. Anderson and A. C. Holt, "Final report for the DARPA impact physics program: physics of high-velocity penetration, October 1986 - September 1988," LLNL Report, UCID-21728, M-3579, C-75, Livermore, CA (November 1988).
16. E. Hauver and A. Melani, "Behavior of segmented rods during penetration," BRL-TR-3129, Ballistic Research Laboratory, Aberdeen Proving Ground, MD (July 1990).
17. K. L. Frank, J. Zook, J. Spangler and M. Keele, "Experiments with high density segmented penetrator element," U. S. Army Research Laboratory, Aberdeen Proving Ground, MD (May 1988).
18. W. S. de Rosset and T. Sherrick, "Segmented rod performance at ordnance velocity," ARL-MR-291, U.S. Army Research Laboratory, Aberdeen Proving Ground, MD (February 1996).
19. Y. Partom, "Projectile-flow effect for long-rod penetration," 15th Int'l. Ballistic Symposium, Israel (1995).
20. W. Herrmann and J. S. Wilbeck, "Review of hypervelocity penetration theories," *Int. J. Impact Engng.*, **5**, 307-322 (1987).
21. D. L. Orphal, R. R. Franzen, S. M. Babcock and R. S. Snedeker, "Experimental measurements of penetration by L/D <1 projectiles," CRT-TR-3294-14, California Research & Technology, Titan Corp., Pleasanton, CA (1993).
22. M. J. Murphy, "Survey of the influence of velocity and material on the projectile energy/target hole volume relationship," 10th International Ballistic Symposium, San Diego, CA (1987).
23. T. W. Bjerke, G. F. Silsby, D. R. Scheffler and R. M. Mudd, "Yawed long-rod armor penetration," *Int. J. Impact Engng.*, **12**(2) 281-292 (1992).

PERGAMON

International Journal of Impact Engineering 23 (1999) 687–698

INTERNATIONAL JOURNAL OF IMPACT ENGINEERING

www.elsevier.com/locate/ijimpeng

HIGHLY OBLIQUE IMPACT AND PENETRATION OF THIN TARGETS BY STEEL SPHERES

D. L. ORPHAL

International Research Associates, Pleasanton, CA 94566, U. S. A.

Summary - Experiments were performed to measure the characteristics of the behind-target projectile fragments (residual projectile fragments) resulting from highly oblique impacts of steel spheres against thin laminated targets. Impact velocity was nominally 4.57 km/s (15,000 ft/s). Impact obliquity ranged from $\theta = 60°$ to $\theta = 80°$. Projectile mass was 222 g. The thickness of the two targets used corresponded to a ratio of target thickness, t, for normal impact to projectile diameter, d, of t/d = 0.6 and t/d = 0.3. The velocity of the residual projectile fragments was measured using multiple flash x-rays. The residual projectile fragments were soft captured and their total mass, as well as information on particle size distribution, was determined. © 1999 Elsevier Science Ltd. All rights reserved.

NOTATION

d	projectile diameter
M_O	mass of impacting projectile = 222g.
M_r	residual projectile mass
t	total thickness of target
v_f	velocity of individual penetrating projectile fragment
v_O	impact velocity
v_r	residual velocity, velocity of leading edge of fragment cloud
θ	impact obliquity

INTRODUCTION

Most previous research concerning hypervelocity impact against thin targets has focused either on normal impact (e. g. Piekutowski [1, 2, 3]) , or, if oblique impact, generally for obliquities less than 60°; an exception is the research reported by Ari and Wilbeck [4]. The objective of this work was to quantify the characteristics of the penetrating projectile fragments for very highly oblique impacts, obliquities from $\theta = 60°$ to $\theta = 80°$.

In this paper the portions of the impacting projectile that penetrate the target are designated as the "residual projectile", or "residual projectile fragments." Correspondingly, quantities such as velocity associated with the residual projectile fragments are denoted as residual quantities, i. e. residual velocity, v_r.

0734-743X/99/$ - see front matter © 1999 Elsevier Science Ltd. All rights reserved.
PII: S0734-743X(99)00114-1

EXPERIMENT DESIGN

The projectiles used in the experiments were 440 C stainless steel spheres with a Rockwell (C) hardness of 32 - 34. Projectile masses were 222 g (1.5 inch diameter), 25 g (0.72 inch diameter), and 1 g (0.25 inch diameter). Only the results for the 222 g projectiles are discussed.

Targets were composite plates of MX-2600 silica phenolic (SP) backed by 2024-T4 aluminum. A zero degree (flat) SP lay-up was used. The projectile impacts the SP surface of the targets. Target plane dimensions were 32 inches by 18 inches (81.28 cm by 45.72 cm) with the long dimension in the direction of impact. Two target thicknesses were used to give ratios of target thickness to projectile diameter for normal impact of t/d = 0.6 and t/d = 0.3. Thickness dimensions for the targets fabricated for the 222 g experiments are given in Table 1.

Table 1. Target plate specifications
Thicknesses (cm)

nominal t/d	*silica phenolic*	*bond*	*aluminum substrate*	*total thickness*	*areal density g/cm2 **
0.6	1.88	0.096	0.318	2.29	4.08
0.3	0.87	0.096	0.18	1.15	2.06

* Nominal densities: SP = 1.63 g/cm^3, bond = 1.63 g/cm^3, aluminum = 2.7 g/cm^3

Figure 1 is a schematic of the experiment geometry. Four flash x-rays were used uprange of the impact point to determine the impact velocity. Four 180 kv flash x-rays were positioned 12 inches, 19 inches, and 31 inches (30.48 cm, 48.26 cm, and 78.74 cm) downrange of the impact point. Three of these flash x-rays were aimed horizontally across the ballistic range and imaged the residual fragment cloud at three different times and positions. The fourth flash x-ray was orthogonal to the x-ray at the 31 inch location. These flash x-rays were used to measure the velocity of the residual projectile fragments. The relatively large separation between the impact and x-ray locations insured that the residual fragments were dispersed and that velocities could be measured for at least some of the individual projectile fragments.

Figure 2 shows the three flash x-rays from Test 5155 (t/d = 0.3, θ = 70°) and the cloud of residual projectile fragments (impact from right to left). The less dense (i. e. lighter) debris in the x-rays is from the target, primarily the aluminum substrate.

A device called the Residual Fragment Collector (RFC) was designed, fabricated, and very successfully used to soft capture the residual projectile fragments. The RFC was located 36 inches (91.44 cm) downrange from the impact point and 5 inches downrange from the orthogonal flash x-rays as shown in Figure 1. The face of the RFC was 48 inches by 24 inches (121.92 cm by 60.96 cm) and centered on the projectile flight line. The depth of the RFC was 18 inches (45.72 cm). The face area of the RFC was designed so that the entire cloud of residual projectile fragments would be "geometrically intercepted." Analysis of the orthogonal x-rays of the residual fragment cloud just in front of the RFC showed that this objective was achieved. In addition, inspection of the impact pattern in

the wax and the "lip" of the RFC face (see Figure 3) indicated that all the penetrating projectile fragments were being captured by the RFC.

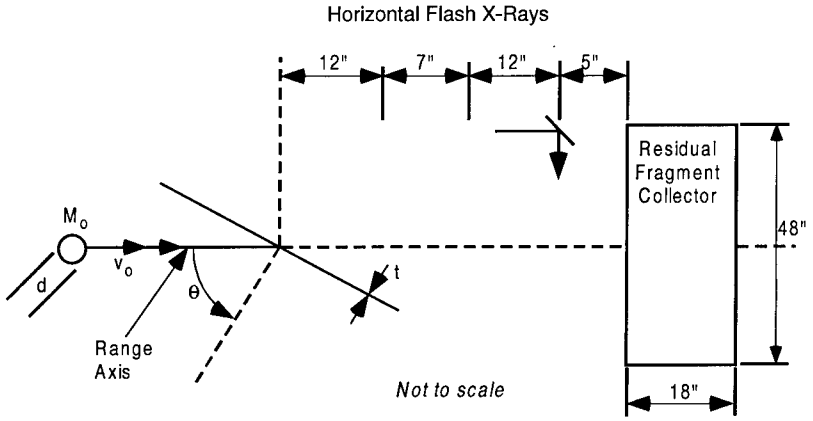

Fig. 1. Schematic of experiment geometry

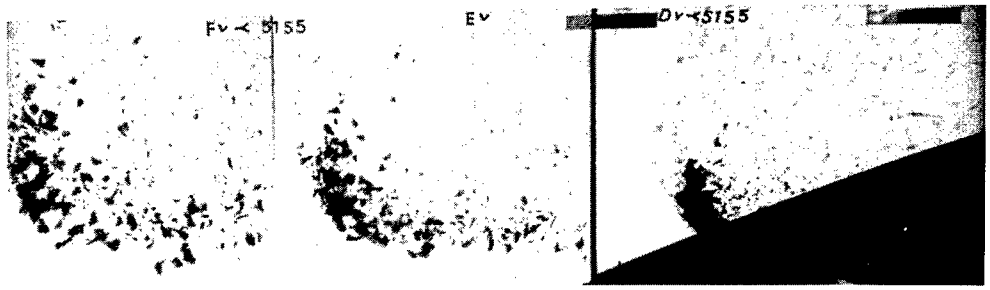

Fig. 2. Flash x-rays from Test 5155 (t/d = 0.3, θ = 70°)
showing residual fragment cloud

The RFC consisted of two components. The first component was a steel box made of 1/2 -inch (1.27 cm) thick steel plates welded and clamped together. This component remained in the range between tests. The second component was an aluminum box sized to just fit into the steel box (nominally 48 inches by 24 inches by 18 inches). The aluminum wall thickness was 0.064 inch (1.626 mm). The aluminum box was filled prior to an experiment to a depth of 12 inches (30.48 cm) with melted microcrystalline wax. The wax was allowed to cool and solidify in an ambient environment to a temperature of 60 - 80° F. The nominal density of the wax at 75° F was 0.93 g/cm^3. The wax-filled aluminum box was inserted into the heavy steel box and the RFC properly positioned in the range before each experiment. Following the experiment the wax-filled aluminum box, now containing the residual projectile fragments, was removed from the range. Figure 3 shows a wax-filled aluminum box after one of the experiments.

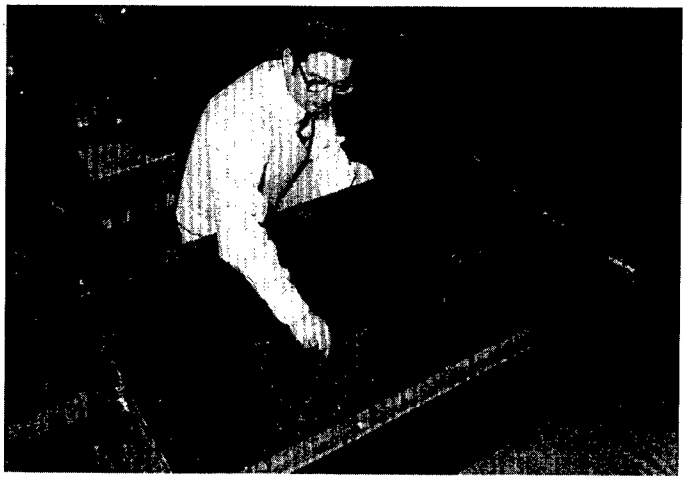

Fig. 3. Residual fragment collector

The wax was melted in a large oven and strained through a fine wire mesh to recover the residual projectile fragments, as well as target debris, etc. The metallic and non-metallic debris was separated magnetically. Mild steel debris (from the test support structure, x-ray cassette covers, etc.) was chemically separated from the 440 C stainless steel residual projectile fragments using nitric acid. The residual projectile fragments were then weighed, sorted, and analyzed.

Figure 4 shows the set up in the range with the target (A), target frame (B), make switch (C), and the RFC (D). The make switch was used to initiate the timing of the downrange flash x-ravs.

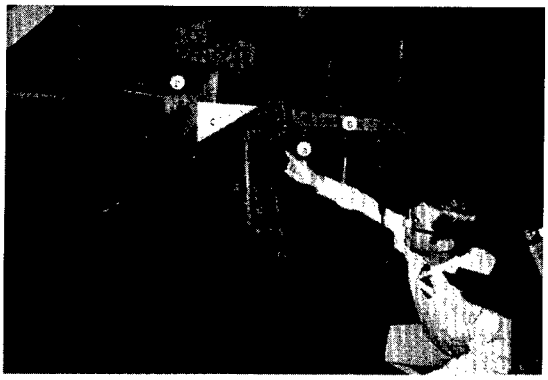

Fig. 4. Experimental set up in ballistics range

EXPERIMENTAL RESULTS

Residual Projectile Mass

An essential phenomenology associated with such highly oblique impacts is that a portion of the impacting projectile ricochets along the front surface of the target. This is shown in Figure 5 for a $\theta = 75°$ test. The impact is from left to right and the actual impact point is out of the view. The projectile fragments penetrating the target are in the upper part of the x-ray ("above" or downrange of the target). The ricocheting projectile fragments are in the lower left of the x-ray moving along the front surface of the target.

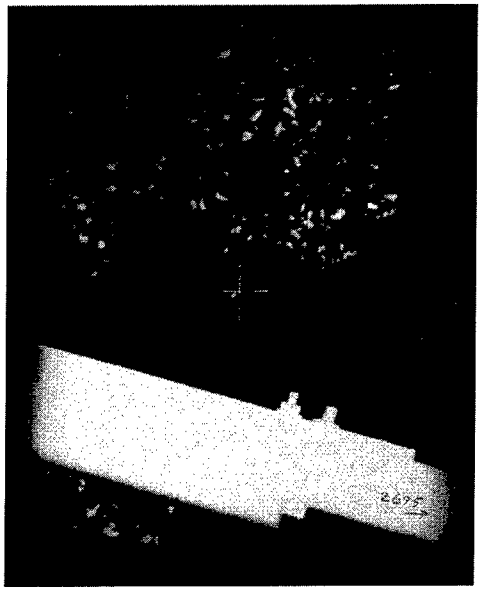

Fig. 5. Flash x-ray showing ricochet of some projectile fragments along front surface of target

As the impact obliquity increases, less of the projectile mass penetrates the target and more ricochets. This is shown in the two flash x-rays in Figure 6. The left-hand x-ray is from a $\theta = 60°$ experiment and the right-hand x-ray is from a 65° experiment. The reduction of the mass of the residual projectile as obliquity is increased from 60° to 65° is evident.

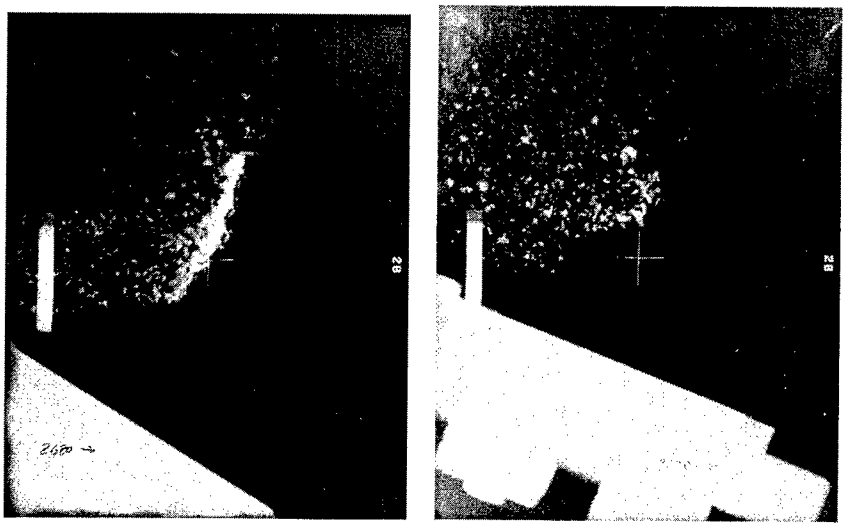

Fig. 6. Flash x-rays showing reduction in residual projectile mass as obliquity increases from 60° (left) to 65°

Figure 7 shows the ratio of the total mass of the residual projectile fragments recovered from the RFC, M_r, to the original projectile mass, M_O, versus impact obliquity. Data are shown for t/d = 0.6 and t/d = 0.3. As expected, the total mass of the residual fragments is greater for the thinner target. For q = 65° only about half the impacting projectile mass ($M_r/M_O \approx 0.5$) penetrates the target, the rest ricocheting off the front surface of the target. The residual mass ratio, M_r/M_O, decreases rapidly as obliquity increases, from about $M_r/M_O \approx 0.46$ at q = 65° to only about $M_r/M_O \approx 0.03$ at q = 80° for the t/d = 6 target.

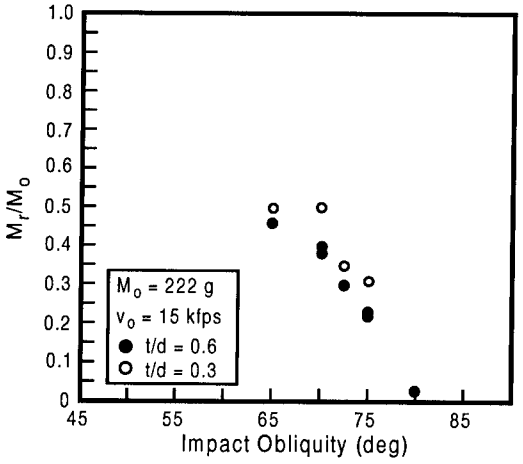

Fig. 7. Residual mass ratio vs. impact obliquity

Residual Projectile Fragment Size

The size distribution of the recovered residual projectile fragments was determined by sorting the fragments through standard sieves. Figure 8 shows the measured fragment size distribution for two nominally identical tests at t/d = 0.6 and θ = 70°. The fragment size distributions are essentially identical. In general it was found that fragment size distribution was remarkably repeatable.

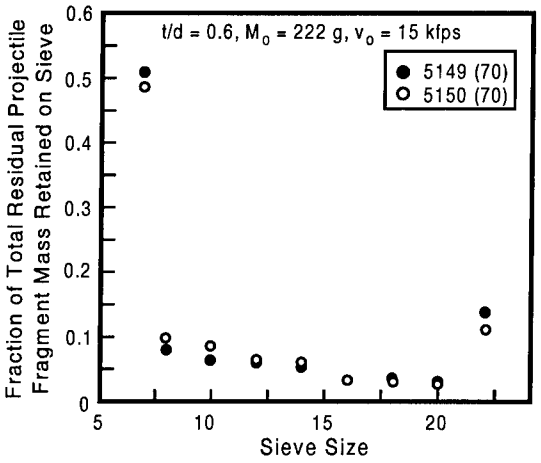

Fig. 8. Comparison of residual fragment size distributions for two nominally identical tests at 70 degrees obliquity

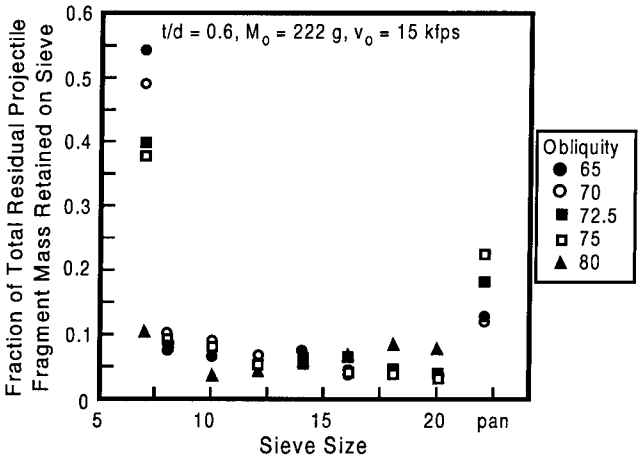

Fig. 9. Variation of residual projectile fragment size with impact obliquity

The percentage of the residual projectile mass with fragment sizes between 0.0331 inch (mesh opening of #20 sieve ≈ 0.84 mm) and 0.111 inch (mesh opening of #7 sieve ≈ 2.82 mm) was found to be essentially independent of impact obliquity. This is shown in Figure 9. However, the fraction of the total residual projectile mass in large fragments (> 0.111 inch/retained on #7 sieve) and in small fragments (< 0.0331 inch/pass #20 sieve) did vary

consistently with impact obliquity as shown in Figure 10. As impact obliquity increases from $\theta = 65°$ to $\theta = 80°$ the percentage of the total residual projectile fragment mass in large fragments (> 0.111 inch) decreases from about 55% to 10% or less while the percentage in small fragment (< 0.0331 inch) increases from about 10 - 15% to 50 - 70%.

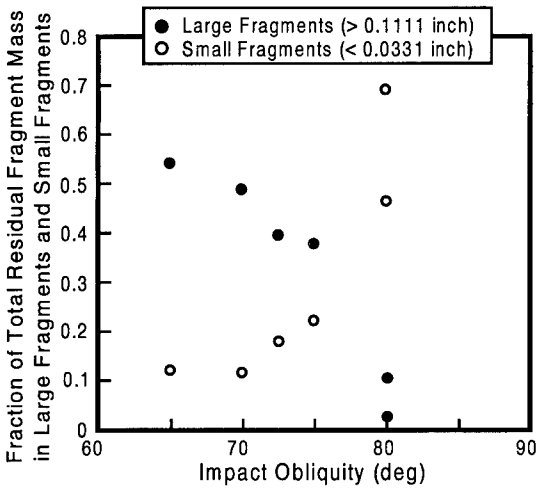

Fig. 10. Variation of the Percentage of Total Residual Fragment Mass in Large and Small Fragments with Impact Obliquity

Distribution of Mass in Residual Projectile Fragment Cloud

The mass distribution in the residual projectile fragment cloud was estimated using a digital analyzer to measure the fragment areas on the x-rays and "sphering" these areas to obtain volumes and thus masses. The absolute total fragment mass obtained in this manner compares only fairly with the total obtained from the recovered fragments from the RFC. This is mostly due to the fact that the fragments tend to be "plate-like", i.e. with a thin dimension, and not spherical. Also, often the fragment cloud is so dispersed only the front portion of it is visible in the x-rays. However, the relative fragment mass as a function of distance behind the cloud front is considered a reasonable estimate. The cumulative fraction of mass in the residual fragment cloud as a function of distance behind the leading edge of the cloud is shown in Figure 11 for four of the tests with impact obliquities ranging from 65° to 75°. The mass in the residual fragment cloud is concentrated just a few centimeters behind the leading edge. There appears to be a tendency for the mass to become somewhat more dispersed as the impact obliquity increases.

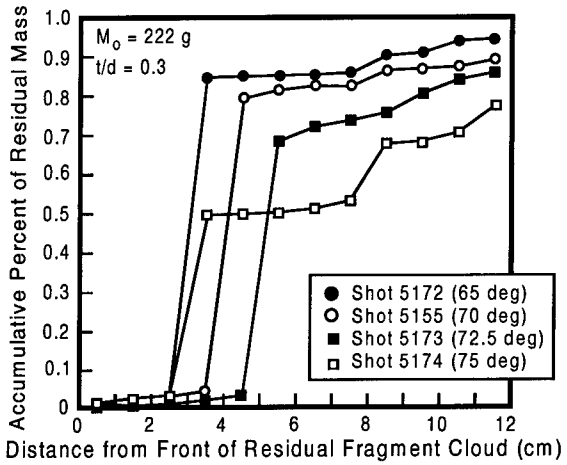

Fig. 11. Accumlative percent of residual mass vs. distance behind the front of residual fragment cloud

Residual Projectile Velocity

The velocity of the leading edge of the residual fragment cloud is designated the residual velocity, v_r. Figure 12 shows the measured residual velocity ratio, v_r/v_o, where v_o is the impact velocity, as a function of impact obliquity. For both targets v_r/v_o decreases rapidly as impact obliquity increases from 60° to 80°. For t/d = 0.6, v_r/v_o decreases from about 0.8 at 60° to only about 0.1 - 0.2 at 80°. The data for t/d = 0.3 exhibit similar behavior but, of course, higher values since the targets are thinner. The residual velocity data approximately collapse to a single curve if the independent variable is selected as the "line-of-sight" target thickness, t/(d cos θ), as shown in Figure 13 for these data. A linear least squares fit to the data gives:

$$v_r/v_o = 1.058 + (-0.255)\ t/(d \cos \theta) \qquad (r = -0.983)$$

where r is the correlation coefficient.

Distribution of Fragment Velocity in Residual Projectile Fragment Cloud

At the x-ray locations the cloud of residual projectile fragments was sufficiently dispersed that some individual fragments could be identified in each x-ray. The velocity of these individual fragments was determined. Figure 14 shows the velocity of these individual fragments v_f, normalized by the impact velocity, versus the distance, x, of the fragment behind the leading edge of the cloud for two tests. The tests have a t/d = 0.3 and impact obliquities of 65° and 72.5°. The fragment velocity decreases very slowly with distance behind the leading edge of the cloud and the variation is remarkably linear. Linear least squares fits to this data give:

5172 (65°)	$v_f/v_o = 0.83 - 0.0048$ x (cm)	(r = -0.6580)
5173 (72.5°)	$v_f/v_o = 0.76 - 0.0105$ x (cm)	(r = -0.9775)

where r is the correlation coefficient.

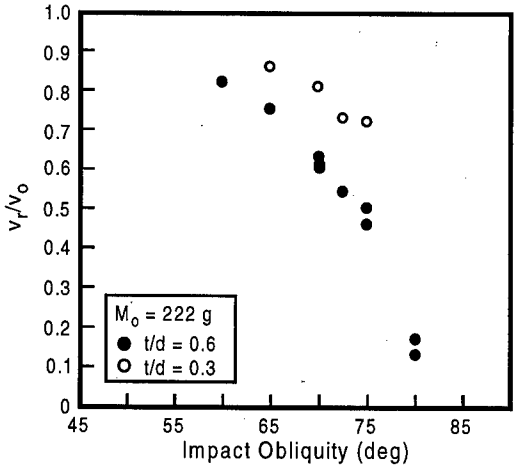

Fig. 12. Residual velocity ratio vs. impact obliquity

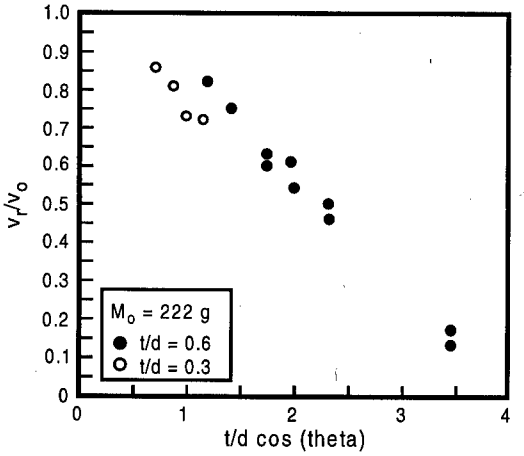

Fig. 13. Residual velocity ratio vs. line of sight target thickness

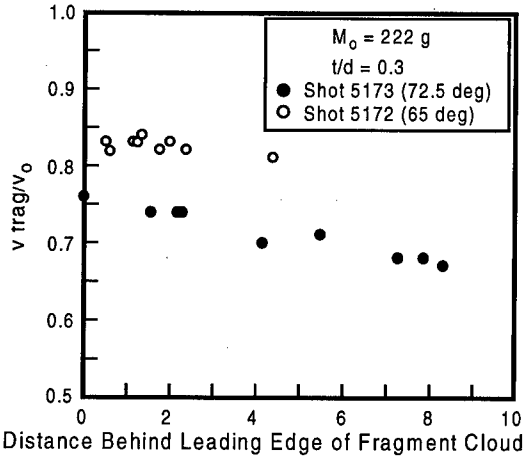

Fig. 14. Fragment velocity vs. distance behind leading edge of the fragment cloud

Momentum and Kinetic Energy of Residual Projectile

The mass in the residual projectile fragment cloud is concentrated very near the front of the cloud (Fig. 11) and the velocity of the fragments decreases very slowly with distance behind the front of the cloud (Fig. 14). Therefore, to a good approximation the momentum and kinetic energy in the cloud of residual projectile fragments are:

$$\text{Residual momentum} = M_r v_r$$

$$\text{Residual kinetic energy} = 1/2\, M_r v_r^2$$

Figure 15 shows the variation in the normalized residual momentum and kinetic energy, $(M_r v_r/M_o v_o)$ and $(M_r v_r^2/M_o v_o^2)$, respectively, as a function of impact obliquity for the t/d = 0.6 experiments. The normalized residual momentum, $M_r v_r/M_o v_o$, decreases from only about 0.35 for $\theta = 65°$ to about 0.1 at 75° and essentially zero at 80°. The kinetic energy of the residual projectile cloud is only about 25% of the original impact kinetic energy at an impact obliquity of 65°. The residual kinetic energy decreases rapidly as the impact obliquity increases beyond 65° and is essentially zero at 80°.

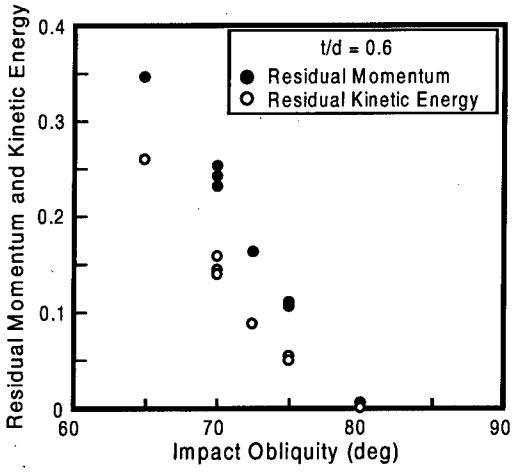

Fig. 15. Variation of normalized momentum and kinetic energy of residual projectile fragment cloud

CONCLUSIONS

These experiments covered a limited range of parameters. Targets were silica phenolic over aluminum with t/d = 0.6 and 0.3; corresponding areal densities were about 4 g/cm^2 and 2 g/cm^2. Projectiles were 440 C stainless steel spheres. Impact velocity was nominally 4.57 km/s (15,000 ft/s). With these limitations in mind, the experiments show:

1. At an impact obliquity of 65° only about half of the projectile mass penetrates the target, the other half ricocheting along the front surface.

2. The fraction of the projectile mass penetrating the target, M_T/M_O, decreases rapidly from about 0.5 at 65° obliquity to essentially zero at 80°.

3. The mass in the residual projectile fragment cloud is concentrated very near the front of the cloud.

4. Size distributions of the residual projectile fragments are quite repeatable.

5. For the t/d = 0.6 targets the fraction of the residual projectile mass represented by large (> 0.111 inch) fragments decreases from about 50% at 65° obliquity to just a few percent at 80°. At the same time the fraction of the residual projectile mass represented by small fragments (<0.0331 inch) increases from about 10% at 65° to nearly 70% at 80°.

6. The velocity of the front edge of the cloud of residual projectile fragments, v_r, decreases rapidly as impact obliquity is increased from 60° to 80°. For t/d = 0.6 the normalized residual velocity, v_T/v_O, decreases from about 0.8 at 60° obliquity to about 0.15 at 80°. The variation of v_T/v_O for t/d = 0.3 is similar but the values of v_T/v_O are about 30 percent or so higher than for the t/d = 0.6 targets.

7. The velocity of individual fragments in the residual projectile fragment cloud decreases very slowly with the distance of the fragment from the front edge of the cloud. The variation of fragment velocity with the distance of the fragment behind the cloud front appears to be linear.

Acknowledgment - These experiments were performed at Range G of the U. S. Air Force Arnold Engineering and Development Center. The assistance of Richard Raper, AEDC Project Engineer, and the entire Range G crew is gratefully acknowledged. The assistance of my wife, Viki, in preparing the manuscript is very much appreciated.

REFERENCES

1. A. J. Piekutowski, Characteristics of debris clouds produced by hypervelocity impact of aluminum spheres with thin aluminum plates, *Int. J. Impact Engng.* **14**, 573 -586 (1993).
2. A. J. Piekutowski, Fragmentation of a sphere initiated by hypervelocity impact with a thin sheet, *Int. J. Impact Engng.* **17**, 627 - 638 (1995).
3. A. J. Piekutowski, Effects of scale on debris cloud properties, *Int. J. Impact Engng.* **20**, 639 - 650 (1997).
4. Nasit Ari and J. S. Wilbeck, Debris fragment characterization in oblique hypervelocity impact, *Int. J. Impact Engng.* **14**, 37 - 48, (1993).

PERGAMON

International Journal of Impact Engineering 23 (1999) 699–710

INTERNATIONAL JOURNAL OF IMPACT ENGINEERING

www.elsevier.com/locate/ijimpeng

STREAMLINE REVERSAL IN HYPERVELOCITY PENETRATION

DENNIS L. ORPHAL* and CHARLES E. ANDERSON, JR.**

*International Research Associates, 4450 Black Ave., Pleasanton, CA 94566 USA; **Southwest Research Institute, Engineering Dynamics Department, P. O. Drawer 28510, San Antonio, TX 78228 USA

Summary—We report a direct observation of the "streamline" reversal of eroded rod material proposed by Allen and Rogers in 1961 [1]. Allen and Rogers suggested that the "turning" of high-velocity long-rod penetrator material at the target interface could be viewed as a reversal of the direction of a "streamline" with only a change of sign in the velocity. Allen and Rogers' streamline reversal model has two important consequences. First, the eroded debris has a speed of $v_d = 2u - v$ relative to the target, where v is the impact velocity and u is the speed of penetration of the rod relative to the target. Secondly, a consequence of $v_d = 2u - v$ is that the length of the rod debris, ℓ_d, is given by the difference in the initial length of the rod, ℓ_o, and the remaining length of the rod, ℓ, i.e., $\ell_d = \ell_o - \ell$. Results of a time-resolved experiment for a tungsten penetrator into a polycarbonate target at 3.61 km/s and a corresponding numerical simulation are consistent with streamline reversal. Numerical simulations are then used in a parametric study to investigate the effects of various density ratios between penetrator and target materials. © 1999 Elsevier Science Ltd. All rights reserved.

NOTATION

d	projectile diameter	u	penetration velocity
ℓ	instantaneous length of projectile	u_{hydro}	hydrodynamic penetration velocity
ℓ_o	initial length of projectile	u_{sim}	penetration velocity from simulation
ℓ_d	instantaneous length of debris	v	impact velocity (tail velocity)
ℓ_{d1}	difference in depth of rod and depth of debris	v_d	debris velocity
ℓ_{d2}	measured length of debris	$(v_d)_{sim}$	debris velocity from simulation
p	penetration depth	v_{sim}	tail velocity from simulation
p_d	depth of rear of debris	Y_p	projectile strength
R_t	target resistance	β	$[\rho_t/\rho_p]^{1/2}$
t	time	ρ_p	projectile density
		ρ_t	target density

INTRODUCTION

In 1961, Allen and Rogers [1] suggested a model for high velocity penetration. In a reference frame stationary with respect to the penetrator-target interface, they viewed the flow of the penetrator material as a simple reversal of a streamline.. For the case of hydrodynamic penetration, if the impacting rod has a higher density than the target, the eroded rod material has a residual velocity, v_d, into the target. If v_d is sufficiently high, the eroded rod material can continue to penetrate the

0734-743X/99/$ - see front matter © 1999 Elsevier Science Ltd. All rights reserved.
PII: S0734-743X(99)00115-3

target after the original rod has been completely eroded away or "consumed". Allen and Rogers named the additional target penetration due to the eroded rod material "secondary" or "residual" penetration. Allen and Rogers reported post-test experimental data for depth of penetration that they believed showed this secondary penetration for high velocity (> 2 km/s) impacts of gold rods into aluminum (7075-T6) targets.

Streamline reversal of the penetrator material results in several phenomenon which may be quantitatively verified by both experiment and numerical simulations. This paper reports the results of both a hypervelocity penetration experiment and a series of numerical simulations performed to examine the Allen and Rogers streamline reversal hypothesis.

THEORY

Allen and Rogers [1] proposed that the flow of penetrator material into and out of the penetrator-target interface could be modeled as a reversal of a streamline in steady-state penetration. In streamline reversal, the direction of the flow changes, but the velocity magnitude remains constant. The flow of penetrator and target material in the laboratory reference frame are shown in Fig. 1(a). Figure 1(b) shows the same event in a reference frame stationary with respect to the penetrator-target interface (i.e., this reference frame is moving at a speed of u with respect to the laboratory frame). The penetrator material flows into the interface at a velocity of (v-u). If the flow of penetrator material is modeled as a streamline reversal then the velocity of the eroded penetrator material or "debris", v_d, is $-(v-u)$. In the laboratory frame

$$v_d = -(v-u)+u = 2u-v \tag{1}$$

Equation (1) is a quantitative result that will be examined experimentally for one case, and for several cases using numerical simulations.

If hydrodynamic behavior is assumed, several other quantitative results may be derived from the Allen and Rogers model. For steady-state hydrodynamic behavior:

$$u = \frac{v}{1+\beta} \tag{2}$$

where $\beta = [\rho_t/\rho_p]^{1/2}$. Substituting Eqn. (2) into (1), v_d is written in terms of the impact velocity and the square root of the density ratio:

$$v_d = \frac{v(1-\beta)}{(1+\beta)} \tag{3}$$

Therefore, for hydrodynamic penetration and $\rho_t = \rho_p$ ($\beta = 1$), $v_d = 0$. For $\rho_t < \rho_p$ ($\beta < 1$), v_d is positive and the eroded penetrator material or debris has a net velocity into the target. For $\rho_t > \rho_p$ ($\beta > 1$), v_d is negative and the penetrator debris has a velocity in the opposite direction of the penetrator. These results are examined below.

Finally, in the stationary frame, the penetrator is being eroded at the rate (u - v) and the eroded penetrator debris is increasing in length at the same rate, (v - u). Thus, at any time, the sum of the length of the remaining penetrator, ℓ, and the length of the debris, ℓ_d, is given by:

$$\ell + \ell_d = \ell_o = \text{constant.} \tag{4}$$

EXPERIMENT

An experiment was performed with a tungsten rod (ρ_p = 19.3 g/cm^3) penetrating a Zelux target (ρ_t = 1.2 g/cm^3). The impact velocity was 3.61 mm/μs (km/s). The experiment was performed in

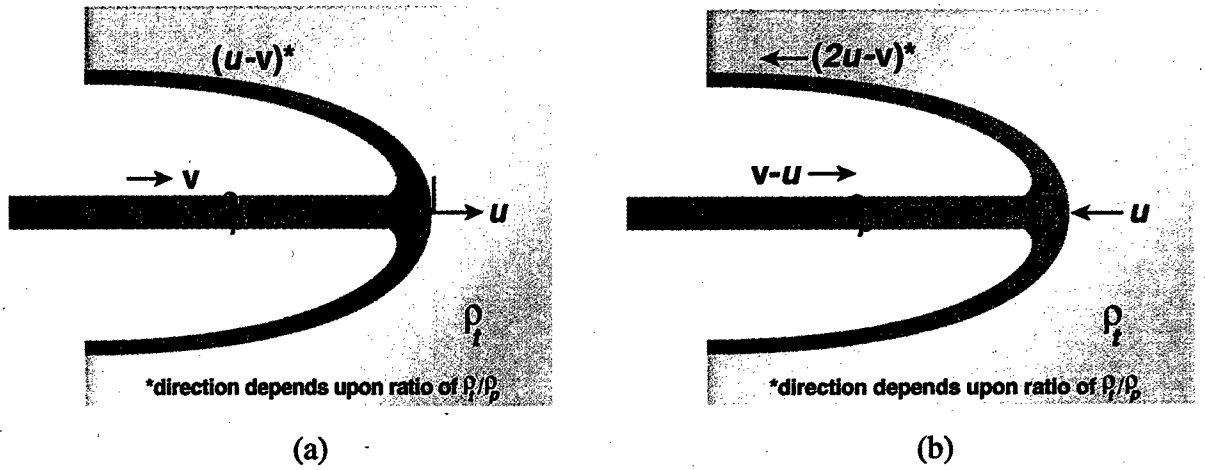

Fig. 1. Schematic of penetration process in (a) the laboratory frame, and (b) in the steady-state reference frame.

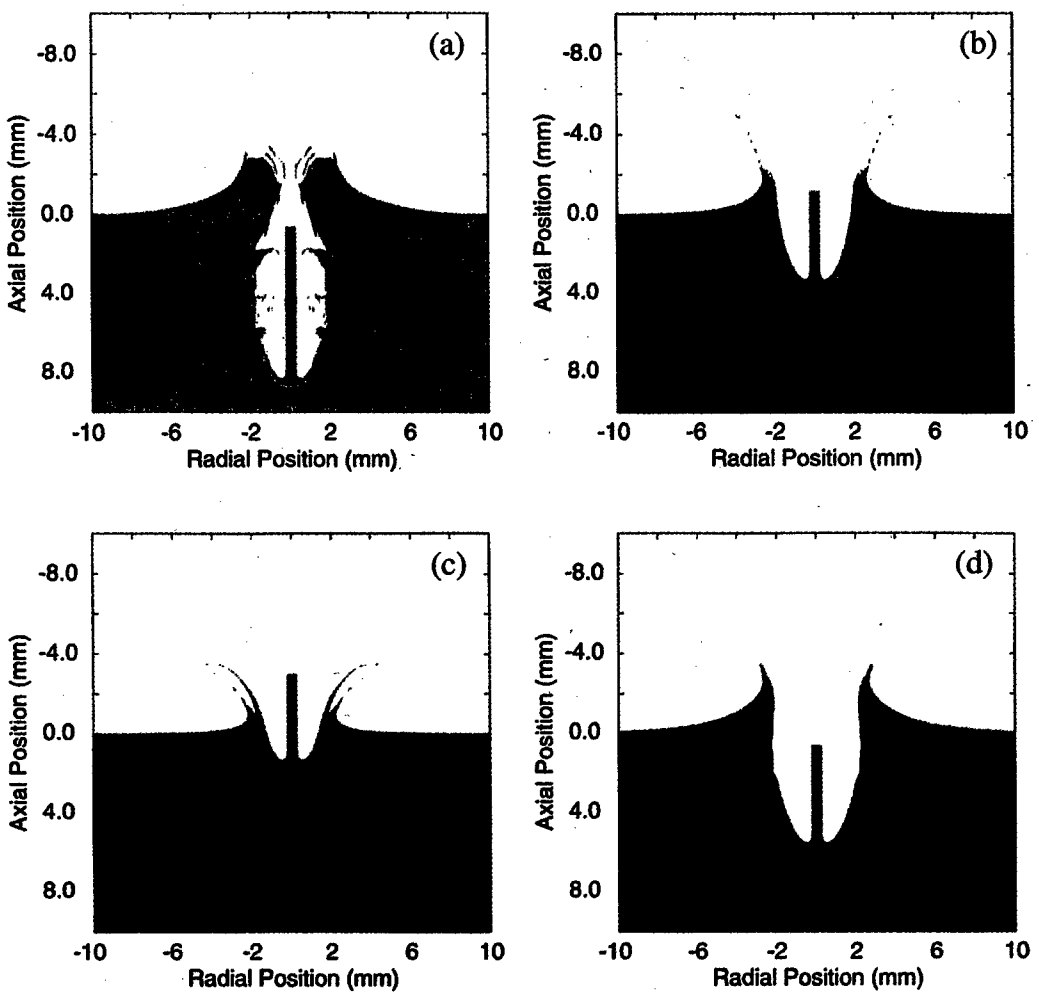

Fig. 5. Material plot of penetration results: (a) tungsten into Lexan (t = 3.0 μs); (b) steel into steel (t = 2.5 μs); (c) aluminum into steel (t = 2.0 μs); (d) tungsten into steel (t = 3.0 μs).

the reverse ballistic mode. The tungsten rod had a diameter $d = 0.508$ mm, length $\ell_o = 50.8$ mm, and thus $\ell_o/d = 100$. The diameter of the target was 25.4 mm; the target length was 114.3 mm.

Primary instrumentation for the experiment was four flash X-rays; the X-ray shadowgraphs are shown in Fig. 2. The first X-ray shows the rod before impact. The remaining three X-rays show the tungsten rod penetrating the Zelux target. The eroded tungsten is obvious in the X-rays. The outer diameter of the eroded tungsten debris is seen to be quite constant and about equal to twice the diameter of the rod.

Measurements from the X-rays are summarized in Table 1. The absolute time of impact (i.e., zero time) is not known for this experiment so the times given in Table 1 are only relative to the first X-ray which shows the projectile and target prior to impact. Times between X-rays are accurate to less than 1 μs. Length measurements were made with a millimeter scale and the accuracy is estimated to be ± 0.5 mm.

Figure 3 shows the depth of penetration, p, and the depth of the rear of the debris, p_d, into the target versus time, where zero-time is taken as the time of the first X-ray, which is actually slightly before impact. The slopes of the two curves are very interesting. Linear, least-squares fits to the penetration-time data are shown as solid lines. The slopes of the curve fits provide the penetration velocity, u, and the debris velocity, v_d; these values are 2.72 ± 0.15 mm/μs and 2.10 ± 0.14 mm/μs, respectively. Assuming that the penetration speed is ideally hydrodynamic, then Eqn (2) gives the hydrodynamic penetration velocity: $u_{hydro} = 0.80v = 2.89$ mm/μs. The slope of the dashed line in

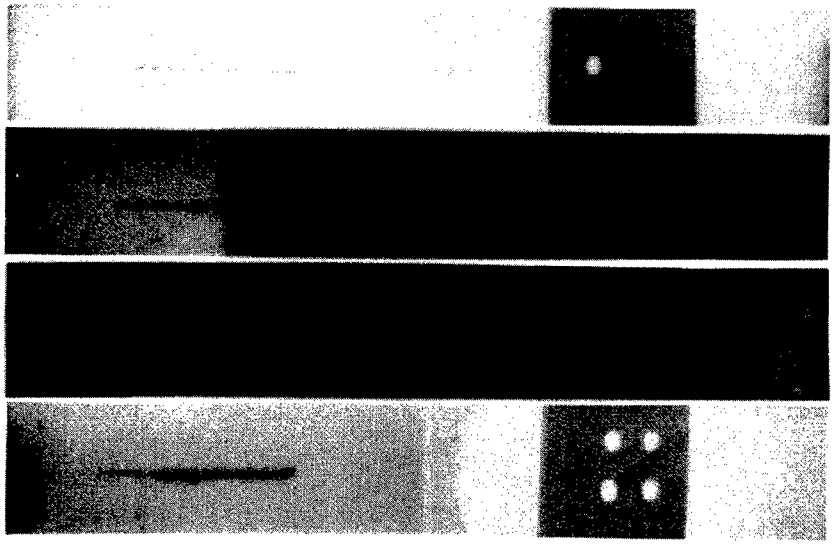

Fig. 2. X-ray shadowgraphs of the experiment.

Table 1. Summary of experimental results

X-Ray	Time (μs)	p (mm)	p_d (mm)	ℓ (mm)	$\ell_{d1} = p - p_d$ (mm)	$\ell_{d1} + \ell$ (mm)	$\ell_d \equiv \ell_{d2}$ (mm)	$\ell_{d2} + \ell$
2	12.2	28.2	22.9	44.1	5.3	49.4	5.3	49.4
3	24.8	65.7	52.5	35.0	13.2	48.2	13.6	48.6
4	37.2	96.1	75.4	27.5	20.7	48.2	19.5	47.0

Fig. 3 is u_{hydro}. The experimental penetration velocity is within 6% of that given by steady-state hydrodynamic theory. The velocity of the debris, dp_d/dt, is into the target, as expected for the condition $\rho_p > \rho_t$. Furthermore, the debris velocity of 2.10 mm/μs agrees reasonably well with that expected from the streamline reversal model, assuming hydrodynamic penetration velocity, $v_d = 2u - v = 2.16$ mm/μs, shown as the dotted line in Fig.3.

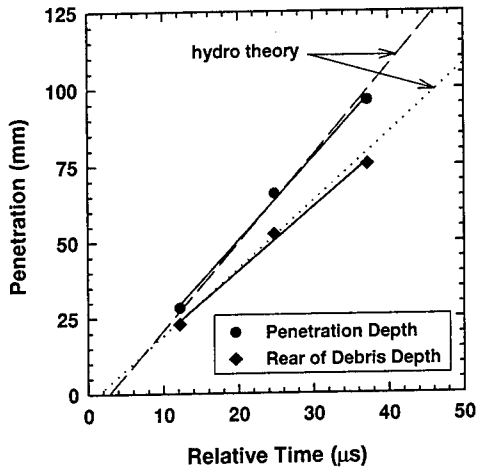

Fig. 3. Depth of eroded rod debris with time: Experimental data compared with Allen and Rogers [1] streamline reversal model.

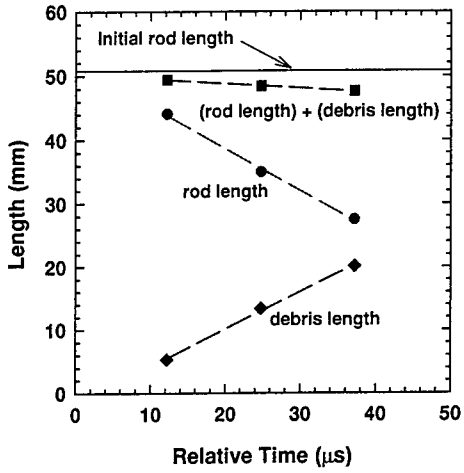

Fig. 4. The length of the rod and eroded debris versus time.

Table 1 also lists the length of the remaining rod, ℓ, and the length of the eroded rod debris, ℓ_d. The length of the eroded rod debris was measured two ways. First, the difference between the depth of the rod and the depth of the rear of the debris, ℓ_{d1}, was measured. Second, the length of the debris was measured directly using a millimeter scale, ℓ_{d2}. Using these two measurements, the sum of the length of the remaining rod and length of the debris was determined ($\ell_{d1} + \ell$ and $\ell_{d2} + \ell$). These two measures agree reasonably well with one another and the differences are an indication of measurement error. The length of the remaining rod and the length of the eroded rod debris are plotted in Fig. 4, along with their sum $\ell_d + \ell$. The size of the symbols is slightly larger than the uncertainty in the measurements (and thus, for purposes of the graph, there is no distinction between ℓ_{d1} or ℓ_{d2}). In all cases, the sum $\ell_d + \ell$ is slightly less, about 3 to 7 percent, than the length of the original rod, shown as the solid horizontal line in Fig. 4. The difference between the sum $\ell_d + \ell$ and ℓ_o appears to increase with time. This probably reflects effects of the strength of the tungsten rod.

It has already been noted that the experimental penetration velocity is less than that predicted from hydrodynamic theory, so the slight decrease in $\ell_d + \ell$ with time is the second observation where there is a slight deviation with hydrodynamic theory. These observed "discrepancies" with hydrodynamic theory are probably not "experimental error" but, instead, are real; they are attributed to the effects of strength. It is clearly demonstrated in Ref. [2] that the effects of strength can be observed experimentally and numerically at impact velocities as high as 4.5 km/s over a wide range of projectile and target materials. The effects of strength are observed in the results from numerical simulations, which will be discussed in the next section.

In summary, the experiment closely approximates hydrodynamic penetration and matches the essential predictions of the streamline reversal model proposed by Allen and Rogers for this case. Specifically, for $\rho_p > \rho_t$: 1) the velocity of the eroded rod debris is into the target; 2) the velocity of the eroded debris closely approximates $v_d = 2u - v$; where u is the hydrodynamic penetration

velocity, Eqn. (2), and 3) the sum of the length of the remaining rod and the eroded rod debris is approximately constant and closely approximates $\ell_d + \ell = \ell_o$.

NUMERICAL SIMULATIONS

Computational Methodology

The nonlinear, large deformation, multi-material Eulerian wavecode CTH [3] was used to simulate the experiment. The 2-D cylindrically symmetric option of CTH was used. CTH uses a van Leer algorithm for second-order accurate advection [4] that has been generalized to account for a non-uniform and finite grid, and multiple materials [3]. CTH also has an advanced material interface algorithm for the treatment of mixed cells [3]. A Mie-Grüneisen equation of state was used to compute the thermodynamic material response except for one case, which is discussed below. CTH allows the flow stress to be a function of strain, strain rate, and temperature [5-6]. Constitutive behavior for the materials was modeled as elastic-viscoplastic, with the Johnson-Cook [7] model used to determine the flow stress σ.

Square zoning, with 10 zones across the projectile radius, defined the computational grid. The radius of the projectile used in the experiments and the simulations was 0.254 mm, thus giving a zone dimension of 0.0254 mm on a side. The zoning was square into the target for 20 mm, and radially for 3.556 mm. Beyond these dimensions, the zoning was allowed to increase at a rate of 5.5% to the dimensions of the target. Although the projectile used in the experiment had an ℓ_o/d of 100, the numerical simulations were conducted with an aspect ratio of 20 to minimize computational time. Quasi-steady-state penetration was achieved in all the numerical simulations. The target was stationary in the simulations, and the projectile was given an initial velocity of 3.61 mm/μs (the experiment was conducted in the reverse ballistics mode).

Four numerical simulations were conducted and analyzed. The first computation simulated the experiment. Then a parametric study was conducted to examine the effects of changes in penetrator and target densities. The four simulations are summarized in Table 2. Zelux is a tradename for a polycarbonate material, so the constitutive properties for Zelux were approximated using Lexan, another polycarbonate material for which the constitutive parameters have been obtained. Assuming hydrodynamic theory applies, the last column gives the debris velocity, where a positive velocity means that the velocity is in the same direction as the projectile. The material properties used in the simulations are summarized in Table 3.

Table 2. Matrix of numerical simulations

Run Number	*Projectile*	*Target*	*Impact Velocity*	*Density*	*Debris Velocity*
1	tungsten	Lexan	3.61 mm/μs	$\rho_p > \rho_t$	$v_d > 0$
2	steel	steel	3.61 mm/μs	$\rho_p = \rho_t$	$v_d = 0$
3	aluminum	steel	3.61 mm/μs	$\rho_p < \rho_t$	$v_d < 0$
4	tungsten	steel	3.61 mm/μs	$\rho_p > \rho_t$	$v_d > 0$

Tungsten into Lexan

Several different simulations of the experiment were performed because the computational results did not agree qualitatively with the experimental X-ray shadowgraphs. The penetration channel was

Table 3. Material properties

Material	*Density* (g/cm^3)	*Bulk Sound Speed* ($mm/\mu s$)	*Poisson's Ratio* (-)	*Initial Flow Stress* (GPa)	*Melt Temperature* (K)
Lexan	1.20	1.93	0.45	0.0759	558
tungsten	19.3	3.85	0.30	1.50	3660
steel	7.85	4.50	0.29	0.793	1818
aluminum	2.70	5.24	0.33	0.265	925

considerably overpredicted, and there was extensive fracturing of the target. In these initial simulations, the Mie-Grüneisen equation of state was used. It was realized that too much energy was going into penetration channel growth; in order for the simulations to mimic the experiment, an additional sink for projectile kinetic energy was required. It is well-known that the Mie-Grüneisen EOS is not appropriate for distended liquid states and vaporization [8]. Considerable energy is absorbed in vaporization, and polycarbonate has a low vaporization temperature. With the assistance of Hertel [9], a tabular EOS for Lucite was obtained [10].[1] Inclusion of vaporization dramatically decreased the diameter of the penetration channel. A computational result at 3 μs is shown in Fig. 5(a). Target material is denoted by the blue color in Fig. 5, and the tungsten projectile is denoted by the red color. The target material is melted and vaporized in and around the penetration channel. The simulations show that the penetration channel is filled with vaporized target material. Note that the eroded debris is mostly near the bottom of the crater; this will be contrasted with other simulations in the next section.

The tail and nose (penetration) velocities as a function of normalized depth of penetration are displayed in Fig. 6. The calculations were only carried out to 9 μs; the depth of penetration is approximately 25 mm at this time, so the experimental results are later in the penetration process. Although the simulation could have been carried further in time, it is quite obvious that penetration achieves and maintains a quasi steady-state velocity after approximately two projectile diameters of penetration. Also displayed in the figure is the hydrodynamic penetration velocity calculated from Eqn. (2). Agreement is quite good between hydrodynamic theory and the simulation results. However, hydrodynamic theory does not account for strength effects, such as deceleration of the tail [11-12], which ultimately affects the penetration velocity. Strength effects do manifest themselves over time (and penetration depth). The tail velocity decreases due to elastic deceleration, and the penetration velocity slowly decays below that of hydrodynamic theory. Thus, the simulations are consistent with the experimental results since the experimental data are for much later times.

Massless tracer particles were placed throughout the projectile to track the material history of penetrator material. A tracer particle initially 4 project diameters from the projectile-target interface, located approximately halfway between the projectile centerline and the outer edge, is used as a representative Lagrangian material point to observe the penetration dynamics of projectile material. The axial and radial velocities versus a nondimensional time are plotted in Fig. 7. A nondimensional time is defined (tv/d) so that the results are nominally independent of the small scale of the experiment. The material point has an initial axial velocity of 3.61 mm/μs (v), but the forward velocity decreases as the "particle" approaches the projectile-target interface. Concurrently, the

[1] A tabular EOS for a polycarbonate material was not available. Although Lucite is a polymerized methyl methacrylate, it has essentially the same density as Lexan–1.19 versus 1.20–and it has a low sublimation temperature. The high temperatures result from plastic work; therefore, the constitutive model for Lexan was used so that the effects of strength and plastic work are computed correctly. Although there are probably inaccuracies, the effect of vaporization is taken into account to at least first order.

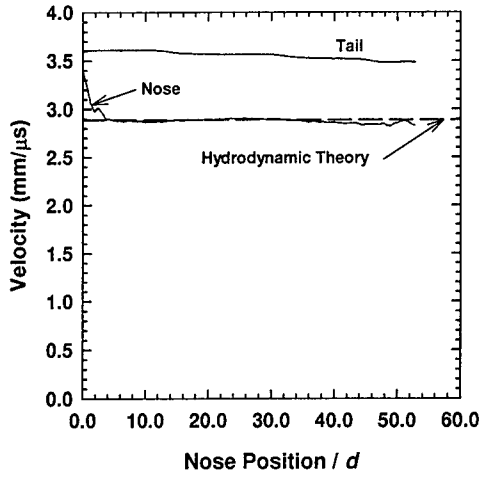

Fig. 6. Tail and penetration velocities versus normalized penetration: tungsten into Lexan simulation.

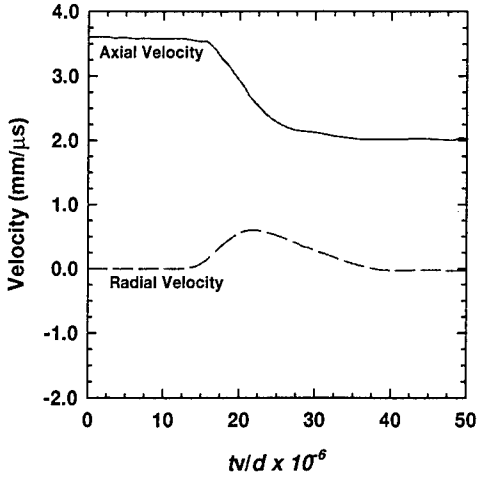

Fig. 7. Axial and radial velocities versus normalized time for tracer particle: tungsten into Lexan simulation. See text for initial location of the tracer particle.

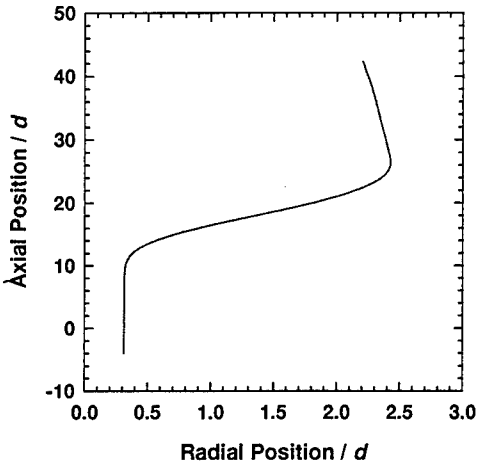

Fig. 8. Lagrangian trajectory of tracer particle: tungsten into Lexan simulation.

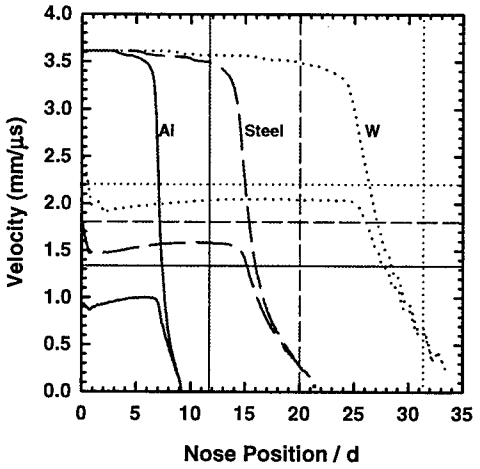

Fig. 9. Tail and penetration velocities verus normalized depth of penetration: parametric study.

radial velocity increases as the particle moves out to the edge of the penetration channel that is established by the deformation flow. Once to the walls of the penetration channel, the radial velocity becomes almost zero (actually, the radial velocity is very slightly negative due to an overall elastic rebound of compressed target material [12]). The erosion debris has an overall forward velocity of approximately 2.0 mm/μs, in nominal agreement with experiment.

The time integral of the axial and radial velocities specifies the trajectory, i.e., streamline, of the tracer particle, Fig. 8. In this figure, the radial position 0.0 is the projectile-target centerline. As the projectile penetrates the target, the tracer particle moves forward axially until it is accelerated radially. The radial displacement scale is highly magnified (by a factor of 20) compared to the axial

displacement scale. Near the end of the trajectory, the outward radial flow reverses since the radial velocity is very slightly negative. Again note that the material tracer continues to move in the direction of penetration, i.e., into the target after it has entered into the erosion debris field.

Parametric Study

As noted earlier, a parametric investigation was conducted where the target material was kept constant and the projectile material was changed so as to explore the effect of different density ratios between the projectile and target. These computer simulations are summarized in Table 2. In all cases, the target was an armor-like steel with a Rockwell C hardness 30. The impact velocity was kept at 3.61 mm/μs. A time snapshot of each of the simulations is shown in Fig. 5. The projectile is approximately half eroded in Figs. 5(b-d); because the penetration velocities depend upon the density ratio, the times are different for each of the figures. The discussion concerning the velocity of the erosion products (debris), relative to Eqn. (3) and the last column of Table 2, is visualized in the figures. For steel into steel, the debris lines the penetration channel from the impact surface. The aluminum erosion products are being ejected from the target, and the tungsten debris–although not as pronounced as it is for the Lexan target–has a forward velocity.

The tail and penetration velocities are plotted in Fig. 9. Because the projectile has a finite length (ℓ_o/d = 20), penetration stops when the projectile is fully eroded. There are a number of observations. First, the penetration velocity, the nonsteady terminal phase, and the penetration depth are strong functions of projectile density. The straight horizontal lines, calculated from Eqn. (3), are the steady-state hydrodynamic penetration velocities. The penetration velocities from the simulations are less than the steady-state hydrodynamic values in all cases, and the disagreement becomes more pronounced as the projectile density decreases. The third and fourth columns of Table 4 provide a summary of values calculated from hydrodynamic theory and from the simulations, respectively.

Table 4. Summary of computational results

Simulation	v *(mm/μs)*	u_{hydro} *(mm/μs)*	u_{sim} *(mm/μs)*	$2u_{hydro}$-v *(mm/μs)*	$2u_{sim}$-v_{sim} *(mm/μs)*	$(v_d)_{sim}$† *(mm/μs)*
W → Lexan	3.61	2.89	2.9	2.17	2.2	2.0
Steel → Steel	3.61	1.80	1.6	0.00	-0.32	-0.32
Al → Steel	3.61	1.33	0.94	-0.94	-1.5	-1.5
W → Steel	3.61	2.20	2.0	0.80	0.54	0.48

† Values determined from tracer particle.

The depth of penetration, as derived from steady-state hydrodynamic theory, is given by:

$$\frac{p}{d} = \frac{\ell_o}{d}\sqrt{\rho_p/\rho_t} \tag{5}$$

The straight vertical lines in Fig. 9 are calculated from Eqn. (5). The depth of penetration for the tungsten projectile exceeds that of the hydrodynamic limit by approximately two projectile diameters as a result of the nonsteady transient phase of penetration (the hydrodynamic limit assumes steady-state penetration). The aluminum projectile only penetrates approximately three-fourths that predicted by the hydrodynamic approximation.

For the steel-into-steel case, the penetration depth is less than that expected from hydrodynamic theory by 10% (2 projectile diameters), in excellent agreement with experimental data [13]. It has

often been assumed, for high impact velocities, that like-into-like materials will behave hydrodynamically. That is, it is assumed that, although the projectile and target have strength, the strengths are equal so they cancel; hence, hydrodynamic-like behavior. That this is not the case can be explained in the context of the modified Bernoulli equation [14], which relates the impact and penetration velocities at the projectile-target interface through the projectile strength Y_p and target resistance R_t:

$$\frac{1}{2}\rho_p(v-u)^2 + Y_p = \frac{1}{2}\rho_t u^2 + R_t \tag{6}$$

The target resistance incorporates the geometrical constraint to radial flow (within the one-dimensional framework of the model) in addition to the strength of the target. Since R_t is considerably larger than Y_p [14], Eqn (6) does not reduce to the steady-state hydrodynamic condition for like-into-like materials. For the tungsten-into-Lexan experiment and simulation, the Lexan is a very weak material, so the target behaves hydrodynamic-like. This is not the case for the armor-like steel target. The deviations from hydrodynamic theory are the result of strength and constraint to radial flow.

Strength also appears to affect the dynamics of the eroded debris. The numerical simulation of the tungsten rod penetrating the very low strength Lexan target agreed quite well, both qualitatively and quantitatively, with the corresponding experiment and the Allen and Rogers model for the case of hydrodynamic penetration. This result is also shown in Table 4 where the $(2u_{hydro} - v)$ column, calculated from the theory, is compared with the debris velocity from the simulation $(v_d)_{sim}$. However, as shown in Table 4, there is poor quantitative agreement between $(2u_{hydro} - v)$ and $(v_d)_{sim}$ for the other three calculations.

Figure 10 shows the axial velocities for the idealized hydrodynamic behavior of a tracer particle, initially located as described above for the tungsten-into-Lexan simulation. The curves in Fig. 10 will be used to compare with the results from the numerical simulations. Axial and radial velocities of tracer particles in the penetrator are plotted in Figs. 11 and 12, respectively. The projectile material is decelerated, Fig. 11, as it approaches the projectile-target interface and is then swept into the eroded debris. Note that the large radial velocities in Fig. 12—the turning of the projectile material—are coincident with the large deceleration of the axial velocity.

A comparison of the axial debris velocities from the simulations, Fig. 11, with idealized hydrodynamic behavior, Fig. 10, show qualitative and quantitative differences. The axial direction of debris flow is into the target for the tungsten projectile, in accordance with the Allen and Rogers model, beginning with a velocity of about 0.5 mm/μs. The $(v_d)_{sim}$ values in Table 4 are from the tracer data and correspond approximately to the "knee" of the curves in Fig. 11. The axial velocity for the aluminum projectile is negative and thus out of the target, also in agreement with the Allen and Rogers model. The axial velocity for the steel tracer is slightly negative, i.e., the direction of flow is out of the target. The Allen and Rogers model gives $v_d = 0$ for hydrodynamic penetration and $\rho_t = \rho_p$. Thus, for the steel into steel case, an effect of strength is to change the direction of flow of the eroded debris from stationary to out of the target.

The streamline trajectories of the tracer points for the three cases (with an exaggerated scale for the radial position) are shown in Fig. 13. For the aluminum projectile, the debris is ejected out of the target along the crater boundary, and thus, the radial position continues to increase with time; see Fig. 5(c). In contrast, for the tungsten and steel projectile cases, the debris approximately follows the radial expansion of the crater.

The penetration and tail velocities from the numerical simulations, u_{sim} and v_{sim}, were used to calculate the quantity $(2u_{sim} - v_{sim})$ for the tracer particle, which is tabulated in Table 4. This value compares well with the last column of Table 4, the debris velocity from the simulation, $(v_d)_{sim}$.

Therefore, numerical simulations do confirm the essential result of the Allen and Rogers model that the debris velocity is given, at least initially, by $v_d = 2u - v$. This is a direct consequence of the assumption of streamline reversal. However, the values of u and v that must be used in calculating the debris velocity must be the ones corresponding to the situation where the projectile and target have strength, and not the hydrodynamic values. A consequence of these strength effects is that the

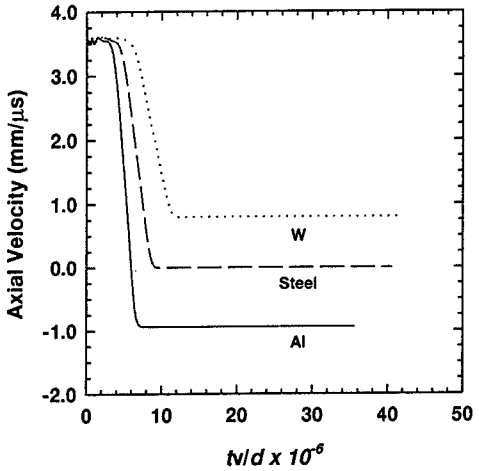

Fig. 10. Idealized (hydrodynamic) axial velocities versus time for tracer particles. The tracer particle is initially 4 diameters from the projectile-target interface.

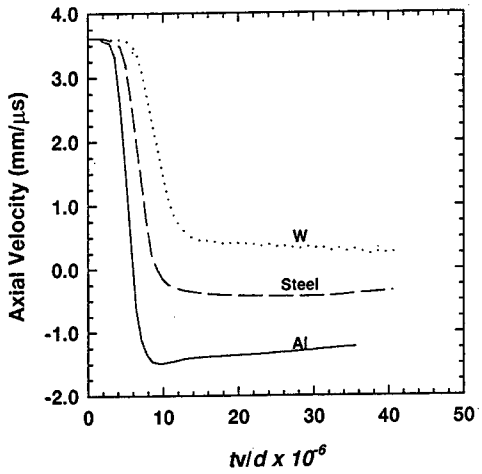

Fig. 11. Axial velocities versus time for tracer particles: parametric simulations.

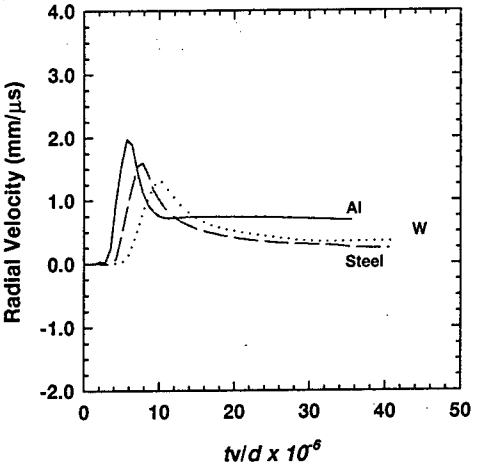

Fig. 12. Radial velocitis versus time for tracer particles: parametric simulations.

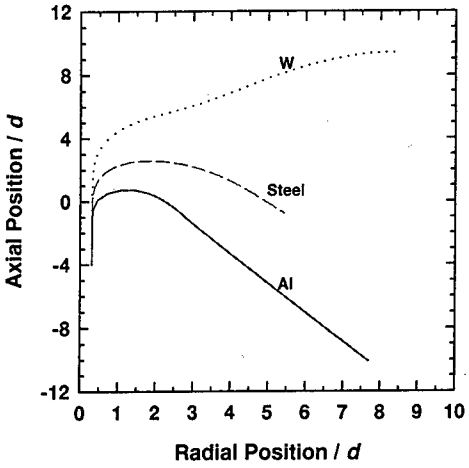

Fig. 13. Lagrangian trajectories of tracer particles for parametric study.

numerical simulations do not confirm the result from the Allen and Rogers model for hydrodynamic penetration that $v_d = 0$ for $\rho_t = \rho_p$ (i.e., steel into steel). As noted above, for this case, the numerical simulation showed that v_d is slightly negative.

It is noted that the axial velocity of the tracer particle (i.e., v_d) for each of the three cases is not constant; the magnitude appears to be decreasing with increasing time, Fig. 11. The mechanics associated with this phenomena are not clear at this time. There are gradients in the debris velocity resulting from transients associated with the formation of debris products, and perhaps other phenomena. The debris may therefore be doing work on itself, with an attendant increase in internal energy, at the expense of kinetic energy. Also, the cavity is not cylindrical. So, for example, in the tungsten projectile case, when the debris velocity is into the target, the debris is probably doing work on the target, again at the expense of debris kinetic energy. Further investigation is required to resolve the mechanics associated with this phenomenon.

CONCLUSIONS

Allen and Rogers proposed a streamline reversal model for high velocity penetration in which the projectile and target materials behave essentially hydrodynamically. An experiment using a very weak target material—polycarbonate— provided data in reasonably good agreement (about 7-10%) with the model, for the specific case of $\rho_t < \rho_p$. A corresponding numerical simulation agrees very well with both the experiment and the model. Numerical simulations using a strong steel target essentially confirm Allen and Rogers' equation for debris velocity, namely $v_d = 2u - v$, at least initially, using the calculated u and v from the simulations. Projectile and target strengths affect both u and v, particularly u, and the relationship between them. If hydrodynamic values for u and v are used, the agreement is poor, even for an impact velocity of 3.61 mm/μs. For example, for a steel projectile into a steel target, the Allen and Rogers model gives $v_d = 0$ for hydrodynamic penetration since $\rho_t = \rho_p$. In the numerical simulations, v_d is not zero but slightly negative (out of the target). The qualitative results often attributed to the Allen and Rogers' model, but which require the additional assumption of hydrodynamic behavior, are affected by strength. Also, it was observed from the numerical simulations that the debris velocity is not constant but appears to be tending to zero with increasing times. Two possible explanation for this phenomenon were suggested. In any case, the results of this research demonstrate that there is much yet to be learned about the dynamics of eroded projectile debris, especially the effects of projectile and target strength on these dynamics.

REFERENCES

1. W.A. Allen and J. A. Rogers, "Penetration of a rod into a semi-infinite target," *J. Franklin Inst.*, **272**, 275-284 (1961).
2. C. E. Anderson, Jr., D. L. Orphal, R. R. Franzen, and J. D. Walker, "On the hydrodynamic approximation for long-rod penetration," *Int. J. Impact Engng.*, **22**(1), 23-42 (1999).
3. J. M. McGlaun, S. L. Thompson, and M. G. Elrick, "CTH: A three-dimensional shock wave physics code, *Int. J. Impact Engng.*, **10**, 351-360 (1990).
4. B. van Leer, "Towards the ultimate conservative difference scheme IV. "A new approach to numerical convection," *J. Comp. Phys.*, **23**, 276-299 (1977).
5. W. W. Predebon, C. E. Anderson, Jr., and J. D. Walker, "Inclusion of evolutionary damage measures in Eulerian wavecodes," *Comput. Mech.*, **7**(4), 221-236 (1991).
6. S. A. Silling, "Stability and accuracy of differencing methods for viscoplastic models in wavecodes," *J. Comp. Phys.*, **104**, 30-40 (1993).
7. G. R. Johnson and W. H. Cook, "A constitutive model and data for metals subjected to large strains, high strain rates and high temperatures," *Proc. 7th Int. Symp. on Ballistics*, pp. 541-547, The Hague, The Netherlands (1983).
8. C. E. Anderson, Jr., T. G. Trucano, and S. A. Mullin, "Debris cloud dynamics, "*Int. J. Impact Engng.*, **9**(1), 89-113 (1990).
9. G. Hertel, Sandia National Laboratories, private communication (1998).
10. G. I. Kerley and T. L. Christian-Frear, "Sandia equation of state data base: seslan file," SAND93-1206, Sandia National Laboratories, Albuquerque, NM, June (1993).
11. C. E. Anderson, Jr. and J. D. Walker, "An examination of long-rod penetration," *Int. J. Impact Engng.*, **11**(4), 481-501 (1991).
12. C. E. Anderson, Jr., D. L. Littlefield, and J. D. Walker, "Long-rod penetration, target resistance, and hypervelocity impact," *Int. J. Impact Engng.*, **14**, 1-12 (1993).
13. V. Hohler and A. J. Stilp, "Hypervelocity impact of rod projectile with L/D from 1 to 32," *Int. J. Impact Engng.*, **5**, 323-331 (1987).
14. A. Tate, "Long rod penetration models–Part II," *Int. J. Engn. Sci.*, **28**, 599-612 (1986).

PERGAMON International Journal of Impact Engineering 23 (1999) 711–722

INTERNATIONAL JOURNAL OF IMPACT ENGINEERING

www.elsevier.com/locate/ijimpeng

HOLES PRODUCED IN THIN ALUMINUM SHEETS BY THE HYPERVELOCITY IMPACT OF ALUMINUM SPHERES

ANDREW J. PIEKUTOWSKI

University of Dayton Research Institute, 300 College Park Avenue, Dayton, Ohio 45469-0182, USA

Summary—The dimensions of holes produced by the impact of 2017-T4 aluminum spheres with various thicknesses of 1100-O, 2024-T3, and 6061-T6 aluminum sheets are presented and analyzed. The sphere diameters ranged from 3.18 mm to 19.05 mm and the bumper-sheet-thickness-to-projectile-diameter ratio, *t/D*, ranged from 0.026 to 0.504 with the majority of the tests having *t/D* ratios of less than 0.234. Impact velocities ranged from 1.98 km/s to 7.23 km/s. The measured hole diameters were normalized by dividing them by the diameter of the sphere that produced the hole. The normalized diameters of the holes produced in the sheets are shown to scale when compared on the basis of *t/D* ratio. Bumper-sheet strength played a role in determining the final diameter of the hole. When the *t/D* ratio was held constant, the holes formed in the lower strength sheets were larger than those produced in the higher strength sheets. When the impact velocity was held constant, a relationship between the *t/D* ratio and the morphology of the lip structure surrounding the hole was noted. As the *t/D* ratio increased, the holes tended to be less circular and the lip morphology became more complex. Micrographs of cross sections of the lip structures are used to confirm that a clear relationship exists between the *t/D* ratio and the morphology of the lip structure. © 1999 Elsevier Science Ltd. All rights reserved.

INTRODUCTION

Holes produced in thin sheets by the impact of hypervelocity projectiles have been the subject of study for more than 40 years. Extensive sets of measurements were taken of holes produced by many of the impact experiments performed during the 1960's and 1970's (e.g., Maiden and McMillan [1], Nysmith and Denardo [2], and Carson and Swift [3]). Hörz *et al.* [4, 5] have performed detailed studies of the holes produced in 1100 aluminum and Teflon sheets. More recently, Gardner *et al.* [6] have derived a new equation for characterizing holes produced in thin foils by hypervelocity particles. The study of holes produced in thin sheets and their description as a function of sheet thickness, projectile diameter, and impact velocity is of interest because the hole produced in the shield or some other component of a spacecraft represents damage that may or may not affect the performance of the spacecraft. In addition, the measurements of holes produced in thin sheets can be used to estimate the properties of the particles that produced the holes.

This paper presents the results of a study that examined the holes produced by the normal impact of 2017-T4 aluminum spheres with various thicknesses and alloys of aluminum sheets. The thickness of the bumper sheets and the diameter of the holes left in the bumper sheets were carefully measured and compared on the basis of the bumper-sheet-thickness-to-projectile-diameter ratio, *t/D*, and impact velocity. Hole diameters increased as the *t/D* ratio and/or impact velocity increased. Micrographic cross sections were made of the edge of the hole and material adjacent to the hole for selected bumper sheets and compared. The micrographic cross sections illustrated that a clear relationship existed between the *t/D* ratio and the morphology of features evident in the cross sections.

0734-743X/99/$ - see front matter © 1999 Elsevier Science Ltd. All rights reserved.
PII: S0734-743X(99)00116-5

EXPERIMENTAL PROCEDURES

All impact tests were performed in the University of Dayton Research Institute (UDRI) Impact Physics Laboratory using a 50/20 mm or a 75/30 mm, two-stage, light-gas gun. Impact velocities for the tests described in this paper ranged from 1.98 to 7.23 km/s. Impact velocity determinations were made with use of four laser-photodetector systems installed at various locations along the flight path of the projectile. Accuracy of the impact velocity determination was better than ± 0.5 percent.

The tests were performed using 3.18-, 6.35-, 9.53-, 12.70-, 15.88-, and 19.05-mm-diameter, 2017-T4 aluminum spheres with nominal masses of 0.046, 0.373, 1.275, 3.000, 5.860, and 10.116 g, respectively. Various thicknesses of 1100-O, 2024-T3, and 6061-T6 aluminum sheets were used as bumpers. The thinner bumpers were 10.8 cm square and were securely taped to a 3.18-mm-thick, 15.2-cm-square aluminum frame that had an 8.9-cm-square opening cut in its center. The thicker bumpers were 15.2 cm square and were held at the corners by screws passing through the sheet into appropriate support posts. All bumpers were installed and impacted normal to the range centerline.

The diameters of the holes left in the bumper sheets were carefully measured by projecting a shadow of the hole on the screen of an optical comparator. Thus, the measured hole diameter represents the diameter of the smallest opening in the sheet for each of the tests. After all hole measurements were complete, small sections of the bumper sheet were removed from the region adjacent to the hole for selected sheets. These small sections were mounted, polished, and the details of the lip morphology were examined using a microscope.

RESULTS AND DISCUSSION

Results of the hole-diameter measurements are presented in Table 1. As shown in Table 1, measurements were taken parallel and perpendicular to the rolling direction of the sheet stock. The average of the two measurements was taken to be the hole diameter, d_h. Of the 52 tests listed in Table 1, 50 tests provided two measurements of the hole diameter. Pieces of the piston used in the operation of the two-stage, light-gas gun struck the bumper sheet for Shot 4-1281 and stretched the hole in one direction. The hole for Shot 4-1353 was very irregular and the diameter shown in Table 1 was the approximate outer diameter of the hole. Twenty-six of the holes, or 52 percent, were larger in the direction parallel to the rolling direction of the sheet. The hole diameter perpendicular to the rolling direction of the sheet was larger for fifteen (30 percent) of the tests; the hole diameter was the same in both directions for nine (18 percent) of the tests. The sensitivity of the hole diameter to very small variations in bumper sheet thickness was obvious during the measurement of the sheet thicknesses and the hole diameters. In a number of instances, two or more tests were performed using the same impact conditions (i.e., sphere diameter, sheet thickness, and impact velocity). The diameters of the holes produced in these tests were nearly identical. Use of the normalized hole diameter, d_h/D, permitted the comparison, on the basis of t/D ratio and impact velocity, of the hole diameters produced by the impact of spheres of different diameters.

The normalized bumper-hole diameter, d_h/D, is shown as a function of impact velocity for selected t/D ratios in Fig. 1. The data plotted in Fig. 1 indicated that the use of this simple geometric scaling technique was a very effective procedure for comparing the dimensions of holes produced by spheres whose diameters ranged from 6.35 mm to 19.05 mm. Although the data sets shown in this figure are limited in their range and the numbers of points, they do indicate that the hole diameter increased as t/D ratio and/or impact velocity increased. The data presented in Fig. 1 also indicated that bumper strength has an effect on the final diameter of the hole. The holes formed in the weaker 1100-O aluminum bumpers were considerably larger than those produced in the higher strength 6061-T6 or 2024-T3 aluminum bumpers. Holes produced in the

Table 1. Bumper hole data

The diameters of the holes were measured perpendicular and parallel to the rolling direction of the bumper-sheet stock and are presented in the units in which they were measured. Typical measurement error was ±0.0005 inch.

Shot Number	$\frac{t}{D}$	*Impact Velocity, (km/s)*	*Hole Diameter, (⊥, in)*	*Hole Diameter, (∥, in)*	*Average Hole Diameter, d_h (in)*	$\frac{d_h}{D}$
1100-O Aluminum Bumper, D = 6.35 mm						
4-1318	0.048	6.64	0.302	0.302	0.302	1.208
1100-O Aluminum Bumper, D = 9.53 mm						
4-1286	0.031	6.42	0.421	0.421	0.421	1.122
4-1288	0.031	6.71	0.421	0.422	0.422	1.125
4-1285	0.032	6.67	0.421	0.421	0.421	1.123
4-1290	0.032	6.67	0.424	0.423	0.424	1.131
2024-T3 Aluminum Bumper, D = 9.53 mm						
4-1282	0.053	6.58	0.431	0.428	0.430	1.147
4-1284	0.053	6.58	0.433	0.430	0.432	1.152
2024-T3 Aluminum Bumper, D = 12.70 mm						
4-1281	0.040	6.46	---[a]	0.549	0.549	1.098
4-1357	0.160	6.38	0.842	0.817	0.832	1.664
6061-T6 Aluminum Bumper, D = 3.18 mm						
4-1851	0.488	6.12	0.334	0.334	0.334	2.672
6061-T6 Aluminum Bumper, D = 6.35 mm						
4-1789	0.048	6.40	0.285	0.286	0.286	1.144
4-1807	0.050	6.06	0.288	0.288	0.288	1.152
4-1449	0.050	7.23	0.294	0.298	0.296	1.184
6061-T6 Aluminum Bumper, D = 9.53 mm						
4-1715	0.026	4.67	0.397	0.393	0.395	1.053
4-1392	0.026	6.54	0.396	0.394	0.395	1.053
4-1395	0.026	6.70	0.392	0.398	0.395	1.053
4-1428	0.049	3.77	0.413	0.413	0.413	1.101
4-1433	0.049	4.71	0.426	0.425	0.426	1.136
4-1394	0.049	5.45	0.426	0.428	0.427	1.139
4-1788	0.049	6.49	0.430	0.431	0.430	1.147
4-1360	0.049	6.62	0.431	0.433	0.432	1.152
4-1633	0.062	3.65	0.434	0.432	0.433	1.155
4-1359	0.062	6.78	0.456	0.460	0.458	1.221
4-1632	0.084	3.47	0.461	0.462	0.462	1.232
4-1631	0.084	3.64	0.466	0.463	0.464	1.237
4-1622	0.084	3.84	0.467	0.473	0.470	1.253
4-1621	0.084	4.62	0.482	0.484	0.483	1.288
4-1289	0.084	6.68	0.509	0.515	0.512	1.365
4-1287	0.084	6.74	0.511	0.517	0.514	1.371
4-1283	0.102	6.72	0.540	0.540	0.540	1.440
4-1722	0.132	2.54	0.472	0.475	0.474	1.264
4-1716	0.135	4.71	0.559	0.561	0.560	1.493
4-1291	0.163	6.71	0.650	0.653	0.652	1.739
4-1717	0.168	4.96	0.618	0.606	0.612	1.632
4-1718	0.233	1.98	0.507	0.504	0.506	1.349
4-1720	0.233	2.44	0.549	0.550	0.550	1.467
4-1719	0.233	2.83	0.577	0.583	0.580	1.547
4-1351	0.233	6.66	0.776	0.776	0.776	2.069
4-1352	0.234	6.64	0.765	0.769	0.767	2.045
4-1353	0.424	6.68	---	---	1.08[b]	2.88
4-1721	0.504	2.23	0.636	0.637	0.636	1.696

Table 1. Bumper hole data (Concluded)

The diameters of the holes were measured perpendicular and parallel to the rolling direction of the bumper-sheet stock and are presented in the units in which they were measured. Typical measurement error was ±0.0005 inch.

Shot Number	$\frac{t}{D}$	*Impact Velocity, (km/s)*	*Hole Diameter, (⊥, in)*	*Hole Diameter, (∥, in)*	*Average Hole Diameter, d_h (in)*	$\frac{d_h}{D}$
		6061-T6 Aluminum Bumper, D = 12.70 mm				
4-1358	0.047	6.26	0.567	0.571	0.569	1.138
4-1770	0.101	6.44	0.711	0.713	0.712	1.424
4-1771	0.101	6.45	0.716	0.713	0.714	1.428
4-1769	0.101	6.50	0.713	0.715	0.714	1.428
4-1765	0.122	6.30	0.759	0.763	0.861	1.552
		6061-T6 Aluminum Bumper, D = 15.88 mm				
4-1762	0.049	6.15	0.727	0.727	0.727	1.163
4-1763	0.097	6.17	0.871	0.868	0.870	1.392
4-1766	0.098	6.12	0.872	0.869	0.871	1.396
4-1767	0.098	6.18	0.869	0.870	0.870	1.392
4-1768	0.098	6.18	0.867	0.870	0.868	1.406
		6061-T6 Aluminum Bumper, D = 19.05 mm				
8-0125	0.084	6.11	0.987	0.986	0.986	1.315

[a] Bumper struck by a piece of piston. Hole was stretched in this direction.
[b] Nearly all of the interior "ring" was missing from the hole. Diameter corresponds to the diameter of the hole without the interior "ring."

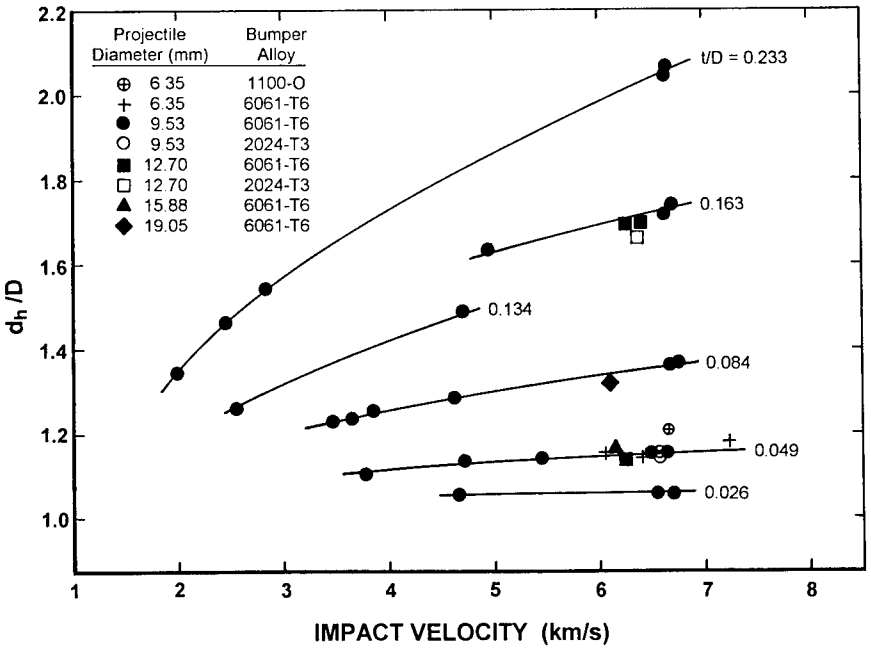

Fig. 1. Normalized hole diameter as a function of impact velocity for six *t/D* ratios.

6061-T6 aluminum bumpers were slightly larger than those produced in the stronger 2024-T3 aluminum sheets. Bumper sheet material strength apparently affected the growth of the hole during the later stages of the hole-formation process when material strength was significantly greater than the residual shock-induced stresses. Selected properties [7] for the sphere and bumper sheet material used in the tests are presented in Table 2.

Table 2. Selected material properties

Aluminum Alloy	Density, (g/cm^3)	Tensile Strength, (MPa)	Yield Strength, (MPa)	Shear Strength, (MPa)
1100-O	2.71	90	35	62
2017-T4	2.80	427	276	262
2024-T3	2.77	483	345	283
6061-T6	2.71	310	276	207

Sufficient data were available in Fig. 1 to provide a reasonable indication of the magnitude of the change in hole diameter that would occur as impact velocity and t/D ratio are varied. Also, the trend in all of the "curves" indicates they could converge on the point $d_h/D = 1$ and $t/D = 0$ when the impact velocity is low (i.e., the diameter of the hole should approach the diameter of the projectile at low impact velocities). The holes produced in the thinnest bumpers ($t/D = 0.026$) were about 5 percent larger than the projectile, regardless of the impact velocity. Many investigators have suggested that a linear relationship may exist between hole diameter and impact velocity for a constant t/D ratio. As shown in Fig. 1, this relationship may hold over a limited range of impact velocities for some t/D ratios, but clearly does not hold for the tests with the lower impact velocities and the higher t/D ratios.

Experimentalists have developed a number of equations used to relate hole diameter to various parameters of the target and projectile. In general form, many of the equations are similar to the following equation given by Maiden and McMillan [1]:

$$d_h/D = 0.45V_0(t/D)^{2/3} + 0.9$$

where V_0 is the impact velocity. Maiden and McMillan's tests were conducted using 3.2-mm-diameter aluminum spheres of an unspecified alloy and 2024-T3 aluminum sheets. Nysmith and Denardo [2] used the following equation to describe the results of tests that used 3.2-mm-diameter, 2017-T4 aluminum spheres and 2024-T3 aluminum sheets:

$$d_h/D = 1.47(t/D)^{0.45}V_0^{0.5}$$

Carey *et al.* [8] developed the following equation to describe the diameters of holes produced by small iron projectiles impacting aluminum foils at velocities ranging from 2 to 20 km/s:

$$d_h/D = 1 + 1.5(t/D)V_0^{0.3}(\,1 / (1 + (t/D)^2V_0^{-n}))$$

where n is given by:

$$n = 1.02 - 4\exp(-0.9\,V_0^{0.9}) - 0.003(20 - V_0)$$

More complicated equations, involving a wide variety of projectile and bumper parameters, have been derived by other investigators.

The equations provided by Maiden and McMillan, Nysmith and Denardo, and Carey *et al.* were evaluated to determine their adequacy for describing the data obtained in this study. The results of the comparison are presented in Fig. 2 for tests with selected t/D ratios. Maiden and McMillan's original equation underestimated (< 2 percent) the hole diameter for the higher velocity, higher t/D ratio tests. It overestimated the hole diameters for the higher velocity, lower t/D ratio tests by as much as 15 percent. Use of this equation for the lower velocity tests worked well for the lower t/D ratio tests but underestimated the hole diameter for the higher t/D ratio tests by about 10 percent. Nysmith and Denardo's equation consistently underestimated the hole diameters by 5 to 10 percent (as t/D ratio decreased) for the higher velocity tests and 10 to 30 percent for the lower velocity tests. Examination of the data used by Maiden and McMillan and

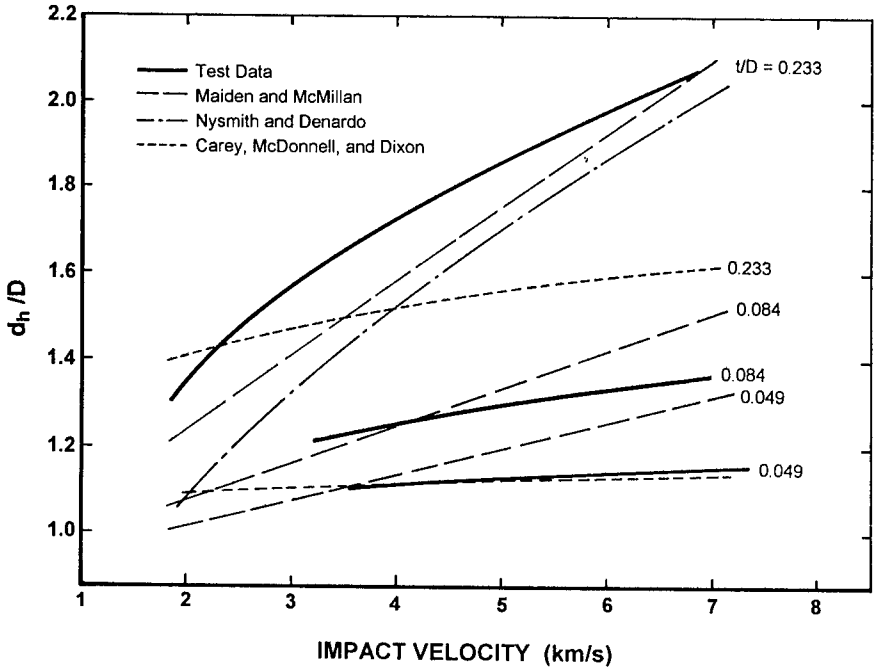

Fig. 2. Comparison of normalized hole diameters obtained from equations provided by Maiden and McMillan [1], Nysmith and Denardo [2], and Carey *et al.* [8] with experimental data in Fig. 1.

by Nysmith and Denardo showed that most of the data were from tests with a limited range of impact velocities and used relatively thick bumper sheets (and high *t/D* ratios). Shot 4-1357 used a 2024-T3 aluminum sheet with a *t/D* ratio of 0.160. The normalized hole diameter for Shot 4-1357 was significantly lower than the normalized hole diameters for the *t/D* = 0.163 tests using 6061-T6 aluminum sheets. The equations would undoubtedly had a better fit to the experimental data had 2024-T3 aluminum, instead of 6061-T6 aluminum, had been used as the target material for the tests described in this paper. Carey *et al.*'s equation described the test data within the experimental error for the lower *t/D* ratio, but significantly underestimated the size of the holes for the tests with the higher *t/D* ratios. Although the hole data presented in this paper exhibit clear trends, there were not sufficient data to develop a general relationship suitable for use in describing hole diameter as a function of impact velocity and *t/D* ratio.

Holes produced by the normal impact of 9.53-mm-diameter, aluminum spheres traveling at 6.70 km/s are shown in Fig. 3 for four *t/D* ratios. An arrow in each hole identifies the location of a portion of the bumper sheet that was removed and used to provide the micrographic cross section shown to the left of the hole photograph. The holes are shown from the front or impacted side of the sheet and the cross sections are shown with their impacted side toward the top of the figure. As the *t/D* ratio increased, the hole diameter, d_h, increased, the holes tended to be less circular, and the structure of the region surrounding the hole became more complex.

The hole photographs and cross sections shown in Fig. 3 illustrate a relationship between *t/D* ratio (or at least sheet thickness) and the morphology of the region surrounding the hole. Flaps or lips developed on both sides of the bumper. The flap on the impacted side of the sheet was larger than the flap on the rear side of the bumper for all of the holes shown in Fig. 3. Grain structure visible in the micrographs indicated that the flaps were formed from portions of bumper that overturned during the hole-formation process. As bumper-sheet thickness increased, the width of the overturned flaps increased. At a *t/D* ratio of 0.102, large cracks were evident in the flaps. As the cracks grew and joined together, pieces of the flap separated from the sheet and reduced the width of the flaps. The cross sections for the tests with *t/D* ratios of 0.163 or greater merely exhibited a small lip on the front and rear surfaces of the bumper sheet. These small lips appeared

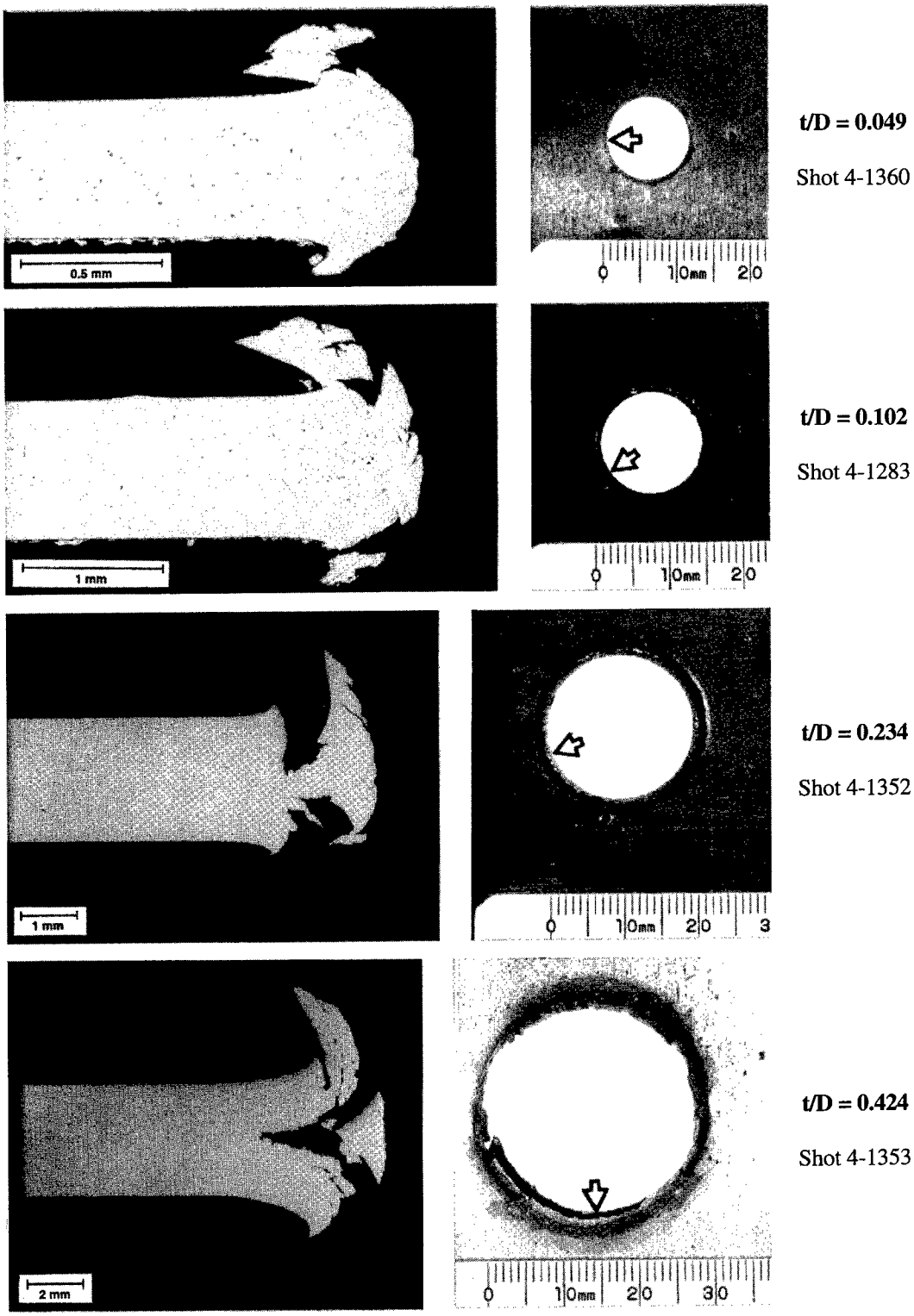

Fig. 3. Photographs and cross sections of holes formed by impact of 9.53-mm-diameter, 2017-T4 aluminum spheres with various thicknesses of 6061-T6 aluminum sheets at 6.70 km/s. Holes are shown from the impacted side of the bumper. Cross sections are shown with the impacted side toward the top of the page.

to be all that remained of the overturned flaps. As the material in the flap overturned, it was strained excessively, cracked, and was separated from the bumper sheet. The newly formed fragments became a part of the ejecta veil and/or the external bubble of debris. The cross sections for these tests also exhibited a large ring of material that was attached to the bumper by a thin web of material at the center of the sheet. The surfaces of the ring that were toward the bumper were concave and appeared to be smooth or polished, in contrast to the more irregular surfaces evident on material closer to the bumper sheet. The smooth appearance of the ring in these regions may indicate that the ring had been in contact with material in the overturned flap. The cross section for the t/D = 0.424 test clearly showed a detached ring with a wedge-shaped cross section, a split in the sheet, and a section of overturned flap that was smooth on the surface which had been in contact with the ring. The split in the sheet extended all around the inside of the hole. The mating surface irregularities in the split section of the sheet and the position of the wedge-shaped ring suggest that the outward motion of the ring may be responsible for the separation of the sheet. It is probable that the wedge-shaped ring was a continuous structure during the hole formation process. As shown in Fig. 3, however, only a portion of the ring remained in the hole after the impact. Additional pieces of the ring were recovered from the target-chamber floor after the test.

The sequence of bumper-sheet cross sections presented in Fig. 3 demonstrated that the hole-formation process could produce a variety of morphological features in the region adjacent to the holes. When a sphere impacts a thin sheet at hypervelocity, a shock forms and propagates into the sheet. The intensity of the shock and the extent of its influence on the sheet material are a function of the t/D ratio and the impact velocity of the sphere [9]. Processes that were latent for tests with low t/D ratios appeared to dominate the formation of lip-region features for tests with high t/D ratios. The changes in the morphology of the lip region may be related to the t/D ratio or they may simply be a result of the change in sheet thickness. The further examination and discussion of test results presented in this paper will focus on establishing a relationship, if one exists, between the t/D ratio and the lip-region morphology. Currently, neither the diameters nor the impact velocities of the particles that produced the damage on recovered spacecraft surfaces are known. An estimate of particle diameter, based on lip-region morphology, would reduce the uncertainty in estimating the impact velocity of these particles.

An examination of the data presented in Table 1 shows that there are a number of sets of data available for use in determining possible relationships between the lip-region morphology and the various test parameters. In addition to the micrographs presented in Fig. 3, cross sections of bumper sheets from other series of tests shown in Table 1 were examined. In the first series, four different sphere diameters, ranging from 6.35 mm to 15.88 mm, were used and the impact velocity and t/D ratio were held constant at 6.25 km/s and 0.049, respectively. The micrographs of the lip regions for the four tests in this series exhibited a structure that was similar to the one shown for Shot 4-1360 in Fig. 3. This similarity of structure may indicate that the morphology of the lip region surrounding the hole is determined solely by the t/D ratio. However, it is possible that the bumper sheets used in the tests were too thin to show sufficient detail for drawing a meaningful conclusion. Micrographs from tests using thicker bumper sheets should be examined to obtain the evidence needed to verify that the hole morphology is determined by the t/D ratio.

Lip-region morphologies of two holes produced by the 6.70 km/s impacts of 9.53-mm-diameter aluminum spheres are compared in Fig. 4. Except for t/D ratio, these tests are the same as for the series shown in Fig. 3. The cross section of Shot 4-1287 (t/D = 0.084) is similar to the cross section of Shot 4-1360 (t/D = 0.049) shown in Fig 3. The cross section for Shot 4-1291 (t/D = 0.163), in Fig. 4, has considerably more structure than seen in the cross sections from Shots 4-1360 and 4-1287. Micrographs from three tests employing 1.55-mm-thick, 6061-T6 aluminum bumper sheets (same thickness as for Shot 4-1291) are compared in Fig. 5. Impact velocity for these three tests was nominally 6.1 km/s. The diameters of the spheres used for the tests were 19.05, 9.53, and 3.18 mm; the t/D ratios of the tests were 0.084, 0.163, and 0.488, respectively. Except

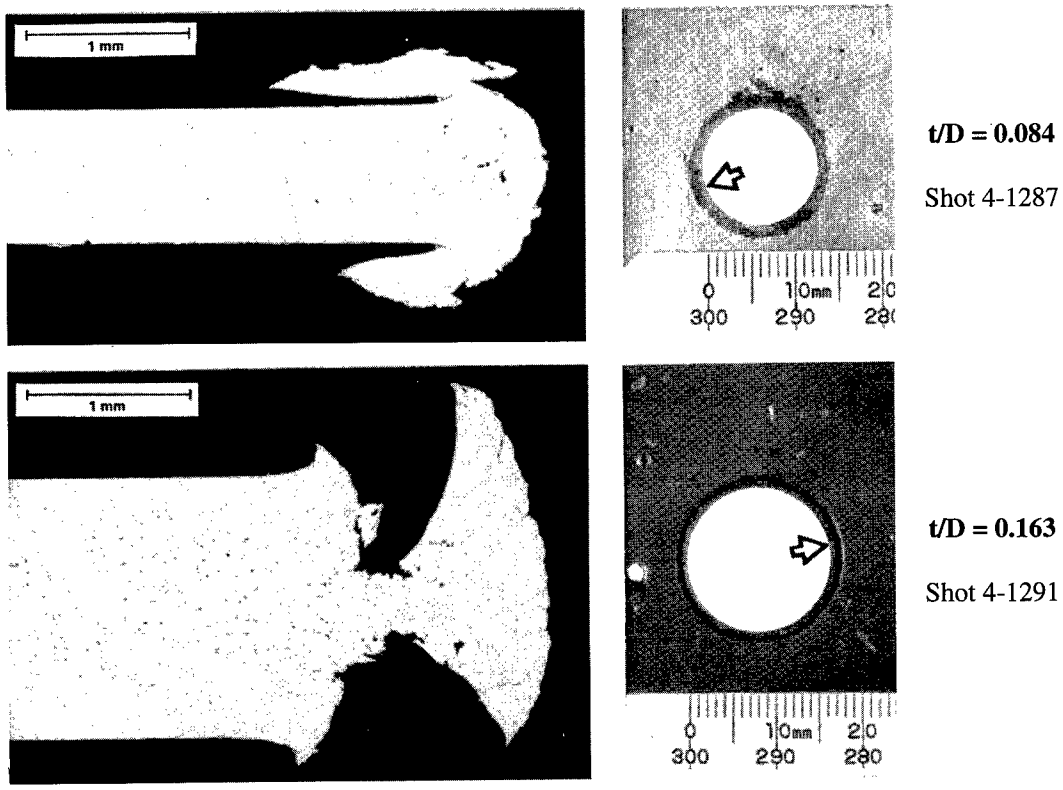

Fig. 4. Photographs and cross sections of holes formed by impact of 9.53-mm-diameter, 2017-T4 aluminum spheres with two thicknesses of 6061-T6 aluminum sheets at 6.70 km/s. Holes are shown from the impacted side of the bumper. Cross sections are shown with the impacted side toward the top of the page.

for the loss of the overturned flaps, the cross section of the lip for Shot 8-0125, shown in Fig. 5, is very similar to the cross section of the lip for Shot 4-1287, shown in Fig. 4, even though the sheet thicknesses for these two tests varies by a factor of 2. Although the cross sections shown in Fig. 5 do not exhibit all of the details of the cross sections of the tests with comparable *t/D* ratios, shown in Figs. 3 and 4, they do indicate the existence of a very strong relationship between lip-region morphology and *t/D* ratio. The lack of a reduced section in the lip region of the hole for Shot 8-0125 is notable. The existence of a reduced section between the internal ring and the remnant of the overturned flap for Shot 4-1851 strongly supports the conclusion that the *t/D* ratio has the greatest influence in the formation of the features exhibited in the lip region of the holes.

The hole shown in Fig. 6 exhibited features that were observed for a number of tests in which 12.70-mm-diameter, 2017-T4 aluminum spheres were fired at 1.976-mm-thick, 6061-T6 aluminum sheets with an impact velocity of about 6.4 km/s. For most of these tests, the major opening in the sheet was defined by a fragile ring of aluminum surrounded by a series of small holes, as shown in Fig. 6. The interior rings were weakly attached to the surrounding bumper sheet and, in some instances, pieces of the ring simply fell from the hole after hole growth ceased. The transition from an attached ring to a detached ring undoubtedly occurred as a result of the loss of material from the thin web that joined the ring structure to the center of the sheet. Features of the bumper-sheet cross section presented in Fig. 6 are very similar to those presented in Figs. 4 and 3 for tests with *t/D* ratios of 0.163 and 0.234, respectively. Several small holes were occasionally observed around the holes in bumper sheets from tests using 9.53-mm-diameter, 2017-T4 aluminum spheres and 6061-T6 aluminum bumper sheets. The average impact velocity and *t/D* ratio for these tests was about 6.4 km/s and 0.21, respectively. While it is possible that

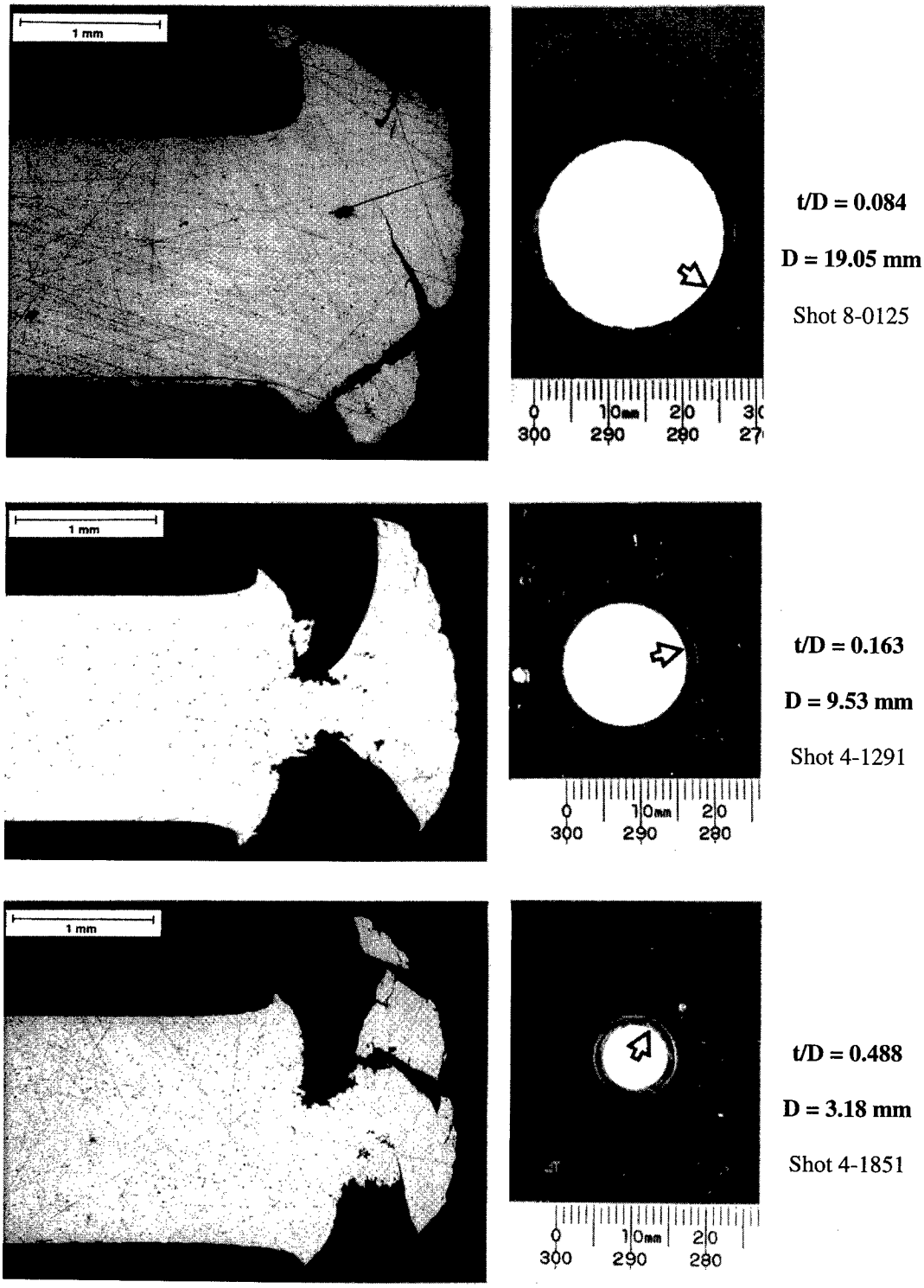

Fig. 5. Photographs and cross sections of holes formed by impact of 19.05, 9.53, and 3.18-mm-diameter, 2017-T4 aluminum spheres with 1.57-mm-thick, 6061-T6 aluminum sheets at 6.1 km/s. Holes are shown from the impacted side of the bumper. Cross sections are shown with the impacted side toward the top of the page.

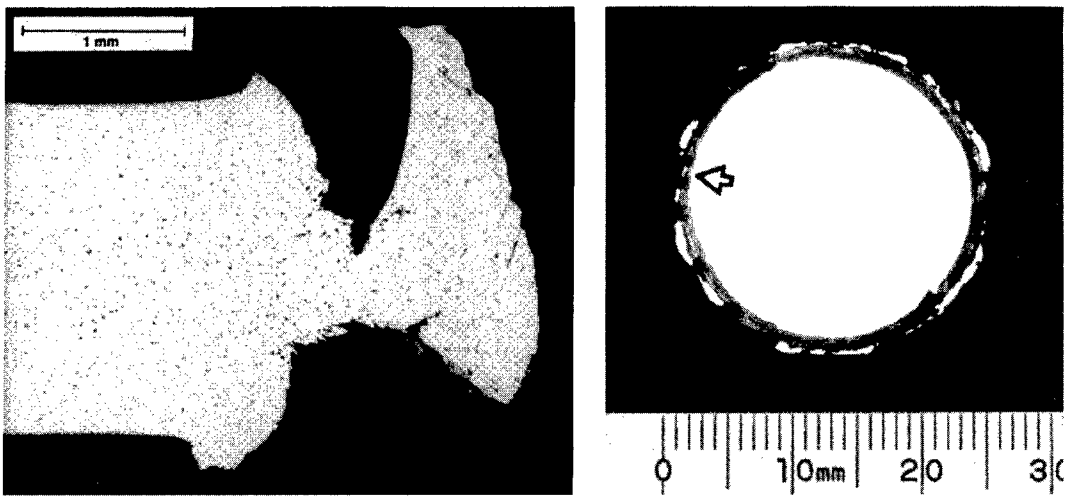

t = 0.0778 inch t/D = 0.156 V_0 = 6.42 km/s

d_h = 0.848 inch (Inside), 0.954 inch (Outside)

Fig. 6. Photograph and cross section of a hole displaying a ring structure surrounded by small holes and openings. Hole was formed by the impact of a 12.70-mm-diameter, 2017-T4 aluminum sphere with a 6061-T6 aluminum sheet.

the formation of a series of small holes around the main opening will only occur when specific conditions of impact velocity and bumper-sheet thickness, strength, and ductility are met, it is probable that the hole features shown in Fig. 6 could be produced by other combinations of sphere diameter, *t/D* ratio, and impact velocity (e.g., the 6.7 km/s impact of a 9.53-mm-diameter sphere with a sheet having a *t/D* ratio greater than 0.234 but less than 0.424). As shown in the information provided in Fig. 6, the difference between the measured diameter of the inner ring and the measured diameter of the hole defined by the irregular opening outside the ring is significant. The normalized diameter of the inner ring fits the data shown in Fig. 1; the normalized diameter of the outer opening does not. For these tests, the post impact hole diameter was determined by the ability of an extremely fragile ring to remain in place after the impact.

CONCLUSIONS

Normalization of the hole-diameter data using the projectile diameter, *D*, permitted the diameters of holes produced by spheres ranging from 6.35 to 19.05 mm in diameter to be compared on the basis of *t/D* ratio. The comparisons indicated that the use of this simple geometric scaling technique was extremely effective for the range of data that was examined. Although the hole data from the tests presented in this paper exhibit clear trends, there were not sufficient data to develop a general relationship suitable for use in describing hole diameter as a function of impact velocity and *t/D* ratio.

Observations made during the measurement of bumper-sheet thicknesses and hole diameters emphasized the sensitivity of the hole diameter to very small variations in sheet thickness. The data also indicated that bumper strength played a significant role in determining the final diameter of the hole.

As the *t/D* ratio increased, the holes tended to be less circular and the structure of the region surrounding the hole became more complex. Micrographs of cross sections of the bumper sheets showed that a clear relationship existed between the *t/D* ratio and the morphology of features evident in the cross sections. The morphological features that were observed in the lip region of

the 6061-T6 aluminum bumper sheets were not observed in the cross sections of the 1100-O aluminum bumpers shown by Hörz *et al.* [4]. The use of thin 6061-T6 aluminum sheets as collectors and surfaces exposed to the impact of micrometeoroids and orbital debris and subsequently recovered for analysis could provide information regarding the diameter of the particle that produced the hole by analyzing of the morphology of the region around the hole.

Impact velocities below 5 km/s failed to produce the lip-region morphological features observed in tests with impact velocities greater than 6 km/s. Data for tests with impact velocities between 5 and 6 km/s were not available.

Acknowledgment—The author wishes to gratefully acknowledge Dr. Joel Williamsen, NASA Marshall Space Flight Center and Dr. Norman Elfer, Martin Marietta Manned Space Systems (MMMSS), for their support of a portion of this work performed under Prime Contract NAS 8-38856 on Subcontract A71447 with MMMSS. He also wishes to gratefully acknowledge the Office of the Director of the University of Dayton Research Institute for support provided for the various range and equipment tests used to provide the most of the data presented in this paper. The author would also like to express his appreciation to fellow associates at UDRI: Kevin Poormon, for his careful assistance in performance of the tests and discussions of test results and Dale Grant, for preparing the micrographs of the bumper-sheet sections.

REFERENCES

1. C. J. Maiden and A. R. McMillan, An Investigation of the Protection Afforded a Spacecraft by a Thin Shield. *AIAA,* **2**(11), 1992-1998, (1964).
2. C. R. Nysmith and B. P. Denardo, Experimental Investigations of the Momentum Transfer Associated with Impact into Thin Aluminum Targets. NASA TN D-5492, October, (1969).
3. J. M. Carson and H. F. Swift, Hole Diameters in Thin Plates Perforated by Hypervelocity Projectiles. AFML/MAY-TM-67-9, November (1967).
4. F. Hörz, M. J. Cintala, R. H. Bernhard, and T. H. See, Dimensionally Scaled Penetration Experiments: Aluminum Targets and Glass Projectiles 50 μm to 3.2 mm in Diameter. *Int. J. Impact Engng.* **15**(3), 257-280, (1994).
5. F. Hörz, M. J. Cintala, R. H. Bernhard, and T. H. See, Cratering and Penetration Experiments in Teflon Targets at Velocities from 1 to 7 km/s. *Int. J. Impact Engng.* **17**, 419-430, (1995).
6. D. J. Gardner, J. A. M. McDonnell, and I. Collier, Hole growth characteristics for hypervelocity impacts in thin targets. *Int. J. Impact Engng.* **19**(7), 589-602, (1997).
7. Materials Selector Issue, *Materials in Design Engineering*, **58**(5), 112-116, Mid-October (1963).
8. W. C. Carey, J. A. M. McDonnell, and D. G. Dixon, Capture Cells: Decoding the Impacting Projectile Parameters. *Lunar and Planetary Science Conference XVIth*, Abstracts, (1985).
9. A. J. Piekutowski, Formation and Description of Debris Clouds Produced by Hypervelocity Impact. NASA CR 4707, February (1996).

PERGAMON

International Journal of Impact Engineering 23 (1999) 723–734

INTERNATIONAL JOURNAL OF IMPACT ENGINEERING

www.elsevier.com/locate/ijimpeng

PENETRATION OF 6061-T6511 ALUMINUM TARGETS BY OGIVE-NOSE STEEL PROJECTILES WITH STRIKING VELOCITIES BETWEEN 0.5 AND 3.0 KM/S

ANDREW J. PIEKUTOWSKI*, MICHAEL J. FORRESTAL**, KEVIN L. POORMON*, and THOMAS L. WARREN**

*University of Dayton Research Institute, 300 College Park Avenue, Dayton, OH 45469-0182, USA
**Sandia National Laboratories, Albuquerque, NM 87185-0315, USA

Summary—We performed a series of depth-of-penetration experiments using 7.11-mm-diameter, 71.12-mm-long, ogive-nose steel projectiles and 254-mm-diameter, 6061-T6511 aluminum targets. The projectiles were made from vacuum-arc remelted (VAR) 4340 steel (R_C 38) and AerMet 100 steel (R_C 53), had a nominal mass of 0.021 kg, and were launched using a powder gun or a two-stage, light gas gun to striking velocities between 0.5 and 3.0 km/s. Since the tensile yield strength of AerMet 100 (R_C 53) steel is about 1.5 times greater than VAR 4340 (R_C 38) steel, we were able to demonstrate the effect of projectile strength on ballistic performance. Post-test radiographs of the targets showed three different regions of penetrator response as the striking velocity increased: (1) the projectiles remained rigid and visibly undeformed; (2) the projectiles deformed during penetration without nose erosion, deviated from the target centerline, and exited the side of the target or turned severely within the target; and (3) the projectiles eroded during penetration and lost mass. To show the effect of projectile strength, we present depth-of-penetration data as a function of striking velocity for both types of steel projectiles at striking velocities ranging from 0.5 and 3.0 km/s. In addition, we show good agreement between the rigid-projectile penetration data and a cavity-expansion model. © 1999 Elsevier Science Ltd. All rights reserved.

INTRODUCTION

Most studies of the penetration of long-rod projectiles launched with high striking velocities have focused on tungsten projectiles impacting steel [1, 2] or confined ceramic [3] targets. Silsby [1] conducted experiments with tungsten alloy long rods and armor steel targets at striking velocities between 1.3 and 4.5 km/s. For those experiments, depth of penetration increased monotonically and eventually reached a limiting depth as striking velocity increased. Anderson *et al.* [2] present data from [1] and five other studies for tungsten rod projectiles with length-to-diameter ratios of 20. When the penetration-depth data were divided by the rod length and plotted versus striking velocity, all six data sets showed small scatter in the normalized plot. This same relationship between penetration depth and striking velocity was reported recently by Orphal *et al.* [3] for confined ceramic targets. For highly resistive steel and confined ceramic targets, the projectile deforms at impact and erodes during the penetration process.

In contrast, penetration experiments that used T-200 maraging steel [4], long-rod projectiles with a 3.0 caliber-radius-head (CRH) nose shape and 6061-T651 aluminum targets [5] showed that the projectiles were visibly undeformed for striking velocities up to 1.46 km/s. For higher striking velocities, post-test radiographs of the targets showed that the projectile shanks fractured into several segments in the penetration channel or cavity. Penetration experiments with the same maraging steel projectiles and 7075-T651 aluminum targets [6] showed that the projectiles

0734-743X/99/$ - see front matter © 1999 Elsevier Science Ltd. All rights reserved.
PII: S0734-743X(99)00117-7

remained visibly undeformed for striking velocities up to 1.26 km/s and fractured in the penetration channel for higher striking velocities. For both of these studies [5 and 6], the depth of penetration increased with striking velocity until the projectile fractured. For the 6061-T651 aluminum targets [5], the maximum normalized penetration depth (penetration depth divided by the rod length) was 4.0. For aluminum targets and steel projectiles, jet theory predicts a normalized penetration depth of 1.7.

In this study, we performed two series of penetration experiments with ogive-nose, steel, long-rod projectiles and 6061-T6511 aluminum targets at striking velocities between 0.5 and 3.0 km/s. The studies were performed to observe the response regions from rigid-body penetration through eroding-rod penetration. To avoid projectile shank fracture, we used moderately hard, vacuum-arc remelted (VAR) 4340 steel projectiles for our first series of experiments. To show the effect of yield strength on ballistic performance, harder AerMet 100 steel projectiles were used for the second set of experiments. In the next sections, we describe our experiments and present our results. In addition, we modified our cavity-expansion penetration model, given in Refs. [5] and [7], to predict the rigid-body response of ogive-nose projectiles. The model showed good agreement with penetration depth data for striking velocities up to 1.8 km/s.

EXPERIMENTS

The dimensions of the ogive-nose, steel projectiles used in both series of penetration experiments are given in Fig. 1. The 6061-T6511 aluminum targets were 254 mm in diameter. The length of the target was determined to be the sum of the anticipated depth of penetration plus the length of the rod. The first series of experiments was performed using VAR 4340 steel [8] projectiles that had a hardness of R_C 38, a tensile yield strength of 1140 MPa (165 ksi), and a fracture toughness of 130 MPa $(m)^{1/2}$ or 120 ksi $(in.)^{1/2}$. The second set of experiments used AerMet 100 steel [9, 10] projectiles that had a hardness of R_C 53, a tensile yield strength of 1720 MPa (250 ksi), and a fracture toughness of 126 MPa $(m)^{1/2}$ or 115 ksi $(in.)^{1/2}$. Thus, both steel projectiles had nearly the same fracture toughness, but the AerMet 100 steel had 1.5 times the tensile yield strength as the VAR 4340 steel.

For striking velocities below 1.3 km/s, the projectiles were launched using a 20 mm powder gun. For striking velocities above 1.3 km/s, the projectiles were launched using a 50/20 mm or a 75/30 mm, two-stage, light-gas gun. Projectile striking velocities were measured with an accuracy of better than 0.5 percent using four laser-photodetector stations installed at various locations along the flight path. The pitch and yaw of the projectile was obtained from radiographs obtained with use of an orthogonal pair of flash x-rays positioned immediately in front of the face of the target. The depth of penetration of the projectile and the final shape of the projectile were determined, after each test, from a radiograph of a 38-mm-thick slice of the target. The slice was cut from each target with special care to ensure the plane of maximum inclination of the rod was

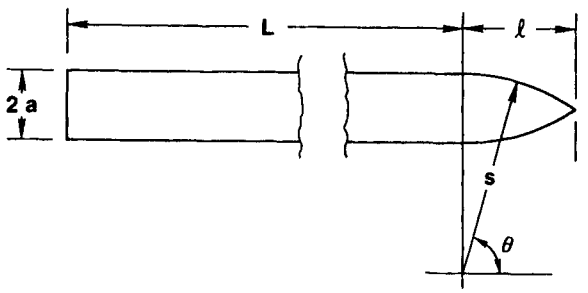

Fig. 1. Geometry for the ogive-nose rod with a 3.0 caliber-radius-head (CRH), L = 59.3 mm, l = 11.8 mm, and $2a$ = 7.11 mm. Note that for a 3 CRH rod, s = 3 x $2a$.

coincident with the plane of the slice. Tables 1 and 2 summarize the penetration data from both series of experiments.

As shown in Table 1, we performed 20 experiments using VAR 4340 steel projectiles. The projectile striking velocities ranged from 0.57 to 2.99 km/s. Depth of penetration increased as striking velocity was increased to 1.40 km/s. For striking velocities below 1.24 km/s, the projectiles remained visibly undeformed and the penetration channels were straight; however, the penetration channels for striking velocities of 1.36 and 1.40 km/s (Shots 4-1829 and 4-1799) exhibited significant curvature and the projectiles were bent. At striking velocities of 1.49 and 1.57 km/s (Shots 4-1800 and 4-1810), the projectiles exited the side of the target. For striking velocities between 1.58 and 1.77 km/s (Shots 4-1801, 4-1831, and 4-1808), the projectiles were severely deformed during penetration, but remained in the target. Finally, for striking velocities between 2.0 and 3.0 km/s (Shots 4-1832, 4-1809, 8-0113, 4-1833, 8-0112, and 8-0104), the projectiles eroded.

Selected radiographs of targets from tests using VAR 4340 steel projectiles are presented in Fig. 2. The radiographs selected for presentation in Fig. 2 illustrate the following changes in

Table 1. Penetration data for VAR 4340, R_C 38, 3-CRH-nosed, steel rods

Targets were 254-mm-diameter bars of 6061-T6511 aluminum with lengths shown below. For Pitch, D = Down and U = Up. For Yaw, R = Right and L = Left.

Shot Number	*Striking Velocity, V_S, (m/s)*	*Penetration[a], (mm)*	*Penetrator Mass, (g)*	*Penetrator Hardness, R_C*	*Penetrator Pitch, Degrees*	*Penetrator Yaw, Degrees*	*Target Length, (m)*
1-0415	569	58	20.38	38.2	0	0.25 R	0.127
4-1805	570	55	20.427	38.1	3.0 U	2.0 R	0.141
4-1806	679	72	20.412	38.1	1.0 U	0.25 L	0.140
4-1796	821	102	20.415	38.9	1.75 U	0.2 R	0.167
4-1797	966	140	20.415	38.0	0.25 U	0.75 R	0.229
1-0412	1147	190	20.41	38.3	---	---	0.248
4-1798	1237	224	20.379	38.0	1.5 U	1.25 R	0.267
4-1829	1365	249 (252)	20.824	39.2	1.75 D	0.75 L	0.343
4-1799	1396	249 (267)	20.418	38.0	2.5 U	0	0.289
4-1800	1493	277[b] (303)	20.383	38.0	0.25 U	1.5 R	0.338
4-1810	1571	(216)[c]	20.480	38.2	1.1 U	0.6 R	0.292
4-1801	1585	105[d]	20.414	38.0	2.0 U	4.5 L	0.363
4-1831	1648	109[d]	20.437	37.7	1.5 D	0.25 R	0.267
4-1808	1770	142[d]	20.444	37.9	1.0 U	0.5 R	0.244
4-1832	1977	123	20.456	39.5	0.25 D	1.25 R	0.216
4-1809	2166	124	20.432	37.9	4.5 U	3.0 R	0.235
8-0113	2193	126	20.423	38.4	0.75 U	5.0 R	0.244
4-1833	2204	121	20.452	39.4	1.5 U	0.25 R	0.216
8-0112	2570	144	20.367	38.2	0.75 U	6.0 R	0.243
8-0104	2988	147	20.390	38.9	0.4 U	1.3 L	0.305

[a] Depth of penetration measured normal to the surface of the target to the *point* of the projectile. Values shown in parentheses are the lengths of the penetration channels when the channels were curved.

[b] Projectile exited side of target at this depth below the target surface. Exit angle was 65 to 70 degrees to the shot-line axis and exit velocity was low. The nose of the rod remained sharply pointed.

[c] Projectile exited side of target at a depth of 141 mm below the target surface. Exit angle was 90 degrees to the shot-line axis and exit velocity was estimated to be 950 m/s. The nose of the rod remained sharply pointed.

[d] Rod appeared to "turn around" during crater formation (i.e., the tail of the rod was at the bottom of the crater and the point of the rod was nearer the mouth of the crater).

Table 2. Penetration data for AerMet 100, R_C 53, 3-CRH-nosed, steel rods

Targets were 254-mm-diameter bars of 6061-T6511 aluminum with lengths shown below. For Pitch, D = Down and U = Up. For Yaw, R = Right and L = Left.

Shot Number	Striking Velocity, V_S, (m/s)	Penetration[a], (mm)	Mass, (g)	Penetrator Hardness, R_C	Pitch, Degrees	Yaw, Degrees	Target Length, (m)
1-0426	794	103	20.908	52.9	0.25 U	1.25 L	0.154
1-0424	1076	160	20.89	53.1	3.5 U	1.5 R	0.230
1-0425	1255	229	20.906	53.1	1.5 U	0.75 L	0.277
4-1840	1348	254	20.914	53.2	1.75 U	2.75 R	0.349
4-1841	1538	332	20.889	53.8	0	2.5 R	0.406
4-1842	1654	389	20.873	53.4	1 U	0.5 L	0.406
4-1843	1786	452	20.912	53.0	1 U	0.25 R	0.470
8-0117	1816	(398)[b]	20.788	53.5	3.25 D	0.25 R	0.559
4-1844	1817	462	20.916	53.3	0.75 U	0	0.559
8-0118	1916	(281)[c]	20.880	53.0	2.25 D	1.75 L	0.559
8-0123	2042	185[d]	20.959	53.3	2.5 D	1.5 L	0.254
8-0121	2438	168[d]	20.872	53.0	4.5 D	1.75 L	0.305
8-0120	2493	168[d]	20.868	53.5	7 D	2.75 L	0.305
8-0119	2963	172[d]	20.912	53.1	3.5 D	2.75 L	0.305

[a] Depth of penetration measured normal to the surface of the target to the *point* of the projectile. Values shown in parentheses are the lengths of the penetration channels when the channels were curved.

[b] Projectile exited side of target at 283 mm below the target surface. Exit angle was 40 degrees to the shot-line axis and exit velocity is estimated at 600 m/s. Splintered rod fragments were recovered.

[c] Projectile exited side of target at 232 mm below the target surface. Exit angle was 60-65 degrees to the shot-line axis and exit velocity is estimated at 1300 m/s. Splintered rod fragments were recovered.

[d] Projectile broken into small fragments.

penetrator response as striking velocity is increased. In Fig. 2a, the penetration channel is straight and coincident with the centerline of the target and the projectile is not visibly deformed. In Fig. 2b, the crater is straight but at an angle to the target centerline; however, the rod is not visibly deformed. The penetration channel is curved and the rod slightly bent in the crater shown in Fig. 2c. In Fig. 2d, the projectile produced a sharply curved channel before exiting the side of the target. In the radiograph shown in Fig. 2e, it is evident that the projectile experienced a sequence of severe deformations and came to rest with the tail of the rod at the bottom of the crater and the nose of the rod nearer the mouth of the crater. (Additional details of the features observed in the crater produced by this test are presented later in this section.) In Fig. 2f, the crater shows evidence of the beginning of eroding-rod penetration. The crater shown in Fig. 2g exhibits the features typically associated with eroding-rod penetration. As shown in Table 1, all of the rods exhibited some inclination, at impact, of their centerline to the shot-line axis and the surface of the target. The trajectory followed by the rod during penetration of the target was in the plane that was determined by the inclination angle of the projectile. This behavior was noted for both types of steel rods.

Penetration data for 14 experiments using AerMet 100 projectiles are presented in Table 2. Striking velocities for these tests ranged from 0.79 to 2.96 km/s. Depth of penetration increased as striking velocity increased to 1.82 km/s. For striking velocities between 0.79 and 1.79 km/s, the penetration channels were straight and the projectiles were not visibly deformed. At striking velocities of 1.82 and 1.92 km/s (Shots 8-0117, 4-1844, and 8-0118), the penetration channels were curved. The projectiles exited the sides of the targets for Shots 8-0117 and 8-0118, but remained in the target for Shot 4-1844. As shown in Table 2, the inclination angles of the rods

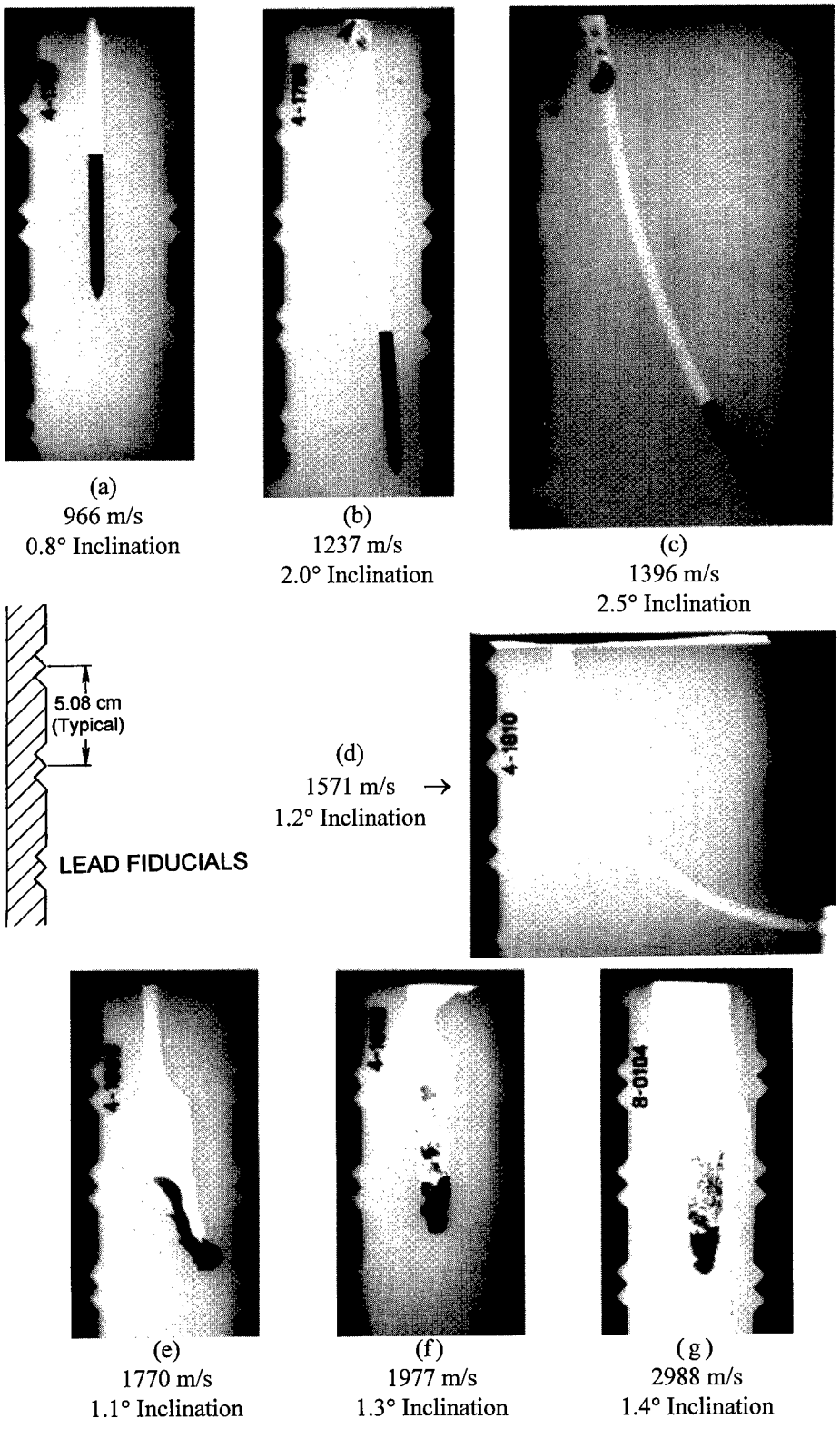

Fig. 2. Radiographs of craters produced by impact of ogive-nosed, VAR 4340 steel rods with 6061-T6511 aluminum targets. Striking velocity and the inclination angle of the rod at impact is noted below each crater.

for Shots 8-0117 and 8-0118 were higher than for the rod for Shot 4-1844. For striking velocities between 2.0 and 3.0 km/s (Shots 8-0123, 8-1021, 8-0120, and 8-0119), the projectiles broke into small fragments or eroded.

Selected radiographs of targets from tests using AerMet 100 steel projectiles are presented in Fig. 3. Again, the radiographs selected for presentation in Fig. 3 illustrate the changes in penetrator response as striking velocity is increased. In Fig. 3a, the penetration channel is straight, coincident with the centerline of the target, and the projectile is not visibly deformed. In Figs. 3b and 3c, the craters are straight but at an angle to the target centerline; however, the rods are not visibly deformed. The penetration channel shown in Fig. 3d is slightly curved and the rod exhibits a very slight bend. In Fig. 3e, the projectile produced a sharply curved channel before exiting the side of the target. In the radiograph shown in Fig. 3f, the projectile appears to have experienced severe deformation after entering the target. The right side of the crater profile for this shot exhibits two large "pouches" that may have been produced by severe bending and fracture of the front part of the rod during the early phase of the penetration event. The lower part of the crater exhibits features more typical of eroding-rod penetration. The crater shown in Fig. 3g exhibits the features usually associated with eroding-rod penetration.

The effect of projectile yield strength on the ability of an ogive-nose, long-rod to penetrate a semi-infinite target is shown in the target radiographs presented in Fig. 4. In this figure, the long, slightly curved penetration channel produced by the impact of an AerMet 100 steel rod is compared to the relatively short and uniquely shaped crater produced by the impact of a VAR 4340 steel rod. The initial conditions of striking velocity and inclination angle were nearly identical for both of the tests. The AerMet 100 steel rod penetrated as a rigid body. The VAR 4340 steel rod, on the other hand, appeared to penetrate normally for the first 40 mm or so and then began to turn sharply to the right. From an examination of the interior surface of the crater, it appears that the front end of the rod bent severely, formed a hook, and continued to penetrate the target. As noted in Fig. 4, the machined surface of the tail end of the rod is clearly evident in the sectioned target. A short section of the tail end of the rod is tightly curved but has broken from the front portion of the rod and is at the bottom of the crater. The nose and the remainder of the rod are pointing toward the mouth of the crater. Clearly, the rod turned around in a cavity that was less than three rod diameters wide while in the process of penetrating the target. More remarkably, the front portion of the rod appeared to straighten itself after it had turned around.

In the next section, we present our cavity-expansion, rigid-body, penetration model. We then compare depth-of-penetration-versus-striking-velocity data for the VAR 4340 and AerMet 100 steel projectiles with our model for the cases where the projectiles remained visibly undeformed.

RIGID-PROJECTILE PENETRATION MODEL

In this section, we present penetration equations for rigid, ogive-nose rods that penetrate 6061-T6511 aluminum targets at normal impact. This model uses the spherical cavity-expansion approximation [11] that closely simulates the two-dimensional target response with results from a dynamic, spherically symmetric cavity-expansion problem. In Ref. 7, Warren and Forrestal presented stress-strain data for 6061-T6511 aluminum at strain rates ranging from $10^{-3}s^{-1}$ to $10^{5}s^{-1}$ and a constitutive equation that includes strain hardening and strain-rate sensitivity. Next, they solved the spherically symmetric, cavity-expansion problem and presented penetration equations for spherical-nose rods. We generalized the penetration equations for a spherical nose to that of an ogive nose with the procedures published in Refs. 5, 6, and 7.

For the 6061-T6511 targets and ogive-nose rod projectiles studied in this work, depth of penetration P is given by

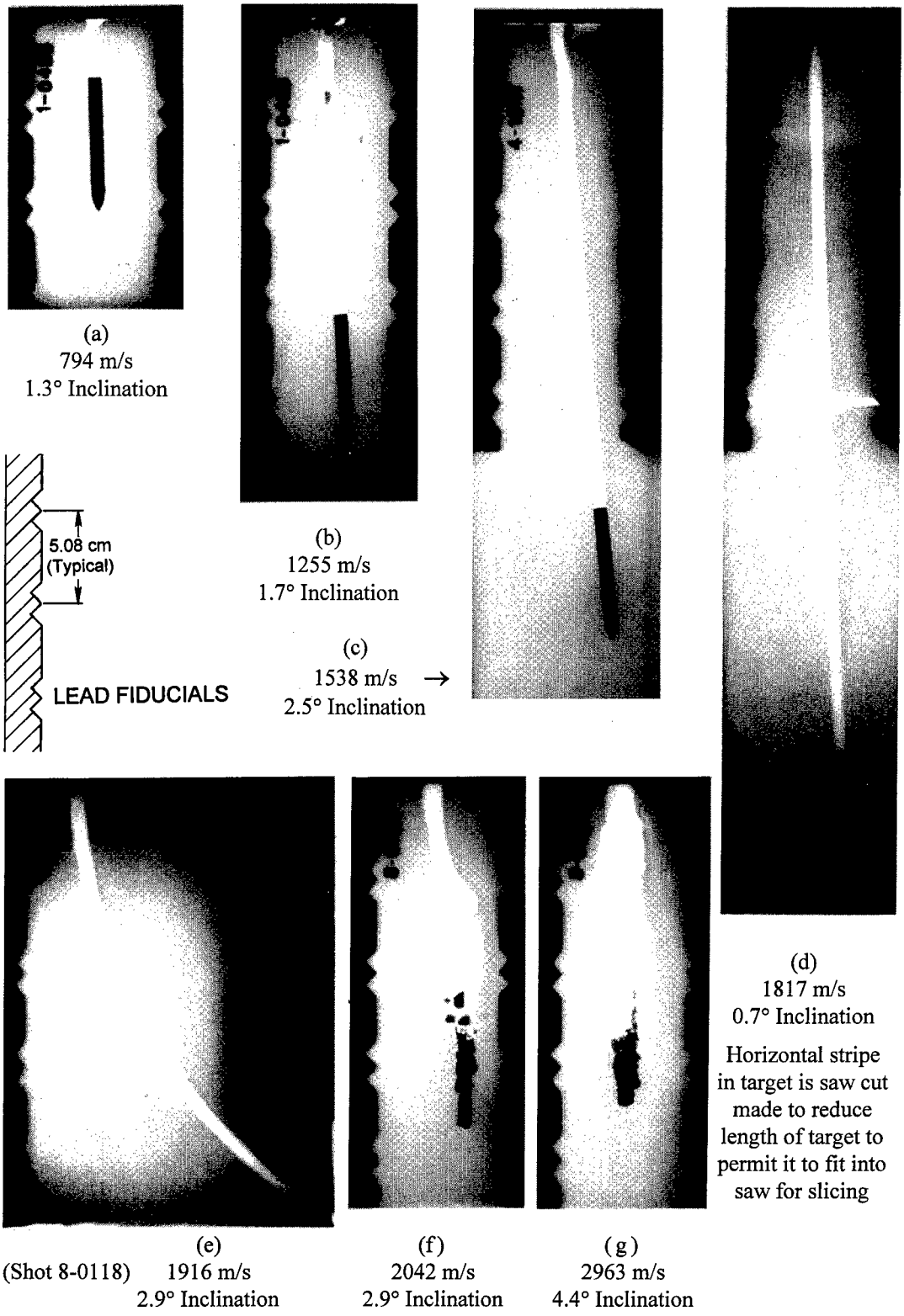

Fig. 3. Radiographs of craters produced by impact of ogive-nosed, AerMet 100 steel rods with 6061-T6511 aluminum targets. Striking velocity and the inclination angle of the rod at impact is noted below each crater.

AerMet 100 Rod
1786 m/s
1.0° Inclination

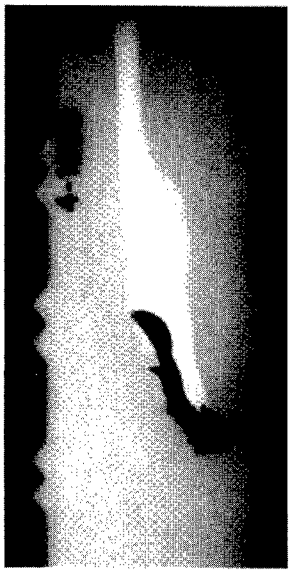

VAR 4340 Rod
1770 m/s
1.1° Inclination

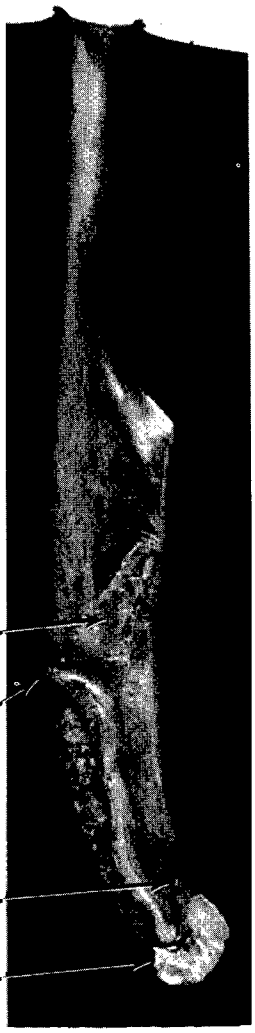

Interior of crater
for Shot 4-1808

Horizontal stripe in target is saw cut made to reduce length of target to permit it to fit into saw for slicing

Fig. 4. Comparison of the crater produced by an AerMet 100 steel rod (left) with the crater produced by a VAR 4340 steel rod (center). Impact conditions for both tests were nearly identical and are noted below the craters. The crater for the VAR 4340 steel rod was cut open to examine the interior surfaces of the crater and the postimpact condition of the rod.

$$\frac{P}{(L+ka)}=\left(\frac{\rho_p}{\rho_t}\right)\frac{1}{2CN}\left\{\ln\left[1+\frac{BN_1}{A}\left(\frac{V_s}{c_y}\right)+\frac{CN}{A}\left(\frac{V_s}{c_y}\right)^2\right]\right\}$$
$$+\left(\frac{\rho_p}{\rho_t}\right)\frac{BN_1}{CN(4ACN-B^2N_1^2)^{1/2}}\left\{\tan^{-1}\left[\frac{BN_1}{(4ACN-B^2N_1^2)^{1/2}}\right]\right. \quad (1)$$
$$\left.-\tan^{-1}\left[\frac{BN_1+2CN(V_s/c_y)}{(4ACN-B^2N_1^2)^{1/2}}\right]\right\}$$

The projectile dimensioned in Fig. 1 has density ρ_p, shank length L, diameter $2a$, and caliber-radius-head ψ. The dimensionless parameters k, N, and N_1 are given by

$$k=(4\psi^2-4\psi/3+1/3)(4\psi-1)^{1/2}-4\psi^2(2\psi-1)\sin^{-1}\left[\frac{(4\psi-1)^{1/2}}{2\psi}\right] \quad (2a)$$

$$N=\frac{8\psi-1}{24\psi^2} \quad (2b)$$

$$N_1=\frac{(4\psi-1)^{3/2}}{3\psi}+\frac{(2\psi-1)^2(4\psi-1)^{1/2}}{2\psi}-\psi(2\psi-1)(\pi-2\theta_o) \quad (2c)$$

$$\theta_o=\sin^{-1}\left(\frac{2\psi-1}{2\psi}\right) \quad (2d)$$

The target is described with density ρ_t and the dimensionless constants A, B, and C determined from the spherically symmetric, cavity-expansion analysis [7]. In addition, V_S is striking velocity and

$$c_y^2=Y/\rho_t \quad (2e)$$

where Y is the quasi-static yield strength of the target [7].

Figure 5 compares our rigid, ogive-nose rod projectile model with the VAR 4340 steel and AerMet 100 steel projectile data given in Tables 1 and 2. We limit the data shown in Fig. 5 to striking velocities below 1.24 km/s for the VAR 4340 steel projectiles and 1.82 km/s for the AerMet 100 steel projectiles. Thus, we only present data in Fig. 5 for nondeforming projectiles. For input to the model, the target parameters are the same as those used or calculated in [7] and are given by $\rho_t = 2710$ kg/m^3, $Y = 276$ MPa, $A = 5.04$, $B = 0.983$, and $C = 0.940$. The projectiles dimensioned in Fig. 1 had $L = 59.3$ mm, $l = 11.8$ mm, $2a = 7.11$ mm, and caliber-radius-head $\psi = 3.0$. The VAR 4340 steel density was 7830 kg/m^3 and the AerMet 100 density was 7890 kg/m^3. In addition, the mass and Rockwell hardness of each projectile are given in Tables 1 and 2. As shown in Fig. 5, the rigid projectile model is in good agreement with model predictions.

If we define

$$\bar{P}=\frac{P}{L+l} \quad (3)$$

where $\bar{P}$ is the penetration depth divided by the total rod length, the data in Fig. 5 cover the range, $0.82 < \bar{P} < 6.36$.

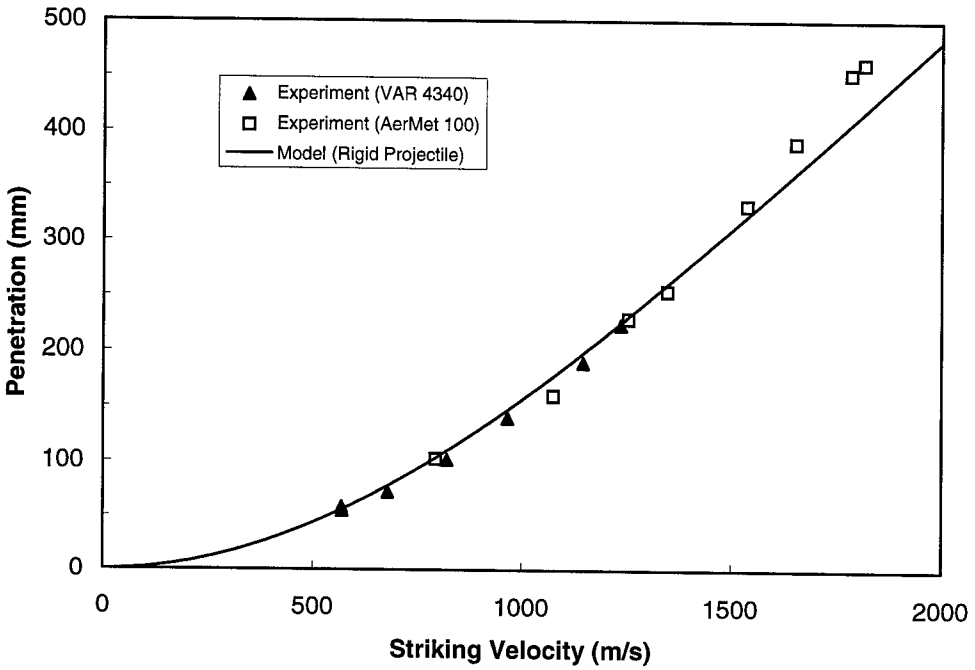

Fig. 5. Penetration depth versus striking velocity for the rigid-projectile response region.

BALLISTIC PERFORMANCE OF VAR 4340 AND AerMet 100 STEEL PROJECTILES

The penetration data given in Tables 1 and 2 for both projectile materials are shown in Fig. 6, along with a prediction from the rigid-projectile model. Not included in this figure are data from the experiments where the projectiles exited the side of the targets or for those tests in which the rod appeared to turn around. For Shots 4-1829 and 4-1799 in Table 1, the projectiles produced a curved penetration channel, so we used the curved path length for penetration depth P.

The data in Tables 1 and 2 and Fig. 6 show the regions of response as striking velocities increase. Response regions for the VAR 4340 steel projectiles include: (1) for $V_S < 1.24$ km/s, the projectiles remain visibly undeformed and the penetration channels are straight; (2) for $1.36 < V_S < 1.4$ km/s, the nose is visibly undeformed but the penetration channels are curved; (3) for $1.49 < V_S < 1.57$ km/s, the penetration channels are curved and the projectiles exited the side of the targets; (4) for $1.58 < V_S < 1.77$ km/s, the projectiles deformed severely and turned around in the targets; and (5) for $2.0 < V_S < 3.0$ km/s, the projectiles eroded and lost mass.

Response regions for the AerMet 100 steel projectiles include: (1) for $V_S < 1.82$ km/s, the projectiles remain visibly undeformed and the penetration channels are straight; (2) for $1.82 < V_S < 1.92$ km/s, the penetration channels were curved and the projectiles exited the sides of the target; (3) for $V_S \approx 2.0$ km/s, the front of the projectile broke into a number of large fragments and the rear of the rod remained intact (see Fig. 3f); and (4) for $V_S > 2.0$ km/s, the projectile fragment size decreased and the rod began to exhibit eroding-rod behavior and lose mass during penetration.

The response regions for both types of steel projectiles exhibit the same qualitative behavior as striking velocities increased. However, as mentioned previously, the AerMet 100 steel has about 1.5 times the tensile yield strength as the VAR 4340 steel for the heat treatment given the rods. Thus, the data presented in Tables 1 and 2 and Figs. 5 and 6 show an increase in projectile performance for the rigid-projectile response region for the AerMet 100 steel projectiles as compared with the VAR 4340 steel projectiles.

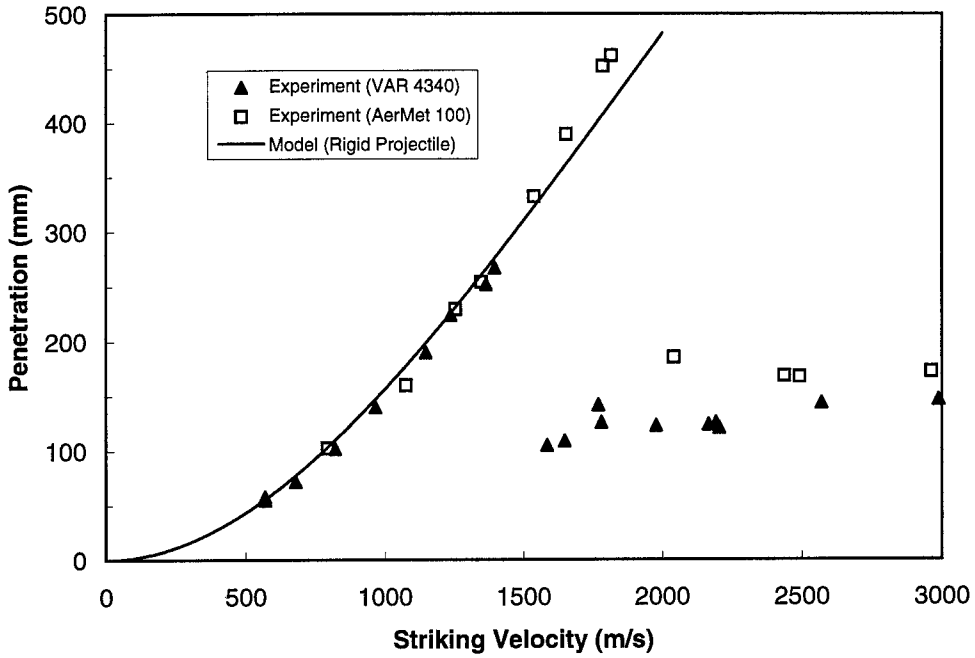

Fig. 6. Penetration depth versus striking velocity.

CONCLUSIONS

We conducted depth of penetration experiments with VAR 4340 (R_C 38) steel and AerMet 100 (R_C 53) steel, ogive-nose rod projectiles at striking velocities between 0.5 and 3.0 km/s. The various response regions for each steel projectile were identified and the ballistic performance of both steel materials was compared. In addition, we presented a rigid-projectile penetration model that accurately predicts the depth of penetration for striking velocities to 1.8 km/s.

Acknowledgment—This work was supported by the United States Department of Energy and the Joint DoD/DOE Munitions Technology Development Program. Sandia is a multiprogram laboratory operated by Sandia Corporation, a Lockheed Martin Company, for the United States Department of Energy under Contract DE-AC04-94AL85000.

REFERENCES

1. G. F. Silsby, Penetration of semi-infinite steel targets by rods at 1.3 to 4.5 km/s. *Proc. 8th Int. Symp. Ballistics*, TB/31-35, Orlando, FL (1984).
2. C. E. Anderson, S. A. Mullin, A. J. Piekutowski, N. W. Blaylock, and K. L. Poormon, Scale model experiments with ceramic laminate targets. *Int. J. Impact Engng* **18**, 1–22 (1996).
3. D. L. Orphal, R. R. Franzen, A. J. Piekutowski, and M. J. Forrestal, Penetration of confined aluminum nitride targets by tungsten long rods at 1.5-4.5 km/s. *Int. J. Impact Engng* **18**, 355–386 (1996).
4. *Data Bulletin–18 Percent Nickel Maraging Steels*, The International Nickel Company, Inc., New York, N.Y. 10005. (1964).
5. M. J. Forrestal, K. Okajima, and V. K. Luk, Penetration of 6061-T651 aluminum targets with rigid long rods. *J. Appl. Mech.*, **55**, 755–760 (1988).
6. M. J. Forrestal, V. K. Luk, Z. Rosenberg, and N. S. Brar, Penetration of 7075-T651 aluminum targets with ogival-nose rods. *Int. J. Solids Struct.* **29**, 1729–1736 (1992).
7. T. L. Warren and M. J. Forrestal, Effects of strain hardening and strain-rate sensitivity on the penetration of aluminum targets with spherical-nose rods. *Int. J. Solids Struct.*, **35**, 3737-3752 (1998).

8. W. F. Brown, H. Mindlin, and C.Y. Ho, *Aerospace Structural Metals Handbook*, Vol. 1, Code 1206, CINDAS/USAF CRDA Handbooks Operation, Purdue University, West Lafayette, IN 47907-1293, (1996).
9. *AerMet 100 Alloy, Alloy Steels 6*, Carpenter Technology Corporation, Carpenter Steel Division, Reading, PA 19612-4662, USA (1992).
10. J. Dahl, AerMet 100 – An advanced steel for the aerospace industry. *Advanced Materials Technology International*, 40–45 (1991).
11. M. J. Forrestal, D. Y. Tzou, E. Askari, and D. B. Longcope, Penetration into ductile metal targets with rigid spherical-nose rods. *Int. J. Impact Engng* **18**, 465–476 (1996).

PERGAMON

International Journal of Impact Engineering 23 (1999) 735–744

INTERNATIONAL JOURNAL OF IMPACT ENGINEERING

www.elsevier.com/locate/ijimpeng

NUMERICAL SIMULATION OF OBLIQUE IMPACT ON ORBITAL DEBRIS SHIELDING

ROBERT J. RABB and ERIC P. FAHRENTHOLD

Department of Mechanical Engineering, University of Texas, Austin, TX 78712

Summary—Hybrid particle-finite element methods have been proposed as a modeling methodology well suited to the problem of hypervelocity impact simulation. To evaluate the use of such numerical methods for orbital debris shielding design, a series of simulations have been conducted using a three dimensional hybrid particle-finite element code now under development. Two sets of oblique impact simulations, one for a single bumper Whipple shield and one for a dual bumper or stuffed Whipple shield, have been compared to published ballistic limit equations, the latter derived from experiment. The results indicate that hybrid particle-finite element methods can provide an accurate and computationally tractable approach to the simulation of orbital debris shield performance. © 1999 Elsevier Science Ltd. All rights reserved.

INTRODUCTION

The design of high performance orbital debris shielding for space structures calls for the evaluation of a wide range of new shielding materials and geometry's. In particular, multi-plate geometry's and composite materials appear to offer significant performance improvements over conventional aluminum Whipple shields, using a protection per unit areal weight metric [1]. To date most research on the shielding design problem has been pursued experimentally. However several factors motivate the development of improved computer aided design tools: (1) promising new materials and shield geometry's have greatly expanded the number of candidate shielding designs, (2) the relatively complex interaction of impact velocity, impact obliquity, and material failure effects means that a rather large number of experiments are needed to fully characterize the three dimensional performance of any single design concept, (3) the desire for faster, cheaper spacecraft design places increased emphasis on simulation as opposed to experiment, and (4) the range of impact velocities and kinetic energies of interest goes beyond the capabilities of conventional light gas guns.

Although experimental research will continue to occupy a critical role in orbital debris shield design, improved computer codes tailored to address the orbital debris impact problem are expected to assume a larger role. Experience to date has shown that conventional Eulerian and Lagrangian hydrocodes are not ideally suited to this simulation task [2, 3], in particular where oblique impact (fully three dimensional) simulations are concerned. Pure particle methods are well suited to three dimensional modeling of the debris propagation portion of the shielding design problem. However their rather approximate treatment of material strength effects can introduce uncertainties in predicting the spacecraft structural response (fracture, spallation, etc.). The latter response can be strongly dependent on strength and material history effects, especially where "near ballistic limit" simulations are concerned.

Recognizing the advantages of particle methods in debris propagation calculations and the sensitivity of the structural response simulation to material strength effects, some code development research has been directed at coupled particle-finite element codes [4] or hybrid particle-finite element methods for use in the simulation of hypervelocity impact. The present paper describes the application of one hybrid particle-finite element method, described in detail by

0734-743X/99/$ - see front matter © 1999 Elsevier Science Ltd. All rights reserved.
PII: S0734-743X(99)00118-9

Fahrenthold and Horban [5], to the specific problem of orbital debris shield design. A series of three dimensional simulations involving oblique impact on single and multi-plate aluminum shields has been performed for comparison to published experimental ballistic limit curves. The results of these simulations demonstrate the utility of particle-finite element methods in the development of a new computer codes tailored to the orbital debris shielding design problem.

NUMERICAL MODELING OF ORBITAL DEBRIS SHIELDING

Space structures face a current and perhaps growing threat of impact with orbiting space debris. For example, inspections of the Space Shuttle orbiters often reveal some impact damage. The frequency of these impacts suggests that the population of small orbital debris is increasing, due to both spacecraft breakups and collisions among existing orbital debris fragments. For long lived space structures, including low earth orbit satellites and the International Space Station (ISS), the probability of a serious impact is significant. The greatest danger arises from fragments one millimeter to one centimeter in length, with a density of 2.8 gm/cc and impact velocities as high as 13 km/s. Larger fragments exist, but the probability of a collision with debris over one centimeter in size is remote [6]. As a result, the focus of much shielding design work, as well as the present simulation work, has been on sub-centimeter sized aluminum particle impacts over the aforementioned velocity range.

Most orbital shielding design research has been experimental, with analytical and numerical modeling playing a secondary role. There are a number of factors which make numerical simulation of oblique impact on orbital debris shielding a very demanding computational problem: (1) equation of state and anisotropic strength models are needed for new composite shielding materials, (2) better "material failure" models are needed for both composite and metallic shields, (3) conventional Lagrangian, Eulerian, and particle codes can be difficult to apply effectively, and (4) computer resource requirements are very large. The large memory and CPU time requirements are due to: (1) oblique impact (three dimensional) effects, (2) large differences in problem characteristic lengths (ratio of shield thickness to standoff distance), (3) a wide range of material effects and corresponding time scales (shock thermodynamics govern shield perforation, while plasticity and fracture govern structural failure of the wall plate), and (4) fluid-structure interaction effects present in pressurized vessel impacts.

The complexity of the numerical modeling problem can appreciated by considering the simplest case of a conventional Whipple shield impact. The simulation problem can be subdivided into three phases. The first phase is shield perforation, a "hydrodynamic" event in which material strength effects are secondary. The second phase is a debris transport calculation, a non-continuum problem which demands very general contact-impact models. The third phase is the wall plate impact simulation, where material strength effects are critical and structural failure may occur relatively slowly. No single Eulerian, particle-based, or Lagrangian code is ideally suited to simulate all three phases of the problem.

Lagrangian finite element codes normally model perforation by "eroding" elements [7], often discarding the internal energy of eroded elements and attaching the eroded element mass to neighboring nodes. Their slideline-based contact-impact algorithms can lack the generality needed for debris cloud transport calculations, and mesh distortion can mandate frequent rezoning. On the positive side, Lagrangian finite element codes provide very accurate material strength models.

Eulerian finite difference (finite volume) codes model perforation as a hydrodynamic event, providing a robust characterization of multi-material impact, at the cost of complex mixed-cell thermodynamics and interface tracking algorithms. An inordinately fine mesh may be required to model debris transport [8]. Finally, strength modeling is approximate, since in general a different collection of material can contribute to the calculation of local material history data at each time step.

Smooth particle hydrodynamic (SPH) codes [9-12] use "Lagrangian" particles but an "Eulerian" internal energy. They provide a very general characterization of contact-impact, although conventional SPH density calculations imply a multi-material mixing effect which is usually ignored. Particle models are ideal for debris transport calculations, but some problems have been experienced with tensile and boundary instabilities [13]. In addition, SPH modeling of strength effects is approximate: different material particle sets can contribute to the calculation of local material history data at each time step, and numerical "fracture" can occur when particles lose contact.

Recognizing the tremendous accomplishments of pure Eulerian (e.g. CTH [14]), Lagrangian (e.g. DYNA3D [15]), and particle (e.g. SPHINX [16]) codes, the preceding discussion suggests nonetheless that some hybrid formulation may be advantageous for oblique debris shield impact simulations. One possibility is some combination of particle and finite element methods - the particle capability can simulate shield perforation and debris transport while the finite element capability can simulate strength dependent (near ballistic limit) effects during the wall plate impact. Published work in this area has emphasized adding SPH options to finite element codes [4]. The questions which arise with such an approach include: (1) are conventional erosion and slideline algorithms sufficiently general? and (2) how will particle-element interactions and element-to-particle transition be represented? The answers to these questions will determine in part the range of contact-impact problems which can be efficiently modeled using this approach.

As an alternative approach, another hybrid particle-finite element formulation has been developed which combines the Lagrangian particle dynamics method of Fahrenthold and Koo [17, 18] with a large strain elastic-plastic finite element formulation. This method, described in detail by Fahrenthold and Horban [5], has been implemented in a three dimensional computer code (EXOS) developed for the simulation of hypervelocity impact on orbital debris shielding. The code can simulate the large strain, elastic-plastic, thermomechanical impact dynamics of solid, fluid, or combined solid-fluid structures and systems. The code is particle based, with a finite element based strength model, and uses a Mie-Gruneisen equation of state. The kinematics, energy functions, and constraints are fully Lagrangian in form. The formulation includes finite strain plasticity, scalar damage variables, decoupled volumetric-deviatoric response, and transient thermal dynamics. The code is three dimensional and includes a plane of symmetry option. A pre-processor simplifies model generation. Although the code is currently undergoing additional development, it has been used to perform the simulations discussed in the sections which follow.

It should be noted here that a number of relatively new numerical modeling techniques including Arbitrary Lagrangian-Eulerian (ALE) methods [19], element free Galerkin methods [20], and alternative particle methods [21] are under development which may prove effective in addressing the orbital debris simulation problem. However to date these methods have not been extensively applied to the application of interest here.

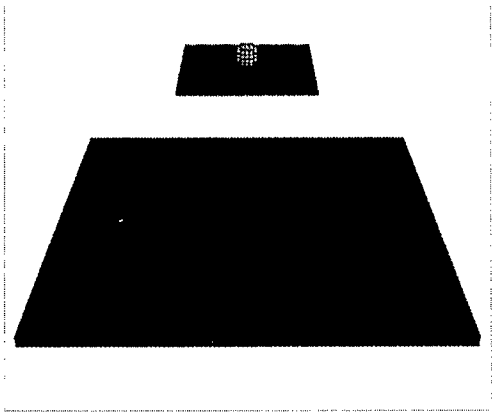

Fig. 1. Example oblique Whipple shield impact simulation (t = 0 microseconds).

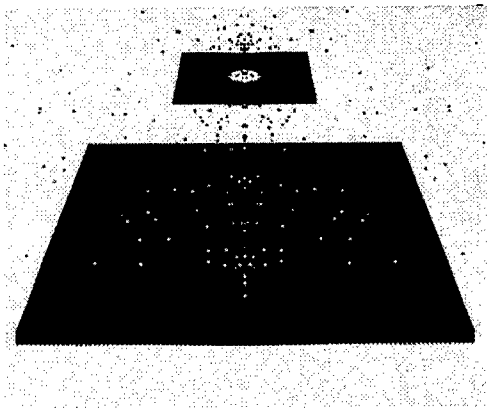

Fig. 2. Example oblique Whipple shield impact simulation (t = 33 microseconds).

SIMULATION METHODOLOGY

As an illustration of the simulations discussed in the sections that follow, Figures 1 and 2 depict the results of a typical oblique Whipple shield impact simulation. The parameters of this example simulation are provided in Table 1 (material properties were taken from Steinberg[22]). The example involves the 7 km/sec impact of a 0.60 cm diameter aluminum sphere on an aluminum Whipple shield and wall plate combination, at an impact obliquity of 15 degrees. Figures 1 and 2 are plots of the simulation results at 0 and 33 microseconds after impact respectively. Consistent with the experimentally derived ballistic limit curve of Christiansen [1], the simulation predicts

perforation of the wall plate. The simulation involved approximately 30,000 particles and required approximately 10 CPU hours on a high performance workstation. Automated rezoning was used every 500 time steps to minimize CPU time (particles moving outside a user specified region above the wall plate were zoned out of the calculation).

Table 1. Example oblique Whipple shield impact simulation

Projectile diameter (aluminum sphere)	=	0.60 cm
Shield thickness (aluminum)	=	0.127 cm
Wall thickness (aluminum)	=	0.3175 cm
Shield-to-wall spacing	=	5.0 cm
Impact velocity	=	7.0 km/sec
Impact obliquity	=	15 degrees
Equation of state type	=	Mie-Gruneisen
Spall stress	=	0.012 Mbar
Failure pressure (tension)	=	0.012 Mbar
Yield stress	=	0.0029 Mbar
Plastic failure strain	=	3.0
Shear modulus	=	0.271 Mbar
Density	=	2.7 g/cc
Melt temperature	=	1,220 degrees K
Number of particles	=	29,422
Total simulation time	=	33 microseconds
Number of time steps	=	4,500

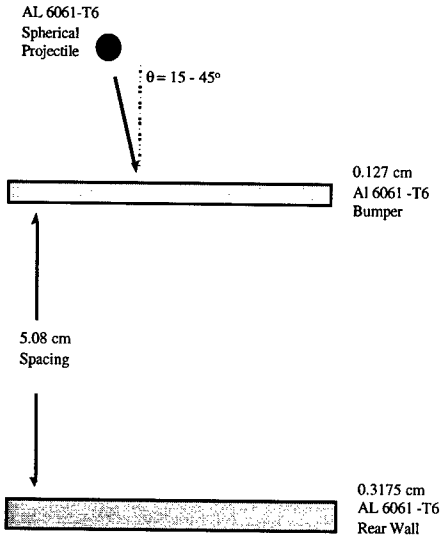

Fig. 3. Geometry for the Whipple shield ballistic limit simulations.

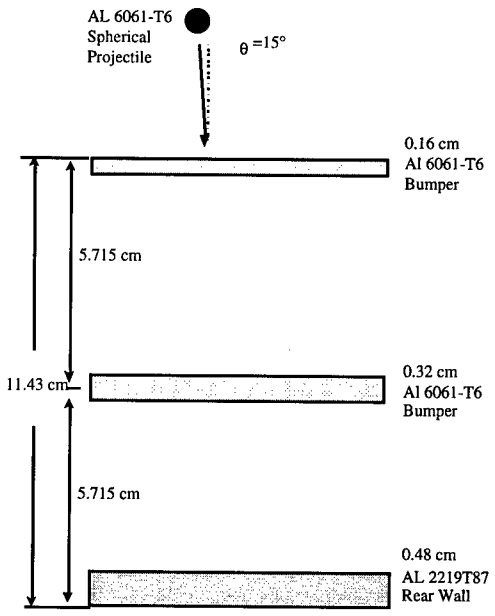

Fig. 4. Geometry for the multi-plate shield ballistic limit simulations.

In order to conduct a systematic evaluation of the utility of hybrid particle-finite element methods in orbital debris shield design, a series of simulations like the one just described were performed, in an attempt to match several experimentally derived ballistic limit curves. Such ballistic limit curves portray graphically the critical projectile diameter required to fail a specific shield and wall plate configuration, as a function of projectile velocity and impact obliquity. Failure is defined as perforation or spall of the wall plate. Ballistic limit curves have been constructed by testing a wide variety of shield geometry's and materials, and are used extensively in orbital debris shield design.

The next section discusses the results of a series of Whipple shield (Figure 3) impact simulations performed at impact obliquity's of 15 and 45 degrees, for various projectile diameters and impact velocities. The results are compared to known ballistic limit curves derived from experiment. In the section which then follows, the results of several simulations involving all-aluminum stuffed Whipple shields (Figure 4) are compared to corresponding experiments and a published ballistic limit curve for a weight equivalent composite-aluminum stuffed Whipple shield. The final section notes the conclusions of this study and plans for future work.

WHIPPLE SHIELD BALLISTIC LIMIT SIMULATIONS

The Whipple shield is the basis for most simple orbital debris shielding designs. The Whipple shield is a thin, sacrificial sheet of material (a bumper) mounted at a fixed standoff distance from the protected structure. An incoming projectile hits the bumper and hopefully fragments or melts, distributing its impact momentum over a wide area of the rear wall. Experiments on aluminum have shown the existence of three distinct projectile response regimes, based on the normal component of the projectile impact velocity. The first regime is located below 3 km/s. At low velocities, the projectile remains nearly intact after impact with the bumper. Shock pressures are low, so the rear wall suffers impact from a deformed but sound projectile. Hence in this regime the critical particle diameter decreases as velocity increases. The second (intermediate) velocity regime is between 3 and 7 km/s. In this velocity range, the projectile fragments and/or melts on impact, reducing its lethality as its velocity increases. The third region consists of normal velocities above 7 km/s, wherein the debris cloud that impacts the rear wall is a multiphase mixture of projectile and bumper components. In this regime the debris cloud becomes more damaging as the impact velocity increases. The solid lines in Figures 5 and 6 are experimental ballistic limit curves [1] for the Whipple shield configuration of Figure 3, for impact obliquity's of 15 and 45 degrees respectively.

Numerical impact simulations were performed for the Whipple shield configuration of Figure 3, for ten different projectile diameter and impact velocity combinations, at each of the two aforementioned obliquity's, in an attempt to match the experimental ballistic limit curves of Figures 5 and 6. In particular, simulations were conducted for projectile diameters slightly smaller and slightly larger than the critical diameter, at velocities of 3, 5, 7, 9, and 11 km/s. In general the code was run to a stop time 6-15 times that required for an unimpeded projectile traveling at the initial velocity to traverse the space between the shield and rear wall. This allowed sufficient time for the debris cloud to impact the rear wall and generate an impulse load. Due to the large number of simulations required and the large CPU time requirements of three dimensional simulation, relatively coarse models of less than 10,000 particles were initially used. In those cases where the coarse models failed to match the ballistic limit curves, finer models (up to 40,000 particles) were used in an attempt to improve the simulation results. CPU times for the coarse and fine models were approximately 20 and 67 CPU hours respectively, on a Cray J90. Particle count and CPU time for each simulation are detailed by Rabb [23]. The simulation results are shown by the open and closed triangles plotted in Figures 5 and 6, indicating good agreement, except at the highest velocity in the 15 degree obliquity case. Tables 2 and 3 describe the wall plate damage predicted by the simulation, including bulging, spallation, and/or perforation.

MULTI-PLATE SHIELD SIMULATIONS

One relatively new system designed to improve spacecraft protection from orbital debris is the multi-plate or stuffed Whipple shield. The simplest stuffed Whipple shield improves upon the basic Whipple by adding an intermediate layer of material between the rear wall and the aluminum bumper (Figure 4). This intermediate layer may be aluminum or a composite material, such as

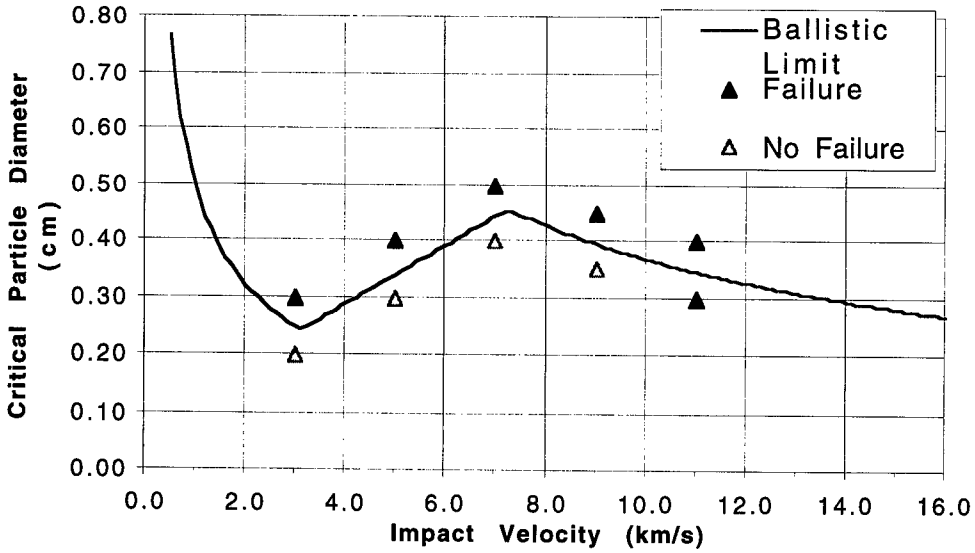

Fig. 5. Ballistic limit curve for the 15 degree obliquity Whipple shield simulations.

Table 2. Predicted damage for the 15 degree obliquity Whipple shield simulations (velocity in km/sec, projectile diameter in cm)

Velocity (diameter)	Shield Failure	Rear Wall Damage Description
3 (0.20)	No	Slight bulge (1 mm deep)
3 (0.30)	Yes	Spallation
5 (0.30)	No	Slight bulge (1 mm deep)
5 (0.40)	Yes	Spallation; Bulge (2 mm deep)
7 (0.40)	No	Slight bulge (2 mm deep)
7 (0.50)	Yes	Perforation; Hole (17 mm diam)
9 (0.35)	No	Slight bulge (2 mm deep)
9 (0.45)	Yes	Spallation; Bulge (25 mm diam, 9 mm deep)
11 (0.30)	Yes	Perforation; Hole (5 mm diam)
11 (0.40)	Yes	Spallation; Bulge (12 mm diam, 2 mm deep)

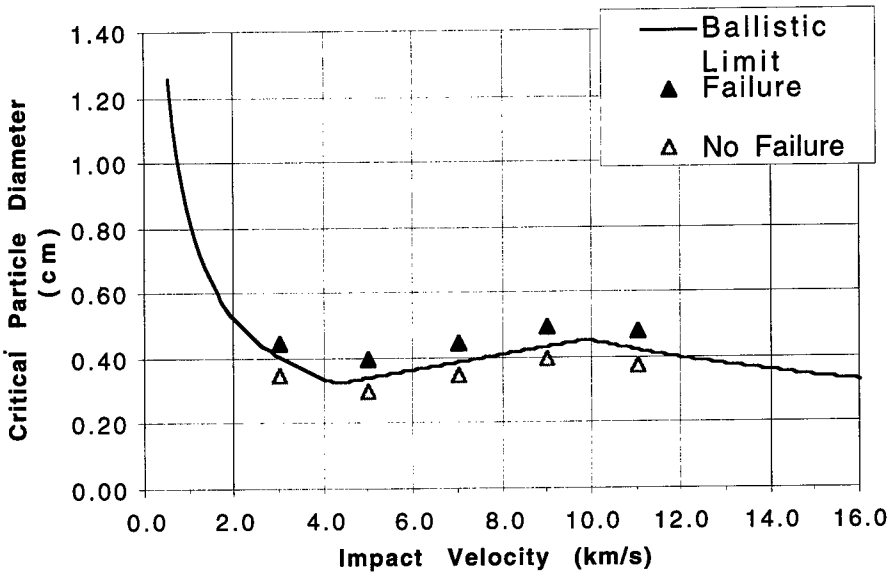

Fig. 6. Ballistic limit curve for the 45 degree obliquity Whipple shield simulations.

Table 3. Predicted damage for the 45 degree obliquity Whipple shield simulations (velocity in km/sec, projectile diameter in cm)

Velocity (diameter)	Shield Failure	Rear Wall Damage Description
3 (0.35)	No	Slight bulge (1 mm deep)
3 (0.45)	Yes	Spallation
5 (0.30)	No	Slight bulge (2 mm deep)
5 (0.40)	Yes	Spallation
7 (0.35)	No	Slight bulge (2 mm deep)
7 (0.45)	Yes	Perforation; Bulge (2 mm deep)
9 (0.40)	No	Slight bulge (1 mm deep)
9 (0.50)	Yes	Spallation; Bulge (3 mm deep)
11 (0.375)	No	Slight bulge (1 mm deep)
11 (0.425)	Yes	Spallation; Bulge (18 mm diam, 3 mm deep)

combination of Nextel and Kevlar. The intermediate layer can generate additional shocks in the projectile and disrupt the moving debris cloud, rendering it less lethal when it reaches the rear wall [24, 25]. Although the additional shield does contribute particles to the debris cloud, these particles are normally much smaller than the projectile fragments. Experiments have shown that the benefits of the intermediate layer outweigh its disadvantages.

Ballistic limit equations for the stuffed Whipple shield are not as well developed as those for simple Whipple shields. However Christiansen and Kerr [25] do provide ballistic limit equations for a specific Nextel-Kevlar-MLI (Multi-Layer Insulation) stuffed Whipple configuration which is of potential interest for ISS shielding applications. The solid line in Figure 7 shows that ballistic limit curve, for a projectile impact obliquity of 15 degrees. The latter authors also cite several experiments on weight equivalent all-aluminum stuffed Whipple shields, demonstrating the superior performance of the composite design. Figure 4 shows the weight equivalent all-aluminum stuffed Whipple shield used in the cited experiments.

In the interest of evaluating the particle-finite element modeling methodology used here on a stuffed Whipple shield configuration, three simulations were performed for the all-aluminum shield configuration of Figure 4, at an impact obliquity of 15 degrees, attempting to duplicate the cited experimental results. The results were also compared to the weight equivalent Nextel-Kevlar-MLI ballistic limit curve shown in Figure 7. No simulations were performed for Nextel-Kevlar-MLI stuffed Whipple designs, due to the lack of equation of state data for the composite materials and the fact that the required anisotropic strength models for the composite materials are still under development [26].

The solid triangles in Figure 7 indicate the projectile diameters and velocities for which simulations were conducted. The simulations were run for 61-66 microseconds, approximately four times that required for an unimpeded projectile traveling at the initial velocity to traverse the space between the first shield and the rear wall. Approximately 35,000 particles were employed, with each simulation requiring about 23 CPU hours on a Cray J90. Each of the simulations predicted similar results, namely slight bulging and spallation failure of the wall plate. The latter results are generally consistent with the experimental data, in that two of the three experiments showed wall plate failure. Note from Figure 7 that the tested velocities and projectile diameters varied only slightly between the three tests. In addition, the simulations indicate that the performance of all-aluminum stuffed Whipple shields is inferior to that of weight-equivalent composite designs, given the predicted failures of the wall plate at particle diameters below the experimental Nextel-Kevlar-MLI ballistic limit curve shown in Figure 7. It should be noted that due to CPU time constraints, the simulations were terminated after the first indication of wall plate failure (spallation). The debris cloud of projectile and bumper particles had not in all cases fully loaded the rear wall. The rear wall could incur additional damage from subsequent loading of the traveling debris.

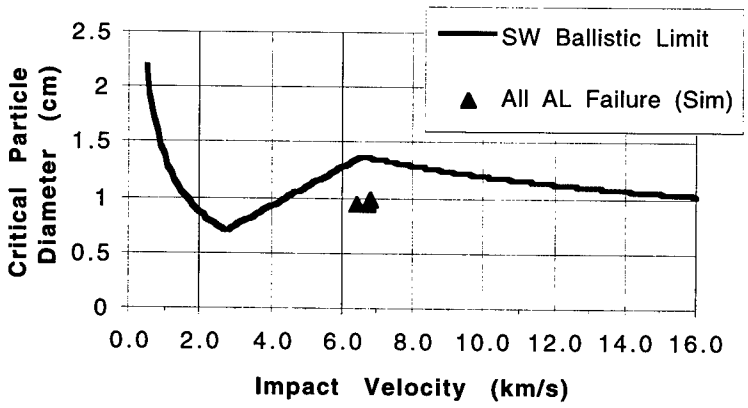

Fig. 7. Ballistic limit curve for the 15 degree obliquity multi-plate shield simulations.

CONCLUSIONS

The present paper has described the application of a new particle-finite element modeling method in the simulation of hypervelocity impact on orbital debris shielding. Three dimensional simulation results were compared to experimentally derived ballistic limit curves for oblique impact on Whipple and multi-plate spacecraft shielding, at velocities ranging from 3 to 11 km/s. In general the simulations show good agreement with the experimental curves, suggesting the further development of coupled or hybrid particle-element methods for hypervelocity impact simulation.

Although the simulation results presented here are encouraging, they represent preliminary work involving a new code and a new numerical modeling scheme. Since the present simulations were evaluated using a fail/no-fail criterion only, the accurate simulation of failure modes was not critically evaluated. In addition, the Mie-Gruneisen equation of state used here is certainly approximate at the high end of the impact velocity range considered. Relatively coarse models were employed, refined somewhat whenever initial simulation results were not consistent with the experimental curves. All of these issues warrant further study.

Additional code verification and testing is needed, as well as development and implementation work on composite equation of state and anisotropic strength models for new shielding designs. However the results presented here do support a trend towards the increased use of computer simulation in orbital debris shield design. Until experimental capabilities are developed to reach all velocities and impact energies of interest, simulations will provide the only estimates of shield performance in some hypervelocity impact regimes.

Acknowledgments—This work was supported by the Space Science Branch of NASA Johnson Space Center under Grants NAG 9-808 and NAG 9-946. Computer time support was provided by the Texas Advanced Computing Center at the University of Texas at Austin.

REFERENCES

1. E.L. Christiansen, Design and performance equations for advanced meteoroid and debris shields, *International Journal of Impact Engineering*, **14**, 145-156 (1993).
2. E.P. Fahrenthold, A Lagrangian model for debris cloud dynamics simulation, *International Journal of Impact Engineering*, **14**, 229-240 (1993).
3. E.P. Fahrenthold, Oblique hypervelocity impact simulation for Whipple shield-protected structures, *International Journal of Impact Engineering*, **17**, 291-302 (1995).
4. G.R. Johnson, E.H. Petersen, and R.A. Stryk, Incorporation of an SPH option into the EPIC code for a wide range of high velocity impact computations, *International Journal of Impact Engineering*, **14**, 385-394 (1993).
5. E.P. Fahrenthold and B.A. Horban, A hybrid particle-finite element method for hypervelocity impact simulation, *International Journal of Impact Engineering*, in press.
6. W.M. Isbell and W.J. Tedeschi, Hypervelocity research and the growing problem of space debris, *International Journal of Impact Engineering*, **14**, 359-372 (1993).
7. T. Belytschko and J.I. Lin, A three-dimensional impact-penetration algorithm with erosion, *International Journal of Impact Engineering*, **5**, 111-127 (1987).
8. E.S. Hertel, Comparison of Analytic Whipple Bumper Shield Ballistic Limits with CTH Simulations, Sandia Report SAND92-0347 (1993).
9. J.J. Monaghan, An Introduction to SPH, *Computer Physics Communications.*, **48**, 89-96 (1988).
10. R.F. Stellingwerf and C.A. Wingate, Impact modeling with smooth particle hydrodynamics, *International Journal of Impact Engineering*, **14**, 707-718 (1993).
11. L.D. Libersky, A.G. Petschenk, T.C. Carney, J.R. Hipp, and F.A. Allahdadi, High strain Lagrangian hydrodynamics, *Journal of Computational Physics*, **109**, 67-75 (1993).
12. W. Benz and E. Asphaug, Simulations of brittle solids using smooth particle hydrodynamics, *Computer Physics Communications*, **87**, 253-265 (1995).
13. G.R. Johnson and S.R. Beissel, Normalized smoothing functions for SPH impact computations, *International Journal for Numerical Methods in Engineering*, **39**, 2725-2741 (1996).
14. J.M. McGlaun, S.L. Thompson, and M.G. Elrick, CTH: a three dimensional shock wave physics code, *International Journal of Impact Engineering*, **10**, 351-360 (1990).
15. J.O. Hallquist, Theoretical Manual for DYNA3D, Lawrence Livermore National Laboratories (1983).

16. C.A. Wingate, R.F. Stellingwerf, R.F. Davidson, and M.W. Burkett, Models of high velocity impact phenomena, *International Journal of Impact Engineering*, **14**, 819-830 (1993).
17. E.P. Fahrenthold and J.C. Koo, Hamiltonian particle hydrodynamics, *Computer Methods in Applied Mechanics and Engineering*, **146**, 43-52 (1997).
18. E.P. Fahrenthold and J.C. Koo, Energy based particle hydrodynamics for hypervelocity impact simulation, *International Journal of Impact Engineering*, **20**, 253-264 (1997).
19. K.G. Budge and J.S. Peery, RHALE: A MMALE shock physics code written in C++, *International Journal of Impact Engineering*, **14**, 107-120 (1993).
20. Y.Y. Lu, T. Belytschko, and M. Tabbara, Element-free Galerkin method for wave propagation and dynamic fracture, *Computer Methods in Applied Mechanics and Engineering*, **126**, 131-153 (1995).
21. D. Sulsky, Z. Chen, and H.L. Schreyer, A particle method for history dependent materials, *Computer Methods in Applied Mechanics and Engineering*, **118**, 179-196 (1994).
22. D.J. Steinberg, Equation of State and Strength Properties of Selected Materials, Lawrence Livermore National Laboratory, Livermore, CA, UCRL-MA-106439 (1996).
23. R.J. Rabb, Numerical Simulation of Ballistic Limit Curves for Orbital Debris Shielding, Master of Science thesis, Department of Mechanical Engineering, University of Texas at Austin (1998).
24. E.L. Christiansen, J.L. Crews, J.E. Williamsen, J.H. Robinson, and A.M. Nolen, Enhanced meteoroid and orbital debris shielding, *International Journal of Impact Engineering*, **17**, 217-228 (1995).
25. E.L. Christiansen and J.H. Kerr, Projectile shape effects on shielding performance at 7 Km/s and 11 Km/s, *International Journal of Impact Engineering*, **20**, 165-172 (1997).
26. E.P. Fahrenthold and B.A. Horban, Hypervelocity impact simulation in composite materials, *Proceedings of the 5th International Conference on Composites Engineering*, Las Vegas, 275-276 (1998).

PERGAMON

International Journal of Impact Engineering 23 (1999) 745–756

INTERNATIONAL JOURNAL OF IMPACT ENGINEERING

www.elsevier.com/locate/ijimpeng

RESEARCH ON FEATURES OF BEHAVIOUR OF ISOTROPIC AND ANISOTROPIC MATERIALS UNDER IMPACT

ANDREW V. RADCHENKO*, SERGEI V. KOBENKO*, IGOR N. MARZENYUK*, IVAN E. KHOREV**, GENADII I. KANEL***, and V. E. FORTOV***

*Tomsk Branch of the Institute for Structural Macrokinetics of Russian Academy of Sciences, Tomsk, GSP-18, 8 Lenin Square, 634050, Russia; **Tomsk university of control system and radioelectronics, Tomsk, 40 Lenin av., 634050, Russia; ***Institute of high temperature of Russian Academy of Sciences, Moscow, 13/19 Izhorskaya street, 127412, Russia

Summary— In paper, the influence of anisotropy degree and orientation of strength properties on destruction of materials under impact is investigated numerically and experimentally. The numerical modeling was carried out in three-dimensional statement by a method of finite elements in frameworks of the continual approach of the mechanics of deformable solid. The destruction is described by tensor polynomial criterion of the fourth degree, which takes into account the influence of hydrostatic pressure.© 1999 Elsevier Science Ltd. All rights reserved.

INTRODUCTION

Development of modern materials production technologies with the given orientation of physico-mechanical and the increasing requirements imposing to optimization and reliability of the operational characteristics of designs, cause the increased interest to the investigations of anisotropic materials behavior in various conditions.

The distinctions in structure and technologies of anisotropic materials creation also predetermine their essential qualitative distinctions in response toward external loading. It results in necessity of complex experimental and theoretical approach to a problem. However investigations in this direction are carried out basically for static conditions of load. The behavior of anisotropic materials under the conditions of dynamic loading is practically not investigated. This is especially the case with experimental investigations as well as with mathematical and numerical modeling.

The investigations of the material damage under impact show that the destruction mechanisms change with the interaction conditions. The experiments identify that in a number of cases the resulting destruction is determined by the combination of several mechanisms. But in the experiments we fail to trace sequence, operation time and the contribution of various destruction mechanisms. Besides, the distractions, obtained at the initial stages of the process can't always be identified in the analysis of the resulting destruction of the materials. For anisotropic materials the strength itself is multivalued and uncertain notion due to the polymorphism of behaviour of these materials under the load. The limiting state of anisotropic bodies may be of different physical nature in dependence on load orientation, stressed state type and other factors. The dependence of the physical nature of limiting states is revealed in the study of the experimental data.

The investigations of hydrostatic pressure effect upon the strength of isotropic materials show that comprehensively the compression exerts a weak action on the resistance of isotropic materials under static loads. Therefore, the classic theories of strength, plasticity and creep are based on assumption about the lack of the effect of fall stress tensor upon strength isotropic materials.

0734-743X/99/$ - see front matter © 1999 Elsevier Science Ltd. All rights reserved.
PII: S0734-743X(99)00119-0

In the experiments with anisotropic materials it was state that flow phenomenon may arise only under the action of hydrostatic pressure. Upon the materials strength is due to the anisotropy. The shape of anisotropic bodies changes under the action of hydrostatic pressure. If these changes reach such values that, they don't disappear under relief, the limiting state should come. Therefore, the postulate of classic strength that hydrostatic pressure can't transfer the material to the dangerous state is not valid for anisotropic materials.

Phenomenological approach to the investigation of dynamics of deformation and destruction of anisotropic and isotropic materials is used in the work. The phenomenological approach to the materials strength requires that the conditions of the transition into the limiting state of various physical nature should be determinated by one equation (criterion). The necessity of such an approach results from destruction polymorphism, being deduced experimentally.

For anisotropic bodies the phenomenological approach has many advantages, since there appears the possibility to use general condition of strength for the material different in composition and technology but similar in symmetry of properties, and also for the materials with substantial anisotropy, for which one and the same stressed state can result in limiting conditions, different in physical nature.

THE BASIC EQUATIONS OF THE MODEL

The problem of interaction of steel striker in the form of compact cylinder with isotropic and anisotropic (transtropic and orthotropic) barriers from organo- and glassplastic is considered.

The system of equations describing non-stationary adiabatic movements of compressing medium in the arbitrary coordinate system (i=1,2,3) includes the following equations:

-continuity equation:

$$\frac{d\rho}{dt} + div\rho\bar{\upsilon} = 0 \tag{1}$$

-equations of motion:

$$\rho a^k = \nabla_i \sigma^{ki} + F^k \tag{2}$$

where

$$\sigma^{ki} = -p\delta_{ki} + S^{ki}\ ;\ \nabla_i \sigma^{ki} = \sigma^{ki}_{,i} + \sigma^{mi}\Gamma^k_{mi} + \sigma^{ki}\Gamma^m_{mi}$$

$$a^k = \frac{\partial \upsilon^k}{\partial t} + \upsilon^i \nabla_i \upsilon^k$$

-equation of energy:

$$\frac{dE}{dt} = \frac{1}{\rho}\sigma^{ij} e_{ij}\,. \tag{3}$$

Here ρ is the medium density; $\bar{\upsilon}$ is the speed vector; a^k are the components of acceleration vector; F^k are the components of vector of mass forces; Γ^k_{ij} are Kristoffel symbols; δ_{ij} is the Kronekker symbol; σ^{ij}, S^{ij} and P are contravariant components of the symmetrical tensor of stress, deviator of stress and the ballpart of tensor of stress-pressure, respectively; E is the specific internal energy; e_{ij} are the components of the symmetric tensor of strain rates:

$$e_{ij} = \frac{1}{2}\left(\nabla_i \upsilon_j + \nabla_j \upsilon_i\right). \tag{4}$$

Supposing that the principal of minimum work of true stress at the increment in plastic deformations is valid for the medium, let's write the relation of the component of tensor of strain rates and stress deviator for the strike material in the form of

$$2G\left(e_{ij} - \frac{1}{3}e_{kk}\delta_{ij}\right) = \frac{DS^{ij}}{Dt} + \lambda S^{ij}, (\lambda \geq 0). \tag{5}$$

Here

$$\frac{DS^{ij}}{Dt} = \frac{dS^{ij}}{dt} - S^{ik}\omega_{jk} - S^{jk}\omega_{ik}$$

where $\omega_{ij} = \frac{1}{2}\left(\nabla_i \upsilon_j - \nabla_j \upsilon_i\right)$, G is shear modulus.

Under elastic deformation the parameter $\lambda = 0$ and under plastic deformation ($\lambda > 0$) is defined with the help of Von Mises law:

$$S^{ij}S_{ij} = \frac{2}{3}\sigma_d^2 \tag{6}$$

where σ_d is the dynamic yield point.

The pressure in the material of the striker was present by the function of the specific internal energy (E) and density (ρ):

$$P = P(\rho, E) \tag{7}$$

The equation of Mie-Gruneisen type [1] and wide-range equation [2] were used and equation of state (7). The components of tensor of stress in the barrier material before the destruction are defined from relations for orthotropic body:

$$\begin{aligned}
&\frac{d\sigma_{11}}{dt} = C_{11}e_{11} + C_{12}e_{22} + C_{13}e_{33}\ , \quad \frac{d\sigma_{12}}{dt} = C_{44}e_{12}\ ; \\
&\frac{d\sigma_{22}}{dt} = C_{12}e_{11} + C_{22}e_{22} + C_{23}e_{33}\ , \quad \frac{d\sigma_{23}}{dt} = C_{55}e_{23}\ , \\
&\frac{d\sigma_{33}}{dt} = C_{13}e_{11} + C_{23}e_{22} + C_{33}e_{33}\ , \quad \frac{d\sigma_{13}}{dt} = C_{66}e_{13}\ ,
\end{aligned} \tag{8}$$

where, C_{ij} are elastic constants.

The elastic constants C_{ij} can be expressed through Young's module E_i and Poisson's ratio ν_{ij}:

$$\begin{aligned}
&C_{11} = \frac{1}{E_2 A}\left(\frac{1}{E_3} - \frac{\nu_{23}^2}{E_2}\right); C_{12} = \frac{1}{E_3 A}\left(\frac{\nu_{31}\nu_{23}}{E_3} + \frac{\nu_{12}}{E_1}\right); C_{13} = \frac{1}{E_2 A}\left(\frac{\nu_{12}\nu_{23}}{E_1} + \frac{\nu_{31}}{E_3}\right) \\
&C_{22} = \frac{1}{E_3 A}\left(\frac{1}{E_1} - \frac{\nu_{31}^2}{E_2}\right); C_{23} = \frac{1}{E_1 A}\left(\frac{\nu_{12}\nu_{31}}{E_3} + \frac{\nu_{23}}{E_2}\right); C_{33} = \frac{1}{E_1 A}\left(\frac{1}{E_2} - \frac{\nu_{12}^2}{E_1}\right) \\
&C_{44} = G_{12}\ ; C_{55} = G_{23}\ ; C_{44} = G_{13} \\
&A = \frac{1}{E_1 E_2 E_3}\left(1 - 2\nu_{12}\nu_{23}\nu_{31} - \frac{E_1}{E_3}\nu_{31}^2 - \frac{E_2}{E_1}\nu_{12}^2 - \frac{E_3}{E_2}\nu_{23}^2\right)
\end{aligned} \tag{9}$$

Tensor-polynomial criterion of the fourth degree [3-7], taking in to account the hydrostatic pressure is used to define the transition of the barrier material into the destructed state:

$$\alpha_{ik\ell m}\sigma_{ik}\sigma_{\ell m} - \left[\frac{\left(\sigma_{ik}\delta_{ik}\right)^2 + \sigma_{ik}\sigma_{ik}}{2}\right]^{\frac{1}{2}} \le 0 \qquad (10)$$

In complex stressed states that tensor-polynomial criterion contains stresses to the second and fourth power; the fourth order of polynomial allows not only to approximate the experimental data better than the second one but also comply with the nature of strongly anisotropic bodies: the strength surface for strongly anisotropic bodies may contain vortex as well as concave sites according to the different character of dangerous state at these sites.

The first summand ($\alpha_{ik\ell m}\sigma_{ik}\sigma_{\ell m}$) is the joint invariant of stress tensor and strength tensor, and the second one expresses the dependence of strength of anisotropic bodies upon two invariants of stress tensor J_1 and J_2. The first summand of this equation is the "plastic potential'' in its extended form. In physical aspect the invariant equation may be considered as the generalization of Mises "plastic potential" for the case when clear dependence of limiting state upon the first invariant of stress tensor (upon hydrostatic pressure J_1) takes place. In completely extended form the criterion (10) is the polynomial of the forth power regarding to the six components of operating stresses. The constants $\alpha_{ik\ell m}$ are (in the Eqn. (10)) the components of the forth range i.e. strength tensor.

It is supposed that the destruction of anisotropic material under the conditions of heavy dynamic loads occurs according to the following scheme:

- if the criterion (10) is disrupted under the conditions of material compaction ($e_{kk} < 0$) it is considered that the material losses its anisotropic properties and its behavior is described by the hydrodynamical model;
- if the criterion (10) is destructed under the tension conditions ($e_{kk} > 0$) it is considered the material has been destructed and the components of stress tensor are to be equal to 0 ($\sigma_{ij} = 0$).

In the cartesian coordinate system XYZ (1 corresponds to the axis $X, 2 - Y, 3 - Z$) the criterion (10) for the orthotropic body can be written as:

$$\frac{\sigma_x^2 + c\sigma_y^2 + b\sigma_z^2 + d\tau_{xy}^2 + p\tau_{yz}^2 + r\tau_{xz}^2 + s\sigma_x\sigma_y + t\sigma_y\sigma_z + f\sigma_x\sigma_z}{\sqrt{\sigma_x^2 + \sigma_y^2 + \sigma_z^2 + \tau_{xy}^2 + \tau_{yz}^2 + \tau_{xz}^2 + \sigma_x\sigma_y + \sigma_y\sigma_z + \sigma_x\sigma_z}} \le [\sigma_0] \qquad (11)$$

where

$$[\sigma_0] = \frac{\sigma_{bx}}{k_b};\ c = \frac{\sigma_{bx}}{\sigma_{by}};\ b = \frac{\sigma_{bx}}{\sigma_{bz}};\ d = \frac{\sigma_{bx}}{\tau_{bxy}};$$

$$p = \frac{\sigma_{bx}}{\tau_{byz}};\ r = \frac{\sigma_{bx}}{\tau_{bxz}};\ s = \frac{4\sigma_{bx}}{\sigma_{bxy}^{(45)}} - c - d - 1;$$

$$t = \frac{4\sigma_{bx}}{\sigma_{byz}^{(45)}} - c - b - p;\ f = \frac{4\sigma_{bx}}{\sigma_{bzx}^{(45)}} - b - r - 1.$$

Here $\sigma_x, \sigma_y, \sigma_z$ and $\tau_{xy}, \tau_{xz}, \tau_{yz}$ are normal and shear components of the stress tensor. The letter σ with the low symbol "b" defines the value of dangerous stress (strength limit) at the tension or compression in the axis direction, corresponding to the second low index; the letter τ defines the same thing at pure shear, at which the right angle is changed between the axes, indicated in the index. The upper index (45) at the letter σ indicates the strength limit in the diagonal direction (at the angle of 45° to the symmetry axes), located in the plane, corresponding to the low indexes.

We shall consider the interaction of the steel strikes with isotropic and anisotropic barrier in a general, three-dimensional case in the cartesian coordinate system XYZ (fig.1). The striker is the compact cylinder, occupying the D_1 region, and limited by the surfaces Σ_1 and Σ_2. At the starting moment the speed vector of the striker coincides with its symmetry axis and forms the angle α with the normal to the barrier. The barrier occupies the D_2 region and it is limited by the Σ_2 and Σ_3 surfaces. The Σ_1 and Σ_3 surfaces are free from the forces, Σ_2 is the contact surface of the cylinder with the plate.

For the equations (1-11), the problem with the initial (at $t = 0$) and present (at the Σ_1, Σ_2, Σ_3 surfaces) boundary conditions is proposed.

Initial conditions ($t = 0$):

$$\sigma_i = \tau_{ij} = E = u = 0 \text{ at } (x,y,z) \in D_1 \cup D_2,\ i,j = x,y,z \tag{12}$$

$$u = \upsilon_0 \sin(\alpha);\ w = \upsilon_0 \cos(\alpha) \quad \text{at } (x,y,z) \in D_1 \tag{13}$$

$$u = w = 0 \quad \text{at } (x,y,z) \in D_2 \tag{14}$$

$$\rho = \rho_i \quad \text{at } (x,y,z) \in D_i,\ i = 1,2. \tag{15}$$

Here u, υ, w are the components of the speed vector along the X, Y, Z axes, respectively.

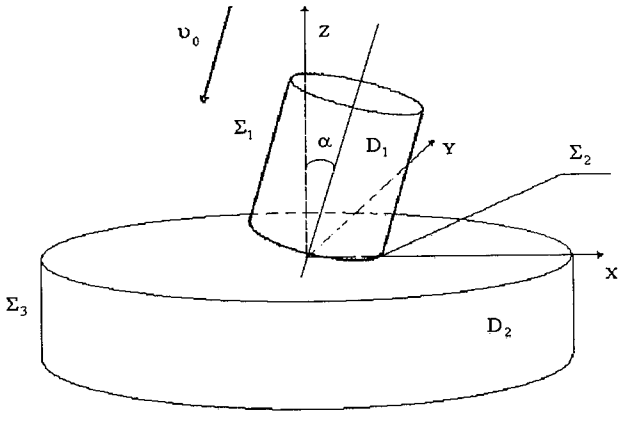

Fig. 1. Statement of a problem.

The boundary conditions have the following form. The following conditions are performed at the free Σ_1, Σ_3 surfaces:

$$T_{nn} = T_{n\tau_1} = T_{n\tau_2} = 0 \text{ at } (x,y,z) \in \Sigma_1 \cup \Sigma_3, \tag{16}$$

at the contact surface Σ_2 the sliding conditions are realized:

$$T_{nn}^{+} = T_{nn}^{-}, T_{n\tau_1}^{+} = T_{n\tau_1}^{-} = T_{n\tau_2}^{+} = T_{n\tau_2}^{-} = 0, \upsilon_n^{+} = \upsilon_n^{-} \text{ at } (x,y,z) \in \Sigma_2. \quad (17)$$

Here $\boldsymbol{n}$ is the unit normal vector to the surface at the point under consideration, τ_1 and τ_2 are the interperpendicular unit vectors in the plane, tangential to the surface at this point; $\boldsymbol{T_n}$ is the force vector at the surface with normal $\boldsymbol{n}$; υ is the speed vector. The low indexes of vector $\boldsymbol{T_n}$ and υ indicates the projections onto the corresponding basis vector, the "+" sign characterizes the value of parameters in the strike, the sign "-" indicates the same in the barrier.

Thus, the equations system (1-11) fully defines the finite problem together with initial and boundary conditions (12-17).

INVESTIGATION RESULTS

In the framework of the preset problem the experimental and numeric investigations of interaction of steel strike with isotropic and anisotropic barrier were conducted. The numeric modeling was carried out through the method of finite elements [8-10]. The plates from isotropic glassplastic and transtropic organoplastic with an anisotropy degree $n=E_{Tx}/E_{Tz}=6.4$ were used. For considered transtropic material $E_{Tx}=E_{Ty}>E_{Tz}$. E_1 values for isotropic material lies in the limits of $E_{Tx}>E_1>E_{Tz}$. Here E_{Tx}, E_{Ty}, E_{Tz} and E_1 are the modules of elasticity for the transtropic and isotropic material, respectively. Coordinate plane XOY lies in the isotropy plane of the transtropic barrier and the axis Z coincides with the normal to it. The compact (the diameter D is equal to length L) steel cylinders with the mass of m=10 (D=L=11.8 *mm*) and m=20 (D=L=14.8 *mm*) grams were used as the striker. In the experiments normal interaction ($\alpha = 0°$) of the strikers with barriers were provided.

Table 1 shown the results of experiments and calculations at the interaction of the striker with mass of 20 grams with the isotropic barrier. The following symbols are introduced into the table and the text: h is the barrier thickness, υ_0 is the initial striker speed, υ_1 is the beyond barrier speed of striker, ε is the relative decrease of the striker height after barrier piercing, δ_υ is the relative divergence along beyond barrier speed of striker in the experiment and calculation.

Table 1. Comparison of results of calculations and experiments

h, mm	υ_0, *m/s*	δ_υ, %	*Experiment*		*Calculation*	
			υ_1, *m/s*	ε, %	υ_1, *m/s*	ε, %
5	992	6.3	928	5.7	870	2.8
9	1163	6.2	1013	8.9	950	5.6
14	1064	4.0	812	10.4	780	9.0

The results on beyond barrier speeds of striker at the interaction of 20-gram striker with transtropic barrier are presented in table 2.

Table 2. Comparison of results of calculations and experiments

h, mm	υ_0, *m/s*	δ_υ, %	*Experiment*	*Calculation*
			υ_1, *m/s*	υ_1, *m/s*
26	1054	8.3	698	640
26	1077	8.2	695	638
18	1012	6.8	897	836
18	956	5.5	838	792

The influence of anisotropy and orientation of the strength properties onto the protective barrier properties can be evaluated by the plots, presented in fig. 2. The figure shows the calculated dependencies of the resistant forces upon the time at the normal striker interaction with 10 gram transtropic and isotropic (n=1) barriers with the thickness of 24 mm.

As the calculations showed the increase in the barrier strength in XOY plane provides more substantial increase in barrier resistance to penetration (curve 3) then the increase in strength along Z (curve 2).

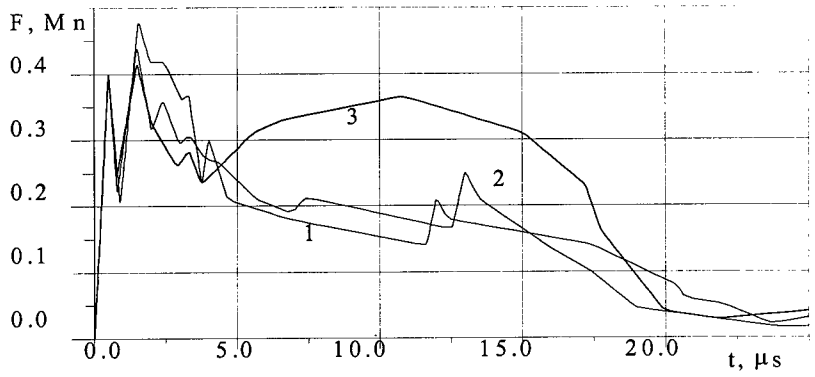

Fig. 2. Resistance force vs time. υ_0=1000 *m/s*, α=0°, 1 – n=1, 2 – n=0.1, 3 – n=10.

The calculated values of beyond barrier speeds of striker with the mass 20 gram are presented in table 3 during its interaction with the thickness of 24 *mm* and at different anisotropy degree (from 0.1 up to 10) at speeds of 2000 *m/sec* and 1000 *m/sec* where $\delta_{\upsilon i}$ is the relative deviation of beyond barrier speed of striker in comparison with isotropic case.

Table 3. Influence of orientation of barrier strength properties and interaction speed on beyond barrier speed of striker

n	0.1	0.3	1	6.4	10
υ_0=2000 *m/s*					
υ_l, *m/s*	1054	1051	1082	1060	1035
$\delta_{\upsilon i}$, %	-2.9	-2.9	0	-2.0	-4.0
υ_0=1000 *m/s*					
υ_l, *m/s*	533	557	578	468	371
$\delta_{\upsilon i}$, %	-8.0	-4.0	0	-19.0	-36.0

The analysis of the results allows to conclude that the anisotropy effect increases with the decrease of interaction speed.

Various resistance of anisotropic and isotropic barriers to the penetration is due to the dynamic of destruction, being developed in them as a result of the impact. Fig. 3 presents the configurations of isotropic (a) and transtropic (b) barriers with the thickness of h=19 *mm*, interacting with the 10 gram striker in ZOX section. The regions, in which the criterion (10) had been destructed at pressing (e_{kk}<0) are fully painted, and the regions of destruction at tension (e_{kk}>0) are cross-hatched. The destruction of the barrier material begins in the compression

wave, being initiated at the impact and developed along the barrier. The tension regions are formed as the result of reflection of compression waves from the free surfaces in the barrier. Initially they are formed at the face in the ring zone along the perimeter of the crater, being formed as the result of the reflection of compression waves from the strike side surfaces and the barrier face. Then they are formed near the end barrier surface as the result of compression wave reflection from the end surface.

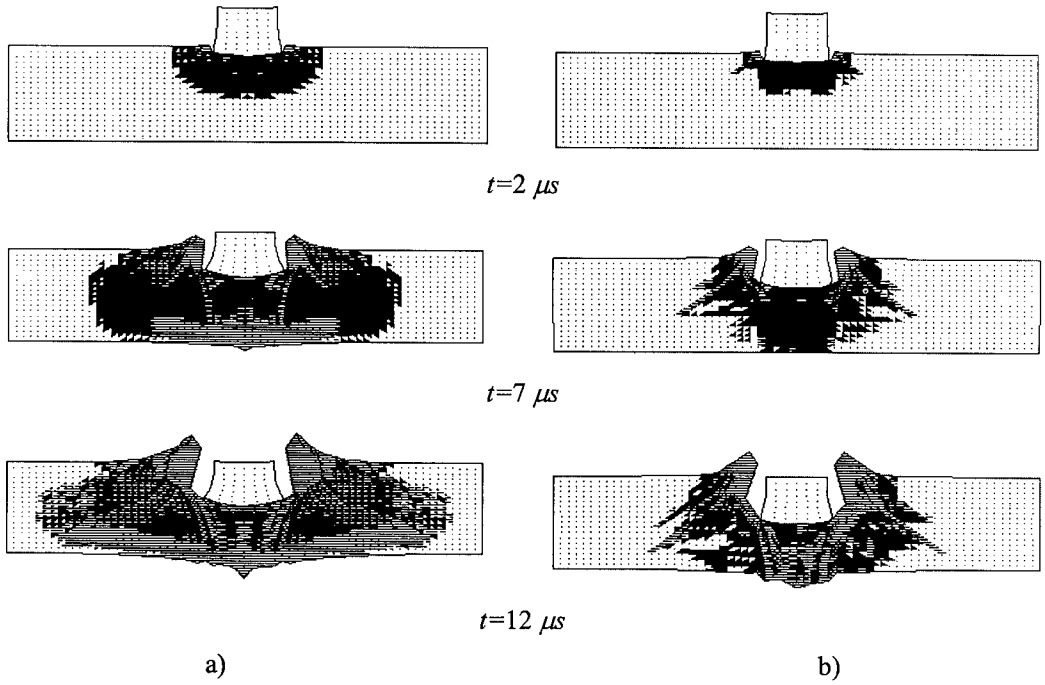

Fig. 3. Evolution destruction areas in isotropic (a) and transtropic (b) barrier. υ_0=1000 *m/s*, α =0°, *h*=19 *mm*, *m*=10 *g*.

The calculations showed that in the case under consideration the diameter of the destructed zone at the face of the transtropic barrier is 1.6 fold less then of the isotropic one and 4 fold less at the end surface (7 μs). In isotropic barrier the destruction region is extended with the propagating of the impact wave retaining vortex (initially spherical and the close to ellipsoid) form. In transtropic barrier the destruction zone in the impact wave is narrowing with its approach to the end surface. Also in transtropic barrier the narrow conic zone of destruction (crack) is separated, being propagated at the angle of 45° to *Z*-axis. Similar differences in the destruction character are explained by the fact that the rates of propagation of discharge waves (of sound) in transtropic barrier along *X*, *Y* and *Z* are various ones: $C_x=C_y>C_z$, $C_x/C_z=2.6$. Owing to this fact the discharge waves, being propagated from free surfaces with the speed, greater then the impact wave one, leads to the increase in the destruction region in the compression wave in the *X* and *Y* direction in its interaction with the latter.

The conducted experiments supported the calculation results. Fig. 4 represents the photos of faces of isotropic (a) and transtropic (b) barriers after the interaction with steel strikes. The starting conditions in the experiments corresponded to the calculated ones. As it is seen from the photos, the diameter of the distracted area in the transtropic barrier is less then the one in isotropic barrier and practically coincides with the strike diameters.

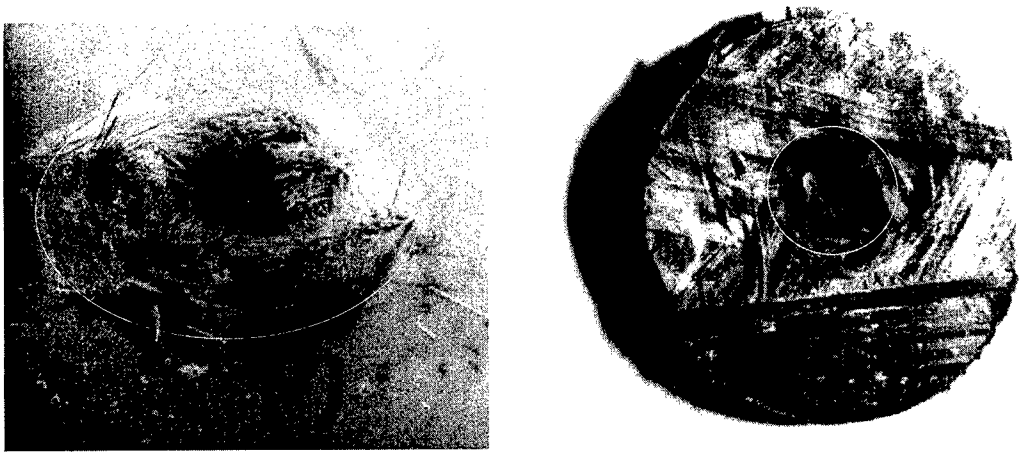

a) b)

Fig. 4. Barrier faces after interaction with striker. υ_0=1000 *m/s*, α=0°, h=19 *mm*, m=10 *g*.

Further the numerical investigations of peculiarities of destruction of isotropic, transtropic and orthotropic barriers from organoplastics were carried out during interaction with 20 gram steel striker in the impact speed range of 1000 – 3000 *m/sec* and at the meeting angles of 0° - 60°. In the calculations the following relation of elastic material properties were provided: for transtropic material $E_{Tx}=E_{Ty}>E_{Tz}$, $n=E_{Tx}/E_{Tz}$=6.8; for orthotropic one $E_{Ox}>E_{Oy}>E_{Oz}$, $n_1= E_{Ox}/E_{Oz}$=6.8, $n_2= E_{Oy}/E_{Oz}$=2.98. For isotropic barrier the elastic characteristics had mean value $E_{Tx}>E_I>E_{Tz}$. The relation between strength parameters was provided in the same manner as for the elastic characteristics.

Fig. 5 shows volume configurations, illustrating the interaction process of the striker with orthotropic barrier.

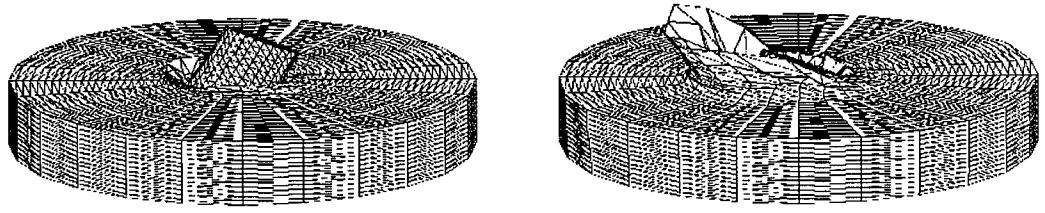

t=6 μs t=11 μs

Fig. 5. Volumetric configurations of striker and orthotropic barrier.
υ_0=1500 *m/s*, α =30°, h=15 *mm*, m=20 *g*.

The results, allowing to compare the destruction in the barriers being realized to the moment of coming out of the impact wave onto the end surface are given in table 4. The values d_T/d_I and d_O/d_I characterize the relation of the destructed region diameter at the face and end surface in transtropic and orthotropic plate to the corresponding diameter in the isotropic plate; d_f/d_e is the relation of the destructed zone diameter at the face to the one of the end barrier surface: I – isotropic, T – transtropic, O – orthotropic.

Table 4. Relation of destroyed areas

Starting conditions	Surface	d_T/d_I	d_O/d_I	d_f/d_e		
				I	*T*	*O*
υ_0=1500 *m/c* α =0°	Face	0.87	0.87	1	1	0.6
	End	0.87	0.53			
υ_0=1000 *m/c* α =30°	Face	1	0.78	0.67	0.46	0.4
	End	0.68	0.47			
υ_0=1500 *m/c* α = 30°	Face	0.95	0.76	0.67	0.64	0.41
	End	0.9	0.46			
υ_0=2500 *m/c* α = 30°	Face	1	0.83	0.73	0.67	0.48
	End	0.91	0.55			
υ_0=1500 *m/c* α = 60°	Face	1	0.78	0.6	0.3	0.28
	End	0.5	0.37			

The analysis of the investigations conducted shows that under considering conditions the diameter of the destruction region is less in anisotropic barriers (transtropic and orthotropic ones). In case the greatest increase in the destruction region is observed in orthotropic barrier: for the face the increase is 13-24 %, for the end surfaces the one is 45-63 %. Also for anisotropic barriers the greater narrowing of the destruction with the face one (d_f/d_e). Thus, if at normal (α=0°) interaction in isotropic and transtropic barrier the narrowing is absent (d_f=d_e) in orthotropic one the diameter of end destruction's is 40% less then at face. In the impact at the angle of (α=30°, α=60°) the narrowing for the isotropic barrier is 27-40%, for transtropic one it is 33-70%, for orthotropic: 40-72%.

Figures 6-8 illustrate (*ZOX* in section) the destruction dynamics of isotropic (fig. 6), transtropic (fig. 7) and orthotropic (fig. 8) barriers at normal interaction with the striker. Fig. 9 shows at the same time configurations of isotropic (a), transtropic (b), and orthotropic (c) barriers at the interaction of the striker at the angle of $\alpha = 30°$. The indication of the destruction region is similar to fig. 3.

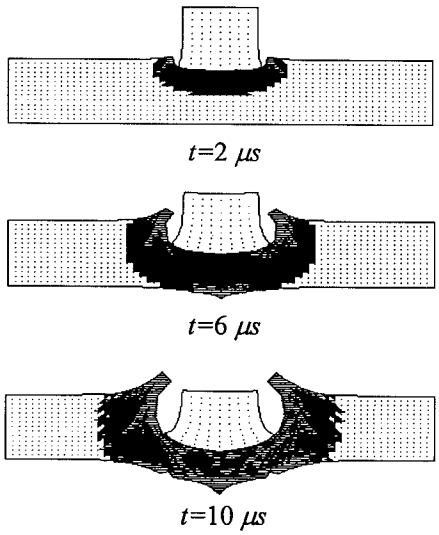

Fig. 6. Destruction areas evolution in isotropic barrier. υ_0=1500 *m/s*, α=0°, *h*=15 *mm*, *m*=20 *g*.

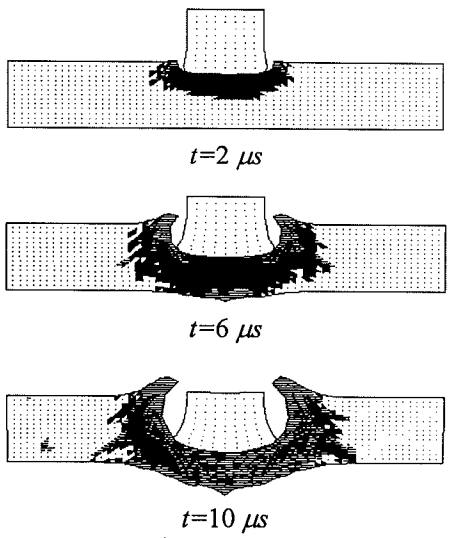

Fig. 7. Destruction areas evolution in transtropic barrier. υ_0=1500 *m/s*, α=0°, *h*=15 *mm*, *m*=20 *g*.

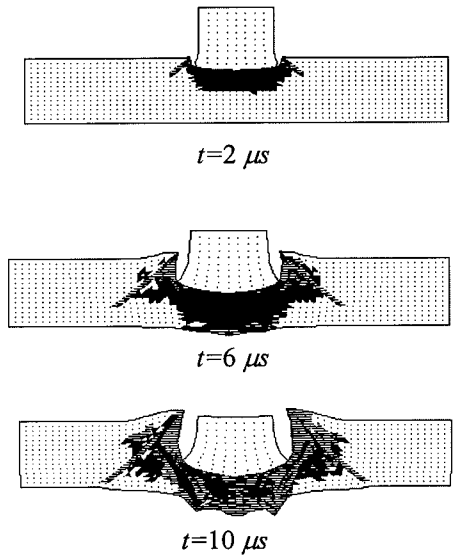

Fig. 8. Destruction areas evolution in orthotropic barrier. υ_0=1500 *m/s*, α=0°, h=15 *mm*, m=20 *g*.

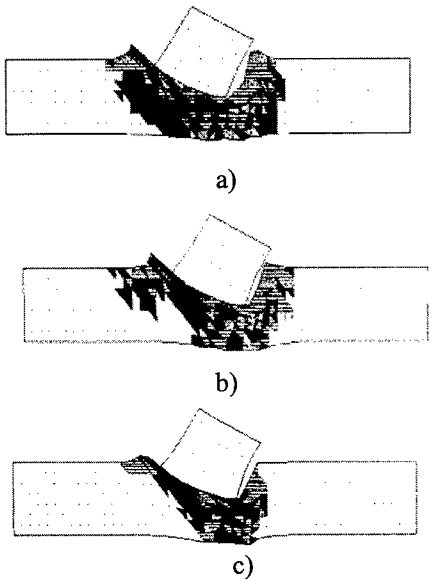

Fig. 9. Comparison of destruction areas. υ_0=1000 *m/s*, α=30°, h=15 *mm*, t=11 *μs*, m=20 *g*.

CONCLUSION

1. The offered model allows to describe adequately main laws of the destruction processes of anisotropic materials under dynamic loads.
2. The investigation showed substantial dependence of configurations and volumes of the destruction regions upon the orientation of elastic and strength material properties that defines, as a result, the resistance of the barrier to the penetration in itself.
3. The qualitative and quantitative discrepancies in the destruction of isotropic and anisotropic materials under the dynamic loads are defined not only by strength parameters but either by the interaction of the compression and tension waves. Different speeds of waves propagation along the directions in anisotropic barriers (C_x=C_y>C_z – for transtropic, C_x>C_y>C_z – for orthotropic) provide the discharge of the impact wave and the narrowing in the destruction region.

REFERENCES

1. M. L. Wilckins, The calculation of elastic-plastic flows. In *Vychislitelniye metody v gidrodinamike,* pp. 212-263, Moscow, Mir (1967).
2. A. V. Bushman, V. K. Gryaznov, G. I. Kanel, L. A. Ni, S. G. Sugak and V. E. Fortov, The dynamic of the condensed media under intensive pulse effect. Thermodynamic material properties at high pressures and temperatures. *Preprint, Chernogolovka, OIHF AN USSR* (1983).
3. E. K. Ashkenazi and A. V. Ganov, Anisotropy of the construction materials, *Spravochnik,* Leningrad (1980).
4. A. M. Vu Phenomenological criteria of the destruction of anisotropic media. In *Mehanika kompozicionnyh materialov,* Moscow, Mir (1985).

5. A. V. Radchenko and N. K. Galchenko, The destruction of isotropic and anisotropic steels under dynamic loads. *Fiziko-himicheskaya mehanika materialov*, 28(3), 80-83 (1992).
6. A. V. Radchenko, I. N. Marzenyuk and S. V. Kobenko, Investigation of Properties of Anisotropic SHS Materials. *4th Int. Symp. on Self - propagation High - temperature Synthesis*, October.6-9,Toledo, Spain (1997).
7. A. V. Radchenko, I. N. Marzenyuk and S. V. Kobenko, The influence of heterogeneous materials anisotropy properties on their behaviour under dynamic loads. *V International Conference "Computer-Aided Design of Advanced Materials and Technologies"*, August 4-6, Baikal Lake, Russia (1997).
8. G. R. Johnson, High Velocity Impact Calculations in Three Dimension. *J. Appl. Mech.*, March, 95-100 (1977).
9. G. R. Johnson, Three-dimensional analysis of sliding surface during high velocity impact. *J. Appl. Mech.*, 6, 771-773 (1977).
10. A. V. Radchenko The application of the finite element method to the calculation of flows in double phase media. In *Chislennye metody mehaniki sploshnoj sredy,* Krasnoyarsk, pp. 106-107 (1989).

PERGAMON International Journal of Impact Engineering 23 (1999) 757–770

INTERNATIONAL JOURNAL OF IMPACT ENGINEERING

www.elsevier.com/locate/ijimpeng

METALLOGRAPHIC OBSERVATIONS OF ARMOR STEEL SPECIMENS FROM PLATES PERFORATED BY SHAPED CHARGE JETS

MARTIN N. RAFTENBERG and CLAIRE D. KRAUSE

U.S. Army Research Laboratory, ATTN: AMSRL-WM-TD
Aberdeen Proving Ground, MD 21005, U.S.A.
TEL: 410-306-0788, FAX: 410-306-0783, e-mail: mnr@arl.mil

Summary—In each of four experiments, a plate of rolled homogeneous armor (RHA) was perforated by a copper jet from a shaped charge warhead. Optical and scanning electron microscopy were performed on RHA specimens prepared from a remaining perforated target plate and from various recovered fragments. In the remaining plate, white-etched (in 2 pct nital) adiabatic shear bands were found to emanate from the hole wall and enter the interior. These blended into dark-etched bands of concentrated shear. Some cracks were found to enter from the hole wall and run along a shear band. Tips of these cracks were planar, suggesting brittle cleavage. A crack not associated with a shear band was formed by the coalescence of ductile voids. Recovered fragments were bounded by white-etched adiabatic shear bands. Shear bands also entered interiors of fragments, where they sometimes meandered and bifurcated. One fragment exhibited a dendritic pattern, possibly indicative of melting. Microhardness measurements were obtained in the dendritic region, a nearby white-etched band, and the martensitic matrix. A mechanism coupling local reductions in spall strength to the presence of adiabatic shear banding is proposed. Published by Elsevier Science Ltd.

INTRODUCTION

Four experiments were performed, each with a shaped charge warhead fired at normal incidence into a plate of rolled homogeneous armor (RHA). The same type of warhead was used in all experiments. The two parameters varied in the series were the standoff, or distance between charge base and the target plate, and the target plate thickness. Optical and scanning electron micrographs of RHA specimens are presented. These micrographs reveal several features: dark-etched (in 2 pct nital) shear banding, white-etched shear banding, a sharp-tipped crack that runs along a white-etched shear band, a crack not associated with shear banding that was formed by void coalescence, and a dendritic structure near the periphery of a fragment that may indicate melting. The purpose was to remind modelers of important micromechanical phenomena active in perforation by a shaped charge jet.

METHODS

The shaped charge warhead had a conical, oxygen-free, high conductivity (OFHC) copper liner with a 42° apex angle, an 81.28-mm outer-diameter base, and a 1.91-mm wall thickness. The explosive fill was Composition-B. The jet tip speed produced by this warhead has been determined to be 7.73 mm/:s [1, 2].

0734-743X/99/$ - see front matter Published by Elsevier Science Ltd.
PII: S0734-743X(99)00120-7

The target plates were composed of RHA, a quenched and tempered, medium-carbon, martensitic steel defined in Ref. [3]. Each plate had a square cross section, with an edge length of either 197 mm or about 254 mm. Two values for target plate thickness d were considered: 13 and 25 mm. Brinell hardness was measured at a single location on each of the entrance and exit surfaces. These hardness measurements are denoted $BHN_{ent.}$ and BHN_{exit}, respectively; they satisfy the hardness requirement in Ref. [3].

In each experiment, the warhead was statically supported on a horizontal platform containing a hole through which the jet passed. Four vertical bolts were attached to the underside of this platform. The target plate was suspended from these bolts by means of a hook welded to each of its four edges. The plate's square cross section was oriented horizontally so that the jet struck at normal incidence. Standoff S, or distance between the base of the conical liner and the entrance face of the RHA target, was controlled by adjusting the elevation of the target plate's attachment to these bolts. Three values of standoff were evaluated: 3.00 charge diameters (C.D.), or 244 mm; 12.00 C.D., or 975 mm; and 15.23 C.D., or 1238 mm. Table 1 presents the values for d, S, cross-sectional dimension, $BHN_{ent.}$, and BHN_{exit} applicable to each experiment.

Table 1. Experiment descriptions

Test	*D (mm)*	*$BHN_{ent.}$*	*BHN_{exit}*	*X-section (mm^2)*	*S (C.D.)*
4099	25.5	364	364	254x256	3.00
4098	12.5	364	340	251x252	3.00
4100	25.6	364	340	251x252	12.00
10771	13.0	364	364	197x197	15.23

The setup included x-ray tubes and associated film cassettes. A witness pack was located 609.6 mm beneath the exit surface of the target plate. The witness pack was used to collect RHA fragments and was disassembled for their retrieval following the experiment. The pack consisted of five mild-steel plates and four styrofoam spacers. Each steel plate and spacer had a square cross section with an edge length of 1219 mm. The thickness of each styrofoam spacer was 25.4 mm. Thicknesses of the steel witness plates, in order of increasing distance from the target plate, were 0.8, 0.8, 1.6, 1.6, and 3.2 mm.

Figure 1 contains a series of radiographs from Test 4099 and another experiment involving the same conditions of 13 mm for d and a 3.00 C.D. standoff. Figure 1 shows that, at this relatively short standoff, the copper jet was still intact and stretching at the time of initial impact and throughout the course of perforation. In contrast, Fig. 2 shows from Test 4100 that at the longer standoff of 12.00 C.D., the jet broke up into particles prior to initial impact. Figure 1 also shows post-perforation debris patterns at five times. At the early times of 17.7 and 33.1 μs after impact, fragments were small and clustered into a dense debris cloud. At the three later times, much larger fragments are apparent. This same general pattern of debris was observed throughout the series of experiments (see Refs. [4, 5] for additional radiographs).

In the case of Test 10771, the perforated RHA plate was sectioned along an approximate hole diameter following the experiment. Microscopy specimens were prepared from the exposed face in the vicinity of the hole. Specimens from Test 10771 were mounted in a bakelite resin. In the case of Tests 4098, 4099, and 4100, witness packs were disassembled following the experiment and assorted fragments of RHA were recovered. Recovered fragments were sectioned to expose the internal structure and mounted in a clear epoxy. Specimens from the four experiments were then ground, polished, and etched in a 2 pct nital solution for approximately 10 s.

Optical microscopy was performed with a Zeiss Axiomat IAC, an inverted reflected light microscope. The scanning electron microscope used was a JEOL JXA-840A. Vicker and Rockwell C hardness measurements were obtained on one fragment specimen by means of a LECO M-400 microhardness tester with 100-g load.

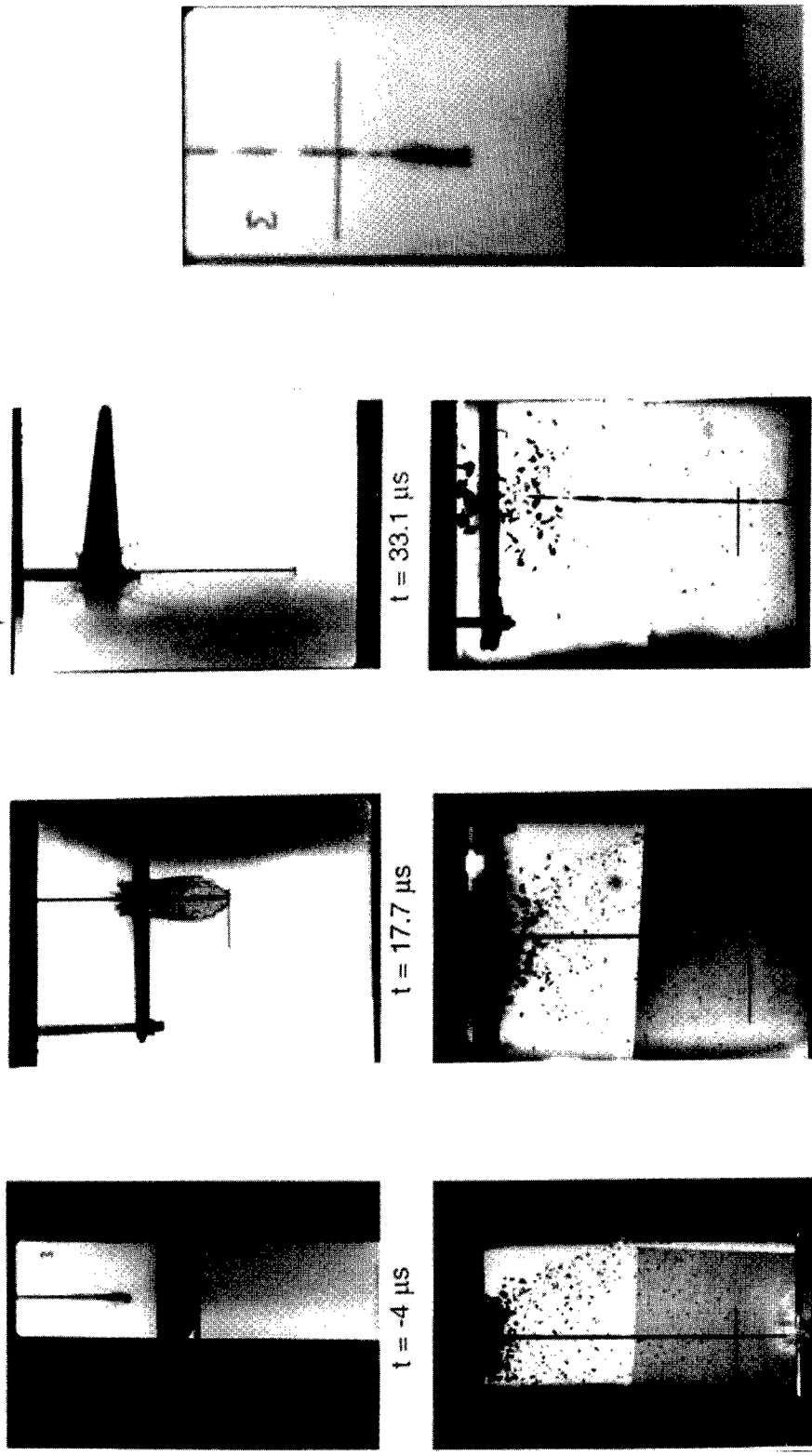

Fig. 1. Radiographs for a standoff of 3.00 C.D. and a target plate thickness of 13 mm.

Fig. 2. Pre-impact radiograph from Test 4100.

OBSERVATIONS

Perforated RHA Plate from Test 10771

Figure 3 shows the surface from which all micrographs from Test 10771 were obtained. Figure 4 shows the microstructure of the tempered martensite that constitutes undeformed RHA.

Figure 5 displays a dark-etched portion of a shear band. The microstructure within resembles that of the surrounding matrix. Martensitic lath alignment with the band indicates large plastic flow.

Figure 6 contains a "white"-etched portion of a shear band. Structure in the central portion of the band is very fine and difficult to resolve in this figure. The band's width in this region is about 6 μm. The martensitic laths adjacent to the band again show some alignment with it.

In Fig. 7, a white-etched region of a shear band grows into a dark-etched region, which in turn blends into the ambient martensite. A crack is found at the other end of the band.

Another case in which a crack and white-etched shear band are associated is contained in Figure 8. This is Crack #1, denoted in Fig. 3. It emanates from the perforation hole boundary and is inclined at about 30° to the shot line. This crack extends for about 0.75 mm (Fig. 8). An enlargement of a portion of Fig. 8 in Fig. 9 shows the crack to be surrounded by the white-etched band. An enlargement of the crack tip region is contained in Fig. 10. The tip, lying within the shear band, appears to be planar, suggesting a brittle cleavage mode of fracture. Further enlargement of this same shear band in its region extending beyond the crack tip is given in Fig. 6.

Crack #2 in Fig. 3 is also inclined at about 30° to the shot line. This crack's width varies greatly with distance along its length (Fig. 11). The crack is not bounded by a shear band, but its two narrow portions may have run along the shear band observed near the crack's tip.

Figure 12 shows a crack that formed by the coalescence of voids on the slice shown in Fig. 3. These voids range in diameter from 1 to 3 μm. The local alignment of martensitic laths along the crack is evidence of extensive plastic flow.

RHA Fragments from Tests 4098, 4099, and 4100

The witness packs from Tests 4098, 4099, and 4100 were disassembled following the experiment, and individual fragments were recovered. Figure 13 from Test 4098 shows a pattern that is familiar from Test 10771. A crack beginning at the fragment's boundary is lined by a straight, white-etched shear band and terminates in the band.

Figure 14 from Test 4099 displays a shear band that both bifurcates and abruptly changes direction. The band thickens near its bifurcation point. This region is enlarged in Fig. 15.

Figure 16 shows shear bands that are not straight, but instead meander around the cross section of this fragment from Test 4100. Two of these bands are continuous with a wider white-etched region, presumably also an adiabatic shear band, that surrounds the fragment. (It was not ruled out that some of this wide "white" region may be deposited copper.)

In Fig. 17 from Test 4099, the fine-grained band near the fragment's periphery includes a dendritic structure. Figure 18 contains an enlargement. Individual dendrites are oriented approximately orthogonally to the fragment's local boundary. Vickers hardness (VHN) measurements were made across the fragment. Indentations from the measurements are visible in Fig. 17. Table 2 contains the results, along with conversions to Rockwell C hardness (HRC). In this table, points are numbered in the order of increasing distance from the fragment's boundary. Vickers hardness is seen to increase from a level of about 350 in the ambient RHA to 483 within the portion of the band that appears solid white. An intermediate value of 450 is found within the dendrites. The dimension of the indentation exceeds a dendrite's width, so a spatial averaging of hardness has occurred in this last measurement.

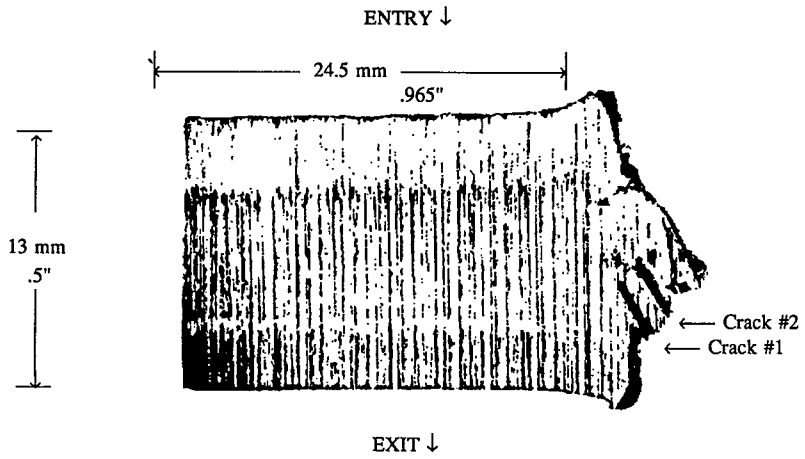

Fig. 3. Slice of target plate from Test 10771 with two cracks emanating from perforation hole indicated.

Fig. 4. Tempered martensite observed in perforated target plate (SEM photograph, 2 pct nital etch, 1350×).

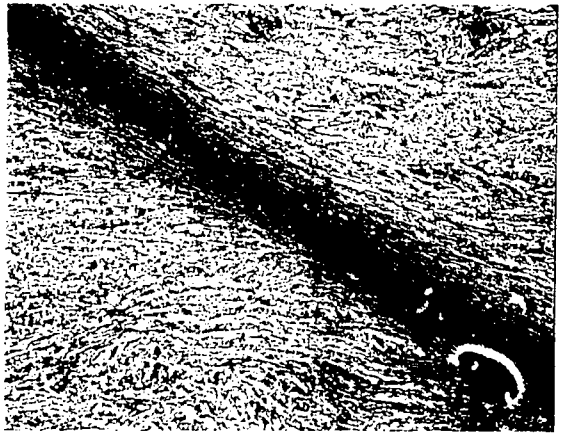

Fig. 5. A dark-etched region of a shear band (Test 10771, SEM photograph, 2 pct nital etch, 2430×).

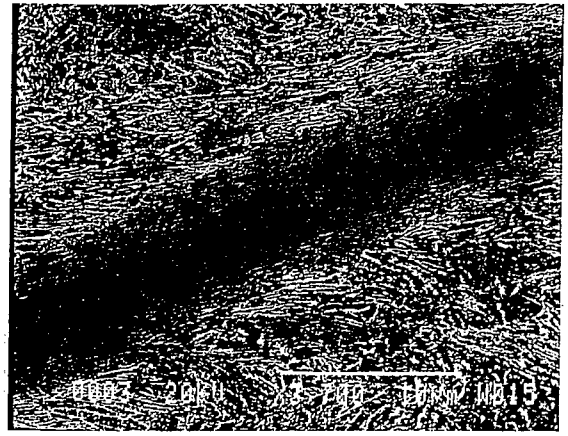

Fig. 6. A "white"-etched region of a shear band (Test 10771, SEM photograph, 2 pct nital etch, 3330×).

Fig. 7. A shear band associated with a crack at one end and blending with the ambient martensite at the other (Test 10771, optical micrograph, 2 pct nital etch, 250×).

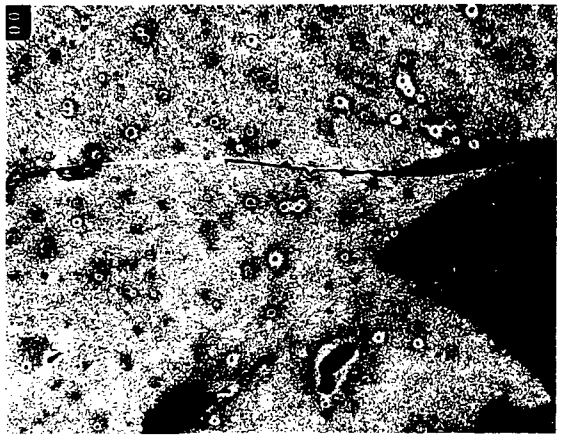

Fig. 8. Crack #1 in Fig. 3 and adjoining shear band (Test 10771, optical micrograph, 2 pct nital etch, 54×).

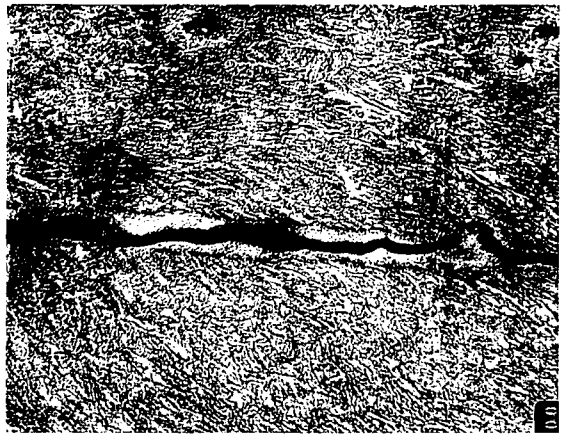

Fig. 9. Enlargement of Fig. 8 showing crack to be surrounded by a white-etched shear band (Test 10771, optical micrograph, 2 pct nital etch, 337×).

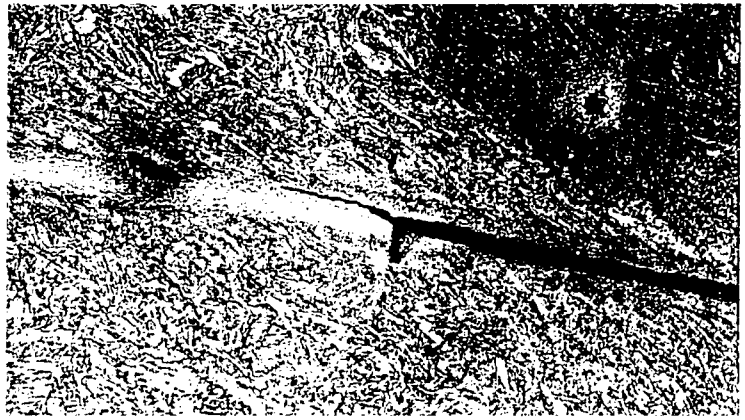

Fig. 10. Enlargement of Fig. 8 showing relationship of crack tip to the shear band (Test 10771, optical micrograph, 2 pct nital etch, 720×).

Fig. 11. Crack #2 in Fig. 3 and adjoining shear band (Test 10771, optical micrograph, 2 pct nital etch, 337×).

Fig. 12. Voids have coalesced to form a crack in RHA (Test 10771, SEM photograph, 2 pct nital etch, 2700×).

Fig. 13. Crack that enters the interior of an RHA fragment and is bound by and terminates in a white-etched shear band (Test 4098, optical micrograph, 2 pct nital etch 54×).

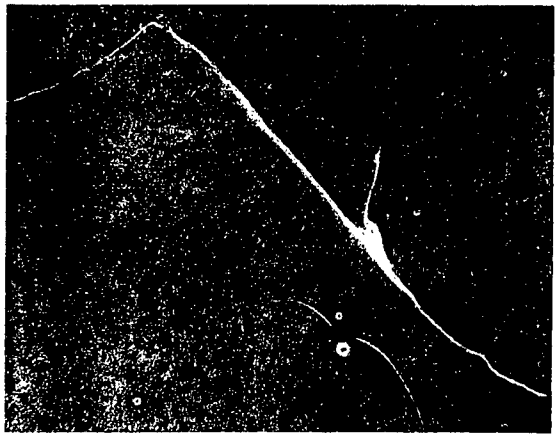

Fig. 14. Shear band that bifurcates and abruptly changes directions in an RHA fragment (Test 4099, optical micrograph, 2 pct nital etch, 54×).

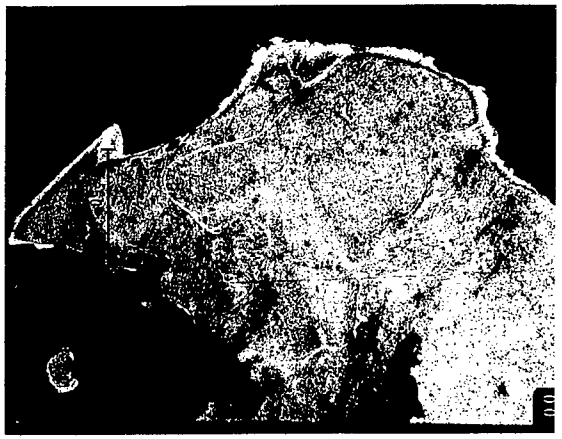

Fig. 16. Shear band that meanders into interior of RHA fragment (Test 4100, optical micrograph, 2 pct nital etch, 67×).

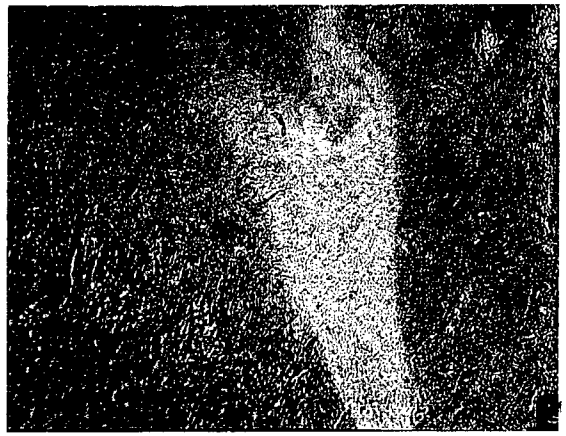

Fig. 15. Enlargement of Fig. 14 in region of shear band bifurcation (Test 4099, optical micrograph, 2 pct nital etch, 422×).

Fig. 17. RHA fragment bounded by a dendrite structured band (Test 4099, optical micrograph, 2 pct nital etch, 67×). Table 2 gives microhardness measurements at indentation points on fragment.

Fig. 18. Enlargement of Fig. 17 with dendritic structure shown (Test 4099, optical micrograph, 2 pct nital etch, 250×).

Table 2. Vickers and Rockwell C hardness measurements across the RHA fragment of Figs. 17 and 18 (100 g load used).

Point	*VHN*	*HRC*	*Comments*
1	464	46.5	solid-white region
2	483	48.0	solid-white region
3	450	45.3	dendrite arms
4	450	45.3	dendrite arms
5	363	36.8	martensite matrix
6	363	36.8	martensite matrix
7	363	36.8	martensite matrix
8	345	35.0	martensite matrix
9	333	33.5	martensite matrix
10	351	35.6	martensite matrix

DISCUSSION

The fragments from the witness pack perforated at least 0.8 mm of mild steel. It is possible that some of their microstructural features were influenced by this interaction.

In Observations, the distinction was made between dark-etching and white-etched portions of a shear band. Rogers and Shastry [6] termed such regions "deformed" and "transformed," respectively, implying in the latter case that steel had re-austenitized and then quenched at a rapid rate. On the basis of observations such as Fig. 7, they proposed that deformed bands frequently act as "precursors" to transformed bands. Rogers and Shastry generated shear bands in quenched and tempered AISI 1040 by means of impact with a flat-nosed steel projectile. They claimed microhardness levels that they measured within white-etched bands to be greater than that obtainable by a martensitic transformation brought on by conventional quench and tempering techniques. They attributed the additional increase in microhardness to the extreme reduction in grain size and the thorough dissolution of carbon into the hot austenite.

Beatty *et al.* [7] and Wittman *et al.* [8] both challenged the assertion of phase transformation within white-etched bands. In Ref. [7], shear bands were generated in hat-shaped specimens of AISI 4340 steel by split Hopkinson bar compression testing. In Ref. [8], shear bands were produced in a hollow cylinder of 4340 steel by detonating an explosive charge along its axis. In both works, similarities in diffraction patterns from transmission electron microscopy (TEM) were found inside and outside the white-etched bands and no remaining austenite was found within these bands. In Ref. [8], microhardness increase within a white-etched band was again attributed to a more uniform distribution of carbides, although Wittman and coworkers claimed that no austenization was required.

The dendritic structure in Figs. 17 and 18 may represent the signature of rapid solidification following melting. This fragment may have received substantial heat via conduction from the jet in addition to heat generated by local plastic deformation. Some RHA melting in the vicinity of the shot line was predicted by wavecode simulations of Test 10771 [1, 2]. Zhou and coworkers [9] measured temperatures as high as 1700 K, which they claimed to be about 90 pct of the melting temperature within shear bands in C-300 maraging steel. Shear bands in their experiments were generated by impacting prenotched specimens at the relatively low speed of 42.8 m/s. The discussion in Ref. [9] implies that higher-speed impact would have produced a larger temperature rise within a shear band. The reasoning is that the increased hydrostatic compression would have retarded crack formation and prolonged plastic flow within the band.

White-etched shear bands have exhibited a variety of geometrical features in Figs. 14, 15, and perhaps 17. Figure 6 displays a straight portion of a band, with a width of about 6 μm. This figure was obtained near the periphery of the final hole. In a perforation experiment, the peak strain rate decreases with increasing radial distance from the path of the projectile. Most shear

band analyses have predicted decreasing band width with increasing local strain rate, e.g., [10, 11, 12]. Perhaps the simplest analysis of this type was presented by Bai and Dodd [13]. By assuming a balance between heat flux and the rate of plastic work, they derived the expression for shear band late-time half-width, δ, for the case of simple shear:

$$\delta = \sqrt{\frac{\kappa\theta_*}{\beta\tau_*\dot{\gamma}_*}}. \tag{1}$$

κ is the thermal conductivity, β is the fraction of plastic work converted into heat, τ_* and $\dot{\gamma}_*$ are the shear stress and shear strain rate, respectively, within the shear band, and θ_* is the temperature difference between the shear band and the material outside the band. Ref. [13] also compares Eqn (1) predictions with torsional split-Hopkinson bar test results and finds the former to be reasonably accurate for several steels, including AISI 4340. Hence, one would expect to find a range of widths in different regions of an RHA target perforated by a shaped charge jet.

Cracks have been seen to occur in association with shear bands, as in Figs. 7 through 10 and 13. It was noted earlier that the planar crack tip within the shear band in Fig. 10 suggests a brittle cleavage fracture. In contrast, the crack in Fig. 12 is unassociated with shear banding and appears to have resulted from ductile void coalescence. A shear band, once quenched, locally increases RHA's hardness. This was demonstrated in closely related AISI 4340 steel by Wittman and coworkers [8], and it may also be demonstrated in Table 2, if the "solid-white" region can be identified with a white-etched shear band. Embrittlement would accompany an increase in hardness. Hence, shear banding may locally change the fracture mode from ductile to brittle cleavage.

Cho *et al.* [14] generated shear bands in 4340 steel by means of torsional split-Hopkinson bar tests. SEM fractography on unpolished fracture surfaces within white-etched shear bands revealed dimples characteristic of ductile fracture. Since SEM fractography was not performed in the present study, it is impossible to definitively assess whether fracture surfaces within shear bands, such as seen in Fig. 10, do indeed represent brittle cleavage rather than ductile void coalescence. A fundamental difference between the dynamic torsion tests in Ref. [14] and the penetration tests of the present study is the presence of large hydrostatic stresses in the latter case. Hence, whereas fractures in Ref. [14] were presumably driven by shear loading, the fracture in Fig. 10 may have resulted from tensile loading. Another fundamental difference may be a much greater time delay between shear band formation and fracture in the present study, enabling fracture to occur at much lower temperatures than in Ref. [14]. Consider the following analysis of dilatational waves during penetration.

When a copper shaped charge jet impacts an RHA plate, shock waves are produced in both materials along the region of impact. The shock wave in RHA travels towards what will be the exit surface, leaving behind material in a large degree of hydrostatic compression. Similarly, the shock in copper leaves behind compressed material as it travels along the jet. As penetration progresses behind the RHA shock, large deviatoric stresses arise near the cavity boundary, and these stresses can give rise to shear banding. Perhaps the superimposed hydrostatic compression suppresses the shear fracture within shear bands observed in Ref. [14]. The compressive RHA shock strikes the exit surface of the target, producing a tensile wave that travels back towards the entrance face and into the shear-banded region. Tensile waves produced from reflections of the compressive shock within the jet may enter the RHA in time to also play a role in RHA fracture. This last consideration would more likely apply to the long-standoff Tests 4100 and 10771, in which the jet had broken up into short particles. In addition, release waves, behind which hydrostatic stresses are near zero, form in RHA along the cavity wall as regions become unloaded. As release waves intersect with the reflected tensile waves, regions of large hydrostatic tension are formed in the shear-banded region near the cavity. If the shear bands are still very hot, the material within would have a smaller flow stress than the original pre-shear-banded material and hence be more susceptible to ductile void growth. Figure 12 in

Ref. [15] (which is produced in Ref. [13] as Fig. 3.7) shows equiaxed voids within a shear band in U-2Mo alloy and apparently illustrates this phenomenon of enhanced ductile void growth within a shear band under tension (the equiaxed geometry suggests growth under tension rather than under shear). If instead the material within the shear band has sufficient time to quench into a material having finer microstructure and greater hardness than the original RHA, then the material would be more susceptible to fracture by means of brittle crack growth. Figure 10 seems to illustrate this phenomenon of increased susceptibility to brittle fracture. The tensile field was insufficient to fail material outside of the shear band; this material possessed microstructure more similar to that of undamaged RHA. The mode of tensile failure has apparently changed from that of ductile void growth (Figure 12) to that of brittle fracture.

Once the driving force has been removed and formation of a shear band in RHA has ceased, the time required for a significant amount of quenching to occur within the band can be estimated from the one-dimensional heat equation. Let x be the spatial coordinate across the shear band and θ the temperature rise within the band. The boundary conditions are $\partial\theta/\partial x = 0$ at $x = 0$, the center of the shear band, and $\theta = 0$ at $x = \delta$, the edge of the shear band at the time of load removal. The solution is

$$\theta(x,t) = \sum_{n=1}^{\infty} a_n e^{-t/t_n} \cos\left[\frac{(2n-1)\pi x}{2\delta}\right], \tag{2}$$

where a_n is evaluated by means of an initial condition, and

$$t_n = \frac{4\rho c\delta^2}{(2n-1)^2\pi^2\kappa}. \tag{3}$$

ρ is density, c is specific heat, and κ is again thermal conductivity. Corresponding to $n = 1$,

$$t_1 = \frac{0.41\rho c\delta^2}{\kappa}. \tag{4}$$

δ is associated with the half-width of a shear band, or about 3 μm according to Figure 6. Ref. [16] gives κ as 37.7 W/m-K for 4140 steel at 694 K. ρ and c are treated as constants and assigned values of 7830 kg/m^3 and 477.8 J/(kg-K), respectively, from Ref. [17] for 4340 steel. Substitution into Eqn [4] yields

$$t_1 \cong 0.37 \ \mu s. \tag{5}$$

Hence, substantial quenching of an RHA shear band occurs within a microsecond after the driving force has been removed. This calculation supports the viewpoint that a tensile wave would encounter brittle material within a shear band. However, the time of driving force removal remains undetermined.

Wittman *et al.* [8] provided an estimate of this quantity. Their premise was that heating within the shear band causes flow stress reduction and, hence, reduction in the rate of plastic work, the source of further heating. In their analysis, the temperature rise at the center of the band was instantaneously brought up to 800°C. The center temperature was maintained at that level until the temperature rise at 4.0 μm from the center (the position they took to be the edge of the shear band) reached 90 pct of the rise at the center. From that time on, the temperature at the band's center was no longer fixed but was allowed to diminish as heat diffused outwards. At 50 μs, the temperature rise at the center had dropped to 300°C, and at 200 μs to 100°C. These are large times relative to the dilatational wave analysis, but their 90 pct criterion seems arbitrary.

CONCLUSIONS

This paper has documented isolated observations of microstructural phenomena in RHA that was perforated by a shaped charge jet. Observations included adiabatic shear banding, apparently brittle fracture within a shear band, ductile fracture unassociated with a shear band, and perhaps melting. Fragment boundaries lined by shear bands and cracks along shear bands in the remaining target plate are evidence of the close association between fragmentation and adiabatic shear banding. A program of more thorough target and fragment evaluation through microscopy would produce a more complete picture of the micromechanics performation.

Acknowledgement—The following colleagues at the U.S. Army Research Laboratory contributed. Dr. Priscilla Kingman and Mr. David E. Mackenzie assisted with use of the scanning electron microscope and with specimen preparation, respectively. Drs. Martin G. H. Wells and John H. Beatty provided insights on interpreting the micrographs.

REFERENCES

1. M. N. Raftenberg, Modeling RHA plate perforation by a shaped charge jet. BRL-TR-3363, Ballistic Research Laboratory, Aberdeen Proving Ground, MD (1992).
2. M. N. Raftenberg, Lagrangian hydrocode simulations of rolled-homogenous-armor plate perforation by a shaped charge jet. *Int. J. Imp. Engng.*, **15**, 619-643 (1994).
3. U.S. Department of Defense. Military specification: armor plate, steel, wrought, homogeneous (for use in combat-vehicles and for ammunition testing). MIL-A-12560G(MR), U.S. Army Materials Technology Laboratory, Watertown, MA (1984).
4. M. N. Raftenberg, Experimental investigation of rolled-homogeneous-armor plate perforation by a shaped charge jet. ARL-TR-328, U.S. Army Research Laboratory, Aberdeen Proving Ground, MD (1994).
5. M. N. Raftenberg, Experimental investigation of RHA plate perforation by a shaped-charge jet. *Proc. 12th Army Symp. Solid Mech.*, edited by S.-C. Chou, U.S. Army Research Laboratory, Watertown, MA, pp. 395-410 (1992).
6. H. C. Rogers and C. V. Shastry, Material factors in adiabatic shear bands in steels. In *Shock Waves and High-Strain-Rate Phenomena in Metals*, (edited by M. A. Meyers, and L. E. Murr) pp. 235-298, Plenum Press, New York (1981).
7. J. H. Beatty, L. W. Meyer, M. A. Meyers and S. Nemat-Nasser, Formation of controlled adiabatic shear bands in AISI 4340 high strength steel. In *Shock Wave and High-Strain-Rate Phenomena in Materials*, (edited by M. A. Meyers, L. E. Murr and K.P. Staudhammer) pp. 645-656, Marcel Dekker, New York (1992).
8. C. L. Wittman, M. A. Meyers and H.-R. Pak, Observations of an adiabatic shear band in AISI 4340 steel by high-voltage transmission electron microscopy. *Metal. Trans. A*, **21A**, 707-716 (1990).
9. M. Zhou, A. J. Rosakis and G. Ravichandran, Dynamically propagating shear bands in impact-loaded prenotched plates - I. Experimental investigations of temperature signatures and propagation speed. *J. Mech. Phys. Solids*, **44**, 981-1006 (1996).
10. F. H. Wu and L. B. Freund, Deformation trapping due to thermoplastic instability in one-dimensional wave propagation. *J. Mech. Phys. Solid*, **32**, 119-132 (1984).
11. D. E. Grady and M. E. Kipp, The growth of unstable thermoplastic shear with application to steady wave shock compression in solids. *J. Mech. Phys. Solids*, **32**, 95-118 (1987).
12. T. W. Wright and H. Ockendon, A model for fully formed shear bands. *J. Mech. Phys. Solids*, **40**, 1217-1226 (1992).
13. Y. Bai and B. Dodd, *Adiabatic Shear Localization, Occurrence, Theories and Applications*, Pergamon, Oxford, pp. 179-182 (1992).
14. K. Cho, Y. C. Chi and J. Duffy, Microscopic observations of adiabatic shear bands in three different steels. *Metallurgical Transactions A*, **21A**, 1161-1175 (1990).
15. G. J. Irwin, Metallographic interpretation of impacted ogive penetrators. DREV R-652/72, Defense Research Establishment, Valcartier, Quebec (1972).
16. American Society for Metals, *ASM Metals Reference Book*. Second Edition, Metals Park, Ohio, p. 210 (1983).
17. G. R. Johnson and W. H. Cook, A constitutive model and data for metals subjected to large strains, high temperatures. *Proc. Seventh Int. Ballistics Symp.*, The Hague, pp. 541-547 (1983).

PERGAMON International Journal of Impact Engineering 23 (1999) 771–782

INTERNATIONAL JOURNAL OF IMPACT ENGINEERING

www.elsevier.com/locate/ijimpeng

IMPACT STUDIES OF FIVE CERAMIC MATERIALS AND PYREX

J. E. REAUGH, A. C. HOLT, M. L. WILKINS, B. J. CUNNINGHAM, B. L. HORD, and A. S. KUSUBOV

Lawrence Livermore National Laboratory Livermore, CA 94551

Summary—We measured the ballistic performance of five ceramic materials (alumina, silicon carbide, boron carbide, aluminum nitride, and titanium diboride) and Pyrex, when they are backed by thick steel plates. The projectile for all tests was a right-circular cylinder of tungsten sinter-alloy W2 with length 25.4 mm and diameter 6.35 mm, fired at velocities from 1.35 to 2.65 km/s. For this threat we determined the minimum areal density of each material that is needed to keep the projectile from penetrating the backup steel. For all of the facing materials studied here, this performance measure increases approximately linearly with projectile velocity. However, the rate of increase is significantly lower for aluminum nitride than for the other materials studied. Indeed, aluminum nitride is a poor performer at the lowest velocity tested, but is clearly the best at the highest velocity. Our computer simulations show the significant influence of the backing material on ceramic performance, manifested by a transition region extending two projectile diameters upstream from the material interface. Experiments with multiple material layers show that this influence also manifests itself through a significant dependence of ballistic performance on the ordering of the material layers. © 1999 Elsevier Science Ltd. All rights reserved.

INTRODUCTION

Ceramics, when used appropriately, can stop a variety of projectiles with less weight per unit area than ballistic steel. The design of ceramic composite armor to stop projectiles and the design of laboratory targets to examine the ballistic behavior of ceramic materials is complicated by the characteristic properties of ceramics — strength in compression and weakness in tension. In the late 60's and early 70's, Wilkins and colleagues[1-5] demonstrated that both properties are important to the defeat of small caliber (7.6 mm) armor-piercing projectiles, and that no single property would correlate ballistic performance for all scenarios. His observations explained why different laboratory targets, which are intended to examine ceramic behavior and which may weight tensile and compressive behavior differently, can produce different rankings among the candidate facing materials. The implication is that one who wishes to measure the ballistic performance of ceramics needs to consciously select a target configuration and projectile combination that tests the particular properties of interest.

For the study reported here, we chose a target configuration that is simple, and that tests the behavior of a facing material when it is well-supported by thick ballistic steel. This eliminates the complex influence of back-plate flexure on ceramic performance.

The projectile chosen is not intended to mimic any specific fielded projectile. It has an aspect ratio (L/D, where L is the projectile length and D is the projectile diameter) of 4, which is intermediate between short projectiles and long rods. It exhibits features of both long rods (quasi-steady penetration) and short projectiles (unsteady end-of-penetration described by Wilkins and Reaugh[6]) With this choice, we were able to defeat the projectile in the velocity range of interest with tile thicknesses of less than about half the lateral dimensions of the tiles available to us.

0734-743X/99/$ - see front matter © 1999 Elsevier Science Ltd. All rights reserved.
PII: S0734-743X(99)00121-9

Table 1. Densities and sound velocities of ceramic facing materials

Ceramic	*Longitudinal velocity[a], km/s*	*Shear velocity[a], km/s*	*Density, g/cc*
Alumina AD96	10.10	5.97	3.75
Alumina AD85	8.80[c]	5.07	3.40
SiC	11.76	7.51	3.16
B4C	13.83	8.72	2.51
AlN	10.76	6.33	3.25
TiB_2	11.08	7.43	4.49
Pyrex	5.64[b]	3.28[b]	2.23

[a] Averaged from several samples of varying thickness
[b] From the AIP handbook, Ref. [7]
[c] From Ref. [3]

EXPERIMENTAL PROCEDURE

Our targets consisted of square tiles of facing material, 102 mm on a side, bonded onto the face of square steel backup plates, 152 mm on a side and 64 mm thick. A photograph of a typical target is shown in Fig. 1. The ceramic tiles were supplied by Dow Chemical Corporation. The Pyrex was of commercial grade. Densities and sound velocities of the facing materials are given in Table 1. We chose 4340 steel hardened to Rc35 as our backing material. This steel was chosen over rolled homogeneous armor (RHA) to eliminate the variability in mechanical properties that we have experienced in RHA in the past. The measured harnesses of our steel backing plates varied from Rc33 to Rc37. The other mechanical properties of the backing steel are given in Appendix B. We expect that the performance of the ceramic facings on this steel will be the same as on RHA. In preparation for target assembly, one side of each steel backup plate was milled lightly to insure a flat, clean and slightly roughened mounting surface. Tile surfaces to be bonded were ground flat and parallel to a tolerance of less than 0.03 mm. Surfaces to be bonded were cleaned with hexane to remove any traces of grease. To insure optimal bonding strength the steel block and ceramic tiles to be assembled were heated to approximately 40° C using infrared lamps. The components of the adhesive, Stycast 1266, were carefully weighed, mixed, and applied to the prepared surfaces. The tiles were then placed on the center of the backup plates. In some cases a single tile was used to produce a target. In others, several tiles were stacked to yield the required facing thickness. Thirty pound weights were placed on top of the tiles being glued to insure a minimal, adhesive layer thickness between the surfaces. The assemblies were then allowed to cure for 24 hours before they were handled. The projectile was a right circular cylinder, D=6.35 mm, and L=25.4 mm of tungsten sinter-alloy W2, manufactured by GTE. The manufacturer's technical specifications for the mechanical properties of W2 are given in Table 2.

Table 2. Material properties of W2 Tungsten alloy

Property	*Value*
Density g/cc	18.36
Hardness, Rc	28 to 31
Ultimate tensile strength, kbar	8.80
Yield strength, kbar	6.95
Elongation at failure, %	5.5

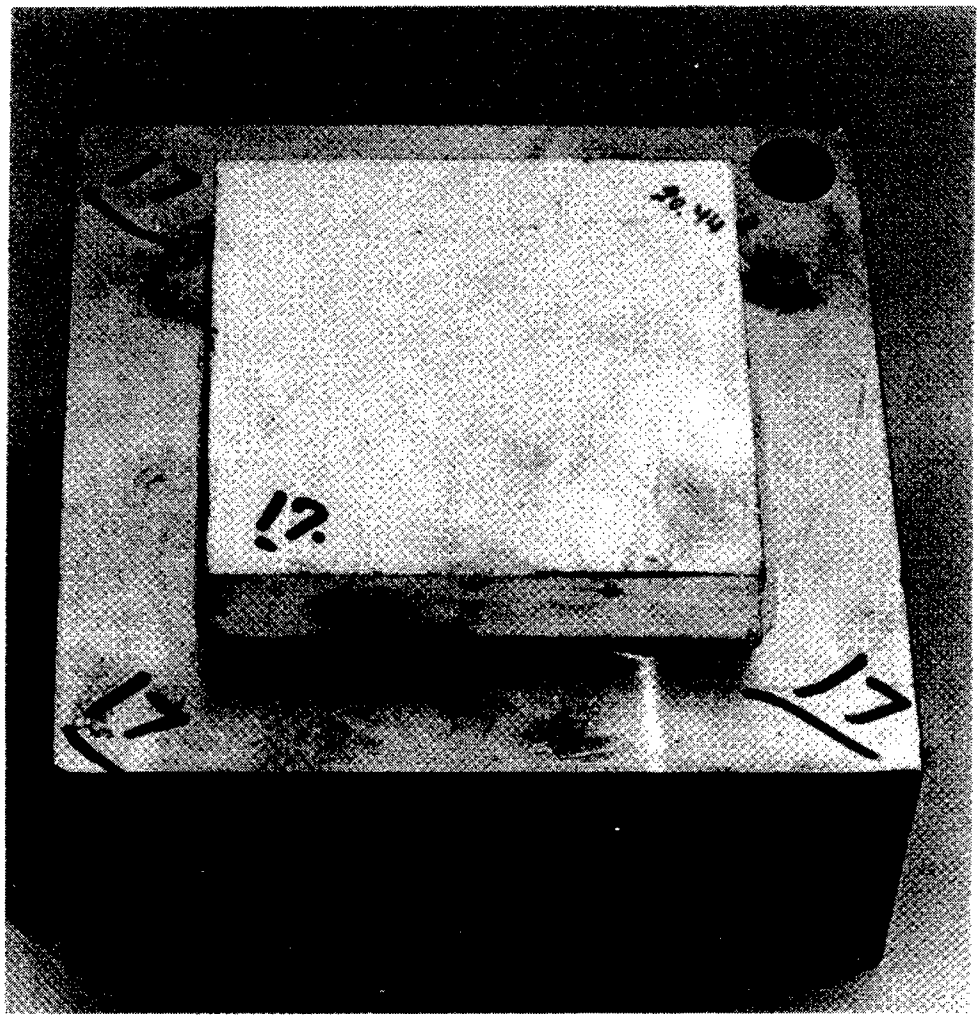

Fig. 1. Target assembly with ceramic tile bonded to the face of a 4340 steel backup plate.

Our experiments were performed at three nominal velocities: 1.35, 1.75, and 2.6 km/s. The experiments at 1.35 and 1.75 km/s were performed using a 14.5 mm powder gun and a 23 mm powder gun respectively, at our ballistic range facility. The Lawrence Livermore National Laboratory two-stage light gas gun was used to accelerate the projectiles for the 2.6 km/s experiments. The shots at 1.35 km/s were fired into air at 1 atmosphere. In the other shots, the projectiles were fired into a vacuum of about 1 Tor. The sabot assembly was stripped from the projectile by a block of low-density foam. Flash x-rays were used to determine tilt and projectile velocity, as well as to verify that the sabot assembly had been separated from the projectile. Average projectile tilt for a representative sample of experiments was less than 2 degrees. Any tilt greater than 4 degrees was considered excessive and the experiment was repeated.

The depth of penetration into the steel backup plate, normal to the impact surface, P_b, was used as a performance measure for each shot. Two methods were used for measuring P_b. The first consisted of measuring the perpendicular distance form the upper surface of the block to the bottom of the crater using a micrometer depth gauge. An inverted U-shaped spacer was employed to straddle the distorted region around the crater opening and to facilitate referencing to the undistorted region of the front face. After measuring the distance from the top of the spacer

Table 3. Linear regression fit to normal impact data, $P_b = P_0 - a\Delta$, for values of the tile thickness Δ exceeding 10 mm. The average velocity of the experiments used for the fit is v.

	Low velocity			*Intermediate velocity*			*High velocity*		
Tile	P_0 *mm*	*a*	*v, km/s*	P_0 *mm*	*a*	*v, km/s*	P_0 *mm*	*a*	*v, km/s*
AD85	17.7	0.44	1.36	31.2	0.68	1.76	50.8	0.80	2.50
AD96	19.5	0.52	1.36	31.3	0.77	1.70	54.1	0.93	2.63
AlN	18.0	0.68	1.29	36.4	1.01	1.79	55.5	1.20	2.60
B_4C	33.9	1.98	1.25	38.9	1.01	1.77	32.1	0.45	2.61
Pyrex	---	---	---	33.2	0.59	1.79	53.2	0.63	2.65
SiC	37.2	2.33	1.37	35.5	1.05	1.72	38.9	0.64	2.65
TiB_2	44.2	4.05	1.35	41.6	2.09	1.70	60.4	1.30	2.65

to the bottom of the crater, the spacer thickness was subtracted to give the hole depth. The end of the depth gauge used is flat with a diameter of 3.2 mm. If the crater was too deep for the first method, or if it were suspected that significant amounts of residual penetrator was present at the bottom of the crater, the steel block was sectioned. Normal depth of penetration was then determined by using a caliper to measure the distance from the deepest point of the projectile penetration to the rear surface of the backup plate and subtracting that value from the (undistorted) backup plate thickness.

EXPERIMENTAL RESULTS

Our measured values of P_b are given in Appendix A. Since we measured the penetration depth into the backup plate as a function of facing thickness, we can estimate the minimum facing thickness necessary to prevent penetration of the backup plate, Δ^*. To this end, we performed a linear regression fit of P_b as a function of facing thickness for each material at each nominal velocity. The fit can then be used to solve for Δ^*. The results are given in Table 3, and plotted in Fig. 3. In that figure we see that the limiting areal density for each ceramic increases approximately linearly with velocity, and that the various ceramics have different rates of increase. In particular, the limiting areal density of aluminum nitride has the slowest increase with velocity of all the materials tested. As a consequence, it is the best of the ceramics tested at high velocity, i.e. requires the least areal density to stop the projectile.

We wondered whether stacking several facing plates to obtain a desired thickness would give a different result in our experiments than if the facing had been a single plate of the same thickness as the total. In order to investigate this question, we repeated the silicon carbide shot at 1.75 km/s with 20 mm of facing. In the original shot, we used a single 20 mm thick tile as facing, and in the second, we stacked two 10 mm plates. The difference in the results was insignificant.

Our simulations, discussed below, suggested that if two layers of different facing materials are used over the steel backup plate, then the order in which they occur might strongly influence their performance. In order to see if this is so, we performed a series of experiments in which titanium diboride plates were used in combination with Pyrex and with AD96 plates. In each case, shots were performed with the TiB_2 next to the steel and then again, with the TiB_2 on the front face. The results of these experiments are given in Table 4. They show a strong dependence on the ordering of the facing materials.

With thin (10mm) tiles of AD96 and TiB_2, the residual penetration is slightly smaller when the TiB_2 is on the outside (Table 4) although the difference is small, 14 versus 16 mm. At equal areal density, an all-AD96 tile would result in the same residual, 15.6 mm, but an all-TiB_2 tile would result in only 5 mm. The thin TiB_2 tile does not perform well. With thicker tiles of TiB_2 and Pyrex the order is more significant. (Table 4) At equal areal density, an all-Pyrex tile would result in 7 mm residual, whereas an all-TiB_2 tile would stop the projectile (no residual). The

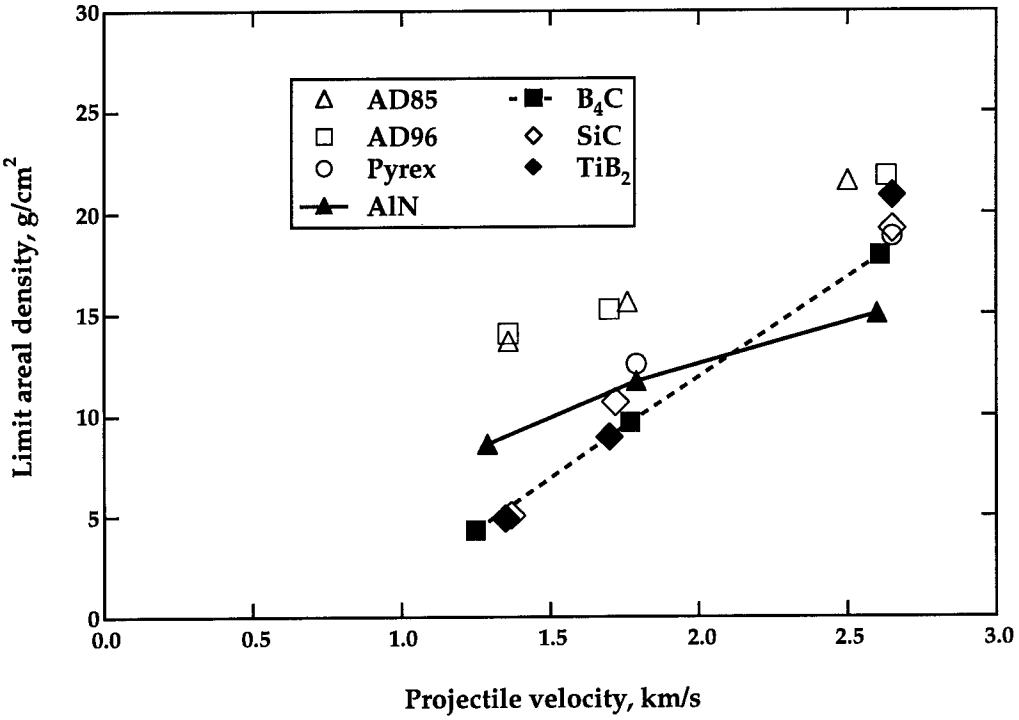

Fig. 3. The limit areal density required to prevent penetration in the backup steel, calculated from fits to the experimental data. The AlN limit value increases slowly with velocity.

combination with Pyrex on the outside has higher residual penetration than either single-material facing. With TiB_2 on the outside, the combination results in less residual than all Pyrex, but more than all-TiB_2. The thin TiB_2 tile performs as badly with thicker Pyrex backing as it does with AD96 backing.

Table 4. Experimental results for 25.4 mm by 6.35 mm diameter tungsten cylinder into steel faced by multiple ceramic plates at normal obliquity.

Upper plate		*Lower plate*		*Projectile*	*Penetration*
Material	*Thickness, mm*	*Material*	*Thickness, mm*	*velocity, km/s*	*into steel, mm*
AD96	10.2	TiB_2	10.0	1.78	16.1
TiB_2	10.1	AD96	10.2	1.76	13.9
Pyrex	13.7	TiB_2	14.8	1.78	12.6
TiB_2	14.7	Pyrex	13.8	1.77	4.8
TiB_2	10.0	Pyrex	18.5	1.77	11.9

COMPUTER SIMULATIONS

We performed computer simulations of some of the experiments using GLO, a two-dimensional multi-material Eulerian finite-difference code under development at our laboratory. The material parameters used to model the 4340 steel backing are those for Rc35 steel given in Appendix B.

Simulations with Pyrex

We selected Pyrex as the first tile material for the simulations. Previous experimental results suggested that the Pyrex fractures and breaks early in the penetration event, and so could be modeled as a broken material throughout the penetration event.

By assuming this, we achieve a significant simplification in the task of modeling ceramics numerically. The reason is that the change in the state from intact to broken is accompanied by a significant reduction in the magnitude of stress, whether fracture takes place in compression or tension. The resulting release of strain energy is propagated through the system with amplitude and period that are proportional to the finite-difference zone size. This numerical noise will, if the zone size is too large, be of sufficient amplitude to trigger the fracture of nearby zones. In contrast, when the material is in a single state (for Pyrex, always broken) the numerical solution is smooth.

The behavior of broken, hard materials is described by the Mohr-Coulomb friction model for granular media, well-known in the literature of soil and rock mechanics (for example[8]). The difference between the maximum principal stress, σ_1, and the minimum principal stress, σ_3, is given by

$$\sigma_1 - \sigma_3 = (\sigma_1 + \sigma_3)\sin\varphi \tag{1}$$

where positive stress is compressive, and φ is the friction angle. A somewhat simpler implementation, which does not require calculation of the principal stresses, is the extended von Mises criterion[8]

$$Y = \alpha P \tag{2}$$

where Y is the equivalent stress and P is the mean stress. When this criterion is fit to the compressive triaxial test ($\sigma_1 > \sigma_2 = \sigma_3$), where σ_2 is the intermediate principal stress, it overestimates the measured strength of granular materials in shear ($\sigma_2 = 0$) and extension ($\sigma_1 = \sigma_2 > \sigma_3$). Nevertheless, we used this latter criterion (Eq. 2) in our computer simulations. So long as the parameter α is less than 1.5, the minimum principal stress is never in tension.

A second feature that accompanies the shear of granular material is dilatency[9], the increase in volume observed when a mass of dense, granular material undergoes shear at constant confining pressure. Although the plastic potential theory of von Mises will generate a plastic volume increase during shear deformation when the extended von Mises criterion (Eq. 2) is used as the potential surface, we have chosen to ignore dilatency. Experiments on granular soils[10] show that there is a characteristic porosity, which is a function of confining stress, that is achieved by a soil mass undergoing large shear deformation. In contrast, naive use of the plastic potential theory (associated flow rule) produces ever-increasing volume with shear deformation at constant normal stress. More complicated flow rules (or more complicated limit surfaces) are required to obtain physically realistic results, and require the specification of additional parameters.

We found the parameter α in the extended von Mises criterion by the expedient of matching results of numerical simulations to experiments by Hord[11], in which a short W2 projectile (L/D = 2.5) was fired into a confined Pyrex column at 1.5 km/s. Flash x-rays were taken during the penetration event to mark the nose and tail position. Results of the experiments and two computer simulations with different values of α are shown in Fig. 4. The final positions and residual projectile lengths are shown also. We chose $\alpha = 0.8$ for the remainder of the computer simulations for Pyrex. Similar experiments in glass with a longer rod were performed by Hohler and Stilp. Calculations of those experiments and the experimental results are reported by Anderson *et al.*[12]

Table 5. Calculated influence of the backing metal on the performance of 20 mm thick Pyrex tiles at 1.75 km/s

Backing metal	P_{0B}, mm[a]	P_B, mm	η_M[b]	η_{MS}[c]
Aluminum	82.5	58.0	1.5	1.9
Steel	36.0	21.2	2.6	2.6
Tungsten	20.6	11.1	3.9	2.9

[a] P_{0B} is the penetration in the backing metal without Pyrex

[b] The differential efficiency, η_M is given by

$$\eta_M = \rho_B (P_{0B} - P_B)/(\rho_C \Delta)$$

where ρ_B is the backing metal density, ρ_C the tile density, and Δ the tile thickness..

[c] The differential efficiency scaled to steel, η_{MS}, is given by

$$\eta_{MS} = \rho_S P_{0S}/(\rho_B P_{0B})$$

where ρ_S is the density of steel and P_{0S} the penetration in steel alone.

With this model for Pyrex, we performed computer simulations of the experimental geometry at 1.75 km/s, in advance of experiments with Pyrex. The comparison of the computed and measured residual penetration in steel is shown in Fig. 5. The good agreement with experiment led us to examine the results of the computer simulations in more detail.

We show the velocity at the projectile nose and tail as a function of the nose position in Fig. 6. There is a noticeable change in the nose (interface) velocity from the value characteristic of Pyrex to the value characteristic of steel over a distance in Pyrex that is approximately two projectile diameters. When we repeated the calculations, replacing the steel backup with aluminum and with tungsten, the transition region had the same two-diameter thickness, but with the final interface velocity being characteristic of aluminum or tungsten as can be seen in Fig. 7. This transition region has a significant effect on the differential efficiency of Pyrex, even when scaled to steel for all cases (Table 5.)

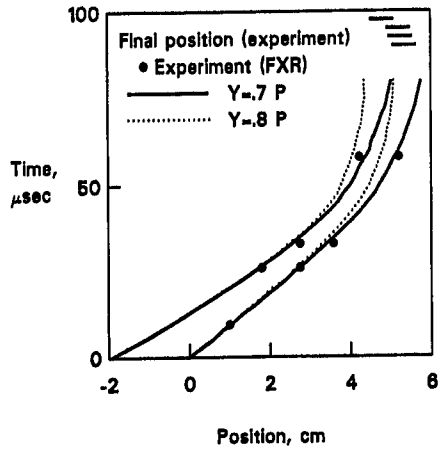

Fig. 4. Position of nose and tail as functions of time from experimental flash x-rays (solid dots) and simulations (solid and dashed lines). Final position and residual length shown by short lines at the top

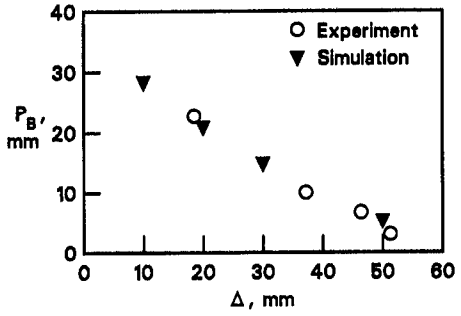

Fig. 5. Residual penetration in the back-up steel as a function of Pyrex thickness from experiment and simulation

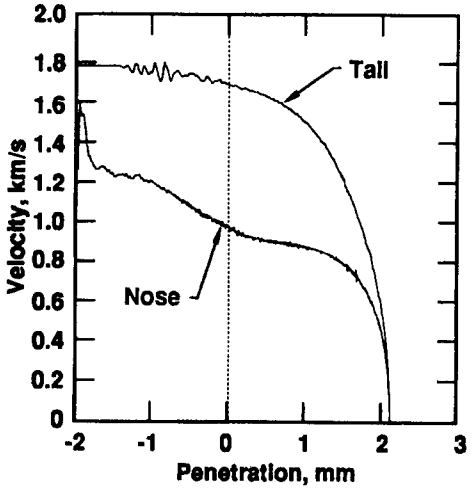

Fig. 6. Calculated nose and tail velocities as a function of nose position in a 20mm Pyrex/steel target. Original position of the interface is at zero.

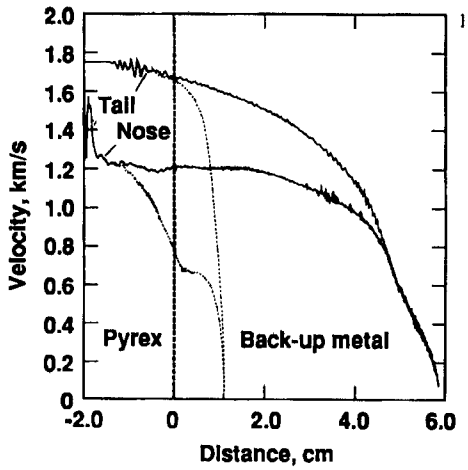

Fig. 7. Calculated nose and tail velocity as a function of nose position for a 20mm Pyrex/metal target using aluminum (solid) and tungsten (dash) to replace steel.

Simulations with Aluminum Nitride

The experimental results with aluminum nitride sufficiently intrigued us that we sought to model those experiments as well. Heard and Cline[13] showed a transition from brittle to ductile failure in quasi-static triaxial compression tests when the confining stress $\sigma_2 = \sigma_3$ exceeded 6 kbar (pressure about 20 kbar). This suggested to us that perhaps at the highest velocity experiments, the mean stress in aluminum nitride was sufficiently large that the material was ductile, even at the strain rates of the impact test (10^5/s). We fit the quasi-static data[13] by an extended von Mises surface Y = f(P), and estimated the strength at the Hugoniot elastic limit to be 68 kbar, as shown in Fig. 8. Figure 9 shows the interpolated/extrapolated experimental penetration in the backup steel as a function of velocity for a 20 mm tile of AlN, together with calculations using the intact strength and the broken strength, where the value of α for broken AlN was arbitrarily taken to be the same value as was used for glass (Fig. 8).

From these results, it is our assessment that AlN is behaving substantially like a broken material at the lower two velocities, although we cannot rule out the possibility that there is a short time when the material retains its intact strength. In any event it is apparent that the calculations using the intact strength of AlN are incorrect at the lower two velocities.

When we examine detailed results of the two lower-velocity calculations that used the intact strength, the first 10% of plastic strain experienced by material in the path of the projectile is achieved at pressures below 30 kbar. At the strain rates achieved in the ballistic test, 10^5/s, we would estimate the brittle-ductile transition to occur at 30 to 40 kbar (20 kbar for the quasi-static tests). Thus we would infer that at the lower two velocities, the AlN fractures and is broken in the penetration path. The case for the higher velocity is less clear-cut. Most of the strain is achieved at pressures exceeding 35 kbar, although the strain from 2 to 4% is achieved at pressures as low as 25 kbar. At somewhat higher velocity, 3.5 km/s, we would anticipate that AlN in the penetration path would behave as a ductile, high strength material, and exhibit excellent resistance to penetration.

The calculations using the extended von Mises criterion for broken AlN are also not accurate except at the intermediate velocity. We note that the value of α chosen was the one for Pyrex, which gives results in substantial agreement with experiment in the velocity range 1.5 to 1.75 km/s, but is otherwise unsupported by independent experiment at different velocities (or confining pressure).

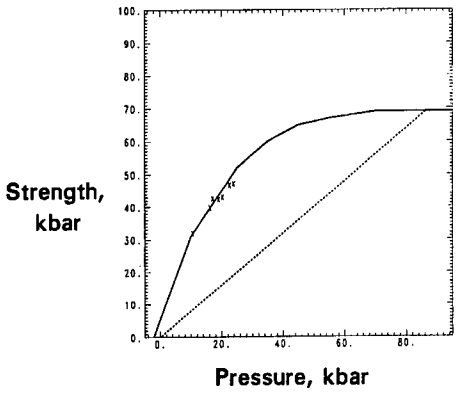

Fig. 8. Measured strength of aluminum nitride (x) and model fit for intact (solid) and broken AlN. The slope for the broken material is the same as was used for Pyrex.

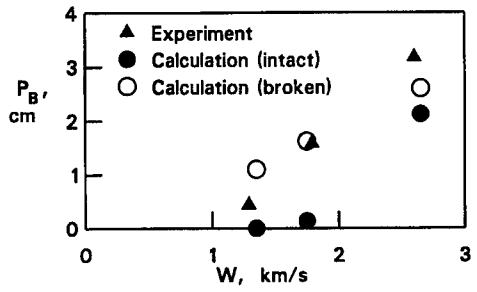

Fig. 9. Penetration in the back-up steel as a function of velocity for 20mm AlN/steel target from experiment and simulations

CONCLUDING REMARKS

Our experimental results show that titanium diboride, boron carbide, and silicon carbide perform equally well when supported by a thick steel backing. They outperform aluminum nitride, Pyrex, and alumina at velocities below 2.0 km/s. Interestingly, the two aluminas have about equal performance in this ballistic test for all three velocities.

At velocities above about 2.0 km/s the aluminum nitride outperforms all the others. Moreover, Pyrex ranks with boron carbide, titanium diboride and silicon carbide at about 2.6 km/s and may outperform them at higher velocities. Our computer simulations for aluminum nitride suggest to us that the superior performance of aluminum nitride at the highest velocity is due to its retention through ductility of a substantial part of its strength at the high confining pressures experienced there, in contrast to the other ceramics, which are substantially broken at high velocity.

Our simulations of the Pyrex experiments show that a target material interface begins to influence the penetration process when the projectile nose is yet a significant distance away. This observation explains why thin layers of a facing material do not perform the same way as thicker ones. It is because the process is entirely within the transition region, where both materials are influencing the penetration process.

Acknowledgments—The authors thank Estella McGuire for performing the GLO computer simulations. This work was performed under the auspices of the U. S. Department of Energy by Lawrence Livermore National Laboratory under Contract No. W-7405-ENG-48 and the U. S. Army/DOE Memorandum of Understanding "Fundamentals of Penetration Program". This work was performed during 1988-89, but distribution of the results was then restricted. More recently, Steinberg used these experimental data to help develop a model for ceramics applied to titanium diboride, and reported his results in[14].

APPENDIX A. RESIDUAL NORMAL PENETRATION IN STEEL

We present the experimental results for the normal residual penetration of a 6.35-mm diameter by 25.4-mm long tungsten projectile into the back-up steel. In the table below, the tile thickness, Δ, is in mm, the projectile velocity, V, is in km/s, the obliquity, θ, in degrees between the flight axis and the normal to the tile. The residual penetration in the backup steel normal to the steel surface, P_b, is in mm.

Table A1. Experimental residual penetration

Tile	Δ	V	θ	P_b	*Tile*	Δ	V	θ	P_b
AD96	10.5	1.35	0	14.5	AD85	6.2	1.33	0	18.5
AD96	15.1	1.35[a]	0	11.1	AD85	14.0	1.35	0	11.8
AD96	20.6	1.36	0	8.7	AD85	22.1	1.35	0	7.5
AD96	30.2	1.36	0	4.0	AD85	32.0	1.37	0	3.8
AD96	20.4	1.68	0	15.8	AD85	6.2	1.75	0	31.0
AD96	31.7	1.72	0	6.4	AD85	14.0	1.75	0	22.0
AD96	40.0	1.70	0	0.0	AD85	29.9	1.75	0	10.0
AD96	40.4	1.80	0	0.5	AD85	42.5	1.77	0	2.7
AD96	15.1	1.69	30	14.0	AD85	20.5	2.50	0	33.6
AD96	29.9	1.74	30	5.5	AD85	39.3	2.50	0	20.6
AD96	15.3	1.80	45	9.5	AD85	59.1	2.50	0	2.6
AD96	25.0	1.72	45	0.0	SiC	10.0	1.37	0	13.9
AD96	10.5	1.74[a]	60	6.7	SiC	15.1	1.36	0	2.0
AD96	15.2	1.74[a]	60	4.1	SiC	20.0	1.37	0	0.0
AD96	20.0	1.74	60	0.0	SiC	30.1	1.31	0	0.0
AD96	15.1	2.63	0	39.2	SiC	20.0[b]	1.69	0	14.3
AD96	30.1	2.63	0	27.8	SiC	20.0[b]	1.75[a]	0	14.5
AD96	51.3	2.62	0	5.9	SiC	29.5	1.77	0	5.7
TiB_2	7.9	1.38	0	12.2	SiC	30.2	1.70	0	2.4
TiB_2	10.0	1.31	0	3.7	SiC	40.0	1.74	0	0.0
TiB_2	15.0	1.36	0	0.0	SiC	15.0	1.75	30	14.9
TiB_2	20.0	1.37	0	0.0	SiC	31.3	1.78	30	1.0
TiB_2	10.1	1.69	0	22.1	SiC	15.1	1.71	45	8.2
TiB_2	14.9	1.70	0	7.3	SiC	25.0	1.81	45	0.0
TiB_2	20.1	1.72	0	1.1	SiC	10.1	1.70	60	6.6
TiB_2	30.0	1.69	0	0.0	SiC	14.9	1.80	60	1.9
TiB_2	10.1	1.70	30	19.5	SiC	20.0	1.69	60	0.0
TiB_2	25.0	1.80	30	0.0	SiC	30.1	2.62	0	18.2
TiB_2	7.7	1.73	45	15.4	SiC	39.9	2.68	0	15.6
TiB_2	20.0	1.69	45	0.0	SiC	59.7	2.64	0	0.
TiB_2	7.8	1.80	60	5.6	B_4C	10.4	1.79	0	28.3
TiB_2	15.0	1.81	60	0.0	B_4C	19.3	1.74[a]	0	19.8
TiB_2	20.1	2.63	0	34.5	B_4C	28.8	1.78	0	9.8
TiB_2	24.9	2.69	0	29.8	B_4C	28.0	1.79	30	3.3
TiB_2	30.3	2.63	0	17.8	B_4C	17.6	1.77	60	2.2
TiB_2	40.0	2.63	0	9.6	B_4C	10.4	1.28	0	13.3
AlN	9.7	1.25	0	10.1	B_4C	15.2	1.22	0	3.8
AlN	14.3	1.30	0	8.9	B_4C	19.2	1.29	0	0.0
AlN	19.6	1.31	0	4.3	B_4C	38.9	2.61	0	14.5
AlN	9.9	1.79	0	27.5	B_4C	58.6	2.61	0	5.6
AlN	19.7	1.79	0	14.3	Pyrex	18.5	1.80	0	22.7
AlN	28.8	1.80	0	8.5	Pyrex	37.2	1.78	0	10.0
AlN	37.0	1.79	0	0.0	Pyrex	46.4	1.78	0	6.7
AlN	28.2	1.76	30	1.6	Pyrex	51.3	1.80	0	3.0
AlN	17.5	1.78	60	0.0	Pyrex	39.4	2.64	0	28.5

Table A1. (concluded) Experimental residual penetration

Tile	Δ	V	θ	P_b	Tile	Δ	V	θ	P_b
AlN	30.3	2.61	0	19.3	Pyrex	58.9	2.65	0	16.3
AlN	39.5	2.58	0	8.3					

[a] Velocity estimated from the powder load

[b] The facing on the first of these two shots was a single 20 mm plate. The facing for the second was two 10 mm plates bonded together.

Table A2. Penetration depth of normal impacts into the back-up steel alone.

V	P_b
1.34[a]	26.8
1.34	27.0
1.34	27.0
1.35	27.8
1.35	28.5
1.74[a]	35.3
1.77	36.0
2.50	43.8

[a] Velocity estimated from the powder load

APPENDIX B. CHARACTERIZATION OF 4340 STEEL

Four-inch diameter billets of 4340 steel were quenched and tempered to achieve nominal Rockwell hardness of Rc35, Rc40, and Rc45. Three 0.5-inch diameter standard tensile specimens (2-inch gauge length, 6 inches long) were machined from each heat treatment, designated 35-1, 35-2, 35-3, 40-1, etc. The specimens were tested in tension on a 56,000 pound Instron machine according to ASTM standard E8 at room temperature. Crosshead speed was 0.01 in/min., except for specimens 35-1, 35-2, 40-1, and 45-1, which were tested at 0.005 in/min. Gauge extension was measured with an Instron 2"-50% extensometer, and load-elongation plots were produced for each test. In addition, a Zygo laser was used to scan 1.7 inches of the 2-inch gauge length at a speed of 0.26 in/s on an interval determined by the deviation of the minimum diameter from the original diameter, ranging from once every five minutes initially to once every 20 sec when the diameter had reduced by 30%. During each sweep, approximately 90 diameter determinations were made and recorded digitally, together with the load at the beginning and end of each sweep.

Table B1. Parameters for the flow stress of 4340 Steel

Nominal hardness, Rc	Measured hardness, Rc	Y_0, kbar	β	n
35	34	10.3	125	0.0700
40	40	12.9	282	0.0389
45	43	13.2	580	0.0350

We followed the procedure of Norris *et al.*[15] to determine the work-hardening functional dependence of the three heat treatments. In that procedure, a computer simulation of the tension test is performed (we used HEMP[16]) with an initial guess at the work-hardening. Results of the computer simulations and experiments are compared, and the work hardening function revised until satisfactory agreement is reached. The results are shown in Fig. B1-B3 for the three heat treatments. In those figures true strain is $-2 \ln(D/D_0)$ where D is the minimum diameter.

Engineering stress is the load per unit area of the original minimum cross-section. The functional form chosen for the flow stress is

$$Y = Y_0(1+\beta\varepsilon^p)^n \tag{B1}$$

where Y is the equivalent stress, and ε^p is the equivalent plastic strain. The fitted parameters are given in Table B1.

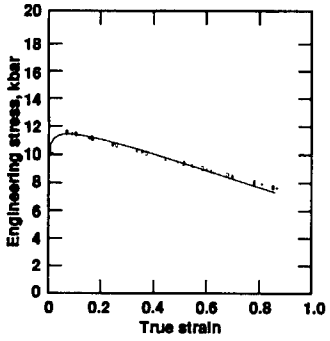

Fig. B1. Engineering stress as a function of true strain for 4340 steel, Rc35 for experiments (symbols) and simulation (line).

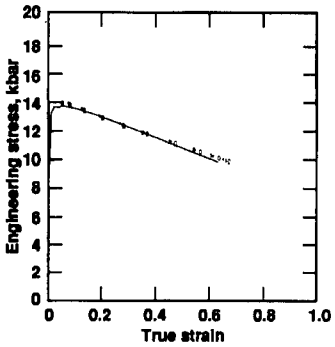

Fig. B2. Engineering stress as a function of true strain for 4340 steel, Rc40 for experiments (symbols) and simulation (line).

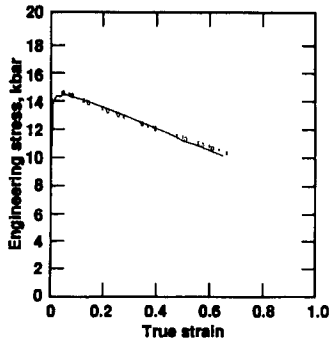

Fig. B3. Engineering stress as a function of true strain for 4340 steel, Rc45 for experiments (symbols) and simulation (line).

REFERENCES

1. M. L. Wilkins, C. Honodel, and D. Sawle, "An approach to the study of light armor," Lawrence Livermore National Laboratory, Livermore, CA Report No. UCRL-50284, June 13, 1967.
2. M. L. Wilkins, "Second progress report of the light armor program," Lawrence Livermore National Laboratory, Livermore, CA Report No. UCRL-50349 Rev. 1, 1967.
3. M. L. Wilkins, "Third progress report of the light armor program," Lawrence Livermore National Laboratory, Livermore, CA Report No. UCRL-50460, July 9, 1968.
4. M. L. Wilkins, C. F. Cline, and C. A. Honodel, "Fourth progress report of light armor program," Lawrence Livermore National Laboratory, Livermore, CA Report No. UCRL-50694, 1969.
5. M. L. Wilkins, "Mechanics of penetration and perforation," *Int. J. Engrg. Sci.*, vol. 16, pp. 793-807, 1978.
6. M. L. Wilkins and J. E. Reaugh, "Computer simulations of ballistic experiments," Lawrence Livermore National Laboratory, Livermore, CA Report No. UCRL-95774, January 23, 1987.
7. D. E. Gray, "American Institute of Physics Handbook," , Third ed. New York: McGraw Hill Book Company, 1972.
8. A. W. Bishop, "Shear strength parameters for undisturbed and remoulded soil specimens," in *Stress-Strain Behavior of Soils*, R. H. G. Parry, Ed. Henly-on-Thames: G. T. Foulis & Co. Ltd., 1972, pp. 7-11.
9. O. Reynolds, "On the dilatency of media composed of rigid particles in contact, with experimental illustrations," *Phil. Mag. S.*, vol. 5, pp. 20, 1885.
10. C. P. Wroth and R. H. Bassett, "A stress-strain relationship for the shearing behavior of a sand," *Geotechnique*, vol. 15, pp. 32-56, 1965.
11. B. L. Hord, Personal Communication, 1986.
12. C. E. Anderson, V. Hohler, J. D. Hohler, and A. J. Stilp, "Time-resolved Penetration of Long Rods into Glass Targets," *Int. J. Impact Engng.*, vol. submitted, 1998.
13. H. C. Heard and C. F. Cline, "Mechanical behavior of polycrystalline BeO, Al_2O_3 and AlN at high pressure," *Mats. Science*, vol. 15, pp. 1889-1897, 1980.
14. D. J. Steinberg and R. E. Tipton, "A new fracture model for ceramics," Lawrence Livermore National Laboratory, Livermore, CA Report No. UCRL-JC-116953, March 14, 1994.
15. D. N. Norris, B. Moran, J. K. Scudder, and D. F. Quinones, "A computer simulation of the tension test," *J. Mech. Phys. Solids*, vol. 26, pp. 1-19, 1968.
16. M. L. Wilkins, "Calculation of Elastic-Plastic Flow," in *Methods of Computational Physics*, vol. 3, B. Alder, S. Fernbach, and M. Rotenberg, Eds. New York: Academic, 1964, pp. 211-263.

PERGAMON

International Journal of Impact Engineering 23 (1999) 783–794

INTERNATIONAL JOURNAL OF IMPACT ENGINEERING

www.elsevier.com/locate/ijimpeng

ORBITAL DEBRIS IMPACT DAMAGE TO REUSABLE LAUNCH VEHICLES

JENNIFER H. ROBINSON

NASA Marshall Space Flight Center, Huntsville, AL 35812 USA

Summary—In an effort by the National Aeronautics and Space Administration (NASA), hypervelocity impact tests were performed on thermal protection systems (TPS) applied on the external surfaces of reusable launch vehicles (RLV) to determine the potential damage from orbital debris impacts. Three TPS types were tested, bonded to composite structures representing RLV fuel tank walls. The three heat shield materials tested were Alumina-Enhanced Thermal Barrier-12 (AETB-12), Flexible Reusable Surface Insulation (FRSI), and Advanced Flexible Reusable Surface Insulation (AFRSI). Using this test data, predictor equations were developed for the entry hole diameters in the three TPS materials, with correlation coefficients ranging from 0.69 to 0.86. Possible methods are proposed for approximating damage occurring at expected orbital impact velocities higher than tested, with references to other published work.
© 1999 Elsevier Science Ltd. All rights reserved.

INTRODUCTION

The National Aeronautics and Space Administration (NASA) and private industry are cooperating to develop new design technologies for reusable launch vehicles (RLV). These tasks include the new application of thermal materials for cryogenic insulation and reentry heating insulation on the external surfaces of the RLV's. The RLV's are planned to be in operation for up to twenty years, launching payloads to low earth orbit, including resupply missions to the International Space Station. Program planners predict each vehicle may be in orbit a total of up to five years over its twenty year life. As a consequence of this low earth orbit exposure, the vehicles will be subjected to potentially damaging impacts by manmade orbital debris.

At the NASA/George C. Marshall Space Flight Center (MSFC), the extent of damage orbital debris can cause to RLV thermal protection systems (TPS) is being studied. In 1994 and 1995, two series of hypervelocity impact tests on preliminary RLV TPS/structure designs were completed. The original purpose of the tests was to determine the ballistic limit for each TPS/composite tank wall design. The test results, damage morphologies, ballistic limits and related penetration probabilities are given in References [1-3]. These same data sets are used in this paper to determine predictor equations for hypervelocity particle entry hole diameters in the TPS tiles and blankets. The TPS includes the cryogenic insulation and the outer heat shield material, bonded to a composite load-carrying structure. In most of the configurations tested, this structure was integral with the pressurized fuel tanks, as shown in Figure 1. Perforation of the heat shield materials by orbital particles could lead to catastrophic failure of the vehicle from penetration of the fuel tank, or during reentry heating of the load-carrying structure.

0734-743X/99/$ - see front matter © 1999 Elsevier Science Ltd. All rights reserved.
PII: S0734-743X(99)00122-0

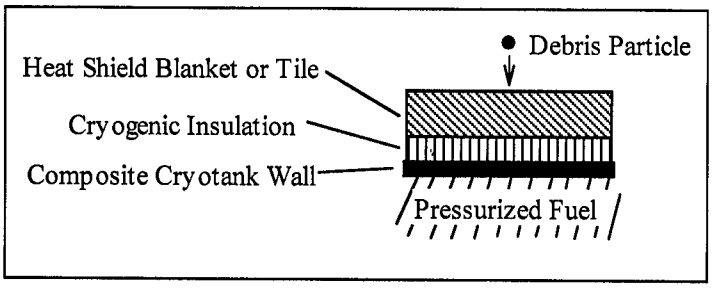

Fig. 1. Typical RLV integral tank cross-section.

TPS AND TANK WALL MATERIALS

Three heat shield materials were included in this study: AETB, Alumina-Enhanced Thermal Barrier-12 (0.192 g/cm^3); FRSI, Flexible Reusable Surface Insulation, a Nomex felt (0.134 g/cm^3); and AFRSI, Advanced Flexible Reusable Surface Insulation (0.160 g/cm^3; avg. break strength assumed 813.73 kg/cm^2). Material thicknesses varied from 0.64 to 7.62 cm. The TUFI coating, Toughened Uni-Piece Fibrous Insulation, coated on the surfaces of the AETB tiles was approximately 0.25 cm thick and approximately 1.32 g/cm^3 (strength approximately 52.73 kg/cm^2).

The cryofoam used in the test sample construction was Rohacell, a rigid, structural, closed cell polymethacrylimide (PMI) foam. Rohacell 51WF (0.051 g/cm^3) was in all but two test samples which contained Rohacell 71WF (0.075 g/cm^3).

Two types of composite cryogenic tank walls were tested: 0.23 cm 16-ply IM7/8552 graphite/epoxy (1.6 g/cm^3); and 0.15 or 0.11 cm thick IM7/8552 graphite/epoxy (1.6 g/cm^3) face sheets sandwiched around the cryofoam.

3M Nextel® 440 ceramic fabric (0.10 cm thick, 12 harness satin weave, non-standard product, 0.719 g/cm^3) and high strength Hexcel Kevlar® 49 fabric (0.03 cm thick, 285 crowfoot weave, 1.24 g/cm^3) were interlayered between heat shield and cryofoam layers in several of the samples to attempt to increase the penetration resistance of the samples. Earlier orbital debris shield design studies indicated that Nextel® and Kevlar® increased penetration resistance when used in certain structural configurations [4-8].

The components of each test sample were bonded together with thin layers of RTV (room temperature vulcanizing) adhesive.

The outer walls of some of the non-integral tank configurations consisted of a heat resistant blanket or tile bonded to composite facesheet honeycomb panels with 0.040 cm IM7/5250-4 graphite/BMI face sheets (1.66 g/cm^3) and a 1.27 cm Nomex honeycomb core (assumed 0.048 g/cm^3). For the remaining non-integral tank configurations, the heat resistant blankets or tiles were bonded to an outer single-thickness wall of 0.10 cm thick IM7/5250-4 graphite/BMI panel (1.66 g/cm^3).

All the materials except the composite panels were typically 15.2 cm square. The composite cryotank wall panels and the non-integral composite structure panels, when used, were 25.4 cm square. Spacing between the composite panels in the non-integral configurations varied between 15.2 and 20.3 cm, as specified in the sketches accompanying the tables describing individual test specimens, in the following sections.

TEST DESCRIPTION

The HVI tests were performed at NASA/Marshall Space Flight Center at the Space Debris Impact Facility [9]. The facility consists of an instrumented two-stage light gas gun (LGG) capable of launching 0.3175 to 1.27 cm diameter particles from 3 to 7 km/sec. Projectile velocity is measured with a pulsed x-ray system and a Hall photographic station. 1100-O aluminum (2.71 g/cm^3) spherical projectiles at approximately 6 km/sec were used for each test. For this test series, the intermediate test chamber (.66 m X .66 m X 1.2 m) was utilized. The barrel and test chamber were pumped to a vacuum of 400 milli-Torr for each test.

Aluminum 2024-T3 witness plates (2.77 g/cm^3) were held in place behind each test sample during impact, as shown in Figure 2. Each witness plate was 0.05 cm thick, and spaced 5.1 cm from the back of the test sample, and 5.1 cm between additional witness plates.

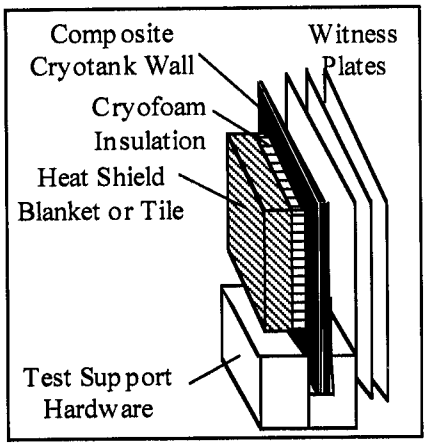

Fig. 2. Typical test setup.

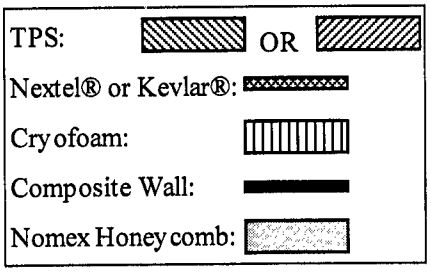

Fig. 3. Materials for table sketches.

TEST DATA REGRESSION RESULTS

Equations were developed for each of the three heat shield materials: AETB, FRSI, and AFRSI, to predict the entry hole diameters formed at the test particle impact velocity. These diameters were measured in-plane with the outer surface of the blanket or tile. The parameters chosen for the equations were those shown to be significant in previous hypervelocity impact studies, as they seemed appropriate in each material's impact process. Non-dimensional analysis methods were the basis for the regressions performed. Most tests were normal surface impacts; #1610 (an AFRSI configuration) was 30° off normal.

Tables describe the test samples, test parameters and results. Where "N" or "K" are shown within the tables indicates the use and location of single Nextel® or Kevlar® blankets. For example, from Table 1, test sample #1652 consisted of 0.41 cm of FRSI, a layer of Nextel® fabric, another layer of 0.81 cm thick FRSI, a layer of Kevlar® fabric, 1.27 cm of cryofoam, and finally the composite cryotank wall. The sketches corresponding to each configuration tested use the material designations shown in Figure 3. The sketches are not to scale, but are simply intended to show the stacking order of the materials in each test sample.

FRSI Regression Results

Table 1 includes sketches of each of the seven FRSI configurations tested, the test sample material thicknesses, and the test parameters and resulting damage to FRSI.

Equation (1) is the predictor equation for the entry hole diameter in the FRSI heat blanket material, formed by entry of the hypervelocity particle at approximately 6 km/s. The sketches in Figure 4 illustrate the configurations for FRSI used to develop Equation (1). The correlation coefficient for this equation is 0.69 for 17 data points.

$$H = 1.261 \{ t_1^{\,3.068} (t_2/t_1)^{0.5513} (d/t_1)^{1.880} (r_1/r_p)^{-1.352} (r_2/r_p)^{0.9380} \}^{0.326} \quad (1)$$

where:
- H = clear entry hole diameter in FRSI, cm
- t_1 = thickness of first FRSI blanket, cm
- t_2 = thickness of second layer (FRSI blanket or Nextel®), if any, cm
- d = particle diameter, cm
- r_p = particle material density, g/cm^3
- r_1 = material density of FRSI, g/cm^3
- r_2 = material density of t_2, if any, g/cm^3
  (for impact velocities 5.5 km/sec ≤ v ≤ 6.5 km/sec, only)

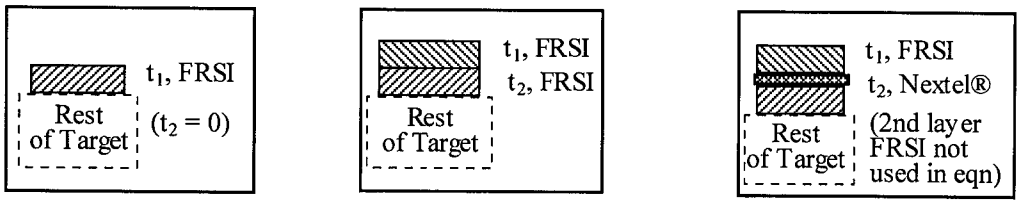

Fig. 4. FRSI configurations.

The parameters chosen for regression of the FRSI data were: particle diameter and material density; and target material thicknesses and densities. Since including impact velocity in the regression produced a very low correlation coefficient, it was dropped as a parameter. The angle of particle impact was not included, since all tests were normal impacts. Due to the felt-like structure of the FRSI, the actual diameter of deformed or damaged material extended out from the clear hole, shown in Figure 5. The material density of FRSI is assumed to be constant throughout the blanket thickness.

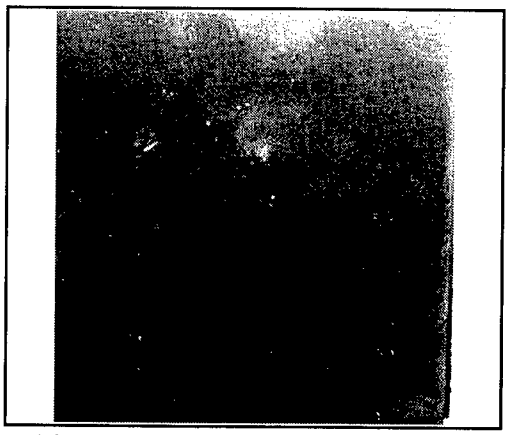

Fig. 5. Damage to #1615 FRSI blanket.

Table 1. FRSI test samples, test parameters and results

		Material Thickness, cm				Test Parameters & Results		
	Test #	FRSI	Cryofoam	Composite Outer Shell	Composite Tank Wall	Particle Diam.,cm	Velocity, km/sec	Hole Diam.,cm
config. FRSI-1	1612	0.89	2.03	-	0.23	0.32	6.07	0.86
	1613	1.27	1.27	-	0.23	0.32	6.30	1.02
config. FRSI-2 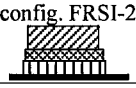	1615	1.27/N	1.27	-	0.23	0.32	6.30	1.02
config. FRSI-3	1634	.41/N/.81	1.91	-	0.23	0.47	6.22	1.83
	1641	.41/N/.81	1.91	-	0.23	0.32	6.18	1.52
	1668	.41/N/.81	1.91 (71WF)	-	0.23	0.47	5.96	1.04
	1670	.41/N/.81	1.91 (71WF)	-	0.23	0.32	6.03	1.02
config. FRSI-4 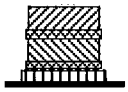	1650	.41/N/.81/K	1.27	-	0.23	0.47	approx. 6	1.30
	1652	.41/N/.81/K	1.27	-	0.23	0.64	6.16	1.50
	1653	.81/N/.81/K	1.27	-	0.23	0.47	6.23	1.32
	1656	.81/N/.81/K	1.27	-	0.23	0.47	approx. 6	1.40
config. FRSI-5 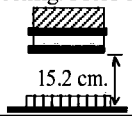	1624	0.91	1.78	.04/.04	0.23	0.64	6.00	2.54
	1630	0.70	1.78	.04/.04	0.23	0.47	6.35	2.29
config. FRSI-6 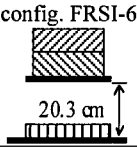	1659	.41/.81	1.91	.10	0.23	0.32	6.11	0.99
	1660	.41/.81	1.91	.10	0.23	0.47	6.00	1.17
config. FRSI-7 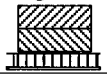	1675	.41/.81	1.27	-	.11/.11	0.47	5.95	2.29
	1676	.41/.81	1.27	-	.11/.11	0.32	6.23	0.69

AFRSI Regression Results

Table 2 includes sketches of each of the eight AFRSI configurations tested, the test sample material thicknesses, and the test parameters and resulting damage to AFRSI.

Equation (2) is the predictor equation for the entry hole diameter in the AFRSI heat blanket material, formed by entry of the hypervelocity particle at 6 km/s. The sketches in Figure 6 illustrate the configurations for AFRSI used to develop Equation (2). The correlation coefficient for this equation is 0.69 for 28 data points.

$$H=1.615\ \{\ t_1^{\ 1.381}\ (t_2/t_1)^{-0.340}\ (d/t_1)^{\ 1.328}\ (k/v)^{\ 0.496}\ (r_1/r_p)^{\ -0.339}\ (r_2/r_p)^{\ -0.444}\ \}^{\ 0.724} \qquad (2)$$

where: H = clear entry hole diameter in AFRSI, cm

t_1 = AFRSI quartz cloth, or Nextel® thickness, cm

t_2 = Remainder of AFRSI or entire AFRSI thickness, cm
d = particle diameter, cm
r_p = particle material density, g/cm^3
r_1 = material density of the AFRSI quartz cloth, or Nextel®, g/cm^3
r_2 = material density of the AFRSI, g/cm^3
v = particle velocity, 5.5 km/s ≤ v ≤ 6.5 km/s only, km/s
k = material variable (0.288 for AFRSI quartz cloth, or 0.170 for Nextel®), km/s

Table 2. AFRSI test samples, test parameters and results

		Material Thickness, cm				Test Parameters & Results		
	Test #	AFRSI	Cryofoam	Composite Outer Shell	Composite Tank Wall	Particle Diam.,cm	Velocity, km/sec	Hole Diam.,cm
config AFRSI-1	1603	1.27	1.27	-	0.23	0.32	6.20	1.04
	1605	2.54	1.91	-	0.23	0.32	6.80	1.02
	1606	2.54	1.91	-	0.23	0.64	5.88	1.52
	1607	2.54	1.91	-	0.23	0.47	5.91	1.73
	1608	1.27	1.27	-	0.23	0.32	6.20	0.66
	1678	1.27	1.27	-	0.23	0.32	6.11	1.02
config AFRSI-2	1604	1.27/N	1.27	-	0.23	0.32	6.30	0.97
	1609	1.27/N	1.27	-	0.23	0.47	6.06	1.57
	1610	1.27/N	1.27	-	0.23	0.47	5.97, 30°	1.47
config AFRSI-3	1635	N/1.91	1.91	-	0.23	0.47	6.20	1.30
config AFRSI-4	1637	N/1.91/N	1.91	-	0.23	0.47	6.20	1.30
config AFRSI-5	1654	N/2.54/K	1.27	-	0.23	0.47	5.93	1.09
	1655	N/2.54/K	1.27	-	0.23	0.47	5.91	0.76
	1657	N/2.54/K	1.91	-	0.23	0.47	approx. 6	0.89
	1658	N/2.54/K	1.91	-	0.23	0.47	6.16	0.91
	1665	N/5.08/K	1.91	-	0.23	0.64	6.16	1.14
	1667	N/5.08/K	1.91	-	0.23	0.47	5.92	0.81
	1672	N/2.54/K	1.27	-	0.23	0.47	5.85	1.07
	1673	N/2.54/K	1.27	-	0.23	0.47	5.76	1.02
config AFRSI-6 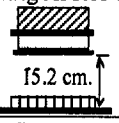	1631	0.64	1.78	.04/.04	0.23	0.47	6.20	2.36
	1632	1.27	1.27	.04/.04	0.23	0.64	5.83	1.78
config AFRSI-7 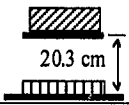	1661	1.91	1.91	.10	0.23	0.47	approx. 6	1.52
	1663	1.91	1.91	.10	0.23	0.64	approx. 6	1.73
config AFRSI-8	1674	2.54	1.27	-	.15/.15	0.47	5.83	0.97
	1677	2.54	1.27	-	.15/.15	0.32	6.06	0.64
	1642	2.54	1.91	-	.11/.11	0.32	6.45	0.97
	1643	5.08	1.91	-	.11/.11	0.32	6.31	1.14
	1671	2.54	1.27	-	.11/.11	0.47	5.97	1.80

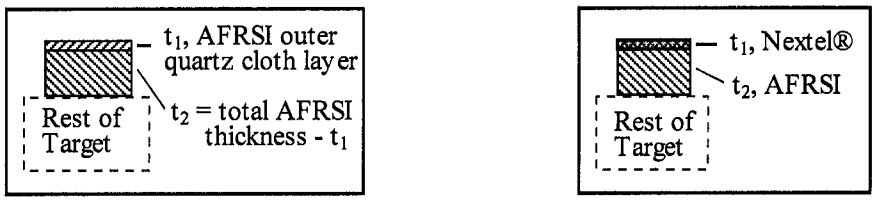

Fig. 6. AFRSI configurations.

The parameters chosen for the regression of the AFRSI data were: particle diameter, material density and velocity; target material thicknesses, densities and the material variable, k = [material strength x (9.8 m/s^2) / material density]^0.5. Unlike the FRSI regression, including the impact velocity did not cause a lower correlation with the data; therefore it was retained in the equation. However, this does not imply the equation can be extrapolated outside the range of velocities tested. The angle of particle impact was not included, since all but one test was normal to the surface. Because the outer surface of AFRSI blankets is a woven cloth, the actual diameter of deformed or damaged material cannot be accurately measured; measurements were made to approximate the clear circular hole diameter through the cloth. The blanket consists of a 0.07 cm thick quartz fabric (0.94 g/cm3) sewn around an internal thickness of felt (assumed same density as complete AFRSI blanket, 0.160 g/cm^3). Figure 7 shows typical hypervelocity impact damage on an AFRSI blanket. Additional test results for AFRSI blankets can be found in Reference [10], along with a proposed ballistic limit predictor equation for AFRSI blankets bonded to a substrate.

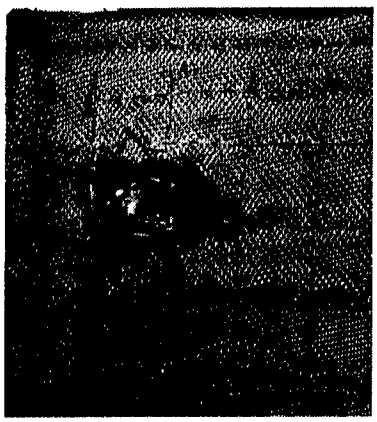

Fig. 7. Damage to #1603 AFRSI blanket.

AETB Regression Results

Table 3 includes sketches of each of the three AETB configurations tested, the test sample material thicknesses, and the test parameters and resulting damage to AETB.

Equation (3) is the predictor equation for the entry hole diameter in the AETB (0.192 g/cm^3) heat tile, formed by entry of the hypervelocity particle at approximately 6 km/sec. The sketches in Figure 8 illustrate the configurations for AETB used to develop Equation (3). The

correlation coefficient for this equation is 0.86 for 10 data points. The improved correlation over the FRSI and AFRSI is probably due to less subjectivity in measurement of the damage in the hard AETB tile. Also, the material density used is likely closer to the actual value than those used for the loosely packed flexible blankets.

$$H = 0.845 \{ (t_1)^{3.477} (t_2/t_1)^{-1.756} (d/t_1)^{3.153} (k/v)^{-0.072} (r_1/r_p)^{2.163} (r_2/r_p)^{-2.753} \}^{0.288} \quad (3)$$

where: H = clear entry hole diameter in AETB, cm
t_1 = estimated AETB coating (TUFI) thickness, cm
t_2 = total AETB thickness minus coating thickness (0.03 cm), cm
d = particle diameter, cm
r_p = particle material density, g/cm^3
r_1 = material density of the TUFI coating, g/cm^3
r_2 = material density of the AETB, g/cm^3
v = particle velocity, 5.5 km/sec ≤ v ≤ 6.5 km/sec only, km/s
k = material variable (0.06307 for AETB's TUFI coating), km/s

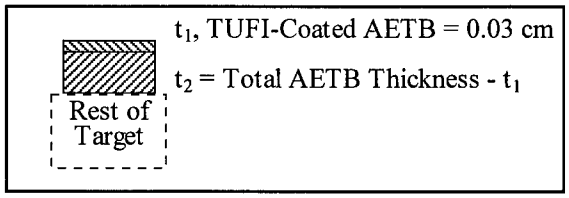

Fig. 8. AETB configuration.

Table 3. AETB test samples, test parameters and results

		Material Thickness, cm				Test Parameters & Results		
	Test #	AETB	Cryofoam	Composite Outer Shell	Composite Tank Wall	Particle Diam., cm	Velocity, km/sec	Hole Diam.,cm
config AETB-1	1616	5.08	1.78	-	0.23	0.32	6.10	1.02
	1617	5.08	1.78	-	0.23	0.64	5.60	1.78
	1618	6.35	2.54	-	0.23	0.64	5.88	1.91
	1619	6.35	2.54	-	0.23	0.95	6.02	3.96
	1620	6.35	2.54	-	0.23	0.80	5.91	2.29
	1621	5.08	1.78	-	0.23	0.80	5.98	2.54
	1625	7.62	3.05	-	0.23	0.80	6.05	2.54
	1626	7.62	3.05	-	0.23	0.95	6.53	NotAvail
config AETB-2	1622	1.27	1.27	0.04/0.04	0.23	0.95	6.35	NotAvail
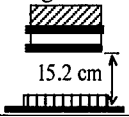	1623	1.27	1.27	0.04/0.04	0.23	0.80	6.10	6.35
config AETB-3 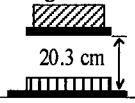	1662	5.08	1.91	0.11	0.23	0.64	6.10	1.91
	1664	5.08	1.91	0.11	0.23	0.80	5.99	2.18

The parameters chosen for the regression of the AETB data were: particle diameter, material density and velocity; material thicknesses, densities and the material variable, k= [material strength x (9.8 m/s^2) / material density]^0.5. As in the AFRSI regression, including the impact velocity did not cause a lower correlation with the data; therefore it was retained in the equation. However, this does not imply the equation can be extrapolated outside the range of velocities tested. The angle of particle impact was not included, since all tests were normal impacts. Figure 9 illustrates typical front surface damage seen in TUFI-coated AETB tiles. Discussion of the damage morphology seen on the test samples was previously published in Reference [1] and is not discussed in detail here. However, several other recent publications show similar reflected-cone-shaped damage in materials with densities of 0.14 g/cm^3 [11], and 0.3 g/cm^3 and 1.9 g/cm^3 [12]. The shape seems due to debris cloud expansion after initial impact, followed by a decrease in energy as it passes through the thickness of the tile. Figure 10 is a simple sketch of this damage shape. Reference [10] also describes a similar damage shape, in addition to a proposed ballistic limit predictor equation for TUFI-coated AETB tiles bonded to a substrate.

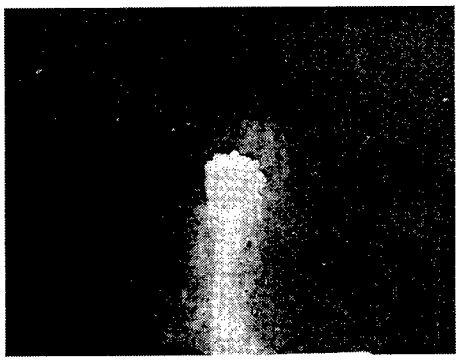

Fig. 9. Damage to #1617 AETB tile.

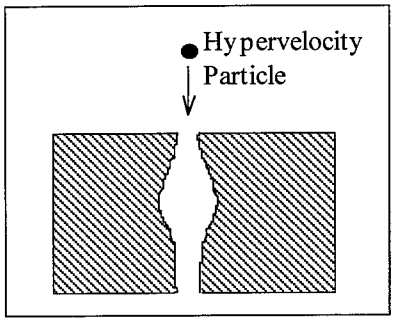

Fig. 10. Typical shape of internal AETB tile damage.

Composite Cryotank Wall Test Results

Several efforts were made to regress the composite cryotank data to form a predictor equation for the hole diameter in the wall. Although the resulting equations mathematically correlated well to the data, too many inconsistencies existed in the equations to allow for publication. With the presentation of the data here, interested researchers may be able to develop an adequate predictor equation. The data presented in Table 7 includes both the integral and non-integral tank configurations; the non-integral configurations are shaded. Sketches of each configuration, and material thicknesses can be found in previous sections of this paper. Typical damage seen in the graphite/epoxy laminate panels [1] was consistent with that reported by Yew and Kendrick [13].

Table 7. Test parameters and composite tank wall results

TPS Type	Test #	Al Particle Diameter, cm	Velocity, km/sec	Impact Angle, degrees	Composite Tank Wall Damage
FRSI	1612	0.32	6.07	0	1.3 x 0.7 cm Hole
	1613	0.32	6.30	0	1.0 cm Hole
	1615	0.32	6.30	0	Rear-side Delam.
	1634	0.47	6.22	0	1.5 x 2.7 cm Hole
	1641	0.32	6.18	0	None Visible
	1668	0.47	5.96	0	1.7 x 3.2 cm Hole
	1670	0.32	6.03	0	Delam., No Hole
	1650	0.47	approx. 6	0	2.1 x 3.3 cm Hole
	1652	0.64	6.16	0	3.4 x 3.9 cm Hole
	1653	0.47	6.23	0	1.0 x 1.4 cm Hole
	1656	0.47	approx. 6	0	2.0 x 2.3 cm Hole
	1624	0.64	6.00	0	4.3 cm Irreg. Hole
	1630	0.47	6.35	0	None Visible
	1659	0.32	6.11	0	None Visible
	1660	0.47	6.00	0	None Visible
	1675	0.47	5.95	0	3.6 x 2.3 cm Hole
	1676	0.32	6.23	0	2.0 cm Long Crack
AETB	1616	0.32	6.10	0	None Visible
	1617	0.64	5.60	0	None Visible
	1618	0.64	5.88	0	None Visible
	1619	0.95	6.02	0	6.4 x 15 cm Hole
	1620	0.80	5.91	0	0.8 x 1.0 cm Hole
	1621	0.80	5.98	0	3.8 x 7.6 cm Hole
	1625	0.80	6.05	0	None Visible
	1626	0.95	6.53	0	Entire Panel Delaminated
	1622	0.95	6.35	0	6.4 x 3.3 cm Hole
	1623	0.80	6.10	0	6 Small Holes
	1662	0.64	6.10	0	None Visible
	1664	0.80	5.99	0	None Visible

TPS Type	Test #	Al Particle Diameter, cm	Velocity, km/sec	Impact Angle, degrees	Composite Tank Wall Damage
AFRSI	1603	0.32	6.20	0	1.1 x 0.6 cm Hole
	1605	0.32	6.80	0	None Visible
	1606	0.64	5.88	0	2.2 x 5.6 cm Hole
	1607	0.47	5.91	0	2.5 x 1.3 cm Hole
	1608	0.32	6.20	0	1.0 x 0.6 cm Hole
	1678	0.32	6.11	0	Pinhole
	1604	0.32	6.30	0	Rear-side Delam.
	1609	0.47	6.06	0	2.3 x 2.3 cm Hole
	1610	0.47	5.97	30	2.8 x 2.0 cm Hole
	1635	0.47	6.20	0	1.8 x 3.6 cm Hole
	1637	0.47	6.20	0	1.7 x 2.9 cm Hole
	1654	0.47	5.93	0	1.9 x 3.2 cm Hole
	1655	0.47	5.91	0	1.5 x 1.7 cm Hole
	1657	0.47	approx. 6	0	1.5 x 2.8 cm Hole
	1658	0.47	6.16	0	1.4 x 2.0 cm Hole
	1665	0.64	6.16	0	6.8 x 3.5 cm Hole
	1667	0.47	5.92	0	None Visible
	1672	0.47	5.85	0	3.3 x 2.0 cm Hole
	1673	0.47	5.76	0	1.0 x 1.8 cm Hole
	1631	0.47	6.20	0	None Visible
	1632	0.64	5.83	0	4 Holes
	1661	0.47	approx. 6	0	None Visible
	1663	0.64	approx. 6	0	0.2 cm Hole
	1674	0.47	5.83	0	2.1 x 2.1 cm Hole
	1677	0.32	6.06	0	None Visible
	1642	0.32	6.45	0	None Visible
	1643	0.32	6.31	0	None Visible
	1671	0.47	5.97	0	2.5 x 2.2 cm Hole

PREDICTING DAMAGE AT HIGHER VELOCITIES

With results from analyses and even from tests at less than 8 km/s, approximations can be made of damage that will occur at projectile impact velocities in orbit, 14 - 20 km/s. When similar predictions result from different methods, the predictions remain unsubstantiated by tests at actual expected impact velocities, and should be regarded as preliminary. For the heat shield materials included in this study, the expected increase in hole diameter may be approximated several ways, although with low confidence.

For laminate composite PEEK and graphite/epoxy plates, Reference [14] proposed a model to predict the entry hole diameter as a function of projectile energy, target thickness and projectile diameter. To predict the hole growth with increasing velocity, the new hole diameter would be proportional to a function of the cubed root of the projectile energy. This relationship held true in an additional study by Taylor, Herbert and Kay [15]. Other references indicate hole diameter growth is proportional to a function of velocity, from hydrocode analyses of metal targets [16], from space station shielding tests (back wall hole growth) [17], and from tests below 8 km/s for thin metal plates [18]. None of these functions are directly applicable to the heat shield blankets and tiles in this study. However, as a first approximation, the proportionality of hole diameter to the cubed root of projectile energy, proposed for laminate composite materials, should provide a reasonable estimate. As an example, from Table 6, test # 1617 in AETB resulted in a hole diameter of 1.8 cm. If proportional to velocity, the hole at 16 km/s would be 5.1 cm diameter. If proportional to the cubed root of the projectile energy, the hole at 16 km/s would be 3.6 cm. Further analyses and tests at higher impact velocities are required for the heat shield materials in this study to improve confidence in approximating the resulting hole diameters.

SUMMARY AND CONCLUSIONS

The three TPS hole diameter equations developed during this study correlate well with the test data for normal impacts at approximately 6 km/s impacts. The less subjective measurements and more consistent material properties through the thickness of the AETB tiles led to a higher correlation than for the FRSI and AFRSI blankets. The equations may be used in the evaluation of impacts suffered on-orbit, however with less confidence since on-orbit impacts will occur at varying impact angles, and particle shapes, materials, and sizes, and at higher impact velocities.

More research is required to fully understand the implications of the orbital debris environment on reentry vehicles. The limited scope of this study should be expanded to include variations of particle density, impact angle and impact velocity, as a minimum, to gain more insight into the survivability of reusable launch vehicles, orbiter-type vehicles, and crew return vehicles.

Acknowledgments—Thanks to Angela Nolen, Mary Hovater and Melanie McCain for their performance of the hypervelocity impact tests at MSFC's Space Debris Impact Facility, and for their untiring assistance in compiling the details of the test parameters and each test sample used in this study.

REFERENCES

1. J.H. Robinson, et al, Meteoroid/orbital debris implications to a reusable launch vehicle thermal protection system. *AIAA Space Programs and Technologies Conference*, AIAA 95-3606 (1995).
2. Dave Wittman, Early on-orbit TPS debris impact tests. Rockwell Aerospace- Space Systems Division, Laboratory Test Report No. LTR 6552-4031 (1994).
3. J.K. Pulley, Test report - debris impact test report - delta testing. Rockwell Aerospace Space Systems Division Report No. Addendum SSD94D0330 (1995).
4. E.L. Christiansen, Advanced meteoroid and debris shielding concepts. *AIAA/NASA/DOD Orbital Debris Conference*, AIAA 90-1336 (1990).
5. B.G. Cour-Palais and J.L. Crews, Multishock concept for spacecraft shielding. *Int. J. Impact Engng*, **10**(1-4), 135-146 (1990).
6. J. Zwiener, A. Mount, K. Herren, A. Nettles, C. Semmel, and J. Sims, Enhanced Whipple bumper system: impact resistance of composite materials. *AIAA Space Programs and Technologies Conference*, AIAA 92-1589 (1992).
7. G.D. Olsen and A.M. Nolen, Advanced shield design for space station freedom. *Int. J. Impact Engng*, **14**(1-4), 541-549 (1993).
8. E.L. Christiansen, J.E. Williamsen, J.L. Crews, J.H. Robinson, and A.M. Nolen, Enhanced meteoroid and orbital debris shielding. *Int. J. Impact Engng* (1995).
9. R.A. Taylor, Space debris simulation facility for spacecraft materials evaluation. *SAMPE Quarterly*, **18**(2) (1987).
10. Larry Jay Friesen and Eric L. Christiansen, Hypervelocity impact tests of X-38 crew return vehicles (CRV) thermal protection materials, part II. JSC 27664, December (1996).
11. Larry Jay Friesen and James Whitney, Hypervelocity impact tests of shuttle material targets. JSC 27315, June (1996).
12. C. Loupias et al., Hypervelocity impacts of orbital debris on an advanced heat shielding material: comparison of ouranos computations to experimental results. *Int. J. Impact Engng*, **20** (1997).
13. Ching H. Yew and Rodney B. Kendrick, Study of damage in composite panels produced by hypervelocity impact. *Int. J. Impact Engng*, **5** (1987).
14. R.C. Tennyson and G.D. Shortliffe, Hypervelocity impact tests on composite boom structures for space robot application. *9th Canadian Aeronautics and Space Conference on Astronautics, Ottowa, Canada* (1996).
15. Emma A. Taylor, Mark K. Herbert and Laurie Kay, Hypervelocity impact on carbon fibre reinforced plastic (CFRP)/ aluminum honeycomb at normal and oblique angles. *Second European Conference on Space Debris, ESOC, Darmstadt, Germany* (1997).
16. Alan J. Watts and Dale Atkinson, Dimensional scaling for impact cratering and perforation. *Int. J. Impact Engng*, **17** (1995).
17. J. Williamsen and W. Schonberg, Empirical models for spacecraft damage from orbital debris penetration and effects on spacecraft survivability. *Second European Conference on Space Debris, ESOC Darmstadt, Germany* (1997).
18. V. C. Frost, Meteoroid damage assessment. NASA SP-8042 (1970).

PERGAMON International Journal of Impact Engineering 23 (1999) 795–802

INTERNATIONAL JOURNAL OF IMPACT ENGINEERING

www.elsevier.com/locate/ijimpeng

ON THE INTERACTION BETWEEN SHAPED CHARGE JETS AND CONFINED EXPLOSIVES AT NORMAL INCIDENCE

Z. ROSENBERG and E. DEKEL

RAFAEL, P.O. Box 2250, Haifa, Israel

Summary — The normal incidence of shaped charge jets on confined explosive sheets is investigated through a series of 2D numerical simulations with the Eulerian code PISCES 2DELK. The basic mechanisms of the interaction are explored using a relatively simple criterion for the sheet efficiency to disrupt the jet, which is based on the undisturbed length of the emerging jet. The simulations are compared with experimental results published several years ago and the agreement is good. Using these simulations we show how one can optimize the efficiency of this interaction by using non-symmetrical confinement plates and stronger explosive sheets. © 1999 Elsevier Science Ltd. All rights reserved.

INTRODUCTION

The interaction between shaped charge jets and inclined reactive cassettes has been the subject of intense research during the past 25 years, due to the high efficiency of these elements in disrupting the jet, making them useful armor devices ([1]-[3]). The main features of this interaction is the continuous interaction between the jet and the moving plates which are propelled by the explosive sheet. Much less attention has been given to this interaction at normal incidence which, obviously, precludes the disruption of the jet by the plates. Still, it has been known for many years that thick blocks of explosives can reduce the penetration efficiency of jets by disrupting parts of the jets which are not directly involved in the penetration of the explosive block.

The most comprehensive work in the published literature, on the subject of normal incidence, is that of Brown and Finch [4]. They performed a series of experiments with explosive sheets, with various thicknesses and diameters, confined between steel plates of various thicknesses. They used X-ray shadowgraphy as their main diagnostics recording the shape of the jets emerging form the interaction. Our work, presented here, compliments the experimental work of Brown and Finch [4] by using 2D numerical simulations to reproduce their findings on the one hand, and performing some optimization studies, on the other. As stated above we were mainly interested in the disruption ability of the confined explosive sheet for which these 2D simulations are extremely useful.

NUMERICAL SCHEME

The Eulerian processor of the PISCES 2DELK code (described in [5]) was used in this study and the computational scheme is described in Fig. 1. In order to avoid lateral release effects we used the FLOW condition on the target lateral edges. This way the target is extended effectively to very large dimensions, in the lateral directions, avoiding any lateral release waves. A copper jet, 3 mm in diameter, impacts the confined explosive at normal incidence with a velocity of 7 km/s. The jet, with no velocity gradients, is long enough but we are only interested in its front

0734-743X/99/$ - see front matter © 1999 Elsevier Science Ltd. All rights reserved.
PII: S0734-743X(99)00124-4

portion and, specifically, in the undisturbed length emerging from the interaction. The jet has 11 cells on its radius with similar cell size in the target to insure convergence of the simulations. The steel plates are described by the Johnson-Cook model [6] with the parameters for RHA. The explosive sheet parameters, in most of these simulations, were those of TNT with $\rho_0 = 1.63$ g/cc, D = 6.93 mm/μsec and PCJ=211. These were inserted into a JWL model to describe the equation of sate for the explosive. The initiation process itself is performed through a Chapman-Junget condition (see [5]). As mentioned above, the disruption efficiency of a given sandwich was determined by the length of the undisturbed jet emerging from the interaction. This intact portion of the jet is responsible for the residual penetration in a witness block behind the sandwich. Thus, the shorter this length, the better protection is afforded by the given sandwich. One should note that all these are semi-quantitative figures of merit and that our analysis is basically a relative one, in which we can point to trends and sensitivities, rather than make accurate predictions.

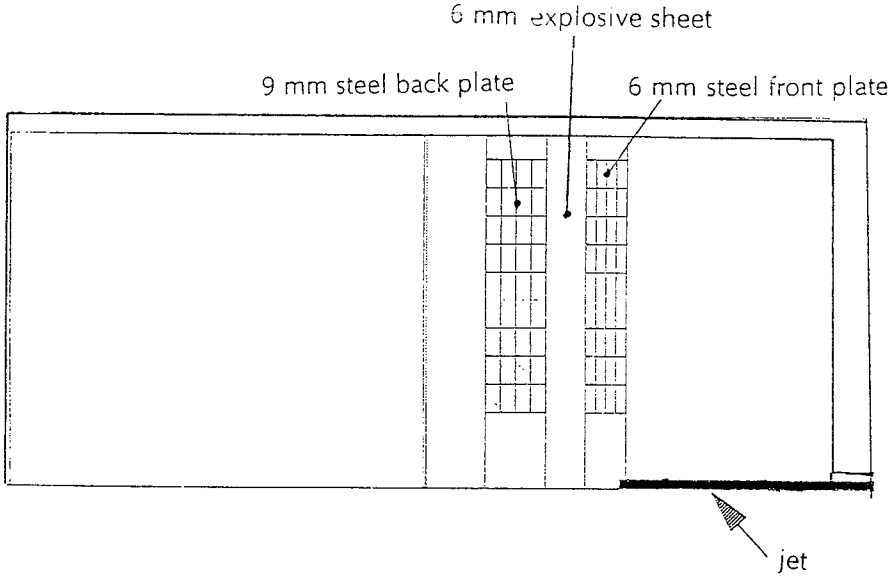

Fig. 1. Numerical scheme for 2D simulations.

RESULTS

Principal Disruption Mechanism

Fig. 2 shows a series of "snapshots" from a simulation using a 6 mm steel front plate, a 6 mm explosive sheet and a 9 mm steel back plate (→6/6/9). One can clearly see that up to 5 μsec after impact there is nothing unusual in the penetration and cratering process. The explosive sheet has been detonated and the jet experiences the well known erosion-inversion process. The relatively large crater diameter is the result of the high impact velocity (7 km/s). However, at later times we can clearly see how the inverted jet and the steel debris around it are pushed by the explosive products towards the symmetry axis. Thus, one can clearly state that the main disruption mechanism of the jet is that by the lateral impact of this debris. As shown in Fig. 2, a jet length of about 40 mm remains intact after the interaction. This is followed by a severely disrupted region which, owing to the 2D nature of the simulation, is probably grossly exaggerated in comparison with the experimental results.

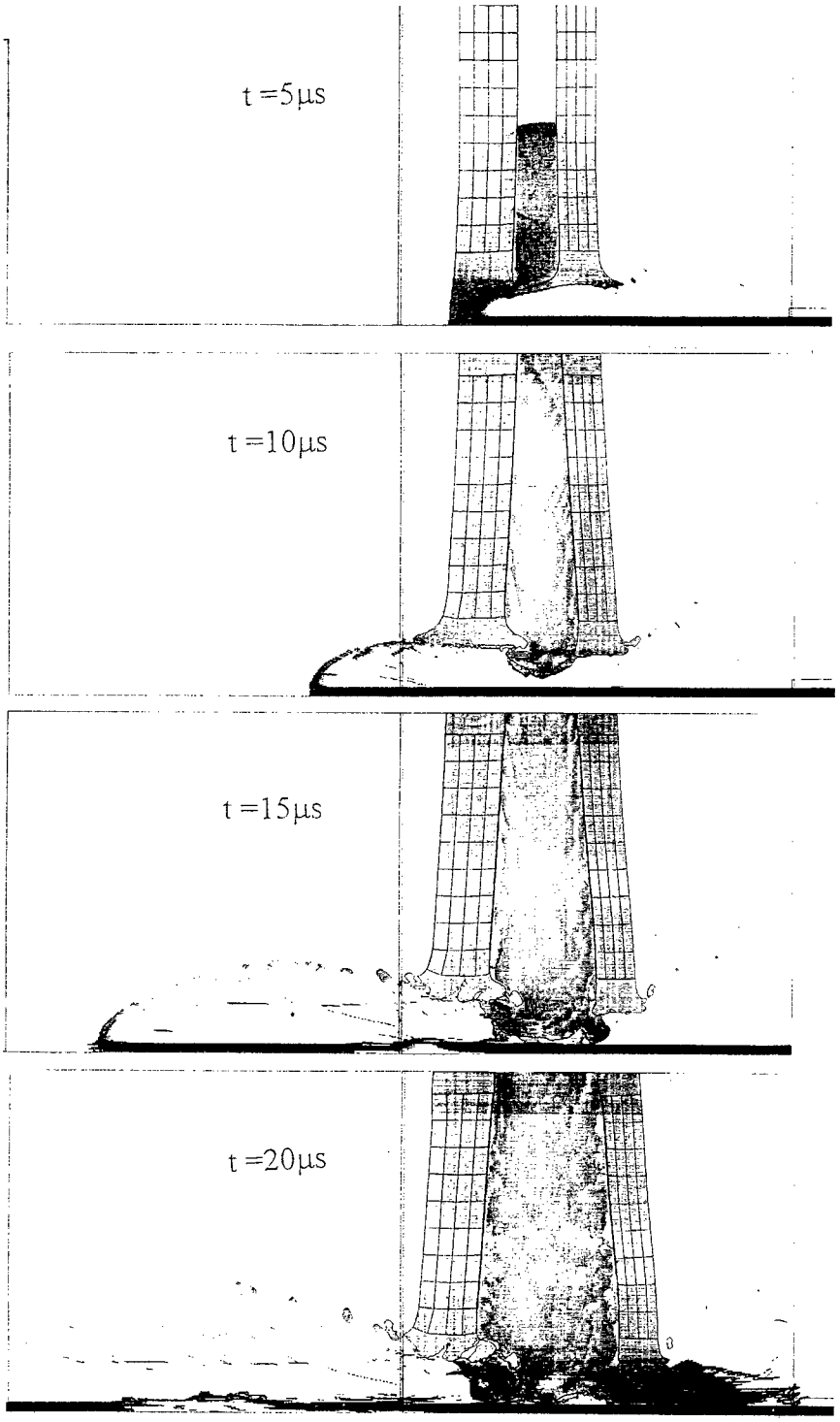

Fig. 2. Stages in a simulation with a sandwich of →6/6/9.

The Influence of Explosive Thickness

Brown and Finch [4] show that in order to have a substantial effect, the confined explosives should be thick enough - at least twice the diameter of the jet. They used a sandwich of →6/X/6 in which they varied the explosive thickness in the 3-12 mm range. We performed similar simulations and our results are shown in Fig. 3, together with those of [4], in terms of residual (undisturbed) jet length as a function of explosive thickness. Note the good agreement between the two sets of results which is quite surprising considering the differences between explosives, the fact that our jet is nonstretching, and that we use stronger steel plates in our simulations (RHA in our simulations vs. mild steel in [4]).

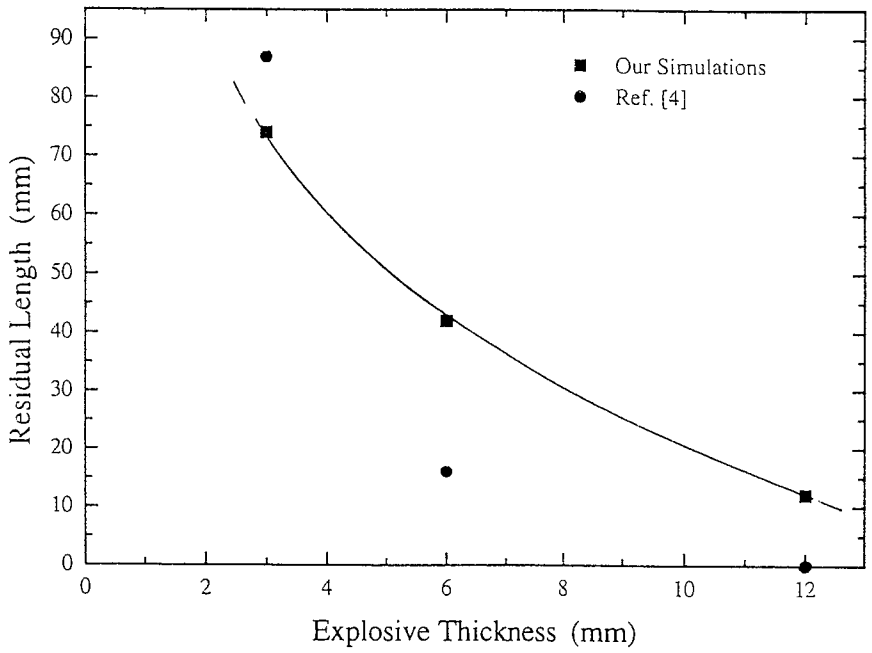

Fig. 3. Comparison of experimental and simulation results for intact jet length, emerging from the interaction.

The Influence of Plates Thicknesses

In order to further explore the nature of this interaction we performed several simulations varying the thickness of the steel plates. We followed the timing for the lateral impact of the inverted jet at the axis which, obviously, determines the length of the intact jet. Fig. 4 shows the results of two simulations with asymmetrical, equal weight, sandwiches: →3/6/6 and →6/6/3. One can clearly see the difference in the performance of these sandwiches, which was also found in [4], as far as the intact jet length is concerned. The sandwich with the lighter front plate resulted in an intact jet of 12 mm only, while for other simulation this length is 80 mm. This difference is due to the very different time of arrival of the debris at the jet location, as can be seen in Fig. 4. The shorter impact times result in shorter jets escaping the interaction.

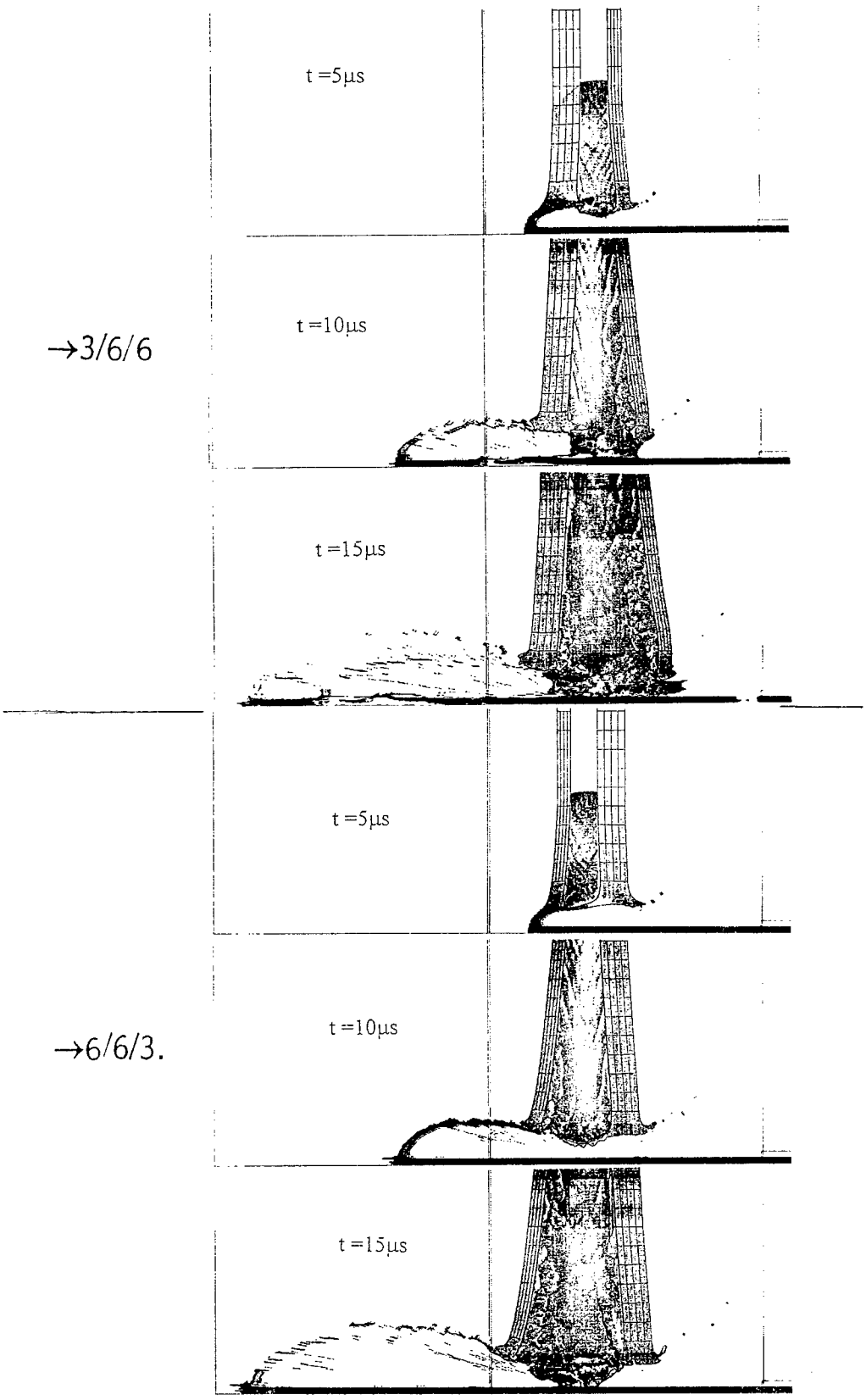

Fig. 4. The difference between the disruption efficiency of two asymmetrical sandwiches.

Another simulation with an equivalent, symmetrical, sandwich (→6/6/6) resulted in an intermediate value of 42 mm for the intact jet length. Thus, asymmetrical sandwiches with light front plates are much more efficient in reducing jet length. As is clearly seen the time of impact, at the axis, is much shorter for the more efficient sandwich so one can conclude that this parameter is most crucial in determining jet lengths. Another interesting result which we obtained concerns the type of material which confines the explosive sheet. We found that replacing the back steel plate with an equal weight aluminum plate did not change the length of the intact residual jet. Thus, it is the weight supporting the explosive sheet which is responsible for its performance. A summary of our simulation results is given in Fig. 5 where they are arranged in three groups of constant weight sandwiches. The three groups differ by the thickness of the explosive layer and, as we can clearly see, the best performance (smallest residual jet) is obtained with front plate thickness of 1.5 to 2 mm This trend is the opposite to the trend we obtained for the interaction of shaped charge jets and inert cassettes [7]. There we found that for a given total weight it is preferable to chose a configuration with a thin (1 mm) back plate. The efficiency of inert cassettes to disrupt the jet was determined by the bulging velocity of the two plates. This is a different criterion than the one we used in the present work, hence the different results. Thus, one can use these sets of simulations to optimize the performance of various combinations of inert and reactive cassettes, even though these are 2D simulations while the actual interactions are clearly 3D. We would like to emphasize, again, that these results should not be viewed as predictions but, rather, as trends from which one can have an idea about the sensitivity of the main mechanisms operating in these interactions.

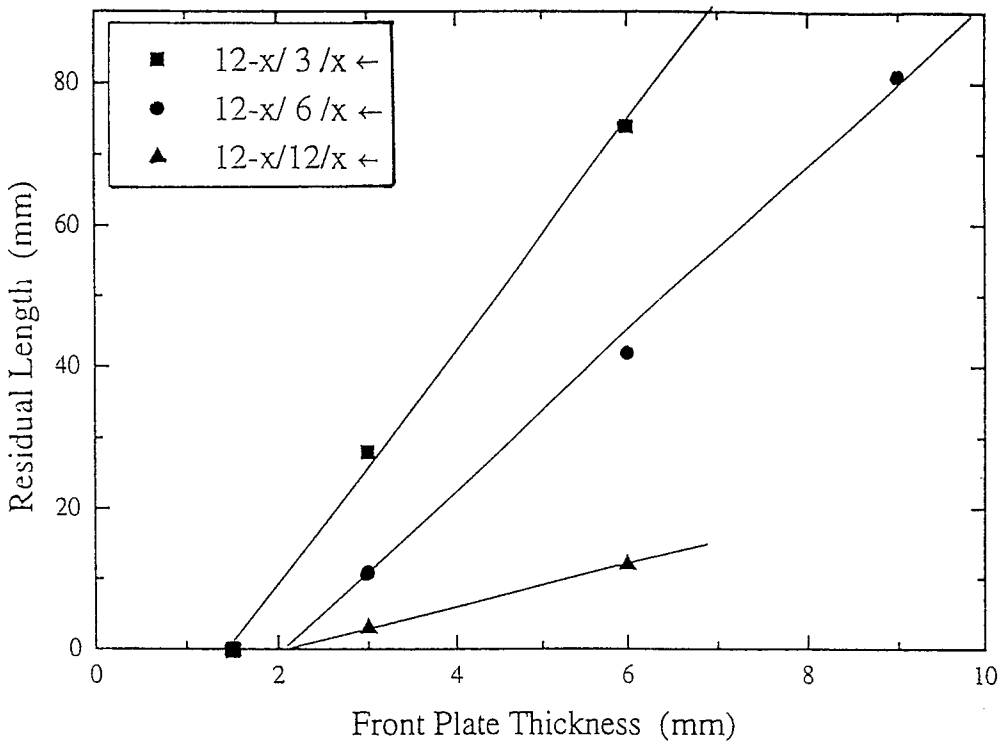

Fig. 5. Summary of our results for constant weight sandwiches.

Varying the Explosive Configuration

The experiments in [4] showed that removing the cover plate (exposing the explosive layer) reduces the effect substantially and the emerging jet is almost undisturbed. A simulation with an explosive layer (6 mm) on a 12 mm steel plate confirms this result showing very little damage to the jet. On the other hand changing the type of the explosive to a stronger one resulted in a much stronger effect for a →6/6/6 sandwich. In fact, an increase of 30% in the explosive strength (PCJ) resulted in a reduction of almost 40% in the length of the intact jet (26 mm) emerging from the interaction. Finally, we simulated the experiments in [4] with discs of explosives, 42 mm in diameter, embedded in steel targets. Fig. 6 shows the results of such a simulation. The configuration is similar to the →6/6/6 sandwich and the intact jets emerging from these interactions have nearly the same length. Thus, a disc of explosive embedded in steel causes a similar disturbance to the jet as that of a continuous explosive sheet.

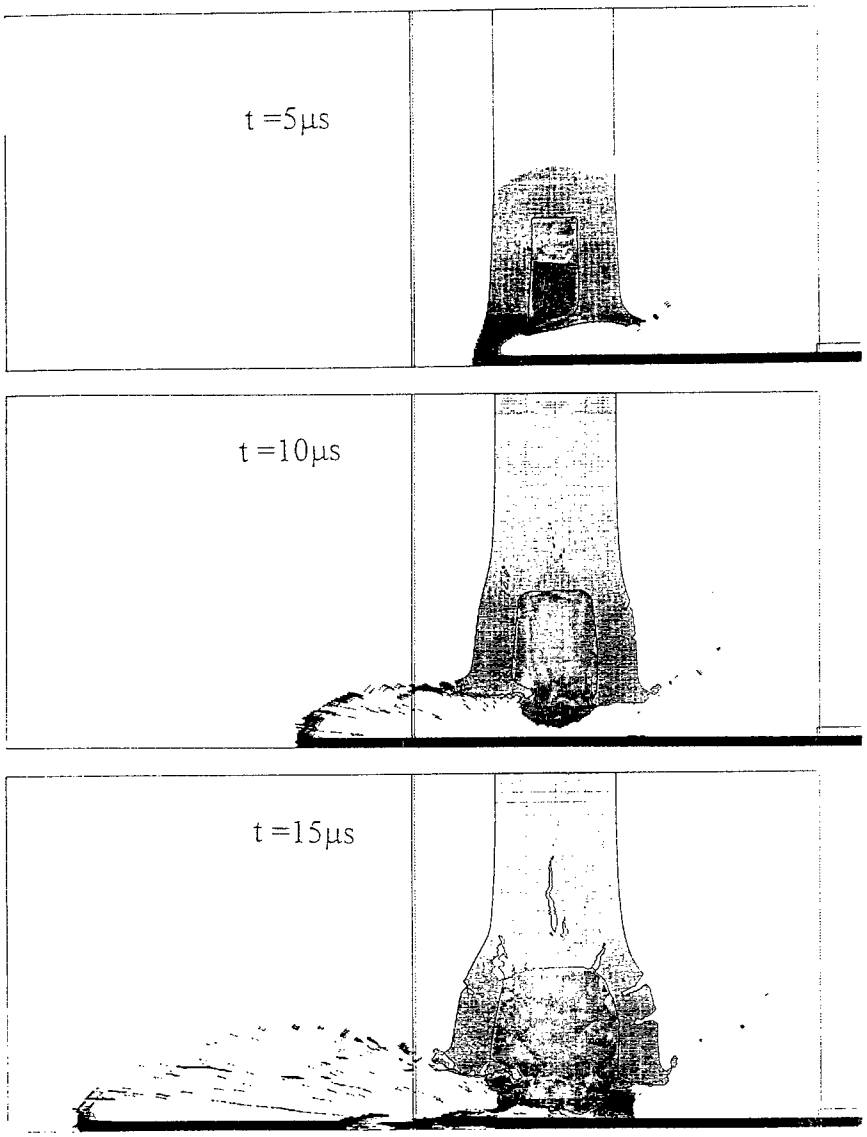

Fig. 6. Simulation results for a disc of explosive, 42 mm in diameter, embedded in a steel plate.

CONCLUSIONS

Two-dimensional simulations of the interaction between normally incident shaped-charge jets and confined explosive sheets, reproduced several experimental features which were published in the literature. The main disruption mechanism to the jet is the lateral impact of the inverted jet particles on its rear portions. The faster this impact takes place, the shorter the emerging jet length and, thus, the better the performance of the sandwich. We found that asymmetrical sandwiches with light cover plates are better than others and that the explosive sheet does not have to be very large, as long as it is well confined in the steel target. Moreover, thicker and stronger explosives cause more damage to the jet, as far as the escaping intact jet is concerned. The main message of these simulations is that one can use these 2D, axially symmetric, calculations to study the main mechanisms and their important parameters in such interactions. Moreover, one can optimize the performance of such disruption mechanisms by using these simulations, saving a lot of effort (and resources) which are needed in a purely empirical study. Obviously, one should check these optimal configurations experimentally throughout the study to validate the simulation work.

REFERENCES

1. M. Held, A structure for protection against projectiles, ERA Patent, Germany, 2008156 (filed 21.2.1970).
2. M. Mayseless, Y. Ehrlich, Y. Falcovitz, D. Weihs and G. Rosenberg, *Proc. 8th Int. Symp on Ballistics*, Orlando, FL, pp. VII-15 - VII-20, (1984).
3. J.S. Nicholson, M.C. Rogers, R.J. Cox and G. Merritt, *Proc. 9th Int. Symp on Ballistics*, Shrivenham, England, pp. 2-403 - 2-410, (1986).
4. J. Brown and D. Finch, *Proc. 11th Int. Symp. on Ballistics.*, Brusselles, Belgium, pp. 211-232, (1989).
5. S.L. Hancock, *PISCES Theoretical Manual*, Physics International Company, San Leandro, CA (1985).
6. G.R. Johnson and W.H. Cook, *Engng. Fract. Mech.*, 21, 31, (1985).
7. Z. Rosenberg and E. Dekel, *Int. J. Impact Eng.*, 21, 297, (1998).

PERGAMON International Journal of Impact Engineering 23 (1999) 803–810

INTERNATIONAL JOURNAL OF IMPACT ENGINEERING

www.elsevier.com/locate/ijimpeng

MATERIAL PROPERTIES EXPERIMENTS USING THE AWE HIGH POWER LASER, HELEN

S. D. ROTHMAN, A. M. EVANS, R. T. EAGLETON, and L. B. PEARSON

AWE plc, Aldermaston, Reading, RG7 4PR, Berkshire, England

Summary—In this report we discuss two experimental programmes recently carried out using the AWE 1 TW Nd-glass laser, HELEN, to determine the properties of materials under shock loading conditions relevant to hypervelocity impacts. In the first experiment a laser heated hohlraum is employed to generate a uniform steady planar shock which is used to derive high accuracy equation of state data using the impedance match method at pressures in excess of those generally available by conventional means and hitherto only achieved in the vicinity of nuclear explosions. The results are shown to be self consistent and reproducible and thus represent a significant new tool in the material modeler's armoury. In the second experiment direct laser illumination at 10^{13} W.cm^{-2} is used to generate an attenuating shock in an aluminium target. Direct evidence of a spall layer is obtained by means of x-ray backlighting for the first time in such laser driven experiments. A cumulative damage model is required to predict the spallation and a preliminary analysis shows that the Johnson model, with parameters derived from conventional experiments at much lower strain rates, can be used to predict the spall thickness at the higher rates associated with the laser experiment. © British Crown Copyright 1999/MOD. Published by Elsevier Science Ltd with the permission of the Controller of Her Britannic Majesty's Stationery Office.

INTRODUCTION

In attempting to model hypervelocity impact phenomena it is important to have a good understanding and prescription of the material properties of both impactor and target over a wide range of pressure and temperature conditions. The initial impact at velocities of 20-40 mm.μs^{-1} will lead to shock pressures in excess of 10 Mb (1 TPa), somewhat higher than those generally obtainable in conventional equation of state experiments. At these pressures deformation of the material is dominated by the fluid equation of state; however in a thick target the pressures attenuate as the shock traverses the material and other properties such as material strength and spallation become increasingly important.

In this paper we discuss the application of high power short pulse (~1 ns) lasers to determine these properties. Two experimental programmes using the AWE 1 TW Nd-glass laser, HELEN, will be described. In the first we address the high pressure equation of state via measurements of the principal shock Hugoniot using an impedance match technique, demonstrating accurate measurements in the regime above 10 Mb which is in excess of that generally accessible using high explosive or gas gun techniques. The second experiment demonstrates a technique for observing spallation phenomena at very high strain rate, ~10^7 s^{-1}. Here the use of the laser allows us to vary the strength of the initial shock and observe the transition from solid to fluid behaviour.

0734-743X/99/$ - see front matter © British Crown Copyright 1999/MOD. Published by Elsevier Science Ltd with the permission of the Controller of Her Britannic Majesty's Stationery Office.
PII: S0734-743X(99)00125-6

HIGH PRESSURE EOS EXPERIMENTS

While conventional high explosive and gas gun techniques have yielded a wealth of experimental data on a wide variety of materials[1] they are in general limited to pressures around a few Mb in high impedance materials. A number of experiments using nuclear drivers have been performed during the underground testing programme[2,3]; however the errors attached to these data are often unquantifiable and the experiments cannot be repeated. Many years ago it was recognised that lasers could be used to generate similar pressures and attempts were made to investigate their possible use for EOS experiments[4,5], using direct irradiation of the sample materials. At that time, beam quality was poor and it proved impossible to generate sufficiently planar shocks for accurate measurements. In the intervening years advances in the inertial confinement fusion (ICF) programme have led to significant improvements in both beam quality and our understanding of how to generate planar shocks. One such technique, the use of a hohlraum to convert direct laser irradiation into a smoother quasi black-body x-ray field, has been used for a number of studies in which it is important to have a relatively uniform drive and has been adopted by AWE as the basis for accurate EOS experiments.[6]

Drive Uniformity

In our experiment, Figure 1, the two beams from the HELEN laser enter the hohlraum (a right circular gold cylinder of 1 mm diameter, 1 mm height) obliquely through entrance holes in the curved surface, irradiating the farther wall at around 10^{15} W.cm^{-2} thereby maximising the conversion to thermal x-rays. The equation of state sample is mounted over a 600 μm hole at one end of the hohlraum. The hohlraum is designed to be conservative in the sense that it does not fill to more than $\frac{1}{10}$ critical density for the frequency doubled, 0.53 μm, light at the end of the 1 ns Gaussian laser pulse, enabling us to make a simple 3D viewfactor estimate of drive uniformity; this shows the drive flux and hence pressure over the central 300 μm to be uniform to better than 1%. These flux uniformity calculations were confirmed experimentally by observing the shock breakout from a flat aluminium foil placed over the end of the hohlraum. Such experiments showed a 0.5% RMS variation in breakout time over the central 300 μm diameter.

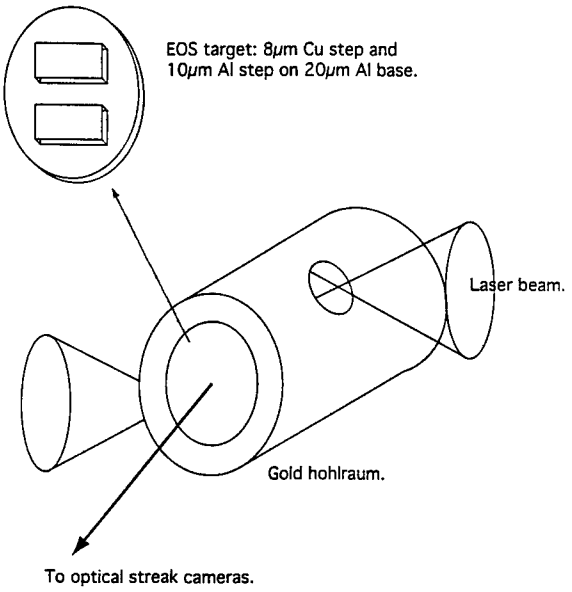

Fig 1. Laser driven EOS target

In its simplest form, the impedance match target is a base layer of aluminium upon which are placed steps of aluminium and the material for which we desire to know the equation of state. In our initial experiment we have used copper as a reasonably simple material for which there is some data from the nuclear experiments. In practice the interaction of the laser radiation with the hohlraum walls is known to produce high energy electrons and gold M-band photons, both of which are highly penetrating when target thicknesses are only of the order of 10 μm; a thin gold preheat shield is therefore included. The final design is thus a thin aluminium layer of 5-6 μm in which the shock wave is generated by ablation due to the thermal radiation field in the hohlraum, a 3-4 μm gold preheat shield, a 20 μm aluminium base layer during the passage through which the shock attains effective steady state conditions and finally steps of 10 μm aluminium and 8 μm copper.

Sample preparation

Such targets are not easy to fabricate and extremely difficult to characterise when the experiment calls for an accuracy of better than 1%. The targets are produced by vapour deposition, the various layers being laid down without releasing the vacuum to ensure good adhesion. Short puffs of oxygen are used to avoid the growth of dendritic structures in the aluminium base layer which would give rise to poor surface quality and spoil the shock breakout measurement; no oxygen was included in the last few microns nor in the steps themselves. The steps were made using suitable moveable masks and have 50-150 μm wells between them, a compromise between having them as close as possible to minimise errors due to any non-uniformity in the shock and the need for a sufficiently flat Al base area, unaffected by the rounded edges of the steps from which to observe the shock breakout. Step heights were initially measured to around 2% using a Zeiss laser scanning microscope, in the later series this was improved using the Zygo New View 100 white light interferometer. Multiple 2D scans for each target both on the microscope slide substrate used for the vapour deposition process and following mounting on the hohlraum end plate structure show the step heights to be accurate to ~0.5%. Surface finish was also measured with the New View and found to be 10-50 nm. A major difficulty lies in determining the density of the individual layers, at present this has not proved possible to better than ~2%. X-ray diffraction measurements indicate that lattice parameters for both aluminium and copper are within 0.05% of the values for standard crystal density but this would not preclude a degree of porosity; nevertheless in the absence of any information to the contrary we assume full crystal density in our analysis.

Optical shock break-out diagnostic

Shocks in the Mb regime produce sufficient temperature to be observed in the visible regime; either on breakout from an opaque surface or during transmission through a transparent material. Our principal diagnostic in determining shock velocities is thus an optical streak camera viewing the face of the target placed over the plane end of the hohlraum. The cameras respond to light in the range 590-750 nm with a spatial resolution at the target of 20 μm and a temporal resolution of 14 ps at the usual streak rate of 80 ps.mm-1. The cameras were calibrated using a train of short pulses produced by an etalon; curvature on the intensifier due to electron time of flight effects was corrected for using a full 2D calibration. Temporal accuracy is thereby assessed as better than 0.7%.

Steady shock and preheat assessment

Before conducting our impedance match experiments it was important to confirm the steady-state nature of the shock. This was done by fielding aluminium wedge targets varying linearly from 10-40 μm in thickness. Breakout from these targets indicate a shock velocity constant to better than 1% over the 500 ps required to transit the wedge. Preheat due to fast electrons and M-shell photons remains a concern as indicated above. With no preheat shield in the target early signals from the thinner part of the wedge are clearly visible. Inclusion of a 3-4 μm gold shield removes this, indicating that any preheat is below the 0.5 eV detection threshold of the streak camera, also, since any expansion of the rear surface would affect the breakout time we conclude any preheat is small. Calculations based on estimates of hot electron production and the hard x-ray spectrum suggest a value of ~0.05eV (~500°K). Subsequent experiments used a Michelson interferometer to investigate motion of the rear surface of similar flat aluminium targets including various thickness of preheat shield. Analysis is ongoing but the initial indications are that preheat using a 3-4 μm gold shield is indeed in the range 500-600°K. The effects of this preheat are difficult to quantify; the targets starts to expand and the subsequent shock is driven through a slightly thicker, lower density material; however calculations suggest that at the high pressures associated with these experiments, the error introduced is again of order 1%.

Experimental Hugoniot Results

Three series of experiments have now been fielded. By varying the input laser energy to the hohlraum we can generate shock pressures in the aluminium varying from 2-10 Mb although at the lowest end there must be some question as to the steady state nature of the shock as the hohlraum driver has not been adequately tuned or characterised. Shock transit times and step height data have been converted to shock velocity; particle velocity and pressure on the aluminium principal Hugoniot are derived from the known equation of state and appropriate reflected Hugoniots are calculated; this permits us to infer the Hugoniot conditions in the copper, the results are presented in table 1 and figure 2. The reference EOS for aluminium was taken from the LANL SESAME table 3715[7] which gives an excellent fit to the large body of experimental data including that derived from the nuclear driven shots of Simonenko[8] and Volkov[9] in the 10 Mb regime. However, it must be noted that although soundly based there is no direct experimental verification of the off-Hugoniot behaviour in this regime and this could give rise to additional errors.

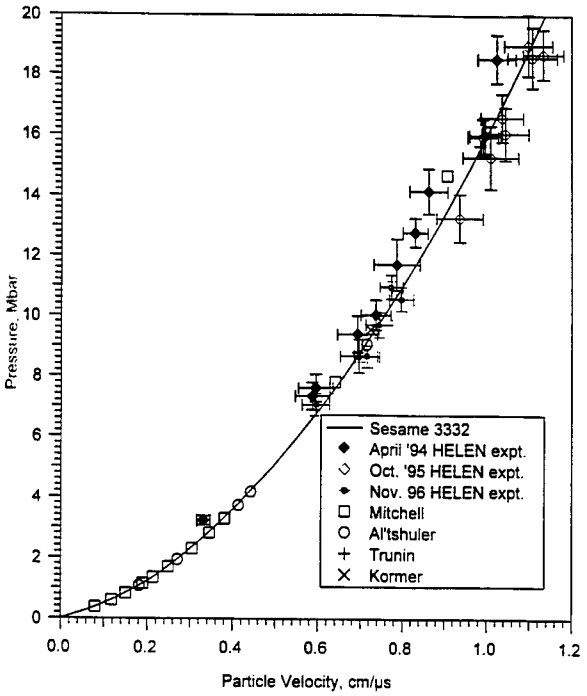

Fig. 2. Copper Principal Hugoniot

Table 1. Measured and calculated parameters for Al/Cu impedance match EOS targets

$mm.\mu s^{-1}$ U_s Al	$mm.\mu s^{-1}$ U_p Al	Mb P Al	$mm\ \mu s^{-1}$ U_s Cu	$mm.\mu s^{-1}$ U_p Cu	Mb P Cu	$g.cm^{-3}$ ρ Cu
12.66 ± 0.2	5.44 ± 0.2	1.86 ± 0.1	11.00 ± 0.2	3.28 ± 0.2	3.19 ± 0.15	12.68
16.91 ± 0.4	9.07 ± 0.3	4.14 ± 0.25	14.21 ± 0.4	5.87 ± 0.4	7.38 ± 0.45	15.16
17.06 ± 0.4	9.20 ± 0.3	4.24 ± 0.25	14.49 ± 0.3	5.92 ± 0.4	7.6 ± 0.45	15.05
18.55 ± 0.5	10.46 ± 0.4	5.24 ± 0.35	15.33 ± 0.4	6.9 ± 0.5	9.36 ± 0.6	16.19
19.17 ± 0.4	10.94 ± 0.3	5.66 ± 0.3	15.4 ± 0.3	7.33 ± 0.4	10.0 ± 0.5	16.98
20.32 ± 0.6	11.87 ± 0.45	6.51 ± 0.45	16.84 ± 0.5	7.86 ± 0.55	11.72± 0.85	16.69
21.14 ± 0.3	12.53 ± 0.25	7.15 ± 0.25	17.42 ± 0.3	8.33 ± 0.3	12.85 ± 0.5	17.06
21.9 ± 0.5	13.14 ± 0.4	7.77 ± 0.4	18.6 ± 0.4	8.62 ± 0.45	14.18 ± 0.75	16.59
24.67 ± 0.5	15.4 ± 0.4	10.26 ± 0.5	20.5 ± 0.4	10.24 ± 0.45	18.6 ± 0.8	17.78
22.05 ± 0.55	13.25 ± 0.46	7.89 ± 0.4	16.04 ± 0.41	9.36 ± 0.55	13.29 ± 0.8	21.37
23.35 ± 0.69	14.31 ± 0.57	9.03 ± 0.63	17.15 ± 0.41	10.09 ± 0.66	15.31 ± 1.04	21.62
23.49 ± 0.36	14.43 ± 0.3	9.16 ± 0.34	18.22 ± 0.31	9.91 ± 0.36	15.99 ± 0.6	19.51
23.55 ± 0.37	14.48 ± 0.3	9.21 ± 0.34	18.20 ± 0.3	9.96 ± 0.37	16.04 ± 0.6	19.66
23.89 ± 0.54	14.76 ± 0.45	9.52 ± 0.21	17.41 ± 0.39	10.44 ± 0.55	16.09 ± 0.87	22.23
24.05 ± 0.49	14.89 ± 0.4	9.66 ± 0.47	18.12 ± 0.32	10.36 ± 0.5	16.62 ± 0.8	20.78
25.24 ± 0.61	15.86 ± 0.51	10.81 ± 0.61	19.01 ± 0.34	11.07 ± 0.58	18.63 ± 1.00	21.31
25.32 ± 0.59	15.93 ± 0.49	10.89 ± 0.59	19.58 ± 0.34	10.98 ± 0.57	19.03 ± 1.0	20.26
25.45 ± 0.49	16.04 ± 0.4	11.02 ± 0.49	18.67 ± 0.3	11.33 ± 0.48	18.73 ± 0.82	22.64
16.80 ± 0.32	8.98 ± 0.27	4.08 ± 0.21	13.45 ± 0.27	5.95 ± 0.32	7.09 ± 0.37	15.96
18.27 ± 0.49	10.21 ± 0.41	5.04 ± 0.34	14.11 ± 0.24	6.96 ± 0.44	8.69 ± 0.55	17.56
18.39 ± 0.32	10.31 ± 0.27	5.12 ± 0.22	13.69 ± 0.17	7.15 ± 0.3	8.67 ± 0.36	18.63
19.10 ± 0.35	10.89 ± 0.29	5.61 ± 0.26	14.75 ± 0.2	7.44 ± 0.32	9.71 ± 0.42	17.96
19.86 ± 0.31	11.51 ± 0.25	6.17 ± 0.23	14.97 ± 0.22	7.97 ± 0.29	10.57 ± 0.40	19.03
19.89 ± 0.30	11.53 ± 0.24	6.19 ± 0.22	16.06 ± 0.25	7.73 ± 0.28	10.98 ± 0.40	17.16

As noted in ref 6 our initial results for the copper Hugoniot form an excellent self consistent set albeit rather harder than the best theoretical data available - SESAME 3332 - which is itself a good fit to the results of Al'tschuler, Trunin and Kormer. It is probably fortuitous that Mitchell's 15 Mb point agrees more closely with our data. The second and third AWE series data are rather softer and better agree with SESAME 3332. We believe the systematic difference with the first set is probably attributable to the target metrology and we place more confidence in the Zygo New View instrument for determining step heights. The second series was disappointing in that it did not show significantly smaller errors; the major contribution here was the rise time of the optical signal which was not as sharp as in the previous experiment and is attributed to the quality of the surface finish. The third series was highly successful in reducing error bars to almost 1% in shock velocity but limitations to the energy available during this series led to our working only in the 10 Mb range.

SPALLATION IN LASER DRIVEN EXPERIMENTS

The second series of experiments formed part of a collaborative programme with LANL to investigate changes in the behaviour of a sample undergoing an attenuating shock as the peak pressure varies. If the pressure is sufficiently low the material will remain in the solid state and there is the possibility of spallation. As the pressure is increased the material will become molten at some point and eventually form a plasma. Direct laser heating provides a suitable means of generating an attenuating pressure pulse with variable peak pressure simply by

adjusting the focal spot intensity. An initial series of experiments was performed using the HELEN laser in a short pulse mode (200 ps Gaussian) to directly irradiate targets at intensities varying from 10^{13} - 8 10^{14} W.cm^{-2}. The targets, Figure 3a, consisted of a plastic (Delrin) ablator some 400 μm thick which was designed to act as a smoothing layer from which the generated shock passed to a 100 μm thick aluminium plug of 200 μm diameter set in a gold tamper. The plug itself is machined from bulk aluminium. Observation of the state of the rear surface of the aluminium was by x-radiography using a 100 ps pulse of the HELEN backlighter beam to illuminate a silver tipped carbon fibre producing L-line emission peaking around 3.2 keV delayed to observe the aluminium after shock breakout.

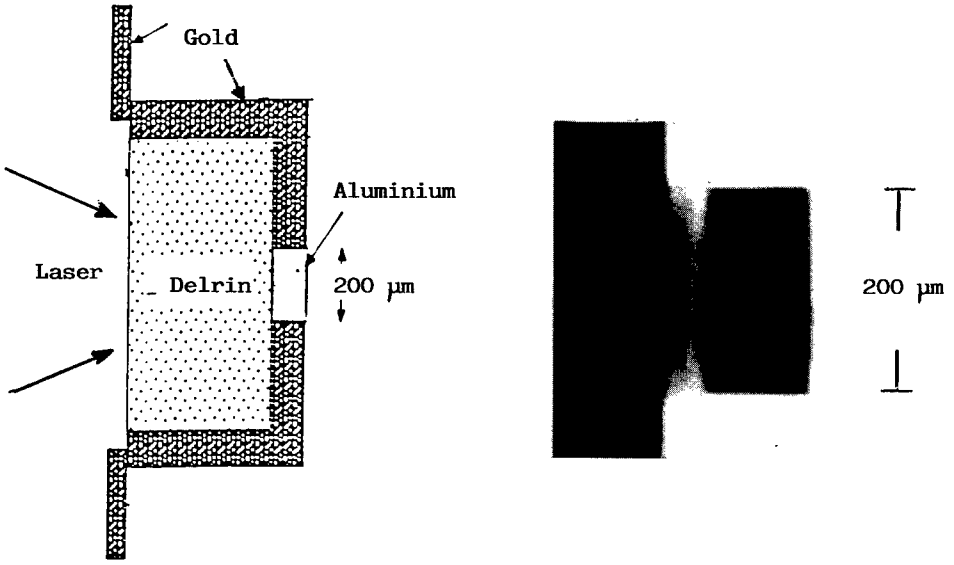

a. Configuration b. Radiograph

Fig. 3. Original spall experiment

Analysis Of First Experiments

Good experimental data were obtained at all intensities with the rear surface of the aluminium staying obviously intact (see figure 3b) at the lower values (1.25 x 10^{13} W.cm^{-2} and 5.10^{13} W.cm^{-2}). Calculations suggest that strains of around 10^7 s^{-1} are attained in these experiments and at the lowest intensity tensions well in excess of the estimated spall strength[10,11] (10-60 kb) would be achieved so that we might expect to observe spallation with a spall thickness of around a few tens of microns. The backlit radiograph is well aligned and shows no sign of a spall layer, the whole 100 μm thick aluminium plug having apparently been blown from the target. This leads us to question the validity of a simple peak tension spallation criterion.

A more satisfactory criterion is that of cumulative damage in which the tensile stress has to act for sufficiently long in order for spallation to occur. A suitable model is that due to Tuler and Butcher[12].

$$\int_0^t (\sigma_R - \sigma)^A \, dt \geq 3.8\,10^4 \quad \text{kb}^2\,\text{ns}$$

where σ_R = -10 kb, A ~ 2 and t is the fracture time. Using this criterion with parameters from our hydrocode calculations it can be shown that at no time does the integral exceed the critical value and spallation would not be expected.

Revised Target Design Results

We have accordingly redesigned the target, in this case rejecting the Delrin smoothing layer in favour of a simple aluminium block (see figure 4a). Calculations suggest that the Tuler-Butcher criterion is exceeded by at least an order of magnitude and we expect spallation to occur. Figure 4b shows the dynamic radiograph of this target some time after breakout of the shock from the rear surface. There is clear evidence of a spall layer some 60 μm thick. The first such radiographic evidence from a laser driven experiment.

Analysis of the experiment is a little complicated and relies on hydrocode simulations of the laser-plasma interaction to provide information on the temporal pressure pulse transmitted into the solid target. However when this is done and the resulting pulse calculated by a hydrocode using the Johnson[13] spall model with parameters chosen to fit published Russian data on aluminium[14] taken at far lower strain rates (10^4 - 10^5 s^{-1}) good agreement with the 60 μm spall layer is obtained.

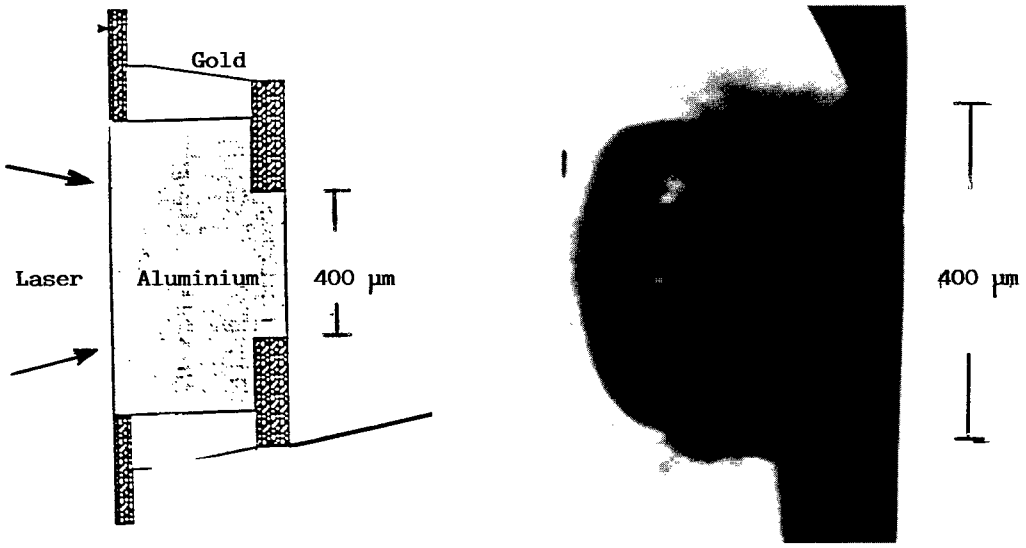

a. Configuration b. Radiograph

Fig. 4. Revised Spall Experiment

CONCLUSIONS

We have demonstrated that hohlraums driven by high energy lasers are a viable source for high pressure equation of state experiments in the region above a few Mb which has hitherto only been addressed by nuclear driven experiments. Accuracy approaching 1% in shock velocity can be achieved provided considerable attention is paid to temporal calibration of shock breakout diagnostics - in our case visible streak cameras - and more particularly characterization of the target dimensions. While this paper has concentrated on the demonstration of the technique using aluminium-copper targets we have obtained data for a number of other materials, including a number of plastics. The advent of higher power lasers will enable us both to address higher pressures and to reduce the burden on target fabrication by employing larger targets. The latter may also be achieved using the larger vacuum hohlraums driven by wire array Z-pinch implosions as recently demonstrated by SNLA[9].

Direct laser driven experiments can be used to investigate spallation effects at high strain rates and thereby complement conventional techniques. Simple peak tensile stress models are inadequate for predicting spall, cumulative damage models prove more appropriate. The Johnson model, easily adapted for use in hydrocodes where physical separation of interfaces is not always possible, has been shown to give good results for the high strain rate case with parameters based on fits to lower strain rate experiments.

ACKNOWLEDGEMENTS—The authors gratefully acknowledge the contributions of the AWE target fabrication and laser operations staff without whose able assistance the experiments could not have been carried out. Brian Thomas and Peter Graham provided much of the basic hohlraum design and flux uniformity calculations while John Maw and Andrew Giles provided the hydrocode calculations of the spall experiment.

REFERENCES

1. S P Marsh ed. *LASL Shock Hugoniot Data* (Univ Calif. Press, 1980)
2. A C Mitchell et al *J. Appl. Phys.* 69 pp 2981-2986 (1991)
3. R F Trunin et al *Sov. Phys. JETP* 29 630/1 (1969)
4. L R Veeser et al *Appl. Phys. Lett.* 35 (10) 761-763 (1979)
5. P C Thompson et al *J. Phys. D.* 14 1215 (1981)
6. A M Evans et al *Laser and Particle Beams* 14 113-123 (1996)
7. V A Simonenko et al *Sov. Phys. JETP* 61 (4) 869 (1985)
8. A P Volkov et al *Sov. Phys. JETP Lett.* 31 (11) 588-592 (1980)
9. J R Asay private communication
10. Elizier, Gilath, Bar Noy *J. Appl. Phys.* 67 (1990)
11. Gilath et al *J. de Physique* C3 (9) (Sept 1988)
12. F R Tuler, B M Butcher *Inter. J. Fracture Mech.* 4 (1968)
13. J N Johnson *J. Appl. Phys.* 52 2812-2825 (1981)
14. G I Kanel et al *Int. J. Impact Eng.* 20 467-478 (1997)

PERGAMON International Journal of Impact Engineering 23 (1999) 811–821

INTERNATIONAL JOURNAL OF IMPACT ENGINEERING

www.elsevier.com/locate/ijimpeng

SIMULATED SPACE DEBRIS IMPACT EXPERIMENTS ON TOUGHENED LAMINATED THIN SOLAR CELL COVER GLASS

ROBERT ROYBAL*, PAWEL TLOMAK*, CHARLES STEIN*, and HEADLEY STOKES**

*Air Force Research Laboratory, Space Vehicles Directorate, VSSE, 3550 Aberdeen Ave., Kirtland AFB, NM, 87117-6008, USA; ** Space Debris Group, Space Department, Defense Research Agency, Farnborough, Hampshire, GU14 OLX, UK

Summary—Increasing demands on the design criteria of space craft components have driven efforts to develop advanced space debris ground simulation techniques suitable to be incorporated into a space environmental effects chamber. A laser driven flyer method suitable in such a chamber was used to conduct an initial investigation of space debris impact on a new toughened solar cell coverglass material. Damage characteristics, including mechanical damage and contamination generated by impact with a 3mm diameter, 3 micron thick aluminum particle accelerated to 4.5 km/s, were looked at. Scanning electron microscopy, optical microscopy, and spectrophotometry were used to measure the mechanical damage and the loss of solar transmission. Because of the limited number of impact tests made in this initial study a quantitative analysis was not possible. However, much insight was obtained from the observed damage. © 1999 Elsevier Science Ltd. All rights reserved.

INTRODUCTION

Spacecraft placed in low-Earth orbit (LEO) are exposed to a large flux of hypervelocity impacts with small particles of natural space micrometeorites and man generated debris, Schneider [1], Rose [2], and Dursch [3]. At risk are the proposed satellite constellation systems. These satellite constellations, predominantly used for communication systems, will be placed in low Earth, nearly polar, orbits. Because of the overall cost associated with the number of satellites required and the environmental issues involved with the orbital location of the satellites, design criteria must include the use of advanced spacecraft materials that reduce launch cost and still maintain high survivability merits, Crowther, *at al.* [4]. The implementation of innovative large area solar panels to reduce the cost and complexity of solar arrays requires the generation of an advanced coverglass capable of providing high operational solar transmission along with the necessary strength for fabrication, launch survival, and debris impact resistance. The solar coverglass designed by Pilkington Space Technology (PST) is an effort to increase the cost efficiency of producing large volumes of spacecraft components, Kitchen, *et al.* [5]. The active cell area is increased substantially, up to $0.1m^2$ in area, reducing the number of components and allowing for the mass production of arrays. The traditional method for producing solar panels requires placement of a large number of interconnected small area cells onto delicate light weight substrates. This traditional method is labor intensive and requires highly skilled fabrication techniques. A large area cell array relies primarily on the toughness of the coverglass. During fabrication the solar cell array and satellite must withstand the rigors of ground handling. Launch and deployment stresses must also be considered in the design strength of the solar cell arrays. A proprietary PST process is used by Pilkinton to produce a strengthened coverglass by toughening both sides of a single large area glass. An active material

0734-743X/99/$ - see front matter © 1999 Elsevier Science Ltd. All rights reserved.
PII: S0734-743X(99)00126-8

such as a cadmium telluride thin-film, may be deposited onto the coverglass sheet which acts as a substrate. To achieve a suitably toughened laminate assembly, a second toughened coverglass is laminated to the first coverglass sheet with a resin layer between them. A cross section of a typical coverglass laminate is shown in Fig. 1. Silicon cells may also be fabricated by adhering two toughened cover glass sheets to a matrix of several large area silicon cells.

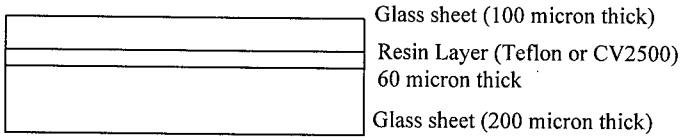

Fig. 1. Cross section of a toughened solar cell coverglass.

EXPERIMENTAL

The technique used to accelerate the particles is a laser driven flyer method as described by Roybal *et al.* [6]. A laser is used to vaporize the interface of a metal foil diffusively bonded to a glass substrate. The vapor reaches high pressures in the giga Pascal range and then cuts out and accelerates a metal disk the diameter of the periphery of the laser beam. Typical dimensions of flyers accelerated with this technique range from diameters of 500 microns to 3 mm with thickness of 3 to 25 microns. Velocities from 4.5 to 7.5 km/s have been achieved by the authors. Higher velocities are reported by Paisley *et al.* [7]. This method is suitable for accelerating small, flat particles to hypervelocity impacts with targets in a space environmental effects chamber. Flyer plate bonding techniques, and the effect of the quality of the laser beam profile on debris particle velocities are topics of interest considered in this paper.

The method used to fabricate the metal to glass laminate, used to create the debris particle, is critical to the particle acceleration technique. A tenacious bond is required to achieve the desired velocities. The bond must allow the highest possible pressure to be reached and the yield or "break loose" stress should be a function of the metal yield strength rather than the interface bond strength. Work to develop and improve the bonding method has continued over the duration of the laser driven flyer experiments. One of the most frequently experienced problems in fabricating a flyer laminate is the occurrence of trapped air bubbles between the glass and the metal foil. The main source of trapped air bubbles is gas adsorbed on the surfaces of the glass substrate and the metal foil. In earlier bonding procedures, the gas on the glass and metal interface surfaces was squeezed out during the bonding. To aid in the removal of the surface gas, the surface of the metal foil was slightly scored with a sanding process forming paths for the escape of the gas. For the most part, the sanding method works well. However, sanding of the metal surface does not completely prevent the trapping of air. When the ambient relative humidity is extremely low the occurrence of trapped air bubbles is more frequent. It has been suggested that a static charge is built up on the glass surface during times of low humidity. The static build up acts as a getter to increase the adsorption of gas on the glass surface and is believed to occur during the cleaning stage of the bonding method when a dry cloth is used to clean and polish the surface.

To remove the adsorbed gas from the glass and metal surfaces and minimize the formation of trapped air bubbles, the bonding process is now done in a vacuum chamber. Initially, the system was evacuated, the metal/glass laminate was heated to the required temperature, and the voltage applied across the laminate. Because the partial pressures of the trace gasses remaining in the vacuum chamber are low enough for ionization to occur, a current discharge occurred on the outer surface of the laminate. This as predicted by Paschen's Law, Llewellyn [8]. This ionization prevents the bonding method from working while under vacuum. To alleviate this problem, the metal /glass laminate is placed under vacuum, heated to the required temperature, and then slowly returned to ambient pressure. The voltage is applied across the laminate while it

is at ambient pressure. This method produces a very high percentage of tenacious bonds with a low appearance of trapped air bubbles.

A neodymium-glass, pulsed laser with energies ranging from 2 -5 joules with a 18 ns pulse was used in this work. The effect of laser beam profile in producing the desired particle acceleration is critical. Not only does the beam profile determine the shape of the flyer but it also determines the effectiveness of the beam coupling with the flyer material. A "flat top" profile is desirable in accelerating the metal flyers. Before obtaining the "flattop" beam profile, a somewhat Gaussian beam profile was used in an attempt to accelerate the particles. As shown in Figs. 2 and 3, "hot spots" existed in the beam profile and there was no sharp drop off in beam energy at the flyers' cross-section boundary. "Hot spots" are considered to be localized, high energy peaks in the beam cross-section.

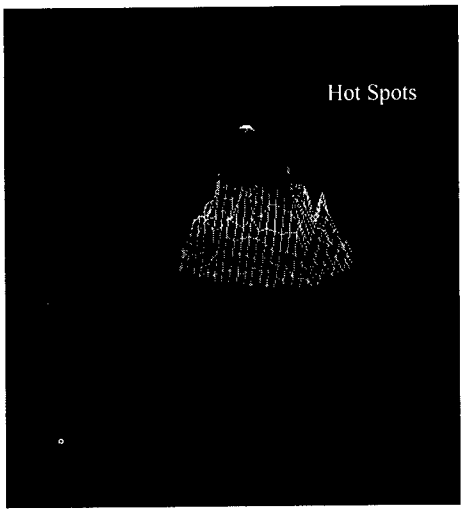

Fig. 2. 3D profile of a poor quality beam.

Fig. 3. Cross-section of a profile with "Hot Spots"

The effect of a poor beam profile is seen in Fig. 4. A beam profile with a tapered boundary causes the foil to pull away from the glass substrate in a way that allows the pressure of the vaporized metal to leak under the foil, reducing the effective use of the built up pressure. "Hot spots" in the beam may also couple with the glass substrate. The energy intensity of a "hot spot" can be orders of magnitude higher than the surrounding beam profile. This high intensity may easily exceed the damage threshold of the glass. A breakdown of the glass reduces the amount of energy that can couple with the metal foil. Another effect that is often seen when a non-uniform beam profile is produced, is the acceleration of a number of small particles producing a "shot gun" effect on the target rather than the described impact of a single, flat particle.

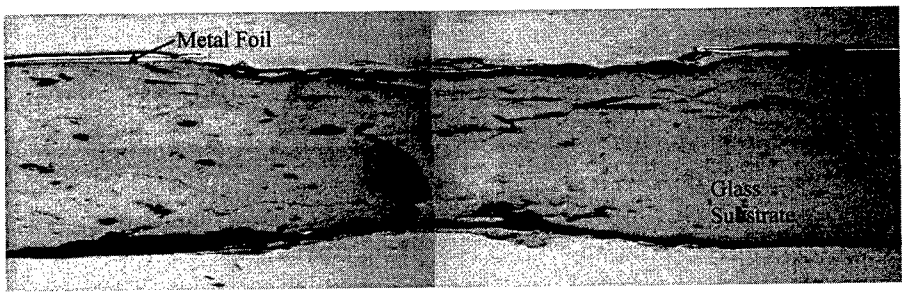

Fig. 4. Optical micrograph of a cross-section of the metal/glass laminate after particle acceleration with poor quality beam.

An optimum beam profile is required to transfer the maximum amount of laser energy into kinetic energy of the particle. The optimum profile for particle acceleration was determined to have a distinct energy step function at the boundary, producing the "flattop" appearance as in Fig.5. The beam profile must also have a uniformly distributed energy cross-section, as in Fig. 6.

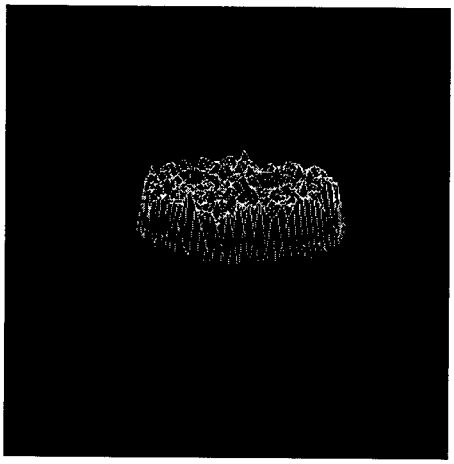

Fig. 5. 3D Beam profile of an acceptable beam.

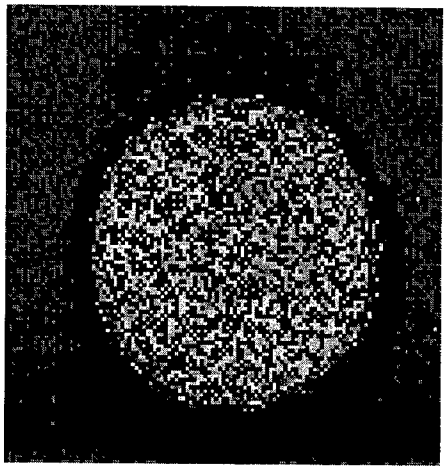

Fig. 6. Cross-section of an acceptable beam.

Figure 7 shows a 50X optical image of a cross-section of the metal foil/glass laminate after a particle has been accelerated from the surface with an optimized laser beam. The image shows that a disk was cut away from the original foil layer, leaving behind a rim of foil that was originally stretched away from the glass substrate and recoiled upon release of the disk. Except for the surface of the glass at the interface, the substrate is relatively free of damage.

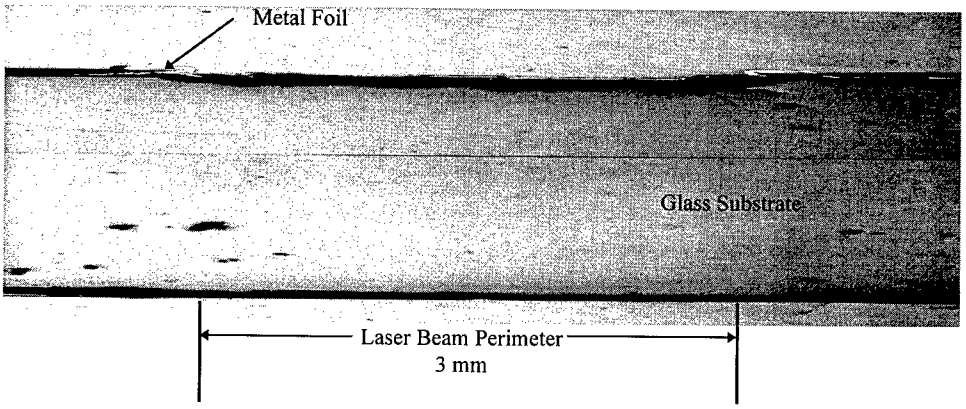

Fig. 7. 50X Cross-section of a metal /glass laminate after particle was accelerated with "flattop" beam.

Impact testing on the Pilkington coverglass has been completed using flat aluminum flyers 3mm in diameter and 3 microns thick. Work using this size particle was performed at Los Alamos National Labs. Further tests using smaller diameter particles are in progress at the Air Force Research Laboratory, Phillips site. The coverglass targets in the present work consist of two thin glass sheets laminated with a thin layer of Teflon or CV2500 resin. The glass varied in thicknesses, such that, laminates were fabricated with a combination of 100 and 200 micron thick glass, as well as with two layers of 300 micron thick glass. Target sample areas of solar

coverglass were 40mm by 40mm. The samples were placed in a small vacuum chamber during testing. In order to minimize the effect of air cushioning the flyer impact. A diagram of the experimental setup is shown in Fig. 8. The coverglass target was held in place with the same o-ring used to maintain vacuum. This mounting method avoids stresses introduced by a rigid fixed mount. The flyer traveled a distance of approximately 12 mm before impacting the target.

Velocity measurements of the flyer were made using a velocity interferometer system for any reflector (VISAR) manufactured by Valyn international, Barker and Hollenbach [9]. This technique uses an interferometer to measure a small Doppler shift in light frequency given to a beam of a "green light" from a diode laser as it is reflected from the moving flyer surface. The Doppler shift produces a number of light fringes in the interferometer proportional to the flyer velocity. Data reduction consists of counting the number of recorded light fringes produced in a given time and multiplying by a velocity-per-fringe constant of the interferometer to obtain a velocity. Since the solar cell coverglass target is transparent, velocity measurements of the flyer may be made through the target.

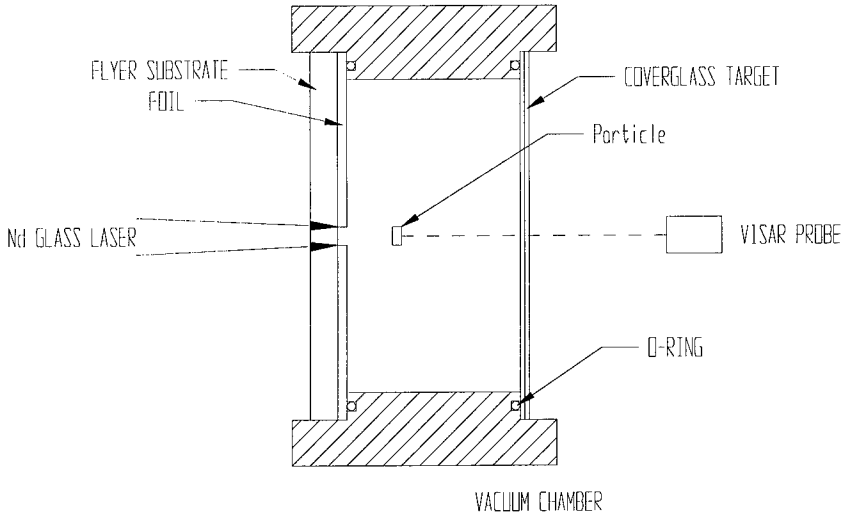

Fig. 8. Schematic of cross-section of experimental setup.

Only one impact was made per target. This was done to assess the amount of redeposited contamination attributed to ejecta from a single impact. The geometry and orientation of the flyer upon impact was determined by inspecting the shape of the impact crater. If a flyer impacted at an angle other than normal to the target, the crater produced would be non-symmetrical. The crater size should closely match the laser spot size if the flyer remained intact. Previous work employed a streak camera to characterize the flyers in flight, Roybal and Tlomak [10]. From this earlier work it was observed that the flyers remained intact and flew parallel to the target for the flight distance used in that experiment. Therefore we assumed another diagnostic for the monitoring integrity and orientation of the flyer is the intensity of the VISAR return signal. If the flyer maintains its' integrity and orientation the return signal is remains continuous.

RESULTS

The damage observed in these experiments included : front surface cratering, front and rear surface radial and concentric cracks, rear surface uplift and spall; and contamination in the form of vaporized material ejected from the crater, some of which redeposited on the front surface. The mechanical damage to the targets was characterized using optical and scanning electron microscopy. Inorder to avoid charging by the electron beam scanning electron imaging required that the sample be electrically conductive. Because the coverglass is made of nonconductive materials, we coated the surface of the sample with a thin layer of gold and palladium which was sputtered onto the target surface. Figure 9 shows a typical optical micrograph image of an impacted coverglass target in which

Fig. 9. 4X Optical image of a coverglass laminate.

the mechanical damage resulted from an impact at 4 km/s. Radial cracks extend from the impact crater to the edge of the 4 cm sample. The dashed circle in the image represents the size and impact location of the 3 mm flyer. Figure 10 is a typical SEM image of the rear surface of an impacted target and shows that some glass material has been removed from the rear surface. The predominant damage observed on the rear surfaces of targets was cracking and uplifting of the glass, however the glass remains attached to the laminate, similar to common safety glass. This effect is shown in the optical micrograph of Fig. 11.

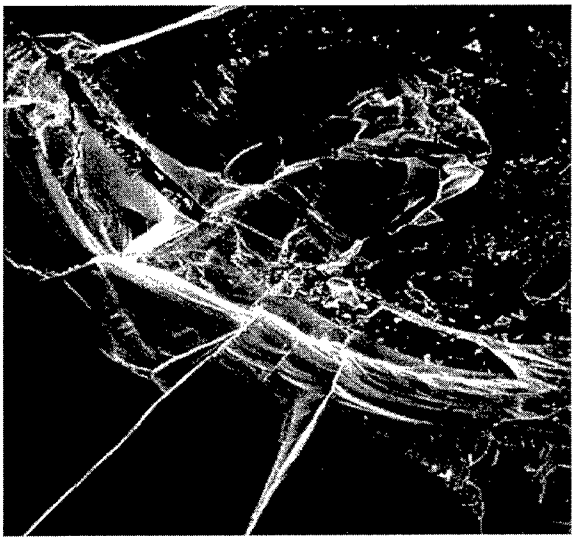

Fig. 10. 40 X Typical SEM image of rear surface of a coverglass laminate.

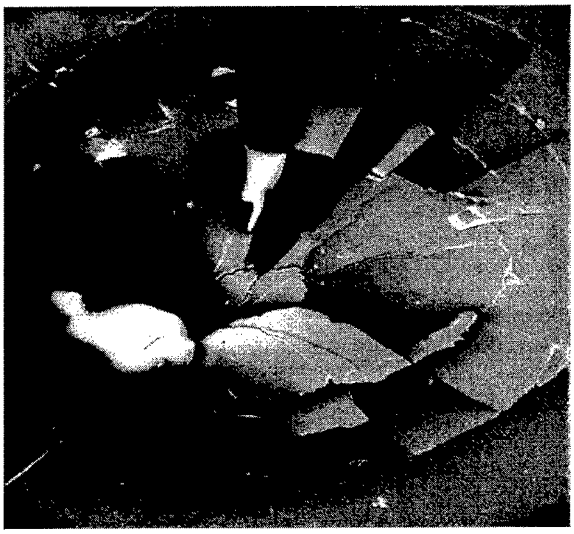

Fig. 11. 10X Optical image of a rear surface of a coverglass laminate.

Images of the cross section of coverglass targets were made and are shown in Figs. 12 and 13. Figure 12 represents an area away from the impact site. The laminate is intact but was slightly damaged from the cross-sectioning process. The layers of glass laminated to a 60 micron thick Teflon resin layer are clearly visible.

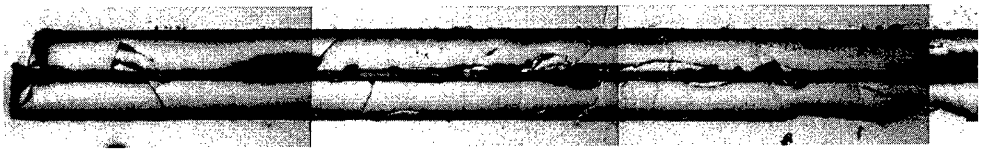

Fig. 12. Optical image of a cross section of a non-impacted laminate.

Figure 13 shows a typical image of the cross-section of an impacted cover glass laminate sample. The impacted side, as well as the surrounding areas, suffered extensive damage to all layers of the glass laminate. The damage included extensive cracking of the glass layers and permanent deformation primarily within the impact area. Upon impact, the aluminum particle formed a crater concave towards the impact direction. As a result, the glass on the impact side was extensively cracked but still remained attached to the deformed laminate. On the other hand, much of the cracked glass on the rear side of the impacted cover glass was uplifted and spalled off.

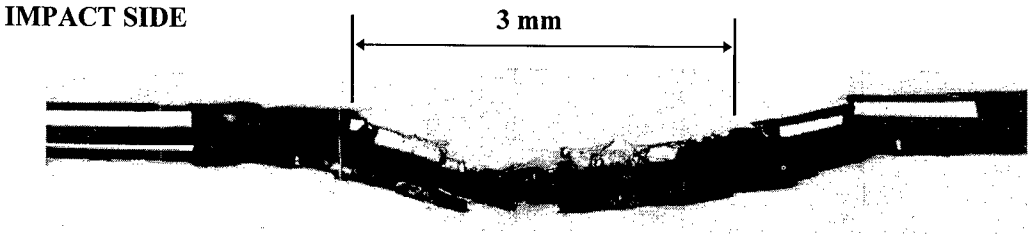

Fig. 13. Optical image of a cross section of an impact site on a coverglass laminate.

Contamination from the vapor blown out of the impact crater may actually be the most serious consequence of damage to the cover glass, when considering the overall efficiency of the solar cell. An interesting phenomena is seen when examining the deposition of ejecta from the impact crater onto the target surface. The ejected material forms bands of different material densities radiating out from the crater. Fig. 14 is a schematic diagram of the impacted sample shown in Fig. 9. Area (A) represents the size of particle impacting the surface. Region (B) is the crater area in which material has been removed from the target. While molten aluminum is found in Area (C). Aluminum is also found on the entire sample in the form of trace deposited vapor. Area (D) remained relatively free of re-deposition. While at a distance of over 1 cm from the impact site, area (E), the surface is heavily coated with the vapor removed from the crater.

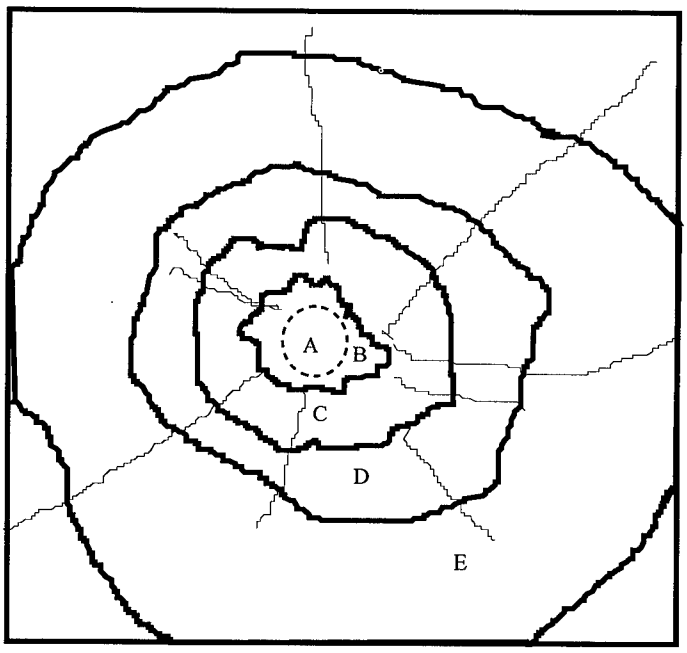

Fig. 14. Schematic of an impact area showing outlines of re-deposition regions.

An elemental analysis of the coverglass surface was completed using a PGT energy dispersive system attached to our scanning electron microscope, and produced the qualitative elemental analysis shown in Figs. 15, 16, and 17. Figure 15 shows a baseline spectra consisting predominantly of silicon and potassium for coverglass sample that has not been impacted. Figure 16 is an energy dispersive spectra of the impact crater, area (A). In the crater area much of the glass is removed revealing the resin layer below resulting in the presence of fluorine and carbon. An energy dispersive spectra in Fig. 17 was collected for area (E) on the coverglass.

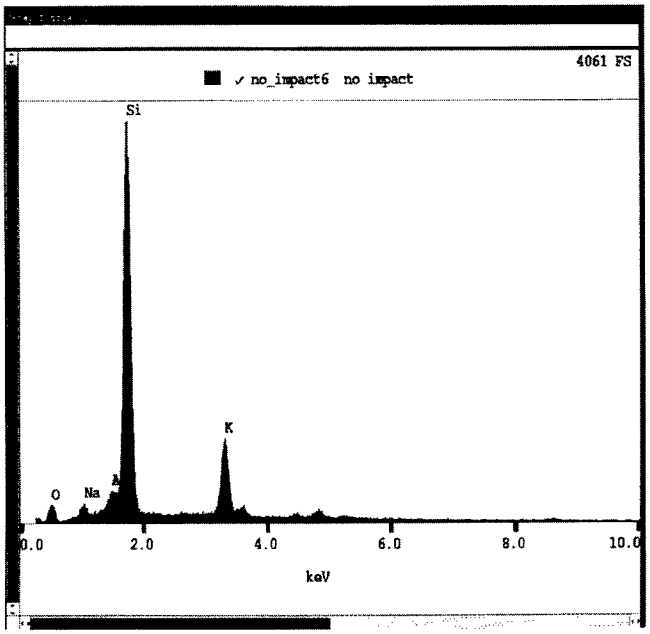

Fig. 15. Energy dispersive spectrum of a non impacted coverglass.

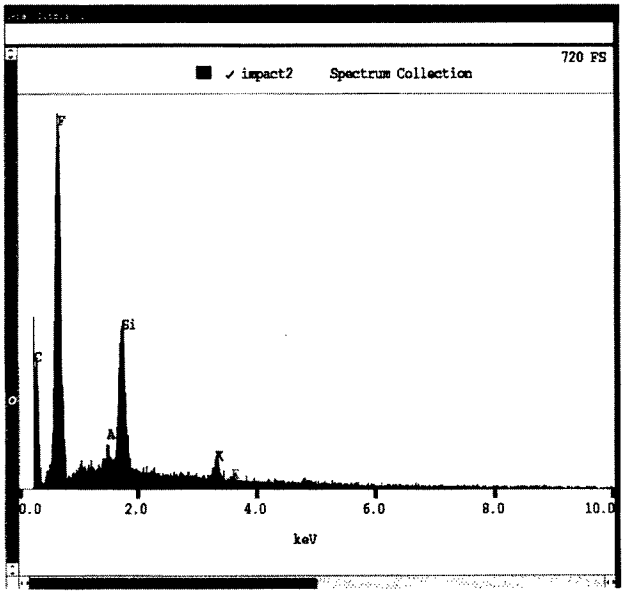

Fig. 16. Energy dispersive spectrum of the crater area (A) on an impacted coverglass.

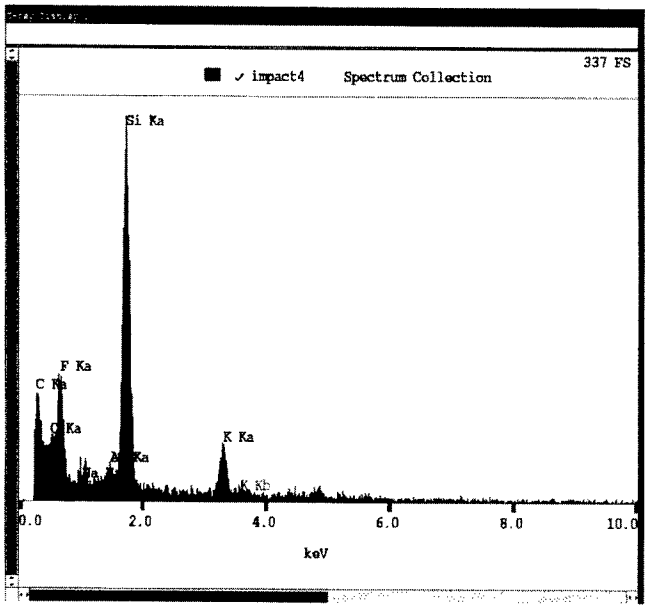

Fig. 17. Energy Dispersive spectrum of area (E) on an impacted coverglass.

The above spectra show that a deposition of fluorine, carbon, and aluminum is now present in regions of the once clean surface. The fluorine and carbon are generated from the vaporization and ejecta of the Teflon resin layer of the laminate. The pribable source of aluminum comes from vaporization of the aluminum flyer.

Light transmission measurements were over the wavelengths from 300 nanometers to 1500 nanometers made using a Cray 5ev Spectrophotometer through impacted targets and control samples. This wave length range covers the useful solar spectra for solar cells. Figure 18 compares transmission spectra of an undamaged control sample to transmission spectra measured in area (E) 1.6 cm from the crater of an impacted sample. These spectra show that a maximum transmittence of 90 percent exists at the wavelengths of interest in a control sample. While degradation in the original sample transmitance of approximately 10 percent was measured across area (E) of the impacted sample.

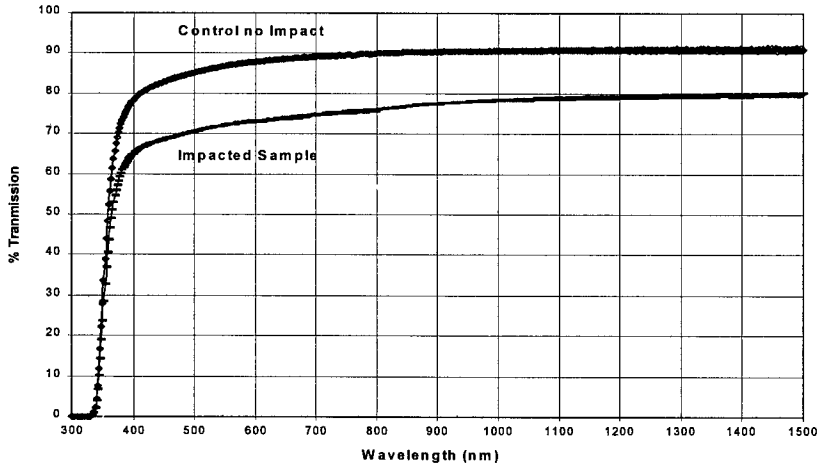

Fig. 18. Transmission spectra of UV light through a coverglass target pre and post impact.

DISCUSSION AND CONCLUSIONS

The results of our investigations revealed a very complex morphology at the damage site of the cover glass samples exposed to hypervelocity impacts by aluminum debris particles at velocities ranging between 2.5 km/s and 5.0 km/s. The range of velocities and energy used in these experiments are relatively small and were limited by the configuration of the laser used in this set of tests. As such, the data reported in this paper are not sufficient to establish a quantitative relationship between the debris' velocity, its kinetic energy and the size and geometry of the post impact damage sites. Nevertheless, the results of our semi-quantitative analyses clearly indicates that there is a typical damage pattern consisting of both mechanical damage and contamination. Formation of the impact crater is accompanied by the presence of molten aluminum and post impact deposition of contamination on the surface of the damaged cover glass sample. The ejecta consists not only of the cover glass laminate material removed from the crater, but some fragments of the aluminum debris particle as well. Over 90 percent of the 40 X 40 mm sample experienced at least a 10 percent loss in initial solar transmission. Degradation of the solar cell efficiency due to loss of solar transmittance may be more critical to the solar cell performance than the actual mechanical damage from impact. Results of our work presented in this paper are a part of our consistent and comprehensive effort to investigate the response of nonhomogeneous and composite materials to a very harsh space environment, including hypervelocity space debris impact damage.

REFERENCES

1. E. Schneider, Micrometeorite impact on solar panels. *Proceedings of the 5th European Symposium: 'Photovoltaic Generators in Space'*, Scheveningen, The Netherlands, 30 September (1986).
2. F. M. Rose, Hypervelocity impact on solar cells. *NASA Technical Report, NASA-CR-192444*, January (1993).
3. H. Dursch, Results from testing and analysis of solar cells flown on LDEF. *Proceedings of the LDEF Materials Workshop, Nasa Langley, Part 2*, pp 649-660, September (1992).
4. R. Crowther, V. Marsh, H. Stokes, R. Walker, Interaction Between Space Systems And The Orbital Environment, *SPIE Conference Proceedings,* Denver, August (1996).
5. C. A. Kitchen, A.A. Dollery, Kmullaney, K. Bogus, Teflon bonding of solar assemblies using Pilkington CMZ and CMG coverglass- Now a production process. *AIAA paper 94-3969*, pp. 257-262 (1994).
6. R. Roybal, J. Shively, C. Stein, C. Miglionico, Laboratory simulation of hypervelocity debris. *Proceedings of the 19th Space Simulation Conference, a NASA Conference Publication 3341*, Baltimore, MD, October 28 - 31 (1996).
7. D. L. Paisley, et. al., In *Ultra- and High-Speed Photography, Videography, Photonics, and Velocimetry, Proc. SPIE* Vol. **1346** ,pp. 172-178 (1990).
8. F. Llewellyn-Jones, Ionization and Breakdown in Gases ,pp 61, John Wiley & Sons, NY (1966).
9. L. M. Barker and R. E. Hollenbach, Laser interferometer for measuring high velocities of any reflecting surface, *J. Appl. Phys.* **43**, pp. 4669-4675 (1972).
10. R. Roybal, P. Tlomak, Hypervelocity space debris testing. *Proceedings of the AIAA Defense and Space Programs Conference*, Huntsville, AL, September 23-25 (1997).

PERGAMON International Journal of Impact Engineering 23 (1999) 823–834

INTERNATIONAL JOURNAL OF IMPACT ENGINEERING

www.elsevier.com/locate/ijimpeng

MODELLING OBLIQUE HYPERVELOCITY IMPACT PHENOMENA USING ELEMENTARY SHOCK PHYSICS

WILLIAM P. SCHONBERG* and AHMED R. EBRAHIM**

*Civil & Environmental Engineering Department, University of Alabama in Huntsville, Huntsville, AL 35899;
**Mechanical & Aerospace Engineering Department, University of Alabama in Huntsville, Huntsville, AL 35899

Summary—During their missions in space, spacecraft are subjected to high velocity impacts by orbital debris particles. Such impacts are expected to occur at non-normal incidence angles and can cause severe damage to the spacecraft as well as to its external flight-critical components. In order to ensure crew safety as well as the proper function of internal and external spacecraft systems, the characteristics of debris clouds generated by such impacts must be known. In this paper, a first-principles-based analytical model is developed for the characterization of the penetration and ricochet debris clouds created by the hypervelocity impact of a spherical projectile on a thin aluminum plate. This model employs normal and oblique shock wave theory to characterize the penetration and ricochet processes. The predictions of the model are compared against numerical and experimental results. © 1999 Elsevier Science Ltd. All rights reserved.

INTRODUCTION

All earth-orbiting spacecraft are susceptible to high-speed impacts by pieces of orbital debris. The impacts of these particles, which can occur at speeds as high as 12 to 14 km/s, can damage flight-critical systems and possibly lead to catastrophic failure of the spacecraft. Therefore, the design of a long duration earth-orbiting spacecraft must take into account the effects of such impacts and must contain protective systems to insure the safety of its occupants and operating systems.

Numerous investigations have been performed over the last 30 years to study the effectiveness of multi-wall structures in reducing the damage threat of high-speed particles. Dual-wall configurations were repeatedly shown through extensive testing and analysis to provide significant increases in protection against perforation by hypervelocity projectiles over equal-weight single-wall structures (see, e.g. [1-3]). However, in the vast majority of the tests performed, the shotline of the projectile was perpendicular to the test specimen, that is, most of the tests were performed under normal impact conditions.

Recent experimental investigations of high-speed impact phenomena have shown that the response of a dual-wall structure to an oblique impact is significantly different from its response to a normal impact (see, e.g. [4,5]). Unlike a normal impact, an oblique impact produces two, not one, inward travelling debris clouds. Additionally, an oblique impact can produce a tremendous amount of ricochet particles. If such an impact were to occur on orbit, these ricochet particles could severely damage external spacecraft instrumentation units. Obliquity effects, therefore, must also be considered in the design of a space structure that will be exposed to the orbital debris environment.

A wide variety of analytical models exist that predict the response of thin plates to normal impact loading. However, only a relatively small number of models have been developed for

0734-743X/99/$ - see front matter © 1999 Elsevier Science Ltd. All rights reserved.
PII: S0734-743X(99)00127-X

oblique impact. Many of these oblique impact models were developed for relative low impact velocities and, as such, are not applicable to the study of oblique hypervelocity impact phenomena. Schonberg and Yang [6] proposed a model of oblique impact response that characterized the mass and velocity quantities for the three debris clouds created in an oblique hypervelocity impact event. However, that model contained a significant number of empirical factors and was therefore limited in its applicability.

Figure 1 shows the oblique impact of a dual-wall structure by a spherical projectile. In such a system, the bumper protects the pressure wall by causing the disintegration of the impacting projectile and the creation of several debris clouds. Two of these debris clouds travel towards and eventually impact the pressure wall: these are the 'normal' and 'in-line' debris clouds. In Figure 1, m_1, m_2, and m_r are the masses of the normal, in-line, and ricochet debris clouds, respectively; the quantities θ_1, θ_2, and θ_r refer to the trajectories of their respective centers-of-mass. The quantities V_{ax1}, V_{ax2}, and V_{axr} are the axial velocities of the three debris clouds, and V_{ex1}, V_{ex2}, and V_{exr} are their expansion velocities. The quantities d_p, V_p, and θ_p are the diameter, velocity, and trajectory obliquity of the impacting projectile; t_b is the bumper thickness.

Thus, in the impact event shown in Figure 1, the number of unknowns to be determined to completely characterize the three debris clouds is twelve: three debris cloud masses, three axial velocities, three expansion velocities, and three center-of-mass trajectories. Conservation of mass, energy, and momentum (horizontal and vertical) provide four equations, far short of the twelve required. This paper presents a shock physics-based model that can be used to determine these twelve quantities. The model is a major improvement over that developed by Schonberg and Yang [6] in that its reliance on empirical equations and parameters is minimal. The validity of the model is assessed by comparing its predictions against numerical and experimental results for a wide range of trajectory obliquities.

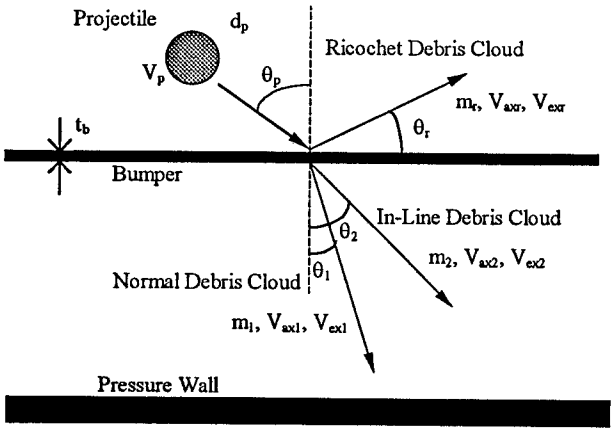

Fig. 1. Oblique high speed impact of a dual-wall structure.

SHOCK LOADING AND RELEASE DUE TO THE INITIAL IMPACT

Shock Loading Analysis

Consider the oblique hypervelocity impact of a projectile on a thin bumper plate. Upon impact, shock waves are set up in the projectile and bumper plate materials. In characterizing the shock loading and subsequent release of these materials, the shock waves are considered to be initially planar. This simplification allows one-dimensional relationships to be used for analyzing the creation and release of shock pressures. The shocked states of the projectile and bumper materials (i.e. the pressures, energies, densities, etc.) are determined the three one-dimensional shock-jump conditions, a linear relationship between the shock wave velocity and particle velocity in each material, and continuity of pressure and velocity at the projectile/bumper interface. As such, the shock loading process in oblique hypervelocity impact is presumed to be the same as that in a normal impact. The primary difference, of course, is that while the initially-planar wave fronts of the shock waves generated by a normal impact are parallel to the projectile/plate interface, in an oblique impact they make an angle with respect to that interface. For the purposes of this study, that angle is presumed to be equal to θ_p, the impact obliquity angle.

While the shock loading of a material is an irreversible process that results in an increase of the internal energy of the shocked material, the release of a shocked material occurs isentropically along an 'isentrope' or 'release adiabat'. The difference between the area under the isentrope and the energy of the shocked state is the amount of energy that remains in the material and can cause the material to melt or even vaporize. In order to calculate the release of the projectile and bumper materials from their respective shocked states, first-principles-based models typically employ either the Mie-Gruneisen or Tillotson equation-of-state to incrementally define the release adiabat. As will be seen in later sections, the mechanisms defining the penetration and ricochet processes in an oblique hypervelocity impact both require closed-form expressions for the respective release adiabats. To meet this need, approximate functional forms are developed in the following section for the isentropes along which the projectile and bumper materials are released from their shocked states following an oblique hypervelocity impact.

Release from Shock Loading

Since the release of the shocked projectile and bumper materials is due to the action of rarefaction waves created at a free surface or at a material interface, we consider the general case of the oblique incidence of a shock wave at an interface between two dissimilar materials (see Figure 2). In this figure, U_{s1} is the speed of a shock wave that encounters the interface between two dissimilar materials A and B. The angle between the incident wave front and the interface is labeled by θ and is a known quantity. The ambient conditions in material A ahead of the shock wave are identified by mass density ρ_0^A, particle velocity u_{p0}, pressure p_0, and internal energy E_0. Behind the shock wave, the shocked material properties are the mass density ρ_1, particle velocity u_{p1}, pressure p_1, and internal energy E_1. As a result of the interaction between the incident shock wave and the interface, part of the energy is reflected as a wave that travels back into material A, and part is transmitted as a shock wave that travels into material B.

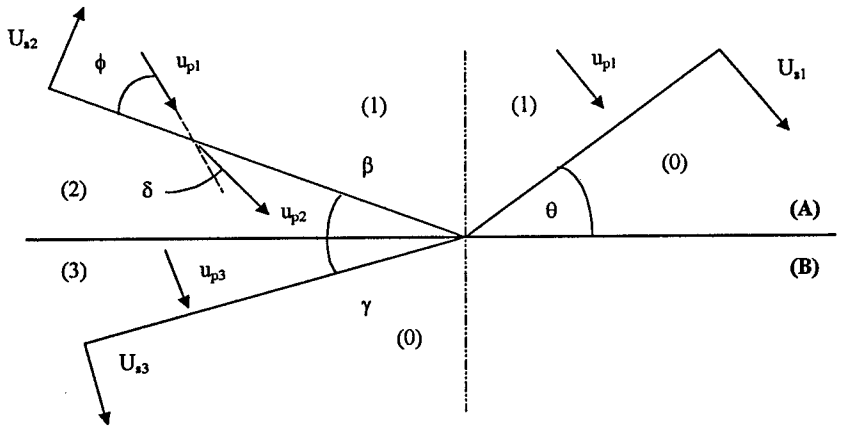

Fig. 2. Oblique incidence of a shock wave at an interface between two dissimilar materials

In Figure 2, the material state behind the reflected wave is represented by "2" subscript. Ahead the reflected wave, the direction of the particle velocity makes an angle ϕ with respect to the wave front and is deflected by an angle δ behind it. The transmitted shock wave moves into the undisturbed material B whose state is represented by "0" subscript. The shocked state behind this wave is identified with "3" subscript. We note that the angles β and γ at which the newly generated reflected and transmitted waves go off from the interface, respectively, are different from the angle at which the incident shock wave strikes the interface. Once the quantities in Figure 2 with a "1", "2", and "3" subscript, as well as the angles ϕ, β, δ, and γ, are obtained, the release adiabat for a material shocked by the passing of an oblique shock wave is found as follows.

One of the basic precepts of oblique shock wave theory states that only the normal components of material particle velocity ahead of and behind an obliquely incident shock or rarefaction wave are affected by the wave's passing [7]. Using this concept, we see from Figure 2 that the particle velocity component that is affected by the passing of the reflected wave U_{s2} is $u_{p1}\sin\phi$. Therefore, the release of material A from its shocked state will start from a point in u_p-p space having the coordinates ($u_{p1}\sin\phi$, p_1). Graphical representations of the curves required for obtaining a release adiabat in case of an oblique hypervelocity impact are shown in Figure 3.

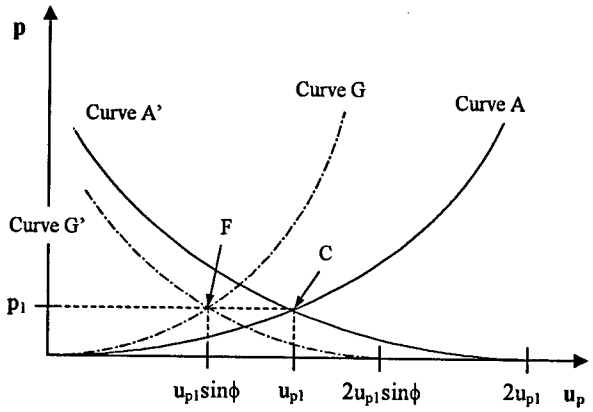

Fig. 3. Graphical construction of release adiabat for an oblique shock wave

In Figure 3, Point C(u_{p1}, p_1) and Point F($u_{p1}\sin\phi$, p_1) define, respectively, the shocked states of a material following the passage of normal and oblique shock waves travelling at speed U_{s1}. Curve A (on which lies point C) represents the principle Hugoniot for the material, while Curve A' is a mirror image of Curve A about Point C. As such, Curve A' represents the release of the material from the initial shocked state as defined by Point C, i.e. due to a normal shock wave (see also [8]). We define Curve G to be the 'modified principle Hugoniot curve' for the same material except that it passes through the 'modified shocked state' represented by Point F. Maintaining the analogy between the case of a normal shock wave and an oblique shock wave, we construct the release adiabat corresponding to Curve G and passing through Point F by reflecting Curve G about a vertical line through Point F. In this fashion, Curve G' represents the release of a material from a shocked state as defined by Point F, i.e. due to an oblique shock wave.

Knowing that Curve G' passes through the points ($u_{p1}\sin\phi$, p_1) and ($2u_{p1}\sin\phi$, 0) allows us to obtain a functional form for Curve G' in the u_p-p plane. Since the functional form for Curves A and G is quadratic, we also write the representation for Curve G' as a quadratic with unknown coefficients. These coefficients are found by substituting the coordinates of the known points into the quadratic equation for Curve G'.

PENETRATION PROCESS MECHANISMS

In this section we develop an shock-physics-based model to calculate the velocities and trajectories of the normal and in-line debris clouds created in an oblique high-speed impact of a spherical projectile on a thin plate. The model to be developed consists of two mechanisms. In the first, referred to as the Single Transmitted Wave mechanism, two new waves are created following the impingement of a shock wave on the bumper rear free surface: a rarefaction wave that is reflected back into the shocked bumper material and a shock wave that is transmitted into the space behind the bumper. The properties of this transmitted wave in effect characterize a "combined" penetration debris cloud.

In the second mechanism, referred to as the Double Transmitted Wave mechanism, three new waves are created: a rarefaction wave that is reflected back into the shocked bumper material and two transmitted shock waves. One of these transmitted waves will correspond to the in-line debris cloud and the other to the normal debris cloud. Although the development of the second mechanism is clearly of primary interest, the first mechanism will be developed first to render the development of the second mechanism more analytically tractable.

Single Transmitted Wave Mechanism

The wave configurations for this mechanism are shown in Figure 2. If we let materials A and B represent the bumper material and the "material" occupying the space behind the bumper, applying conservation of mass, momentum, and energy across each wave front in Figure 3 results in the following sets of equations. First, across the incident shock wave U_{s1}:

$$\rho_0^A U_{s1} = \rho_1 (U_{s1} - u_{p1}) , \qquad p_1 = \rho_0^A U_{s1} u_{p1} \tag{1,2}$$

$$E_1 = U_{s1} u_{p1} - \frac{1}{2} u_{p1}^2 - \frac{p_1}{\rho_1}, \qquad U_{s1} = c_0^A + k^A u_{p1} \tag{3,4}$$

Across the reflected wave U_{s2}:

$$\rho_1 (U_{s2} + u_{p1} \sin\phi) = \rho_2 [U_{s2} + u_{p2} \sin(\phi - \delta)] \tag{5}$$

$$p_2 - p_1 = \rho_1 (U_{s2} + u_{p1} \sin\phi)[u_{p1} \sin\phi - u_{p2} \sin(\phi - \delta)] \tag{6}$$

$$E_2 - E_1 = \frac{1}{2}(u_{p1} \sin\phi)^2 - \frac{1}{2}[u_{p2} \sin(\phi - \delta)]^2 + U_{s2}[u_{p1} \sin\phi - u_{p2} \sin(\phi - \delta)] + \frac{p_1}{\rho_1} - \frac{p_2}{\rho_2} \tag{7}$$

Continuity of the tangential particle velocity is written as follows:

$$u_{p1} \cos\phi = u_{p2} \cos(\phi - \delta) \tag{8}$$

Across the transmitted shock wave U_{s3}, the governing equations are identical to equations (1-4), with 'B' replacing 'A' and '3' replacing '1'. The boundary conditions at the plate free rear surface are continuity of pressure and particle velocity.

In equations (1-8), p_1 is known – it is the Hugoniot impact pressure. Equations (1), (2), and (4) are then used to solve explicitly for u_{p1} and ρ_1. This completely defines the shocked state of the bumper material behind the initial shock wave. The next step is to determine the state of the material following the passage of waves U_{s2} and U_{s3}. This is accomplished using equations (5-8) and invoking the boundary conditions at the interface. This results in the following system of four equations in six unknowns, i.e., u_{p2}, U_{s2}, p_2, ρ_2, β and γ:

$$\rho_1 [U_{s2} + u_{p1} \sin(90 - \theta - \beta)] = \rho_2 [U_{s2} + u_{p2} \sin(90 - \beta - \gamma)] \tag{9}$$

$$p_2 - p_1 = \rho_1 [U_{s2} + u_{p1} \sin(90 - \theta - \beta)][u_{p1} \sin(90 - \theta - \beta) - u_{p2} \sin(90 - \beta - \gamma)] \tag{10}$$

$$u_{p1} \cos(90 - \theta - \beta) = u_{p2} \cos(90 - \beta - \gamma) \tag{11}$$

$$p_2 = \rho_0^B (c_0^B + k^B u_{p2}) u_{p2} \tag{12}$$

Two additional equations are required to render these equations solvable for the unknowns. One of these equations is that of the reflected Hugoniot which characterizes the release of the bumper material from its shocked state, which has the following functional form:

$$p_2 = \frac{\rho_0^A (c_0^A + k^A u_{p1})}{\sin\phi} \left[2 - \frac{u_{p2} \sin(\phi - \delta)}{u_{p1} \sin\phi} \right] u_{p2} \sin(\phi - \delta) \tag{13}$$

The second equation is obtained by assuming a Snell's law type of relationship between the angles at which the new waves emerge from the bumper rear free surface:

$$\frac{\sin\beta}{U_{s2}} = \frac{\sin\gamma}{U_{s3}} \tag{14}$$

These six non-linear equations are solved using the second-order Newton-Raphson method. Once these six unknowns have been determined, the remaining quantities are readily obtained.

We note that the formulation presented thus far assumes that material B is a real material. In an actual spacecraft multi-wall system, the medium surrounding the bumper is a vacuum. In this case, if we take $\rho_0^B = 0, c_0^B = 0,$ and $k^B = 1.0$, the particle velocity u_{p3} represents the rear free surface velocity of the plate, that is, $u_{fs} = u_p$. Also, the internal energy of the transmitted wave is denoted by $E_{trans} = E_3$. This internal energy will be used in the solution for the leading edge velocities and center-of-mass trajectories of the normal and in-line debris clouds in the Double Transmitted Wave mechanism.

Double Transmitted Wave Mechanism

The wave configuration for this mechanism is shown in Figure 4. The governing equations relating the states ahead and behind waves U_{s1}, U_{s2}, and U_{s3} are identical to those presented in the preceding section. The equations for wave U_{s4} are very similar to those for U_{s1}, with some changes in variables as required.

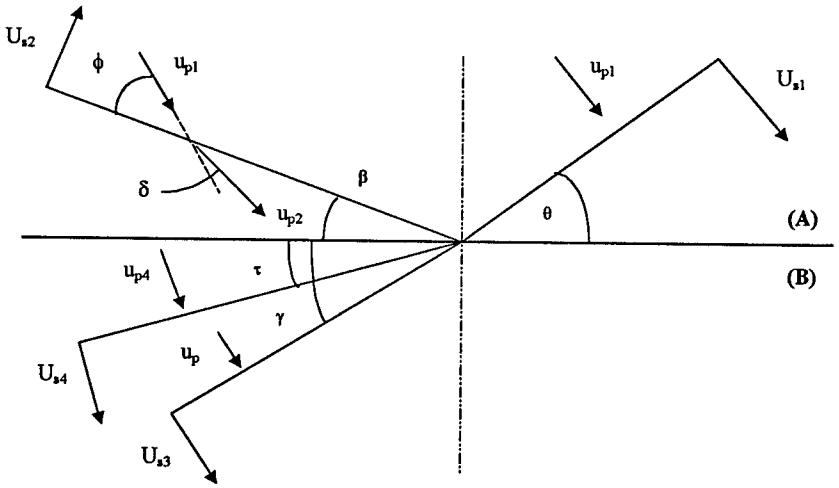

Fig. 4. Oblique incidence of a shock wave at an interface between two dissimilar materials, double transmitted wave mechanism, unsteady coordinate system.

The boundary conditions at the interface between material A and material B are continuity of pressure, normal particle velocity, and tangential particle velocity written as follows:

$$p_2 = \kappa_1(p_3 + p_4) \tag{15}$$

$$u_{p2}\sin(\theta+\delta) = \kappa_2(u_{p3}\sin\gamma + u_{p4}\sin\tau) \quad , \quad u_{p2}\cos(\theta+\delta) = \kappa_2(u_{p3}\cos\gamma + u_{p4}\cos\tau) \tag{16,17}$$

where κ_1 and κ_2 are constants that represent the contributions to the pressure and the particle velocity, respectively, at the interface by the two shocked states within material B. The values of these constants are determined such that the predicted values of the normal and in-line debris

cloud center-of mass trajectories compare well with experimental data. Following the same procedure as in the case of the Single Transmitted Wave mechanism, we obtain a system of eight equations which, when taken together with the boundary conditions as written in equations (15-17), are solved simultaneously for the twelve unknowns (i.e. u_{p2}, u_{p3}, u_{p4}, U_{s2}, p_2, p_3, p_4, ρ_2, β, γ, τ, and δ) that characterize the various states of materials A and B.

One more equation is needed to make the solution for the unknowns possible. This equation is obtained by equating the internal energy associated with the transmitted shock wave in a Single Transmitted Wave mechanism to the sum of the internal energies associated with the two transmitted shock waves in the Double Transmitted Wave mechanism. This system of equations unknowns is solved using the second-order Newton-Raphson iteration method. In the particular case of material B being vacuum, the calculated particle velocities $u_{p4} = V_{1e1}$ and $u_{p3} = V_{1e2}$, are the bumper rear free surface velocities that correspond to the leading edge velocities of the normal and in-line debris clouds, respectively. Moreover, the angles $\tau = \theta_1$ and $\gamma = \theta_2$ correspond to the trajectory angles of the normal and in-line debris clouds' centers-of-mass, respectively.

RICHOCHET PROCESS MECHANISM

In modeling a high-speed normal impact, since the initial shock wave front is parallel to the bumper surfaces, the interaction between this shock wave and the bumper upper free surface is typically ignored. However, in an oblique impact, the shock wave front is inclined with respect to the bumper upper free surface and the interaction cannot be ignored. This interaction generates a rarefaction wave that is reflected back into the bumper material, and a shock wave that is transmitted into the medium above the bumper.

The wave configurations for this mechanism are shown in Figure 5. In this figure, the interface is between the bumper material and the medium above it, referred to as material C, and U_{s1} is the shock wave generated by the initial impact. At the point of encounter O, a rarefaction wave U_{s5} is reflected back into the shocked bumper material while a shock wave U_{s6} is transmitted into material C which in an ambient condition. Behind the rarefaction wave, the state of the bumper material is identified with "5" subscript, while the state of material C after the passage of the transmitted shock wave is labeled with "6" subscript.

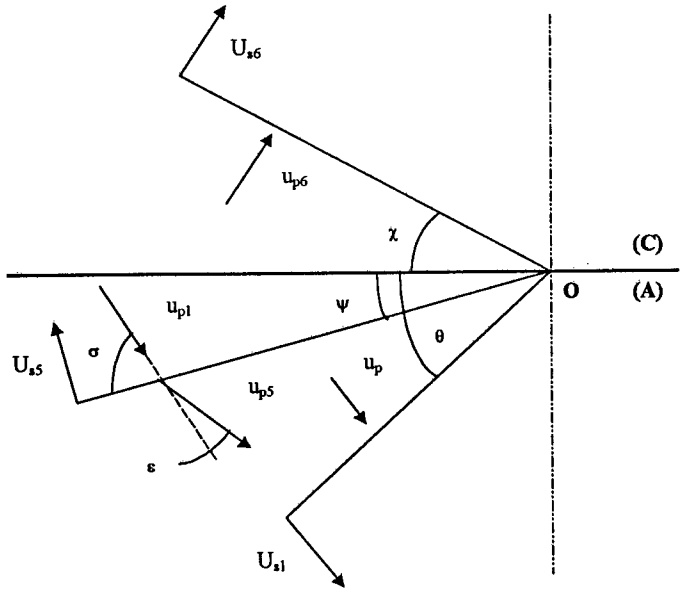

Fig. 5. Wave configurations for ricochet mechanism, unsteady coordinate system.

The conservation equations governing the relation between material state ahead and behind shock wave U_{s1} are given by equations (1-4) while those for U_{s5} are very similar to equations (5-8) with the appropriate changes in variables as required. The equations for the transmitted shock wave U_{s6} are similar to those for U_{s1}, also with some changes in the variables as required. The interaction between the three shock waves and the plate upper surface is regulated by the boundary conditions at the interface, which are again continuity of pressure (i.e. $p_5=p_6$), and normal and tangential particle velocities:

$$u_{p5}\cos(\sigma-\varepsilon-\psi)=u_{p6}\cos(90-\chi), \qquad u_{p5}\sin(\sigma-\varepsilon-\psi)=u_{p6}\sin(90-\chi) \tag{19a,b}$$

Following the same procedure used previously results in a of six non-linear equations in six unknowns, namely, u_{p5}, U_{s5}, p_5, ρ_5, ψ and χ. This system of equations is solved for the unknowns using the second-order Newton-Raphson iteration method. Once the solution is obtained, the parameters associated with the passage of shock wave U_{s6} are readily obtained. In the particular case of the medium above the plate being a vacuum, the particle velocity at the interface $u_{p6} = V_{ler}$ represents the free surface velocity of the bumper upper free surface and the leading edge velocity of ricochet debris cloud. Moreover, the angle that denotes the trajectory of the center of mass of ricochet debris cloud is given by $\theta_r = 90-\chi$.

CHARACTERIZATION OF DEBRIS CLOUDS IN OBLIQUE IMPACT

In this section we present a semi-analytical model for determining the remaining nine unknown quantities (i.e. the masses, axial velocities, and expansion velocities). In this model, the leading edge velocities of the three debris clouds (V_{le1}, V_{le2}, and V_{ler}) are known quantities as obtained using elementary shock physics solutions.

Debris Clouds Masses

Mass conservation before and after the impact of the projectile on the bumper plate yields the following expression:

$$m_p + m_b = m_1 + m_2 + m_r \tag{20}$$

where m_p and m_b are the masses of the impacting projectile and the bumper hole out material. Since the mass m_r of the ricochet debris cloud consists of projectile and bumper material, we write

$$m_r = P_{rp}\, m_p + P_{rb}\, m_b \tag{21}$$

where P_{rp} and P_{rb} are the percentages of projectile and bumper particles that ricochet away from and penetrate through the bumper, respectively. These percentages were determined from a regression analysis of data obtained from a series of SPH runs simulating the high speed oblique impact of a spherical aluminum projectile on thin aluminum plates. These runs were performed for a wide variety of impact velocities, trajectory obliquities, and projectile diameters [9]. The following empirical equations for P_{rp} and P_{rb} were obtained:

$$P_{rp} = 0.137 d_p^{-0.116} e^{5.164\theta_p} V_p^{-0.142} \quad , \quad P_{rp} = 67.01 d_p^{-0.479} e^{2.058\theta_p} V_p^{+0.390} \tag{22,23}$$

where d_p is measured in cm, θ_p in radians, and V_p in km/s. The correlation coefficients R^2 for equations (22) and (23) are 0.989 and 0.963, respectively, which indicate a good fit to the data. Now that m_r is defined, m_1 and m_2 are obtained as follows.

It has been hypothesized that the material in the normal debris cloud is primarily bumper plate material, while the material in the in-line debris cloud is primarily projectile material [10]. Using

this hypothesis and substituting equation (21) into (20) yields the following relations for the normal and in-line debris cloud masses, respectively:

$$m_1 = (1-P_{rb})m_b \quad , \quad m_2 = (1-P_{rp})m_p \tag{24,25}$$

This completes the calculation of the masses of the three debris clouds generated in an oblique impact, leaving six remaining unknowns to be determined.

Debris Clouds Characteristic Velocities

The characteristic velocities of interest in an oblique hypervelocity impact include the axial and expansion velocities for each debris cloud. As in [11], we presume the following relationships among the leading edge velocity, axial velocity, and expansion velocity, for each debris cloud:

$$V_{le1} = V_{ax1} + V_{ex1} \quad , \quad V_{le2} = V_{ax2} + V_{ex2} \; , \quad V_{ler} = V_{axr} + V_{exr} \tag{26a-c}$$

Conserving energy before and after the initial impact of the projectile on the bumper plate and ignoring the energy lost in the light flash:

$$\frac{1}{2}m_p V_p^2 = \frac{1}{2}m_1\left(V_{ax1}^2 + V_{ex1}^2\right) + \frac{1}{2}m_2\left(V_{ax2}^2 + V_{ex2}^2\right) + \frac{1}{2}m_r\left(V_{axr}^2 + V_{exr}^2\right) + m_p E_{lost}^{proj} + m_b E_{lost}^{bmpr} \tag{27}$$

where E_{lost}^{proj} and E_{lost}^{bmpr} are the amounts of specific energy lost in the projectile and bumper materials due to shock heating. Applying conservation of momentum before and after the initial impact of the projectile on the bumper plate, the following two equations are obtained:

$$\eta m_p v_0 \cos\theta = m_1 v_{ax1} \cos\theta_1 + m_2 v_{ax2} \cos\theta_2 - m_r v_{axr} \sin\theta_r \tag{28}$$

$$\varsigma\, m_p v_0 \sin\theta = m_1 v_{ax1} \sin\theta_1 + m_2 v_{ax2} \sin\theta_2 + m_r v_{axr} \cos\theta_r \tag{29}$$

where η and ζ are adjustment factors introduced to account for momentum due to back splash and any momentum transferred to the bumper plate. Since this adds two more unknowns to the system of equations, two additional equations are required. These equations are obtained by relating debris cloud velocities to spread angles for the normal and in-line debris clouds, namely:

$$\frac{V_{le1} - V_{ax1}}{V_{ax1}} = \tan\left(\frac{\gamma_1}{2}\right) \quad , \quad \frac{V_{le2} - V_{ax2}}{V_{ax2}} = \tan\left(\frac{\gamma_2}{2}\right) \tag{30,31}$$

where γ_1 and γ_2 are the cone angles for the normal and in-line debris clouds, respectively. For aluminum-on-aluminum impacts, the empirical equations for γ_1 and γ_2 have the following forms:

$$\frac{\gamma_1}{\theta_p} = 0.417\left(\frac{V_p}{c_b}\right)^{0.228} \cos^{0.225}\theta_p \left(\frac{t_b}{d_p}\right)^{-0.491} \quad , \quad \frac{\gamma_2}{\theta_p} = 2.539\left(\frac{V_p}{c_b}\right)^{1.217} \cos^{2.972}\theta_p \left(\frac{t_b}{d_p}\right)^{0.296} \tag{32,33}$$

where c_b is the speed of sound in the bumper material. These equations were obtained through a multiple linear regression analysis of test data [5]; their correlation coefficients are 0.738 and 0.925, respectively.

Since the leading edge velocities are known, equations (27-31) together with equations (26a-c), constitute a system of 5 equations in 5 unknowns, namely, V_{ax1}, V_{ax2}, V_{axr}, η, and ζ. The solution of this system for the unknowns is again carried out using the second-order Newton-Raphson

iteration method. Having determined the axial velocities of the three debris clouds, their expansion velocities can be determined by substituting the axial velocities values into equations (26a-c). This completes the development of the model characterizing the three debris clouds created in an oblique hypervelocity impact of a spherical projectile on a flat plate.

COMPARISON WITH EXPERIMENTAL AND NUMERICAL RESULTS

The predictions of the model developed herein are compared against the predictions of empirically-based regression equations [5], the predictions of regression equations based on hydrocode results, and high speed impact test data. These comparisons are presented in Figures 6-8 for the center-of-mass trajectories of the normal, in-line and ricochet debris clouds, respectively, for the case of a spherical projectile with a 0.475 cm diameter impacting a 0.20 cm thick plate at a speed of 6 km/s at angles of obliquity between 45 and 75 degrees. Table 1 shows the values of the adjustment factors η and ζ for the obliquity angles considered herein.

Table 1. Adjustment factor values

θ_P (deg)	45	50	55	60	65	70	75
η	0.115	0.258	0.404	0.537	0.648	0.739	0.843
ζ	1.59	1.50	1.42	1.35	1.308	1.308	1.349

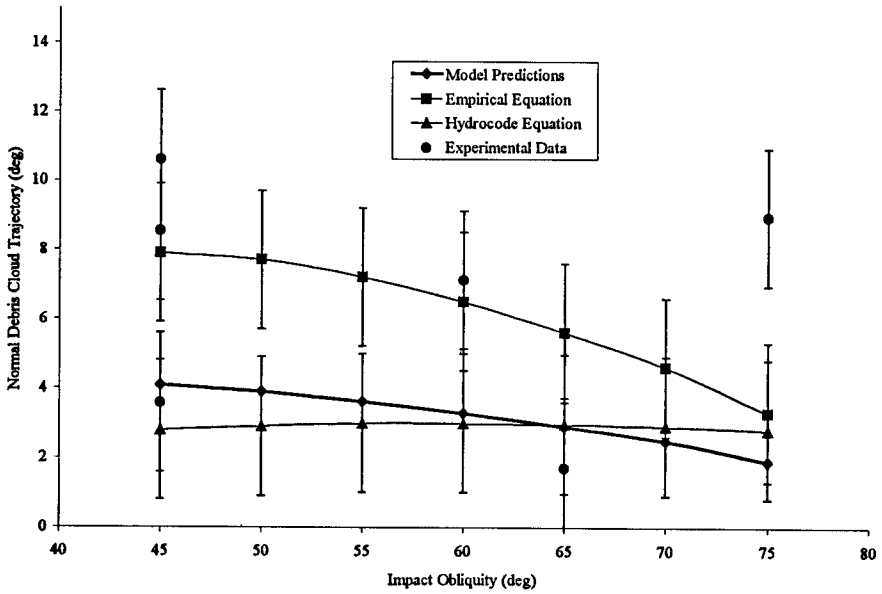

Fig. 6. Comparison of model predictions with experimental and hydrocode results for θ_1.

The hydrocode-based regression equations for θ_1, θ_2, and θ_r were derived through a multiple regression analysis of oblique hypervelocity impact simulation results obtained using the SPH hydrocode for a variety of impact velocities, trajectory obliquities, and projectile diameters (see again [9]).

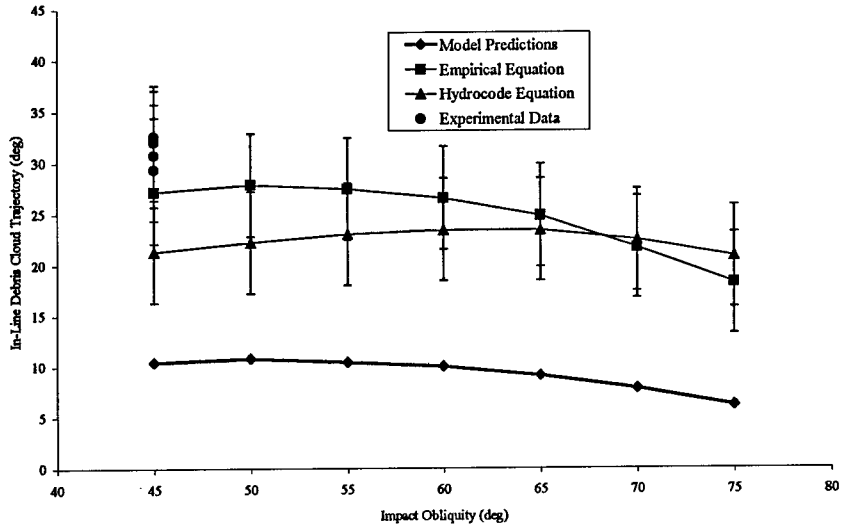

Fig. 7. Comparison of model predictions with experimental and hydrocode results for θ_2.

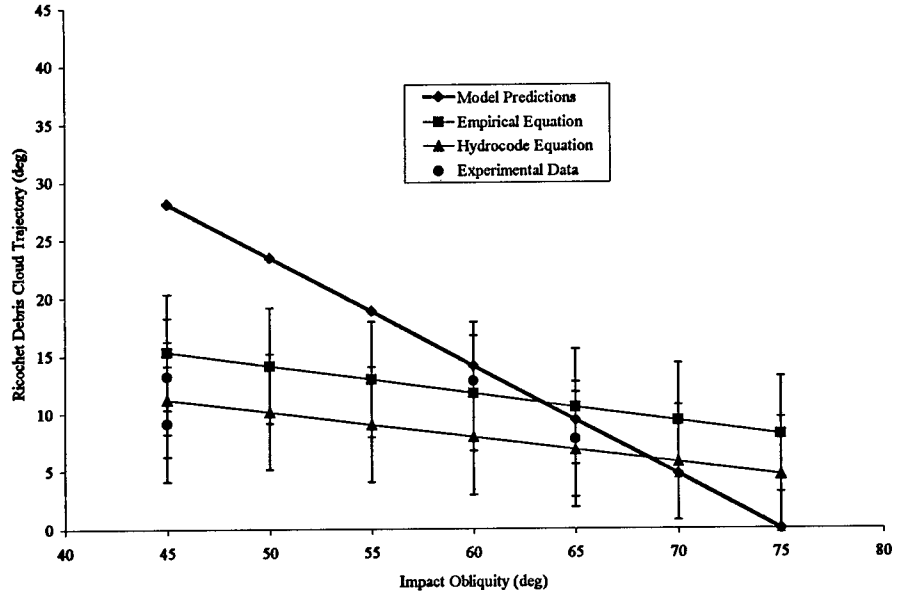

Fig. 8. Comparison of model predictions with experimental and hydrocode results for θ_r.

It is clear from Figures 6-8 that the model and the regression equations show similar trends in predicting the normal, in-line, and ricochet debris clouds center-of-mass trajectories as functions of the impact obliquity angle. The agreement between model predictions and the predictions of the hydrocode and experimental regression equations is best for θ_1 and least for θ_2; the agreement for θ_r becomes reasonable when the impact angle exceeds 60 degrees. It is also interesting to note that the model prediction trend for θ_2 in Figure 7 exhibits a peak near $\theta_p = 60$ degrees. This behavior in θ_2 as a function of θ_p was previously observed from an analysis of experimental debris cloud trajectory data [4].

Comparing the values obtained from the empirically-based regression equations with those obtained from the model, it is seen that the former gives higher values of θ_1 and θ_2, and a lower value of θ_r than those obtained from the model predictions. This can be due to the fact that at the impact velocity considered, the material in the debris clouds is not completely molten and includes some solid particles. As a result, shear waves are generated and the debris cloud particles experience a component of lateral motion larger than that if it were completely fluid [12]. This in turn increases angles of emergence θ_1 and θ_2 and decreases θr. However, the model formulation assumed that the material behaves as a fluid in which no shear waves are generated at the bumper free surfaces. As a result, the model predictions of θ_1 and θ_2 will be less than the experimental results, while the predictions of θ_r will typically exceed the experimental results.

SUMMARY

In this paper, a new first principles-based analytical model for the characterization of the penetration and ricochet debris clouds created in an oblique hypervelocity impact has been developed. Debris cloud masses, characteristic velocities, and trajectories were found by applying conservation equations before and after the impact event, the results of elementary shock physics analysis, and several regression equations. The model predictions of the center-of-mass trajectories of the normal, in-line, and ricochet debris clouds were compared against the experimental and hydrocode results. While the trends predicted by the model compared favorably with the experimental results, there were some discrepancies in the actual values of the various center-of-mass trajectories. A possible reason for the discrepancies is the assumption of pure hydrodynamic behavior in the model development.

Acknowledgement—The authors are grateful for the support provided by the Civil and Environmental Engineering and the Mechanical and Aerospace Engineering Departments at the University of Alabama in Huntsville. The authors are also grateful to the NASA/Marshall Space Flight Center for providing the SPH results and the experimental data that made part of this investigation possible.

REFERENCES

1. A.R. Coronado, M.N. Gibbins, M.A. Wright and P.H. Stern, Space station integrated wall design and penetration damage control. *Final Report NAS8-36426*, Boeing Aerospace Company, Report No. D180-30550-1, Seattle, Washington (1987).
2. A.K. Hopkins, T.W. Lee, and H.F. Swift, Material phase transformation effects upon performance of spaced bumper systems. *J. Spacecraft and Rockets*, 9(5), 342-345 (1972).
3. W.P. Schonberg and R.A. Taylor, Exterior spacecraft subsystem protective shielding analysis and design. *J. Spacecraft and Rockets*, 27(3), 267-274 (1990).
4. W.P. Schonberg, Penetration and ricochet phenomena in oblique hypervelocity impact. *AIAA Journal*, 27(5), 639-646 (1989).
5. W.P. Schonberg, Hypervelocity impact penetration phenomena in aluminum space structures. *J. Aerospace Engineering*, 3(3), 173-185 (1990).
6. W.P. Schonberg and F. Yang, Response of space structures to orbital debris particle impact. *Int. J. Impact Engng.*, 14, 647-658, (1993).
7. B.K. Hodge and K. Koenig, *Compressible Fluid Dynamics with Personal Computer Applications.* Prentice-Hall, New Jersey (1995).
8. W.C. Moss, Using the Hugoniot to approximate the release adiabat. In *Shock Waves in Condensed Matter*, pp. 157-163, Plenum Press, New York (1986).
9. A.R. Ebrahim, *Modeling the Oblique Hypervelocity Impact of Orbital Debris Particles on Spacecraft Structures Using Elementary Shock Physics.* PhD Dissertation, University of Alabama in Huntsville, June (1998).
10. G.T. Burch, Multi-plate damage study. *AFATL-TR-67-116*, Eglin Air Force Base, Florida (1967).
11. A.J. Piekutowski, Debris clouds generated by hypervelocity impact of cylindrical projectiles with thin aluminum plates. *Int. J. Impact Engng.* 5, 509-518 (1987).
12. J.S. Rinehart, Transient stress wave boundary interactions. In *Stress Waves in Anelastic Solids*, (edited by H. Kolsky and J. Prager), pp.193-206, IUTAM Press (1963).

PERGAMON International Journal of Impact Engineering 23 (1999) 835–846

INTERNATIONAL JOURNAL OF IMPACT ENGINEERING

www.elsevier.com/locate/ijimpeng

ANALYTICAL HOLE DIAMETER AND CRACK LENGTH MODELS FOR MULTI-WALL SYSTEMS UNDER HYPERVELOCITY PROJECTILE IMPACT

WILLIAM P. SCHONBERG* and ESSAM MOHAMED**

*Civil & Environmental Engineering Department. University of Alabama in Huntsville, Huntsville, AL 35899;
**Mechanical & Aerospace Engineering Department, University of Alabama in Huntsville, Huntsville, AL 35899

Summary—All long-duration spacecraft in low-earth-orbit are subject to high-speed impacts by meteoroids and orbital debris. In the event of a perforation, the pressure wall of a dual-wall structure impacted by a high-speed particle can also experience cracking and petaling. If such cracking were to occur on-orbit, unstable crack growth could develop which could lead to an unzipping of the impacted spacecraft module. This paper presents a summary of the development of a first-principles-based crack length and hole size model for a spacecraft module pressure wall that has been perforated in an orbital debris particle impact. Predictions of the crack length model are compared with experimental data. Modifications to the model that are required to bring its predictions in closer agreement with the experimental results are then presented and discussed. © 1999 Elsevier Science Ltd. All rights reserved.

INTRODUCTION

All long-duration spacecraft in low-earth-orbit are subject to high speed impacts by meteoroids and orbital debris. As a result, the threat of damage from such high speed impacts has become a significant design consideration in the development and construction of long duration earth-orbiting spacecraft. Historically, significant amounts of resources have been devoted to developing shielding for such structures as a means of reducing the penetration potential of high speed on-orbit impacts. Many studies have concluded that the level of protection afforded a spacecraft by a multi-wall structure significantly exceeds the protection level provided by an equal weight single wall of the same material. These studies have typically focused on simply whether or not the inner (or 'pressure') walls of candidate multi-wall structural systems would be perforated. The extent of pressure wall damage following a penetration has only recently begun to be explored (see, e.g. [1,2]).

In addition to a hole, the pressure wall of a multi-wall structure impacted by a high speed particle can also experience cracking and petaling [3-5]. If such cracking were to occur on-orbit, unstable crack growth could develop which could lead to an unzipping of the impacted module [6]. Thus, it is imperative to be able to characterize the cracking phenomena associated with the penetration of multi-wall systems used in long-duration earth-orbiting spacecraft, such as the International Space Station (ISS).

This paper presents the results of a study whose objective was to develop an analytical, first-principles-based model of hole diameter and maximum tip-to-tip crack length for a spacecraft module pressure wall that has been perforated in an orbital debris particle impact. These models can be incorporated directly into a survivability analysis (see, e.g. [7]) to determine whether or not module unzipping would occur under a specific set of impact conditions. The prediction of hole diameter can also be used as part of a survivability analysis to determine the time available for module evacuation prior to the onset of incapacitation due to air loss.

0734-743X/99/$ - see front matter © 1999 Elsevier Science Ltd. All rights reserved.
PII: S0734-743X(99)00128-1

The analytical hole diameter and crack length models presented herein are developed by sequentially characterizing the phenomena comprising the orbital debris impact event. These phenomena include the initial impact, the creation and motion of a debris cloud within a multi-wall system, the impact of the debris cloud on the pressure wall, pressure wall deformation prior to crack formation, pressure wall crack initiation, propagation and arrest, and finally, pressure wall deformation following crack initiation and growth. We note that the analytical treatment presented herein considers only normal impacts on the multi-wall structure.

Two types of multi-wall systems were considered in this study: a Whipple-type system and an enhanced shielding system. In both cases, the outer wall or 'bumper' protects the module and its inhabitants by disrupting impacting particles. The difference between the two wall systems is that in a standard Whipple system, the inner wall is a multi-layer thermal insulation (MLI) blanket, while in an enhanced system, the inner wall consists of several layers of Kevlar and Nextel cloth added to an MLI blanket (see Fig. 1).

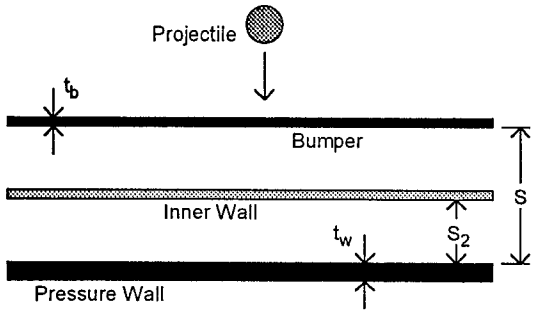

Fig. 1. Hypervelocity impact of a generic multi-wall system.

Following a summary of the shock loading and release analysis used to characterize the state of the debris cloud created by the initial impact on the bumper, the modeling of the debris cloud motion in the multi-wall system is presented and discussed. The form of the pressure wall loading function is then developed, followed by the pressure wall deformation model. Predictions of the crack length model are compared with empirical data. Model adjustments that are required to bring its predictions in closer agreement with the data are then discussed.

INITIAL IMPACT SHOCK LOADING AND RELEASE MODELING

Consider the normal hypervelocity impact of a projectile on a thin plate (e.g. the bumper of the multi-wall system shown in Fig. 1). Upon impact, shock waves are set up in the projectile and bumper materials. In calculating the shock loading and subsequent release of the projectile and bumper materials, the shock waves are considered to be initially planar. This simplification allows one-dimensional relationships to be used for analyzing the creation and release of shock pressures. The shock pressures, energies, etc., in the projectile and bumper materials are calculated using the three 1-D shock-jump conditions, a linear relationship between the shock wave velocity and particle velocity in each material, and continuity of pressure and velocity at the projectile/bumper interface. In this manner, the shocked states of the projectile and bumper materials due to the initial impact are completely defined.

While the shock loading of a material is an irreversible process that results in an increase of the internal energy of the shocked material, the release of a shocked material occurs isentropically along an 'isentrope' or 'release adiabat'. The difference between the area under the isentrope and the energy of the shocked state is the amount of residual energy that remains in the material and can cause the material to melt or even vaporize. In order to calculate the release of the projectile and bumper materials from their respective shocked states, an appropriate equation-of-state is needed for each material. To keep the analysis relatively simple, the Mie-Gruneisen equation-of-state [8] was used in this study.

DEBRIS CLOUD CHARACTERIZATIONS

Following the impact of the projectile on the bumper, a debris cloud is created that travels towards and eventually impacts the inner bumper of the multi-wall system. This in turn creates another debris cloud that travels towards and eventually impacts the pressure wall. These debris clouds area referred to as the "primary" and "secondary" debris clouds, respectively. This section is concerned with calculating the masses and velocities of these debris clouds. .

Primary Debris Cloud Mass Content, Distribution, and Characteristic Velocities

The mass of the primary debris cloud consists of the original impacting projectile mass plus the mass of the removed bumper material. No mass is considered lost to backsplash of the bumper and projectile materials; hence, since all of the mass is presumed to be directed in towards the pressure wall, the model to be developed should yield conservative results. The contribution of the bumper material to the primary debris cloud mass can be determined once the bumper hole diameter is known. This diameter can be calculated using any empirical equation for hole diameter in a thin plate due to a high speed impact (see, e.g. [9]).

X-ray photographs of debris clouds created by hypervelocity impacts of spherical and cylindrical projectiles on thin metallic plates have shown that the primary debris cloud material is not uniformly distributed throughout the debris cloud; rather, the projectile material is typically nested within a hollow shell containing bumper material. Therefore, for the purposes of this study, the bumper material was assumed to be contained in a hollow spherical shell while the projectile material was assumed to be contained within a solid spherical mass. In addition, the leading edge of the projectile material coincided with the leading edge of the spherical shell containing the bumper material.

The four characteristic velocities of interest for the primary debris cloud are the axial and expansion velocities of the projectile and bumper material debris cloud components. These velocities are obtained using a technique similar to one used in a study in which similar velocity quantities were required [10]. This method is based on conservation of momentum and energy before and after the impact event. Conservation of momentum provides the following equation:

$$m_p V_p = m_p V_{ax,p} + m_b V_{ax,b} \tag{1}$$

where V_p is the impact velocity, m_p and m_b are the projectile and bumper hole-out masses, respectively, and $V_{ax,p}$ and $V_{ax,b}$ are the axial velocities of the projectile and bumper material components of the primary debris cloud, respectively. Because the initial impact occurs at such a high velocity, momentum transfer to the bumper itself is ignored. Furthermore, again because of the rapidity of the impact event, the only significant energy losses are to the accompanying light flash and the shock heating of the bumper and projectile materials. If we neglect the energy associated with the light flash, and assume constant axial and expansion velocities, then the energy balance is written as follows:

$$\frac{1}{2}m_p V_p^2 = \frac{1}{2}m_p V_{ax,p}^2 + \frac{1}{2}m_p V_{exp,p}^2 + \frac{1}{2}m_b V_{ax,b}^2 + \frac{1}{2}m_b V_{exp,b}^2 + E_{sr,p}m_p + E_{sr,b}m_b \tag{2}$$

where $V_{exp,p}$ and $V_{exp,b}$ are the expansion velocities of the projectile and bumper material components of the primary debris cloud, respectively, and $E_{sr,p}$ and $E_{sr,b}$ are the waste heats per unit mass produced by the shock heating and release of the projectile and bumper hole-out materials, respectively. By neglecting energy losses such as those due to light flash, and by assuming constant axial and expansion velocities, the results obtained herein should also be conservative in nature.

Since the leading edge of the projectile component has been assumed to be coincident with that of the bumper material component, the leading edge velocities of the two debris cloud components must be equal. As in [10], we postulate that the leading edge velocity is the sum of the axial and expansion velocities for each of the material components. This provides us with the following two additional equations:

$$V_{ax,p} + V_{exp,p} = V_{le} \ , \qquad V_{ax,b} + V_{exp,b} = V_{le} \tag{3a,b}$$

However, the leading edge velocity is itself an unknown, and so while the number of equations available is now four, the number of unknowns has risen to five. The fifth and final equation is provided by assuming that the ratio of the expansion velocities of the two debris cloud components is inversely proportional to their masses:

$$\frac{V_{exp,p}}{V_{exp,b}} = \frac{m_b}{m_p} \tag{4}$$

Equations (1-4) are manipulated to yield the following equation for the leading edge velocity:

$$AV_{le}^2 + BV_{le} + C = 0 \tag{5}$$

where

$$A = \frac{1}{4}(m_p + m_b)\left(\frac{m_b}{m_p} + \frac{m_p}{m_b}\right) \ , \qquad B = -\frac{1}{2} m_p V_p \left(\frac{m_b}{m_p} + \frac{m_p}{m_b}\right) \tag{6a,b}$$

$$C = E_{sr,t} + \frac{1}{4} m_p V_p^2 \left(\frac{m_p}{m_b} - 1\right) \ , \qquad E_{sr,t} = E_{sr,p} m_p + E_{sr,b} m_b \tag{7a,b}$$

Once Eqn. (5) is solved for V_{le}, axial and expansion velocities are readily obtained.

Secondary Debris Cloud Mass Content, Distribution, and Characteristic Velocities

The characterization of the secondary debris cloud mass content is very similar to that of the primary debris cloud with the exception that it also includes the mass of the removed inner wall material. As before, no mass is considered lost to backsplash of the inner wall and primary debris cloud materials. The contribution of the inner wall material to the secondary debris cloud mass can be determined once the inner bumper hole diameter is known. This quantity is taken to be given by the diameter of the projectile material component of the primary debris cloud as it passes through the plane defining the position of the inner wall.

The distribution of the mass within the secondary debris cloud is analogous to that assumed for the primary debris cloud: a solid sphere of projectile material is surrounded by a hollow sphere of bumper and inner wall materials. In order to maintain a parallel with the discussion concerning the primary debris cloud, the bumper and inner wall materials in the spherical shell are hereafter referred to as 'bumper material'.

The axial and expansion velocities of the projectile and bumper components of the secondary debris cloud are calculated in a manner very similar to that used for the primary debris cloud. In fact, it is found that the equations are identical with the exception that the inner wall hole out mass must be added to that of the bumper hole out mass wherever the bumper hole out mass term appears in the original set of equations. That is, wherever there appears in equations (1-7) the quantity m_b, it is simply replaced by the quantity m_b+m_{ib}, where m_{ib} is the inner bumper hole-out mass. In this manner, the solution of equations (1-4) using the modified bumper mass term yields the five velocity quantities that characterize the motion of the secondary debris cloud.

PRESSURE WALL LOADING FUNCTION

The function defining the load on the pressure wall due to the impact of the debris cloud was developed to possess the following characteristics.

- The primary debris cloud delivers the load to the pressure wall at time t=0; the load due to the bumper material begins a short time later.
- The duration of each component load is defined as the time between the first contact of the debris cloud leading edge on the pressure wall and the time when the debris cloud trailing edge passes through the plane defining original pressure wall position.
- The combined load of the two debris cloud components at a given instant of time is given simply as the sum of the individual component loads at that instant of time.
- The pressure wall area over which the load of each debris cloud component is applied is assumed to be circular and of constant radius.
- The footprint area radius for each debris cloud component is the projection of the sphere defining each component on the pressure wall at the time of first contact with the pressure wall.

Based on these characteristics, the pressure wall loading function takes the following form:

$$p(r,t) = p_{op}R_p(r)[H(r) - H(r - R_{wp})]T_p(t)[H(t) - H(t - t_{dp})] + p_{ob}R_b(r)[H(r) - H(r - R_{wb})]T_b(t)[H(t - t_1) - H(t - t_1 - t_{dp})] \quad (8)$$

where $R_p(r)$ and $R_b(r)$ are dimensionless functions characterizing the pressure wall load area radii of the projectile and bumper material components of the debris cloud, $T_p(t)$ and $T_b(t)$ are dimensionless functions characterizing the position of each debris cloud component, p_{op} and p_{ob} are the relative maximum magnitudes of the two debris cloud component loadings, H(*) is the Heavyside Function, and t_1 is the time delay between the impact of the projectile and bumper material components of the primary debris cloud.

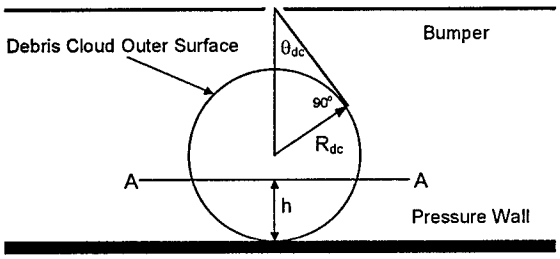

Fig. 2a. Debris cloud arrival at pressure wall upper surface.

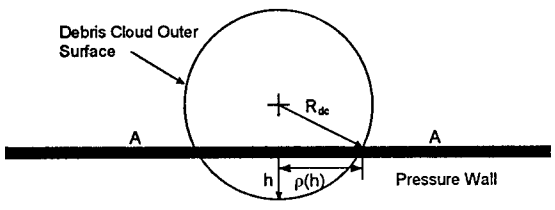

Fig. 2b. Debris cloud having moved through pressure wall plane a distance 'h'.

Figure 2a shows a debris cloud component just at the instant of its impact on the pressure wall, while Fig. 3b shows the position of the same debris cloud component at a short time later when Section A-A of the debris cloud, which was at a height 'h' above the pressure wall plane, arrives at the pressure wall. In Fig. 2b, ρ(h) is the actual radius of the debris cloud footprint area at that instant in time.

Since the pressure wall areas over which the debris cloud component loads are applied are assumed to be constant, the dimensionless functions $R_p(r)$ and $R_b(r)$ must each be equal to unity. The functions $T_p(t)$ and $T_b(t)$ are found by using the variation in ρ(h) for each debris cloud component as a measure of the fraction of each debris cloud that has passed through the plane defining the original undeformed position of the pressure wall. For each

debris cloud component, the function $\rho(h)$ is normalized by R_{dc}, the debris cloud radius at the instant of impact on the pressure wall, to keep each T(t) function non-dimensional. Thus, in generic form, we can write for each T(t) function the following expression:

$$T_i(t) = \left(\frac{\rho_i[h_i(t)]}{R_{dci}} \right)^2 \quad , \quad i = b \text{ or } p \tag{9}$$

The expression in Eqn. (9) is squared to avoid the complications that arise when a radical is used in subsequent calculations. The geometry shown in Figures 2a,b can be used to readily obtain expressions for each R_{dc} and $\rho(h)$.

The expression for h(t) is found by using a linear interpolation between a debris cloud's leading edge and the trailing edge velocities, $V_{ax}+V_{exp}$ and $V_{ax}-V_{exp}$, respectively, together with the assumption that the progress of the portion of the debris cloud that has not yet struck the pressure wall is not impeded by the portion of the debris cloud that has.

The constants p_{op} and p_{ob} are found by conserving axial momentum for each debris cloud component before and after the impact of the particular component on the pressure wall. This conservation equation is written as follows:

$$(m_b + m_{ib})V_{ax,b} + m_p V_{ax,p} = \pi p_{ob} R_{wb}^2 I_b + \pi p_{op} R_{wp}^2 I_p \tag{10}$$

where R_{wb} and R_{wp} are the radii of the bumper and projectile component load area footprints on the pressure wall,

$$I_p = \frac{1}{\alpha_p}\left(2 - \frac{1}{\alpha_p}\right)t_{dp} - 2\left(\frac{\gamma_p}{\alpha_p}\right)\left(1 - \frac{1}{\alpha_p}\right)\ln\left(1 + \frac{t_{dp}}{\gamma_p}\right) - \frac{1}{\alpha_p^2}\left(\frac{t_{dp}\gamma_p}{t_{dp} + \gamma_p}\right) \tag{11}$$

$$\alpha_p = \frac{V_{exp,p}}{V_{ax,p} + V_{exp,p}} \quad , \quad \gamma_p = \frac{2R_{dcp}}{V_{exp,p}} \tag{12,13}$$

and t_{db} and t_{dp} are the impact durations for the bumper and projectile components of the debris cloud, respectively. The expression for I_b is the same as that for I_p, but with 'b' replacing 'p' in Eqns. (11-13). We note that Eqn. (10) is but one equation in two unknowns. A second equation relating p_{ob} and p_{op} is obtained by assuming that the peak pressure delivered by each component is proportional to its axial momentum:

$$\frac{p_{op}}{p_{ob}} = \frac{m_p V_{ax,p}}{(m_b + m_{ib})V_{ax,b}} \tag{14}$$

Equations (10) and (14) now yield the required solution for p_{ob} and p_{op}.

Finally, the impact duration for each debris cloud component is obtained by noting that when the debris cloud trailing edge passes through the plane defining the original position of the pressure wall, i.e., when $h=2R_{dc}$.

PRESSURE WALL DEFORMATION

Pressure wall deformation is presumed to begin the instant the debris cloud leading edge strikes the pressure wall. The model developed herein contains the following features:

- pressure wall movement prior to the onset of fracture;
- a family of radial cracks initiating at the center of impact on the pressure wall and their subsequent propagation;
- petalling of the pressure wall between adjacent cracks following propagation; and,
- calculation of maximum tip-to-tip crack length and equivalent hole diameter.

In modeling the response of the pressure wall to the impact loading of the debris cloud, the following assumptions were used to render the model analytically tractable:

- pressure wall deformation is modeled as that of a fully clamped circular plate;
- the pressure wall is made of a rigidly plastic material;
- the pressure wall material is controlled by the Tresca yield condition and its associated flow rule;
- the pressure wall starts to yield at time t=0 (elastic deformations are negligible);
- the pressure wall thickness is small enough to allow the use of thin plate theory; and,
- the thickness of the pressure wall varies linearly from a minimum value at the impact footprint area center to a maximum value at the outer perimeter of the footprint area.

The "thinning" of the pressure wall material within the impact footprint area is included to account for the erosion of the pressure wall by the many grinding impacts of the many debris cloud particles. The expression defining the linearly varying thickness of the pressure wall is stated as follows:

$$h(r) = h_o\left[\frac{r}{r^*} + \varepsilon\left(1 - \frac{r}{r^*}\right)\right] \tag{15}$$

where r^* is the radius of the pressure wall affected by the impact of the debris cloud (i.e. either R_{wp} or R_{wb}), $h_o=t_w$ is the nominal thickness of the pressure wall beyond r^*, and ε is the ratio of the thinnest pressure wall thickness value (i.e. at r=0) to its nominal thickness value. The pressure wall deformation model is presented as a sequence of discrete stages which when taken together form a complete pressure wall response model.

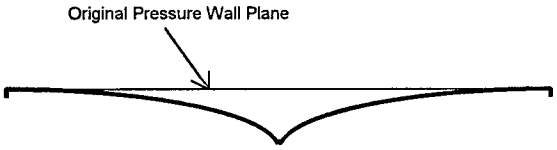

Fig. 3. Pressure wall deformation due to impulsive loading.

Stage 1: Pressure Wall Deformation Prior to Crack Initiation

Prior to crack initiation, the pressure wall deformation is that of a plastic clamped circular plate under a uniform impulsive loading (see Fig. 3). The deformation of such a plate under this type of loading is obtained using the procedure in [11-13]. In this procedure, expressions for the velocity of the plate center and the location of the plastic hinge must be determined. The location of the plastic hinge depends on the magnitude of the applied load [11,12]. Since our problem is concerned with very high loads, and because the load due to the impact of the bumper component is expected to be spread out over a larger area than that due to the projectile component, it is reasonable to assume that the plastic hinge occurs at $r_1 = R_{wb}$.

In obtaining an expression for velocity of the plate center, we must consider several possibilities. First, crack initiation may occur during the application of the debris cloud loads. Second, crack initiation may occur after the debris cloud loads have ended. Based on these possibilities, velocity expressions are needed while a load is being applied as well as after the applied load has been removed. Naturally, the possibility that the motion of the plate will cease without a crack ever having been formed must be considered as well. The process by which we obtain expressions for moments, velocities, and displacements is one in which the governing equation of motion for a clamped rigid-plastic circular plate is solved under the Tresca Yield Condition and its associated flow rule.

Of interest is the definition of r_1 in the case of pressure wall deformation following load removal. Previous studies have all found that the variation of r_1 during this plate deformation phase is very small (i.e. on the order of 2%-4%) and can be neglected [11-14]. Hence, for the purposes of this study, r_1 in this phase is kept constant at its previous value, that is, $r_1 = R_{wb}$.

Stage 2: Dynamic Crack Propagation and Crack Arrest

In the event that the pressure wall has ruptured at the center of the impact footprint area, the model proceeds with the analysis of the propagating cracks (see Figure 4). In the analysis of these cracks, it is presumed that they propagate at speeds far greater than that of the deforming pressure wall. Hence, the creation and growth of these cracks does not significantly affect any subsequent motion of the pressure wall and vice versa. The crack propagation and arrest calculations are performed using the theoretical development presented in [15-17] where the governing equation for Mode I crack propagation under elasto-plastodynamic conditions is based on a relationship between the instantaneous dynamic stress intensity factor, the static stress intensity factor, and the material's dynamic resistance to crack propagation. In this development, all of the resulting cracks are presumed to be equal in length. Hence, the maximum tip-to-tip crack length is simply calculated as twice the final calculated length of any given crack.

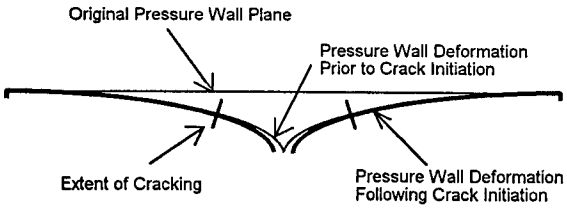

Fig. 4. Pressure wall deformation following crack initiation.

Stage 3: Pressure Wall Petalling Deformation

Following the creation of cracks in the pressure wall, the nature of the deformation of the pressure wall changes dramatically. The portion of the pressure wall beyond the cracks continues to deform plastically. However, the pressure wall material between two adjacent cracks begins to petal (see Figure 5). The shape of the pressure wall petals is determined using the theoretical development in [18] which presents a means to calculate the large deformation of a cantilever beam as the free end of the beam experiences curling. However, whereas the method in [18] assumes a cantilever beam with a constant-width and constant depth rectangular cross-section, pressure wall petals are typically triangular when viewed from the top or bottom. The sharpness of the petal tips at the point of crack formation resulted in singularities that, unfortunately, could not be avoided. An alternative approach was developed by Walker, *et al.* [19] to obtain an impulse-deflection relationship for a petal without a sharp tip at the free end. Therefore, in order to be able to use the method in [18], each petal was modeled as a constant-width and constant-depth cantilever beam with average depth and width properties based on actual petal cross-section and width properties

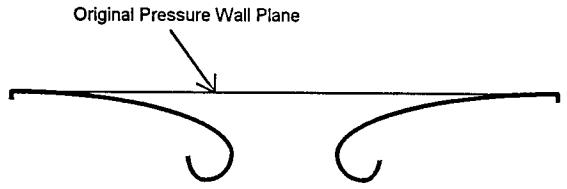

Figure 5. Advanced Stage of Pressure Wall Cracking with Petals Shown

Onset of Pressure Wall Petalling

In examining damaged pressure walls from a variety of different high speed impact tests, it became apparent that not all pressure walls exhibited petalling upon perforation. Rather, some perforated pressure walls holes retained their flatness and contained what may be called "cookie-cutter holes", that is, holes with jagged edges from which pressure wall material had been simply punched out. Therefore, it is necessary to possess a means by which it would be possible to

determine, a priori, whether a pressure wall perforation would be in the form of a petaled hole or a cookie-cutter hole. Further examination of damaged pressure walls revealed that the likelihood of petalling occurring increased:

- when the inner bumper was closer to the pressure wall;
- when the inner bumper was made from a relatively heavy material;
- for higher impact velocities;
- for larger projectile diameters;
- for thinner pressure walls; and,
- for normal impacts.

Based on these observations, a petalling limit function f_{pet} was developed such that if, for a given set of impact conditions and geometric parameters, its value exceeded a certain critical value f_{cr}, then pressure wall perforation would be accompanied by petalling. Alternatively, if the value of the petalling limit function was less than the critical value f_{cr}, then pressure wall perforation would be in the form of a cookie-cutter hole. The development of this function is presented in [20].

Pressure Wall Crack Initiation

To determine the instant of time at which crack growth begins (and hence the deformed configuration of the pressure wall at that time), we apply Gillemot's criterion of critical plastic work per unit volume [21]. This criterion states that material failure will occur when

$$\gamma_{1f}^2 + \gamma_{1f}\gamma_{2f} + \gamma_{2f}^2 = \varepsilon_{1f}^2 \tag{16}$$

where γ_{1f} and γ_{2f} are the principal in-plane strain components and ε_{1f} is the ordinate workability index of fracture strain. For our axially symmetric coordinate system, we have $\gamma_{1f} = \gamma_{rr}$ and $\gamma_{2f} = \gamma_{\theta\theta} = 0$. If in-plane plate displacements are small compared to the transverse plate displacement, and Eqn. (16) reduces to the following expression for the time t_c of pressure wall crack initiation:

$$\frac{\partial w(0,t_c)}{\partial r} = \sqrt{2\varepsilon_{1f}} \tag{17}$$

We note that implicit in Eqn. (17) is the assumption that pressure wall cracking will commence at the center of the pressure wall loading area, i.e. at r = 0. This appears to be a reasonable assumption since it is at this point where strains attain their maximum value.

Equivalent Hole Diameter

The method for calculating equivalent hole diameter depends on whether or not the perforation was accompanied by petalling. If it was not, then the diameter of the hole created is simply equal to the radius of the projectile component debris cloud. However, if it was a petalling perforation, then the equivalent hole diameter is taken to be that of a circle with an area equal to the see-through area of the petaled pressure wall.

COMPARISON WITH EXPERIMENTAL RESULTS

The predictions of the model presented herein are compared against those of the empirically-based equation for maximum tip-to-tip crack length for three ISS wall configurations. These equations were derived from experimentally obtained pressure wall hole diameter and maximum tip-to-tip crack length data and can be found in Reference [1]. The ISS wall systems considered herein are the baseline US Lab Cylinder (BLC), the enhanced US Lab Cylinder (ELC), and the

Endcone (LEC). Table 1 presents a summary of the geometric parameters defining these wall systems. Tests were performed using spherical projectiles at impact velocities of 6.5 ± 0.3 km/sec with a two-stage light gas gun and at 11.3 ± 0.5 km/sec using an inhibited shaped charge launcher (ISCL).

Theoretical predictions of maximum crack length for each of the three multi-wall systems described above were compared against values generated by the empirical equations for three impact velocities: 6, 9, and 12 km/s. Review of these results revealed some interesting trends in the predictions of the analytical model.

First, when the projectile diameter was less than the petalling limit diameter, the predictions of the analytical model greatly exceeded the empirical equation values. Thus, the use of the diameter of the debris cloud projectile component to calculate the diameter of the resulting hole in the pressure wall greatly overestimated actual hole diameter values.

Table 1. Multi-wall system geometries

Wall System	t_b *(mm)*	*Inner Wall*	S *(cm)*	S_2 *(cm)*	t_w *(mm)*
BLC	1.27	MLI[a]	11.43	5.72	4.78
LEC	1.91	MLI[a]	22.15	18.33	4.78
ELC	2.03	6N+6K[b]	11.43	5.72	4.78

[a]20 layers of multi-layer thermal insulation

[b]6 layers of Nextel AF62 cloth backed with 6 layers of Kevlar 710 cloth

Second, when the projectile diameter exceeded the petalling limit diameter, analytical model predictions ranged from being fairly close to the empirical equation predictions to being significantly lower than the empirical predictions. Thus, in most of the cases where petalling occurred, the pressure wall petals did not open up sufficiently during the curling process, which in turn resulted in underpredicted pressure wall hole diameters.

Based on these results, some adjustment of the analytical model was required to bring it more in line with experimental results. Modification functions were introduced into the model so that it would take on appropriate values for a given multi-wall system geometry and for a specific set of impact parameters. The specific forms of the correcting factors used depended on the multi-wall system and were functions of projectile diameter, trajectory obliquity, and impact velocity. Table 2 contains a summary of the comparisons between the predictions of the modified analytical model and those of the empirical equations.

Table 2. Comparison of model predictions and empirical equation predictions

	LEC			*BLC*			*ELC*		
V_p *(km/s)*	d_p *(cm)*	D_h *Ratio*	L_{tt} *Ratio*	d_p *(cm)*	D_h *Ratio*	L_{tt} *Ratio*	d_p *(cm)*	D_h *Ratio*	L_{tt} *Ratio*
	0.92	1.194	1.184	0.75	1.001	1.013	1.21	1.094	1.109
	1.16	0.987	1.027	1.03	1.159	1.141	1.38	0.833	1.113
6	1.41	1.006	1.002	1.33	1.001	0.999	1.55	1.006	1.001
	1.66	0.891	0.876	1.62	0.999	1.041	1.73	1.057	0.969
	1.91	1.001	1.001	1.91	1.000	1.028	1.91	1.005	0.999
	0.93	1.166	1.188	0.75	0.503	0.951	1.25	1.018	1.014
	1.17	1.012	1.008	1.03	0.633	0.814	1.41	0.959	1.082
9	1.41	0.594	0.764	1.32	1.002	0.999	1.57	1.001	1.000
	1.66	1.180	1.275	1.61	1.532	1.039	1.74	1.017	0.973
	1.91	1.006	1.003	1.91	0.997	1.026	1.91	1.005	1.001
	0.77	1.108	1.129	0.64	1.004	1.013	1.14	1.116	1.086
	1.03	1.009	1.005	0.95	0.529	0.911	1.32	0.941	1.138
12	1.33	1.049	1.592	1.27	0.998	0.999	1.52	1.005	1.001
	1.62	0.958	1.208	1.59	2.396	0.989	1.71	1.001	0.969
	1.91	1.004	1.001	1.91	1.003	1.000	1.91	1.003	.999

In Table 2, d_p is the diameter of the projectile, while entries in the D_h and L_{tt} columns are the ratios of the empirical prediction equation values to the modified analytical model values for hole diameter and crack length, respectively. This table reveals a fairly high level of predictive accuracy for the modified model. However, there still exist some differences between the predictions of the modified model and the predictions of the empirical equations, especially for normal impacts of BLC wall system at impact velocities of 9 km/s and above.

Further validation of the analytical model developed herein was obtained by comparing its predictions against actual empirical hole diameter and crack length data from several individual high speed impact tests. Model predictions were obtained for six impact scenarios: one for an impact velocity near 6.5 km/s and and one for a velocity near 11 km/s. Table 3 contains the experimental and model values of hole diameter and crack length for the six impact scenarios considered. Also shown in Table 3 are the hole diameter and crack length values predicted by the empirical equations.

Table 3. Comparison of modified model predictions and actual empirical data

Wall System	*Test No.*	*V_p (km/s)*	*d_p (cm)*	*Hole Diameter (cm)*			*Crack Length (cm)*		
				Exp. Res.	*Model Pred.*	*Emp. Eqn.*	*Exp. Res.*	*Model Pred.*	*Emp. Eqn.*
	HS-11	6.41	0.95	3.25	7.69	2.70	5.66	3.50	3.34
BLC	7698-1	11.70	1.47	3.96	1.81	4.05	10.29	10.97	10.94
	1722	6.78	1.42	11.20	3.98	3.43	32.39	8.79	10.04
ELC	7698-3	11.64	1.32	22.17	22.91	20.79	41.91	39.35	45.11
	1699	6.67	1.42	7.12	6.46	5.93	18.67	19.59	18.76
LEC	7698-7	11.37	1.32	6.25	4.04	7.68	13.72	14.15	23.49

As can be seen from Table 3, the predictions of the modified analytical model, in general, compare rather favorably with actual experimental data values. However, there do again exist instances where the model predictions and empirical data are somewhat divergent. Of some concern is the discrepancy between the predicted and experimental values of hole diameter and crack length for Test No. 1722. However, analysis of the data for tests conducted under similar impact conditions revealed that the damage sustained by the pressure wall in this test was anomalous.

SUMMARY

This paper presents the development of a first-principles-based model of crack length and hole diameter for a spacecraft module pressure wall that has been perforated by a normal orbital debris particle impact. The model is developed by sequentially characterizing the phenomena comprising the orbital debris impact event, including the initial impact, the creation and motion of a debris cloud within the dual-wall system, the impact of the debris cloud on the pressure wall, the deformation of the pressure wall due to debris cloud impact loading prior to crack formation, pressure wall crack initiation, propagation, and arrest, and finally pressure wall deformation following crack initiation and growth. The predictions of the model are compared against the predictions of empirically-based equations for three ISS wall configurations and against data from individual impact tests. Initial model predictions did not compare favorably with the experimental data, especially for cases in which pressure wall petalling did not occur. Several modifications were made to the original model to bring its predictions closer in line with the experimental results. Following the adjustment of several empirical constants, the predictions of the modified analytical model were in much closer agreement with the experimental results.

Acknowledgment—The authors are grateful for the support of the NASA Marshall Space Flight Center under contract NCC8-28. The authors would also like to acknowledge Dr. Joel Williamsen and Mr. Ben Hayashida for their many helpful comments and guidance during the course of this effort.

REFERENCES

1. W.P. Schonberg and J.E. Williamsen, Empirical hole size and crack length models for dual-wall systems under hypervelocity projectile impact. *Int. J. of Impact Engng.*, **20**, 711-722 (1997).
2. B.E.P.Lutz and C.J. Goodwin, Catastrophic failure modes assessment of the international space station alpha. *NASA CR-4720*, Marshall Space Flight Center, AL (1996).
3. G.T. Burch, Multi-plate damage study. *AFATL-TR-67-116*, Eglin Air Force Base, FL (1967).
4. W. P. Schonberg, A.J. Bean and K. Darzi, Hypervelocity impact physics. *NASA CR-4343*, Washington, D.C. (1991).
5. W.P. Schonberg, Aluminum 2219-T87 vs. 5456-H116: A comparative study of pressure wall materials in dual-wall structures under hypervelocity impact. *Acta Astronautica*, **26**, 799-812 (1992).
6. SSFPO, Common module shell unzipping due to meteoroid/orbital debris strikes. *Space Station Freedom Program Office, Report No. GSS-40.05-RPT-6-001*, Reston, VA (1994).
7. J.E. Williamsen, Vulnerability of manned spacecraft to crew loss from orbital debris penetration. *NASA TM-108452*, Marshall Space Flight Center, AL (1994).
8. M.H. Rice, R.G. McQueen, and J.M. Walsh, Compression of solids by strong shock waves. *Solid State Physics*, Vol/ VI, (edited by F. Seitz and D. Turnbull), Academic Press, New York (1958).
9. W. Jolly and W.P. Schonberg, Analytical prediction of hole diameter in thin plates due to hypervelocity impact of spherical projectiles. *Shock and Vibration*, **4**, 379-390 (1997).
10. W.P. Schonberg and J. Serrano, Internal effects model for spacecraft modules perforated by orbital debris. *J. Spacecraft and Rockets*, **34**, 325-332 (1997).
11. A.L. Florence, Clamped circular rigid-plastic plates under blast loading. *J. Applied Mech.*, **33** (2), 256-260 (1996).
12. A.L. Florence, Clamped circular rigid-plastic plates under central blast loading. *Int. J. Solids and Structures*, **2**, 319-335 (1966).
13. A.J. Wang and H.G. Hopkins, On the plastic deformation of built-in circular plates under impulsive load. *J. Mechanics and Physics of Solids*, **3**, 22-37, (1954).
14. D. Krajcinovic, Dynamic analysis of clamped plastic circular plates. *Int. J. Mechanical Sciences*, **14**, 225-234 (1972).
15. T.L. Anderson, *Fracture Mechanics: Fundamentals and Applications*, CRC Press, NY (1991).
16. M.F. Kanninen and C.H. Popelar, *Advanced Fracture Mechanics*, Oxford University Press, Oxford, England (1985).
17. D.K. Roberts and A.A. Wells, The velocity of brittle fracture. *Engineering*, **178**, 820-821, (1954).
18. T.C.T. Ting, Large deformation of a rigid ideally plastic cantilever beam. *J. Applied Mech.*, **32**(2), 295-302 (1965).
19. J.D. Walker, D.J. Grosh and S.A. Mullin, Experimental impacts above 10 km/s. *Int. J. of Impact Engng.*, **17**, 903-914, (1995).
20. W.P. Schonberg, Onset of petaling in a thin spacecraft wall perforated by an orbital debris particle. *Proc. SPIE Symposium on Characteristics and Consequences of Space Debris and Near-Earth Objects,* San Diego, CA (1998).
21. A. Atkins, *Elastic Plastic Fracture*, John Wiley and Sons, NY (1985).

PERGAMON International Journal of Impact Engineering 23 (1999) 847–858

INTERNATIONAL JOURNAL OF IMPACT ENGINEERING

www.elsevier.com/locate/ijimpeng

3D HYDRODYNAMIC CODE SOVA FOR MULTIMATERIAL FLOWS, APPLICATION TO SHOEMAKER-LEVY 9 COMET IMPACT PROBLEM

V.V. SHUVALOV, N.A. ARTEM'EVA, and I.B. KOSAREV

Russian Academy of Sciences, Institute for Dynamics of Geospheres, 38 Leninsky Prosp. (bldg.6), Moscow, 117979, Russia e-mail: shuvalov@idg.chph.ras.ru

Summary–A totally conservative Eulerian 3D numerical code which conserves mass, momentum and energy both in the source and remap steps is developed. Mass, momentum and kinetic energy are conserved simultaneously during the remapping. The use of special form of linear viscosity makes the code more tolerant to the time step, leaving the second order of accuracy. Multimaterial flows including those contaminated by dust particles may be investigated using this program. The performance of the code is illustrated by modeling the Shoemaker-Levy 9 impact against Jupiter. Penetration of nonuniform fragments with complex structure into the Jovian atmosphere is investigated. © 1999 Elsevier Science Ltd. All rights reserved.

INTRODUCTION

The SOVA code was developed to model multidimensional, multimaterial, large deformation gasdynamics flows including those contaminated by dust particles. Radiation transfer is also taken into account using assumptions of thermal conductivity, volume radiation or one-dimensional approximations. General description of the code is given in [1]. In the present paper the main features of the code are described, and its performance is illustrated by modeling the impact of S-L9 Comet fragments in assumption of there inhomogeneous structure.

A two-step Eulerian solution scheme is exploited to integrate the problem through time. This scheme is in many ways similar to that used in the CTH System [2]. But several principal advances are made. The two-step procedure is more suitable for multimaterial problems. In the first step the Lagrangian forms of equations are solved, then the distorted cells are remapped back to initial mesh (or some new mesh changing in time). At the beginning of the remap step a boundary (or boundaries) between different materials are constructed.

The finite volume approximations of the conservation equations have been designed to conserve mass, momentum and energy both across the Lagrangian and remap steps. The main problem is to conserve the mass, momentum and kinetic energy across the remap, because these three quantities are usually calculated using two equations. From the physical point of view it means that a combination of two or three volumes in the process of remapping is similar to nonelastic impact (the velocities becomes equaled). This leads to deficiency of

0734-743X/99/$ - see front matter © 1999 Elsevier Science Ltd. All rights reserved.
PII: S0734-743X(99)00129-3

the kinetic energy. Sometimes (similar to nonelastic collision) this energy discrepancy is transformed into the heat [2]. But this procedure is not quite correct, though it provides a conservation of the total energy. In reality two opposite processes take place at each time step: a coupling and separation of finite volumes. The volume added to any cell is removed from some other cell. The kinetic energy (and momentum) distribution between the parts of separating volume should be determined from conservation conditions for coupling and separation simultaneously. An attempt to provide such a conservation is made in the SOVA code. One more substantial improvement is the consideration of dust particles transfer in the frame of multimaterial code.

The solution scheme and some details of the code are described in the next section. The performance of the code is illustrated by modeling the impact of Shoemaker-Levy 9 Comet against Jupiter. This unique event continues to be a remarkable test for modern and future hydrocodes connected with high velocity impacts. In this paper nonhomogeneous fragments with complex structure are considered, which needs a use of multimaterial code. Some conclusions are presented in the final section.

DESCRIPTION OF THE CODE

Computational Mesh and Variable Positions

Three-dimensional rectangular and two-dimensional cylindrical and rectangular geometries are used to generate the computational mesh. Each cell (i, j, k) is restricted by spatial coordinates: $x_i \le x \le x_{i+1}$, $y_j \le y \le y_{j+1}$, $z_k \le z \le z_{k+1}$ (for the 3D case). All quantities are cell centered except the velocities, which are centered on appropriate cell faces (see Fig.1). A staggered mesh is constructed for the momentum conservation equation. The staggered cell boundaries pass through midpoints of the adjacent cells, so the mass of staggered cell equals one half the mass of two adjacent cells.

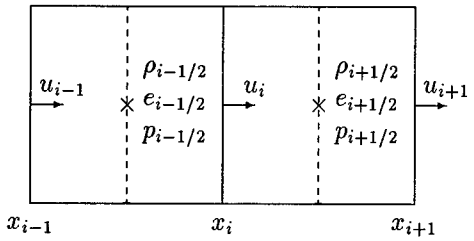

Fig. 1. Original (solid lines) and staggered (dashed lines) mesh and variable positions.

The process of multidimensional equation integration is simplified by using operator splitting techniques which replaces the multidimensional equations with a set of one-dimensional equations. This techniques is used both in the Lagrangian and remap steps. The operator splitting technique is used to separate gasdynamic, gas-dust interaction and radiation steps also.

Lagrangian Step

Nondivergent form of energy equation is used for numerical approximation. Therefore special efforts should be undertaken to conserve the total energy [2]. The use of alternative (conservative) form of the energy equation provides the total energy conservation automatically but leads to some problems in the case of nearly inertial flows, where a small value of

thermal energy is determined as a difference between two large values of the total and kinetic energies. The one-dimensional rectangular geometry forms of the finite-difference equations are

$$\rho^n_{i+1/2}(x^n_{i+1} - x^n_i) = \tilde{\rho}_{i+1/2}(\tilde{x}_{i+1} - \tilde{x}_i) \tag{1}$$

$$\tilde{x}_i = x^n_i + 0.5(u^n_i + \tilde{u}_i)\tau \tag{2}$$

$$\frac{\tilde{u}_i - u^n_i}{\tau} + \frac{p_{i+1/2} - p_{i-1/2}}{0.5(\rho^n_{i-1/2}(x^n_i - x^n_{i-1}) + \rho^n_{i+1/2}(x^n_{i+1} - x^n_i))} = 0 \tag{3}$$

$$\frac{\tilde{e}_{i+1/2} - e^n_{i+1/2}}{\tau} + p_{i+1/2}\frac{u^n_{i+1} + \tilde{u}_{i+1} - u^n_i - \tilde{u}_i}{2\rho^n_{i+1/2}(x^n_{i+1} - x^n_i)} = 0 \tag{4}$$

where ρ, e, p, u are the cell average density, thermal energy, pressure and velocity respectively, τ is the time step, index n corresponds to the values at the time level n, and symbol ~ marks the values at the end of the Lagrangian step. Such a form of approximation provides energy conservation if the same value of pressure is used in both Eqn. (3) and (4) [3].

The pressure $p_{i+1/2}$ is obtained by extrapolation from time level n to $n + 1/2$ assuming that the entropy S remains constant [4]

$$p_{i+1/2} = p^n_{i+1/2} + \left(\frac{\partial p}{\partial \rho}\right)_S \frac{\partial \rho}{\partial t}\frac{\tau}{2} \tag{5}$$

This expression can be rewritten in the form

$$p_{i+1/2} = p^n_{i+1/2} - \rho^n_{i+1/2}\left(c^n_{i+1/2}\right)^2 \frac{\tilde{u}_{i+1} - \tilde{u}_i}{x_{i+1} - x_i}\frac{\tau}{2} \tag{6}$$

where c is the sound speed. Involving of the velocities from $n + 1$ time level increases the stability of the scheme. In some sense it is similar to including some portion of implicit linear viscosity. As a result the time step τ is restricted not by usual Courant conditions but by a weaker condition

$$\tau \leq \min\left(\min_i \frac{x_{i+1} - x_i}{|u_i|}, \min_i \frac{x_i - x_{i-1}}{|u_i|}\right). \tag{7}$$

Equation (3) with the pressure (6) is solved using a sweep method. Quadratic artificial viscosity $q = \nu\rho_*(\Delta u)^2$ is used to model shocks (if $\Delta u < 0$). In case of multimaterial cell ρ_* is defined as a minimum of material densities.

Equations (1-4) define the total thermal energy and density in the cell. If the cell contains more than one material, thermodynamic parameters of each component are determined from the following equations:

$$p_l(\tilde{e}_l, \tilde{\rho}_l) = p_m(\tilde{e}_m, \tilde{\rho}_m) \qquad \forall l, m \tag{8}$$

$$\sum_m \alpha_m \tilde{\rho}_m = \tilde{\rho} \tag{9}$$

$$\tilde{e}_m = e^n_m + p\left(\frac{1}{\tilde{\rho}_m} - \frac{1}{\rho_m}\right) \tag{10}$$

where l and m are material numbers, α is material volume concentration and p is defined by (6).

Remap step

The velocities, densities and energies updated at the Lagrangian step must be remapped to the initial (or some other) mesh. The second order Van Leer scheme [5] replacing a uniform distribution in the donor cell with a linear distribution is used to remap density and internal energy. The mass, momentum and kinetic energy cannot be conserved simultaneously if the same scheme is applied to calculate the velocity. For this reason a special algorithm is used for the velocity remapping. The momentum and kinetic energy exchange between two adjacent cells is described by conservation laws:

$$m_i^n\tilde{\tilde{u}}_i + m_{i+1}^n\tilde{u}_{i+1} = (m_i^n - \triangle m)\tilde{u}_i^{n+1} + (m_{i+1}^n + \triangle m)\tilde{\tilde{u}}_{i+1} \tag{11}$$

$$m_i^n(\tilde{\tilde{u}}_i)^2 + m_{i+1}^n(\tilde{u}_{i+1})^2 = (m_i^n - \triangle m)(\tilde{u}_i^{n+1})^2 + (m_{i+1}^n + \triangle m)(\tilde{\tilde{u}}_{i+1})^2 \tag{12}$$

where m is a staggered cell mass, $\triangle m$ is a mass flux across a cell face, $\tilde{\tilde{u}}_i$ is the velocity obtained after momentum-energy exchange between $i-1$ and i cells. The resulting equations are:

$$u_i^{n+1} = \frac{m_i^n\tilde{\tilde{u}}_i + m_{i+1}^n\tilde{u}_{i+1}}{m_i^n + m_{i+1}^n} + \frac{\tilde{\tilde{u}}_i - \tilde{u}_{i+1}}{m_i^n + m_{i+1}^n}\sqrt{\frac{(m_{i+1}^n + \triangle m)m_i^n m_{i+1}^n}{m_i^n - \triangle m}} \tag{13}$$

$$\tilde{\tilde{u}}_{i+1} = \frac{m_i^n\tilde{\tilde{u}}_i + m_{i+1}^n\tilde{u}_{i+1}}{m_i^n + m_{i+1}^n} + \frac{\tilde{u}_{i+1} - \tilde{\tilde{u}}_i}{m_i^n + m_{i+1}^n}\sqrt{\frac{(m_i^n - \triangle m)m_i^n m_{i+1}^n}{m_{i+1}^n + \triangle m}} \tag{14}$$

For $\triangle m \ll m_i^n$ and $\triangle m \ll m_{i+1}^n$ Equation (13) leads to the momentum flux $\triangle m(\tilde{\tilde{u}}_i + \tilde{u}_{i+1})/2$, which corresponds to the second order of accuracy. This procedure is not symmetric, different results are obtained in the cases where index i increases or decreases. The asymmetry is minimized by permuting the direction of calculations.

The algorithm described above provides the conservation of all physical quantities, it is totally conservative according to terminology [3].

Some interface reconstruction techniques are necessary to remap density and internal energy in the case of multimaterial cells. The SLIC scheme [6] is used in SOVA for three-dimensional mesh. The high resolution interface tracker developed in CTH [2] is exploited in the case of two-dimensional geometry.

A special probabilistic algorithm was supposed in CTH to calculate the motion of small (less than one cell) fragments surrounded by different material. In the SOVA code, an additional, optional technique is used to describe interaction of the flow with small particles including dust and aerosole particles. This technique based on solving equations of motion for some number ($10^3 - 10^5$) of representative particles (markers). Each of these markers represents a motion of large number ($10^5 - 10^{10}$) of real dust grains having similar trajectories. The Monte-Carlo method is used to calculate diffusive spreading of the dust. Implicit procedure is applied to calculate the dust-gas interaction.

Our experience shows that, in some cases, pressure equalization after remapping using Eqn.(8-10) improves the results. Simple 1D numerical tests demonstrate that the results of the SOVA code correlate rather well with those obtained with the high resolution CTH code, transforming kinetic energy discrepancy into the heat. In the explosion-like tests the SOVA code allows to cut computational time by several times with the same accuracy.

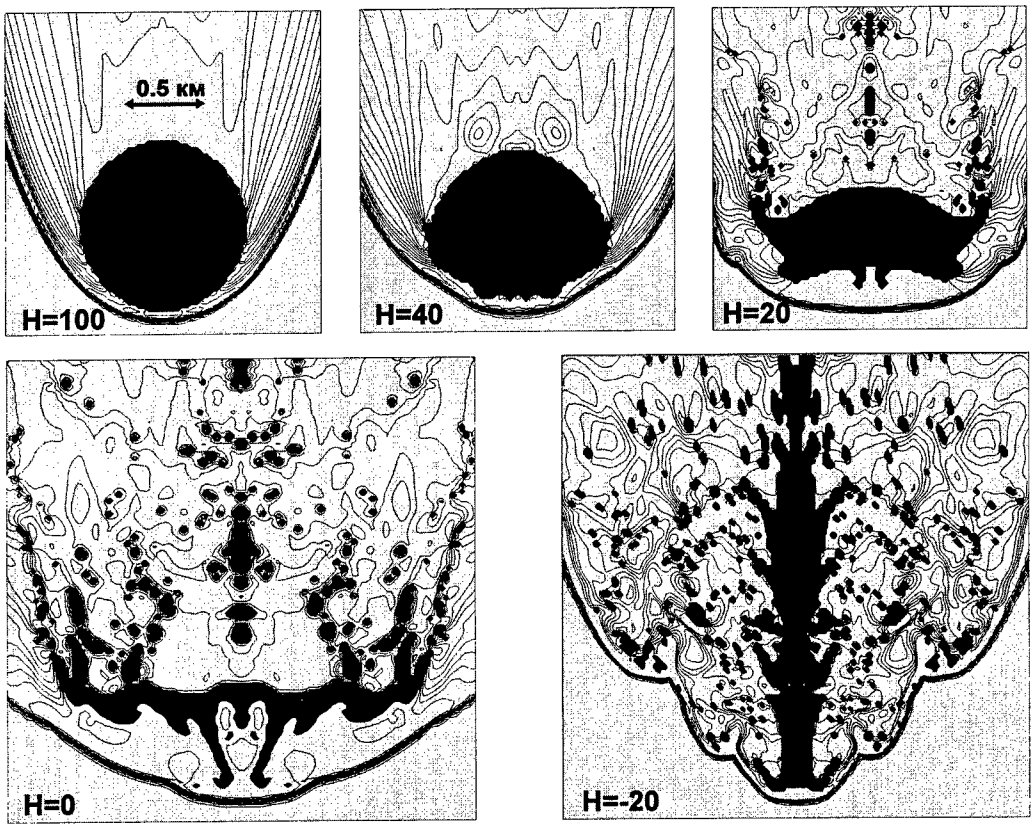

Fig. 2. Initial configuration and evolution of the uniform fragment. Density contours are presented. Dark gray shading marks comet material. H, km, is an altitude above (or below) 1 bar level.

NUMERICAL SIMULATIONS OF S-L9 IMPACT

The interest in the impacts of large cometary and asteroidal fragments with planetary atmosperes has been rekindled in recent years [7], in particular in connection with the impact of Comet S-L9 into the Jovian atmosphere in July 1994 [8]. This powerful collision was an unprecedented event with no direct analogy observed in nature. Even prior to the Comet impact, several research groups all over the world made attempts to simulate this phenomenon to predict penetration depth of the fragments, the energy deposition as a function of the depth and the luminosity of the observable events [9-14]. Whereas the qualitative picture of the event was nearly the same in all the simulations and coincided as a whole with observed data [15-18], quantitative estimates differed from one another drastically depending on the assumed mass and radius of the fragments, on the physical processes involved in the simulations and even on the hydrocode in use. Four years later intensive simulations and discussions do not stop [19-25].

In the recent papers [20] and [24] the influence of radiation on fragment evaporation, on the energy release and bolide luminosity was taken into account. But, the role of radiation at the late stage of the impact (below 1 bar pressure level) is not yet clear. At these altitudes, the radiative flux is substantially less than the hydrodynamic one, however, the total surface of the disrupted and dispersed fragments increase drastically. This can result in increase in evaporation.

One more question concerns fragment structure. In all the previous investigations the fragments of S-L9 Comet have been treated as uniform bodies with some average density

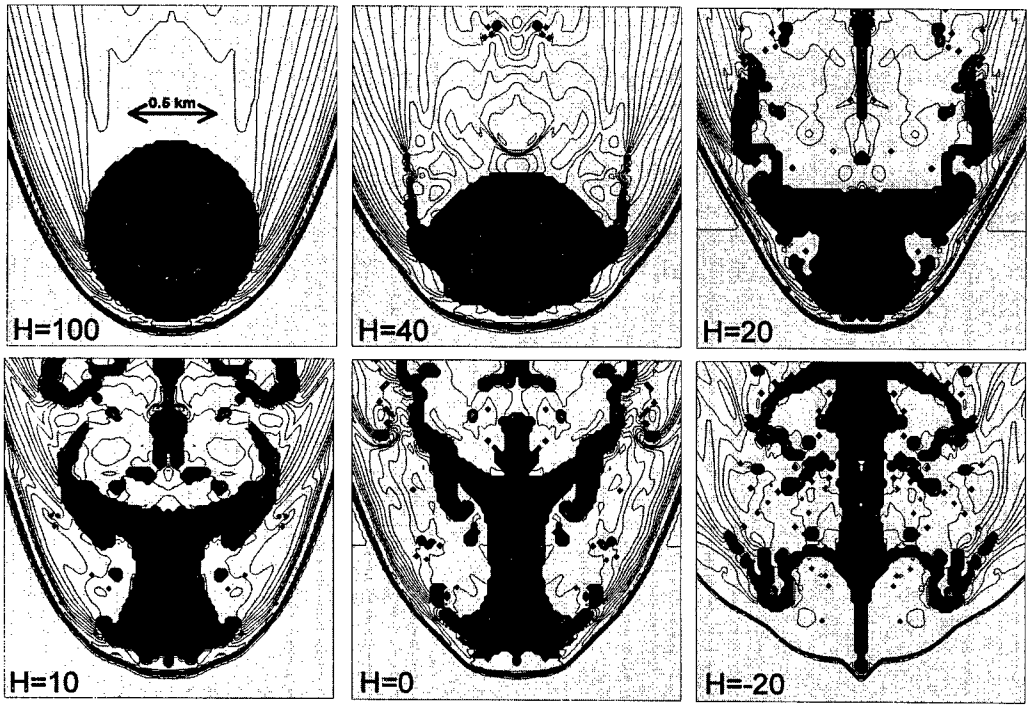

Fig. 3. Initial configuration and evolution of the fragment with heavy kernel (``cherry''). Density contours are presented. Black shading marks high density material, dark gray corresponds to low density component. H, km, is an altitude above (or below) 1 bar level.

that is usually less than 1 g/cm^3. It seems plausible that the real structure of the Comet may be more complex and each fragment is a mixture of different materials with different densities, strengths and equations of state. It is not evident in advance if the impact process is defined by the mass and energy of the fragment only or if structure is important too.

The main purposes of the present simulations are as follows:

1. To clear the role of radiation transfer at the late stage of the penetration.
2. To demonstrate the impact process for fragments with different structure and the influence of structure on energy deposition.
3. To compare numerical results with semianalytical models of meteoroid breakup.

Physical Model of the Impact

In the context of the same simulations we attempt to consider the uniform body with density of 0.22 g/cm^3 as a basic model and two types of nonuniform fragments, composed of heavy (with the density of 1 g/cm^3) and light (with the density of 0.1 g/cm^3) components.

Two-dimensional geometry (cylindrical and rectangular) is exploited in the impact simulations. Calculation mesh consists of 200 × 200 cells. The central portion of the mesh (60 × 100 cells) with constant spatial step $\Delta x = 0.02$ km moves together with the fragment. The spatial step increases outside the central high resolution region to the boundaries. The mesh spans the region of 300 km along the trajectory and 20 km in perpendicular direction.

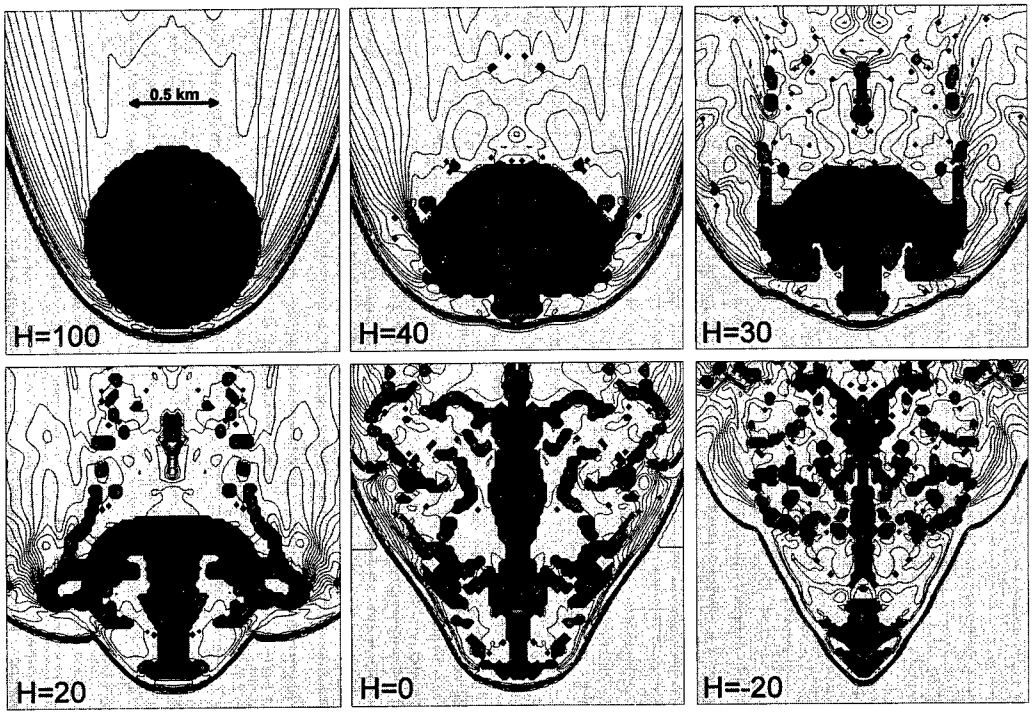

Fig. 4. Initial configuration and evolution of the fragment with heavy grains (``muffin"). All designations are the same as in Fig.3.

Tabularized equation of state ond opacity tables presented in the papers [21, 26] were applied for the comet vapor and Jovian atmospheric gas. The comet material was described by Gruneisen-like equation of state:

$$p = \rho_{00} C_0^2 (y^3 - y^2) + p_T(\rho, e_T) \tag{15}$$

where p and ρ are the pressure and density of the substance, ρ_{00} and C_0 equal density and sound velocity of the cold material, $y = \rho/\rho_{00}$ is the degree of compression, p_T and e_T are the thermal parts taken from [21]. As it has been shown in the previous investigations intensive deceleration and disintegration of the S-L9 fragments take place near the 1 bar pressure level, where the atmospheric density equals $10^{-4} - 10^{-3}$ g/cm^3. The pressure at the stagnation point at this level exceeds the critical in Van-der-Waals sense. Thus, the use of simplified equation of state (15) is justified.

The failure of the fragment itself, i.e. the loss of the strength, has not been considered in this paper. The simulations started at the altitude of 100 km, and it was assumed that at this altitude the fragment failed totally, but conserved its initial mass, size and shape and therefore may be treated as a liquid.

As shown in [21, 24] the process of fragment evaporation should be the major object of simulations at the altitudes of about 100–200 km. This is the process which results in the formation of the vapor cloud around the fragment. The radius of this cloud exceeds the initial radius of the fragment by 2–3 times. Ablation may substantially change the bolide brightness at these altitudes, but doesn't considerably diminish the fragment mass. The evaporation rate sharply decreases at the altitudes of less than 100 km due to screening effects. And, finally, at the altitudes of about 50 km ablation caused by radiation can be completely neglected [26]. The role of radiation may increase again at the altitudes of $H < 0$, where the total surface of the dispersed body increases drastically. At these altitudes optical

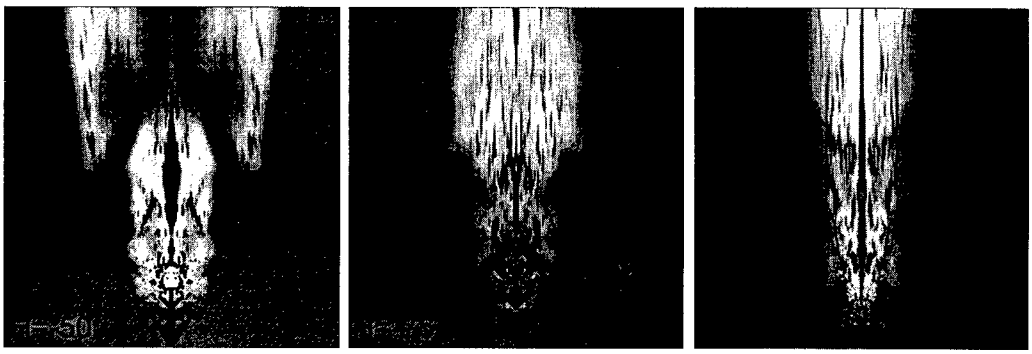

Fig. 5. Density destribution in the jet resulting from disruption of the ``cherry'' fragment. Shading intensity is proportional to density. H, km, is an altitude below 1 bar level.

thickness of the shock compressed gas is significantly greater than unity. Therefore the radiative transfer is taken into account in the thermal conductivity approximation.

Results of Numerical Simulations

The first one of the nonuniform fragments consists of the heavy kernel and light shell. From now on it is called "cherry". The second represents a light shell with some amount of heavy grains (hereafter referred to as "muffin"). All the fragments have the same radius of 0.5 km, the same mass of $1.22 \cdot 10^{11}$ kg, the same initial velocity of 60 km/s and consequently the same initial kinetic energy equal to $2 \cdot 10^{20}$ J. The calculations started at the altitude of 100 km.

Figures 2–4 illustrate the initial stage of the fragment deceleration. At the altitudes of about 40–50 km the fragments start to deform. The development of Rayleigh-Taylor and Kelvin-Helmholtz instabilities results in wave-like disturbances at the surface and formation of the separate drops. At this stage the results of the numerical simulations coinside qualitatively with the results of well-known semianalytical models of meteoroid breakup [27-30]. For example, the third plate in the Fig.2 demontrates a typical "pancake". Nevertheless, at the moment of doubling of the initial radius (or even earlier in the case of complex structure) the total disruption occurs and the fragments transform into a cloud of drops, that are concentrated mainly near the axis of the trail. It should be emphasized that at this stage the velocity of the fragments averaged over the mass diminishes slightly, only by 1–2 km/s, and the velocity of the head part remains constant. Thus, intensive deceleration and energy release take place not at the stage of "pancake", but later, when the fragments transform to the debris jet, which consists of the small liquid drops and vapors, mixed with atmospheric gas. Deceleration process is defined by the jet composition, which, in turn, is defined by the initial structure of the fragment.

Let us consider the deceleration process for each type of fragment in detail. The uniform fragment is flattened under the aerodynamic loading, transforming into a "pancake" with radius twice the initial size. Then, the development of instabilities produces the debris jet with radius practically equal to the initial radius of the undispersed body (Fig.2). The breakup of the "cherry" (Fig.3) differs substantially from the simplified pancake-model. A low density envelope is deformed and decelerated early, while the heavy kernel becomes the leader. The shadowed envelope is exposed to weaker aerodynamic loading, its disruption continues only due to the removal of the comet materail from the edges. At the same time the leading kernel behaves as an isolated uniform body with smaller radius (see above). Finally, the kernel forms the jet with smaller radius than in the previous case. The narrowest jet is

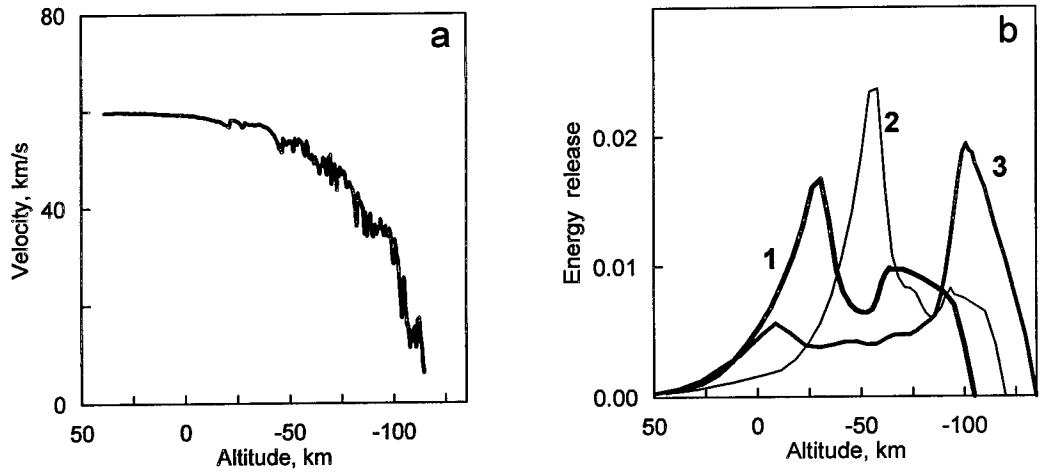

Fig. 6. (a) Bolide velocity versus altitude for the "cherry" fragment. (b) Normalized energy deposition versus altitude at the moment of 9 s. 1 - uniform fragment, 2 - "cherry", 3 - "muffin".

generated in the case of "muffin"-like fragment (Fig.4), where the leading role is connected with one of the small grains. Its deformation and tranformation take place later. The envelope is deformed and dispersed even earlier than this grain.

The later jet evolution (Fig.5) characterized by intensive deceleration and energy release holds the greatest interest for astronomers and physicists, and is not trivial. For example, the velocity of the heavy constituents of this jet diminishes faster than the velocity of the low density part. This fact is based on the leading role of the heavy components. These are the pieces which generate the shock wave and experience a high drag, while the light pieces move within the rarefied wake and are exposed to smaller drag and deceleration. When decelerated heavy pieces slide to the back, some other nondecelerated pieces become leaders and so on. As a whole the jet evolution demonstrates the collimation effect [31, 32], i.e. concentration of the material in the trail instead of the dispersion. The jet doesn't decelerate as a uniform body, but in each moment of time, most of its components have velocity close to the maximum or minimum ones. The velocity of the head exceeds the average velocity in 1.5–2 times and, hence, the jet stretches along the trajectory for many tens of kilometers. At altitudes of about -50 – -100 km the penetration of a substantially decelerated jet into the deeper layers of the Jovian atmosphere continues due to particles from the inner part of the jet, where velocity is large enough.

The complex evolution of the jet results in considerable fluctuations of the visible bolide velocity, i.e. the velocity of the leading edge of the shock wave. The time dependence of this velocity is shown in Fig.6a. The same velocity variations may occur in the case of bolide motion in Earth's atmosphere. Thus, the value of dynamic mass obtained in the analysis of the bolide trajectory may differ substantially both from the total mass of the meteoroid and from the mass of the individual fragments.

The energy release curves for each type of fragment are shown in Fig.6b at the time of 9 s after the beginning of the simulations. These curves have been obtained by calculating the energy excess in comparison to the initial atmospheric energy for each altitude. It should be mentioned that these curves change over time. As indicated above, the jet is stretched along the trajectory and its different parts decelerate and release energy at different altitudes and at different moments of time. Moreover atmospheric gas also moves along the trajectory: downwards in the near wake and than upwards due to the break in hydrostatic equilibrium. For all cases the energy curves have two peaks. The first is connected with the maximum radius of the fragment at the initial pancake-stage of the impact, the second – with the

deceleration of the inner part of the jet. The uniform fragment decelerates more intensively and has an energy peak at the altitude of about -20 km, but continues to move and reaches the maximum depth of about -100 km. Nonuniform fragments form more narrow jets and penetrate deeper.

The set of simulations with and without the thermal conductivity have shown that radiation influences the dynamics of deceleration insignificantly, but results in considerable increase of the comet material temperature. The internal energy of the vapor reaches 5–7 kJ/g and exceeds the evaporation energy by far, while in the sets without radiation the comet material remains cold. The heating may change the spectrum of the generated plume, which may be detected by satellite and Earth-based equipment.

CONCLUSIONS

This work introduces a new multimaterial multidimensional hydrodynamic code SOVA, which allows investigation of a wide range of gasdynamical and geophysical problems. The mass, momentum and energy are conserved both across the Lagrangian and remap step although a nondivergent form of the energy equation is used. Different forms of the equation of state (analytical and tabularized) may be exploited. The code allows the study of flows contaminated by aerosol particles, which is important for most geophysical applications. Radiation transfer in several assumptions can also be optionally taken into account if necessary. A preliminary version of this code has already been used for modeling the Shoemaker-Levy 9 Comet collision with Jupiter [22, 24] and meteoroid impacts against the Moon [33].

The use of the multimaterial multidimensional SOVA hydrocode allows modeling the impact of S-L9 fragments with complex structure. It has been shown that the process of deceleration may be divided into two clearly defined stages. At the first stage, the strengthless body is flattened and converts to a debris jet with practically the same velocity as initially. The parameters of the jet strongly depend on the initial structure of the fragment. At the second stage the jet decelerates and releases its energy into the Jovian atmosphere, forming the plume. A narrow jet penetrates deeper into the Jovian atmosphere. Only the first stage (flattening and break-up) of the impact may be described properly by semianalytical models. Two peaks in the energy release curve, obtained in the more justified model [23], also correspond to the break-up stage of the impact and are caused by two types of instabilities.

Taking radiation transfer into account does not considerably influence the penetration process and atmosphere-fragment energy exchange, but raises the vapor temperature and, hence, may change the spectrum of the plume.

REFERENCES

1. V.V.Shuvalov, Multimaterial hydrodynamic code SOVA for interfacial flows, application to thermal layer effect. *Shock Waves* (submitted) (1998).
2. J.M.McGlaun, S.L.Thomson and M.G.Elrick, CTH: a three-dimensional shock wave physics code. *Int.J.Impact.Engineering* **10**, 351–360 (1990).
3. Yu.P.Popov and A.A.Samarsky, *Finite Difference Methods for Gas Dynamic Problems.* Nauka, Moscow, 101–108 (1980) (in Russian).
4. S.M.Barhrah, Yu.P.Glagoleva, M.S. Samugin, B.D.Frolov, N.N.Janenko and Yu.V.Janilkin, Calculations of gasdynamic flows on the base of concentration method. *Docl Acad Nauk SSSR*, **257**, 566–569 (1981) (in Russian)
5. B.Van Leer, Towards the ultimate conservative difference scheme IV. A new approach to numerical convection. *J. Comput. Phys.*, **23**, 276–299 (1977).
6. W.F.Noh and P.Woodward, SLIC (simple line interface calculation). *Springer Lecture Notes in Physics*, **59**, 330–340 (1976).

7. V.V.Adushkin and I.V. Nemtchinov, Consequences of impacts of cosmic bodies on surface of the Earth. In: *Hazards due to Comets and Asteroids* (edited by Gehrels T.). Univ. of Arizona Press, Tucson, Arizona (1994).
8. S.L.Shoemaker, E.M.Shoemaker and D.H.Levy, Comet Shoemaker-Levy . *IAU Circ*, 5725 (1993).
9. T.J.Ahrens, T.Takata, and J.D.O'Keefe, Impact of Comet Shoemaker-Levy 9 on Jupiter. *Geophys. Res. Lett.*, **21**(11), 1087–1090 (1994).
10. M.B.Boslough, D.A.Crawford, A.C.Robinson and T.G.Trucano, Mass and penetration depth of Shoemaker-Levy 9 fragments from time-resolved photometry. *Geophys.Res.Lett.*, **21**(14), 1555–1558 (1994).
11. V.K.Gryaznov, B.A.Ivanov, A.B.Ivlev, B.A.Klumov, S.V.Utyuzhnikov and V.E.Fortov, Collision of the Shoemaker- Levy 9 with Jupiter: Interpretation of observed data. *Earth, Moon and Planets*, **66**, 99–128 (1994).
12. M.-M.Mac Low and K.J.Zahnle, Explosion of comet Shoemaker-Levy 9 on entry into the Jovian atmosphere. *Astrophys. J.*, **434**(1, pt.2), L33–L36 (1994).
13. E.M.Shoemaker, P.J.Hassing and D.J.Roddy, Numerical simulations of the Shoemaker-Levy 9 impact plumes clouds: a progress report. *GRL*, **22**(13), 1825–1838 (1995).
14. V.V.Svetsov, A comet fall in the Jovian atmosphere. *Solar System Research*, **29**(4), 331–340 (1995).
15. C.R.Chapman, W.J.Merline, K.Klaasen, T.V.Johnson, C.Heffernan, M.J.S.Belton and the Galileo Imaging team, Preliminary results of Galileo imaging of SL-9 impact sites. *GRL*, **22**(12), 1561–1564 (1995).
16. H.B.Hammel, R.F.Beebe, A.P.Ingersoll, G.S.Orton, J.R.Mills, A.A.Simon, P.Chodas, J.T. Clarke, E.DeJong, T.E.Dowling, J.Harrington, L.F.Huber, E.Karkoschka, C.M.Santori, A.Toigo, D.Yeomans and R.A.West, HST imaging of atmospheric phenomena created by the impact of Comet Shoemaker-Levy 9. *Science*, **267**(3), 1288–1296 (1995).
17. P.D.Nicholson, P.J.Gierasch, T.L.Hayward, C.A.McGhec, J.E.Moersch, S.W.Squyres, J.VanCleve, K.Matthews, G.Neugebaur, D.Shuppe, A.Weinberger, J.W.Miles, B.J.Conrath, Palomar observations of the IR spectra of the R impact of Comet Shoemaker- Levy 9: Spectra. *GRL*, **22**,(22), 1617–1620 (1995).
18. H.A.Weaver, M.F.A'Hearn, C.Arpigny, D.C.Boice, P.D.Feldman, S.M.Larson, P.Lamy, D.H. Levy, B.G.Marsden, K.J.Meech, K.S.Noll, J.V.Scotti, Z.Sekanina, C.S.Shoemaker, E.M.Shoemaker, T.E.Smith, S.A.Stern, A.D.Storrs, J.T.Trauger, D.K.Yeomans and B.Zellner, The Hubble Space Telescope (HST) observing campaign on Comet Shoemaker-Levy 9. *Science*, **267**, 1282–1288 (1995).
19. M.B.Boslough and D.A.Crawford, Shoemaker-Levy 9 and plume-forming collisions on Earht, in *Near-Earth Objects* (edited by J.L. Remo), N.Y. Academy of Sciences, New York, 236–282 (1997).
20. D.A.Crawford , Fragment size and mass estimates from light flux observations. *LPSC XXVIII* (1997).
21. I.V.Nemtchinov, V.V.Shuvalov, I.B.Kosarev, N.A.Artemieva et al., Assessment of comet Shoemaker-Levy 9 fragment sizes using light curves measured by Galileo spacecraft instruments. *Planet.Space.Sci.*, **45**(3), 311–326 (1996).
22. I.V.Nemtchinov, N.A.Artem'eva, I.B.Kosarev, V.V.Shuvalov, V.V.Svetsov, G.Neukum, G. Hahn and D.De Niem, Luminosity of the bolides created by SL- 9 comet fragments in the Jovian atmosphere. *Int.J.Impact.Engineering*, **20**, 591–599 (1997).
23. M.S.Roulston and T.J.Ahrens, Impact mechanics and frequency of SL9-type events on Jupiter. *Icarus*, **126**, 138–147 (1997).
24. V.V.Shuvalov, N.A.Artem'eva, I.B.Kosarev, I.V.Nemtchinov and I.A.Trubetskaya, Numerical Simulation of the Bolide Phase of the Impact of Comet Shoemaker-Levy 9 Fragments on Jupiter. *Solar System Research*, **31**(5), 393–400 (1997).
25. K.Zahnle and M.-M.MacLow, A simple model for the light curve generated by a Shoemaker-Levy 9 impact. *JGR*, **100**(E8), 16,885-16,895 (1996).

26. I.B.Kosarev, T.V.Loseva and I.V.Nemtchinov, Vapor optical properties and ablation of large chondrite and ice bodies in the Earth's atmosphere. *Solar system research*, **30**(4), 265–278 (1996).
27. S.S.Grigorian, Motion and disintegration of meteorites in planetary atmospheres. *Cosmic Research*, **17**(6), 724 (1979).
28. K.Zahnle, Airburst origin of dark shadows on Venus. *JGR*, **97**(E6), 10243–10255 (1992).
29. C.F.Chyba, P.J.Thomas and K.J.Zahnle, The 1908 Tunguska explosion: atmospheric disruption of a stony asteroid. *Nature*, **361**, 40–44 (1993).
30. J.G.Hills and M.P.Goda, The fragmentation of small asteroids in the atmosphere. *Astronom.J.*, **105**, 1114–1144 (1993).
31. P.H.Schultz and S.Sugita, Penetrating and Escaping the Atmospheres of Venus and Earth. *LPSC XXV*, 1215–1216 (1994).
32. N.A.Artemieva and V.V.Shuvalov, Interaction of shock waves during the passage of disrupted meteoroid through atmosphere. *Shock waves*, **5**(6), 359–367 (1996).
33. I.V.Nemtchinov, V.V.Shuvalov, N.A.Artem'eva, B.A.Ivanov, I.B.Kosarev and I.A.Trubetskaya, Light flashes caused by meteoroid impacts on the lunar surface. *Solar System Research*, **32**(2), 99–114(1998).

PERGAMON International Journal of Impact Engineering 23 (1999) 859–867

INTERNATIONAL JOURNAL OF IMPACT ENGINEERING

www.elsevier.com/locate/ijimpeng

AN INVESTIGATION OF CERAMIC/ALUMINIUM COMPOSITES AS SHIELDS FOR HYPERVELOCITY IMPACTS

V.V. SILVESTROV, A.V. PLASTININ, V.V. PAI, and I.V. YAKOVLEV

Lavrentyev Institute of Hydrodynamics, Siberian Division of Russian Academy of Sciences, Lavrentyev Avenue 15, Novosibirsk, 630090 Russia

Summary—The protection efficiency of single-shield bumpers made of composites based on the aluminum matrix containing the disperse ceramic inclusions of SiO_2 or Al_2O_3 is considered for a Whipple-type shield. The aim of the paper is to compare the protection efficiency of the first bumpers made of the metal composites with that for the duralumin shield by impact of spherical steel projectile with the velocity of 5.5 and 7.5 km/s. Mass fraction of the ceramic inclusions accounts for 15 and 30 percent of the total composite. A thick backwall plate was used, and the maximum depth of fragment craters on the witness plate is taken as a protection characteristic of shields made of different materials: reference aluminum alloy, composites under study, and loosely-packed metal powder bumpers. The bumpers made of the metal composites, Al-matrix plus embedded ceramic inclusions, are shown to have the poorer protection efficiency than those made of the duralumin alloy when used with steel impactors. It is shown that by impact of the hypervelocity steel projectile the shield material strength, if it is rather low but not zero, may essentially affect the damage pattern of the backwall in spite of the high level of realized impact pressures. © 1999 Elsevier Science Ltd. All rights reserved.

INTRODUCTION

The shielding system used against meteoroid/debris impacts now universally accepted involves the use of different multi-screen modifications of the Whipple shield. The principal part of the system is a thin outer bumper plate located a certain standoff distance from the protected wall. The function of the first screen is to rupture and to disperse a projectile with a view of decreasing the local action of its fragments on subsequent constructional elements. Considerable advances has been made in creating the effective shielding for practical spacecraft systems from meteoroid and orbital debris impacts [1–3].

However, a search for materials and the inner structure of the first bumper to shatter more effectively a projectile and to disperse more intensively a bumper material is in progress. Stilp and Weber have shown that the impedance mismatch and the order of the layers in two-layer bumpers strongly influences the debris cloud velocities and the fragment number and size [4]. Other shielding approach is the use of metal composites based on a plastic aluminum matrix containing dispersed ceramic inclusions [5]. Robinson and Nolen have studied an impact of an aluminum projectile with the velocity of 4–5 km/s on the composite bumpers consisting of the aluminum matrix with 20–25 v/o SiC inclusions. The authors have reasoned that, owing to collision of high-velocity projectiles against the shield made of a material containing the embedded inclusions and having a shock impedance different from that of the matrix material, the projectile will be more broken than for homogeneous aluminum bumpers. Also, they have concluded with care that similar material applications in the antimeteoroid protective systems are in sight.

0734-743X/99/$ - see front matter © 1999 Elsevier Science Ltd. All rights reserved.
PII: S0734-743X(99)00130-X

As described in Ref. [6], the crater depth in semi-infinite targets of aluminum matrix metal composites containing ceramic inclusions is considerably reduced as compared to plastic matrix materials. Hence, this paper deals with the use of metal composites based on aluminum matrix containing the disperse SiO_2 or Al_2O_3 inclusions as the first bumper in the single-shield system. The aim of the paper is to compare the protection efficiency of bumpers made of the disperse metal composites with that for the duralumin shield by impact of spherical steel projectile with the velocity of 5.5 and 7.5 km/s.

EXPERIMENTAL PROCEDURE

Two-component composite plates of thickness t_s = 1–1.3 mm are prepared by hot pressing of mechanical mixtures of a fine aluminum powder and SiO_2 or Al_2O_3 powders at 450°C followed by annealing. Mass fraction of the second component, ceramic, accounts for 15 and 30 % of the total composite. The mean sizes of powder grains are 10–20 μm for aluminum, 50–100 and 5–10 μm for SiO_2 and Al_2O_3, respectively. The porosity of composite materials, Π, is defined by measured values of density, ρ_s, and the theoretical maximum density, ρ_{th}, calculated by the mixture rule (Table 1). The areal density of the composite shields is nearly constant and equal to $t_s\rho_s$ = 0.27–0.33 g/cm^2.

Table 1. The characteristics of test materials

	D16T	*Pressed Al*	*15%SiO_2*	*30%SiO_2*	*15%Al_2O_3*	*30%Al_2O_3*
ρ_{th}, *g/cc*	2.78	2.71	2.67	2.64	2.82	2.06
ρ_s, *g/cc*	2.78	2.62	2.66	2.62	2.55	2.57
Π, *%*	–	3	1	1	10	13
τ_s, *MPa*	185–260	100–120	50–60	50–60	25–30	25–30
	Shock pressure for two impact velocities (unidirectional calculations)					
$P_{5.5}$, *GPa*	105	99	100	98	95	95
$P_{7.5}$, *GPa*	165	159	162	160	153	153

The impact of steel projectiles normal to the bumper is investigated. The 1 mm diameter steel balls are accelerated by a tubular explosive accelerator at velocities up to V_p = 5.5 and 7.5 km/s [7]. The final projectile diameter, d_p, is 0.9 and 0.83 mm, respectively. The test setup is conventional as follows: the bumper target being tested is located 50 mm from a witness plate (D16 aluminum alloy, 5 mm in thickness). The bumper plates 60 mm in diameter is supported by a steel flange which protects the witness plate from action of explosion products. The flange is mounted on the duralumin tube 150 mm in inner diameter which is closed by the witness plate. The explosive gun is vertically positioned 60 cm uprange the bumper. The volume between bumper and backwall is not pumped out and is filled with air at atmospheric pressure. The decrease of gas pressure below 1 atm did not significantly increase the maximum depth of the largest craters on the thick backwall even for the aluminum projectile [8] but complicates the experiments. As a reference bumper to be compared, the 1 mm duralumin plate (made of the aluminum alloy D16T) is used.

After the impact of a projectile with a shield, a debris cloud involving fragments of the projectile and the shield materials forms behind the bumper. The protection efficiency of the bumper can be judged by the fracture pattern of the backwall, such as the bending deflection, the wall perforation, the size of the damage zone and the depth of secondary fragment craters [5, 9]. In this work a thick backwall plate was used, and the maximum depth of fragment craters, P_c, on the witness plate did not exceed 1 mm. Thus the backwall could be considered semi-infinite, and the and maximum value of P_c is taken as a protection characteristic of shields made of different

materials. The measurement accuracy of P_c is ±0.02 mm. The crater depths given in Fig. 1 are normalized to the projectile diameter which is known with an accuracy of 5 % [10].

RESULTS AND DISCUSSION

Figure 1 gives the data on the relative penetration, P_c/d_p, on the backwall plate for the eight bumper materials under study at V_p = 5.5 and 7.5 km/s. For each bumper material a number of data are presented for three to five of the deepest craters. With incorporation of the disperse ceramic inclusions into the shield material the crater depth increases by 10–30 % relative to the values for the duralumin shield. The influence of inclusions SiO_2 or Al_2O_3 and their concentration and dispersity was not evident within the accuracy of P_c/d_p defining. Notice that the pressed aluminum powder shield results are essentially coincident with the data for the homogeneous duralumin bumpers.

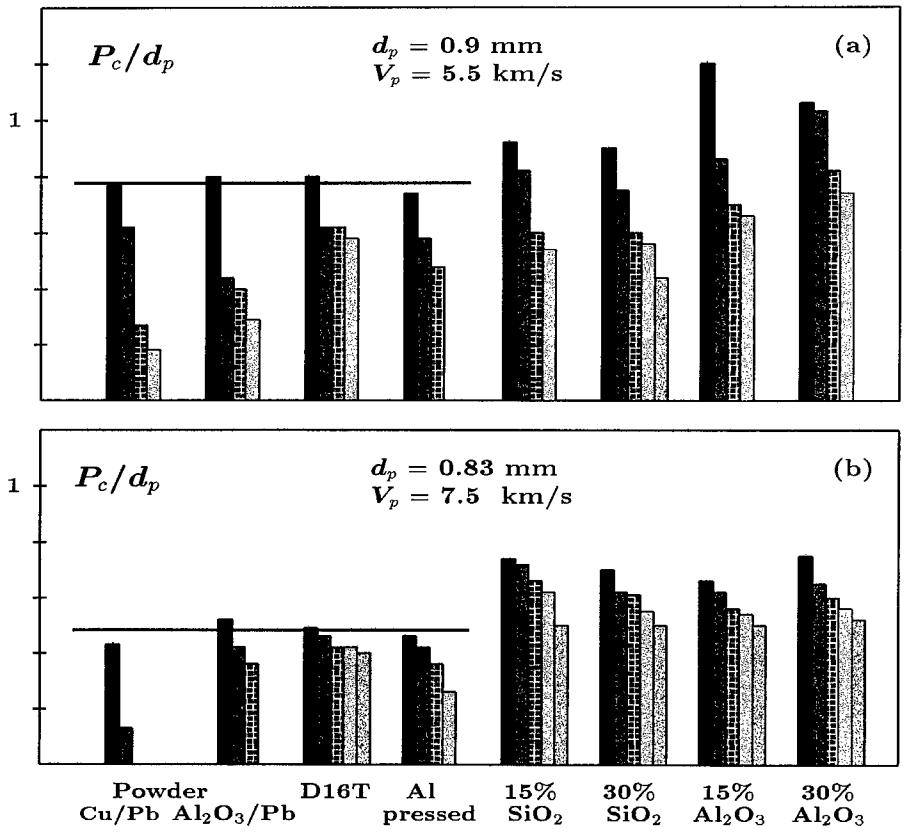

Fig. 1. Relative depth of craters on the back wall for the different bumper materials by the impact of the steel projectile with velocity of 5.5 (a) and 7.5 km/s (b).

Figure 2 shows the impact crater pattern on the witness plate of debris cloud for several bumpers at two impact velocities. In the case of the composite bumpers the debris cloud fragments are mainly spread over the narrower area than damaged one for duralumin bumper. The diameter of effective damaged area, D_d, involving 90 % of total area of all fragment craters is reduced about 1.5 times for tests with composite bumpers. This statement is demonstrated in Fig. 3 which shows the radial distribution of the sum of areas for all craters lying outside the circle with the radius R (the centre of circle placed in the centre of damaged area; the areas' sum is normalized to the total area of all craters on the witness plate). For instance, at the steel/Al im-

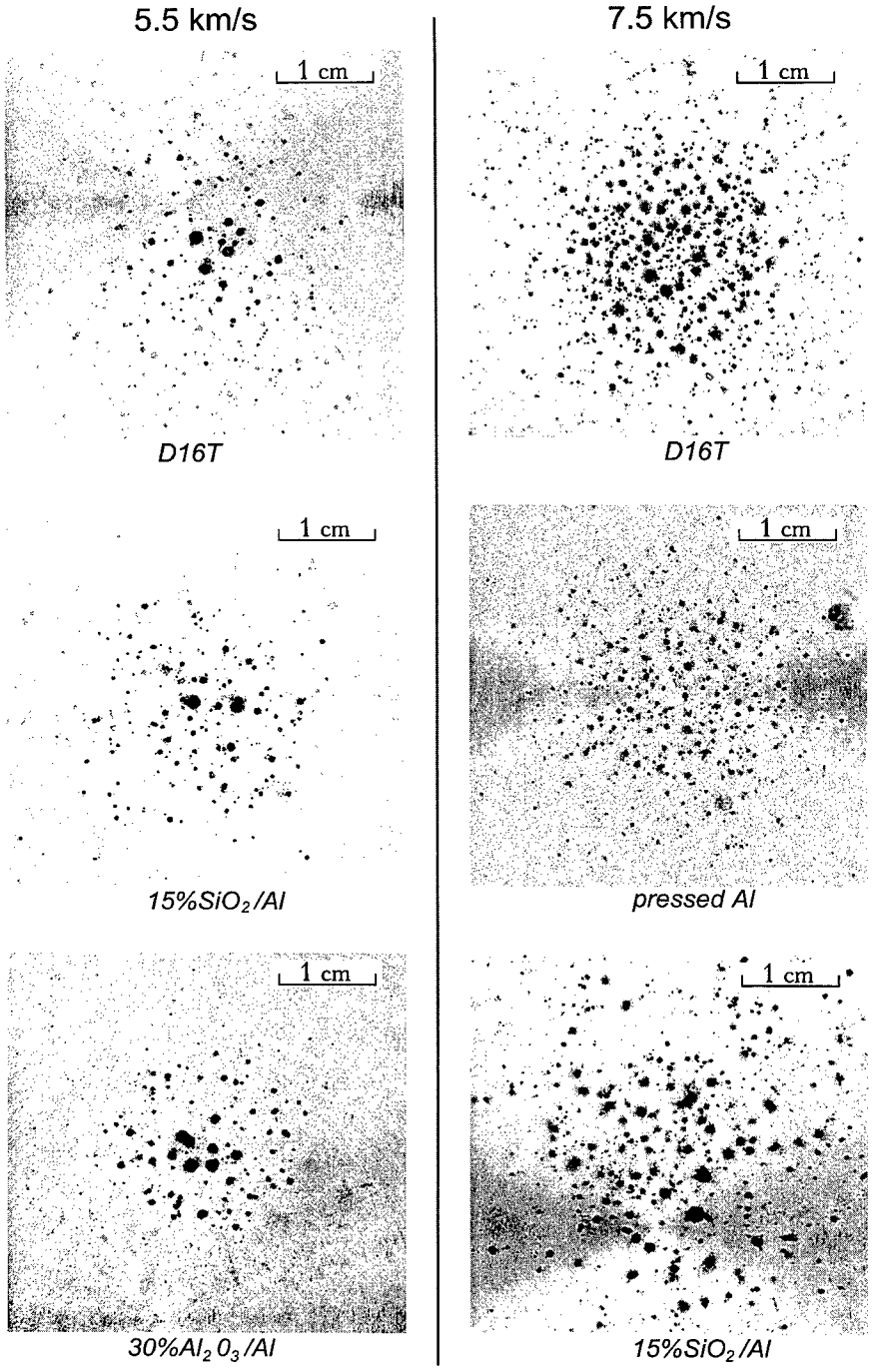

Fig. 2. A back wall viewed from the impact side at velocities 5.5 and 7.5 km/s.

pacts the values of D_d are 35 and 60 mm at V_p = 5.5 and 7.5 km/s, respectively; at the steel/composite impacts the corresponding values of D_d decrease to 23 mm and 43 mm.

Let us consider some possible reasons of decreasing the protection efficiency of bumpers made of metal composites with the embedded ceramic inclusions:

1. *Shield Thickness Variability.* The relative thickness of shields, t_s/d_p, in experiments ranges from 1.1 to 1.3, i.e. shields are rather thick. According to [9], a minimum of P_c/d_p is attained for

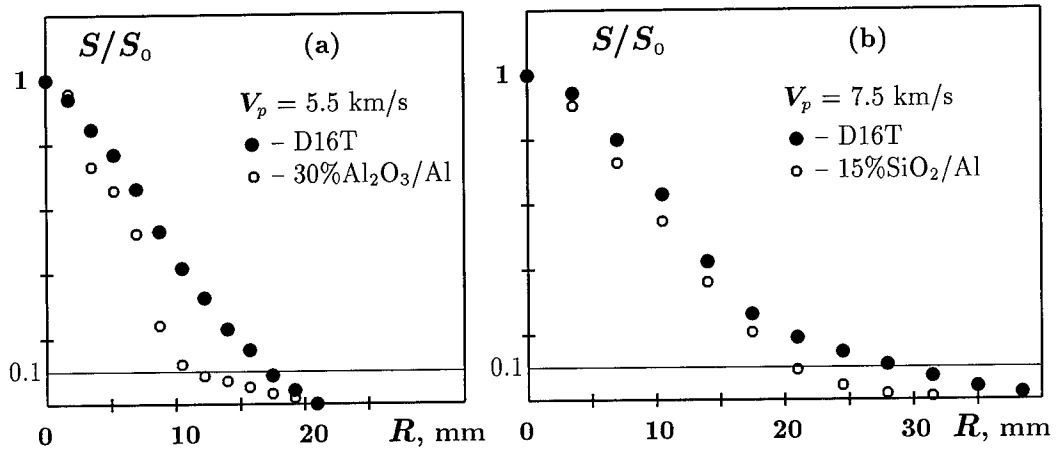

Fig. 3. Radial distribution of areas' sum for all craters lying outside the circle with the radius R for duralumin and composite bumpers.

steel/aluminum impacts with the velocity of 5.5 km/s and t_s/d_p values of 0.6–1.3. Within these t_s/d_p limits the P_c/d_p is essentially invariant. With the impact velocity of 7.5 km/s, the minimum of P_c/d_p is attained at t_s/d_p = 0.4–0.8. For the thicker shields the crater depth increases as $\Delta(P_c/d_p) \cong 0.6\Delta(t_s/d_p)$. For actual $\Delta(t_s/d_p)$ = 0.2, the estimate of P_c/d_p increasing is about 0.12 and can not properly explain the observed increase in the fragment crater depths for the composite shields containing ceramic inclusions.

2. *The Influence of Variations in Impact Pressure.* The composite densities in our experiments are lower than the theoretical value calculated by the mixture rule. The porosity of the materials used ranges from 1 to 3 percent for bumpers made of pressed aluminum powder or the mixture of aluminum and quartz sand. The mixture of aluminum with fine alumina powder has a material porosity of 10–13 percent. Hence, the impact pressure may be considerably changed for shields made of different materials. The shock compressibility of two-component mechanical mixtures is calculated as a sum of the components' compressibilities [11]. Hugoniots of individual components are taken from Ref. [12]. The effect of the composite porosity is considered by the formal simple Thouvenin approach [13]. The initial impact pressures calculated as an unidirectional approximation are presented in two last rows of Table 1.

The estimate of the impact pressure of a steel projectile against porous shields indicates that the pressure is reduced, at most, from 5 to 10 percent with respect to that realized during the impact of a projectile with a duralumin shield. The strength of the metal composites discussed in this study is low, however, their density and shock impedance are rather high and can produce high pressures at collision. Yet, the evident worsening of shielding properties of metal composite bumpers is noted.

At this stage in our research we have concluded that the metal composite bumpers rupture an impacting projectile worse than aluminum bumpers, and the largest craters on witness plate are formed by projectile fragments. At first glance this view is supported by the results described in the next subsection 3 of the paper. Yet, the results of the subsequent experiments with powder bumpers (subsections 4 and 5) has revised our viewpoint.

3. *The Influence of Shear Strength of Shield Materials.* The following two factors are assumed to cause the high-velocity projectile failure at impact: the projectile velocity defines the stress level in its body, and the relative thickness of the shield defines the time of the interaction the projectile with the bumper. The mechanical strength of a bumper material is not an unimportant factor. The last inference is based on the data obtained in experiments on metal shields: aluminum alloys, steel, copper, brass, etc., having different but high values of strength of the order of 100 MPa and above.

Suppose that the deterioration of shielding properties of the pressed composite bumpers is due to a decrease in shear strength of a shield material. During perforation of a thin shield by a high-velocity projectile, the impact pressure value is quickly reduced by rarefaction waves. When a projectile passes through a shield, the level of mechanical stresses at the lateral periphery of the projectile can be reasonably determined by the force interaction at the contact surface dividing the materials of the projectile and the shield. Shear stresses operate principally over the contact surface. The shear strength of the least strength material will define a mechanical stress level at the projectile periphery.

To check this assumption, the measurements of the shear strength, τ_s, of materials used have been performed using the split Hopkinson pressure bar as a punching test device [14]. The method consists of dynamically punching a plate from the test material using a cylindrical indentor. Disk-shaped specimens with 20 mm diameter and 2 mm thickness were tested. Diameters of the indentor and the hardened steel backup ring were equal to 8 and 9 mm, respectively, in the tests. In Table 1, measured values of τ_s are presented for tests done using a strain rate of 40–100 s^{-1}.

Figure 4 gives the results of measuring the maximum crater depth on the backwall plate and the shear strength of materials for the outer bumper. As indicated in the figure, the shielding action of bumpers made of different materials correlates with the shear strength of the material, i.e. the lower the shield material strength, the poorer its shielding action. This inference is true for relatively low values of $\tau_s < 100$ MPa. The conclusion concerning the influence of bumper strength on the degree of dispersion of the projectile striking at the velocity above 5 km/s is inconsistent with present concepts. Conceivably the observed correlation is due to a number of test factors disregarded or not properly considered.

4. *Impact against Shields Made of Powders.* To understand the above correlation of the protective action of shield materials possessing shear strength, we have performed some experiments with a bumper material having zero strength. By keeping the impact velocities such as for the tests with the no-shear strength bumpers, two parameters that determinate, in our view, the fracture of a impacting projectile — the impact pressure P_s and the shield relative

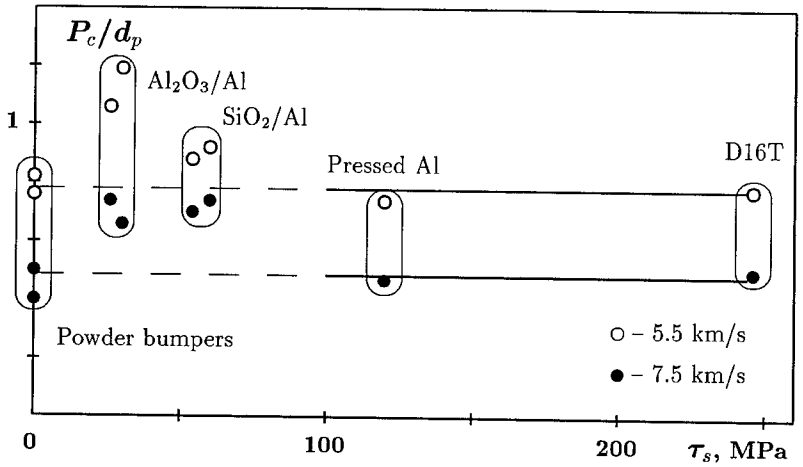

Fig. 4. Maximum crater depth versus the shear strength of bumper materials.

thickness t_s/d_p — have been kept the same. The central idea of these experiments is to remove craters on the backwall due to an impact by bumper fragments and to answer the question: Are the deepest craters in the above tests formed by the impact of debris from the steel projectile or a bumper? When nullifying the shield material strength, a projectile is shattering into the less number of the larger fragments, then a maximum depth of craters is to increase. If the rupture of a projectile is determined by the impact pressure which has to be retained the same as in the

considered experiments, the maximum depth of craters will not vary as against the results of the experiments with duralumin bumpers.

To do this, a thin layer of loosely-packed metal powder was placed on a paper sheet 10 μm thick and used as a bumper. In order to obtain the same necessary values of P_s the following high-porosity mixtures were used: (1) a mixture of lead and copper powders having a density ρ = 3.8 g/cc with the size of particles ranges from 10 to 20 μm, the copper mass fraction μ = 40 %, the porosity Π = 63 %, and (2) the mixture of lead and alumina powders (ρ = 3.5 g/cc, μ = 43 %, Π = 43 %). Although the layer thickness is 1 mm, the areal density of the shield exceeds that of previous experiments by about 1.2–1.4 times. The same calculated estimate of the impact pressure provides 100–104 and 168–172 GPa at impact velocities of 5.5 and 7.5 km/s, respectively, which is close to the impact pressure of a projectile against the duralumin shield. The shear strength of these materials appears to be equal to zero.

Figure 5 shows the distribution of craters on the backwall plates for the similar impacts against two different bumpers made of powder mixtures. A powder bumper significantly reduced the number of fragment craters to 50–60 as compared to 500–1000 for impacts against the duralumin shield. A drastic change in the backwall failure is due to the absence of large fragments of shield material. The occurrence of rather deep craters with $P_c \approx 0.5$–0.8 mm cannot be attributed to the small size of individual grains making up a bumper. All the craters observed appear to be formed by debris from the steel projectile. The depth of the largest craters on a witness plate is close to the data for pressed aluminum and duralumin shields (Figs. 1, 4). It is noted, that the area distribution of craters has the random nature for powder bumpers, and it has not the axisymmetric pattern which is typical for solid bumpers (Figs. 2, 5).

For all tests with solid, composite and powder bumpers the impact pressure, the bumper areal density and the bumper thickness are nearly constant. But the maximal crater depth formed by debris fragments is greater in the case of composite bumpers. If not assuming that in this case a projectile is broken up into the less number of fragments for a variety of uncertain reasons, the observed increase of the crater depth on the witness plate in the tests with composite bumpers is caused by appearing the larger fragments of the composite shield material in a debris cloud.

The results of these qualitative experiments provide a support for the view that the impact pressure play a basic role in damage an impacting projectile. However, the shield material strength (unless it is zero or more than 100 MPa) affects the degree of dispersing a shield material. A low strength is favorable to the formation of rather large fragments of bumper material in

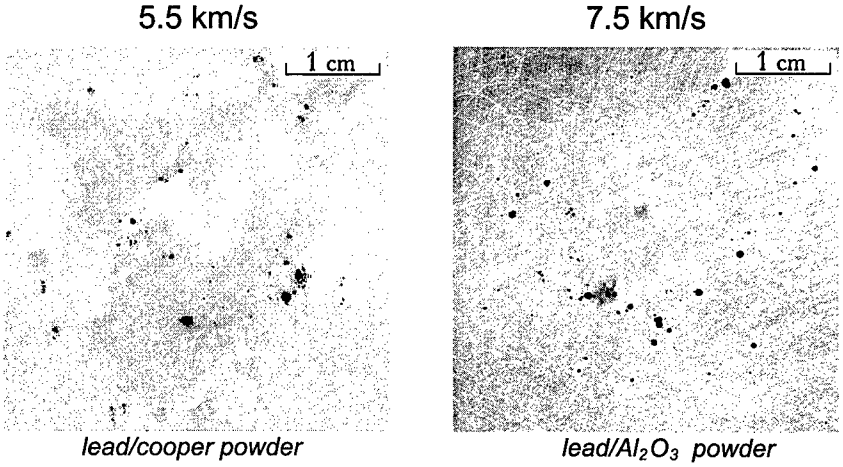

Fig. 5. A back wall viewed from the impact side in case of powder bumpers. Bumper materials are as follow: at left – a lead/copper powder screen, V_p = 5.5 km/s; at right – a lead/Al_2O_3 powder screen, V_p = 7.5 km/s.

the debris cloud and results in a decrease of the efficiency of shields made of pressed dispersed metal composites.

5. *Effect of The Bumper Areal Density.* It is qualitatively clear that not only the shield thickness effects on the time of interaction a projectile with the bumper but its areal density as well. The larger density is favourable for increasing the interaction time, and the energy sharing lost by the projectile during the perforation of a bumper (as in numerical simulations by Riney at the impact velocity of 15 km/s with aluminum projectiles against laminated bumpers with changing their areal density five-six times [15]). In our experiments the $t_s\rho_s$ has changed no more than 1.3 times. Most likely, this being so, we have not observed the effect of $t_s\rho_s$ on the results. This view is qualitatively supported by the results of the next two tests, wherein on keeping the impact pressure the areal mass of shields made of powders has been changed twofold with increasing or decreasing a bumper volume density. With a low impact velocity, this has enabled us to simulate an impact at the higher velocity by increasing the impact pressure caused by rising the shock impedance of the bumper material, and conversely.

In the first test a 1 mm thick layer of lead powder having a bulk density of $\rho_s = 6.67$ g/cc and $t_s\rho_s = 0.67$ g/cm^2 is used as a bumper. For the steel/bumper impact at $V_p = 5.5$ km/s the calculated impact pressure equals to 172 GPa, which corresponds in pressure to the projectile impact at $V_p = 7.5$ km/s with the above shields. The depth of the deepest crater on the backwall $P_c/d_p \leq 0.4$ is not over the value of 0.5 typical for impacts at the velocity of 7.5 km/s (Figs. 1, 3).

In the second test the projectile impacts upon the 1 mm layer of copper powder having $\rho_s = 1.61$ g/cc and $t_s\rho_s = 0.16$ g/cm^2 at $V_p = 7.5$ km/s. The impact pressure of 105 GPa is compatible with the pressure which relized by projectile impact at the velocity of 5.5 km/s against aluminum shields with $t_s\rho_s \cong 0.3$ g/cm^2. The depth of penetration rises sharply to $P_c/d_p \approx 1$, which is higher by 25 percent than the value of 0.8 characteristic for impacts with the velocity of 5.5 km/s. The diameter of the damage area in the back wall is reduced to 20 mm as against 40–60 mm in the case of the denser shields. The results uniquely show that in parallel with the impact pressure not only does the shield thickness plays the important role in rupturing the impacting projectile, but the bumper areal density also plays. The effect of areal density appears to be reflected by changes in the effective time of interacting the projectile with the shield and in the remaining kinetic energy of projectile fragments.

So, the results of tests with porous powder bumpers allow (1) to understand the reason of formation of the deeper craters on the backwall for tests with metal composite bumpers, and (2) to favour once more the view that the impact pressure and the shield thickness, and more precisely, it's areal density play a crucial role to shatter the impacting projectile.

CONCLUSION

The protection efficiency of thin shields made of metal composites based on the aluminum matrix containing the disperse ceramic inclusions of SiO_2 or Al_2O_3 (at a mass fraction of 15 and 30 percent) by impact of a spherical steel projectile at the velocity of 5.5 and 7.5 km/s is considered for a Whipple-type shield. The bumpers made of these materials are shown to have the poorer protection efficiency than those made of the duralumin alloy when used with steel impactors. There is a need to perform further researches with the resulting justified advisability of using the metal composites, Al-matrix plus embedded ceramic inclusions, as the first bumpers for constructing the meteoroid protection schemes in case of hypervelocity aluminum projectiles.

It is shown that by impact of the hypervelocity steel projectile the shield material strength, if it is rather low but not zero, may essentially affect the damage pattern of the backwall in spite of the high level of realized impact pressures.

Acknowledgements—This research was supported by the Russian Foundation for Basic Researches, grants 96-01-01951 and 96-15-96264.

REFERENCES

1. B. G. Cour-Palais and J. L. Crews, A multi-shock concept for spacecraft shielding. *Int. J. Impact Engng.*, **10**(1–4), 135–146 (1990).
2. E. L. Christiansen and J. H. Kerr, Mesh double-bumper shield: a low-weight alternative for spacecraft meteoroid and orbital debris protection. *Int. J. Impact Engng.*, **14**(1–4), 169–180 (1993).
3. E. L. Christiansen, J. L. Crews, J. E. Williamsen, J. R. Robinson, and A. M. Nolen, Enhanced meteoroid and orbital debris shielding. *Int. J. Impact Engng.*, **17**(1–6), 217–228 (1995).
4. A. J. Stilp and K. Weber, Debris clouds behind double-layer targets. *Int. J. Impact Engng.*, **20**(6–10), 765–778 (1997).
5. J. H. Robinson and A. M. Nolen, An investigation of metal matrix composites as shields for hypervelocity orbital debris impact. *Int. J. Impact Engng.*, **17**(1–6), 685–696 (1995).
6. V. V. Silvestrov, A. V. Plastinin, V. V. Pai, and I. V. Yakovlev, Hypervelocity impact on isotropic composites with metal or ceramic inclusions. *Int. J. Impact Engng.*, **20**(6–10), 733–742 (1997).
7. V. M. Titov, Yu. I. Fadeenko, and N. S. Titova, Acceleration of solid particles by cumulative explosion. *Doklady Akademii Nauk SSSR*, **180**(5), 1051–1052 (1968).
8. F. Schäfer, E. Schneider, M. Lambert, and M. Mayseless, Propagation of hypervelocity impact fragment clouds in pressure gas. *Int. J. Impact Engng.*, **20**(6–10), 697–710 (1997).
9. L. A. Merzhievskii and V. M. Titov, Shielding properties of thin bumper at hypervelocity impact. *J. Applied Mechanics and Technical Physics*, **2**, 135–139 (1977).
10. V. M. Titov and V. V. Silvestrov, Acceleration of solid spherical projectiles by cumulative explosion of tubular charge of high explosive. Report of Lavrentyev Institute of Hydrodynamics, Novosibirsk (1994).
11. A. N. Dremin and I. A. Karpukhin, A method of Hugoniot determination for the disperse matter. *J. Applied Mechanics and Technical Physics*, **3**, 184–188 (1960).
12. Compendium of shock wave data. General Editor M. van Thiel. Lawrence Livermore Laboratory, University of California. Vol. 1–2 (1977).
13. J. Thouvenin, Effect of a shock wave on a porous solid. *Proc. Fourth Symposium (Int.) on Detonation*, pp. 258–265, October 12–15, White Oak, Maryland (1965).
14. C. Mazeau, L. Beylat, P. Longère, and P. F. Louvigné, On the quantitative evaluation of adiabatic shear banding sensitivity of various titanium alloys. *Journal de Physique IV*, **7**, 429–434 (1997).
15. T. D. Riney, Numerical evaluation of hypervelocity impact phenomena. In *High-Velocity Impact Phenomena*, (edited by Kinslow), pp.166–177, Academic Press, New York and London (1970).

PERGAMON International Journal of Impact Engineering 23 (1999) 869–882

INTERNATIONAL JOURNAL OF IMPACT ENGINEERING

www.elsevier.com/locate/ijimpeng

APPLICATION OF STEADY STATE MAXIMUM ENTROPY METHODS TO HIGH KINETIC ENERGY IMPACTS ON CERAMIC TARGETS

LARRY L. SMALLEY* and JAMES K. WOOSLEY**

* Department of Physics, University of Alabama in Huntsville, Huntsville, AL 35899
**Teledyne Brown Engineering, 300 Sparkman Drive, Huntsville, AL 35807

Summary—The maximum entropy method is used to investigate the fragmentation and pulverization of ceramics subjected to high energy impacts. Since the exact physical processes that occur during high energy impacts on ceramic targets is not completely known, the calculation of the details of these interactions can at best be approximate. However, many of the general features of what will happen are known, such as conservation of energy-momentum and thermodynamic laws act as constraints on any model. The maximum entropy incorporates by the method of constraints everything known to be correct into the model. The more constrained the system, the better the model. Several important developments arise: It is important that the ceramic be confined long enough for the ceramic to be pulverized; and there will be, in general, a lower bound on the minimal size of the pulverized ceramics consistent with the properties of the ceramic and the kinetic energy of the penetrator. A sample application for a steady state erosion process due to the abrasive ceramic powder acting on the penetrator is discussed. The transfer of energy-momentum from the penetrator to the ceramic is shown to depend on the degree of pulverization and characteristic frequency associated with the impact event. Improvements and future directions for study are described in the conclusions. © 1999 Elsevier Science Ltd. All rights reserved.

1 Introduction

1.1 General Considerations

Impact analysis is in the strength dominated regime of impacts from about $0.5 - 2.0 km/s$[1] which is difficult to quantify. The behavior of high strength materials straddles the relatively easy hydrodynamics response in the hypervelocity range and the *elastic/plastic* response at lower velocities. Experimental configuration, material preparation, material history, crack dynamics, porosity, amongst other considerations, can result in 10 -100% (or more) variation in penetration resistance, even for samples of similar material composition and total areal density. The brittleness of ceramic targets complicates the impact response even further since even the experimental configuration, *e.g.* lateral confinement of ceramic tiles, can have enormous consequences.

An improved impact model should depend more on basic physical properties, both microscopic and macroscopic that is t independent of experimental details and configurations. A strictly analytic

*Supported in part by U S. Army Contract No. DAAE07-91-C-R007
†Email: smalley@pluto.cs.uah.edu

0734-743X/99/$ - see front matter © 1999 Elsevier Science Ltd. All rights reserved.
PII: S0734-743X(99)00131-1

model is still only possible in the phenomenological or probabilistic sense. The general approach is to begin with what is known and predict from that *as well as possible*. The maximum entropy method will do just that – the prediction is only as good as the known principles satisfied which are included as constraints. Once the known constraints on the variables are consistently incorporated into the solution, an improved foundation for incorporating momentum balance or hydrodynamics to solve the deterministic aspect of the problem exists.

The maximum entropy method is highly suited for single events involving global conservation laws such as conservation of energy or other features that occur such as constancy of volume. As a first step towards a time dependent process, a steady state maximum entropy method is assumed with uniform rates In this simple steady state model of fragmentation, an erosion dominated effective penetration depth of the impactor can be predicted.

1.2 Maximum Entropy Method – Equilibrium Processes

The maximum entropy method very closely parallels the calculation of the entropy for a thermodynamic system. The entropy S is

$$S = k \ln w, \tag{1}$$

where w is the number of ways that states can be distributed in phase space given that every distribution is equally likely and k is a constant which in thermodynamic problems is given by the Boltzmann constant. In reality, the maximum entropy process determines k *inter alia* from the constraint forces. In terms of the distribution p_n, this is written, up to a constant entropy term,

$$S = -k \sum_{n=0} (p_n \ln\ p_n - p_n). \tag{2}$$

If the distribution, p_n, is changed, the trend is to decrease S because of the additional information about the state of the system. This is contrary to the Second Law of Thermodynamics which states that $\Delta S \geq 0$. Thus S is subject to the condition that it is maximized with respect to certain constraints, many of which are readily intuitive:

$$\text{Normalization}: \quad \sum_n p_n = 1, \quad \text{Energy}: \sum_n e_n p_n = E, \tag{3}$$

where E is the total energy and e_n is the energy of the n^{th} particle, and so forth.

Suppose the distribution of a set of states is sought such that the energy of the n^{th} state is given by $e_n = ne_o$. [This might be a collection of states distributed over a complete set of quantum states.] This is equivalent to a variational problem such that

$$\delta S = k\delta \left\{ \sum_n [-p_n ln p_n + p_n + \lambda p_n - \beta e_n p_n] \right\} \equiv 0, \tag{4}$$

where λ and β are Lagrange multipliers for the normalization and energy constraints respectively. Then

$$p_n = e^{\lambda} e^{-\beta e_n p_n} p_n = \frac{e^{-\beta e_n}}{Z}. \tag{5}$$

where for $e_n = ne_o$

$$Z = \sum_n e^{-\beta e_n} = \frac{1}{1 - e^{-\beta e_o}}, \tag{6}$$

is called the partition function. The average value of n is then

$$< n >= \frac{\sum_n n e^{-n\beta e_o}}{Z} = -\frac{\partial}{\partial(\beta e_o)} \ln\ Z = (e^{\beta e_o} - 1)^{-1}, \tag{7}$$

and the average energy is simply $< e_n >=< n > e_o$.

In Sect.2 the equilibrium maximum entropy process is discussed for fragmentation and extended to steady state processes in Sect.3. The properties of ceramic materials during high kinetic energy collisions is discussed in the last section.

2 Total Fragmentation Processes

Englman, Rivier and Jaeger [2] have extended the maximum entropy method to the total fragmentation (or shattering) of a system due to an explosion or a high energy impact. They subject their system to an additional constant volume constraint for the total of all fragments. The fragments are assumed to be roughly spherically shaped with linear size a_i. The energy of a particle is then given by

$$e_i = \frac{2}{3}\pi\rho a_i^3 u^2 + \frac{2}{5}\pi\rho a_i^5 \dot{\epsilon}^2 + \frac{4}{6}\pi a_i^3 \frac{\sigma^2}{K} + C a_i^{4.5} + 4\pi\gamma a_i^2 (1 - \frac{a_i}{R}), \tag{8}$$

where ρ is the density. The first term is the Kinetic energy (KE) of the center of mass (CM). The second is the KE about the CM where $\dot{\epsilon}$ is the trace of the stretching tensor rate which is called the dilation (or strain) rate. Given a rate of fractional change of volume (about the CM)

$$\frac{\partial}{\partial t}\left\{\frac{\Delta V}{V}\right\} = \frac{\partial}{\partial t}\left\{\frac{\Delta a^3}{a^3}\right\} = \frac{\partial}{\partial t}\left\{3\frac{\Delta a}{a}\right\} = \frac{3}{a}\frac{\partial a}{\partial t} = 3\dot{\epsilon}, \tag{9}$$

where each part of a particle experiences a velocity $\dot{a} = a\dot{\epsilon}$.When the rate $\dot{\epsilon}$ is constant, then [3]

$$KE_{dil} = \int \frac{1}{2}(a_i\dot{\epsilon})^2 dm = \frac{2}{5}\pi\rho a_i^5 \dot{\epsilon}^2. \tag{10}$$

For a uniform expansion of the particle, the strain energy of distortion is zero and only hydrostatic strain energy is involved. This means that the fragments are stress free upon formation so that the third term represents the stored elastic energy available for *fragmentation*[3] where σ is the stress and K is the bulk modulus.[1] The fourth term indicates that a particle may suffer internal damage (crack) giving an energy term proportional to the particle volume to the 3/2 power. The last term is the incremental surface energy acquired by a particle.[3] The surface energy of a fragment is

$$\Gamma_i = 4\pi a_i^2 \gamma, \tag{11}$$

where the surface energy density γ is given in terms of the density, ρ, fracture toughness, K_{IC} ,and the sound velocity, c, by

$$\gamma = \frac{K_{IC}^2}{2\rho c^2}. \tag{12}$$

The form of the fifth term depends on the assumption of an original volume $V = \frac{4}{3}\pi R^3$. If all particles fractured to the same size a_i, then there would be $N = (R/a_i)^3$ particles. Since the surface energy of the original body is $\Gamma = 4\pi R^2\gamma$, then

$$N_i = N(4\pi a_i^2\gamma) = 4\pi a_i^2 \gamma \left\{\frac{R}{a_i}\right\}^3 = \Gamma\frac{R}{a_i}. \tag{13}$$

[1]Note the missing exponent on σ in Ref.1.

Then the incremental surface energy acquired per particle is

$$\frac{\Delta\Gamma}{N} = \frac{\Gamma}{N}\{\frac{R}{a_i} - 1\} = \Gamma_i\{1 - \frac{a_i}{R}\}. \tag{14}$$

Several comments concerning these terms are possible: First, in the impact situation, the particles do not acquire the large translational KE as in an exploding solid since the material is confined to a region below the impactor. Secondly the volume of the ceramic does not remain constant during impact. Some of the ceramic may be ejected to the side and rear of the projectile. New material continually comes under the grinding influence of the impactor whereas much more of the material may be forced as a whole to move in the direction of the impactor. Here the fragmentation and pulverization of the ceramics during impact is assumed to be a steady state process.

In the region of the ceramic in front of the impactor, there develops a Hertzian crack zone called the fracture conoid.[4, 5, 6, 7] The conical fracture surface allows the force of the impact to be spread over a larger cross sectional area, say over some backup plate behind the ceramic.[8]

As the impact proceeds, the ceramic within the conoid region is fractured by the multi reflection of the shock wave and continually pulverized by the compressive force of the advancing impactor. [An interesting description of this fracture zone is shown in a figure based upon a calculation by Mescall & Tracy for alumina under confinement.[9] The multi reflection pattern of the hoop tensile failure is quite evident.] Eventually the ceramic becomes sufficiently pulverized so that either the impactor forces the particles out of the way into the crack zones, or the particles become sufficiently small to flow around the impactor in the aft direction. This latter effect further degrades the impactor through erosion. Thus hard, abrasive ceramics,[8] such as alumina, should be very effective at eroding the penetrator compared with solely metallic targets. In the literature there are statements such as, "...the fracture of the ceramic consumes a negligible amount of energy compared to that required for erosion..."[10] However what is missing from this quote is that the amount of energy consumed in fragmentation depends on how finely the ceramic is pulverized. The efficiency of pulverization depends strongly on shear strength of the comminuted ceramic in the near region below the impactor. As long as the ceramic is subjected to a confining pressure, the shear strength remains high.[11] It is not difficult to show in the model described above, that the energy necessary to pulverize the ceramic maximizes as the mean size of the particle goes to zero. Thus at some point in the pulverization process, there must be a cross over particle size for which the energy degradation due to crushing competes favorably with other energy absorption mechanisms.

Lastly the model described above assumes that the crushing process produces *roughly* spherically symmetric particles. Experimentally this is not the case since in many cases the shapes of fragments are more comparable to to parallelepiped geometry. For example, the shape distribution of particles observed in the fragmentation of asteroids (large ceramic objects) during collisions[12] is found to be ellipsoidal and to have an average aspect ratio for the semimajor axes of $2 : \sqrt{2} : 1$. The same effect with approximately the same aspect ratios has been found in the fragmentation of ceramics, such as SiC, under high rates of strain in the laboratory.[13] This has two immediate consequences:

1. The energy e_i of the particles in the above model is missing three rotational degrees of freedom.
2. The grinding efficiency of rotating ellipsoidal particles is enhanced over spheres due to the increased in friction between the contacting (eroding) surfaces.

The incorporation of a rotational KE term uses an effective moment of inertia, I_{eff}

$$\bar{e}_{i,rot} = \frac{3}{2} I_{eff}\omega_i^2 = \zeta\pi a_i^5\omega_i^2, \tag{15}$$

where ζ is a parameter that describes the effective 1–D moment of inertia, and ω_i is the average angular velocity of an ellipsoidal particle which is modeled with aspect ratios $2 : \sqrt{2} : 1$. As indicated earlier, for microscopic particles, equipartition of energy implies $a_i\omega_i \approx u$.

Finally the incremental surface energy acquired in the model of Englman, *et al*,[2] is modified since it depends on the original characteristic size of the body R. This has no exactly equivalent meaning for the case of the impacts. For the case of long rod penetrator on ceramics a relevant dimension could be the cylindrical radius of the impactor. Another possibility is to let R be the thickness of the ceramic plate. Alternatively since $R \gg a_i$, neglecting the a_i/R part of the term for the incremental surface energy just gives an upper bound which can not be very much larger than the entire original term. This latter approach is adopted.

3 Maximum Entropy Method – Non-Equilibrium Processes

3.1 Steady State Processes

Experimentally, the particles are lumped into discrete bins with "linear" *sizes* [2]

$$(i - \frac{1}{2})\ell < a_i \leq (i + \frac{1}{2})\ell, \tag{16}$$

with $i = 1, 2, ...I_b$, where ℓ is some experimentally motivated minimal size, and ℓI_b is consistent with the size of the original system (for example in our case this might be the thickness of the ceramic plate or the distance that the penetrator moves in some characteristic time).

There are at least two ways to describe the fragmentation process. One is a generalization of the method which seeks the number of fragments per unit time n_i for the i^{th} particle class of size a_i. Details of this method can be found in Englman, et al.[2] An inherent difficulty in this method occurs because the variation is applied to each individual bin. Since the energy constraint is over the entire system, there can not be any overall constraint (such as on the energy) for the individual bins. Thus because of the way the probability distribution comes into the average number of particles per bin and the total energy, along with the normalization condition, the interpretation of the Lagrange multiplier for the energy constraint β is therefore non standard.

The second method proposed here treats the bins collectively. The number of fragments per unit time n_i in the i^{th} bin associated with particle class of size a_i is sought. The numbers n_i and i will have a probability distribution $p(n_i, i)$ which satisfies

$$\sum_i \sum_{n_i} p(n_i, i) = 1. \tag{17}$$

Note that for a uniform rate process, the $p(n_i, i)$ are constants, but now we must treat the n_i as rates which progress uniformly in time. The "average" value of n_i is assumed to be given

$$\sum_{n_i} n_i p(n_i, i) =< n_i >, \tag{18}$$

which then represents the "average" number of *particles/time* found in the i^{th} bin. The significance of this average will be discussed later. Equation (*18*) will also impose restrictions on the probability distribution $p(n_i, i)$. The average value of the total number of particles for all bins then requires a sum over i in Eq. (*18*). However the total number of particles is not a good constraint in the variational problem.

In principle there is some characteristic frequency ν (the inverse time constant τ) associated with the steady state impact process. Note that the sums over n_i in Eqs.(*17-18*) make sense only

if we can define the time independent summation index, $\bar{n}_i = n_i/\nu$ where ν is the characteristic frequency discussed above. The bar notation, except where a difficulty might arise in interpretation, will be suppressed.

The distribution over the bins is described in terms of the minimum particle size ℓ associated with the fragments as shown in Table I.

So far this is similar to the method of Englman,*et al;* [2] however both indices i and n_i in Eq.(*17*) are summed in comparison with just n_i in the first method.

The joint probability distribution is written

$$p(n_i, i) = p(n_i)p(i), \tag{19}$$

where $p(n_i)$ is a probability distribution over particle numbers in the i^{th} bin, and p_i is a probability distribution of a particle being in the i^{th} bin.The normalization is still given by Eq.(*17*)

$$\sum_i \sum_{n_i} p(n_i, i) = 1. \tag{20}$$

but the hypothesis of joint probability now implies

$$\sum_{n_i} p(n_i) = 1, \quad \text{and} \quad \sum_i p_i = 1, \tag{21}$$

are satisfied simultaneously. Therefore Eq.(*18*) is true for every p_i, or using the probability $p(n_i)$ alone, the "average" is

$$\sum_{n_i} n_i p(n_i) =< n_i >' . \tag{22}$$

Note from Eq.(*18*) the average number of particles in the i^{th} bin is now

$$< n_i >= p_i < n_i >' . \tag{23}$$

Table I. Bin distribution using minimum fragment dimension ℓ. Each bin is depicted by a pair of vertical bars $|\cdots|$. The width of the individual bins is given by ℓ and the center-to-center distance between bins is also given by ℓ.

	ℓ	ℓ	ℓ	ℓ	ℓ	
Bins	$\leftarrow\cdots\mid$	$\cdots\rightarrow\leftarrow\cdots\mid$	$\cdots\rightarrow\leftarrow\cdots\mid$	$\cdots\rightarrow\leftarrow\cdots\mid$	$\cdots\rightarrow\leftarrow\cdots\mid$	$\cdots\rightarrow$
Bins	$\cdots\rightarrow\mid$	$\leftarrow\cdots\cdots\rightarrow\mid$	$\leftarrow\cdots\cdots\rightarrow\mid$	$\leftarrow\cdots\cdots\rightarrow\mid$	$\leftarrow\cdots\cdots\rightarrow\mid$	$\leftarrow\cdots$
		ℓ	ℓ	ℓ	ℓ	ℓ
Bin label	0	1	2	3	4	$5\cdots i$
Fragment size	0	ℓ	2ℓ	3ℓ	4ℓ	$5\ell\cdots i\ell$
Particles in bin i	n_0	n_1	n_2	n_3	n_4	$n_5\cdots n_i$

The rate of total energy is now given by

$$E = \sum_i \sum_{n_i} e_i n_i p(n_i, i) = \sum_i e(li) p_i \sum_{n_i} n_i p(n_i), \tag{24}$$

where in this model

$$e_i = \frac{2}{3}\pi\rho a_i^3 u^2 + \zeta\rho a_i^5\omega^2 + \frac{2}{5}\pi\rho a_i^5\dot{\epsilon}^2 + \frac{2}{3}\pi a_i^3\frac{\sigma^2}{K} + Ca_i^{4.5} + 4\pi\gamma a_i^2. \tag{25}$$

Since this represents the steady state (uniform) amount of energy supplied to the target (or removed from the penetrator) per unit time, then the energy described by Eq.(*24*) is a good constraint. Another good constraint is found if the volume rate of material removed from the target is also uniform

$$V = \sum_i \sum_{n_i} a_i^3 n_i p(n_i, i) = \sum_i \ell^3 i^3 p_i \sum_{n_i} n_i p(n_i). \tag{26}$$

Since particle number conservation in the variation is not imposed, then if E increases, the volume may or may not change depending on how the energy is distributed over the bins.

3.2 Variational Problem

The variational problem now becomes

$$\begin{aligned} \delta S = k\delta \textstyle\sum_i \sum_{n_i} \{ & -p(n_i)p_i \ln[p(n_i)p_i] + p(n_i)p_i + \lambda p(n_i)p_i \\ & -\beta e(\ell i) n_i p(n_i)p_i + \xi \ell^3 i^3 n_i p(n_i)p_i \} \end{aligned} \tag{27}$$

where β and ξ are the Lagrange multipliers associated with the energy and volume constraints respectively. Note that the Lagrange multipliers β and ξ depend on time so the the $p(n_i)$ are constant probabilities. The variations, using the variables $p(n_i)$ and p_i yields the same results for the joint probability function

$$p(n_i)p_i = e^{\lambda} \exp[-\beta e(li) n_i + \xi \ell^3 i^3 n_i]. \tag{28}$$

Using the normalization condition Eq.(*21*) on the joint probability given by Eq.(*28*) gives

$$p_i = e^{\lambda} Z_i, \tag{29}$$

where the time independent partition function associated with the i^{th} bin is

$$Z_i = \sum_{\bar{n}_i} \exp[-\bar{\beta} e(li) + \bar{\xi} \ell^3 i^3] = \frac{1}{1 - \exp[-\bar{\beta} e(li) + \bar{\xi} \ell^3 i^3]}, \tag{30}$$

where for the steady state process $\beta = \bar{\beta}\tau$ and $\xi = \bar{\xi}\tau$ are introduced such that $\tau\nu = 1$. Substituting Eq.(*29*) into Eq.(*28*) gives the number probability for the i^{th} bin

$$p(n_i) = \frac{1}{Z_i} \exp[(-\beta e(li) + \xi \ell^3 i^3) n_i]. \tag{31}$$

Applying the normalization conditions Eq.(*21*) to Eq.(*29*) gives the Lagrange multiplier λ for probability conservation

$$e^{\lambda} = \frac{1}{Z} = \frac{1}{\sum\limits_i Z_i}, \tag{32}$$

where the total partition function is defined in the last step. The number probability distribution Eq.(*31*) can be used in the volume constraint Eq.(*26*) along with Eqs.(*29, 30 & 32*)

$$V = \sum_i \sum_{n_i} \ell^3 i^3 n_i \frac{p_i}{Z_i} \exp[(-\beta e(li) + \xi \ell^3 i^3) n_i] = \nu\, e^{\lambda} \sum_i \frac{\partial Z_i}{\partial \bar{\xi}} = \nu \frac{\partial}{\partial \bar{\xi}} \ln\, Z. \tag{33}$$

Similarly the energy constraint Eq.(*26*) becomes

$$E = \sum_i \sum_{n_i} e(li) n_i \frac{p_i}{Z_i} \exp[(-\beta e(li) + \xi \ell^3 i^3) n_i] = -\nu \frac{\partial}{\partial \bar{\beta}} \ln\, Z. \tag{34}$$

The average number of particles for the i^{th} bin given by Eq.(*23*) now becomes, using Eqs.(*29* & *31*),

$$< n_i >= p_i \sum_{n_i} n_i p(n_i) = \frac{\nu}{Z} \left\{ \left[1 - \exp[(-\bar{\beta} e(li) + \bar{\xi} \ell^3 i^3) n_i] \right] \left[\exp[(\bar{\beta} e(li) + \bar{\xi} \ell^3 i^3) n_i] + 1 \right] \right\}^{-1} \quad (35)$$

The average number of particles for all bins is then

$$< n >= \sum_i < n_i >' p_i = \sum_i < n_i > . \quad (36)$$

Thus the problem has been reduced to finding the total partition function Z.

It may seem reasonable in the impact process that the volume term should not be included because the penetrator is losing energy. Except for the steady state process discussed here, this would certainly be the case. As its energy is degraded, the volume of the ceramic removed from the target per unit time is (normally) a decreasing function. However for thin plates (and the steady state process), including a volume (rate) term in the variational problem may have some merit since the degradation would be small.

Although $e_i \to 0$ as $a_i \to 0$, in the pulverization process E converges to its largest value as $a_i \to \ell$ will be shown. This is obscured by the fact that the summand in Eq.(??) for $i = 0$ goes to infinity. However for $i = 0$, a_i lies outside the physical range since its smallest value is ℓ. From earlier discussion this means that in the limit of very finely pulverized powder, the surface term dominates the particle energy term for these classes of particles providing ℓ is sufficiently small. Thus at some particular size, a_i, the energy to form a surface becomes greater than the CM KE. In fact because of the specific a_i dependence of each term in e_i in Eq.(*25*), the surface term dominates all the other terms in e_i for sufficiently small a_i, depending however, on the individual parameters in Eq.(*25*). Roughly this occurs when the sum of the first two terms in e_i is of the same order of magnitude as the last term, *i.e.* when

$$\gamma \geq \rho a_i u^2. \quad (37)$$

Alternatively this occurs, using Eq.(18), when the particle size satisfies

$$a_i \leq \frac{K_{IC}^2}{2\rho^2 u_p}^4 , \quad (38)$$

where the speed of sound is taken equal to the CM velocity which is about equal to the particle velocity for a powder (*e.g.* the speed of sound in sand is about 100 m/s). Nominally for alumina, this limit occurs for $a_i \simeq 0.02\ \mu$. Another measure is given by the nominal fragment diameter found by Grady for dynamic fragmentation[14]

$$d = 2a_i = \left[\frac{\sqrt{20} K_{IC}}{\rho c \dot{\epsilon}} \right]^{\frac{2}{3}} , \quad (39)$$

which is obtained by minimizing the energy of the third and sixth terms in e_i. Note that c in Eq.(*39*) is the speed of sound in bulk matter. For alumina this can be as large as *11.6 km/s* for sapphire. Typically the size given by Eq.(*39*) is several orders of magnitude larger than the previous limit cited above in Eq.(*38*), but the exact values depend on the strain rate. However the energy associated with these terms at their minimum is of the order of 0.1% of the KE of CM described previously.

The energy given by Eq.(*34*) is considered in the limit that the surface term dominates the particle energy. For this case the thermal parameters $\bar{\beta}$ and $\bar{\xi}$ are also assumed sufficiently small so that $\bar{\beta}e(\ell i)$ and $\bar{\xi}\ell^3 i^3$ are both less than *1* for small i. Equation (*34*) becomes

$$E = \frac{\nu}{Z}\sum_i \left\{ \frac{e(\ell i)}{\left[e^{\bar{\beta}e(\ell i)-\bar{\xi}\ell^3 i^3} - 1\right]\left[1 - e^{-\bar{\beta}e(\ell i)+\bar{\xi}\ell^3 i^3}\right]} \right\}. \tag{40}$$

Both the summand and Z go to infinity for small i. When $i \to 0$, they depend strongly on the surface particle energy $e(\ell i) \approx 4\pi\gamma\ell^2 i^2$. Thus to lowest order

$$E = \nu \lim_{i\to 0}\left\{ \frac{4\pi\gamma\ell^2 i^2}{\bar{\beta}} 4\pi\gamma\ell^2 i^2 - \bar{\xi}\ell^3 i^3 \right\} = \frac{\nu}{\bar{\beta}}. \tag{41}$$

However a similar lowest order approximation of Eq.(*33*) for the volume gives

$$V = \nu \lim_{i\to 0}\left\{ \frac{\ell^3 i^3}{\bar{\beta}} 4\pi\gamma\ell^2 i^2 - \bar{\xi}\ell^3 i^3 \right\} = 0, \tag{42}$$

which does not give a reasonable estimate of the volume rate. Thus the partition function Z will be considered directly.

First it is noted in both Eqs.(*41-42*) that the limit of $i \to 0$ is **not** in the physical range of the particle fragments. Experimentally there are no particles in the 0^{th} bin. The first physical bin corresponds to $i = 1$, *i.e.* the minimum experimental value of $a_i = \ell i$. This is most evident in the infinite value from the direct calculation of Z from Eqs.(*30* & **??**). Thus it is required that the sum start from $i = 1$ which corresponds most closely with experiment, *i.e.*

$$Z = \sum_{i=1}^{\infty}\left\{ \frac{1}{1 - e^{-\bar{\beta}e(\ell i)+\bar{\xi}\ell^3 i^3}} \right\}. \tag{43}$$

Assuming that the surface term in the energy dominates and converting Eq.(*43*) to integral form

$$Z \approx \int_1^{\infty}\left\{ \frac{di}{1 - e^{-\bar{\beta}e(\ell i)+\bar{\xi}\ell^3 i^3}} \right\}. \tag{44}$$

Since the major contribution to the integral comes from small i, the exponential is approximated to first order so that integration of Eq.(*44*) gives

$$Z = \left\{ \frac{1}{\bar{\beta}} 4\pi\gamma\ell^2 + \frac{\bar{\xi}^2}{\bar{\beta}} 16\pi^2\gamma^2\ell \ln(1-\zeta) \right\}. \tag{45}$$

where $\zeta = \frac{\bar{\beta}4\pi\gamma}{\bar{\xi}\ell}$. Note that the second term in Eq.(*45*) is now a function of $\bar{\xi}$. Thus using Eqs.(*33-34*) directly, again to lowest "physical" order, it is found, respectively

$$V = \frac{\nu}{\bar{\xi}}, \quad \text{and} \quad E = \frac{\nu}{\bar{\beta}}. \tag{46}$$

In arriving at Eq.(*46*), the parameter ζ is treated to be of order *1* and is further constratined by the logarithm term in Eq.(*46*) to $0 \le \zeta < 1$. Substituting Eqs.(*46*) into ζ, an approximate equation of state for the steady state penetration process is obtained

$$E = \zeta \frac{\ell}{4\pi\gamma} V. \tag{47}$$

The lower limit on ζ maintains the positivity of the relationship between E and V in Eq.(*47*), whereas the upper limit is a reality condition for Z.

Experimentally ℓ is the minimum particle size. The partition function Z, as can be seen from Eq.(*43*), is strongly dependent on small ℓ. The energy, however, is only weakly dependent because of the cancellations in Eq.(*41*) for small ℓ. This weak dependence on small ℓ is somewhat deceptive because we have ignored the frequency ν in our discussions since ν occurs linearly in V and E in Eqs.(*33-34*). In fact, the pulverization of the ceramic to smaller sizes tends to maximize the energy transfer since more energy is continually required to fracture the ceramic to smaller and smaller sized fragments. Thus it is important that the maximum energy, consistent with conservation of momentum, be transferred from the impactor to the ceramic thereby producing the maximum pulverization, *i.e.* the finest ceramic powder possible. But in order for this to happen, **the ceramic must be confined long enough** for the ceramic to be pulverized.

3.3 Confinement of Ceramic

Confinement has several meanings. The standard situation is as follows: In addition to a ceramic tile with a backup plate to prevent tensile failure (spall) of the ceramic, it is well-known that lateral confinement increases the quasi static compressive strength of the ceramic.[15] Including a face plate may or may not improve performance. Penetration experiments show that there is a threshold velocity below which a face plate does not seem to help.[6, 16] However under dynamic loading (ceramics under impact conditions), ceramics are found to exhibit inelastic as well as elastic deformation plus a large stain rate with dependence on confining pressure.[17] Thus confinement seems to be important in the consideration of the ballistic performance of ceramics. An additional effect that we are not considering here is the additional symmetric shock effects that will occur to the penetrator. There are indications that these shocks can lead to substantial fragmentation of the penetrator and could compete favorably with the erosion process during collisions.[18]

3.4 Minimum Ceramic Particle Size

Finally it is necessary to discuss how one might obtain a lower bound on the minimal size of the pulverized ceramic. After the shock has been completely relieved in the ceramic, then the energy deposition by the impactor into the ceramic is carried away at the speed of sound in the **fractured** ceramic. Whereas the speed of sound in bulk alumina may be as high as *11.6 km/sec* (sapphire or highly densified alumina), the speed of sound in highly fragmented ceramic matter is much less than the bulk value. By comparison, the speed of sound in sand is of the order of *100 m/s* which can not be too different from that for fragmented alumina. The center to center distance for fragments is certainly of the order of the size of the particles. Thus the speed of sound in the "grainy" ceramic is of the order of the actual particle velocity u_p which we noted earlier was also of the order of *100 m/s* Therefore this center-to-center distance represents a cut off (minimum) wavelength of sound that can not be transmitted by the motion of the fragments. This can also be expressed as a maximum frequency

$$\nu_{\max} = \frac{c}{\lambda_{\min}}. \tag{48}$$

It is possible to estimate $\nu_{\max}$ by considering a typical time scale of about *0.1* μs which could be interpreted as the time for the wave to transit a fragment, *i.e.* the period of the wave. Then $\nu_{\max} = 10^7 MHz$ and $\lambda_{\min} = 10\ \mu m$. However frequencies higher than $\nu_{\max}$ are not transmitted, but their energy **can** be deposited in nearby grains which then can lead to tensile fracture within the grains. Thereafter the energy can be transmitted to the next level of grains, and so forth. Thus

the frequency spectrum associated with the impact event ultimately determines the minimum size of the fragments, and *a fortiori*, the energy rate as given by Eq.(*41*).

4 Erosion Models

Even if the fracturing of the ceramic does not initially consume much energy from the penetrator (*i.e.the* case of large $a_{\min}$), a simple assumption on erosion given the particle distribution $< n_i >$, is that the work done by erosion, which can be very large, is equal to the yield strength of the ceramic times the volume of the target removed.[6] *A* better model adapts the steady state maximum entropy model to the erosion model of Rabinowicz[19] based upon a relatively simple empirical model of the erosion process of a metal by an abrasive such as a ceramic.[2] Following Rabinowicz, the erosive wear equation for the volume of metal removed (from the penetrator P) is

$$V_P = \frac{k_e m_c v^2 \theta}{p}, \tag{49}$$

where k_e is the wear constant for the metal, m_c is the total mass of ceramic (abrasive) particles impacting the penetrator, which is the same as the mass removed from the target, v is the average velocity of the abrasive particles which for the ceramic powder is the relative velocity of the penetrator and powder, *i.e.* on the average *1500 m/s*, p is the penetration hardness of the surface, and θ is an angular attitude impact factor which is *1* for angles between 10° to 60° and $\frac{1}{2}$ otherwise. Here it is assumed that $\theta = 1$. For tungsten, $k_e \simeq 3\ x\ 10^{-2}$ and $p = 4250\ N/mm^2$. We should note that the Rabinowizc model is also very primitive since it does not take into account the temperature of the process, the hardness of the abrasive nor the dependence on the particle size in the erosion process.[3]

In the steady state penetration problem, the volume rate of ceramic removed is

$$\dot{V}_c = \sum_i a_i^3 < n_i > . \tag{50}$$

The rate of mass removal of ceramic is then

$$\dot{m}_c = \rho_c \dot{V}_c = \rho_c \sum_i a_i^3 < n_i >, \tag{51}$$

so that the rate of mass eroded from the projectile is

$$\dot{m}_P = \frac{\rho_p \rho_c k_e v^2 \theta}{p} \sum_i a_i^3 < n_i >, \tag{52}$$

and in the continuum limit, this becomes, using Eq.(*46*)

$$\dot{m}_P = \frac{\rho_p \rho_c k_e v^2 \theta}{p} \frac{\nu}{\bar{\xi}}. \tag{53}$$

[2]For the sake of completeness, it is mentioned that the elaborate model of Rao & Buckley [20] which is based upon an empirical parameterization in terms of various physical quantities, is limited at the present time because of the lack of relevant experimental data for our case. Further more, this parameterized model is not easily adaptable to the Maximum Entropy model and therefore limits the usefulness of this model.

[3]No doubt some of these variables are empirically incorporated into k_e, θ and p although the experimental controls imposed are not known.

For massive penetrators and thin targets (or thin slices of a thick target), an approximately steady state process can be assumed during the time of the event. In this case, the penetrator moves through the "thin" ceramic target with nearly undiminished speed. For a target thickness of *2.5 cm*, the "characteristic time τ" could be taken as the transit time which is approximately $\tau = 0.2\ \mu s$; however the numerical value of this time is only coincidental to the time which was discuss in Section 3(*c*) which corresponds to the transit time across a grain. The differential mass removed ΔM_p corresponding to the characteristic time τ would be

$$\Delta M_P = \dot{m}_p \tau = \frac{\rho_p \rho_c k_e v^2 \theta}{p} \frac{1}{\bar{\xi}}, \tag{54}$$

which now depends on the time independent thermodynamic parameter $\bar{\xi}$. Nevertheless Eq.(*54*) depends on our interpretation of the characteristic time τ. If the projectile is allowed to pass through a series of identical ceramic layers of "thickness" L, we can calculate an upper bound for penetration since the steady state process does not take into account the degradation of the energy of the projectile. A rough estimate of the total penetration of the long rod projectile, impeded only by erosion of the ceramic, is then given by

$$P_{UB} = \frac{M_P}{\Delta M_P} L = \frac{\bar{\xi} V_p p L}{\rho_c k_e v^2 \theta}. \tag{55}$$

If L is interpreted as the ceramic grain diameter, then ΔM_P would represent the mass of the penetrator removed after passing though the distance L. This simplified approach does not adequately take into account the degradation in the energy of the projectile due to enhanced pulverization and removal of the ceramic target nor the fracturing of the projectile by the same process that fractures the ceramic target and therefore the intrinsically non-steady state process of penetration. However, the exact value of $a_{\min}$ depends strongly on the length of time that the projectile and the ceramic are dynamically interacting with one another. Several approximations of Eq.(*55*) show strong dependance on the value of $a_{\min}$. If $a_{\min} = 10$ Angstroms, then the denominator in the integral in Eq.(*44*) can be approximated along the lines described. Alternately if the Grady limit, *e.g.* $a_{\min} = 0.1\ \mu$ is assumed, then both βe and $\bar{\xi} a_i^3$ are large so that the relative difference and the sign in the exponential term becomes important. The equation of state given by Eq.(**??**) can be used for comparison of the terms, but the major contribution still occurs near the lower limit of integration. Thus the ambiguities discussed appear to be a limitation of the steady state approach at this time. It is tempting to compare this model with the experimental data of Orphal [21] for long rod penetration of various materials as a function of initial impact velocity. There are two reasons why this can not yet be done: First the process is, at best quasistatic as indicated by Orphal in the first two stages of penetration, and therefore does not correspond to a steady state process. Finally the removal of target material below the impactor and the fracturing of the penetrator is not adequately accounted for in this model. The first issue tends to overestimate the penetration; and the lack of the second, underestimates penetration.

5 Conclusions

Some of the necessary elements have been considered in adaptation of the maximum entropy method to fragmentation processes and erosion of high energy penetrators during the impact process. The real process has been approximated as a steady state process. Confinement does seem to enhance energy loss of the penetrator since this corresponds directly to our understanding of the time constant τ of the process. Nevertheless the penetration of a projectile into a target is a time

dependent and intrinsically non-equilibrium case. Thus it is necessary to adapt the maximum entropy process to time dependent systems which could be considered as a series of steady states processes. Each stage in the penetration process is considered as in a state of quasi equilibrium which obey local thermodynamic equilibrium yet have an overall system state but with internal thermal gradients or non equilibrium processes such as radiation. This approach is somewhat analogous to the nearly steady state process during the penetration of a "thin" target. For this reason, the maximum entropy method may yet provide useful information for comparison with the data of Orphal[21] for penetration in the quasistatic regions.

Of the two impactor energy degradation effects obtained from the maximum entropy approach in this work, only the erosion due to the ceramic particles acting on the penetrator has been incorporated into a penetration depth model for the purpose of demonstration. The energy loss due to the fracturing of the ceramic directly by the impact can be easily added to the zeroth order model presented here using a straight forward kinematic framework. A better model for the penetration of a projectile will include fracture effects in the penetrator due to the shock wave that also occurs in the penetrator. This "shock" erosion effect will include energy losses due to both penetrator fragmentation and subsequent parasitic erosion to the impactor. The important lesson that is presented here is that these mechanisms can be treated by the maximum entropy method.

References

[1] For a discussion of the characteristics of the various impact regimes, see, for example, the course notes for, *A Short Course on Penetration Mechanics* by J. S. Wilbeck, C. E. Anderson, A. B. Wenzel, P. S. Westine & U. S. Lindholm, (Southwest Research Institute, San Antonio).

[2] R. Englman, N. Rivier, and Z. Jaeger, "Fragment-Size Distribution in Disintegration by Maximum-Entropy Formalism," Phil. Mag. *B* 56, 751 (1987).

[3] L. A. Glenn and A. Chudnovsky, "Strain-Energy Effects on Dynamic Fragmentation," J. Appl. Phys. **59**, 1379 (1986).

[4] F. C. Frank and B. R. Lawn, "On the Theory of Hertzian Fracture," Proc. Royal Soc. **299**, 291 (1967).

[5] B. R. Lawn, "Partial Cone Crack Formation in a Brittle Material Loaded with a Sliding Spherical Indenter," Proc. Roy. Soc. **299**, 307 (1967).

[6] M. L. Wilkins, "Armor Penetration Phenomena," Third Progress Report of Light Armor Program, Lawrence Radiation Laboratory Report (July, 1968); Fourth Progress Report UCRL-50694 (1969); Fifth Progress Report UCRL-50980 (1971).

[7] L. Yingzhi and D. A. Hills, "The Hertzian Cone Crack," ASME J. Appl. Mech. **58,** 120 (1991).

[8] D. J. Viechnicki, M. J. Slavin, and M. I. Kliman, "Development and Current Status of Armor Ceramics," Ceramic Bull. **70**, 1035 (1991). [10]See A. M. Rajandran and W. H. Cook, "A Comprehensive Review of Modeling of Impact Damage in Ceramics," AFATL-TR-88-143 (1988), *p.*32.

[9] J. F. Mescall and C. A. Tracy, "Improved Modelling of Fracture in Ceramic Armors," presented at Army Science Conf., June 17-19, 1986.

[10] See review by A. M. Rajendran and W. H. Cook, "A Comprehensive Review of Modeling of Impact Damage in Ceramics," AFATL-TR-88-143, (1988), pp. 72-5.

[11] Z. Rosenberg, D. Yaziv, Y. Yeshurum, S. J. Bless, "Shear strength of shock loaded alumina as determined with longitudinal and transverse manganin gauges,: J. Appl. Phys. **62**, 1120 (1987).

[12] R. Bianchi, *et al*, "Experimental Simulation of Asteroidal Fragmentation by Macroscopic Hypervelocity Impacts Against Free Falling Bodies," Astron. Astrophys. **139**, 1 (1984).

[13] J. Lankford and C. R. Blanchard, "Fragmentation of Brittle Materials at High Rates of Loading," J. Mater. Sci. **26**, 3067 (1991).

[14] D. E. Grady, "Local Inertial Effects in Dynamic Fragmentation," J. Appl. Phys. **53**, 322 (1982).

[15] R. Arrowood and J. Lankford, "Dynamic charaterization of an alumina ceramic," Southwest Res. Inst. Rpt. SwRI-6724, San Antonio, TX, 1982; G. R. Johnson, T. J. Holm1quist, H. Lankford, C. E. Anderson, J.Walker, "A computational Constitutive Model and Test Data for Ceramics Sujected to Large Stains, High Strain rates and high pressure, "Final Report, DE-AC04-87AL-42550, Los Alamos National Laboratory, 1990.

[16] D. Puckett, Private communication, July, 1991.

[17] See A. M. Rajandran and W. H. Cook, "A Comprehensive Review of Modeling of Impact Damage in Ceramics," AFATL-TR-88-143 (1988), *p.*80.

[18] J. A. Zukas, High Velocity Impact Dynamics, (John Wiley, NY, 1990), pp.16-25.

[19] E. Rabinowicz, "The wear equation for erosion of metals by abarasive particles," in Proceedings of Fifth International Conference on Erosion by Liquid and Solid Impact, Newnham College, Cambridge, UK, 3-6 Sept 1979, (Cavendish Laboratory, Cambridge, 1979), paper 38.

[20] P. V. Rao and D. H. Buckley, "Solid Impingement Erosion Mechanism and Characterization of Erosion Resistance of Ductile Metals," in Liquid-Solid Flows and Erosion Wear in Industrial Equipment, Ed. M. C. Roco, Energy Sources Technology Conference, Feb. 12-16, 1984 (ASME, 1984).

[21] D. L. Orphal, "Int.J. Impact Eng., **20**, 601 (1998).

PERGAMON

International Journal of Impact Engineering 23 (1999) 883–893

INTERNATIONAL JOURNAL OF IMPACT ENGINEERING

www.elsevier.com/locate/ijimpeng

HYPERVELOCITY IMPACT ON CARBON FIBRE REINFORCED PLASTIC / ALUMINIUM HONEYCOMB: COMPARISON WITH WHIPPLE BUMPER SHIELDS

E. A. TAYLOR, M. K. HERBERT, B. A. M. VAUGHAN and J. A. M. MCDONNELL

Unit for Space Sciences and Astrophysics, School of Physical Sciences, University of Kent at Canterbury, Canterbury, Kent, CT2 7NR, U. K.

Summary—Normal and oblique incidence hypervelocity impact tests (velocity range 4-6 km s^{-1}) were carried out to determine the ballistic limit of a 1.6 mm carbon fibre reinforced plastic facesheet bonded to 45 mm aluminium honeycomb core, as typically used in Low Earth Orbiting spacecraft. The internal honeycomb damage was determined as a function of the impactor parameters. The ballistic limit data showed a strong dependence with impact angle. The internal honeycomb damage was found to be independent of impact angle for constant impact energy for $\Theta < 50°$. An empirically-determined damage equation linking honeycomb damage to impact energy was developed. For the highest impact energy perforating impacts, the debris cone angles for the primary and secondary debris cones were determined. As the impact angle increased, the centre of the damage cones rotated away from the line of flight. The data have been compared with the ballistic limit curve defined by the modified Cour-Palais aluminium Whipple bumper equation and show broad agreement with the equation predictions. A reduced value of the rear facesheet thickness is required to bring the normal and 15° incidence data into agreement with the ballistic limit curve.
© 1999 Elsevier Science Ltd. All rights reserved.

NOTATION

Al-HC	Aluminium Honeycomb
CFRP	Carbon Fibre Reinforced Plastic
LEO	Low Earth Orbit
LGG	Light Gas Gun
LOF	Line of Flight
L/D	Length/Diameter
MLI	Multi-Layer Insulation
NP	Non-Perforating
P	Perforating
α	Primary cone angle (°)
β	Secondary cone angle (°)
ε	Turning angle (°)
Θ, θ	Impact angle (°)
V, v	Impact velocity (km s^{-1})
ρ_p	Projectile density (g cm^{-3})
ρ_b	Back-wall density (g cm^{-3})
σ	Yield strength of back-up wall (ksi)
D_{eq}	(Equivalent) Diameter of CFRP hole (mm)
D_{dam}	Honeycomb blast damage area (mm^2)
D_{prim}	Primary cone diameter (mm)
D_{sec}	Secondary cone diameter (mm)
d_{crit}	Critical diameter for perforation (cm)
d_p	Projectile diameter (mm)
E	Impact energy (J)
t_b	Bumper thickness (cm)
t_w	Back-up wall thickness (cm)
S	Whipple spacing (cm)
A_h	Area of CFRP hole (mm^2)
A_f	Area of CFRP hole (front) (mm^2)
A_r	Area of CFRP hole (rear) (mm^2)

INTRODUCTION

Spacecraft external walls are typically made of aluminium honeycomb core and an aluminium or woven composite material (CFRP) facesheet, bonded to the core using a resin. This material (referred to as spacecraft honeycomb) provides good performance in terms of high strength, low weight and low thermal distortion and, augmented by externally-mounted multi-layer insulation,

0734-743X/99/$ - see front matter © 1999 Elsevier Science Ltd. All rights reserved.
PII: S0734-743X(99)00132-3

provides the primary shielding protection against space debris and meteoroid particle impact for unmanned spacecraft. The predicted increase in the LEO space debris population (linked to the rise in total satellite mass launched), correlated with the increase in average satellite size, has meant that the issue of hypervelocity impact onto spacecraft honeycomb is of increasing concern. Impact tests are required to characterise the hypervelocity impact response of the honeycomb, as computational modelling of hypervelocity impacts onto honeycomb is at an early stage [1]. However, ground based tests are not possible over the whole range of impactor conditions (typical parameters: velocity range 5-20 km s^{-1}, density 1-8 g cm^{-3}, impact angle 0° - 75°), so experimental data must be used to develop a predictive damage equation which can be extrapolated to LEO impact conditions.

The response of spacecraft honeycomb to hypervelocity impact has been poorly characterised to date. Previous work in this field focused initially on the use of honeycomb for manned spacecraft, quantifying the hazard due to meteoroid impact. Cadmium shields were therefore used to investigate impacts onto equivalent aluminium shields at impact velocities > 7 km s^{-1} with the honeycomb represented by a 6061-T6 aluminium cylinder. Channelling was observed and the cell wall thickness was found not to significantly affect the impact performance of the target [2]. Tests on different aluminium alloys - 2024, 5052 and 7075 - as honeycomb cell-equivalent cylinders, showed no significant difference in their performance [3]. Tests were carried out on honeycombs with deep cores (equivalent to large Whipple bumper spacings) and the influence of the cell diameter on the required rear sheet thicknesses for prevention of perforation was investigated [3].

The channelling action of the honeycomb was also investigated for 0°, 45° and 60° incidence shots [4]. 4.76 mm Lexan cylinders were fired onto 24.1 mm thick aluminium honeycomb. For the velocity range tested (3-7 km s^{-1}), the debris clouds produced contained primarily solid fragments. The velocity required to reach the ballistic limit of the structure rose from 4.3 to 7.2 km s^{-1} as the impact angle was increased from 0° to 60°, with a velocity of 6.7 km s^{-1} required to perforate at 45° incidence. Note that, unlike the previous tests, 'real' hexagonal honeycomb was used instead of equivalent diameter cylinders. Shots onto honeycomb beyond the ballistic limit were also carried out for honeycomb placed outside nickel-hydrogen batteries and Space Station radiator panels [5, 6]. For impacts beyond the ballistic limit, the facesheet is delaminated from the honeycomb core and the whole structure is warped. Impact tests have also been carried out onto CFRP facesheet/aluminium honeycomb covered with a layer of MLI [7, 8, 9, 10]. The addition of MLI has been shown to increase significantly the ballistic limit of the honeycomb structure. No direct comparison between the performance of aluminium and CFRP honeycombs has yet been made and a damage equation incorporating the target parameters - honeycomb depth, cell size, cell wall thickness, alloy type, bumper and back-up wall thickness - has not yet been developed.

Hypervelocity impact tests onto CFRP/Al-HC at velocities in the range 4-6 km s^{-1} were carried out using the two stage Light Gas Gun (LGG) at the University of Kent at Canterbury [11]. The spherical projectile densities (nylon, aluminium, titanium and steels) represented a large range of densities present in LEO and were fired over a wide range of impact angles (0-75°). The combined data are used here to explore scaling of honeycomb damage with an aluminium Whipple bumper equation and the influence of impact angle on the ballistic limit.

The ballistic limit of the target has been identified to be strongly dependent on impact angle; the ballistic limit rose from 25-30 J at normal incidence to 55 J at 15°, then to 156 J for 45° incidence, as identified by marginal perforation of the rear facesheet. This impact angle dependence is greater than that shown by previous tests on honeycomb [4]. An empirically-determined damage law relating the internal areal damage of honeycomb as a function of impact energy for spherical projectiles at incidences of 0°-50° has been derived. The angular spread and composition of debris clouds resulting from perforation of the 47.2 mm target by solid nylon cylindrical projectiles have been characterised. An aluminium Whipple bumper damage equation has been used to predict the ballistic limit for an aluminium target equivalent to the CFRP facesheet and spacing used. Modification of the rear wall thickness to a reduced value is required to bring the 0° and 15° incidence data into agreement with the ballistic limit curve.

MATERIALS AND METHODS

The target material was a honeycomb structure, consisting of CFRP facesheets and an aluminium core (Al-HC), as typically used for a LEO space platform. The CFRP/Al-HC lay-up and material properties are given in Table 1. The shot programme is given in Table 2.

Table 1. Target material

Face sheets	*Face sheets*	*Honeycomb core*	*Honeycomb core*
Prepreg matrix	4 ply satin woven carbon fibre epoxy HMF371-7714B	Section type	Aeroweb
Fibre Orientation	0°/90°/90°/0°	Material	Al Alloy 3003
Thickness	1.62 mm	Core density	83 kg m^{-3} (5.2 lb ft^{-3})
Density	1800 - 1850 kg m^{-3}	Cell size	6.4 mm (0.25 inches)
Modulus of Elasticity	69.1 - 69.5 kN mm^{-2}	Cell foil thickness	0.06 mm (25 x 10^{-4} inches)
		Core thickness	45 mm
		Film adhesive	Redux 609 or 312

Table 2. Shot programme

Parameter	*This work + Ref. 12*	*Ref. 13*
d_p (mm)	0.8, 1.0, 1.2, 1.5, 2.0, 4.35	0.8, 1.0, 1.2, 1.5, 2.0
v (km s^{-1})	4.71-5.8	4.5-6.2
ρ_n (g cm^{-3})	1.15, 2.78, 3.99, 4.51, 7.75	1.15, 2.78, 3.99, 4.50, 7.75, 8.47
Θ (°)	0, 15, 30, 45, 60, 75	0
No. shots	28	14

Two mounting arrangements were used for the targets. For the perforating shots, the target was mounted as shown in Fig. 1; held between two aluminium plates, with a witness plate offset at 100 mm behind the target and parallel to the target inclination. The witness plates were manufactured from 2024 Al alloy and were 1 mm thick. The witness plates were between 203 and 286 mm wide and 203 and 273 mm in height and were sized so as to catch the full extent of the debris cloud projected from the rear of the honeycomb target. Higher incidence shots ($\Theta >$ 45°) could not be carried out as the witness plates were limited in size by the internal dimensions of the target chamber. For the non-perforating shots, the targets were angled on a support beam and clamped into place. This allowed the positioning of witness plates to catch ricochet ejecta from highly oblique shots.

The target damage morphology is described in Fig. 2. The front and rear holes were digitally imaged and the projected area of the holes ($A_{h(front)}$ and $A_{h(rear)}$) were calculated via a pixel recognition/counting program and the appropriate scaling factor. By defining the hole damage A_h as an ellipse, the equivalent diameter (D_{eq}) was calculated using Eqn. 1, excluding any delamination damage of the surface. (Delamination damage is defined as material removed around the central hole which does not fully penetrate the surface.) An estimate of the reproducibility of the shots was provided by analysis of two pairs of shots using identical projectiles, impact angles and velocities. The variation in the crater features was used to estimate the 'reproducibility' errors applied to the data.

$$D_{eq} = (4A_h / \pi)^{0.5} \quad (1)$$

The internal honeycomb damage was measured using 30 keV X-rays. A Polaroid film recorded the cell damage integrated over the target thickness. The resulting morphology was compared to that defined in Fig. 3 and the maximum damage area (D_{dam}) was determined using the same technique as for the CFRP hole. Due to the difficulty in accurately estimating the boundaries of the honeycomb damage, an error was placed on each value of D_{dam} to represent operator bias.

The witness plates from the three perforating shots (using solid cylindrical nylon projectiles) were examined under low magnification and the type of damage identified (based on classifications derived in [13]. The diameters of the damaged regions (primary and secondary damage) identified after this classification were measured, as was the deflection of the centre of the damaged region from the line of flight (LOF) of the projectile. These angles and measurements - D_{prim}, D_{sec}, α, β, ε - are defined in Fig. 4. The diameter of the base of the cones was found by averaging the measured diameters in four orthogonal directions; the damaged areas were circular to within 5-10 %. The witness plate perforations were also identified and measured.

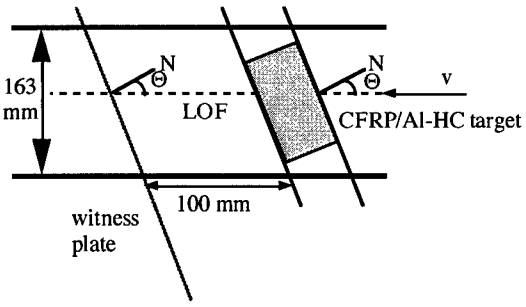

Fig. 1. Target and witness plate mounting

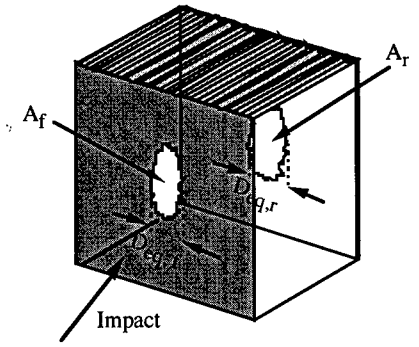

Fig. 2. Target damage parameters

Fig. 3. Internal honeycomb damage morphology. (Definitions from [12])

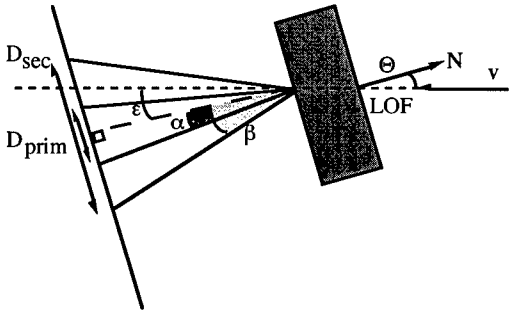

Fig. 4. Debris cloud cone angles

The targets were classified as perforating (rear hole present; beyond the ballistic limit) or non-perforating (no rear hole; below the ballistic limit). The influence of impact angle, impact energy and projectile density for constant impact angle on the ballistic limit was assessed. Previously published impact data on honeycomb were used to determine a ballistic limit scaling factor between normal and oblique incidence impacts, which was compared to the data [4]. The parameter D_{dam} was analysed as a function of the impactor parameters (impact angle, projectile density and impact energy) and a least squares fit carried out between E and D_{dam}. The modified Cour-Palais aluminium Whipple bumper equation [14] was used to predict the critical projectile diameter (d_{crit}) required to perforate the honeycomb-equivalent aluminium Whipple shield (Eqns. 2-4). Eqn. 2 is valid for velocities < 3 km s^{-1} and Eqn. 3 is valid for normal impact velocities greater than 7 km s^{-1}. Eqn. 4 represents a linear interpolation between 3 and 7 km s^{-1}. For oblique incidence impacts the normal component of velocity is used to define the regions. The equivalent thickness of aluminium for the CFRP facesheets was calculated by scaling the areal density of CFRP against that of aluminium. The honeycomb core depth was equated to the Whipple bumper spacing, S. A comparison was made between the d_{crit} values estimated and the particle diameters tested to determine how accurate a Whipple bumper equation is at estimating the ballistic limit of a honeycomb target. A modification to the rear wall thickness was applied to bring the normal and near-normal incidence data into agreement with the ballistic limit curve.

$$d_{crit}=\left\{\left[\frac{\left(t_w\left(\frac{\sigma}{40}\right)^{0.5}+t_b\right)}{\left(0.6\rho_p^{0.5}(\cos\Theta)^{5/3}V^{2/3}\right)}\right]^{\frac{18}{19}}\right\} \tag{2}$$

$$d_{crit}=\left\{\left[3.918t_w^{2/3}\rho_p^{-1/3}\rho_b^{1/9}S^{1/3}\left(\frac{\sigma}{70}\right)^{1/3}(V\cos\Theta)^{-2/3}\right]\right\} \tag{3}$$

$$d_{crit}=\left\{\left[\frac{\left(t_w\left(\frac{\sigma}{40}\right)^{0.5}+t_b\right)}{\left(1.248\rho_p^{0.5}\cos\Theta\right)}\right]^{\frac{18}{19}}\left(1.75-\frac{(V\cos\Theta)}{4}\right)\right\}+\left\{\left[1.071t_w^{2/3}\rho_p^{-1/3}\rho_b^{-1/9}S^{1/3}\left(\frac{\sigma}{70}\right)^{1/3}\right]\left(\frac{(V\cos\Theta)}{4}-0.75\right)\right\} \quad (4)$$

RESULTS AND DISCUSSION

The morphology of the impacts noted on the shots is similar to that noted in previous tests [12, 13]. The circularity of the entrance crater for impacts up to 45 degrees is confirmed (Fig. 5a, c, e). The rear damage for the impacts at ~ 900 J (solid nylon cylindrical projectiles) also includes asymmetric exit holes (Fig. 5d) and facesheet splitting (Fig. 5f). For these impact energies the rear facesheet is on the threshold of delamination from the honeycomb core. The internal honeycomb damage morphology in Fig. 3 (from [12]) is again seen in the solid nylon sabot shots (Fig. 6). The influence of impact angle is seen in the series of shots (0°, 30°, 45°); the arrow signifies the direction of impact. The unusual shape of the honeycomb blast area for the 30° shot could be explained by a slightly rotating impactor (cylinder), although the entrance hole (Fig. 5c) does not show any strong evidence of this. The lighter area at the top of the image denotes the facesheet 'overhang' over the honeycomb core; although the honeycomb damage appears truncated, it did not extend beyond the facesheet and no honeycomb damage was visible from the target exterior. Note also that the type of honeycomb damage increases with impact angle: moving from primarily 'burst' cells to 'blasted' cells. The areal damage also increases by a factor of two from 0° to 30°. There is much more delamination of the core to the facesheet around the entrance and exit holes (superimposed in the X-ray) than noted for earlier shots (Fig. 6 compared to Fig. 3). A summary of the target damage is presented in Table 3.

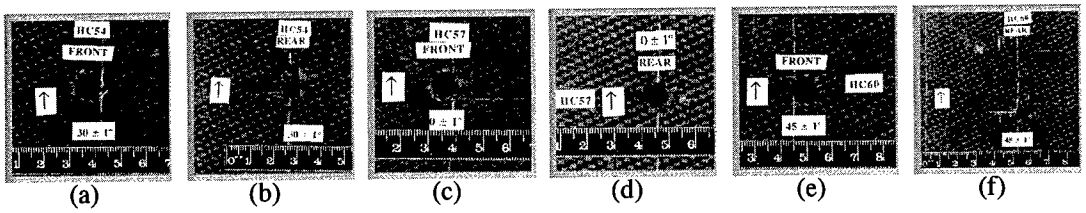

(a) (b) (c) (d) (e) (f)

Fig. 5. Target morphologies beyond the ballistic limit as a function of impact angle (solid nylon cylindrical projectile).

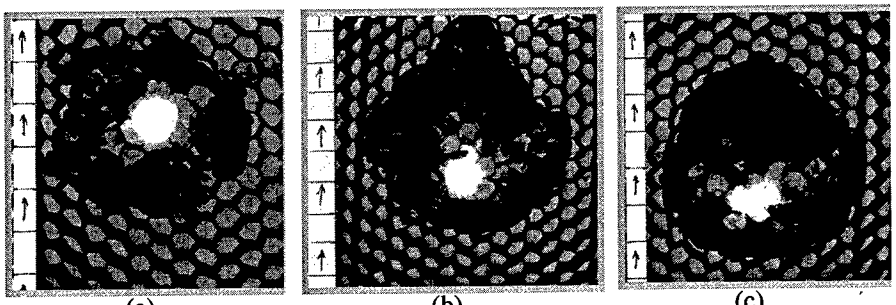

(a) (b) (c)

Fig. 6. Honeycomb blast damage. (a) $\Theta = 0°$ (b) $\Theta = 30°$ (c) $\Theta = 45°$.

The impact results for the normal incidence shots are presented in Fig. 7, sorted by impact energy and projectile density. They are divided into perforating (P) and non-perforating (NP) shots. The ballistic limit of the target for aluminium projectiles is between 25 and 30 J, but at an impact energy of 60 J a nylon projectile is below the threshold for perforation of the target. The ballistic limit for a nylon projectile is poorly defined, lying between 60 and ~900 J, as projectile diameters between 2.0 and 4.3 mm (cylinder) cannot be fired in the LGG. The impact tests into a similar target agree well with the results presented [10]. As previously noted, the projectile density at constant impact energy may influence the ballistic limit [13].

Table 3. Results of LGG shots on CFRP/Al-HC honeycomb . (HC01-HC18 previously published in [13]).

Shot ID	d_p *(mm)*	ρ_p *(g cm^{-3})*	v *(km s^{-1})*	*E(J)*	$\theta(°)$	D_{eq} *(front)*	D_{eq} *(rear)*	*Comments*
HC01	2.00	7.75	5.87	559	0.0	8.06	9.79	Rear larger than front
HC02	1.00	7.75	6.14	76.5	0.0	2.17	4.05	Rear larger than front
HC03	1.00	8.47	6.23	86.1	0.0	2.71	6.01	Rear larger than front
HC04	1.50	1.45	4.89	30.6	0.0	3.99	none	No rear perforation
HC05	1.50	8.47	5.00	187	0.0	3.56	4.86, 4.40	Rear larger than front, two exit holes
HC06	1.50	7.75	4.95	168	0.0	7.74	7.77	Rear equal to front
HC07	2.00	8.47	4.75	400	0.0	8.31	6.15	Rear smaller than front
HC08	1.00	4.50	4.46	23.4	0.0	3.40	none	No rear perforation
HC11	1.20	1.15	4.62	11.1	0.0	2.76	none	No rear perforation
HC13	2.00	1.15	5.00	60.2	0.0	4.33	none	No rear perforation
HC15	1.00	2.78	5.42	21.4	0.0	2.71	none	No rear perforation
HC16	1.20	2.78	4.86	29.7	0.0	3.51	1.80	Rear smaller than front
HC17	1.50	2.78	5.93	86.4	0.0	3.92	4.77	Rear larger than front
HC18	2.00	2.78	5.08	150	0.0	4.56	6.45	Rear larger than front
HC20	1.50	2.78	4.84	58.0	46.6	5.4	none	No rear perforation
HC21	1.20	2.78	5.23	34.6	44.3	4.2	none	No rear perforation
HC22	1.50	2.78	4.99	61.6	74.6	4.2	none	No rear perforation
HC23	1.20	2.78	4.96	31.2	74.4	3.1	none	No rear perforation
HC24	1.50	3.99	4.73	78.8	74.7	4.3	none	No rear perforation
HC25	1.50	2.78	5.11	64.6	74.7	4.4	none	No rear perforation
HC26	1.20	2.78	4.99	31.5	14.3	3.7	none	No rear perforation
HC27	1.50	2.78	4.94	60.4	14.7	5.0	5.6	Rear larger than front
HC28	0.80	7.75	5.09	26.9	14.4	3.6	none	No rear perforation
HC29	1.00	7.75	5.76	67.3	16.0	3.2	1.6	Rear smaller than front
HC33	1.20	2.78	5.15	33.6	24.5	2.7	none	No rear perforation
HC34	1.20	2.78	5.17	33.9	63.5	3.4	none	No rear perforation
HC35	1.20	2.78	5.24	34.8	59.7	3.9	none	No rear perforation
HC36	1.00	7.75	5.07	52.2	74.4	3.9	none	No rear perforation
HC37	1.00	7.75	5.30	57.0	45.0	4.4	none	No rear perforation
HC38	1.50	3.99	4.91	84.9	45.0	4.6	none	No rear perforation
HC41	1.20	4.51	5.04	51.8	73.4	3.4	none	No rear perforation
HC43	1.20	4.51	5.18	54.7	44.5	4.0	none	No rear perforation
HC44	1.20	4.51	5.06	52.2	17.0	3.7	none	No rear perforation
HC45	1.20	4.51	5.10	53.0	14.8	3.3	none	No rear perforation
HC46	1.20	4.51	5.13	53.7	74.1	3.9	none	No rear perforation
HC47	2.00	2.78	4.71	57.6	130.1	5.2	none	No rear perforation
HC51	2.00	2.78	4.80	16.2	135.1	7.3	3.5	Rear smaller than front
HC54	4.34 (L/D = 1.04)	1.15	4.80	30.0	886.0	10.3	9.1	Rear smaller than front (cylindrical projectile)
HC57	4.34 (L/D = 1.04)	1.15	4.75	0.0	864.0	13.4	23.7	Rear larger than front (cylindrical projectile)
HC60	4.34 (L/D = 1.04)	1.15	4.82	45.0	890.0	10.2	8.4, 4.9	Rear smaller than front, two exit holes. (cylindrical projectile)
HC61	2.00	2.78	5.18	29.2	156.2	5.0	5.4	Rear larger than front
HC62	2.00	2.78	5.19	44.0	156.8	5.4	1.0	Marginal perforation of rear

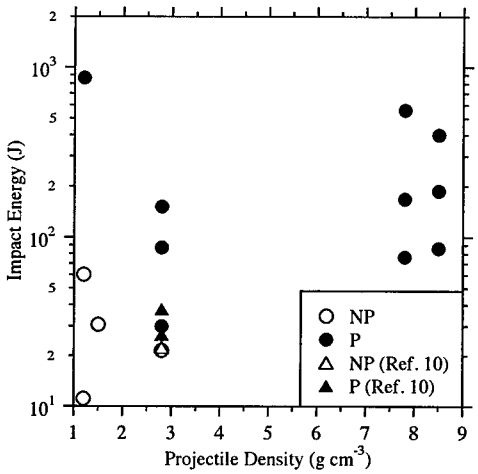

Fig. 7. The dependence of the ballistic limit on impact energy and projectile density for normal incidence impact (NP: non-perforating impact; P: perforating impact)

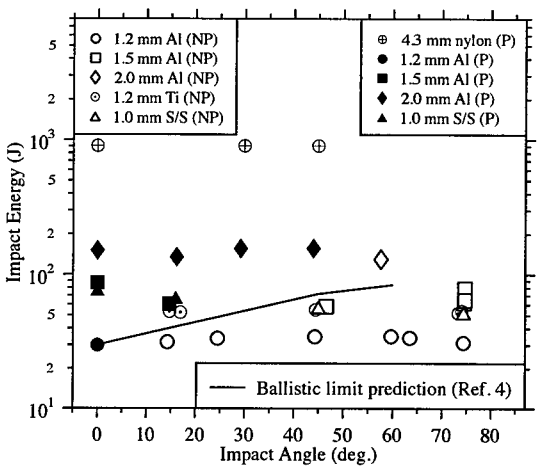

Fig. 8. The dependence of the ballistic limit on impact angle and impact energy. The ballistic limit prediction is scaled from Al/Al-HC data. (NP: non-perforating impact; P: perforating impact).

However, the majority of impacts in space will be at non-normal incidence. The results of some 28 shots, covering a projectile density range of 1.15 to 7.75 g cm^{-3}, are plotted in Fig. 8. The ballistic limit of the honeycomb has been observed previously to be affected by the obliquity of the impactor; the line of flight of the projectile will encounter progressively more layers of honeycomb (analogous to 'thin aluminium bumpers') as the impact angle is increased [4]. The ballistic limit of the CFRP/Al-HC target increased from 25-30 J to ~55 J as the impact angle was increased from 0 to 15°. The ballistic limit at 45° is well defined at 156 J (the 2 mm projectile just perforating the rear facesheet. At 57° it is greater than ~140 J. As the velocity range of these data is 4.5 and 5.5 km s^{-1}, the influence of velocity on the ballistic limit cannot be evaluated. However, previously-published tests onto an aluminium honeycomb (t_b = 0.076 cm, t_w = 0.051 cm (both 7075-T6); S = 2.286 cm; HC core cell size = 4.76 mm (5052-H39)) which cover a velocity range of 4-8 km s^{-1} can be used to assess the dependence of the ballistic limit on velocity for one projectile type (a solid Lexan sabot, 4.76 mm diameter, L/D = 1) [4]. Using these data, the impact energies required to reach the ballistic limit of the target at 45° and 60° were calculated to be 2.3 times and 2.8 times that at 0° respectively. These scaling factors are normalised to the impact energy of 30 J (taken from Fig. 7). In Fig. 8, the impact angle dependence predicted by the data in Ref. [4] is not in agreement with the data from this shot programme. The well-defined ballistic limit values at 15° and 45° are under-predicted, with the observed energy at 45° being over twice as large as that predicted by Ref. 4 (69J compared with 156 J). The ballistic limit is again under-predicted by at least 40 J at ~ 60°. These observed differences may be due to the different shock pressures generated in the projectile and the resulting solid/liquid proportions of the debris cloud (a function of bumper type, thickness and impact velocity), or to the target properties (aluminium versus composite), or, indeed, to the influence of different honeycomb cell core depths.

For four spherical projectile types (1.2, 1.5 mm Al; 1.2 mm Ti; 1.0 mm steel) a series of shots was carried out over the full range of impact angles to explore the effect of impact angle on the honeycomb blast damage area. The impact energies for each projectile type were tightly grouped as the impact velocities were similar. The results are plotted in Fig. 9 and show that, for the range of projectiles tested, the honeycomb damage does not vary significantly for impact angles between 0° and 50°. Above this point, the data tail off rapidly. Therefore, it can be assumed that, for impacts within this range, the damage area at <50° is the same as at 0°. The impact data for these angles are grouped by projectile density in Fig. 10 and show that the four projectile densities are in broad agreement. A damage equation produced by least squares fit to the data (for impact energies between 20 and 400J) for impacts by spherical projectiles is given in Eqn. 5 (E is in joules, D_{dam} in mm^2).

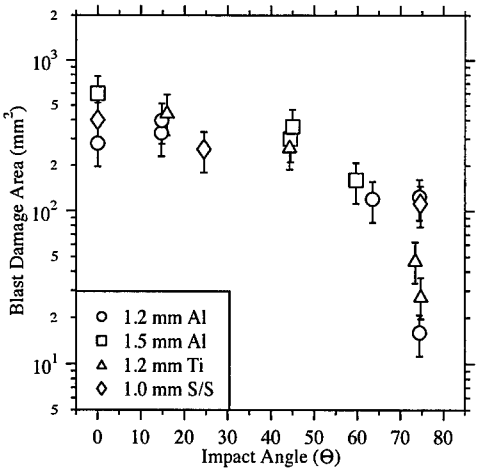

Fig. 9. Honeycomb blast damage area as a function of impact angle for four projectile types at ~ 5 km s^{-1}.

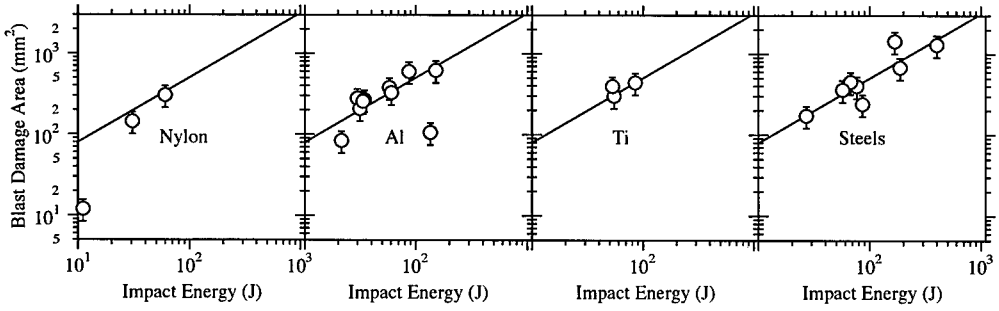

Fig. 10. Honeycomb blast damage for impact angles 0-45°, sorted by projectile density. The line (Eqn. 5) represents a least squares fit to all data with an impact energy < 400 J.

$$D_{dam}=10^{1.1\pm0.2}E^{0.8\pm1.1}\ (r^2=0.8) \quad (5)$$

Table 4. Witness plate angles

Plate	*Impact angle Θ (± 5°)*	*Primary cone angle α (± 5°)*	*Secondary cone angle β (±5°)*	*Turning angle ε (±5°)*
HC57	0	23	43	-6
HC54	30	21	44	36
HC60	45	28	42	48

The primary and secondary ejecta damage morphologies were used to calculate the angles α, β and ε. The values of α, β and ε are given in Table 4 for the three witness plates studied. Two perforations were also recorded in HC57 (measuring 3x2 mm and 6x2 mm). The features in the primary damage cone α are typically near-circular and represent projectile and honeycomb target fragments travelling at velocities close to that of the original impactor. The secondary damage features are shallower and include carbon fibre fragments from the rear of the cone. The values of α are equal within experimental error for 0° and 30° incidence, then increase at 45°, as expected by comparison with [15]. A sharp dependence on turning angle with impact angle is also recorded (Table 4). The anomalous rotation away from this normal measured for HC 57 is probably due to internal honeycomb effects on the passage of the debris cloud.

Considering the qualitative results above, the functional form for a honeycomb-specific damage equation will include target parameters such as the spacing, front and rear facesheet thicknesses and honeycomb cell size and cell wall thickness, in addition to target material parameters. A

detailed test and modelling programme, varying each of these parameters individually, is required to fix the form and exponent values of such an equation.

A simpler, intermediate approach is to scale the impact data with the modified Cour-Palais Whipple bumper equation, as shown by Eqns. 2-4 [14]. This equation consists of a low velocity part (Eqn. 2) and a high velocity part (Eqn. 3), with a linear interpolation between 3 and 7 km s^{-1} (Eqn. 4). The performance of the Whipple shield is governed by the state of the debris cloud, consisting of projectile and bumper fragments. In Eqns. 2-4, the normal component of the impact velocity governs the damage potential of the debris cloud. Therefore if the smallest diameter projectile required to reach the ballistic limit for a normal incidence impact is at 3 km s^{-1}, the corresponding velocity for the minimum particle diameter will be at 6 km s^{-1} for a 60° impact. The minimum particle diameter for the oblique incidence impact will be larger than that for the normal incidence impact. Both the dependence on impact angle and on the spacing (equivalent to honeycomb core depth) may be different for honeycomb, as compared to Whipple bumpers. The dispersion of the debris cloud is hampered by the honeycomb for both normal and oblique incidence impacts, with the normal component of the cloud being channelled by the honeycomb cells. The analysis, of both the debris clouds and the internal honeycomb blast, in the section above shows that the honeycomb affects the development of the debris cloud. This is shown by the increase in particle diameter required to reach the ballistic limit at 5 km s^{-1}, from a 1.2 mm spherical aluminium projectile at normal incidence to a 2 mm projectile of the same density at 45° incidence. The greater damage-causing potential of the debris cloud for the 45° incidence impact (due to the presence of more solid fragments) may be counterbalanced by the presence if the honeycomb. Note that the shock pressures generated in the composite material and projectile cannot be assumed to be the same as for an aluminium-aluminium impact. This also adds uncertainty to the calculation.

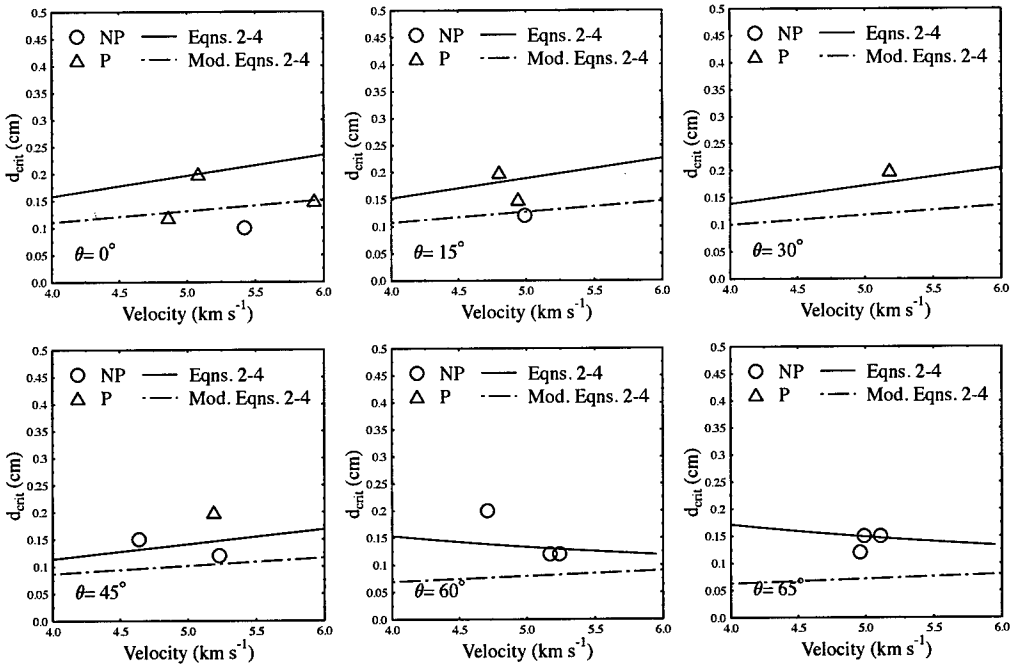

Fig. 11. Modified Cour-Palais Whipple bumper equation predictions compared with aluminium normal and oblique incidence shots. Dashed curve corresponds to ballistic limit curve derived using the scaled rear facesheet thickness.

With these constraints in mind, the impact data (below and above the ballistic limit of the target) can be compared to the Whipple equation predictions for a critical diameter for perforation (d_{crit}). The composite facesheets were converted to equivalent thickness aluminium sheets (1.2 mm thick) and the yield strength values for the front and rear bumpers set to 40 and 70 ksi respectively. For the aluminium impactors in Table 3 (velocity, density, target set-up), the modified Cour-Palais

Whipple bumper equation was used to predict the critical diameter at which the equivalent shield would perforate as a function of velocity (ballistic limit curve). The results for the aluminium projectile data (0°, 15°, 30°, 45° and 60°) are shown in Fig. 11. For the 0° and 15° incidence impacts, the data are below the ballistic limit curve, suggesting that modification of Eqns. 2-4 may be necessary. The 30° and 45° incidence perforating shots are consistent with the curve. However, the non-perforating higher obliquity impacts ($\Theta > 45°$) are above the ballistic limit curve. The performance of the honeycomb is thus conservatively modelled. For normal incidence impacts, the debris cloud has been shown to be 'channelled' [15], therefore increasing the areal damage on the rear facesheet (analogous to the rear wall in a Whipple bumper). Therefore is it expected that the shielding effectiveness of the rear facesheets is reduced, compared with a spaced Whipple bumper. A scaling factor has been applied to the modified Cour-Palais Whipple bumper equation in the version implemented in the ESA ESABASE debris modelling software [16]. The rear wall thickness (t_w) can by modified by the use of a scaling factor for both the low and high velocity terms. To bring the normal and near-normal incidence data into agreement with the ballistic limit curve, the rear wall thickness was modified by a scaling factor of 0.5, reducing the effective thickness of the rear facesheet by 50%. The results are again shown in Fig. 11 (dashed curves). Now, the normal incidence perforating shots lie on the scaled ballistic limit curve. For a conservative ballistic limit curve for this honeycomb structure, the value of t_w should be reduced by 50%. Further optimisation of the scaling factor is not recommended, given the number of assumptions made in converting the honeycomb composite facesheet to an equivalent thickness of aluminium.

CONCLUSIONS

The impact response of a 47.2 mm thick CFRP/Al-HC has been characterised as a function of projectile density, impact angle and impact energy for impact energies between 10-1000 J. The energy required to reach the ballistic limit rises with impact angle; it is doubled for impacts going from 0 to 15° incidence. At 5 km s^{-1}, a 1.2 mm aluminium projectile impacting at normal incidence just perforates the rear of the target, whilst a 2 mm projectile is required to perforate at 45° incidence. The honeycomb blast damage area for impacts at equal energies does not significantly change for Θ = 0-50°, thus an empirically-determined damage law relating the internal areal damage and impact energy for this range of angles has been derived. The debris cone angles for impacts 0-45° have been characterised; the rotation of the cone with respect to the line of flight increases with impact angle, as expected. The modified Cour-Palais aluminium Whipple bumper damage equation has been used to predict the ballistic limit for an aluminium target equivalent to the CFRP facesheet and Al-HC used. A modification to the rear facesheet thickness (as used in the ESA triple wall equation) is required to bring the normal incidence data into line with the ballistic limit curve.

Acknowledgements—Thanks are due to the Particle Physics and Astronomy Research Council (PPARC) for funding of the Light Gas Gun hypervelocity impact facility. E. A. Taylor would like to acknowledge funding from Matra Marconi Space (UK) and the University of Kent at Canterbury. Thanks are also due to Dr. J. Hodgkinson of the Centre for Composite Materials, Imperial College, U. K. for providing the X-ray facilities.

REFERENCES

1. C. C. Poteet, Computational study of hypervelocity impacts on metallic thermal protection systems, *Proc. 8th AIAA International Space Planes and Hypersonic Systems and Technologies Conference*, AIAA-98-1611, pp. 572-584, April 27-30, Norfolk, VI (1998).
2. C. J. Maiden, A. R. McMillan, R. E. Sennett and J. W. Gehring, Experimental investigations of simulated meteoroid damage to various spacecraft structures, *NASA CR-65222* (1965).
3. R. E. Sennett and B. L. Lathrop, Effects of hypervelocity impact on honeycomb structures, *J. Spacecraft and Rockets*, **5**, 1496-1497 (1968).
4. D. W. Jex, A. M. Miller and C. A. Mackay, The characteristics of penetration for a double-sheet structure with honeycomb, *NASA TM X-53974* (1970).
5. D. T. Frate and H. K. Nahra, Hypervelocity impact testing of nickel hydrogen battery cells, Proc. *AIAA Space Programs and Technologies Conference*, AIAA 96-4292, September 24-26, Huntsville, AL (1996).
6. G. L. Shephard and S. A. Scheer, Secondary debris impact damage and environment study, *Int. J. Impact Engng.*, **14**, 671-682 (1993).
7. F. Terrillon, H. R. Warren and M. J. Yelle, Orbital debris shielding design of the Radarsat spacecraft, *42nd International Astronautical Congress*, IAF-91-283, October 5-11, Montreal, Canada (1991).

8. G. A. Sanchez and J. H. Kerr, Advanced X-ray astrophysics facility (AXAF) meteoroid and orbital debris test report, JSC 27354 (1996).
9. C. L. Frost and P. I. Rodriguez, AXAF hypervelocity impact test results, *Proceedings of the Second European Conference on Space Debris*, ESA SP-393, pp. 423-426 (1997).
10. M. Lambert, Hypervelocity impacts and damage laws, *Adv. Space Res*, **19(2)**, 369-378 (1997).
11. M. J. Burchell, M. J. Cole, J. A. M. McDonnell and J. C. Zarnecki, Hypervelocity impact studies using the 2 MV Van de Graaff accelerator and two-stage light gas gun of the University of Kent at Canterbury, *Meas. Sci. Tech.*, in press (1999).
12. E. A. Taylor, M. K. Herbert and L. Kay, Space debris hypervelocity impact on carbon fibre reinforced plastic (CFRP)/Al honeycomb at normal and oblique angles, *Proceedings of the Second European Conference on Space Debris*, ESA SP-393, pp. 429-434 (1997).
13. E. A. Taylor, M. K. Herbert, D. J. Gardner, L. Kay, R. Thomson and M. J. Burchell, Hypervelocity impact on carbon fibre reinforced plastic (CFRP) / aluminium honeycomb, *Proceedings of the Institution of Mechanical Engineers Part G : Journal of Aerospace Engineering*, **221(Part G)**, 355-366 (1998).
14. E. L. Christiansen, Design and performance equations for advanced meteoroid and debris shields, *Int. J. Impact Engng.*, **14**, 145-156 (1993).
15. J. W. Gehring, Chapter IX : Engineering Considerations, *High Velocity Impact Phenomena*, (ed. R. Kinslow), pp. 482-489, Academic Press, New York (1970).
16. G. Drolshagen and J. Borde, ESABASE Debris-Meteoroid/Debris Impact Analysis Technical Description, ESA ESTEC, ESABASE-GD-01/1, Noordwijk, Netherlands (1992).

PERGAMON

International Journal of Impact Engineering 23 (1999) 895–904

INTERNATIONAL JOURNAL OF IMPACT ENGINEERING

www.elsevier.com/locate/ijimpeng

HYDROCODE MODELLING OF HYPERVELOCITY IMPACT ON BRITTLE MATERIALS: DEPTH OF PENETRATION AND CONCHOIDAL DIAMETER

E. A. TAYLOR*, K. TSEMBELIS*, C. J. HAYHURST**, L. KAY* and M. J. BURCHELL*

*Unit for Space Sciences and Astrophysics, School of Physical Sciences, University of Kent at Canterbury, Canterbury, Kent, CT2 7NR, U. K.; **Century Dynamics Limited, Dynamics House, Hurst Road, Horsham, West Sussex, RH12 2DT, U. K.

Summary—The Johnson-Holmquist brittle material model has been implemented into the AUTODYN hydrocode and used for Lagrangian simulations of hypervelocity impact of spherical projectiles onto soda-lime glass targets. A second glass model (based on a shock equation of state and the Mohr-Coulomb strength model) has also been used. Hydrocode simulations using these two models were compared with experimental results. At 5 km s^{-1}, the Mohr-Coulomb model under-predicted the depth of penetration, whilst adjustment of the Johnson-Holmquist model bulking parameter was required to match the experimental data to the simulation results. Neither model reproduced the conchoidal diameter; a key measured parameter in the analysis of retrieved solar arrays, so two failure models were used to investigate the tensile failure regime. A principal tensile failure stress model, with crack softening, when used with failure stresses between 100 and 150 MPa and varying bulking parameters, reproduced the conchoidal diameter morphology. Empirically-determined, power-law damage equation predictions for the range 5-15 km s^{-1} were compared with simulations using both models since no experimental data was available. The power-law velocity dependence of the depth of penetration simulations was found to be significantly lower than the 0.67 predicted by the empirically-determined damage equations. © 1999 Elsevier Science Ltd. All rights reserved.

INTRODUCTION

An understanding of the response of brittle and ductile materials under hypervelocity impact is required for analysis of the space debris and micrometeoroid impact flux via retrieved spacecraft surfaces. Brittle material surfaces exposed in Low Earth Orbit include solar arrays and windows. Laboratory experiments are able to access only a small fraction of the impactor parameters encountered in space (velocity, diameter, density, shape, composition and impact angle), this experimental work alone is insufficient to explore impact cratering on space-exposed surfaces. However, hydrocodes, such as AUTODYN, can be used to understand and predict the response of materials beyond the laboratory calibration regime [1]. Equally, empirically-determined, power-law damage equations can also be extrapolated and compared to hydrocode simulations. Previous hypervelocity impact work onto ductile targets using AUTODYN includes semi-infinite crater formation at normal incidence [2] and oblique incidence [3, 4] and debris cloud and bumper shield studies [5]. Previous hypervelocity impact brittle material hydrocode modelling (soda-lime glass and quartz) at typical space (Low Earth Orbit) velocities [6, 7, 8] have used simple models to model the hypervelocity impact response of the material. For a more realistic simulation of hypervelocity impacts on brittle targets at micrometeoroid and debris velocities (typically 5-20 km s^{-1}), an equation of state which can model shock response and phase changes accurately and a strength/failure model which can reproduce brittle fracture are required.

In this paper the Johnson-Holmquist (JH) brittle material model [9, 10] has been implemented into the AUTODYN hydrocode and used for Lagrangian simulations of hypervelocity impact of

0734-743X/99/$ - see front matter © 1999 Elsevier Science Ltd. All rights reserved.
PII: S0734-743X(99)00133-5

spherical projectiles onto semi-infinite soda-lime glass targets. An alternative model, based on the shock equation of state and the Mohr-Coulomb (MC) strength model, has also been used, using existing material data. A three stage research program was carried out: (1) The JH and MC model predictions were compared with the experimental data using hypervelocity impact tests onto soda-lime glass at velocities in the range of 5 km s^{-1} for a range of projectile diameters and densities. (2) The formation of the brittle material conchoidal diameter was investigated using the principal tensile stress failure model, with and without a crack softening model. (3) The JH and MC model predictions of depth of penetration for 5-15 km s^{-1} were compared with empirically-determined, power-law brittle material damage equation predictions (due to the absence of experimental data).

The Mohr-Coulomb model simulations under-predicted the depth of penetration results at 5 km s^{-1}, whilst the Johnson-Holmquist model results were matched to the data by varying the bulking parameter. The use of a failure model (principal stress and crack softening) in addition to the JH model resulted in the conchoidal diameter morphology (caused by brittle material tensile failure) being reproduced. The depth of penetration results for 5-15 km s^{-1} show that the velocity dependence of the depth of penetration of the hydrocode simulations is less than the damage equation predictions, with the dependence on velocity to the power 0.33 (MC) and 0.35 (JH) compared with the damage equations (0.67).

MATERIAL MODELS

Johnson-Holmquist Model

The JH model [9, 10] is applicable to brittle materials subjected to large strains, high strain rates and high pressures and gives the yield strength as a function of pressure. The equation of state is a simple polynomial with the Grunseisen Gamma set to zero, and therefore is not appropriate for modelling the phase changes that occur at impacts in the range 5-15 km s^{-1}. The strength model incorporates the experimental observation that a brittle material has some compressive strength but no tensile or spall strength after fracture, and includes strain rate and bulking effects. The yield strength is also a function of damage, the residual strength in fractured material, dilation (bulking, reported in [11]) and strain rate effects. The strength model does not include thermal softening. Dilation occurs because brittle materials fail by cracking, leading to free surfaces and increase in volume. The JH model dimensionless constants (A, N, B, M, C, D_1, D_2) (Table 1) were obtained from flyer plate tests and ballistic long-rod penetration tests onto soda-lime glass at 1.5-2.4 km s^{-1} [10]. The remaining constants (for the hydrostat, damage and fractured material strength) were determined partly by a computational iterative technique. The JH strength and failure models are given in Figs. 1 and 2 respectively.

Mohr-Coulomb Model + Shock Equation of State

The MC model parameters are presented in Table 2. The strength of the material in the Mohr-Coulomb model is defined by four points on the yield stress-pressure curve. As the MC model only allows one curve in the yield stress-hydrostatic pressure curve, the maximum tensile hydrostatic presure and calibration data from the biaxial static tests in data were used [10]. The shock equation of state constants c_o and S used (determined by fitting the Hugoniot curve from [10] to a linear U_s-u_p (shock velocity-particle velocity relationship) are 3.3 km s^{-1} and 1.5 respectively and correspond well to previous values used [12]. The Gruneisen Gamma was obtained from a previous soda-lime glass hydrocode modelling publication [3]. For simulating the onset of failure, the principal stress failure criterion was used. Two values were required; maximum tensile failure stress and the maximum shear stress. The former was taken from [6] and the latter calculated as the product of the shear modulus and the maximum plastic strain.

Principal Stress Tensile Failure + Crack Softening Model

The JH and MC models are suited to modelling of the compressive regime, but not the tensile regime. Therefore, modelling of the conchoidal diameter (formed during tensile crack propagation) requires the use of an appropriate failure model. Two such failure models have been used with the JH model [9, 10]. The baseline principal stress tensile failure model produces

Table 1. Johnson-Holmquist model constants

Parameter	*Value*
A	0.93
N	0.77
B	0.088
M	0.35
C	0.003
T (GPa)	0.15
HEL (GPa)	5.95
D1	0.053
D2	0.85
SFMAX	0.5
K1 (GPa)	45.4
K2 (GPa)	-138.0
K3 (GPa)	290.0

Table 2. The Mohr-Coulomb model constants

Parameter	*Value*
ρ (g cm^{-3})	2.23
c_o (km s^{-1})	3.3
S	1.5
Γ	1.32
G (GPa)	27.9
Y_1 (GPa)	0
P_1 (GPa)	-0.15
Y_2 (GPa)	0.42
P_2 (GPa)	0.08
Y_3 (GPa)	0.58
P_3 (GPa)	0.11
Y_4 (GPa)	0.62
P_4 (GPa)	0.12
Tensile stress (GPa)	0.21
Shear stress (GPa)	1.40

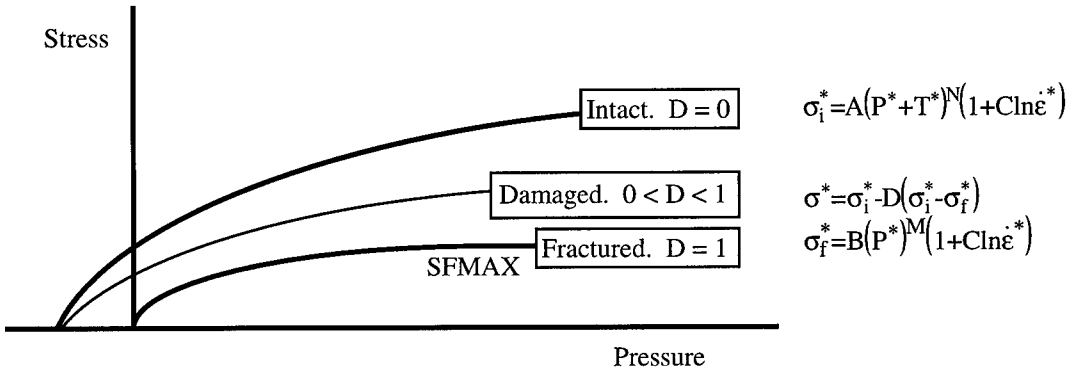

Fig. 1. The Johnson-Holmquist model

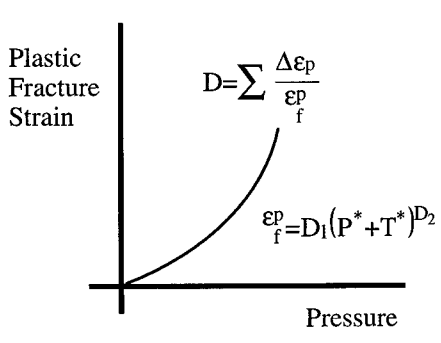

Fig. 2. Johnson-Holmquist failure model

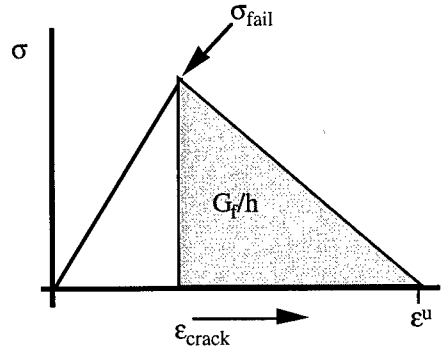

Fig. 3. Crack softening model

material failure when the tensile load in a cell exceeds a specified value. Tensile failure in isotropic brittle materials usually takes place because of maximum tensile stresses and strains which include both volumetric and deviatoric components. However, the principal stress tensile failure model gives instantaneous strength loss, with bulk compression at later times. In practice, brittle materials do not fail instantaneously but gradually lose their load-carrying capacity as cracks propagate through the material. A tensile 'crack-softening' model, recently implemented in

AUTODYN, can improve the description of the post-failure response. It is based on fracture mechanics and isotropically reduces the load-carrying capacity of a cell as a function of the crack opening strain, once the principal stress failure criterion has been reached. A Rankine (principal stress) failure surface with an associative inelastic flow rule is used to monitor crack opening and increment crack strain (damage). The stress-strain curve is given in Fig. 3, with the slope of the softening curve, h, given by Eqn. 1, where L is a characteristic cell dimension, G_f, the mechanical (fracture) energy release rate, and f_i, the stress at failure initiation. G_f is closely related to K_{1c}, the stress-intensity factor for mode I cracking in soda-lime glass [13]. The value of G_f used is 10^4 N mm^{-1}.

$$h=L\, f_i^2 / 2\, G_f \tag{1}$$

SIMULATIONS

Simulations have been carried out using the MC model at 5 km s^{-1} for the projectiles described in Table 3. In addition, simulations were also carried out for a 1 mm aluminium, titanium and stainless steel projectile at 5 km s^{-1} using the JH model. Dilation effects were included for the JH simulations and the effect of varying the bulking parameter was assessed. However, the strain rate dependency was set to zero, since the very low value of the Johnson-Holmquist constant C suggested that the effects would not be significant. The material models for aluminium 2024, stainless steel 304 (Tillotson equation of state and Steinberg-Guinan strength model), titanium (Shock equation of state and Steinberg-Guinan strength model) and nylon (Shock equation of state and Von Mises strength model) are as defined in the AUTODYN material library [1]. Simulations of a 53 μm soda-lime glass sphere impacting a soda-lime glass target at 4.31 km s^{-1} were carried out using the JH model plus the principal stress failure criterion and the crack softening model; the results were compared with the multiple-projectile shot described in the next section. The values of the prinicipal stress failure criterion were varied between 50 and 150 MPa and the crack softening model used to investigate the effect on the crater morphology, including the formation of the conchoidal diameter. A simulation was run to 1.0 μs to ensure that the conchoidal diameter formation was completed. Simulations of a 1 mm aluminium sphere impacting on semi-infinite soda-lime glass from 5 to 15 km s^{-1} were carried out using both the JH and MC models. Again, dilation effects were included but strain rate effects were not for the JH simulations. The simulations at 5 km s^{-1} were compared with experimental results from the hypervelocity impact shot programme and the damage equation predictions.

Table 3. Experimental data.
(#: number of shots; v: velocity of impact; d_p: particle diameter; ρ_p: particle density)

#	*v (km s^{-1})*	*d_p (mm)*	*ρ_p (g cm^{-3})*	*Projectile type*
2	5.37, 5.34	1.2, 1.5	1.15	Nylon
1	5.44	1.5	1.45	Cellulose Acetate
6	5.00, 5.05, 5.07, 5.42, 5.18, 4.44	0.8, 1.0, 1.2, 1.2, 1.5, 2.0	2.78	Aluminium alloy (Al) 2017
1	4.99	1.0	4.51	Titanium
3	5.00, 4.88, 4.90	0.8, 0.8, 1.5	7.92	Stainless Steel (SS) AISI 304
1	5.01	1.0	8.03	Stainless Steel (SS) AISI 316
1	5.17	1.0	8.47	Phosphor Bronze (PBR)
4	4.69, 5.00, 5.20, 5.14	0.8, 0.8, 1.0, 1.2	7.83	Chrome Steel (CS) AISI 52100

EXPERIMENTAL DATA AND DAMAGE EQUATIONS

Two hypervelocity impact test programmes (using the two stage light gas gun at the University of Kent at Canterbury [14]) were carried out to provide experimental data for comparison. The morphology observed and crater parameters measured on glass targets are given in Fig. 4, and are the same as measured on retrieved solar cell [15] and lunar rock surfaces [16].

Experimental data. Soda-lime glass targets were mounted so that there was a free rear surface. The single projectiles were loaded into a sabot and fired onto the targets. The depth measurements were made by two techniques; crater profiling and by depth gauges attached to microscopes. The experimental programme data (Table 3) have an average velocity of 5.02 km s^{-1}. The depth of penetration data were normalised to an impact velocity of 5 km s^{-1} (using a scaling factor derived from the depth of penetration equations described in the following section). To test the reproducibility of the glass results and to fire sub-millimtre sized projectiles, multiple projectiles with a projectile diameter of 53 μm (finely graded glass beads, example in Fig. 5) were loaded into a sabot (projectile holder) and fired onto 50.8 mm diameter, 10 mm thick soda-lime glass targets at 4.31 km s^{-1}. The spread in crater dimensions for impacts under one set of conditions can then be found. An aluminium plate (3 mm thick), with a 20 mm diameter aperture, was mounted ~120 mm in front of the aluminium target holder, as shown in Fig. 6. The 25 multiple impact sites on the glass and aluminium plates were measured and an average value, plus the standard deviation of the average, was determined. The scatter in the aluminium crater diameters is used as a check on the spread of velocity and projectile diameter within the projectile cloud. The variation in the aluminium crater diameter values was typically ± 2 %, caused by velocity and particle diameter variation. The higher standard deviation of the average conchoidal diameter as measured on brittle targets, as compared with impacts on ductile targets, has also been noted on impacts on solar cell borosilicate glass (N. R. G. Shrine, personal communication).

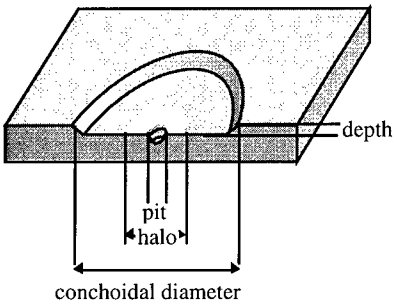

Fig. 4. Brittle material crater morphology.

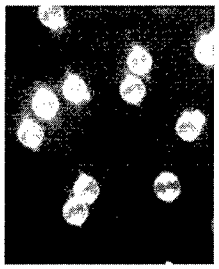

Fig. 5. Multiple glass projectiles.

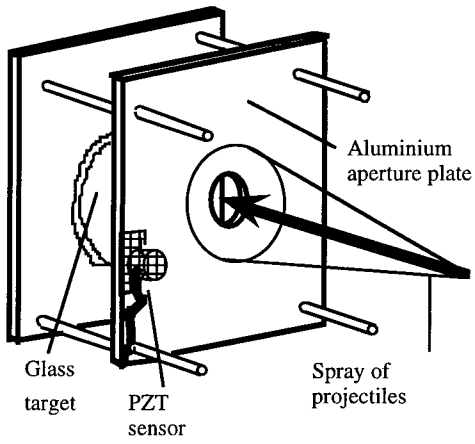

Fig. 6. Experimental set-up for multiple projectile firing.

Damage equations. In Low Earth Orbit, the impact velocities go beyond what can be achieved with laboratory accelerators for macroscopic particles, therefore three published equations (Eqns. 2, 3 and 4, Refs. 17, 23, 24; units are cgs, except velocity which is in km s^{-1}; target density has been assumed to be 2.3 g cm^{-3} for Eqn. 3) have been used to provide calibration data for the higher velocity simulations. Depth of penetration power-law damage equations are derived by least squares fits to experimental data then extrapolated to predict damage features at velocities (or other impactor parameters) beyond the calibration data set. A range of brittle target materials (fused silica, aluminosilicate glass basalt, granite) and impactor parameters (borosilicate glass, aluminium, polystyrene, iron, pyrex; micron to millimetre sized projectiles; velocities between 1-17 km s^{-1}) were used in their development. The performance of the damage equations is checked using a database of over 300 data from impacts onto aluminosilicate glass, basalt, basalt glass, fused quartz and silica, granite, pyrex, soda-lime glass, covering similar impactor ranges as the

source data for the damage equations (data from Refs. 17-22). Note that some of the data used to test the damage equations have also been used in their initial development. The three equations are close to the simple relationship between impactor and target where crater volume is proportional to kinetic energy [25]. This defines the values of exponents for d_p, v and ρ_p as 1, 0.67 and 0.33 respectively. (The symbols are defined as T_c - depth of penetration, ρ_p - projectile density, v_p - projectile velocity, d_p - projectile diameter.)

$$T_c=0.54d_p^{1.071}\rho_p^{0.524}v_p^{0.714} \quad (2)$$

$$T_c=0.64d_p^{1.2}\rho_p^{0.5}v_p^{0.67} \quad (3)$$

$$T_c=0.53d_p^{1.06}\rho_p^{0.5}v_p^{0.67} \quad (4)$$

The three depth of penetration equations were found not to predict accurately the data over the experimental range tested, as shown in Fig. 7. Two show significant scatter in the data with size, suggesting that adjustment of the projectile diameter exponent may be required. The dimensional scaling of Eqn. 3 does not show a trend with projectile diameter (d_p) over the data set, suggesting that the exponent value of 1.2 is appropriate. Eqn. 3 provides the best fit to data and shall be used for comparison with the hydrocode simulations. It should be noted that whilst the average trend in Eqn. 3 is correct, individual results differ from the predicted values by a factor of up to 2.

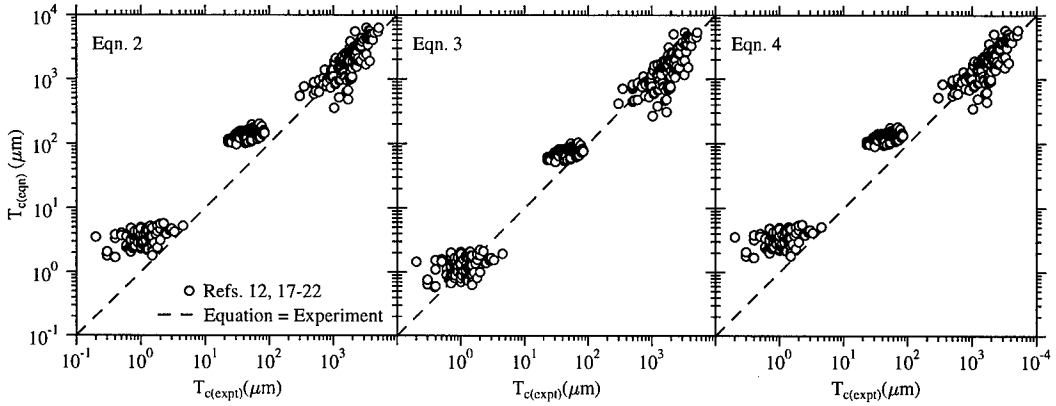

Fig. 7. Depth equation predictions versus experimental data. The dotted line signifies when experimental datum is equal to the equation prediction.

RESULTS AND DISCUSSION

Depth of Penetration Compared with Experimental Data

The MC simulation results are compared with the experimental data in Fig. 8. The aluminium data in Fig. 8a are in good agreement with the hydrocode simulations for d_p = 0.8-1.5 mm, as is the 1.2 mm nylon simulation. However the depth of penetration for the 1.5 mm nylon and 2.0 mm aluminium simulations underpredict the experimental data, by 25% and 20% respectively. This size dependence should be a function of the strength models. A reduced dataset (for clarity) of the steels, chrome steels and phosphor bronze data (density ~ 8 g cm^{-3}; similar depth of penetration predicted by the damage equations Eqns. 2-4) is compared with the MC simulations in Fig. 8b. The simulations under-predict the experimental data results by 10-20%, although the 0.8 mm SS304 datum is in agreement with the simulation results. The results of the JH simulations for a 1 mm diameter sphere at 5 km s^{-1} are compared with the hypervelocity impact soda-lime glass data and the MC model simulations in Table 4. The JH simulations over-predict the depth of penetration; this over-prediction is least when the bulking parameter is set to 0.25. By comparison, the MC simulations underpredict the glass data by 6% (aluminium), 17% (titanium) and 16% (steels) for a 1 mm projectile. The decrease in the predicted depth of penetration with

decreasing bulking parameter may be explained qualitatively by considering the accumulation of dilation pressure given in Eqn. 5 (which describes the dilation pressure contribution to the equation of state, represented graphically in Fig. 2). The second term decreases and thus leads to a smaller value of ΔP. Therefore, the actual pressure exerted on the material will decrease and thus less material will be excavated.

$$\Delta P_{t+\Delta t} = -K1\mu_{t+\Delta t} + \sqrt{(K1\mu_{t+\Delta t} + \Delta P_t)^2 + 2\beta K1\Delta U} \tag{5}$$

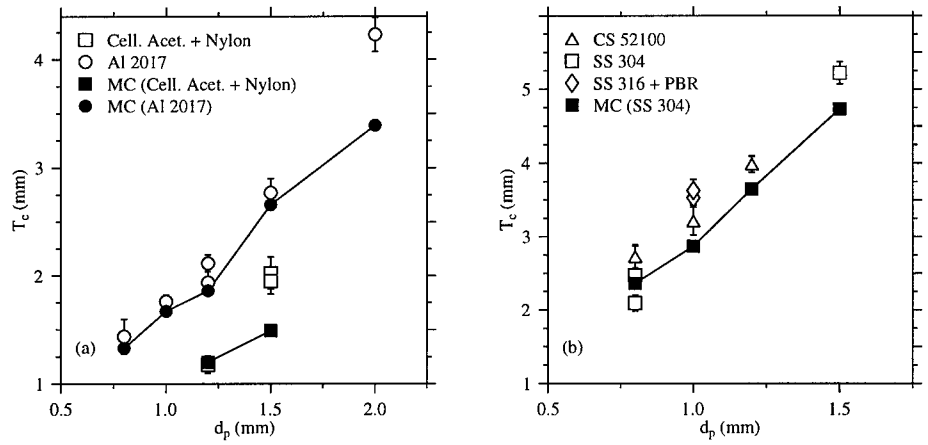

Fig. 8. MC model hydrocode simulations compared with data. Crater depth is plotted against projectile diameter (a) Nylon, cellulose acetate and Al 2017 (b) stainless steels 304, 316, chrome steel 52100 and phosphor bronze.

Table 4. Mohr-Coulomb and Johnson-Holmquist simulations of crater depth compared with experimental data (Al: aluminium; Ti: titanium; SS: stainless steel)

Simulation	T_c (Al) (mm)	T_c (Ti) (mm)	T_c (SS) (mm)
JH, β = 0.25	1.98	2.61	3.41
JH, β = 0.5	2.03	2.67	3.55
JH, β = 1	2.12	2.73	3.62
MC	1.67	2.18	2.87
Expt. data	1.78	2.62	3.49
Expt data (normalised to 5 km s^{-1})	1.77	2.62	3.43

Conchoidal Diameter Compared with Experimental Data

The JH model alone appears to model a reasonable crater formation and a damaged region around the crater can be seen in Fig. 9a . The radial features of this damage region are too deep and narrow to be a reasonable representation of conchoidal failure but could be compared with the shattered (halo) region (Fig. 4). The addition of the principal stress failure criterion produces more realistic surface damage which again may correspond to the shattered region. The failure stress values of 100 and 150 MPa produce near identical results, whilst the value of 50 MPa produces a greatly increased damage region. No conchoidal failure is clearly visible in these plots. Figure 9b shows the damage for the principal stress failure criterion set equal to 150 MPa. When the crack softening model is used with a failure stress of 100 and 150 MPa, a characteristic failure plane is developed at about 20 μm under the surface. This failure plane is present in both simulations. The principal stress failure value of 150 MPa used in this calculation is also in reasonable agreement with the value used in the JH model derivation. The failure plane is shown in Fig. 9c. The progression of crack growth with time for the JH model plus principal stress and crack softening is shown in Fig. 10. The conchoidal diameter produced with $\beta = 0$ was 280 μm and with $\beta = 1$,

660 μm. When the simulation was run for an extended time, the crack extended to produce a conchoidal diameter of 800 μm, for $\beta = 1$, although beyond 660 μm the rate of crack growth slowed significantly. The conchoidal diameters were found to vary between 280 and 660 μm, which suggested that an intermediate value of the bulking parameter, β, (between 1.0 and 0.25) may reproduce a value of the conchoidal diameter more in line with experiment ($D_{co} = 451 \pm 61$ μm).

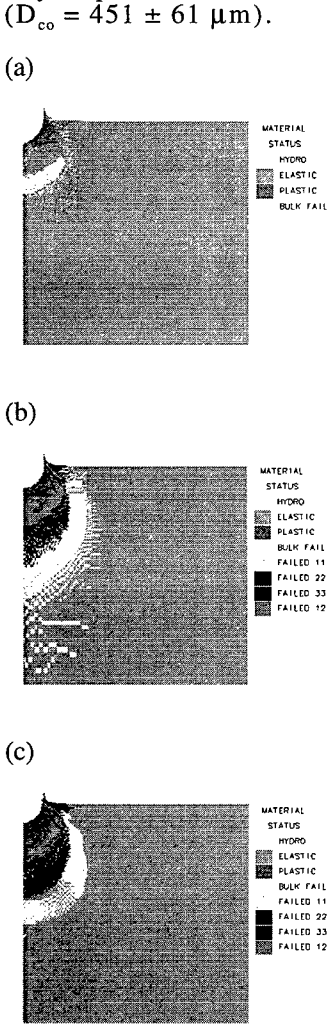

Fig. 9. Crater morphology for 53 μm glass projectile impacting a glass target at 4.31 km s^{-1} (a) JH model (b) JH model and principal stress failure set to 150 MPa (c) JH model plus crack softening and principal stress failure set to 150 MPa

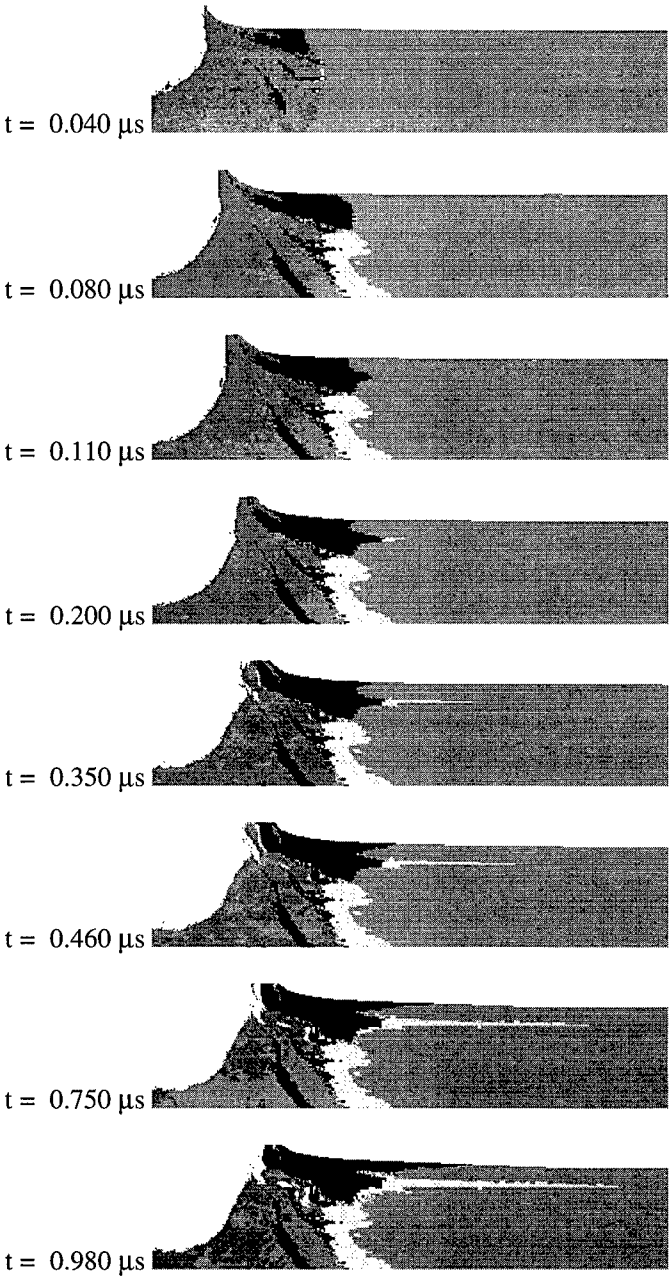

Fig. 10. Progression of crack growth with time for the JH model plus principal stress (150 MPa) and crack softening

Depth of Penetration Compared with Damage Equation Predictions

The depth of penetration simulation results for a 1 mm aluminium projectile are compared with Eqn. 3 and experimental data at 5 km s^{-1} in Fig. 11. At 5 km s^{-1}, the MC simulations and the Eqn. 3 predictions are within the range of experimental values. The JH simulation depth of

penetrations were higher than the MC results at 5 km s^{-1} and this difference increased with impact velocity; a fit to the MC results produced a velocity dependence of $v^{0.33}$, whilst the fit to the JH simulations produced $v^{0.35}$. These values are lower than those suggested by Eqn. 3 ($v^{0.67}$). The velocity exponent, obtained from a fit to the MC hydrocode simulations, is 0.33 instead of 0.67, implying that the depth of penetration is a function of impact momentum, not kinetic energy. This is contrary to the basic model of cratering, used as a basis for the development of the published damage equations outlined earlier. The MC model description of the yield strength does not include a decrease in the yield strength as damage increases. The JH simulations, with the velocity exponent of 0.35, are again much less than the equation prediction of velocity dependence. The depth values at 5 km s^{-1} are greater than the experimental data. Decreasing the bulking parameter from the value of 1 used would bring the experimental values more into line with the data at 5 km s^{-1}, but would not alter the velocity dependence. The JH model only has a polynomial equation of state which does not take into account energy dependence.

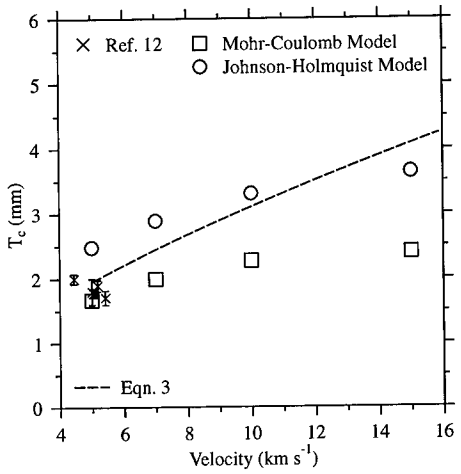

Fig. 11. Johnson-Holmquist and Mohr-Coulomb simulations compared with damage equation predictions and experimental data.

CONCLUSIONS

Two glass models - the Johnson-Holmquist and the Mohr-Coulomb model (based on a shock EOS and the Mohr-Coulomb strength model) - have been tested against depth of penetration experimental data at ~ 5 km s^{-1} and damage equation predictions in the range 5-15 km s^{-1}. Both models were found not to reproduce the conchoidal diameter. Preliminary results using the Johnson-Holmquist model overestimate the depth of penetration at ~5 km s^{-1} when the bulking parameter is set to 1.0. This difference may be due to the rapid accumulation of damage leading to loss of strength in the material early in the calculation. When the bulking parameter is set to 0.25, the experimental data values are reproduced more closely. The Mohr-Coulomb results match the experimental data to within. The depth of penetration is under-predicted by the hydrocode simulations as velocity increases, with velocity exponents of 0.33 (Mohr-Coulomb) and 0.35 (Johnson-Holmquist). Two failure models have been used and tested for their ability to reproduce the conchoidal diameter: (i) principal tensile stress failure, and (ii) principal tensile stress failure initiation with a crack softening model. The crack softening model reduces the tensile strength of the material as a function of the crack-opening strain and thus better simulates brittle, tensile crack growth based on the fracture toughness of the material. When the crack softening model was used with failure stresses of 100 and 150 MPa, the simulations revealed the development of a characteristic failure plane about 20 μm under surface which is associated with the development of a conchoidal failure diameter. The experimentally observed conchoidal diameter (using 53 μm diameter soda-lime glass projectiles at 4.31 km s^{-1}) shows broad agreement with these

simulations, although the influence of the bulking parameter on the simulations will need to be further investigated.

Acknowledgements—Thanks are due to the Particle Physics and Astronomy Research Council (PPARC) for funding of the Light Gas Gun hypervelocity impact facility. E. A. Taylor would like to acknowledge funding from Matra Marconi Space (UK) and the University of Kent at Canterbury. Thanks are also due to Lee Abell of Century Dynamics for assisting in the simulations of the conchoidal diameter, carried out as part of a European Space Agency contract (11887/96/NL/JG)(managed by G. Drolshagen, ESTEC, ESA).

REFERENCES

1. Anon., Century Dynamics, AUTODYN user documentation (1998).
2. S. A. Quinones and L. E. Murr, Correlations of computed simulations with residual hardness mappings and microstructural observations of high velocity impact craters in copper, *Phys. Stat. Sol. (a)*, **166**, 763-789 (1998).
3. C. J. Hayhurst, H. J. Ranson, D. G. Gardner and N. K. Birnbaum, Modelling of microparticle hypervelocity oblique impacts on thick targets, *Int. J. Impact Engng.*, **17**, 375-386 (1995).
4. D. J. Gardner and M. J. Burchell, Thick target hypervelocity impact crater morphology: the influence of impact angle, speed and density ratio, *Proc. 2nd Euro. Conf. Space Debris*, ESA SP-393, pp. 481-486, March 17-19, ESOC, Darmstadt, Germany (1997).
5. C. J. Hayhurst and R. A. Clegg, Cylindrically symmetric SPH simulations of hypervelocity impacts on thin plates, *Int. J. Impact Engng.*, **20**, 337-348 (1997).
6. D. Alwes, Columbus-viewport glass pane hypervelocity impact testing and analysis, *Int. J. Impact Engng.*, **10**, 1-22 (1990).
7. F. McSherry, Numerical simulations of hypervelocity impacts on solar arrays, ESA Contract No., 11693/95/NL/JG (1996).
8. D. F. Medina, P. J. Serna and F. A. Allahdadi, Reconstruction of a hypervelocity impact event in space, *Characteristics and Consequences of Orbital Debris and Natural Space Impactors,* SPIE Proceedings 2813, pp. 137-147, August 8-9, Denver, CO (1996).
9. G. R. Johnson and T. J. Holmquist, An improved computational constitutive model for brittle materials, *High Pressure Science and Technology*, June, Colorado Springs, CO (1994).
10. T. J. Holmquist, G. R. Johnson, D. E. Grady, C. M. Lopatin and E. S. Hertel, Jr., High strain rate properties and constitutive modeling of glass, *Proc. 15th Int. Symp. Ballistics*, May 21-24, Jerusalem, Israel (1995).
11. G. Solve and J. Cagnoux, The behaviour of pyrex glass against a shaped charge jet, *Shock Compression of Condensed Matter - 1989*, (edited by S. C. Schmidt, J. N. Johnson and L. W. Davidson), pp. 967-970, Elsevier Science Publications B. V. (1990).
12. E. A. Taylor, C. J. Hayhurst and K. Tsembelis, Hydrocode modelling of space debris hypervelocity impact on soda-lime glass using the Johnson-Holmquist brittle material model, *Proc. 2nd Euro. Conf. Space Debris*, ESA SP-393, pp. 449-454, March 17-19, ESOC, Darmstadt, Germany (1997).
13. B. Lawn, Fracture of brittle solids - second edition, Cambridge solid state science series, Cambridge University Press (1993).
14. M. J. Burchell, M. J. Cole, J. A. M. McDonnell and J. C. Zarnecki, Hypervelocity impact studies using the 2 MV Van de Graaff accelerator and two-stage light gas gun of the University of Kent at Canterbury, *Meas. Sci. Tech.*, in press (1999).
15. N. R. G. Shrine, E. A. Taylor, H. Yano, A. D. Griffiths and J. A. M. McDonnell, Using solar cells as micro-particle detectors in low earth orbit, *Characteristics and Consequences of Orbital Debris and Natural Space Impactors,* SPIE Proceedings 2813, pp. 76-87, August 8-9, Denver, CO (1996).
16. F. Hörz, J. B. Hartung and D. E. Gault, Micrometeorite craters on lunar rock surfaces, *J. Geophys. Res.*, **76**(23), 5770-5798 (1971).
17. A. H. McHugh and A. J. Richardson, Hypervelocity particle impact damage to glass, North American Aviation, STR-241 (1974).
18. J. C. Mandeville, unpublished data in L. Berthoud and E. A. Taylor, Work package 2 report (analysis of impact calibration tests), Meteoroid and debris flux ejecta models, ESA contract no. 11887/96/NL/JG (1996).
19. R. E. Flaherty, Impact characteristics in fused silica, *Conf. AIAA*, AIAA 69-3647 (1969).
20. K. S. Edelstein, Hypervelocity impact damage tolerance of fused silica, *43rd International Astronautical Congress,* August 28-September 5 , Washington DC, IAF 92-0334 (1992).
21. E. Schneider, A. J. Stilp and G. Kagerbauer, Meteoroid/debris simulation experiments on MIR viewport samples, *Int. J. Impact Engng.*, **17**, 731-737 (1995).
22. J. C. Mandeville. Etude de crateres formes sur des surfaces de verre par l'impact de micrometeoroides artificielles, Ph. D. Thesis, Universite Paul Sabatier de Toulouse (1972).
23. D. E. Gault, Displaced mass, depth, diameter and effects of oblique trajectories for impact craters formed in dense crystalline rocks, *Moon*, **6**, 32-44 (1973).
24. B. G. Cour-Palais, Hypervelocity impact investigation and meteoroid shielding experiments related to Apollo and Skylab, *Orbital Debris*, CP-2360, pp. 247-275 (1982).
25. Yu Shanbing, Sun Gengchen and Tan Qingming, Experimental laws of cratering for hypervelocity impacts of spherical projectiles into thick target, *Int. J. Impact Engng.*, **15**(1), 67-77 (1990).

PERGAMON

International Journal of Impact Engineering 23 (1999) 905–919

INTERNATIONAL JOURNAL OF IMPACT ENGINEERING

www.elsevier.com/locate/ijimpeng

ANALYSIS OF THE FRACTURE OF GAS-FILLED PRESSURE VESSELS UNDER HYPERVELOCITY IMPACT

IGOR Y. TELITCHEV*, FRANK K. SCHÄFER†, EBERHARD E. SCHNEIDER†, and MICHEL LAMBERT‡

*Samara State Aerospace University, 34 Moskovskoye Shosse, Samara, SU-443086 Russia,
†Ernst-Mach-Institut - Fraunhofer Institut für Kurzzeitdynamik, Eckerstr. 4, D - 79104 Freiburg i. Br., Germany,
and
‡ESA-ESTEC, Postbus 299, NL-2200 AG Noordwijk, The Netherlands

Summary—The first part of the study summarizes the results of hypervelocity impact tests on unshielded thin-walled cylindrical pressure vessels made of aluminium alloy. Impact damages ranged from simple front wall perforation with no further damages inside the vessel to catastrophic bursting into many pieces. Two types of catastrophic bursting were observed: front side and rear side failure. Front side failure was initiated at the rim of the front side impact hole. The second part of the study analyzes the physical mechanisms that are involved in the hypervelocity impact process on pressure vessels and simulates the experimental results presented in the first part. In order to treat this problem, the fragment cloud that was generated from the front side impact was assumed to be completely ablated and decelerated in the gas, which is in correspondance with experimental observations for pressures exceeding a few atmospheres. In the presented model the impact event was divided in different stages, that are treated separately. These are: perforation of the front wall and generation of a strong gas shock wave, propagation and damping of the gas shock wave, impact of the gas shock wave on the rear wall and reflection thereof, propagation of the gas shock wave to the front side and interaction with it. Models for the treatment of front and rear side failure mechanisms are presented. The validity of the presented analysis was proven by simulation of the experimental results obtained in the first part of the paper.© 1999 Elsevier Science Ltd. All rights reserved.

NOTATION

a	Half crack length [mm]
D	Vessel diameter [mm]
D_{crack}	Damage zone adjacent to perforation hole [mm]
D_{hole}	Perforation hole diameter [mm]
E	Young's Modulus [MPa]
E_{kin}	Kinetic energy of projectile [J]
K_c	Static fracture toughness [MPa $m^{1/2}$]
K_c^{dyn}	Dynamic fracture toughness [MPa $m^{1/2}$]
K_F	Stress intensity factor for a petalled hole, defined by Folias [13]
K_r	Coefficient of reflection for a gas shockwave
K_σ	Stress intensity factor
p_0	Vessel pressure [bar]
p_c^{stat}	Reduced static burst pressure of a damaged (notched) pressure vessel [bar]
P_1	Pressure behind shock [bar]

0734-743X/99/$ - see front matter © 1999 Elsevier Science Ltd. All rights reserved.
PII: S0734-743X(99)00134-7

P_r	Pressure behind shock after reflection of the gas shockwave from the vessel's rear wall [bar]
R_m	Ultimate Tensile Strength [MPa]
$R_{p0.2}$	Yield Strength [MPa]
t	Wall thickness of vessel [mm]
v_f	Longitudinal velocity of the leading particle in a fragment cloud [km/s]
v_p	Projectile velocity [km/s]
v_r	Radial velocity of the fragment cloud [km/s]
Δp_s	Shock wave pressure [bar]
γ	Adiabatic coefficient
Π_1	Amplitude of the initial gas shockwave [bar]
σ_0	Compressive stresses acting in the plastic zone of the crack [MPa]
σ_h	Wall hoop stress [MPa]
$\sigma_{h,max}$	Reference hoop stress, calculated from experimental burst pressure [MPa]
σ_l	Wall longitudinal stress [MPa]
τ	Pulse duration of the gas shock [μs]

INTRODUCTION

Pressure tanks are important structural parts onboard spacecraft. In case such tanks are attached to the outer spacecraft wall they are exposed directly to the micrometeoroid and debris environment. This threat is nowadays recognized by the space agencies. Impacts of meteoroids and debris on pressure vessels can lead to catastrophic failure of vessels and terminate prematurely spacecraft missions. It is therefore necessary to explore and define the laws that govern pressure vessel's burst process in function of projectile and vessel characteristics. Impact experiments conducted at the Fraunhofer Institut für Kurzzeitdynamik–Ernst-Mach-Institut (EMI) [1, 2], showed that two main types of pressure vessel catastrophic failure are likely to occur: pressure vessel fracture from the front side and failure from the rear side.

While there has been a considerable experimental effort to simulate in the laboratory a great variety of damages by hypervelocity impact tests on pressurized containers, there has been little effort to treat the physical phenomena analytically.

In the first part of this paper an overview on the results of a hypervelocity impact test campaign on pressure vessels that has been performed under ESA contract is given. In the second part a theory for the description of the physical phenomena is provided, which is capable to predict vessel failure from the front and the rear side as a function of projectile parameters and vessel pressure. This theory is then applied to the test cases.

EXPERIMENTAL TEST PROGRAM

The purpose of this study [1, 2] was the experimental determination of impactor energies at hypervelocity and corresponding vessel pressures that lead to catastrophic failure of a thin-walled pressure vessel. The test samples were cylindrical vessels, with a wall thickness of 1 mm, a length of 350 mm and a diameter of 150 mm, made of Al 5754 (AlMg3), an aluminium magnesium alloy with a moderate strength of R_m = 261 MPa, an elongation of A = 8 % and a static fracture toughness of K_c = 21.6 MPa $m^{1/2}$. The aluminium vessels were manufactured from drawn tubes. Plane caps were welded to the vessel ends. The wall was then machined down to the final thickness of nominally 1.0 mm. The manufacturing process introduced local wall thickness variations of up to 20 %.

Quasi-Static Inflation Tests

Two quasi-static inflation experiments were conducted on Al 5754 vessels. At inflation rates of around 0.3 bar/s, the burst pressures were 22.5 bar and 25.6 bar (minium wall thickness 0.9 mm and 1.0 mm, respectively). From the latter burst pressure a reference hoop stress ($\sigma_{h,\,max}$) was calculated. 3 static burst experiments involved vessels with well defined defects (notches) of different geometry. The first defect consisted of a circular impact hole which was created by impact of a projectile 2 mm in diameter at a velocity of 6.9 km/s. In a second vessel a hole of the same diameter as the impact damage was drilled, and a third had a machined slit in axial direction of a length equal to the hole diameter. All defects were closed by thick flexible rubber-sheets to prevent air exhaust during inflation. Burst pressures amounted to 27.0 bar, 24.4 bar, and 26.1 bar, respectively, which means basically no difference to the unnotched vessels. The large scatter of these results reflects the uncertainties in the wall thicknesses.

Hypervelocity Impact Tests

All projectiles were aluminium spheres, impacting at velocities v_p of around 7 km/s at normal incidence in the center of the vessels cylinder wall. Projectile diameters (d_p) ranged from 2 mm to 4.9 mm, at impact velocities between 6.6 km/s and 7.5 km/s, having a kinetic energy of 260 J to 4150 J. Inflation pressures (p_0) ranged between 1.8 bar and 24.6 bar. To determine the projectile diameters and vessel pressures that result in catastrophic rupture, for a given kinetic energy the vessel pressure was increased in subsequent tests until catastrophic failure occurred. This was done for several energy levels. Variation of kinetic energy was realized by variation of projectile diameters. The experimental results are listed in Table 1.

Table 1 Experimental parameters of hypervelocity impact tests on Al-pressure vessels

No.	Experimental parameters					Damage
	d_p [mm]	v_p [km/s]	E_{kin} [J]	p_0 [bar]	$\sigma_h/\sigma_{h,\,max}$	rupture [type†]
Al-1	2.0	$6.7^{\pm 0.2}$	260	2.0	0.08	no
Al-2	2.0	7.5	320	6.0	0.23	no
Al-3	2.0	7.5	320	10	0.39	no
Al-4	2.0	6.9	270	19.2	0.75	no
Al-5	2.0	7.1	290	24.6	0.96	no
Al-6	3.0	7.1	930	19.1	0.75	no
Al-7	3.5	6.7	1300	12.7	0.50	no
Al-8	3.5	6.9	1380	23.0	0.90	yes [f.s.]
Al-9	4.1	6.6	2240	8.4	0.33	no
Al-10	4.1	6.8	2380	11.7	0.46	yes [f.s.]
Al-11¶	4.1	7.0	2520	13.0	0.51	yes [r.s.]
Al-12¶	4.4	7.2	3200	6.7	0.26	yes [r.s.]
Al-13	4.4	7.3	3290	ca. 7.9	0.31	no
Al-14	4.4	7.1	3120	15.6	0.61	yes [f.s.]
Al-15	4.4	7.3	3290	16.0	0.63	yes [f.s.]
Al-16	4.9	6.9	4030	1.8	0.07	no
Al-17	4.9	6.9	4030	2.9	0.11	no
Al-18	4.9	6.9	4030	4.3	0.17	yes [r.s.]
Al-19	4.9	7.0	4150	18.3	0.71	yes [r.s.]

† f.s.: front side; r.s.: rear side

¶ experiments failed

At low pressures impact damages at the rear wall of the vessel are craters, perforation holes, bulges and spallations, generated by fragment impact, and thus depending strongly on the projectile diameter (Figure 1). The wall stresses were not sufficient to propagate cracks to cause catastrophic rupture. As the pressure is increased, the interaction of the hypervelocity fragment cloud with the gas is increased. The fragments of the smaller and medium sized projectiles were ablated and decelerated strongly, thus leaving no or few impact traces at the vessel's backwall.

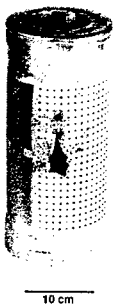

Figure 1

Exp. Al-17 (rear view)
d_p=4.9 mm, v_p=6.9 km/s
p_0=2.9 bar, $\sigma_h/\sigma_{h,max}$=0.11

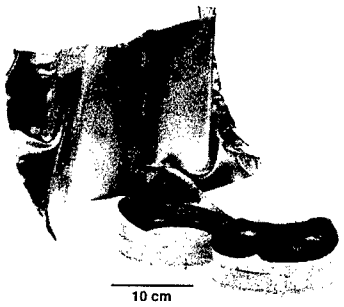

Figure 2

Exp. Al-10 (front view)
d_p=4.1 mm, v_p=6.8 km/s
p_0=11.7 bar, $\sigma_h/\sigma_{h,max}$ =0.46

Figure 3

Exp. Al-18 (rear view)
d_p=4.9 mm, v_p=6.9 km/s
p_0=4.3 bar, $\sigma_h/\sigma_{h,max}$ =0.17

Figure 4

Exp. Al-19
d_p=4.9 mm, v_p=7.0 km/s
p_0=18.3 bar, $\sigma_h/\sigma_{h,max}$ =0.71

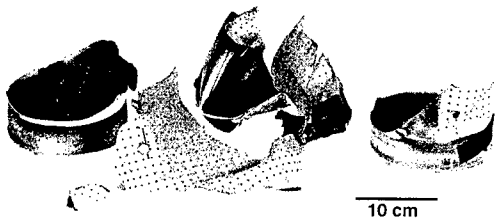

If large pressures are considered, the hoop stresses are high enough to propagate cracks from the rim of the impact hole into the wall and thus cause front side rupture of the vessel, even when small projectiles impact (Figure 2). If the loading conditions (projectile kinetic energy and gas pressure) are high enough, the rear wall is strongly bulged outwards due to the generated strong gas shockwave. Rear wall failure (Figure 3) and complete catastrophic failure (Figure 4) is induced by large projectiles.

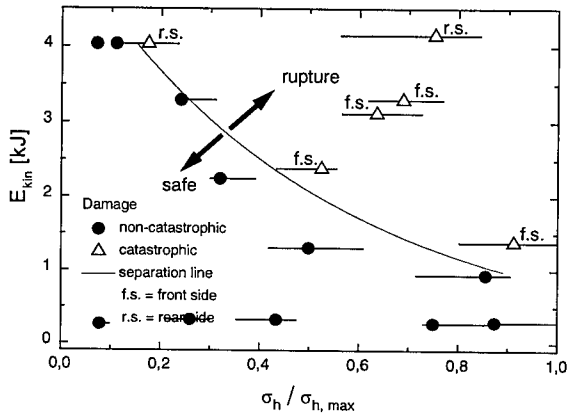

Figure 5 Test results - Hypervelocity Impacts on Pressure Vessels

At high pressures, in none of the experiments impact craters were identified in the vessel's rear wall. In Figure 5, all results are compiled in a diagram with the normalized hoop stresses as abscissa and the projectile kinetic energy as ordinate. Error bars account for uncertainties in wall thickness and associated wall stresses. The experimental results are divided into 'catastrophic' and 'non-catastrophic'. The borderline that separates the parameter regimes has been fit. Experimental parameters taken from below this line result in front wall perforation and different types of non-catastrophic rear- and front side damage, whereas catastrophic rupture occurs for experimental parameters taken from above the curve.

MECHANICAL PROPERTY ANALYSIS FOR AlMg3 (Al 5754) ALUMINUM ALLOY

In gas-filled cylinder shells the stresses in circumferential direction (hoop stress σ_H) are twice the longitudinal stresses σ_L. Thus, in process of fracturing the cracks tend to run longitudinally, perpendicular to the hoop stress. For this reason material properties in circumferential direction were tested. The test samples were cut from cylindrical vessels, which had a wall thickness of 1 mm, a length of 350 mm and a diameter of 150 mm. As a result of the conducted tests the following input data were selected and recommended for the further computation: Ultimate Tensile Strength R_m=261 MPa; Yield Strength $R_{p0.2}$=183 MPa; Youngs Modulus E=71000 MPa; Static Fracture Toughness K_c=21.6 MPa·$m^{1/2}$; Dynamic Fracture Toughness K_c^{dyn}=24.0 MPa·$m^{1/2}$. Strain rates for the dynamic tensile tests were in the order of 100 s^{-1}.

FRACTURE OF DAMAGED PRESSURE VESSELS UNDER QUASI-STATIC INFLATION

Computation of burst pressures of notched vessels under quasi-static inflation

The approach described in [3, 4] was used for the computation of the critical hoop stress $\sigma_{h,max}$ that corresponds to the burst pressure of an impact damaged pressure vessel if inflated quasi-statically. The diameter of the model hole is equal to the diameter of perforated hole (D_{hole}). The model presented in [3, 4] postulates the existence of two radial cracks emanating at the boundary of a circular hole. The radial cracks are normal to the hoop stress. The length of the cracks is bounded by a damage zone (D_{crack}), which is a zone of spall cracks adjacent to the perforated hole (Figure 6).

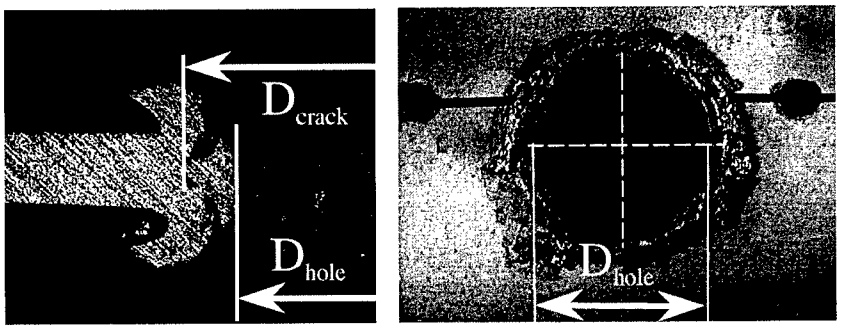

Figure 6 Damage zone adjacent to the perforated hole

A load scheme corresponding to a cylinder shell was built (Figure 7, 8). The load applied to the crack surfaces accounts for the influence of shell hoop stress σ_H and shell longitudinal stress σ_L. The problem was solved numerically by the method of singular integral equations, Ref. [5]. Comparison of the calculated results to the quasi-static inflation test results of notched pressure vessels showed good agreement. Variations did not exceed 5 %, thus the proposed models and the developed program can be used for the analysis of the pressure vessels fracture behavior under hypervelocity impact.

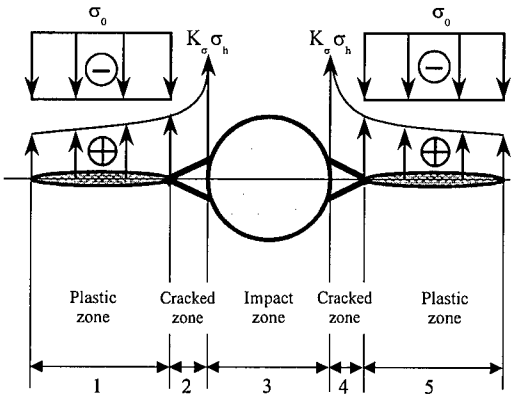

Figure 7 Load scheme (K_σ: stress intensity factor, σ_0: compressive stresses acting in the plastic zone of the crack)

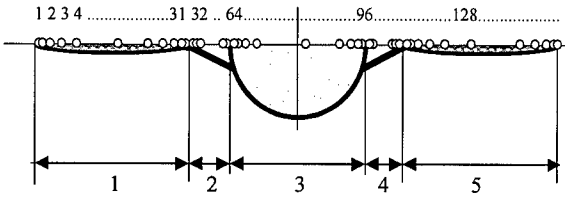

Figure 8 Chebyshev's nodes on the damage surface

Computation of critical stresses that lead to catastrophic front-side bursting of impact-damaged pressure vessels

In the following paragraph, a hypothetical explanation for the front side failure mechanism is given. This approach is then used to calculate the critical pressures and impact parameters that lead to front side failure of the pressure vessels.

During hypervelocity impact the projectile penetrates and perforates the front side, generating a fragment cloud (Figure 9). The expanding fragment cloud propagates to the vessels rear side. It is subject to a strong interaction with the gas. The model makes the assumption that a strong gas shock wave is generated that travels along with the fragment cloud. A second assumption suggested for the case of front wall fracture is that the fragments in the cloud are completely ablated during their propagation in the gas, thus mechanical impact damages are not accounted for by the model. This second assumption is reasonable and corresponds to the observations in experiments where gas pressures exceeded a few bars. The shock wave reaches the rear side, reflects, travels to front side and produces a pressure pulse there. The amplitude of this wave will, in certain conditions, be high enough to cause initiation and propagation of cracks from the rim of the front side impact hole.

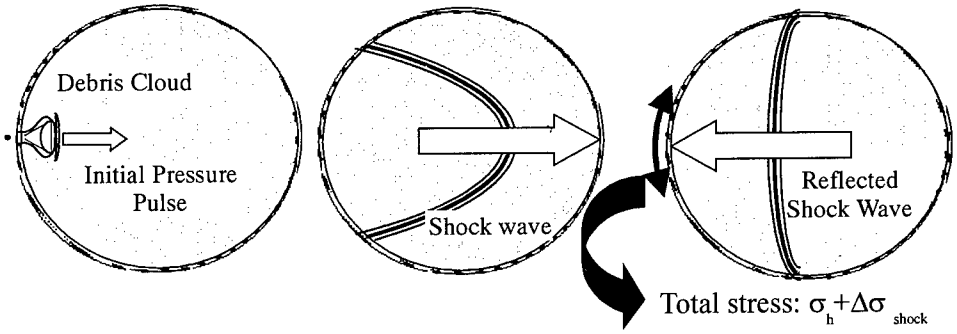

Figure 9 Basic stages of penetration, shock wave generation, -propagation and -reflection

In the following it is assumed that type and size of the front side impact damage is solely determined by the properties of the space debris particle. The pressure inside the vessel is not considered to influence the size of the front side impact damage. Given a specific impact size, i.e. hole diameter and damage zone, the reduced static burst pressure (p_c^{stat}) that would be measured in a quasi-static inflation experiment, can be calculated.

The hypothesis proposes that front side failure occurs when inflation pressure p_o and an additional shock wave pressure Δp_s that is reflected from the front side, exceeds a certain critical limit, which is the above mentioned reduced static burst pressure (p_c^{stat}). Thus failure will occur, when

$$(p_o+\Delta p_s) \geq p_c^{stat}(K_c) \tag{1}$$

The calculated value for the reduced burst pressure p_c^{stat} can be considered as an upper estimate for the static burst pressure p_o for the case of an impacted pressure vessel. p_c^{stat} can be calculated as a function of impactor parameters (i. e. projectile velocity and diameter). By using Eq. (1), it is assumed that a pressure pulse amplitude behaves like an extra static pressure load to the shell and thus transforms directly into shell stresses.

For the computation of the maximum stresses in hypervelocity impact tests, the dynamic fracture toughness was used:

$$\sigma_{h,max} \cong \sigma_{h,max}\left(K_c^{dyn}\right) \tag{2}$$

For the calculation of the critical (static) inflation pressures and corresponding critical stresses $\sigma_{h,max}(K_c)$ of impact damaged pressure vessels, the "static" K_c was used. The damage parameters (D_{hole} and D_{crack}) were determined by taking measurements on impact damaged samples.

The procedure described in [3, 4] was used for the computation of $\sigma_{h,max}(K_c)$ and $\sigma_{h,max}(K_c^{dyn})$. The results of the computation for $\sigma_{h,max}(K_c)$ and $\sigma_{h,max}(K_c^{dyn})$ are presented in Figure 19.

For increasing particle diameter (at constant impact velocity), hole and damage zone diameters increase. As a consequence, the maximum stresses $\sigma_{h,max}(K_c)$ and $\sigma_{h,max}(K_c^{dyn})$ decrease. This trend can be observed in the curves of Figure 19.

FRACTURE OF PRESSURE VESSELS FRONT WALL UNDER HYPERVELOCITY IMPACT

The purpose of the present analysis is to determine the critical values of projectile diameter, impact velocity and inflation pressure, that lead to front side failure.

Evaluating of the characteristics of debris clouds in pressure vessels

An approach suggested by H. F. Swift et. al. (Ref. [6]) was used to evaluate the characteristics of debris clouds inside pressure vessels. The following assumptions were made:

- Material behavior is governed by the laws of fluid-dynamics;
- The debris cloud behind the pressure vessel front wall is a symmetrically expanding sphere the center of which moves from the front side of a pressure vessel to the rear side;
- All of the material within the sphere is concentrated at its surface;
- Negligible momentum is transferred to the impacted pressure vessel or to the debris plume projected from the front surface of the pressure vessel's front wall

Using the procedure described in Ref. [6], the velocities of the leading particles v_f in a fragment cloud that correspond to impacting projectile diameters of 2.01 mm, 2.97 mm, 3.45 mm, 4.13 mm, 4.39 mm, 4.93 mm at an impact velocity of 7.0 km/s were calculated.

Generation and propagation of shock waves in gas

In the following the generation of a shock wave inside a pressure container by a hypervelocity debris cloud is analyzed. To this purpose, motion of gas under impulsive load will be considered. For the evaluation of the initial parameters the approach suggested by Zeldovich, Ref. [7], was used. The following assumptions were made:

- The half-space $x > 0$ is occupied by a perfect gas with constant specific heats;
- Initially, at time zero, the density of the gas is everywhere uniform, and the pressure, temperature, and initial speed of sound are zero;
- All of the material within the fragment cloud is concentrated at its surface;
- The surface of the fragment cloud is continuous (contains no gaps).

Let the gas surface be subjected to an expanding debris cloud (Figure 10). A pressure pulse of short duration (impulsive load) is applied to the external surface of the gas. By this method the action of a fragment cloud to gas inside a pressure vessel is modeled.

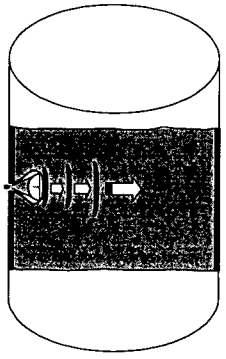

Figure 10 Debris cloud inside pressure vessel

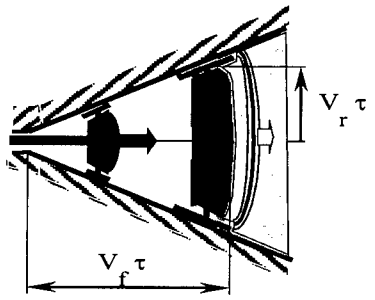

Figure 11 Expanding piston pushing into the gas

In a short time interval τ an expanding planar piston is pushed into the gas with a velocity v_f (Figure 11). The impact of the plate creates a shock wave in the gas, which propagates with a velocity close to v_f. From the energy and momentum conservation it is possible to evaluate the initial pressure pulse amplitudes Π_1 and pulse duration τ.

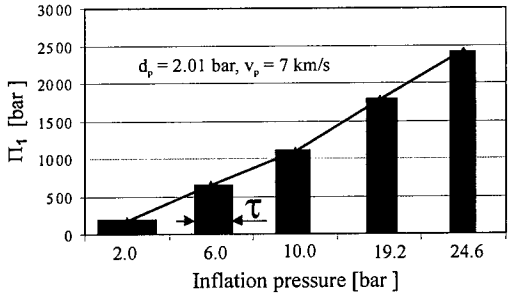

Figure 12 Initial pressure pulses calculated that correspond to the test conditions

Figure 12 shows the initial pressure pulse amplitudes and durations calculated for test parameters that correspond to some of the EMI tests. For increasing inflation pressure, the pressure amplitude increases also whereas the pulse duration decreases.

Phase of motion and damping out of the shock wave in gas

This part of study analyzes the damping of the amplitude of a shock wave that travels in gas to the pressure vessel rear side. The problem is to determine the state of the gas at a time which is large compared to the impact time τ. The above problem was formulated and analyzed in a paper [8] in which the physical features of the resulting motion and of the mathematical solution were explained. The following assumptions were made:

- The gas inside the pressure vessels is a perfect gas with constant specific density;
- The gas-dynamic solutions in the vicinity of the pressure vessel's rear side are self-similar;
- The shock wave propagates through a gas of uniform density;
- The gas in the plane x = 0 is always at rest (bounded by a rigid wall).

One-dimensional adiabatic flows of perfect gas with constant specific heats are considered. It is rather evident that close to the rear side, when the shock wave encompasses a mass M, the motion is self-similar. The pressure behind the front decreases with an increase in the mass M as $P_1 \sim M^{-n}$. Here, the constant n is the exponent corresponding the Lagrangian coordinate. The test pressure vessels contained gaseous Nitrogen (N_2). For a diatomic gas $\gamma = 7/5$ (γ = exponent of the isentropic curve). In [7] it is shown that if the gas in the plane x = 0 is bounded by a rigid wall, then n = 1 (for the case of $\gamma = 7/5$).

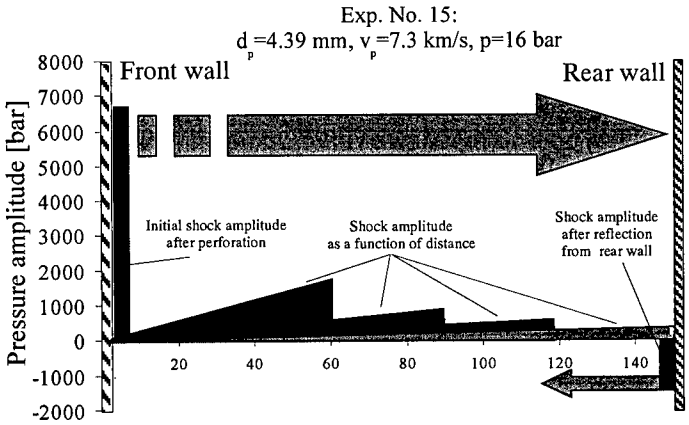

Figure 13 The motion, damping out, and reflection of a shock wave that propagates to the vessels rear side

Using the self-similar solution [7, 8], the pressure amplitude of the shock wave can be evaluated at any point for the shock wave propagation to the rear side. This is illustrated in Figure 13, where the evolution of the pressure amplitude that corresponds to EMI experiment No. Al-15 is shown.

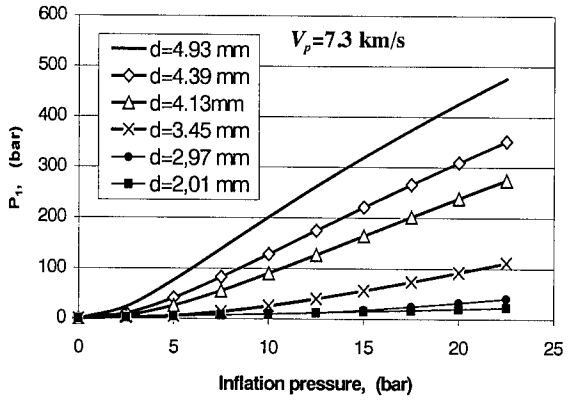

Figure 14 Pressure amplitude just before reflection of the shock wave from the rear wall

Figure 14 illustrates the relationship between pressure amplitude just before reflection from the rear side and inflation pressure. It can be seen that as the inflation pressure is increased the pressure amplitude increases also. This fact corresponds to the proposed earlier assumption that a higher gas density is more efficient in transferring the debris cloud's kinetic energy into shock wave energy. At the same time however, for increasing inflation pressure the shock wave damping is enhanced. The calculated pressure amplitude at the vessel's rear side that is produced by a particle diameter of 2.01 mm is of the same order as the inflation pressure, which is to say that the shock wave was damped completely.

Figure 15 illustrates the process of the damping out the shock wave and stresses the fact that the gas shock waves that are generated by impact of particles with a diameter of less than 3 mm damp out completely at the rear side.

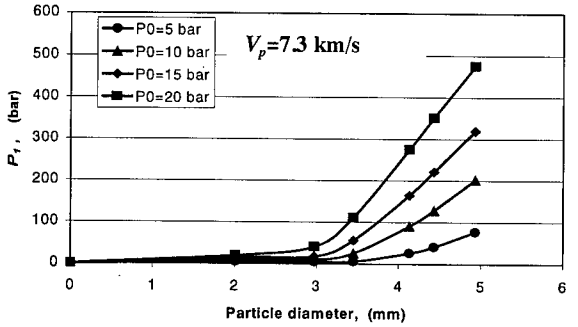

Figure 15 Pressure amplitude just before reflection of the shock wave from the rear wall

Reflection of the shock wave from the vessel's rear side

Here, the reflection of the shock wave from the pressure vessel's rear wall is considered. In this chapter the enhancement of the pressure amplitude upon reflection from the rear side is calculated according to an approach suggested by Stanyukovich [8] for a plane stationary stream (Figure 16). The following assumptions were made:

- The front of the shock wave is plane;
- The gas stream is stationary;
- The rear wall is an absolutely rigid, stationary, plane wall;
- The velocity of the stream is perpendicular to the rear wall.

It is assumed that both stream and reflected shock wave are stationary and therefore the parameters obtained for the reflected shock wave will be valid only for the first instants after reflection.

Figure 17 illustrates the relationship between the coefficient of reflection (K_r) and inflation pressure (p_0). It can be seen that for increasing inflation pressure the coefficient of reflection increases. As a consequence the pressure amplitude of the reflected shock wave increases, too.

Figure 16 Reflection of the shock wave from the rear wall

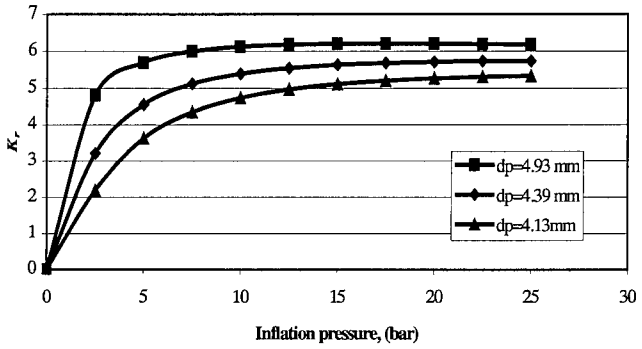

Figure 17 Relationship between coefficient of reflection and inflation pressure

Damping of the shock wave as it travels from the rear- to the front side of the vessel

It can be assumed that the shock wave reflected from the pressure vessel rear wall obeys the laws of self similar motion of gas (Ref. [8]). Let us imagine the half-space $x > 0$ occupied by a perfect gas with constant specific heats. Initially, at $t = 0$, the density of the gas is everywhere uniform, and the pressure, temperature and initial speed of sound are zero. In the plane $x = 0$ the gas is bounded by a rigid wall (pressure vessel rear wall).

Let a pressure pulse of short duration (impulsive) be applied to the surface of the gas. In a short time interval a plane piston (rear wall) is pushed into the gas, creating a pressure P_r. After the time interval the piston is "instantly" removed.

The general method of finding the self-similar solution for the problem of an impulsive load does not differ in principle from the method of solving the problems described in above section of this paper. Some results of the calculation are presented in Figure 18. This diagram illustrates the process of the damping of the shock wave that travels to the front (impact damaged) wall after reflection from the rear wall. Evolution of the pressure amplitude corresponds to EMI experiment No 10 [1].

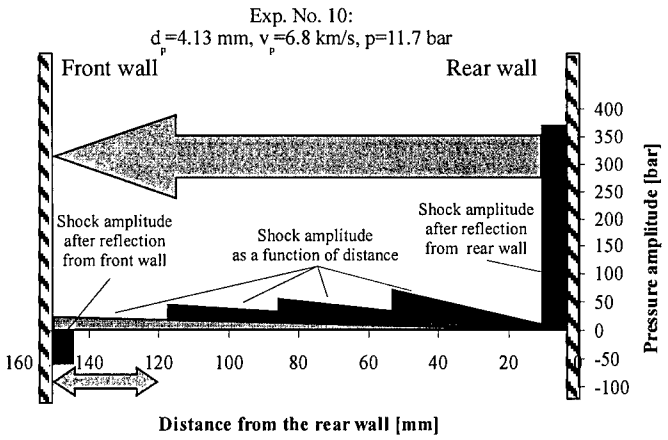

Figure 18 Damping of the shock wave that is reflected from the rear wall. Reflection from the front wall

Shock wave reflection the from the pressure vessel's front wall

For the evaluation of the pressure amplitude that is reflected from the front wall the approach described in previous part of this paper was used. Reflection of a shock wave from the front wall, i.e. the impact damaged shell, can cause catastrophic fracture if the hoop stress exceeds the calculated critical hoop stresses $\sigma_{h,max}(K_c^{dyn})$. The critical hoop stress $\sigma_{h,max}(K_c)$ corresponds to the cases where shock waves are damped out. According to the computational results this situation occurs when $d_p < 3.45$ mm completely (border 1, Figure 19). Front wall fracture is governed then by the effect of the inflation pressure and corresponds to a burst under quasi-static inflation.

Fracture of pressure vessels impacted by hypervelocity particles with a diameter larger than 3.45 mm is governed by the combination of inflation pressure and additional shock pressure (border 2, Figure 19). In this case, the dynamic material properties have to be taken into account.

Using the described procedure and the developed program, the critical parameters (E_{kin}, p_0), which correspond to the border between simple perforation and catastrophic rupture of front wall, were calculated. The results of calculation are illustrated in Figure 19.

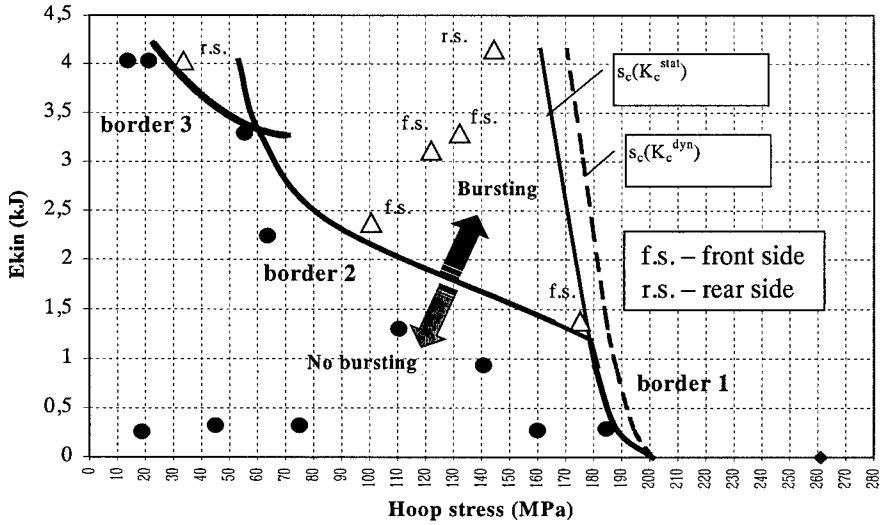

Figure 19 The border line between simple perforation and catastrophic fracture of impact damaged pressure vessels

FAILURE OF THE REAR WALL UNDER HYPERVELOCITY IMPACT

Evaluation of the damage parameters of the pressure vessel rear wall

For the analysis of rear side failure the combined effect of fragment impact and impact of the gas shockwave has to be taken into consideration, which is in contrast to the analysis performed for front side failure, that was solely based on the effect of the gas shock wave. For this reason the effect of the fragment cloud will be considered hereafter. In a hypervelocity impact on a gas-filled pressure vessel, the vessel's front wall fulfills the function of the shield for the vessel's rear wall [10]. In the absence of gas inside the vessel, almost the full analogy with a classical Whipple shield can be drawn, except - of course - for the curvature of the walls.

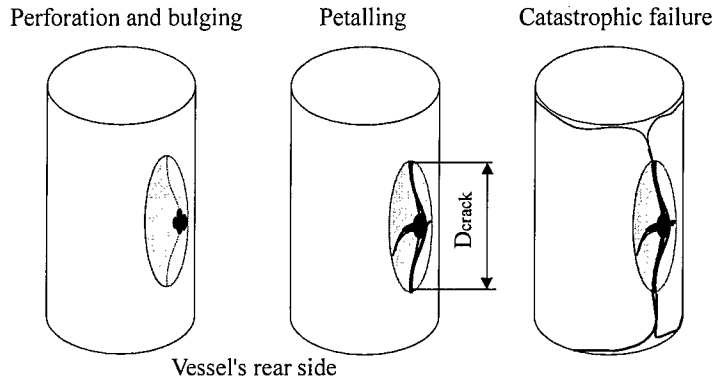

Figure 20 Basic stages of pressure vessel failure from the rear side

When an unpressurized vessel is impacted by a hypervelocity projectile, a fragment cloud is generated that expands inside the vessel and produces an impact damage on the vessel's rear wall over some area. The cloud fragments spread radially, therefore the size of rear wall damage increases with the distance between front and rear wall. Owing to the debris cloud's radial extension the spacing between the individual fragments increases. If the vessel diameter is small, a large central perforation hole as a result of the joint action of the fragments is produced in the rear wall. If the distance from the front wall to the rear wall is rather large (150 mm and higher), the integral rear wall damage will be rather composed of a great number of small-sized damages (tiny perforations / craters) due to the individual impact of fragments.

If the vessel is filled with gas, the fragments are decelerated and ablated. This is witnessed by a change in the shape of the cloud [11]. It is known, that the largest fragments are located nearby the leading edge of the cloud on the symmetry axis, and smaller sized fragments are located off-axis. The large fragments decelerate and ablate less than small-sized fragments, therefore the cloud's off-axis part separates from the central part [11]. In this process the cross-sectional size of the off-axis part of the cloud increases due to its radial expansion velocity. The leading edge part of the cloud propagates along the extension of the original projectile trajectory, thus its cross-sectional size remains almost unchanged. As a result of the velocity dispersion, the debris cloud takes the shape of a wedge. This wedge encounters the rear wall and can cause rear wall bulging and petaling. The gas medium inside the vessel reduces the fragments clouds kinetic energy and thus decreases the amplitude of the loading pulse on the rear wall. However the gas does not always execute a protective function, because at a certain gas density a strong gas shock wave is generated, that impacts the rear wall and can cause rear side failure.

If the projectile kinetic energy is great enough and inflation pressures are below a certain level, the rear wall will be perforated by the leading fragments (Figure 20). The off-axis

fragments that overcame the resistance of the gas medium can produce high radial and circumferential tensile stresses and the characteristic deformation pattern (bulging) upon impact on the vessel's rear side. Particularly high stresses are generated in the central rear wall area if it was already perforated by the leading fragments. The high stress concentration can initiate the growth of axial cracks, which develop from the rim of impact hole or at the top or bottom of the bulge. The sectors so formed are then pushed back by the residual impulse of the fragment cloud to form petals. In distinction to the "classical" petal hole this type damage is only produced in a cylindrical shell which is in under stress as a result of the gas pressure within the vessel. As a consequence of the stress distribution in a cylindrical shell, the longitudinal size of the damage is roughly 1.5-2.0 times larger than the circumferential one.

Calculation of critical impact parameters which lead to the catastrophic failure of pressure vessel rear wall

Once petalling or crack formation starts in the vessel's rear wall, the wall stresses act as a driving force for the cracks. It is evident that there is some critical pressure under which crack propagation and subsequent catastrophic failure takes place. In this case the marginal crack tends to run axially because firstly, the size of petal damage is largest in this direction and secondly, this direction is perpendicular to the wall hoop stresses.

In order to perform a survivability analysis of a vessel with a thin wall subjected to hypervelocity impact, it is necessary to have the relationship between rear shell damage parameters (i.e. hole and petal sizes) and projectile and target parameters. Unfortunately there is no comprehensive collection of semi-empirical relations for impact damages of curved Whipple shields filled with gas. In order to overcome this lack of data, to a first approximation, the rear side damage parameters can be taken from relations obtained in classical Whipple shield impact tests, for example from [12]. This paper performes the analysis of the double-bumper shield impact tests of the pressurized module COLUMBUS. Using the results of the mentioned reference, it is possible to estimate the main spray angle of the debris cloud generated upon impact of spherical particles on a thin bumper wall (which corresponds to the vessel's front wall), the size of cratered area on the backwall plate (i. e., the vessel's rear wall) and the size of the petalled hole in the backwall.

In order to take into account the influence of gas inside a vessel, the damage sizes were drawn from the impacted samples from [1] by inspection of the impacted vessels. The petal damage was considered as a thin slit having an overall length equal to the axial distance between the petal tips. Having these information, the method of singular integral equations [3, 4, 5] was applied for solving numerically the structural response of a thin-shell cylindrical structure containing an axial crack. Since under the action of the internal pressure the edges of cracks that emerge from the petalled hole are bent outward, the stress intensity coefficient increases. Folias [13] suggested a factor of $K_F=(1+1.61a^2/(D/2)t)^{1/2}$, where ($D_{crack}$ = 2a) - crack length (Figure 20), D - vessel diameter. The reduction of the crack driving force due to air leakage through the perforation holes was neglected.

The results of computation are illustrated in Figure 19 as a curve (border 3) which corresponds to the border line between simple perforation of the vessel and catastrophic failure initiated at the vessel's rear wall. The combination of impact parameters (E_{kin}, p_0) that correspond to points above this curve result in catastrophic fracture. The result compares well with the experimental data. Thus, the presented analysis provides a powerful means of predicting catastrophic rupture of hypervelocity impacted pressure vessels.

CONCLUSIONS

While our investigation is continuing, the following conclusions can be reached:

- Comparison of the calculated results to the quasi-static inflation test results of notched pressure vessels showed good agreement. Variations did not exceed 5 %, thus the proposed models and the developed program can be used for the analysis of the pressure vessels fracture behavior under hypervelocity impact
- Shock waves generated in gas from impact of particles with diameters less than 3.45 mm damp out completely inside the pressure vessel for the presented vessel geometry and the considered impact velocity. In this case, fracture occurs from the vessel's front side and is governed by the effect of the inflation pressure, thus corresponds to a burst under quasi-static inflation
- Fracture of pressure vessels of the presented geometry which are impacted at 7 km/s by particles with a diameter larger than 3.45 mm is governed by the combination of inflation pressure and additional shock pressure. In this case, the dynamic materials properties have to be taken into account. Bursting can occur from the vessel's front or rear side
- The intensity of a shock wave inside a hypervelocity impacted gas pressure vessel increases as the particle's kinetic energy and inflation pressure increases
- The developed procedure can be used by the designers of pressure vessels to answer the question if a hypervelocity impact will result in catastrophic burst. This applies to burst initiated at the rim of the impact hole (front side burst) or at the vessel's rear wall (rear side burst)

REFERENCES

1. F. Schäfer and E. Scheider, "Impact Testing – Impact on Pressure Vessels, Hypervelocity Impacts on Aluminum Pressure Vessels", Report No. EMI-HVI-PVI 001, Ernst-Mach-Institut, Freiburg, Germany, May 15, 1996
2. F. Schäfer, E. Schneider, and M. Lambert, "Hypervelocity Impacts on Cylindrical Pressure Vessels - Experimental Results and Damage Classification", PVP-Vol. 351, Structures under Extreme Loading Conditions, Proc. 1997 ASME Pressure Vessels and Piping Conference, Orlando, FL, USA, 28. - 31.07.1997
3. I. Ye. Telitchev et al., "Residual Toughness of Spacecraft Structural Elements Damaged by Space Debris", Int. J. Impact Engn. Vol. 20, 1997
4. I. Ye. Telitchev et al., "Space Station Pressurized Module Design Considering Space Debris Hazard", Proc. 2-nd Europ. Conf. On Space Debris, ESA SP-393, p.553-556, Darmstadt, Germany, 1997
5. M. P. Savruk, P. N. Osiv, and I. V. Prokopchuk, "Numerical Analysis of Crack Theory Problems", Naukova Dumka, Kiew, 1989
6. H. F. Swift et al., "Designing space vehicle shields for meteoroid protection: A new analysis", Adv. Space Res. Vol. 2, pp. 219-234, 1983
7. Ya. B. Zel'dovich, Yu. P. Raizer, "Physics of Shock Waves and High-Temperature Hydrodynamic Phenomena", Academic Press, 1967
8. K. P. Stanyukovich, "Unsteady Motion of Continuous Media", Academic Press, 1960
9. Yu. P. Raizer, "Motion of a gas under the action of a concentrated impact along ist surface (as a result of an explosion on the surface)", Zh. Pricl. Mekhan. I Tekhn. Fiz., 1963, No. 1, 57-66
10. E. L. Christiansen et. al, "Debris Cloud ablation in Gas-Filled Pressure Vessels", Int. J. Impact Engn. Vol. 20, 1997
11. F. Schäfer, E. Schneider, M. Lambert, and M. Mayseless, "Propagation of Hypervelocity Impact Fragment Clouds in Pressure Gas", Int. J. Impact Engng. Vol. 20, 1997
12. Hans-G.Reinmerdes et al., "Ballistic Limit Equations for the COLUMBUS-Double Shield Concept", Proc. 1st Europ. Conf. On Space Debris, ESA SD-01, p.433-439, Darmstadt, Germany, 1991
13. E. S. Folias, Int. J. Fracture Mech., (1), p.104, 1965

PERGAMON

International Journal of Impact Engineering 23 (1999) 921–932

INTERNATIONAL JOURNAL OF IMPACT ENGINEERING

www.elsevier.com/locate/ijimpeng

CRATERING MODEL OF ASTEROID AND COMET IMPACT ON A PLANETARY SURFACE

ALEXANDER V. TETEREV

Faculty of Applied Mathematics and Computer Science, Belarus State University, Minsk, 220050, Belarus

Summary—A discrete model of crater formation describing the ejection of rock fragments from a crater has been developed. This model takes into account elastic-plastic behavior of media, energy transfer by radiation, contact boundaries, thermal and force interaction of gas and fragments of ejected rock. The results obtained in the course of computational experiments demonstrate versatility and flexibility of the developed model in application to different variants of problems on impact and explosive cratering. They will be presented in a second part of the paper. © 1999 Elsevier Science Ltd. All rights reserved.

INTRODUCTION

The studies on mechanics of cratering upon explosion and hypervelocity impact have a long history [1-3]. The works on numerical simulation of this phenomenon [4-9] occupies a special place in these studies since a computational experiment is the only method that allows obtaining the data on crater parameters and rock outburst dynamics for such problems as the fall of large meteorites on planetary surfaces. A great number of factors determining the after-effects of powerful energy release near the surface of a condensed medium are interdependent. Therefore, a physical-mathematical model is required which self-consistently takes into account all the totality of processes and properties both in gaseous and condensed media to perform a numerical experiment adequately simulating the above phenomenon. The following phenomena are to be referred to such processes: hydrodynamic rock material flow in the approximation of a condensed medium in the nearest energy-release zone; its elastic-plastic behavior in the regions where a load value decreases with changing strength properties; formation of cracks, their growth and merging which lead ultimately to rock fracture with a well determined granulometric composition of fragments and dust; formation of a crater bottom surface representing a region where it is necessary to proceed from a description of the fractured rock material in the form of a continuous medium to a discrete representation of movement of separate fragments; ejected rock movement in a gaseous medium with allowance for gravity, resistance, heat and mass transfer due to evaporation and condensation. Besides, the model has to take into account occurring changes in parameters, characteristics, media properties and relief of the terrain.

It is quite clear that a model of such a complicated phenomenon can be at first constructed only in some approximation. The results obtained on the basis of such a model are a source of its further improvement. In can be said that at present such a physic-mathematical model has been developed and can be applied to simulation of cratering for a two-dimensional

0734-743X/99/$ - see front matter © 1999 Elsevier Science Ltd. All rights reserved.
PII: S0734-743X(99)00135-9

case. The model elements have been tested and allow obtaining certain results to carry out investigations. Some features and limitations of the developed model are considered below.

CRATERING MODEL

Physical aspects and premises for the developed cratering model

At an intensive energy release in the immediate vicinity of the interface of gaseous and condensed media, their essential spatial transport occurs, accompanied, as a rule, by interpenetration of different substance phases. In this case, the selection of Euler's approach to describe the above phenomenon seems quite natural. At the initial stage of energy release, when the strength properties of a solid can be usually neglected, the transport is commonly described in the hydrodynamic approximation of a condensed medium representing the differential equations of mass, momentum and energy conservation. If in addition the speed of a cosmic body exceeds 15 km/s, then to correctly describe the processes proceeding in the planet atmosphere, it is necessary that the energy transfer by radiation should be taken into account in that or another approximation [10,11].

Formally, the cratering can be divided into three stages depending on the flow direction in the neighborhood of a target surface. The first stage is characterized by penetration of striker material into a target, energy and momentum transfer from a striker to a target and transition of kinetic to heat energy. At the second stage, inverse flow of a substance and formation of a crater bottom are initiated. At the third stage, the substance ejected from a crater partially falls out inversely forming its final shape. With reference to time, those stages do not have a distinct boundary since they can exist simultaneously but in different spatial regions. The crater development stages are substantially distinguished by the fact that if at the first stage the crater boundary moves in direction of the substance flow, at the second and third stages its dislocation is opposite to the substance flow.

At the first stage the determination of a contact boundary is of special importance. To this effect, a variant has been developed for a method of the large particles [12] including a procedure of explicit determination of a contact boundary [13]. This approach permits a spatial division of media on the Eulerian grid and consideration of their individual thermodynamic properties, which considerably improves the accuracy of calculations.

At the second stage of an intensive ejection a contact boundary is of no use since the vaporous component of an impacting body and target are mixed. The process is primarily stipulated by the flight of a condensed ejection from a crater through that zone. The algorithm of a contact boundary in the cratering model is changed so that it becomes transparent for a target substance being in a gaseous phase. Besides, a target substance that lost continuity and is moving in the form of discrete formations can cross it. This take place when, as a result of target scattering, its density drops lower than a minimal value at which the medium can be still continuous. If such vacuum of the medium appears not on the target surface but in the internal region, in this case the pressure is usually zeroized. Thus, the initially given contact boundary on the target surface becomes a boundary of the crater bottom. When a velocity of the ejected substance falls lower than some minimal value, the boundary again loses its transparency for overflow of the target material. The minimal value of velocity is meant to be a value at which a substance raised from the crater bottom cannot leave its boundaries and again falls on its bottom under gravity. The substance falling on the crater bottom and target surface surrounding the crater forms an ejecta blanket. The volume occupied by the blanket becomes inaccessible for a gaseous medium thereby forming a real surface of the final crater profile.

It is reasonable to assume that a rock substance subjected to substantial compression and then rarefaction as a result of impact loads will represent a dust- or drop-wise substance. Since in this case none of approaches to fracture is applicable, to assign a granulometric composition in such a

region, still at the stage of hydrodynamic flow, one can use e.g. a lognormal distribution based on an assumption of multiplicity of the fracture process. The formation of a granulometric composition is an independent problem and requires a separate consideration. It is only worth noting that use can be made of both a common approach based on application of fracture criteria and more precise methods describing in paper [14].

The most complex material flow occurs in the region where separate fragments of fractured rock seem to escape the region, in which the substance is considered as a continuous medium, and keep moving in the form of discrete particles of definite physical characteristics. The computational model describing the above process has to form a granulometric composition, its thermodynamic parameters and realize a smooth transition of the ejected material description from a continuous medium approach to a discrete one. In this case, use is made of the crushed region parameters obtained as a result of simulation of rock fracture dynamics. To this end, the calculation of particle-markers was introduced into the model described. As opposed to common markers, which passively follow the substance movement, and to particles used to calculate the flows of substance parameters, the particle-markers reflect the state of a substance. Moving over the computational region along with a substance similarly to common markers, they bear information about its evolution history. In particular, if a substance underwent loads, which resulted in its fracture, this will be evidenced by the data on a granulometric composition of the fragments formed. Such information is required when a substance is found in the outburst region.

The ejection of significant masses of fragmented material in the form of solid and liquid particles into the air at a high-power explosion or hypervelocity impact has a great influence on its thermodynamic and optical characteristics, causing alteration of the current pattern in the vicinity of the funnel. Thus a feedback is created during the ejection. Therefore, the flight dynamics of particles of ejected rock and their interaction with the gas medium must be taken into account when creating a physical-mathematical model adequately describing such phenomena. The previously created so-called continuous model [15] described feeding of rock as a condensed phase polydispersed particle system. The multitemperature and multiple-velocity approximation, which is based on application of continuous environment mechanics methods, is used in this case for mathematical description of the mixture of particles and gas. In this case, particles supplied to the gas medium are integrated by dimensions into groups, which are described as interpenetrating continuums. The given model allows detailed description of the dynamics of basic interphase interaction processes. In particular, the force interaction of particles moving in flows of gas, thermal and mass exchange in evaporation and condensation processes and the weight redistribution of particle mass as per dimension associated with this, the influence of gravity, are accounted for with good accuracy. However, this model is not free of significant drawbacks, associated, first of all, with the philosophy of the continuous approach. Namely, the replacement of discrete particles by a solid environment leads to additional uncontrollable interactions inside each separate group of particles that, in turn, can render strong influence on the spatial time distribution of particle concentration, and, consequently, on all the remaining calculation parameters. These drawbacks can be eliminated in the case of transition to a discrete model. It is clear, that it is technically impossible to calculate the interaction dynamics of each particular soil particle with the environment. Therefore it is necessary to consider some representatives, implying under this concept one chosen particle from a certain set of particles having very close parameters. Such an approach, as from the physical point of view, and in respect to its algorithm is similar to the method of particles in cells [16]. It follows from the condition of independence of trajectories of separate particles that for each of representatives it is necessary to have its velocity. This essential difference of representatives from marker particles and from particles in a cell, for which the velocity is determined from the condition of environment continuity as per the field of velocities in computational cells.

Let us underline some characteristic features of the discrete model and limitations, which are necessary for its application. Calculation of trajectories of particles and all processes, which were

considered in the continuous model, is possible if the coordinates, velocity, energy, mean radius of particles, full mass are specified for each representative, i.e. the sum of masses of all particles related to it, i.e. their quantity. Besides, for more accurate account of exchange with the environment, it is possible to introduce the mean radius of the zone, in which particles of the given representative are located. However it is more simple to demand such partition of particles as per representatives, that the mean maximum size of their zones, both at initial ejection, and at their further evolution would be commensurable with the size of computational cells, and interaction with the environment would be implemented on parameters corresponding to representative coordinates, as it is done, for example, in the method of particles in cells. Note that violation of the condition that the dimensions of the area of particles of one representative in case of their intensive momentum, energy or mass exchange could result in saltatory evolution of environment parameters. Of course this is not so critical as density oscillation in the method of particles in a cell, since exchange between the environment and particles in this case leads only to certain increments to already available values.

Processes of heating, evaporation, condensation, braking or the carrying away of particles by the gas flow are described through parameters of representatives and ambient gas similarly as for the continuous model, the only difference being in that separate representatives of particles, the radii of which vary during evaporation and condensation, are considered instead of fixed-dimensions groups of particles.

The main advantage of the discrete approach for describing the motion of particles as compared with the continuous approach is that it allows to trace the spatial-time evolution of each subset of particles, mapped by means of its representative for the entire duration of its existence, i.e. it guarantees trajectory independence. Application of the discrete model also gives an opportunity to improve the description of particles cooling or heating. For small particles it is quite justified to leave the former model of instantaneous heating, while for large particles it is possible to attempt to follow the dynamics of their heating by using any simplified model and introducing additional characteristics of representatives (such as the thickness and temperature of the heated layer. Application of the discrete model allows not only to follow the behavior of particles in a gas flow, but also to consider from a quantitative point of view their deposition or fallout processes at investigation of volcano dome formation and at forecasting contamination of an area by volcanic ejection. The considered model is applicable not only for calculation of the ballistics of large fragments of rock, but also for the description of the dynamics of interaction the finely dispersed dust environment. Moving along certain trajectories in space, the representative intersects the boundaries of the Eulerian computational grid cells. Once a representative is inside a computational cell, the particles of the given representative are uniformly distributed in it at a density equal to the ratio of the representative's mass and the cell's volume. Then the interaction of particles with the cell's gas medium, which results in alteration of their parameters (energy, momentum, dimensions, etc.), is calculated. The velocity, mass, and energy of the representative as a whole are changed accordingly. When several representatives are simultaneously in the same cell, the calculation algorithm is similar to the algorithm of the multigroup continuous model with a quantity of groups equal to the number of representatives. However, particles corresponding to different representatives are described by the discrete model completely independently from each other, and, contrary to the continuous model, there is no redistribution of mass and other parameters between representatives. During evaporation and condensation the dimensions of particles, corresponding to different representatives, vary continuously. The calculation of particle parameters proceeds in the given cell as their representative moves inside it. As soon as the representative intersects the cell boundary and enters an other cell, the entire calculation procedure is transferred to the new cell. If the intersected boundary is the surface of a planet, the given representative is omitted from calculations and an act of particles fallout from the cloud of ejection is registered.

Mathematical model describing physical processes accompanying cratering

From the mathematical point of view this model of the phenomena under consideration in the general case of interacting continua of continuous and discrete media is sets of non-stationary systems of partial and ordinary differential equations [17]. The equation of continuity, which describes the law of mass conservation of continuous media in the three-dimensional Cartesian system of coordinates, is:

$$\frac{\partial \rho}{\partial t}+\frac{\partial\left(\rho u_i\right)}{\partial x_i}+\delta\rho(\mu)=0, \tag{1}$$

where ρ - is the density of substance, in the case of gas medium, $\rho=\sum_{k=1}^{N}\rho^k$, N is the number of gases in the mixture, including the vapor of the discrete component ρ_v, u_i - are the components of velocity, $\delta\rho(\mu)$ is the variation of density due to exchange with the discrete component. The motion equation, which describes the law of momentum conservation, is:

$$\frac{\partial\left(\rho u_i\right)}{\partial t}+\frac{\partial\left(\rho u_i u_j-\sigma_{ij}\right)}{\partial x_i}=\rho\left(F_i+g_i\right)+\delta I(\Delta I), \tag{2}$$

where σ_{ij} - is the stress tensor, F_i - is the force per unit mass, g_i - is the acceleration due to gravity, $\delta I(\Delta I)$ - is the variation of the momentum in the gas medium due to interaction with the discrete component. The equation describing the law of energy conservation with account of external sources

$$\frac{\partial\left[\rho\left(\varepsilon+u_i u_i/2\right)\right]}{\partial t}+\frac{\partial\left[\rho u_j\left(\varepsilon+u_i u_i/2\right)-u_k\sigma_{ij}\right]}{\partial x_j}=\rho u_k F_k+Q, \tag{3}$$

$$Q=Q_R+Q_T+\delta\varepsilon(\Delta\varepsilon),$$

Q_R, Q_T - are the sources of heat due to radiation transfer and thermal conductivity respectively, $\delta\varepsilon(\Delta\varepsilon)$ - is the external source of energy, for example, in the case of energy transfer with discrete phase. The flux of heat due to thermal conductivity is proportional to the temperature gradient, and the source of heat associated with the flux is the divergence of this flux

$$Q_T=\frac{\partial}{\partial x_j}\left(\kappa_T(T)\frac{\partial T}{\partial x_j}\right), \tag{4}$$

where $\kappa_T(T)$- is the thermal conductivity coefficient, T is the temperature. In order to calculate the sources of heat due to energy transfer by radiation

$$Q_R=\frac{\partial}{\partial x_j}\left(S_j\right) \tag{5}$$

it is necessary to solve the equation of radiation transfer

$$\frac{1}{c}\frac{\partial I_\nu}{\partial t}+\Omega_i\frac{\partial}{\partial x_i}\left(I_\nu\right)+\kappa_\nu I_\nu=\kappa_\nu I_{\nu e}\ , \tag{6}$$

where I_ν is the spectral intensity of radiation, ν is the frequency of radiation, c is the light speed, Ω_i is the unit vector of the spatial angle, κ_ν is the absorption coefficient, I_{ve} is the equilibrium spectral intensity of radiation. Then the radiation flux

$$S_i = \int_0^\infty \int_{4\pi} I_\nu \Omega_i d\Omega \, d\nu \tag{7}$$

must be determined.

In some cases the radiation flux can be found in a simpler way. For example, in the case of optically thick layer the approximation of radiation thermal conductivity is acceptable, when the radiation flux is defined by the expression

$$S_i = -\frac{16\sigma l_R T^3}{3}\frac{\partial T}{\partial x_i},$$

where σ is the Stefan-Boltzmann constant, l_R is the Rosseland average run. In the optically thin layer we can use the expression for divergence of radiation flux

$$Q_R = \frac{\partial S_i}{\partial x_i} = 4\sigma\kappa T^4,$$

where κ is the Plank average of the absorption coefficient.

For closure of the system (1)-(7), it is necessary to define the equation of state $p = p(\rho,\varepsilon)$, $T = T(\rho,\varepsilon)$, thermal conductivity coefficients $\kappa_T = \kappa_T(T,\varepsilon)$ and $\kappa_e = \kappa_e(T,\varepsilon)$, absorption coefficients and the equation of dynamics of medium which describes the relationship between the stress tensor and strains, for example, in the form of the generalized Hooke law

$$\sigma_{ij} = E_{ijkl}\varepsilon_{kl}.$$

The whole set of equations for particles represents an aggregate of sets of equations, each of which describes the change of all parameters for a separate particle (or for a separate representative). Thus, total number of the equations set for particles coincides with the number of representatives, available at a given moment in the computational area. Similarly, for the continuum of discrete formations represented as condensed particles we can write down the equation of continuity

$$\frac{dm}{dt} = \mu, \tag{8}$$

where m is the mass of a particle, μ is intensity of mass exchange.

The law of momentum conservation has the form

$$\frac{d}{dt}(mw_i) = m(f_i + g_i) + \Delta I_i, \tag{9}$$

where w_i is the velocity of a particle, f_i is the density of the force acting on the particle from the side of gas medium, ΔI_i is the variation of momentum of the particle due to evaporation or condensation of substance of the particle.

The energy equation for a particular particle has the form

$$\frac{d}{dt}(m\varepsilon_p) = mq + \Delta\varepsilon + f_i w_i, \tag{10}$$

where ε_p is the energy of the particle, q is specific intensity of heat transfer with the surrounding environment, and $\Delta\varepsilon$ is the variation of the energy of the particle due to evaporation or condensation.

The motion equation for the particle has the form

$$\frac{dR_i}{dt} = w_i, \tag{11}$$

where R_i is the radius vector of a particle.

Intensity of heat exchange of the particle and the surrounding gas is determined by the sum of intensities of molecular q_T and radiation q_R heat exchange

$$q = q_T + q_R = \frac{3}{2\rho} Nu\chi \frac{T - T_p}{r^2} + \frac{3\omega}{gr}\sigma\left(T^4 - T_p^4\right), \tag{12}$$

where χ is the thermal conductivity coefficient of gas, T_p is the temperature of a particle, Nu is the Nusselt number considered as the function of the Reynolds Re and Prandtl Pr numbers for the particle in the gas stream, ω is the coefficient of blackness of the particle.

Intensity of mass exchange can be calculated in the supposition of diffusive mechanism of evaporation [18]:

$$\mu = 2\pi\, Sh\, D\, r_p\left(\rho_v - \rho_s\right), \tag{13}$$

where ρ_v and D is the density of vapors and diffusion coefficient of vapor molecules in gas, Sh is the Sherwood number, ρ_s is the density of saturated vapors at particle temperature. The resistance force of the particle F_i per unit mass is determined by the formula [19]:

$$f_i = f_0\left(w_i - w_{ip}\right), \quad f_0 = \frac{3}{8\rho_p}\frac{1}{r} C_D \rho \left|\mathbf{w} - \mathbf{w}_p\right|, \tag{14}$$

where C_D is the resistance coefficient, which is dependent on the number Re of relative motion of vapor and particles in gas.

The equation

$$\varepsilon = \frac{3k}{m} T_p - \lambda, \tag{15}$$

where k is the Boltzmann constant, λ is the sublimation energy per unit, was taken as the equation of state.

2D numerical model

Finite difference approximation of described system of equations was performed on the basis of splitting on physical processes. Difference scheme for calculation of gas-dynamic part of equations was constructed according to the large particles method [12]. Finite difference approximation of the system of equations describing the elastically plastic behavior of solid medium was performed according to [20]. In the process of reduction of the intensity of a shock wave propagated on rock material, at a certain moment the tenaciousness properties of the medium begin to noticeably influence the flow parameters. In this case it is necessary to switch to a model accounting for the behavior of solid-state bodies at loads comparable to the yield point. We shall employ a model of elastically ductile flow, which describes both the elastic

properties of a medium, and its plastic flow originating when loads exceed the structural limit of substance and continuously transferring to the hydrodynamic approximation at their further magnification. The system of equations connected with the deviatory part of the tensor of stresses and responsible for elastically plastic behaviour of the material is [20]:

$$\begin{aligned}
\rho\frac{\partial u}{\partial t} &= \frac{\partial S_{zz}}{\partial z} + \frac{\partial S_{rz}}{\partial r} + \frac{S_{zz}}{r},\\
\rho\frac{\partial v}{\partial t} &= \frac{\partial S_{zz}}{rz} + \frac{\partial S_{rz}}{\partial z} + \frac{2S_{rr} + S_{zz}}{r},\\
\rho\frac{\partial \varepsilon}{\partial t} &= S_{rr}\left(\frac{\partial v}{\partial r} - \frac{v}{r}\right) + S_{zz}\left(\frac{\partial u}{\partial z} - \frac{v}{r}\right) + S_{rz}\left(\frac{\partial v}{\partial z} + \frac{\partial u}{\partial r}\right),
\end{aligned} \tag{16}$$

where S_{ij} - deviator of the stress tensor.

The tensor of stresses can be represented as a sum of the deviatory and spherical parts:

$$\sigma_{ij} = S_{ij} + \sigma\delta_{ij},$$

where $\sigma = \sigma_{ii}/3$. The deviatory part of the tensor characterizes the tensioned state corresponding to the shape-changing strain, and the spherical part (the tensioned state of multifold compression) correspond to volumetric deformation. The arithmetical mean of the three stresses is the hydrostatic pressure with an inverse sign $\sigma = -p$, $p > 0$. Using the expression obtained from the equation of continuity

$$\dot{\varepsilon}_{ii} = \dot{V}/V,$$

where ε is the strain tensor and V is volume, the indicial equation for a medium governed by the law of Hook, can be represented as a relation between the stress tensor deviator and strain speed tensor [21]:

$$\dot{S}_{ij} = 2\mu\left(\dot{\varepsilon}_{ij} - \delta_{ij}\frac{\dot{V}}{3V}\right), \tag{17}$$

where μ is the shift module, and the dot, as in formula for the strain tensor, denotes a derivative on time along the trajectory.

Relation (17) provides a convenient connection for the definition of the deviator of the tensor of stresses through the strain of the element referred to the current configuration. We shall employ the von Mises's condition of fluidity written the in the natural basis [22] for the definition of the elastic flow area:

$$f = 2\left(S_{rr}^2 + S_{zz}^2 + S_{rz}^2 + S_{rr}S_{zz}\right) \le \frac{2}{3}Y_0^2, \tag{18}$$

where Y_0 is the shift stress of fluidity. As soon as the condition (18) is violated during calculation, the components of the deviator of the tensor of stresses must be returned to the fluidity circle. This requires the following normalization:

$$S_{ij} = Y_0\left(3/2f\right)^{-1/2}S_{ij}.$$

In the general case the dependence of the fluidity limit on the thermodynamic state of matter, deformation speed and loading history is complicated. The strengthening of matter can be taken into account by considering that Y_0 is a function of deformation energy, and the supposition

about loss of plastic strength at the temperature of melting is implemented by zeroing this magnitude. Such behavior of the fluidity limit can be described by expression [23]:

$$\widetilde{Y}_0 = \left(Y_0 + Y_1\mu + Y_2\mu^2\right)\left(1 - \varepsilon/\varepsilon_0\right),$$

where $\mu = \rho/\rho_0 - 1$; ε_0 is the internal energy of matter at the melting temperature, Y_1 and Y_2 are experimentally defined constants. Since at $\widetilde{Y}_0 = 0$ the deviator of the tensor of stresses automatically becomes zero and therefore the stresses themselves are reduced to hydrostatic pressure, automatic transition to a purely gas-dynamics approximation will take place.

The general equation of medium governed by Hooke law (17), the system of equations (16) together with the appropriate initial and boundary conditions represent a closed system and allow to simulate the elastically-plastic flow of the material and to find loading parameters at each point of the material. These equations, written in the finite difference form on a fixed grid, are the basis of a separate stage of calculation, included in the general scheme of the program complex for simulation of crater formation dynamics.

Simulation of energy transfer by radiation was carried out in the multigroup approximation using the S_n method [24] when the radiation flux is simply the sum of group radiation fluxes:

$$S_r = \sum_{k=1}^{N} S_r^k, \quad S_z = \sum_{k=1}^{N} S_z^k,$$

where N is the number of spectral groups. A multigroup two-dimensional equation of transfer was used for definition of intensity and radiation fluxes. In a cylindrical coordinates this equation has the form [25]:

$$\sqrt{1-\gamma^2}\left(\mu\frac{\partial I^k}{\partial r} + \frac{1-\mu^2}{r}\frac{\partial I^k}{\partial \mu}\right) + \gamma\frac{\partial I^k}{\partial z} + \kappa^k I^k = \frac{\kappa^k \sigma^k T^4}{\pi},$$

$$S_r^k = \int_{-1}^{1}\frac{\mu d\mu}{\sqrt{1-\mu^2}}\int_{-1}^{1}\sqrt{1-\gamma^2}\,I^k d\gamma, \quad S_z^k = \int_{-1}^{1}\frac{d\mu}{\sqrt{1-\mu^2}}\int_{-1}^{1}\gamma I^k d\gamma,$$

where I^k is the emission power in the k^{th} spectral group; T is temperature of substance. The following notations for angular variables are used here: μ – cosine of angle φ between the projection of the direction of flight of photon $\vec{\Omega}$ on a plane perpendicular to the axis of symmetry and the position vector conducted through the considered point and a point on the axis of symmetry; γ – cosine of the angle φ between the direction of flight of the photon and axis of symmetry z. σ^k is determined by expression:

$$\sigma^k = \frac{2k^4\pi}{c^2h^3}\left[\sigma\left(\frac{h\nu^{k+1}}{kT}\right) - \sigma\left(\frac{h\nu^k}{kT}\right)\right], \text{ where } \sigma(x) = \int_0^x \frac{x'^3}{e^{x'}-1}dx',$$

and the group absorption coefficient κ^k is determined with the help of averaging formulas similar to Planck averaging or according to Rosseland

When the processes of heat transfer described by equations (4)-(5) were not decisive, these equations were approximated by the explicit difference scheme [26]. Depending on the problem, the equations of state and the optical properties of the media was given analytically [27] or tabularly [28].

The special feature of the system (8)-(15) is that the mass of the particle can change up to zero. In this case the application of explicit schemes for numerical solution of the system can

3lead to undesirable results. If one introduce the parameter $x = \hat{r}/r$, the following finite difference approximation for numerical solution of the system can be obtained:

$$\hat{\varepsilon} = \varepsilon + x\left(\hat{q}_T\tau + \left(\hat{H}_T - \varepsilon\right)\frac{\hat{\mu}}{m}T\right) + x^2\hat{q}_R\tau,$$

$$x^3 - 1 = x\frac{\hat{\mu}}{m}\tau,$$

$$\hat{w}_{ip} = \frac{w_{ip} + \left(\varphi w_i - x^3 g_i\right)\tau}{1 + \varphi\tau},$$

$$\hat{R}_i = R_i + w_i\tau,$$

$$\varphi = x^2 f_0 + x\frac{\hat{\mu}}{m}\theta\left(\hat{\mu}\right),$$

where H is the enthalpy, τ is the time step, θ is the Heaviside function.

The final step of the given algorithm is calculation of increments of mass, momentum and energy, obtained during interaction with a separate representative. The calculation is performed with the help of the already known new values of particle parameters:

$$\begin{aligned}
&\rho_p^{(1)} = M_p^{(0)}/V,\\
&\delta(\rho u)_g = \rho_p^{(0)}\left[u^{(0)} - x^3\left(u^{(1)} + g\tau\right)\right],\\
&\delta(\rho v)_g = \rho_p^{(0)}\left(v^{(0)} - x^3 u^{(1)}\right),\\
&\delta(\rho E)_g = \rho_p^{(0)}\left(E^{(0)} - x^3 E^{(1)}\right),\\
&\delta\rho_g = \delta\rho_V = \rho_p^{(0)}\left(1 - x^3\right),
\end{aligned} \tag{19}$$

where $\rho_p^{(0)}$ is the mean density of particles, described by a representative with mass M_p in volume V of the spatial cell.

The algorithm is applied sequentially to all representatives located in a separate computational cell. Increments computed according to (19) are concurrently totaled; thus full changes of gas dynamic parameters due to interaction with all particles in the computational cell are obtained.

Application of then described semi-implicit scheme of calculation of interaction of ground with the gas medium allows to calculate the parameters of particles with arbitrary time step values provided the gas parameters are steady in time. Thus, in order to ensure reliability of calculating the interaction of rock erupted from a crater with gas, it is necessary to ensure stability of calculation of gas dynamic parameters for these processes. The given requirement is satisfied by limitation of the time step on conditions imposed on the magnitude of relative change of gas energy and density per one layer:

$$\left\{-\frac{\sum\delta\rho_g}{\rho_g}\right\}_{max} \le C_1 < 1; \left\{-\frac{\sum\delta E_g}{E_g}\right\}_{max} \le C_2 < 1.$$

In this case the increments are totaled on all representatives in the computational cell, C_1 and C_2 are positive constants.

CONCLUSION

The carried out calculation showed the satisfactory consistency of the developed model with the theories of the crater formation [29,30]. These results will be presented in a second part of

paper. Further improvement of the model (refinement of description of processes of formation of the ejected rock fragments, their fall out, putting into the model the separately developed model of rock destruction) should substantially improve the results of numerical simulation. At the moment a three-dimensional variant of the presented model is being tested. Flexibility of the computational program complex allows modeling of a wide range of radiative gas-dynamic problems and problems of mechanics of continua dealing with explosion, hypervelocity impact phenomena and some others.

The developed model provides a self-consistent description of formation of a condensed phase of an ejecta cloud at cratering. It takes into account all main processes of interaction of separately moving rock fragments with the surrounding gas. The model includes the algorithms of breakdown of representative particles as well as the algorithms of their merging and formation of areas with a continuous medium. The continuous medium, in its turn, can also be broken down depending on its prehistory.

Acknowledgements — I thank L. V. Rudak and N. I. Misychenko for coding and carrying out calculations. This work was carried out on the ISTC project No B-23 at financial support by the USA.

REFERENCES

1. J. D. O'Keefe and T. J. Ahrens, Shock effects from a large impact on the moon. Proc. LPSC VI, 2831-2844 (1975).
2. P. H. Schultz, Ejecta emplacement and crater formation on Venus. *J. Geophys. Res.*, **97**, 16183-16248, 1992b.
3. H. J. Melosh, Impact Cratering: A geological process, Oxford Univ. Press, New York, Clarendon Press, Oxford (1989)
4. T. J. Ahrens and J. D. O'Keefe, Impact on the Earth, ocean and atmosphere. *Int. J. Impact Eng.* **5**,13-32 (1987).
5. D. L. Orphal, Calculations of explosion cratering. In: *Impact and Explosion Cratering*. N.Y.: Pergamon Pres, 897-918 (1977).
6. I. V. Nemchinov, T. V. Loseva, A. V. Teterev, Impacts into ocean and seas. *Earth, Moon and Planets*. **72**, 405-418 (1996).
7. B. A. Ivanov, D. Deniem, and G. Neukum, Implementation of dynamic strength models into 2D hydrocodes: applications for atmospheric breakup and impact cratering. *Int. J. Impact Engng.* **20**, 411-430 (1997).
8. P. H. Schultz and D. E. Gault, Atmospheric effects on Martian ejecta emplacement, *J. Geophys. Res.*, **84**, 7669-7687 (1979).
9. P. H. Schultz, Effect of impact angle on vaporization. *J. of Geophysical Research*, **101**(E9), 21117-21136 (1996).
10. G. S. Romanov, L. V. Rudak, A. V. Teterev, The role of radiation processes by ultra-high velocity impact. *Chemical Physics*. **12**, No 5, 749-752 (1993), in Russian.
11. A. V. Teterev, L. V. Rudak, N. I. Misychenko, G. S. Romanov, Radiation of meteorite track in the earth's atmosphere. Radiative Plasma Dynamics IV, Moscow, p.229-230, (1997), in Russian.
12. O. M. Belotserkovsky, Yu. M. Davidov. Method of large particles in gas dynamics, Moscow, Nauka, p.392, (1982), in Russian.
13. A. V. Teterev, N. I. Misychenko, L. V. Rudak, I.V. Nemchinov, G.S. Romanov, A.S. Smetannikov, Atmospheric breakup of a small comet in the earth's atmosphere. LPSC XXIV, Houston, Texas, 1417-1418 (1993).
14. D. R. Curran, D. A. Shokey, L. Seaman, M. Austin, Mechanisms and models of cratering in earth media. In: *Impact and Explosion Cratering*. N.Y.: Pergamon Press, p.1057-1087 (1977).
15. G. S. Romanov, I. M. Kozlov, A. V. Teterev, Particles influence on parameters of light-erosive flares, Dep. in VINITI No. 1972282, (1982), in Russian.
16. M. W. Evans, F. H. Harlow, The particle-in-cell method for hydrodynamic calculations, Los-Alamos Scientific Lab. Rep. No. LA-2139 (1957).
17. A. A. Samarskii, A. P. Mikhailov, Mathematical modelling: Ideas. Methods. Examples. Moscow, Nauka, 320 p. (1997), in Russian
18. G. S. Romanov, V. K. Pustovalov, Evaporation in cloudy medium containing water drops under the action of intensive monochromatic radiation, Preprint, Physics Institute of Academy of Sciences of BSSR, Minsk (1975), in Russian.
19. R. G. Boothroyd, Flowing Gas-Solid Suspensions. Chapman and Hall Ltd., London (1971).
20. C. L. Mader, Numerical modeling of detonations. Univ. of California Press, 384 p. (1979).
21. M. L Wilkins, Elastic plastic flow. In: Methods Comput. phys., **3** (1964).

22. H. Liebowitz (Ed.), Fracture, **2**, N.Y., Academic press (1968).
23. J. O. Erkman, A. B. Chrstiansen, Attenuation of shock waves in aluminum. *J. Appl. Phys.*, **38**, 5395-5403 (1967).
24. P. N. Stevens, Use of the discrete ordinates S_n method in radiation shielding calculations. *Nucl. Engin. and Design*, 13, 395-408 (1970).
25. B. N. Chetverushkin, Numerical simulation problems of radiative gas dynamics. Nauka, Moscow (1985), in Russian.
26. G. S. Romanov, Yu. A. Stankevich, A.V. Teterev, Urban V.V., Numerical investigation of radiative processes in unsteady plasma flows. Transact. of XV-th ICPIG, Contr. Papers, Part II. Minsk, 899-900 (1981).
27. T. J. Ahrens and J. D. O'Keefe, Equations of state and impact-induced shock-wave attenuation on the moon. In: *Impact and explosion cratering*, N.Y.: Pergamon Press, p.639-656 (1977).
28. G. S. Romanov, Yu. A. Stankevich, L. K. Stanchits, K. L. Stepanov, *Int. J. Heat and Mass Transfer*, **38**, No.3, 545-565 (1995).
29. O. S. Barnouin-Jha and P. H. Schultz, Ejecta entrainment by impact-generated ring vortices: Theory and experiments. *J. of Geophysical Research*, **101**(E9), 21099-21115 (1996).
30. D. E. Maxwell, Simple Z model of cratering, ejection and the overturned flap, *Impact and Explosion Cratering*, edited by D. J. Roddy, R. O. Pepin and R. B. Merrill, pp.1003-1008, Pergamon Press, New York,1997.

PERGAMON International Journal of Impact Engineering 23 (1999) 933–944

INTERNATIONAL JOURNAL OF IMPACT ENGINEERING

www.elsevier.com/locate/ijimpeng

HYPERVELOCITY SHRAPNEL DAMAGE ASSESSMENT IN THE NIF TARGET CHAMBER

R. E. TOKHEIM*, D. R. CURRAN*, L. SEAMAN*, T. COOPER*, A. T. ANDERSON, A. K. BURNHAM**, J. M. SCOTT**, J. LATKOWSKI**, and D. SCHIRMANN*****

*Poulter Laboratory, SRI International, Menlo Park, CA 94025, USA;**Lawrence Livermore National Laboratory, Livermore, CA 94551, USA;***Centre d'Etudes Atomique, France

Summary—In the National Ignition Facility (NIF) target chamber, hypervelocity shrapnel may be produced as the result of neutron and x-ray deposition in target and diagnostic support rods, photon shields, and other objects in the chamber. This shrapnel may pose a hazard for optics debris shields and chamber wall materials. This paper presents the results of a computational and experimental effort to develop a predictive methodology for assessing hypervelocity shrapnel damage. The methodology begins with computations of the size and velocity distributions for the shrapnel, which is typically computed to consist of sizes ranging from submicron to a few hundred micrometers and to span a velocity range from a few hundred m/s to tens of km/s. Damage algorithms were developed based on prior dimensional analyses and hydrocode cratering computations, hypervelocity data from the hypervelocity impact community, and laboratory impact data at a few hundred m/s. The predictions of the algorithms agreed well with the damage observed in the Lawrence Livermore National Laboratory NOVA and the French Commissariat à l'Énergie Atomique PHEBUS laser facilities. The algorithms were then used to calculate damage maps in the NIF chamber for typical source conditions. © 1999 Elsevier Science Ltd. All rights reserved.

INTRODUCTION

The NIF will have 192 laser beams focusing on the target with 1.8 MJ of total energy, enough to expect a fusion yield of nominally 20 MJ. Typically, the neutron, x-ray, and debris source energies from the capsule-hohlraum configuration will be 16 MJ, 3.8 MJ, and 2 MJ, respectively. The diameter of the NIF chamber will be 10 m. The hohlraum converts 0.35-μm laser radiation (3-ω) to x rays via the gold walls and provides sufficiently uniform radiation to implode the capsule containing deuterium, or tritium and deuterium, to produce fusion.

Because we cannot yet perform experiments in NIF, we must find other ways to validate and improve our computational models for cratering and penetration. We present here the important issue of shrapnel generation and the effects of shrapnel impact at the debris shields, which are used to protect the laser optics. Shrapnel is defined as solid or melted (droplets) material with enough velocity to become a threat to exposed surfaces as a consequence of its impact. Debris is defined as vapor, gas, and ionized material; we address debris only in regard to its influence on shrapnel.

Typical NIF experiments will be of two types: (1) low neutron yield shots in which the capsule is not cryogenically cooled and (2) high yield shots for which cryogenic cooling of the capsule is required. For noncryogenic shots, shrapnel would be produced by spalling, melting, and vaporizing "shine shields" exposed to unconverted 1-ω and 2-ω laser radiation. For cryogenic shots, shine shields will not be present, but shrapnel would be generated through shock wave splitting, spalling, and droplet formation of the cryogenic tubes following neutron energy deposition. Motion of the shrapnel is determined not only by particle velocities resulting from the neutron deposition, but also by both x-ray and ionic debris loading arising from explosion of the hohlraum. In this paper, we make predictions only for the nominal 20-MJ high yield shot for NIF, because it represents the typical worst-case scenario, and only for shrapnel generated by the basic hohlraum configuration, not by diagnostics or other objects near the source.

0734-743X/99/$ - see front matter © 1999 Elsevier Science Ltd. All rights reserved.
PII: S0734-743X(99)00136-0

Before we present NIF predictions, we first show comparisons of our computational model with NOVA and PHEBUS experimental data.

METHODOLOGY

Evolution of Shrapnel Particles

We have established a methodology for predicting shrapnel generation [1] and the effects of cratering at first surfaces that can be applied to NIF; preliminary results are encouraging. We compute the evolution of shrapnel using one-dimensional (SRI PUFF) and two-dimensional (L2D) stress wave propagation codes with shock wave material models. In the one-dimensional case, PUFF accurately describes material failure by using our nucleation-and-growth and fragmentation failure models. Initiation of hohlraum and shine-shield computations for our codes is usually based on internal state quantities obtained from the radiation transport (HYADES, originated by J. Larson, Cascade Applied Sciences, Inc.) hydrocode through energy deposition times. In the two-dimensional cases, the free-Lagrangian L2D code continues the computations, handles severe cell distortions, and describes material damage.

Our methodology contains the following assumptions: (1) there are no shrapnel particle collisions, (2) the debris-wind moves molten particles from the cryotubes at its own velocity, but acts on solid particles by the usual drag equations, (3) effects of x-ray gas blowoff are ignored, (4) angular incidence correction in unconverted light is ignored, (5) constant blackbody temperature within the hohlraum during explosion is assumed, (6) the approximation is made of a one-dimensional HYADES run(s) for representing the hohlraum wall behavior, and (7) radiation transport effects are ignored at times after deposition.

Shrapnel Particle Sizes

We defined shrapnel as molten or solid material particles generated by the target source terms. We refer to whatever is vaporized or ionized by these source terms as debris. Unconverted laser light, x rays, and neutrons are all energy sources that can cause portions of objects to become heated but remain solid, to melt, to vaporize, or to ionize. Heated solid material can spall, if the dynamic tensile strength of the material is exceeded and may break up sufficiently under certain conditions to produce shrapnel. Completely melted material will produce droplets (with sizes determined by the loading conditions) that constitute shrapnel. Also, material between incipient and complete vaporization will contain some droplets, depending on the proximity to the liquid end of the "vapor dome" of the equation of state. Material with internal energy between incipient and complete melt will also likely have some contribution to droplet formation, but this mixed-phase contribution is not well understood. In general, we refer to solid and melted material as candidates for shrapnel generation, and vaporized and ionized material as candidates for debris.

In our analysis of the fragmentation of the liquid, we follow the approach of Grady [2]. Grady considers that the spall process (cavitation) may be dominated either by surface tension or by viscosity. His results show that surface effects dominate for all practical strain rates of interest to us. His expression for the average droplet diameter is

$$S_{avg} = (48\gamma/\rho\dot{\varepsilon}^2)^{1/3} \tag{1}$$

where γ is the surface energy per unit area of new fragment surface and is proportional to the surface tension, and both are defined up to the critical temperature. The quantity ρ is the density, and $\dot{\varepsilon}$ is the strain rate. Grady gives examples of good agreement (within a factor of 1.4) of this formula for copper at high strain rates (1.5×10^5/s).

His formula for a material behaving like a ductile solid is based on energy balance at end states and leads to

$$S_{avg} = (8Y\varepsilon_C/\rho\dot{\varepsilon}^2)^{1/2} \tag{2}$$

where Y is the flow stress in simple tension (for a given temperature and strain rate), ε_C is the void volume fraction before fragmentation occurs, and $\dot{\varepsilon}$ is the volumetric strain rate. He recommends $\varepsilon_C = 0.15$ as a reasonable value independent of material and material state.

Grady's analysis of comminution for brittle material led to the following relation:

$$S_{avg} = (24^{1/2} K_c/\rho_0 C\dot{\varepsilon})^{2/3} \quad (3a)$$

where C is sound speed and K_C is the fracture toughness. The fracture toughness should be adjusted for temperature. Grady suggested a temperature modification of the following form (with T_m as the melt temperature) for hard steel:

$$K_c = \frac{K_{co}}{1-T/T_m} \quad (3b)$$

Actual fragment size distributions are usually of the Poisson type. We can use Grady's equisized fragment size distribution to obtain a plausible Poisson distribution that is usually consistent with actual fragment size distributions [3]. Thus, the Poisson droplet size distribution is given by (assuming spherical particles)

$$N_g(S) = N_O \exp(-3S/S_{avg}) \quad (4a)$$

where $N_g(S)$ is the number of droplets per unit volume with diameters greater than S, with the mean particle size given by $S_{avg}/3$, and N_O is the total number of droplets per unit volume, given by

$$N_O = 27/\pi S_{avg}^3 \quad (4b)$$

To compute the total particle-size distribution, we first run the hydrocodes long enough (to the time $t = t_1$) to establish the direction of computational mass cells. We then assume that these cells will continue with their velocity vectors until the mass reaches the first surface. We assume the strain rates at time t_1 can be used to determine the average particle size for each cell. The number of particles per cell is determined from Eqn. (4a) times the cell mass divided by the initial failure density. The particle-size and angular/spatial distributions at some target in the chamber will then be given by integrating the distributions for all cells, and expressed per unit target area. Similarly, we can obtain the distribution for crater damage diameters by using the algorithms for crater diameter as a function of impacting particle size (given in the next section). Applications of this approach are shown for specific configurations described later in this paper.

DAMAGE ALGORITHMS

Cratering Algorithms

The cratering algorithms were first calibrated with the NASA hypervelocity data of Refs. [4, 5, 6] and then supplemented with SRI BB-gun low velocity data of Ref. [1] and the thin film data of Ref. [7]. The morphologies of the observed BB gun craters in glass (fused silica) looked identical to those of the NOVA debris shield: hemispherical subsurface fractured regions surrounding a smaller, heavily fractured, inner rubblized region, and sometimes with a few Herzian cone cracks extending somewhat farther into the target. Because this inner rubblized crater diameter is hard to define, we use the outer "fracture crater" dimension, with diameter Ds obtained from energy considerations as

$$Ds/D = \beta[\alpha\rho v^2/Y_t]^{1/3} \quad (5)$$

where D, ρ, and v are impacting particle diameter, density, and velocity, respectively, and Y_t is the target yield strength.

For brittle material targets, we found that

$$\alpha = \mathrm{Min}[0.1\rho v^2/Y_t, 1] \quad (6)$$

For fused silica, we found that $\beta = 10$ and $Y_t = 1$ GPa. Other results are given in Ref. [1]. The above brittle and ductile formulas are based on observations of hemispherical cratering; data typically fit within a scatter factor of 1.5. However, if the impacting particle is stronger than the target, it may penetrate the target by producing a long hole.

Shrapnel Penetration Algorithm

Considering an impacting particle with mass m at velocity v decelerating in a target according to the approximate equation

$$mdv/dt = -2Y_tA/3 - c_D\rho v^2A/2 \tag{7}$$

where A is the impacting area and c_D is the drag coefficient, we find when v = 0, the maximum depth is obtained as

$$x_{max}/D = (2\rho/3\rho_t c_D)\ln(3\rho_t c_D v_o^2/4Y_t + 1) \tag{8}$$

where ρ_t is the target density and v_0 is the particle impact velocity. Typical values give maximum penetrations in excess of 20 projectile diameters.

However, the initial resistance of the projectile requires

$$2Y/3 \geq 2Y_t/3 + c_D\rho v_o^2/2 \tag{9}$$

where Y is the particle yield strength, which leads to the condition

$$v_o \leq [4(Y - Y_t)/3c_D\rho_t]^{1/2} \tag{10}$$

thereby giving an upper limit to the shrapnel velocity that can lead to in-depth penetration.

For greater velocities, the shrapnel will penetrate with erosion and produce hemispherical craters.

CORRELATIONS WITH NOVA AND PHEBUS EXPERIMENTS

Because we cannot yet perform experiments in NIF, we must find other ways to validate and improve our computational models for cratering and penetration. We find NOVA to be invaluable in this regard because, even though it does not test the effects of neutrons and capsule debris, it is an excellent testbed for determining the effects of hohlraum debris, x rays, and 1-ω and 2-ω laser light on shine shields. Moreover, it provides a source for x rays as well as a source for shrapnel from shine shields or other adjacent objects. Although the blackbody temperature of the NOVA hohlraum is only two-thirds of that expected in the NIF hohlraum, it is still high enough to ionize the hohlraum, cause significant heating in surrounding materials, and produce many of the responses expected with NIF.

Computations for 2-ω NOVA Hohlraum Shine-Shield Experiment

Figure 1 is a sketch of the experimental configuration for a 2-ω NOVA shot (#26090407, also designated DHK_LOWTRT_38). The total 2-ω energy was given as 21.6 kJ for the 8 beams. A one-dimensional LASNEX run was made to guide our computational assumptions for L2D, which led us to assume that 13.4 kJ was the beam energy retained inside the hohlraum, to be spread evenly over the non-laser-entrance-hole (LEH) area, giving 17.2 kJ/cm^2 available as x-ray energy. We assumed a 4-ns deposition. The run showed essentially no x-ray emission through the hohlraum walls. For the 1-ω light on the shine shield, we assumed 8.43 kJ per beam, and based on an incoming average 1.95-cm-diameter circular beam, we obtained a maximum intensity of 7.26 kJ/cm^2 for four beams on each end of the hohlraum.

We used L2D to compute the disassembly of this hohlraum configuration. In this case, partly because the deposition time was long enough for the hohlraum to be filled with vaporized gold, initialization was done by relating the cell locations and associated densities, the internal energies, and the velocities from the one-dimensional HYADES run to the two-dimensional L2D configuration. The blackbody temperature assumed was based on multichannel x-ray spectrometer measurements (88 eV) and a fluence internal to the hohlraum. The loading of the shine shields was determined from HYADES runs representing fluences based on the exposure pattern of unconverted laser light, determined as a function of radius. We assumed that no x-ray energy would come through the hohlraum to the shine shields. During these computations, we

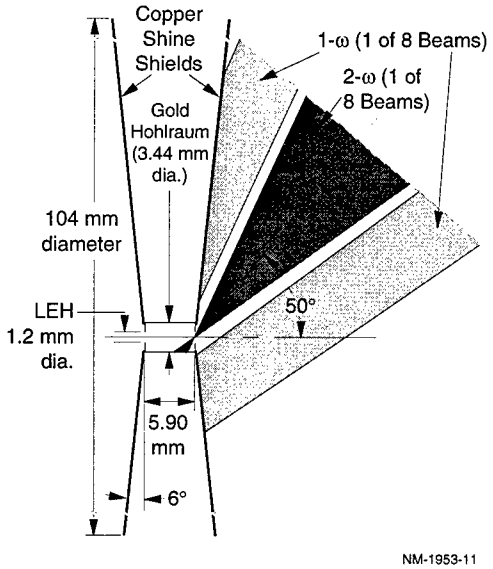

Fig. 1. Configuration assumed for 2-ω NOVA hohlraum shine shield experiment and computations.

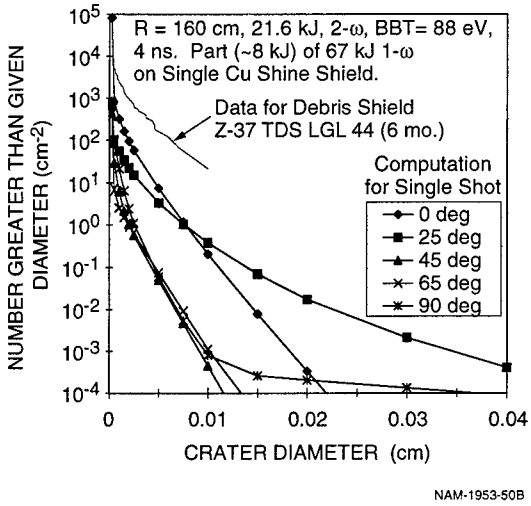

Fig. 2. Computed and observed crater diameter distributions for NOVA debris-shield.

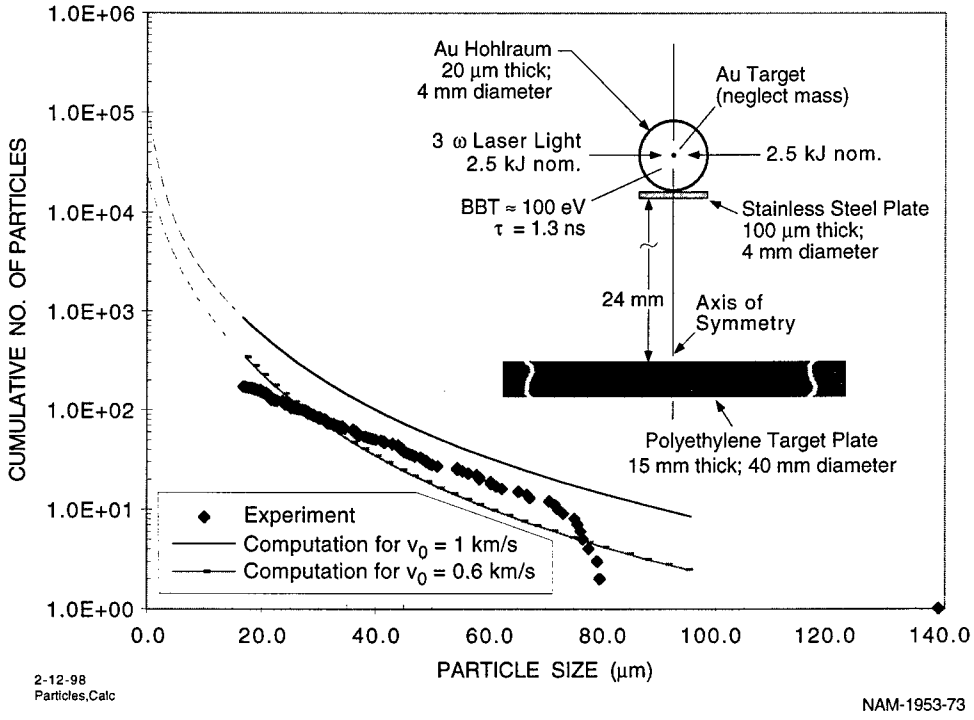

Fig. 3. Observed and computed shrapnel particle distributions in PHEBUS experiment.

maintained cell-boundary separation of phases of material states (solid, melted, and vaporized) during rezoning.

After 512 ns, most of the shine shield is intact except for blowoff and some melt arising from absorption of the 1-ω laser light, which is most intense near the region of the LEH. The radius computed for the inner diameter of the solid portion of the shine shield at 0.5 μs is 2.25 mm—the same as the radius of the 1-ω laser beam. Also, there is some evidence of curling of the inner lip. These results are in agreement with experimental observations of the shine shields. The velocity flow field for the gold confines the flow of the copper somewhat and moves symmetrically about the hohlraum axis and between shine shields.

We assumed that all cells can be ray-traced (except the intact solid) or projected to the first surface. Normally, we would apply this only to material cells that we believe have well-established trajectories at the ending time of the L2D computation. The amount of melted copper is one to two orders of magnitude below that of solid copper. Vaporized and ionized copper is one order of magnitude lower than the melted copper in amount. The gold is mostly ionized, or vaporized, as expected. We computationally projected the melted copper to the optics debris-shield distance of 160 cm.

Comparison with Cratering Observed in NOVA Debris Shield

The silica debris shield protecting the optics in NOVA is replaced after approximately 6 months of exposure because of laser and impact surface damage from shrapnel in the target chamber. The retired debris shield experienced 6 months of NOVA shots at ~20 shots/week, although not all at high energy nor all beamlines, and 2-ω as well as 3-ω types of shots. To provide a basis for comparison with our computations, we measured the size distribution of craters from NOVA debris shield Z-37 TDS LNL 44, which had a variety of target experiments in its history. Figure 2 shows the results of examination (including with the image analyzer) of a sample taken from a segment of the debris shield a few inches from the edge. Most craters were circular, but some had aspect ratios typically up to 1.3:1.

Results of our computations, assumed to be typical, at the 160-cm debris-shield location for the (melted) copper shrapnel are also shown in Figure 2 for numbers of craters versus crater size, with polar angle as a parameter. The comparison is favorable if we consider multiplying the distribution by the number of shots over the history of the debris shield—probably by a couple orders of magnitude. Also the distribution of craters is in reasonable agreement for the angle of the beam (~50 deg). Of course, we do not know what craters were caused by copper shrapnel and what by other materials, or how these craters grew with subsequent exposure to laser light.

Comparisons were also made with 3-ω experiments performed in NOVA under a similar source environment, and results were also favorable, showing similar crater numbers and distribution shapes caused by copper after a couple of exposures [1]. Later exposures in these experiments still showed craters, but the copper had been mostly vaporized.

Correlations with PHEBUS Shrapnel Experiment

The NIF yield target configuration described later uses stainless steel cryotubes. It was desired to perform some experiment to verify our shrapnel predictions of stainless steel at the high strain rates expected in the NIF configuration. This section presents the results of such an experiment performed by Commissariat à l'Énergie Atomique (CEA) at their PHEBUS facility in Limeil-Valenton, near Paris. We used our computational models to simulate this experiment and compared our results with the experimental fragment data.

The experiment proposed and conducted by CEA consists of an exploding spherical hohlraum driving a thin sample, whose fragments are collected in a plastic witness plate. CEA successfully performed such experiments for several materials that provided useful information on shrapnel. We examined only the results from the experiment with the stainless steel sample plate.

The main chamber of PHEBUS has two beams, each with an energy of one of NOVA's beams. A schematic of the experimental setup is given in Figure 3. Each of the two 3-ω laser beams had a nominal 2.5 kJ of energy with a pulse duration of 1.3 ns, giving a measured blackbody temperature of approximately 100 eV. The laser beams entering on opposite sides of the hohlraum ionize the gold target sphere, thereby providing an x-ray source that loads the gold hohlraum and vaporizes it. The nonuniform loading on the sample plate causes it to expand through the thickness when impacted by the hohlraum and to break up into fragments as a result of the high tensile strain rate. Fragments are collected by the polyethylene target.

The experimental data began with radiographs showing locations of shrapnel in the polyethylene target. The resolution of identified particles was reported to be about 20 μm. Figure 3 plots the cumulative number of particles greater than a given size (diameter) versus particle size. Only a small fraction of the stainless steel sample material was recovered by the witness plate, which suggests that much of the sample material was vaporized or melted, either as generated or after impact with the polyethylene plate.

The hohlraum and plate configuration were modeled using our two-dimensional free-Lagrangian hydrocode (L2D). To account for thermal transport physics and corresponding hydrodynamic behavior at early times, we used the results of a HYADES computation for the spherical hohlraum. Another HYADES computation was performed with an outer spherical layer corresponding to the stainless steel plate to get some estimate for the initial internal energy within the plate. The HYADES computation was performed assuming a constant blackbody temperature of 100 eV at the inner hohlraum surface over the 1.3-ns duration of the laser pulses. The absorbed energy should be close to actual because the calculation excludes hohlraum internal front-surface radiative energy loss.

We initialized L2D after 5 ns with the particle velocity, density, internal energy, and cell locations from the HYADES computation. It is assumed that most radiation transport effects have occurred in the gold hohlraum by this time. Also, by this time the hohlraum has expanded to be in contact with the stainless steel plate off the symmetry axis.

L2D results show the development of a thin foil of nearly initial density material facing the hohlraum that appears to remain mostly intact. Much of the remaining material is liquid, and an appreciable amount of much-expanded material is below incipient melt. The axial strain rate dominates and is of the order of 10^7/s for most of the material.

Material is moving at lower velocities is near the end of the sample plate farthest from the expanding hohlraum and on the top side of the plate. Velocities are typically 0 to 5 km/s. The velocity vectors show material mostly moving along the axis of symmetry, except near the outer end of the plate. The final state of the entire configuration at 218 ns gives expansion of the gold hohlraum around the end of the steel plate and the severe plate distortion that results.

The computations further give the following partition of mass in the various states: liquid droplets 35%, solid shrapnel 19%, solid foil 45%, and vapor 1%. The solid foil is assumed to have a density greater than 6 g/cm^3. Solid shrapnel is assumed to be material that has a lower density than 6 g/cm^3 and is unmelted. We can now estimate average shrapnel particle sizes (S_{avg}) from Grady's formulas and the distribution function referred to above. Based on the strain rate of 10^7/s for the stainless steel plate, we expect liquid droplets to have an average size of about $S_{avg} \approx 6$ μm based on Eqn. (1a). The Grady formula for ductile solid material gives $S_{avg} \approx$ 20 μm, assuming a density of 6 g/cm^3 for the solid fragments formed.

We used the cratering-penetration criterion to provide an estimate for the maximum particle velocity for penetration into the witness plate. Particles that meet this criterion will penetrate the target because their densities and yield strengths are greater than those of the target. Particles that do not meet it will be either reflected or melted upon impact and will create surface craters in the target. For the stainless steel shrapnel and the polyethylene witness plate, this gives a maximum particle velocity of about 0.6 km/s.

Correlation of the shrapnel particle size distribution we obtained using the above assumptions is shown in Figure 3. The amount of solid shrapnel mass moving below this velocity is computed to be 1% of the total stainless steel plate mass. These results are consistent with the observations, which give 0.64% mass recovery, based on our particle count. (We also computed results for 1 km/s to determine the sensitivity of results to the maximum cut-off velocity.) The agreement is very encouraging. The smaller particle-size end of the distribution is dashed because it is below the resolution of the radiography.

The particle-size cutoff will be determined by the part of the stainless-steel plate thickness that fragments, increased by the ratio of original density to failure density. The maximum particle size would then be 133 μm, corresponding to the original plate thickness. A PUFF computation we performed for on-axis loading from the hohlraum indicated 55 μm would spall; this would suggest the primary particle-size cutoff at 75 μm. These results are consistent with the observed maximum of 140 μm and the dominant value of 80 μm.

NIF PREDICTIONS

We made two NIF predictions for the 20-MJ yield condition with a cryogenic hohlraum configuration. We describe in greater detail the predictions for the sapphire cryorod

configuration, which appears more promising. The other configuration involves liquid-helium-filled stainless-steel cryotubes.

20-MJ Sapphire Cryorod Configuration

Figure 4 shows a cross section of the cryorod configuration. The two sapphire cooling rods provide mechanical support for the hohlraum and carry heat away from the hohlraum to maintain its temperature near absolute zero (18 K). These rods are mounted at either end of the hohlraum. We are considering a 20-MJ fusion experiment in which the rods are radiated with neutrons and x rays and are then struck by debris from the hohlraum. The neutron radiation defines the material state along the rods: mixed liquid and vapor nearest the hohlraum, then liquid for a centimeter, and the rest remains solid. The sudden heating from this radiation leads then to comminution of the rods into droplets near the hohlraum and small solid particles for the rest of the rods. The droplets and particles are thrown to the walls of the chamber by a combination of the heating from radiation and the drag caused by the passing debris from the hohlraum. When the particles reach the walls, they penetrate and cause cratering damage.

The state and motion of the sapphire rod material during the 20-MJ test are defined by the neutron and x-ray energy deposited in the rods and by the motion of the hohlraum debris sweeping past the rods. The neutron energy is deposited fairly uniformly within the rods (uniform along a radius of the rod, but varying along the length of the rod). The neutron energy deposited into the sapphire rods heats the near-target material into the vapor range, but just leaves the farther parts of the rods warm. This sudden heating defines the state (solid, liquid, or vapor) of the rod material. This heating also causes shock waves within the rods, which produce large radial velocities and subsequently fracture of the rods. The liquid material becomes submicron-size droplets, whereas the solid material comminutes into fragments with dimensions on the order of micrometers. This uniform outward expansion of the rods is modified by the arrival of the x rays, which act only on the surface facing the hohlraum. The x rays vaporize a very thin surface of the rods and provide an outward impulse to the rod fragments, acting primarily in the direction of the hohlraum axis. Then the debris from the hohlraum (vaporized material of the hohlraum) arrives as a strong wind moving approximately radially from the hohlraum center. This wind catches the sapphire particles and droplets and drags them along in the direction of the wind.

We compute the response of the sapphire material to the neutrons, x rays, and debris to determine the particle sizes and velocities. Later these sizes and velocities are used to determine where the particles strike the wall and debris shields in front of the laser focusing optics and to determine the crater damage these particles cause.

The x-ray radiation was provided by a point source definition with the following characteristics: (1) 89-eV blackbody with 2.5 MJ of energy and (2) 18-eV blackbody with 0.2 MJ of energy. The loading duration (10% to 90%) was 49 ns for each x-ray source. We calculated the energy deposition into the sapphire rods by using the FSCATT radiation code [8]. Although the duration of the x-ray radiation was fairly long and the rods had been previously heated by the neutron radiation, the amount of expansion under this heating was still fairly small and fracture had just begun. Therefore, for the x-ray loading, we assumed that the rods were still in the initial positions. Then we computed the impulse delivered by the x rays at specific points along the rods, accounting for the angle between the rod direction and the radial direction to the point source.

The 3.1 MJ of energy deposited into the hohlraum creates plasma or vapor states. This superheated debris material expands rapidly, acting like a wind sweeping past the materials farther out, such as the sapphire rods.

Initiation for the L2D run is based on a HYADES code run that includes the necessary radiation transport physics at early times. The HYADES run assumes one-dimensional cylindrical geometry for the gold shell, 30 μm thick and having a radius of 2.75 mm. The interior of the hohlraum is filled with 2 mg/cm^3 of helium gas. The code run begins at room temperature. The innermost node of the hohlraum is held at a blackbody temperature of 0.4 keV for 6.3 ns. The problem ends up with about 5 MJ present, which follows the true case to first order [9]. Material phase boundaries are maintained.

The L2D run was initialized with the neutron deposition in hohlraum, heater ring, heat sink coupler, and silicon heat. We then deposited the total 6.5-ns energy (internal plus kinetic) from the HYADES run over the deposition time of 6.3 ns. We would have preferred to continue computations based on cell position, density, velocity, and internal energy initialization, but the

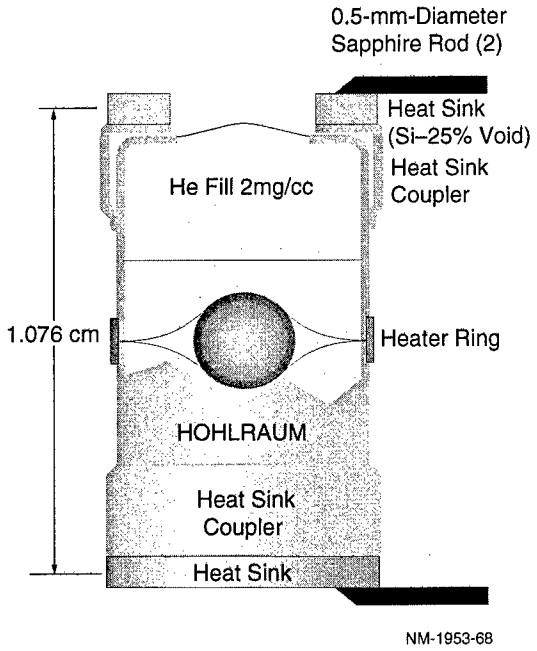

Fig. 4. Cross-sectioned view of NIF sapphire cryorod hohlraum configuration.

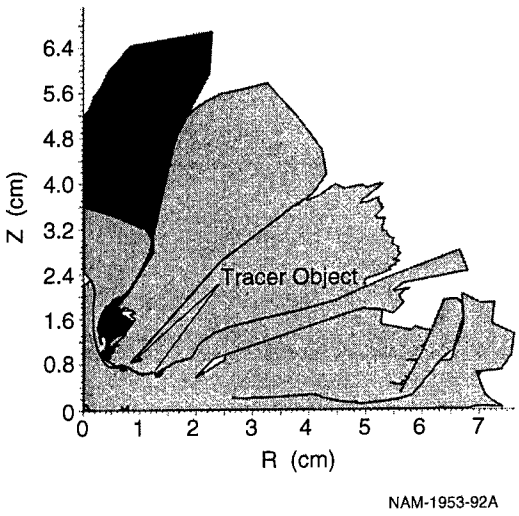

Fig. 5. L2D material position history for 20-MJ NIF cryorod case at 49 ns.

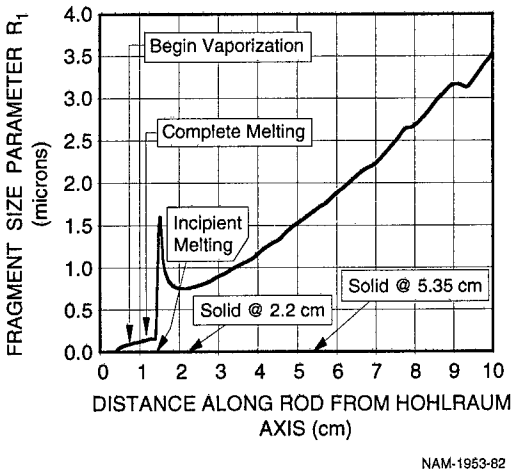

Fig. 6. Computed fragment size parameter R_1 versus distance along sapphire rods from neutron radiation in 20-MJ test.

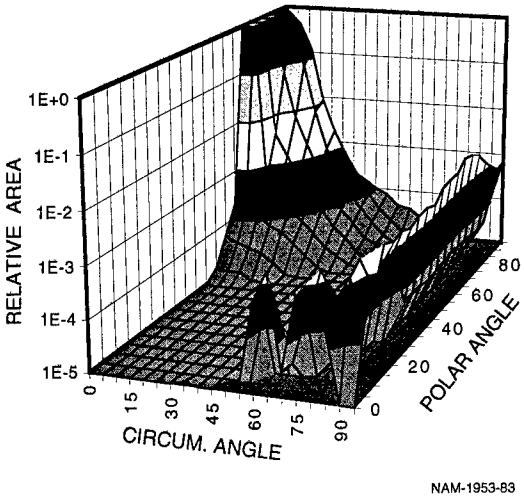

Fig. 7. Relative areal damage in fused-silica wall in 20-MJ computation.

distortion after 6.3 ns was too excessive if we were to include the cryogenic cooling/heater parts of the configuration that could not be included in the one-dimensional HYADES run.

We assumed that the heat sink coupler and heater ring received the same internal energy as the outside of hohlraum. L2D shows that the heat sink coupler will be in contact with the hohlraum by 1 ns. We estimated the x-ray loading from blackbody temperature of 0.4 keV (exiting the LEHs) as a Lambertian distribution, with angle-dependent fluence of 1.84 MJ $\cos\theta/2\pi r^2$ (distance from aperture center r is in cm). We ran HYPUF (a code similar to HYADES) to estimate the shape of deposition profile into the silicon heat sink for an average angle, but retained the radial dependence of fluence in deposition of energy into the silicon over 6.3 ns.

The debris wind velocities were determined primarily from the L2D computations. Tracer objects (1 mm diameter) were placed along the locations of the rods at 0.5, 1.2, 2.0, and 7.0 cm. The motions of these objects were tracked, and radial and axial velocities were obtained. At all points, the predominant motion was radial from the hohlraum axis, but there was also an outward axial component for locations to 1.5 cm along the rods. Velocities ranged from about 10^7 cm/s out to about 1 cm from the hohlraum axis and decreased to about 10^6 cm/s at 2 cm. One L2D position history of the configuration is shown in Figure 5 for $t_1 = 49$ ns..

The resultant velocities are computed for small segments along the rod. Each segment is shaped like a piece of pie about 0.04 cm long with an included angle of 2.5°. Corner points of each segment were assigned velocities from the debris wind, neutron deposition, and x rays according to its location in the rod, and the resultant velocity is determined by vector addition. Then each segment was further subdivided into five subsegments representing four points near the outer corner points and one central subsegment. Each subsegment was assigned a velocity according the distance of its center from the four corner points.

At each location along the rods, the neutron heating brings the material to a uniform compressive stress state, independent of the radius. Following deposition, unloading occurs from the outer radius, reducing the stress to a tensile state. We see that the rods will experience tensile stresses that exceed the tensile strengths throughout their lengths (~20 cm); hence, we can expect that the rods will be fully fragmented. The computed strain rate then varied along the rods as a function of the neutron energy deposited at that location.

With the computed strain rate, the droplet and particle sizes were determined using the equations of Grady. The resulting sizes (particle radius $R_1 = S_{avg}/6$) are shown in Figure 6. The labels in the figure show the boundaries of the material state. The nearest material is in the liquid-vapor state above the critical temperature (assumed to be 8000K) and it does not appear as particles. Next are the submicron droplets of the liquid state, followed by a region of large particles up to 1.6 μm; these are in the hot solid range where the material is fairly ductile. As we proceed out past 1.5 cm, the fracture toughness decreases and the particle size decreases back below 1 μm. At greater distances, the decreasing strain rate leads to larger particle sizes. The hump in the particle size curve near 1.6 μm is associated with our assumption that the material acts in a brittle manner (following Eqns. 3a and 3b) at all temperatures up to melting. But the material may become more ductile near melting and exhibit quite different behavior.

With the known particle sizes, velocities, and masses striking each area of the wall, we computed the cratering damage on the wall from our damage algorithms. The results provided the fractional area of fused-silica debris shield material that is cratered. The maximum cumulative damage tolerable is a few percent. A view of the areal damage on debris shields is shown in Figure 7. We see that the damage is very localized at a circumferential angle of 0° (in a horizontal line with the sapphire rods) and at a polar angle of 65° to 85° from the top of the chamber. Thus, the rod material has been blown mainly radially back toward the wall, but with enough upward velocity to land between 5° and 25° above the horizon. A similar damage pattern occurs just below the horizon. The damage is extremely localized to this small region.

The major damage is caused by material in states ranging from room temperature to liquid. Neither the material above the incipient vaporization range nor that in the cold solid range causes significant damage. Particles cause serious cratering damage in two narrow regions just above and below the horizon of the chamber and in line with the rods. The regions are about 10° wide (circumferential direction) and 20° high, centered 15° above and below the horizon. In these spots, the surfaces of any debris shields present would be completely cratered. (Further study of an erosion concept for multiple particle impacts is needed to make good estimates of possible debris shield perforation and first wall depth of removal.) We therefore estimate based on debris shield locations that no indirect drive debris shield quads would be affected, although those at the direct drive locations would suffer damage, if unprotected.

20-MJ Stainless-Steel Cryotube Configuration

A similar analysis was performed for the preliminary, indirect-drive, cryogenic target yield design having small capillary cryogenic tubes of stainless steel leading to the hohlraum [1, 9]. These tubes filled with liquid helium at 10 K and 200 atm are used to remove heat from the target assembly due to wall thermal loading and tritium decay. The NIF hohlraum configuration is similar to the cryorod configuration, with the tube pairs substituted for each cryorod. We analyzed the effects of neutron deposition in the helium and tubes, the loading of x rays, and the loading of debris wind.

The debris shield suffers from small as well as large particles because a shallow depth of damage is sufficient to reduce transmittance of the shield. For a given velocity, smaller particles are more effective in increasing the damaged surface area. However, larger particles with sufficient velocities can produce significant in-depth damage. Only a few hundred of the larger shrapnel particles are produced, but 10^7-10^8 of the smaller particles. The predicted level of damage was sufficient to render 10 (of 48) of the indirect-drive debris-shield quads (~40 debris shields) ineffective—5 in the upper quadrant, and 5 in the lower quadrant.

SUMMARY AND CONCLUSIONS

Experiments and computations have shown NOVA to be an excellent testbed for investigating many aspects of NIF. The NOVA hohlraum was used to provide x-ray fluences like those expected in NIF (although having a colder blackbody temperature). A NOVA hohlraum shine-shield configuration provided a shrapnel source for model calibration for many NIF candidate materials. Also, we showed computationally that a NOVA configuration can display hohlraum debris behavior similar to that expected in NIF.

Correlations show that our computational modeling is reasonable and provides some validation of our methodology in predicting shrapnel size distributions compared with NOVA and PHEBUS experiments.

Our computations for NIF hohlraum designs show that using sapphire cryorods results in substantially lower potential damage to the NIF final optics than using helium-filled stainless steel tubes. The low damage for the sapphire rods resulted from deflection of the hohlraum debris wind by the silicon heat sinks. In addition, the overall spread in damage was reduced by the focusing effect of the high debris-wind-coupled shrapnel velocities. Moreover, we learned from our computations that damage was due primarily to particles having a mean diameter of several micrometers. In contrast, our computations for the stainless-steel cryotube case showed excessive damage to 10 debris-shield quads, owing largely to the lack of a debris-deflecting mechanism as was present in the sapphire rod case.

REFERENCES

1. R. E. Tokheim, D. R. Curran and L. Seaman, "Damage and hardening assessments for the National Ignition Facility target chamber design," Summary Report UCRL-CR-128686 for University of California, Lawrence Livermore National Laboratory (February 1998).
2. D. E. Grady, "Spall and fragmentation in high-temperature metals," *High-Pressure Shock Compression of Solids II: Dynamic Fracture and Fragmentation* (edited by L. Davison, D. E. Grady, and M. Shahinpoor), Chapters 9 and 12, Springer-Verlag, New York, (1996).
3. D. R. Curran and L. Seaman, "Simplified models of fracture and fragmentation," *High-Pressure Shock Compression of Solids II: Dynamic Fracture and Fragmentation* (edited by L. Davison, D. E. Grady, and M. Shahinpoor), Chapter 13, Springer-Verlag, New York (1996).
4. F. Hoerz, M. Cintala, R. P. Bernhard, F. Cardenas, W. Davidson, G. Haynes, T. H. See and J. Winkler, "Cratering and penetration experiments in Teflon targets at velocities from 1 to 7 km/s," NASA Technical Memorandum 104797 (July 1994).
5. F. Hoerz, M. Cintala, R. P. Bernhard, F. Cardenas, W. Davidson, G. Haynes, T. H. See and J. Winkler, "Penetration experiments in aluminum 1100 targets using soda-lime glass projectiles," NASA Technical Memorandum 104813 (July 1995).
6. K. S. Edelstein and M. L. Fudge, "Penetration and surface spalling due to hypervelocity impact into fused silica," personal communication (1995).
7. N. Pailer and E. Grun, "The penetration limit of thin films," *Planet. Space Sci.* **28**, 321-331 (1980).

8. R. H. Fisher and J. W. Wiehe, *A user's guide to the FSCATT code*, Final Report DASA 2618 by Systems, Science, and Software, for Defense Atomic Support Agency (November 1970).
9. R. E. Tokheim, L. Seaman, T. Cooper, B. Lew and D. R. Curran (SRI International), and J. Sandhez, A. Anderson and M. Tobin (LLNL), "Calculating the shrapnel generation and subsequent damage to first wall and optics components for the National Ignition Facility," Fusion Technology **30**, 745-751 (December 1996).

PERGAMON International Journal of Impact Engineering 23 (1999) 945–956

INTERNATIONAL JOURNAL OF IMPACT ENGINEERING

www.elsevier.com/locate/ijimpeng

A PENALTY APPROACH FOR CONTACT IN SMOOTHED PARTICLE HYDRODYNAMICS

R. VIGNJEVIC and J. CAMPBELL

College of Aeronautics , Cranfield University, Cranfield, Bedfordshire, MK43 0AL, UK

Summary—This paper describes the development and testing of a contact algorithm for SPH. The treatment of contact boundary conditions in SPH has not been adequately addressed, and the development of the normalised smoothing function approach has highlighted the need for correct treatment of boundary conditions. A particle to particle contact algorithm was developed for 2D. The penalty formulation was used to enforce the contact condition, and several equations for the penalty force calculation were considered. The contact algorithm was tested for one and two dimensional problems for the velocity range between 0.2 and 4.0 km/s to determine the best penalty force equation and the best approach for applying the contact force. The tests showed that the zero-energy mode problem in the SPH method had to be addressed, as contact excited a zero-energy mode that caused non-physical motion of particles. The test results were compared to the DYNA3D results for the same problems. Background to boundary condition treatment in SPH is given in Section 1. In Section 2 the development of a contact algorithm for SPH in 1 and 2D is described. Testing of the contact algorithm in 1 and 2D is described in Section 3. Conclusions are presented in Section 4. © 1999 Elsevier Science Ltd. All rights reserved.

INTRODUCTION

The Smoothed Particle Hydrodynamics (SPH) method offers considerable promise as a numerical method for modelling hypervelocity impact. Originally developed for treating astrophysics problems [1, 2], it was first extended to solid mechanics problems by Libersky [3] and the method proved capable of modelling hypervelocity impact [4]. However the SPH method had several problems that were detailed in a study by Swegle [5]. These problems were the tensile instability, lack of consistency and zero-energy modes. Swegle and co-workers developed the conservative smoothing approach as a cure for the tensile instability [6]. Johnson developed the normalised smoothing approach to give the method linear consistency [7].

The method improvements in accuracy and stability achieved by kernel re-normalisation or correction have not come for free. The kernel normalisation acts as a correction for the lack of neighbours at the boundary. For instance, with the stress free condition not enforced unphysical behaviour was observed, with stress and shock waves not being reflected from a free surface. Therefore, it is necessary to treat the essential boundary conditions in a rigorous way.

The approximations in SPH do not have the property of strict interpolants so that in general they are not equal to the to the particle value of the dependent variable, i.e. $u^h(x_j) = \sum_I \phi_I(x_j) u_I \neq u_j$. Consequently it does not suffice to zero u_I at the boundary positions to enforce homogeneous boundary conditions.

Campbell [8] made an early attempt to introduce a more systematic boundary condition treatment by re-considering the original kernel integral estimates and taking into account the boundary conditions through residual terms in the integral by parts. Randles and Libersky [9] were first to propose a more general treatment of the free surface boundary condition based on

0734-743X/99/$ - see front matter © 1999 Elsevier Science Ltd. All rights reserved.
PII: S0734-743X(99)00137-2

an extension of the ghost particle method. In this approach, the boundary was considered to be a surface one half of the local smoothing length away from the so-called boundary particles. A boundary condition was applied to a field variable by assigning the same boundary value of the variable to all ghost particles generated outside the boundary. A constraint was imposed on the boundary by interpolating it smoothly between the specified boundary particle value and the calculated values on the interior particles. This served to communicate to the interior particles the effect of the specific boundary condition. This was the approach we adopted for treatment of the free surface boundary condition.

Like the stress free boundary condition, contact has been successfully ignored in SPH. Contact between two bodies could be reasonably handled through the conservation equations. When a particle from one body is within the smoothing distance of a particle of a second body, they each become neighbour particles of the other. They then interact through the sums over neighbour particles. This method can produce good results when modelling hypervelocity impact, see for example Libersky et al.[4].

However, when using this method a degree of penetration and mixing occurs at the contact surface, typically the first one to two particle rows of each body pass each other. This occurs, as SPH does not require the velocity field to be single valued. Monaghan proposed a modification to prevent this penetration, which he called XSPH [10]. While Monaghan's modification does prevent penetration it does nothing to solve two other problems with treating contact in this manner:

- Generation of tensile forces, resisting separation of two bodies.
- Generation of shear stresses preventing friction-less or low friction sliding.

Different contact algorithms have been used with SPH when combining the SPH method with the FE method [11, 12], but the only purpose of the algorithms were to allow SPH nodes to interact with an FE mesh.

From a literature survey and our experience in dealing with the contact problem in the finite element method, it was concluded that the penalty method would be a good starting point for contact in SPH due to its simplicity and computational efficiency.

An attempt was made to preserve the conceptual simplicity of SPH by developing a particle to particle general contact algorithm. In order to remove the need to define the material boundary as a line in 2D, the SPH particles were considered to be spheres of a known size. In common with the treatment of the free-surface condition, the location of the boundary was fixed at h/2 from the particle centres. So contact was between spheres of radius h/2.

Due to non-uniqueness of the surface normal at vertices it was necessary to calculate two surface normals for each boundary particle, and detect a corner particle when the angle between the two normals exceeds a specified angle. For a corner particle with no contact the free-surface condition was applied by considering both surface normals, for a corner particle with contact the free-surface condition was only applied in the direction of the surface normal not used by the contact algorithm. This is very important because ignoring, not enforcing, free surface boundary conditions on corner particles resulted in their non-physical motion.

Different methods for the penalty force calculation and the contact constraint enforcement were evaluated in 1D. This included expressions for the contact force based on penetration and penetration velocity. Different penalty force algorithms were evaluated by comparison with contact enforced by including all materials in the kernel sum. The favoured methods were extended to 2D, where the treatment of free-surfaces and corners with contact was assessed. Few simple illustrative impact problems were analysed to demonstrate accuracy and numerical efficiency of the contact algorithm developed.

CONTACT ALGORITHM

Having defined position of the boundary using the approach proposed by Libersky [13], contact detection and contact force application was considered. There are two principal choices: particle to surface contact, and particle to particle contact. Figure 2.1 shows an example of both cases. The arrows denote the unit normal vector to the particle calculated by the gradient of unity method [13], the dashed lines represent the surfaces used to determine if there is contact.

In the particle to surface case a straight line is drawn between points that lie $h/2$ along the particle normals, if this line intersects the circle with radius $h/2$ from the oncoming particle then contact has occurred. The normal to the surface at the point of contact is defined by the normal to the line, and a contact force is applied in the same direction as the surface normal. The force would have to be divided between the two particles at either end of the contact line. The contact algorithm can be made more reliable by making it is symmetric, which means that each node is considered as a slave node, and a node on the master surface.

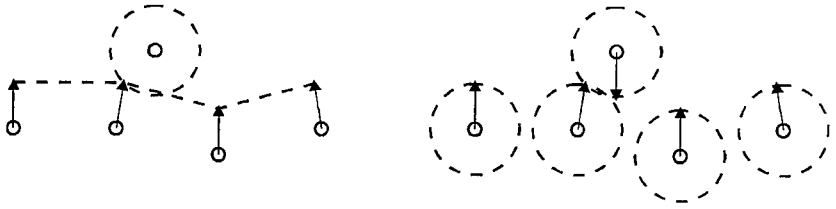

a b

Fig. 2.1: a) Particle to surface contact, b) Particle to particle contact

In the particle to particle form contact occurs when the circles around two particles intersect. This can be easily determined by checking the inter-particle distances, making the detection of contact considerably simpler than with the particle to surface version of contact. Using this method, only the interaction of two particles is considered at any one time, removing the need to consider each particle twice in the algorithm. This approach has many similarities with Belytschko's pinball contact algorithm [14, 15].

The particle to particle approach was investigated first because as using only particle to particle interaction is more in keeping with the meshless approach, and its extension to 3D would not be complex. Extending the particle to surface algorithm to 3D would be complicated by the need to define a boundary surface. Furthermore, this surface needs to be redefined regularly as bodies in contact deform.

In the particle to particle method determination of the direction of the contact force is an obvious problem. The contact force should be applied in a direction normal to the contact surface, however except in special cases, this results in a force vector that does not pass through the centre of mass of the particles in contact, generating a moment. Applying the contact force along the vector connecting the particle centres solves this problem, but the contact force now has a component tangential to the contact surface. Algorithms for both cases were developed, and are described below.

Contact Force Applied Between Particle Centres

Penalty contact algorithms are based on the assumption that there is certain amount of penetration between the bodies in contact. The contact force is usually function of penetration, penetration rate or both. Thus, penetration calculation is an important part of this type of contact algorithm.

In this simple case, penetration is detected if:

$$p = \frac{h_i + h_j}{2} - |r_{ij}| \geq 0 \tag{2.1.1}$$

Where: $r_{ij} = x_j - x_i$ (2.1.2)

p is penetration,

r_{ij} is the vector from the centre of particle i to the centre of particle j,

h_i, h_j are smoothing distances for particles i and j respectively.

The actual penetration is defined by equation 2.1.1. The contact force is applied along vector r_{ij}.

Contact Force Applied Along Average Normal

For the stress-free boundary condition the surface normal at each boundary particle has been found, but it is not possible to assume that the normals on the particles in contact are equal and opposite. An estimate to the normal to the contact surface is found by taking the difference between the two unit normal vectors resulting in a vector that when normalised is the average of the two vectors.

This average normal vector is the vector along which the contact force is applied. So the magnitude of the penetration can be defined as the relative displacement of the particle positions in the direction of the average normal that would result in zero penetration, equation 2.2.1. This is the definition of penetration that is used in the pinball algorithm [14].

$$p = \sqrt{d^2 - r_{ij}^2 + (n_{av} \cdot r_{ij})^2} - (n_{av} \cdot r_{ij}) \tag{2.2.1}$$

Where: $d = (h_i + h_j)/2$,

n_{av} is average normal vector.

Enforcing the Contact Condition

Once contact is detected a method is required to enforce the contact condition. The penalty method was chosen to enforce contact as the simplest and most straight-forward method. Penetration is detected only when the distance between the two particles is $< 0.5(h_i + h_j)$. If the two particles completely pass each other then penetration is no longer be detected, and no contact force is applied. Prevention of this from happening places a lower limit on the magnitude of the penalty force.

Three different expressions for the penalty force were investigated, and implemented into the code. This allowed the sensitivity of the contact algorithm to the contact force type to be tested.

The first contact force considered was the force used by Belytschko in the pinball algorithm, see [15] for details.

The second contact force, referred to later as type 2, considered was:

$$F = K_p \begin{cases} \max(F_1, F_2) & \dot{p} > 0 \\ 0 & \dot{p} < 0 \end{cases} \tag{2.3.1}$$

Where: K_p is a scale factor,

$$F_1 = \frac{mp}{\Delta t^2} \tag{2.3.2}$$

$$F_2 = \frac{2mcp}{\Delta t \Delta x} \qquad \Delta x = |x_j - x_i| \tag{2.3.3}$$

Equation 2.3.2 is used by Swegle [16] for contact between SPH nodes and finite elements. It is derived by assuming that the rate of penetration can be defined as $p/\Delta t$ and applying a force sufficient to bring the node penetrating finite element mesh to rest over a single time step. Equation 2.3.3 can be derived by assuming that $m_i = m_j = m$ and applying a force sufficient to bring to rest a body of mass $2m$ travelling at the relative velocity of the two particles, v':

$$F = \frac{2mv'}{\Delta t} \tag{2.3.4}$$

Then substituting $v' = cp/\Delta x$, where $\Delta x/c$ is an approximation to the time over which the penetration has occurred, gives (2.3.3).

The equation $\sigma = \rho c v$ for the stress behind a one-dimensional elastic wave is equivalent to (2.3.3) if the following substitutions are made: $\sigma = F/A$ and $v = p/\Delta t$.

The third contact force, referred to later as type 3, considered was:

$$F = \begin{cases} \dfrac{|v_j - v_i|}{\dfrac{\Delta t}{m_i} + \dfrac{\Delta t}{m_j}} & \dot{p} > 0 \\ 0 & \dot{p} < 0 \end{cases} \tag{2.3.5}$$

This was derived, by considering the force required to bring the two particles to rest with respect to each other, while conserving momentum, in an ideal plastic collision. The contact force in one time step applies the same impulse to both contact particles:

$$F\Delta t = m_i \Delta v_i \qquad F\Delta t = m_j \Delta v_j \tag{2.3.6}$$

If the particles are to be brought to rest with respect to each other, then the rate of change of penetration has to be, $\dot{p} = \Delta v_i + \Delta v_j$, which combined with equation 2.3.6 yields:

$$\dot{p} = \frac{F_1 \Delta t}{m_i} + \frac{F_1 \Delta t}{m_j} \tag{2.3.7}$$

Substituting the relative velocity $|v_j - v_i|$ for $\dot{p}$ in equation 2.3.7 results in the third contact force expression. No scale factor or other correction term is required for this type of contact force.

Contact With Two Particle Normals

The contact algorithm was tested in 2D by modelling the normal symmetrical impact of two steel blocks. Each block was 1.0 cm by 0.4 cm and consisted of 50 particles by 20 particles, giving a total of 2000 particles in the whole model. The two block's initial relative velocity was 4.0 km/s.

Test results quickly showed that the contact algorithm required improvement in its treatment of corner particles. When the stress free boundary condition was not applied to the corner

particles in contact, this caused incorrect behaviour at the corner particles at either end of the contact surface. As the stress free condition was not applied release waves were not generated correctly at the corner particles. The result was that the horizontal velocity of the corner particles was too low.

In order to treat the corner particles correctly two surface normal vectors were required. If the corner particle was not in contact then the stress free boundary condition was applied for both particle normals. If the particle was in contact then the stress free boundary condition was only applied in the direction of the free surface particle normal. This allowed for the correct behaviour of the corner particles.

For contact it was necessary to find the best normal to use. The best normal was defined as the normal, which gives the maximum value of $n \bullet r_{ij}$. Where r_{ij} is the vector between the centres of the two particles in contact and n is the unit normal vector.

The best normal was then used for the contact algorithm as if it were the single particle normal. The stress free boundary condition was not applied for that surface normal used in contact. For contact boundary particles that lie on a flat or near flat boundary it was necessary not to apply the stress free boundary condition. To differentiate between a corner particle and a surface particle the angle between the two normal vectors was calculated. If this angle exceeded a set value then the particle was considered to be a corner particle and both contact and free surface boundary conditions were applied in the directions of corresponding normals. The set value used in the tests was 45°.

TESTS OF CONTACT ALGORITHM

The SPH code used for both the 1D and 2D tests of the contact algorithm uses the kernel normalisation derived by Randles and Libersky [13]. The multi-dimensional conservative smoothing function proposed by Randles and Libersky [13] was used in all tests to prevent the tensile instability problem.

1D Tests

The first set of tests was in 1D. The aim of these was to test the effects of the different contact (penalty) force algorithms, in exclusion from any effect that could occur in 2D from the two different methods of calculation of the vector along which the contact force was applied.

The test problem used was a symmetrical impact of two 0.4 cm long steel bars. 100 particles were placed along the 1D line, 50 particles in each bar. The smoothing length was 0.008 cm and the initial inter-particle space was equal to the smoothing length. The space between the two contact particles was 0.01, so there was no initial penetration. Each bar was given an equal but opposite initial velocity of 2 km/s.

To provide a reference point the problem was first analysed using DYNA and SPH with no contact, using kernel sums to allow interaction between the two bodies. DYNA and kernel contact results were almost identical in the period between the initial contact and the point in time when release waves reach contact interface. Therefore, only the kernel contact results are shown. With the kernel sums the two end particles were initially in contact as the distance between the two was $1.25h$. Figure 3.1.1 shows the resulting stress profiles. At time $0.2\mu s$ the shock waves are propagating away from the point of contact. The value of k, time step scale factor, used for the results shown was k=0.5. The problem was also run with a value of k=1.5 with no problems, the only difference observed was a higher amplitude, by a factor of 3 to 4, in the stress oscillations behind the shock wave.

With this reference point established, runs were made to compare the different contact force types. Both the type 1 and the type 2 contact forces resulted in similar overall behaviour, therefore results are presented for the contact force types 2 and 3 only.

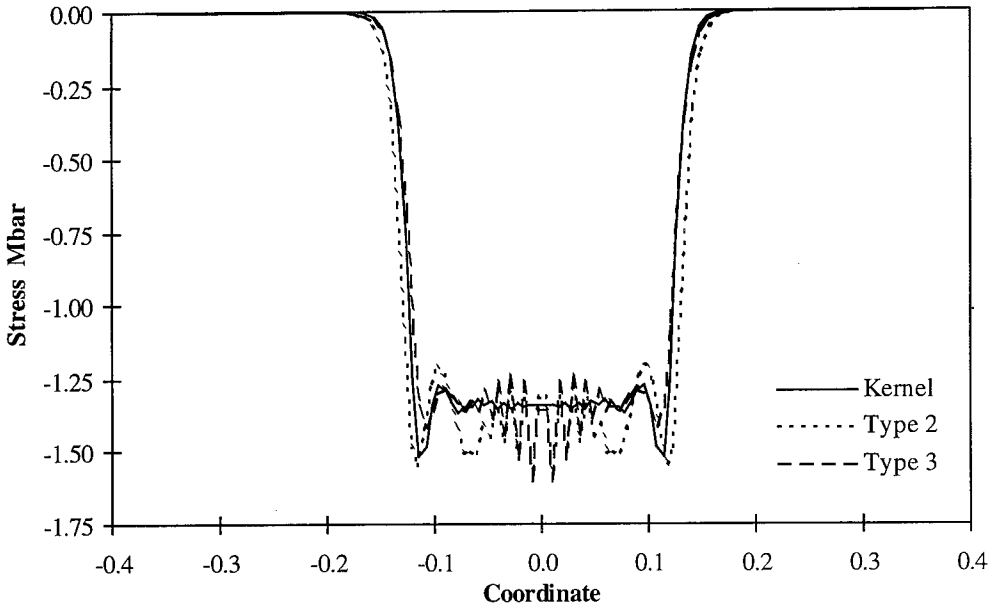

Fig. 3.1.1: Stress profiles at 0.2μs for kernel contact, contact force types 2 and 3. Contact force scale factor for the contact force type 2 was K_p=0.05. Time scale factor was k=0.5.

In figure 3.1.1, considerable oscillation can be seen in the stress at the interface for both cases. A sensitivity analysis was performed in which the contact force scale factor K_p was varied between 0.008 and 0.2 for the contact force type 2. Best results were obtained for K_p = 0.05, the amplitude of the spurious stress oscillations was significantly reduced.

This oscillation was described by Swegle [16] who observed it when modelling the 1D impact of two initially separated bodies using kernel contact. This oscillation corresponds to a zero energy mode, for which stress field does not cause particle accelerations that would reduce the stress amplitude. Swegle showed that this was a characteristic of the SPH method, as the SPH estimate to the stress field has its local maxima and mimima at the particles giving the stress field gradient of zero. In the SPH method no acceleration will be produced at a particle if the stress at the two neighbour particles is equal, this is independent of the stress at the particle itself. This is the stress version of the SPH zero-energy mode where an alternating velocity field does not generate stresses in the material to resist the particle motion. Swegle attempted to control the oscillation by varying the time step, the artificial viscosity coefficient and the smoothing length, all without success.

The stress oscillation in the region of the contact did not change significantly during contact. Figure 3.1.2 compares the stress profiles at 0.7μs. This showed that only a small decrease in the stress amplitude has occurred.

The contact algorithm, using the third type of contact force, showed the best agreement with the velocity profile seen with kernel contact. However, the stress profiles showed that the stress oscillation was present with this contact force type.

If the spurious stress oscillation did not have any affect on the results of the calculation then it would have been possible to ignore it. During the early stages of the calculations, as have been discussed so far, it was not significant. It was found that it can have a significant effect once the release waves arrive at the contact surface. The spurious stress oscillation caused high tensile stresses in the material when the release waves reach the contact interface by affecting the behaviour of the nodes in contact. The root cause of this tensile stress was the incorrect

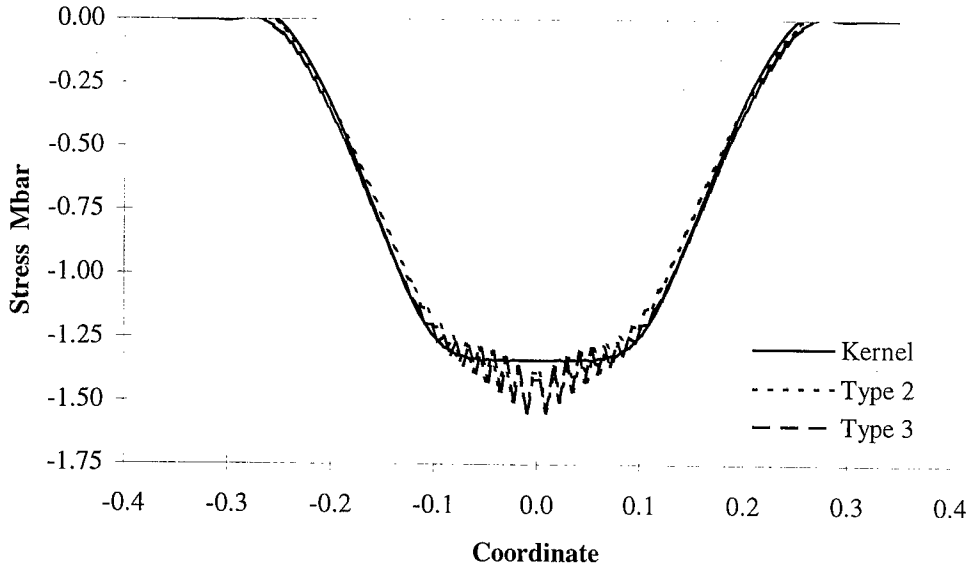

Figure 3.1.2: Stress profiles at 0.7μs for kernel contact, contact force types 2 and 3. Contact force scale factor for the contact force type 2 was K_p=0.05. Time scale factor was k=0.5.

behaviour of the boundary particles due to the spurious stress oscillations. This can be explained by considering the momentum equation.

In 1D, considering only the nearest neighbours, the momentum equation for an internal particle reduces to:

$$\frac{dv_i}{dt}=\left[-\left(\frac{m_{j1}}{\rho_{j1}}(\sigma_{j1}-\sigma_i)\frac{dW_{ij1}}{dx}\right)-\left(\frac{m_{j2}}{\rho_{j2}}(\sigma_{j2}-\sigma_i)\frac{dW_{ij2}}{dx}\right)\right] \tag{4.1.1}$$

Where $j1$ and $j2$ are the two neighbour particles. So when $\sigma_{j1}=\sigma_{j2}$ the acceleration is zero.

For a boundary this equation is:

$$\frac{dv_i}{dt}=\left[-\frac{m_j}{\rho_j}(\sigma_j-\sigma_i)\frac{dW_{ij}}{dx}\right]B \tag{4.1.2}$$

as the stress oscillation causes $\sigma_j\neq\sigma_i$ then the boundary particle has a non-zero acceleration. In all cases the stress oscillation caused by contact had $\sigma_j>\sigma_i$, which causes the boundary particle to have an acceleration away from its neighbour particle.

In most cases the effect that the tensile stress had on the final result was to delay the separation of the two bars, and to generate a tensile stress wave that propagated through the material. In one case the stress was high enough to cause numerical fracture, splitting the particles near the contact point from the remainder.

The effect of the spurious stress oscillation has been established. As it had significant effect on the results it needed to be controlled. Tests were performed to find the effect of varying the time step, contact force and initial material velocity on the oscillation. The amplitude of the oscillation was most sensitive to the magnitude of the contact force. Reducing the contact force gave a significant reduction in the amplitude. Reducing the impact velocity, which also has the effect of reducing the contact force, also reduced the stress oscillation. At the higher velocities the contact force can not be reduced to a level that controls the oscillation, as a low contact force

leads to a large penetration which causes the contact algorithm to break down. Reducing the time step and the contact force gave a significantly reduced amplitude, and offered a way of controlling the amplitude of oscillating stress component. The disadvantage of this was that the tests with a reduced time step were using a time step of 5% of the maximum stable value. In higher dimensions with the consequent larger numbers of particles this size of time step would increase the computational cost of the calculation by an order of magnitude over the cost when using the kernel to provide contact.

2D Tests

The second set of tests was in 2D. The aim of these test was to compare the effects of applying the restoring force along an average particle normal, or along the vector between the two particle centres. As the 1D tests showed that the behaviour of penalty force types 1 and 2 were similar, only penalty force types 2 and 3 were used in the 2D tests. The solid block impact problem described in Section 2.3 was used. The contact boundary particles in each body were initially spaced h apart, so the initial penetration was zero. The results were compared to the result from a DYNA3D analysis for the same problem. The difference in stresses and velocities between was within 5%.

The following four basic cases were considered:

- Average normal contact with penalty force type 2.
- Average normal contact with penalty force type 3.
- Between centres contact with penalty force type 2.
- Between centres contact with penalty force type 3.

For all four runs k was 0.1, and for penalty force type 2 K_p was 0.05. All four sets of results were very similar, with the corner particles behaving correctly, and the two bodies separating later in the calculation, figure 3.2.1. In all of these cases the particles in the two bodies were initially aligned, so that there was no difference between the average normal vector and the vector between the particle centres.

To test for the difference between the two methods, the lower block was given an initial horizontal, along the x axis, offset of $0.25h$. This offset causes that the two vectors to be no longer aligned, while not allowing a contact particle to be in contact with more than one other contact particle during the early stages of the calculation. To measure the difference between the cases, the total x momentum of each of the two blocks was recorded. To reduce the effect of the offset at the corners, a lower initial relative velocity of 200 m/s was used. Initially the x momentum in each body was zero and in the ideal case it would have remained zero throughout the run. The x momentum time histories for the four cases are shown in figure 3.2.2.

The difference between the two force vectors was clearly seen. With both penalty force types the between centres algorithm has resulted in a higher x momentum in the two bodies. The

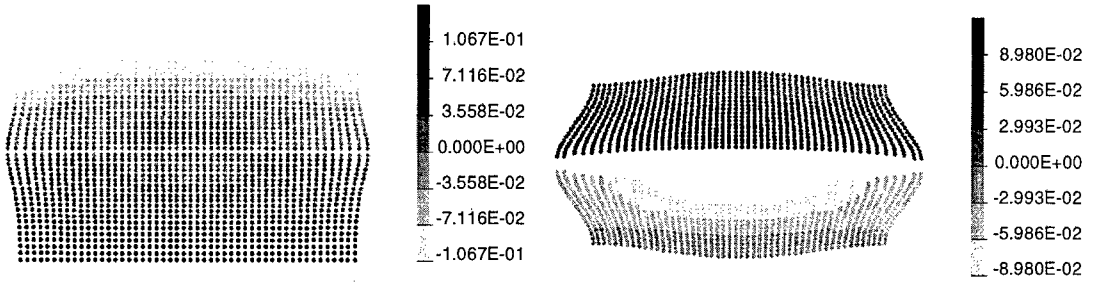

a) b)

Fig. 3.2.1: a) vertical velocity at 0.4 μs. b) vertical velocity at 1.8 μs. for average normal contact, k=0.1. Impact velocity 4 km/s.

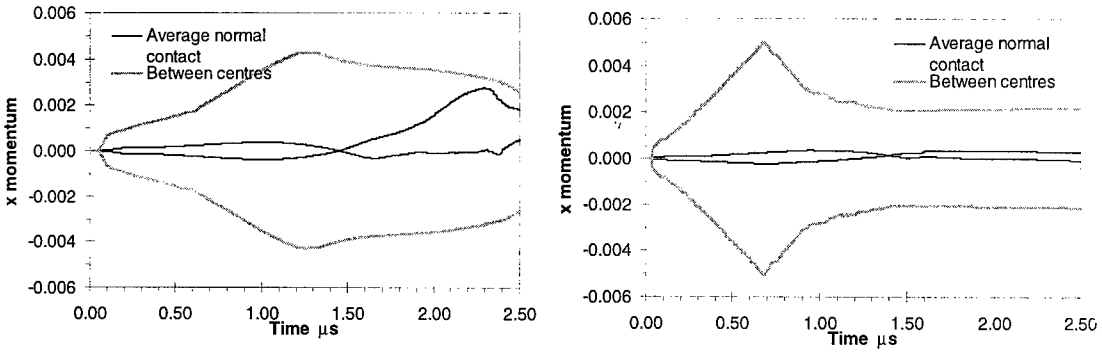

Contact force type 2 Contact force type 3

Fig. 3.2.2: x momentum time histories for the different force vectors. Impact velocity 200 m/s.

maximum value for the average normal contact was at time 0.98μs, the larger value that occurred later will be commented on shortly. There was an order of magnitude difference between the two cases, but was this difference significant? Each block was 1cm by 0.4 cm, and the initial material density was 7.89 g/cm^3, giving each block a total mass of 3.156g. An x momentum of 5.04×10^{-3} is equivalent to the average horizontal velocity of the block of 0.0016 cm/μs, 16% of the initial vertical velocity of the block.

Applying the penalty force along the vector between the two centres has resulted in each block gaining a significant horizontal momentum. The maximum momentum values are given in Table 1. In all cases the momentum drops after reaching its maximum value.

Table 1. Maximum x momentum for the fore contact treatments considered

	Maximum x momentum
Average normal contact, penalty type 2	3.79×10^{-4}
Between centres contact, penalty type 2	4.30×10^{-3}
Average normal contact, penalty type 3	3.63×10^{-4}
Between centres contact, penalty type 3	5.04×10^{-3}

This is because the horizontal motion has resulted in a given contact particle coming into contact with the neighbour of its initial contact particle, the resulting penalty force has an x component of opposite sign to the force from contact with the initial particle. By doubling the number of particles in the model maximum value of the x momentum was reduced ten times.

These tests represent a worst case, where the particle spacing of the two contact surfaces were the same, and all particles were offset in the same direction. In practice it is most likely that the particle spacing of both surfaces would not be identical, and so any forces tangent to the contact surface would not have such a significant global effect.

The momentum time history for the average normal contact with contact force type 2 showed a large change in momentum after 1.5μs. The cause of this change was an instability that developed near both ends of the contact surface. This instability caused visible, non-physical, particle motions. These motions were largest in this case, but were also visible in the other normal contact case and the between centres with contact force type 2. The only case where visible particle motion was not seen was for the between centres with contact force type 3.

This instability was related to the saw-tooth stress oscillation observed in the 1D tests, as the stress oscillation occurs near the corners before the particle motions become significant. The stress oscillation was pronounced at the two ends of the contact surface. No stress oscillation was

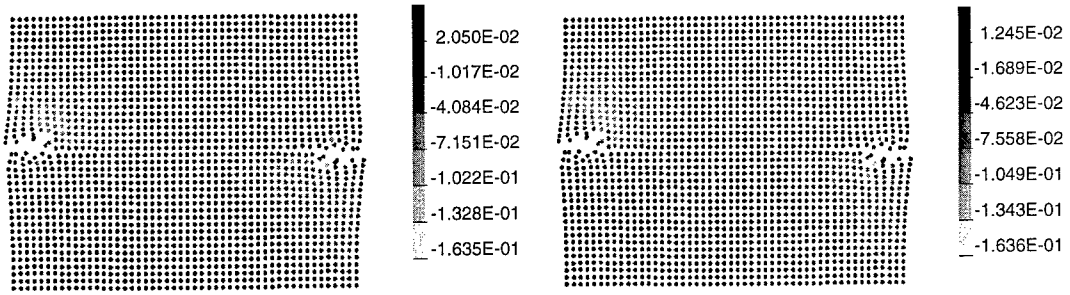

a) b)

Fig. 3.2.3: a) σ_{xx} stress component (horizontal) and b) σ_{zz} stress component (vertical) at 1.4μs for average normal contact. k=0.1. Instabilities at either end of the contact surface. Impact velocity 200 m/s.

observed in the σ_{zz} stress. The stress oscillation was also present in the two other cases where the instability caused visible particle motion.

Examining the particle stresses for the four runs without an initial particle offset showed that the stress oscillation was also present in those results. The instability was also present in 200 m/s impact velocity tests. Like the offset results, the average normal contact with contact force type 2 showed the most extensive instability. Figure 3.2.3 shows plots of the σ_{xx} and σ_{zz} stress components at 1.4μs for this case. Well developed instabilities and related errors in the stress distribution can be seen at either end of the contact surface for both stress components.

The presence of the instability appeared to be related to the spurious stress oscillation. The 1D tests showed that reducing the time step scale factor and the penalty force reduced the amplitude and extent of the stress oscillation. Also reducing the impact velocity, with the corresponding decrease in the contact force, reduced the oscillation. Tests were carried out in 2D to find whether this instability sensitive to the same factors.

The first four tests mentioned in this section, for 4 km/s impact and k=0.1 did not show any visible evidence of the instability. These four tests were repeated with k=0.3 and all four calculations developed the instability. The instability caused visible particle motions by 0.4μs.

The instability was closely related to the stress oscillation as it occurs in locations where the stress oscillation was already present. The severity of the instability is reduced in the same way as the severity of the stress oscillation reducing time step and contact force. The contact algorithm used had a strong effect on the instability, with the instability being most apparent when applying the contact force along the average normal vector, and least apparent when applying the contact force between the particle centres.

Further tests are required before a solid conclusion can be drawn as to whether applying contact force between the particle centres or along an average normal is better. These tests are complicated by the presence of the instability, as over a large range of initial conditions this instability will grow to a point where it prevents the calculation from reaching the termination time or has a significant effect on the global behaviour of the problem. The instability problem related to the zero energy modes must be addressed before further development of the contact algorithms can be carried out.

CONCLUSIONS

A penalty method for contact in SPH has been developed. The method retained the conceptual simplicity of the SPH method by considering only particle-particle contact. Impact and separation in the velocity range between 0.2 and 4 km/s were successfully modelled.

- Penalty approach is a viable way for contact treatment in SPH.
- Contact excites a stress oscillation in the region of the contact interface. In both 1D and 2D the oscillation resulted in non-physical motion of particles, in some cases rendering the final results completely inaccurate.
- Reducing the time step and contact force significantly reduced the severity of the spurious stress oscillation.
- The stress oscillation is a characteristic of the SPH method.
- The spurious stress oscillation requires (zero energy mode problem) addressing and controlling.

REFERENCES

1. R.A. Gingold and J.J. Monaghan, Smoothed particle hydrodynamics: Theory and application to non-spherical stars. *Mon. Not. R. Astron. Soc.*, **181**, 375–389 (1977).
2. L.B. Lucy, A numerical approach to the testing of the fission hypothesis. *Astron. J.*, **82**(12), 1013–1024 (1977).
3. L.D. Libersky and A.G. Petschek, Smooth Particle Hydrodynamics with strength of materials. In H.E. Trease, M.J. Fritts and W.P. Crowley, eds., *Advances in the Free-Lagrange Method*, 248–257. Springer-Verlag (1990).
4. L.D. Libersky, A.G. Petschek, T.C. Carney, J.R. Hipp, and F.A. Allahdadi, High strain Lagrangian hydrodynamics. *J. Comput. Phys.*, **109**, 67–75 (1993).
5. J.W. Swegle, S.W. Attaway: M.W. Heinstein, F.J. Mello, and D.L. Hicks, An analysis of smoothed particle hydrodynamics. Technical Report SAND93-2513, Sandia National Laboratories, (1994).
6. Y. Wen, D.L. Hicks, and J.W. Swegle, Stabilising S.P.H. with conservative smoothing. Technical Report SAND94-1932, Sandia National Laboratories, (1994).
7. G.R. Johnson, R.A. Stryk and S.R. Beissel, SPH for high velocity impact computations. *Comput. Methods Appl. Mech. and Engrg.*, **139**, 347–373 (1996).
8. P.M. Campbell, Some new algorithms for boundary value problems in smooth particle hydrodynamics. Technical Report DNA-TR-88-286, Mission Research Corporation, (1989).
9. P.W. Randles and L.D. Libersky: *Private communication*, October 1997.
10. J.J. Monaghan, On the problem of penetration in particle methods. *J. Comput. Phys.*, **82**, 1–15 (1989).
11. G.R. Johnson: Linking of Lagrangian particle methods to standard finite element methods for high velocity impact computations. *Nucl. Engrg. Des.*, **150**, 265–274 (1994).
12. S.W. Attaway, M.W. Heinstein, and J.W. Swegle: Coupling of Smooth Particle Hydrodynamics with the finite element method. *Nucl. Engrg. Des.*, **150**, 199–205 (1994).
13. P.W. Randles and L.D. Libersky, Smoothed Particle Hydrodynamics: Some recent improvements and applications. *Comput. Methods Appl. Mech. and Engrg.*, **139**, 375–408 (1996).
14. T. Belytscko and M. Neal, Contact-impact by the pinball algorithm with penalty and L.agrangian methods. *Int. J. Num. Meth. Engrg.*, **31**, 547–572 (1991).
15. T. Belytschko and I. Yeh, The splitting pinball method for contact-impact problems. *Comput. Methods App. Mech. Engrg*, **105**, 375–393 (1993).
16. J.W. Swegle, S.W. Attaway, M.W. Heinstein, F.J. Mello, and D.L. Hicks, An analysis of Smoothed Particle Hydrodynamics. Technical Report SAND93-2513, Sandia National Laboratory, (1994).

PERGAMON

International Journal of Impact Engineering 23 (1999) 957–966

INTERNATIONAL JOURNAL OF IMPACT ENGINEERING

www.elsevier.com/locate/ijimpeng

A MODEL FOR PENETRATION BY VERY LOW ASPECT RATIO PROJECTILES

JAMES D. WALKER

Southwest Research Institute, San Antonio, Texas 78228

Summary—As the aspect ratio (L/D) of a projectile decreases and the projectile becomes more disk like, the penetration mode changes. A model for the penetration of low L/D projectiles has been developed to explain and predict the low L/D penetration event. The model divides the penetration into two phases: first a flyer plate type impact, and second, a crater growth phase. Calculations provided insight into the physical mechanism involved. Shortly after impact, the projectile enters a long period of constant velocity penetration. This behavior leads to the depth of penetration scaling with projectile diameter. A large crater grows in the target, and the projectile travels into a debris filled crater as a free body. The velocity is "frozen" in when release waves arrive from the free surface. In the model, the crater in the target is analyzed by assuming plastic constitutive response, with the motion caused by an impulsive load due to the impact. The final depth of penetration is obtained by combining a one-dimensional depth of penetration and a plastic target cratering response. The model compares well with both large scale numerical simulations and experimental data. © 1999 Elsevier Science Ltd. All rights reserved.

INTRODUCTION

When a long rod penetrator is broken into segments the ultimate depth of penetration can be increased. Questions arise as to how thin the segments can be and still yield increased penetration, and what the effect of higher impact velocities are on penetration. In order to understand these effects, a model has been developed for low L/D projectiles impacting a target. This model has two parts. First is an explanation and prediction of velocities seen in the projectile and in the target material beneath the projectile during penetration. The behavior is dominated by wave mechanics. Second, a mechanical model to predict the depth of penetration is presented based on a combination of plastic crater growth in the target material and one-dimensional impact.

The depth of penetration model uses a technique that gives remarkably good results. The technique integrates the momentum balance along the centerline. Velocity profiles are assumed in both the target and the projectile in order to carry out the integration. To determine the shear stress required in the integral, a constitutive model for the target material and a three-dimensional velocity field within the target are assumed. The technique was first applied to metal targets being penetrated by long rods [1], and has subsequently been successfully applied to thick ceramic targets [2] and to thin targets comprised of thin ceramic tiles backed by thin substrates [3].

Here the somewhat different phenomena seen when low length-to-diameter (L/D) ratio projectiles are impacted against targets are explained. The model focuses on target response, explains certain features of the response, and also provides predictions for experimental depths. These predictions are compared against numerical calculations and experiments. Results from this model were first presented at the 1992 Hypervelocity Impact Symposium [4], and a subsequent paper employed this model to provide theoretical limits on the performance of segmented penetrators [5].

LOW L/D IMPACT

In conjunction with [4], numerical simulations of low L/D impact were performed. In these calculations, tungsten projectiles of L/Ds ranging from 1/4 to 1/16 impacted steel targets. The calculations were performed with CTH [6], using Mie-Grüneisen equations of state for the tungsten and the 4340 steel, the Johnson-Cook constitutive model for 4340 steel [7], and an elastic-perfectly plastic constitutive model for the tungsten, with a flow stress of 2 GPa. Zoning was 10 cells across the length of the projectile, with square zoning in the penetration region.

0734-743X/99/$ - see front matter © 1999 Elsevier Science Ltd. All rights reserved.
PII: S0734-743X(99)00138-4

The calculations provide insight into the physical mechanism involved in a low L/D impact event. Shortly after impact, the projectile enters a long period of constant velocity penetration. The behavior of the projectile is seen in Fig. 1. For very low aspect ratio projectiles (L/D=1/8 and 1/16), a lengthy constant velocity plateau is achieved. The velocity of the projectile is set by the arrival of release waves from the free surface, and an explicit expression for the velocity will be presented in Section 3. When rarefactions from the edge of the projectile arrive at the centerline, target material fractures. Figure 2 shows the time sequence for an L/D = 1/16 impact at 3.0 km/s. Rarefactions arrive from the outer projectile edge at the centerline at roughly 1 μs, opening up voids (fracture) in the target material directly underneath the projectile. The target debris in the crater moves at a constant velocity until it collides with the intact target material. A large crater grows in the target, and the projectile travels into a debris filled crater as a free body. The final craters and residual penetrators for calculations from L/D=1 to 1/16 and impact velocities from 1.5 to 5.0 km/s are shown in Fig. 3.

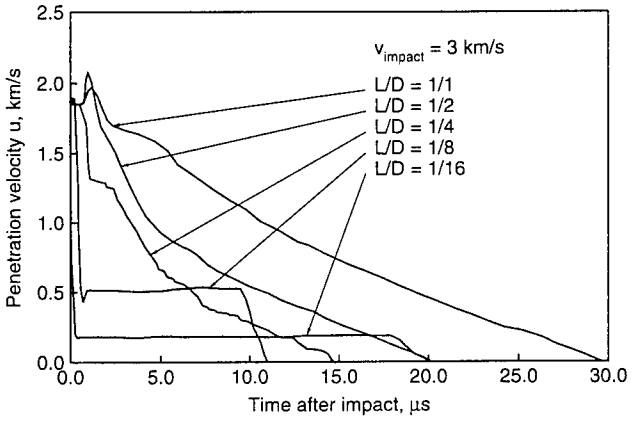

Fig. 1. Computed centerline penetration velocity for L/D = 1, 1/2, 1/4, 1/8 and 1/16 projectiles at 3 km/s impact velocity (from Franzen *et al.*, 1994).

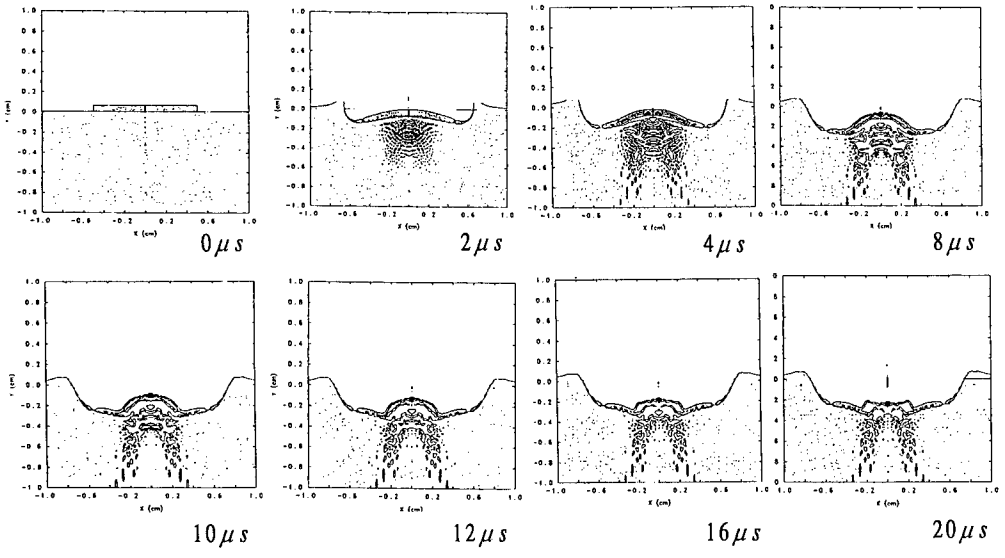

Fig. 2. Impact sequence for L/D=1/16 impactor at 3.0 km/s.

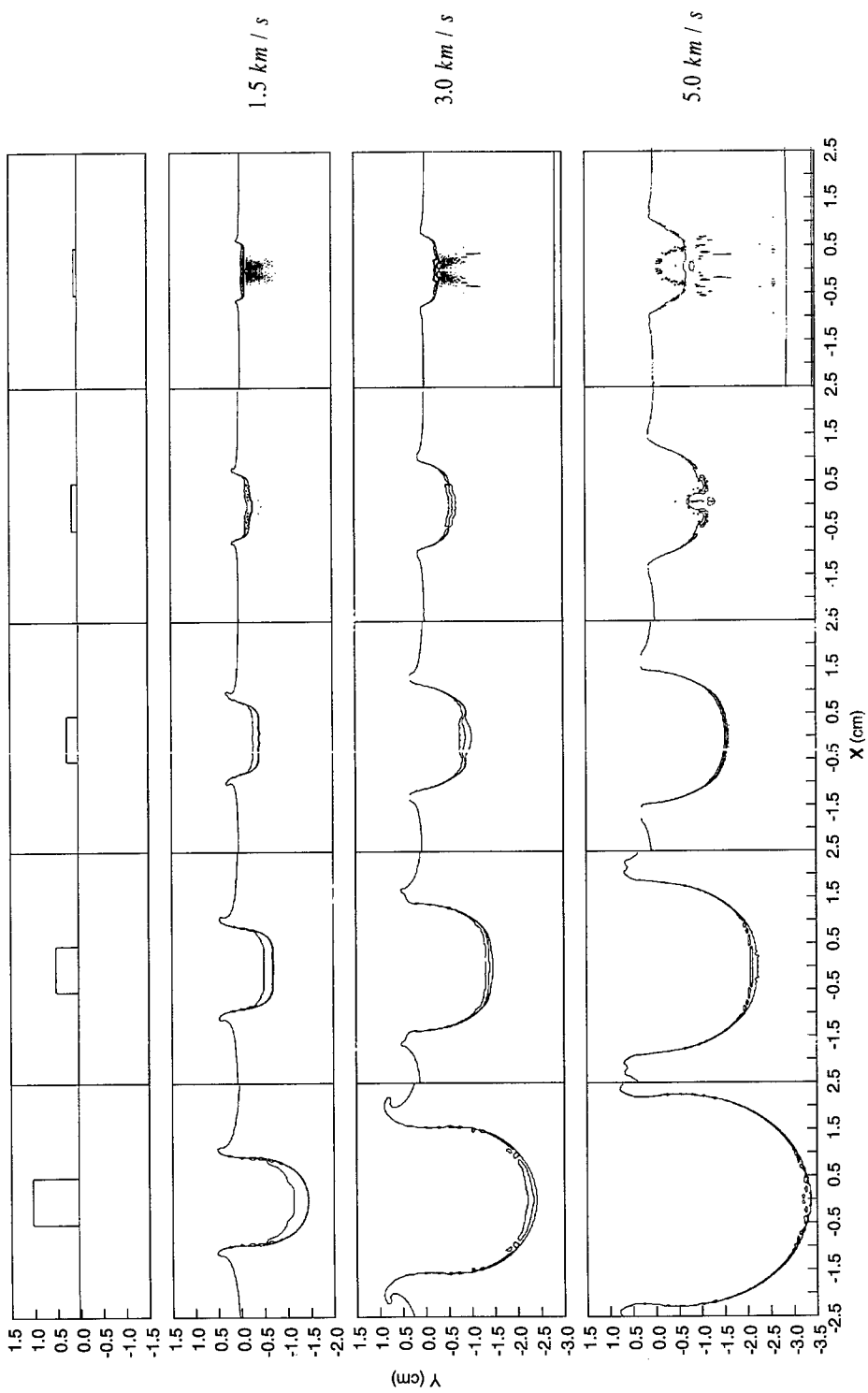

Fig. 3. Final crater profiles and residual projectiles for calculations of L/D = 1, 1/2, 1/4, 1/8, and 1/16 tungsten projectiles impacting steel targets at velocities 1.5, 3.0 and 5.0 km/s.

VELOCITIES WITHIN THE TARGET

The early stages of impact are very much one dimensional along the axis of symmetry. It is possible to see the step deceleration of the projectile in the numerical simulations as waves reflect back and forth. At a time given by the radius of the projectile divided by the sound speed of the target, the rarefaction waves arrive from the side of the impact area, and the pressure along the centerline is released. Though the pressure is released, *the axial velocity of the material is unchanged.* The target material is fractured due to the now tensile stresses. The fractured target material then travels at the velocity it had when released. This material continues to travel until it collides with the cavity wall, where is comes to rest.

To quantitatively model the impact scenario, a 1-D small deformation elastic impact is considered. The two materials have an acoustical impedance $z_m = \rho_m c_m$, and the impedance of the projectile material is assumed to be greater than that of the target material.

Upon impact, an elastic wave is formed in the projectile that travels from the interface, reflects off the rear surface of the projectile, and travels back to the interface. Because of the material mismatch, a new reflected wave is formed with a lower stress, and the cycle continues. The time for the wave to travel from the interface, reflect off the back, and back to the interface is $2L/c_p$, where c_p is the sound velocity in the projectile.

Velocities are found by equating stresses at the interface:

$$\sigma = \rho c u \tag{1}$$

where c is the sound velocity and u is the particle velocity, assuming the material was initially at rest. This leads to a series of equations:

$$\rho_p c_p (u_p^i - u_p^{i+1}) = \rho_t c_t u_p^i \tag{2}$$

where the superscript i refers to the number of reflections off the projectile-target interface. With

$$B = \frac{z_p}{z_p + z_t} \tag{3}$$

($1/2 < B < 1$ by assumption), the target-projectile interface velocity is

$$u_p = \begin{cases} B\mathrm{v}, & 0 \le t \le 2L/c_p \\ (2B-1)B\mathrm{v}, & 2L/c_p \le t \le 4L/c_p \\ (2B-1)^2 B\mathrm{v}, & 4L/c_p \le t \le 6L/c_p \\ \cdots & \cdots \end{cases} \tag{4}$$

The total depth of penetration for the one-dimensional linear elastic model is given by the sum of the interface velocity multiplied by the time the interface is travelling at that velocity:

$$P_e = B\mathrm{v}\frac{2L}{c_p} + (2B-1)B\mathrm{v}\frac{2L}{c_p} + (2B-1)^2 B\mathrm{v}\frac{2L}{c_p} + \ldots = \frac{B\mathrm{v}}{(1-B)c_p}L \tag{5}$$

Though we have explicitly solved this problem, it is qualitatively more clear to examine an approximate solution. An approximate equation for the interface velocity is

$$\frac{du_p}{dt} \approx \frac{\Delta u_p^{i+/2}}{\Delta t} = \frac{u_p^{i+1} - u_p^i}{2L/c_p} = \frac{(2B-1)^{(n+1)}B\mathrm{v} - (2B-1)^n B\mathrm{v}}{2L/c_p} = \frac{(B-1)}{L/c_p}u_p^i \tag{6}$$

To get the right hand side at $i + 1/2$,

$$u_p^{i+1/2} \equiv \frac{u_p^{i+1}+u_p^i}{2} = Bu_p^i \tag{7}$$

The approximate differential equation is then

$$\frac{du_p}{dt} = -\frac{(1-B)}{BL/c_p}u_p \tag{8}$$

This equation is valid for small L/c_p. Chosing to match the initial velocity v at the initial time, the solution to the differential equation is

$$u_p = \mathrm{v}\exp\left\{-\frac{c_p}{L}\frac{(1-B)}{B}t\right\} \tag{9}$$

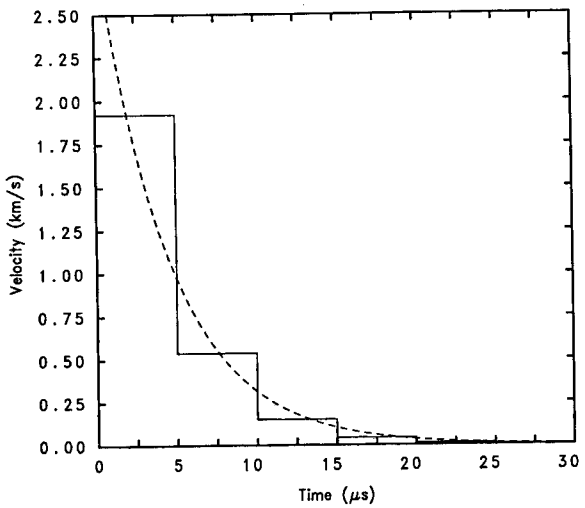

Fig. 4. Velocity of interface versus time.

Figure 4 shows the velocity of the interface versus time from Eq. (4) (solid line) and the approximate velocity from Eq. (9) (dashed line) for a tungsten into steel impact at 3.0 km/s. The plateaus around 500 m/s and 150 m/s seen in Fig. 1 for the L/D = 1/8 and impact calculations 1/16 are seen as interface velocities from Eq. (9) in Fig. 4.

Equation (9) provides a time profile of the velocity at the target-projectile interface. It also matches the depth of penetration for the exact solution, from Eq. (5). The velocity of the interface yields the spatial velocity profile in the target by noting that the wave travels from the interface into the target at the sound speed of the target:

$$u_z(z) = \mathrm{v}\exp\left\{-\frac{c_p}{L}\frac{(1-B)}{B}(t-z/c_t)\right\} \tag{10}$$

The rarefaction wave from a corner of the projectile reaches a point z on the centerline at roughly

$$t = \frac{\sqrt{z^2+(D/2)^2}}{c_t} \tag{11}$$

As noted above, the release essentially "freezes" the current axial velocity of the material. The numerical simulations show extensive fracturing of the material at this time. An expression for the frozen velocity is

$$u_z^{release}(z) = \min\left(Bv, v\exp\left\{-\frac{c_p}{c_t L}\frac{(1-B)}{B}(\sqrt{z^2+(D/2)^2}-z)\right\}\right) \tag{12}$$

An adjustment has been made for early time to match the initial penetration velocity for the first wave half transit. The velocity in Eq. (12) is used to plot material position versus time for the L/D=1/16 impact case at 3 km/s in Fig. 5. The figure shows the material versus time for 5 points located in the steel target at 0, 0.5, 1.0, 1.5, and 2.0 mm for a D = 1 cm impactor. Figure 6 shows the similar plot from the CTH calculation. The release velocity is an increasing function of the initial coordinate z, which gives rise to the "fan" behavior seen in both figures. In the numerical simulation, when the impulsively loaded crater comes to rest, the fractured material within the crater also comes to rest - this can be seen at the top of the figure, where the forward motion of the target material ceases.

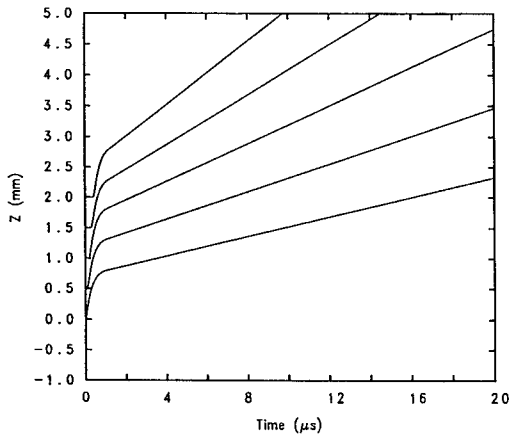

Fig. 5. Position versus time for points in the target for L/D = 1/16 and a 3 km/s impact velocity, using Eq. (12).

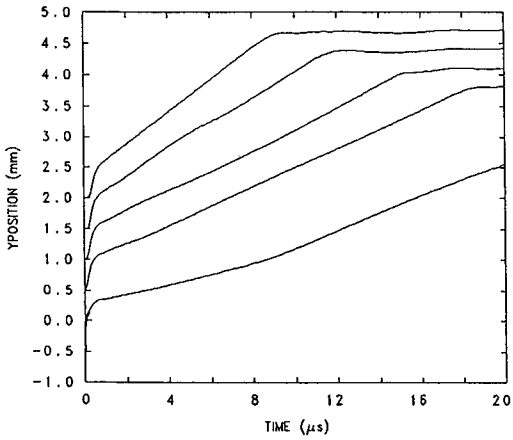

Fig. 6. Position versus time for points in the target for L/D = 1/16 and a 3 km/s impact velocity, from a CTH calculation.

DEPTH OF PENETRATION

The crater in the target is formed mostly by a plastic target response, caused by an impulsive load at the impact pressure. An expression for the final depth of penetration will be derived by combining a 1-D depth of penetration and the plastic target cratering response which includes three-dimensional effects. The model provides an explicit expression for the penetration in terms of material properties and initial impact conditions.

First the response of a plastic target to an impulsive load is examined. To simplify the problem, the projectile is viewed as a thin layer on the inside of a hemisphere in a perfectly plastic half space. The extent of the initial hemisphere is obtained by equating surface areas of the actual low L/D projectile, and the hemisphere:

$$\pi(D/2)^2 = 2\pi R_0^2 \tag{13}$$

Thus, the initial extent is $R_0 = D/2\sqrt{2}$. The impact of the projectile gives rise to an impact stress, which is viewed as an impulsive load which expands the hemisphere. A plastic flow field is assumed in the target half space.

The study of the plastic crater expansion begins with an examination of the momentum balance (see [1] for an example of the technique). The momentum balance along the z-axis, which is the axis of symmetry, simplifies to:

$$\rho \frac{\partial u_z}{\partial t} + \frac{1}{2}\rho \frac{\partial (u_z)^2}{\partial z} - \frac{\partial \sigma_{zz}}{\partial z} - 2\frac{\partial \sigma_{xz}}{\partial x} = 0 \tag{14}$$

The stresses are positive in tension. Equation (14) is integrated along the z-axis from the target-projectile interface ($z_i(t)$) to deep within the target. Assuming that the change in density in the target is small, so that the density term can be pulled out of the integral, we obtain

$$\rho_t \int_{z_i}^{+\infty} \frac{\partial u_z}{\partial t} dz + \frac{1}{2}\rho_t u_z^2 \Big|_{z_i}^{+\infty} - \sigma_{zz}\Big|_{z_i}^{+\infty} - 2\int_{z_i}^{+\infty} \frac{\partial \sigma_{xz}}{\partial x} dz = 0 \tag{15}$$

A velocity field in the target of form

$$u_z(z) = \begin{cases} \dfrac{u}{\alpha^2 - 1}\left[\left(\dfrac{\alpha R}{r(z)}\right)^2 - 1\right] & R \le r(z) < \alpha R \\ 0 & \alpha R \le r(z) \end{cases} \tag{16}$$

is assumed. This field has a hemispherical behavior, and is incompressible. In this equation, $r(z) = z - z_i(t) + R$, where R is the *crater* radius. The profile displays a similarity to that displayed from the numerical simulations. The velocity profile in the target is only over a finite domain, from R to αR, and this can be viewed as the extent of the plastic zone in the target.

It will be assumed that α is constant, and that the crater radius is equal to the interface location, so that $z_i(t) = R$ and hence $r(z) = z$. R is time dependent. These assumptions give

$$\int_{z_i}^{+\infty} \frac{\partial u_z}{\partial t} dz = \int_R^{\alpha R} \frac{\partial u_z}{\partial t} dr = \dot{u} R \frac{\alpha - 1}{\alpha + 1} + 2u\dot{R}\frac{\alpha}{\alpha + 1} \tag{17}$$

Assuming the target is perfectly plastic, it can be shown that ([1,2])

$$\int_R^{\alpha R} \frac{\partial s_{xz}}{\partial x}\bigg|_{x=0} dz = -\frac{7}{6}\ln(\alpha) Y_t \tag{18}$$

where Y_t is the constant flow stress for the target material.

Combining these pieces leads to an equation for the crater radius:

$$\rho_t \left\{ \frac{\alpha - 1}{\alpha + 1} R\ddot{R} + \frac{3\alpha - 1}{2(\alpha + 1)}(\dot{R})^2 \right\} = -\frac{7}{3}\ln(\alpha) Y_t - \sigma_z(R) \tag{19}$$

If the right hand side of Eq. (19) is viewed as constant, then it is autonomous (meaning that it does not depend explicitly on t). We write the equation as

$$aR\ddot{R} + b(\dot{R})^2 = -A \tag{20}$$

(As a note, an approximate spherical cavity expansion solution gives rise to this same equation, with the coefficients a, b and 7/3 being only slightly different. This fact argues that Eq. (20) is the right kind of equation to model crater growth.) Equation (20) can be reduced in order by making the substitution $S = dR/dt$, leading to

$$\frac{dR}{dt} = \begin{cases} \sqrt{\frac{|A|}{b}}\frac{\sqrt{R^{2b/a} - R_0^{2b/a}}}{R^{b/a}}, & A < 0 \\ \sqrt{\frac{A}{b}}\frac{\sqrt{\tilde{R}^{2b/a} - R^{2b/a}}}{R^{b/a}}, & A > 0 \end{cases} \tag{21}$$

where R_0 and $\tilde{R}$ are constants and

$$\frac{2b}{a} = \frac{3\alpha - 1}{\alpha - 1} \tag{22}$$

In particular, for large α, $2b/a \approx 3$.

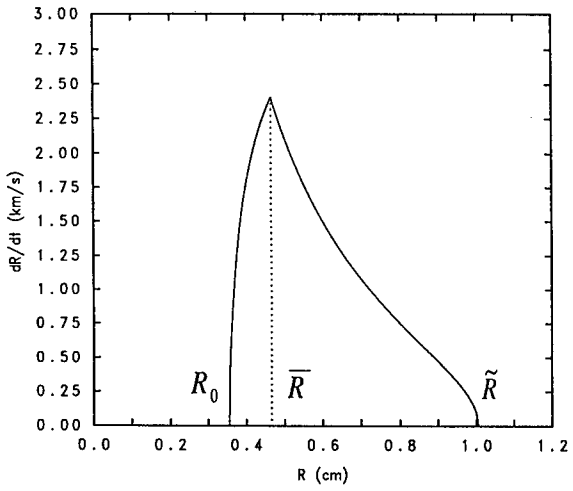

Fig. 7. Interface velocity versus crater radius.

The impact produces an impulsive loading at stress σ_0 for a given time. The initial loading and acceleration of the crater is followed by a dissipative expansion of the crater. The $A < 0$ solution holds for the initial loading, and the $A > 0$ solution holds for the subsequent decelerating expansion, where R_0 is the initial radius of the projectile and $\tilde{R}$ is the final crater radius. Figure 7 shows the velocity versus time from Equation (21) for a L/D = 1/8 impact at 3.0 km/s. The final penetration $\tilde{R}$ is solved for by equating the two solutions at the value of the displacement when the impulsive load is removed, $\overline{R}$:

$$\sqrt{\frac{|A_0|}{b}}\frac{\sqrt{\overline{R}^{2b/a} - R_0^{2b/a}}}{\overline{R}^{b/a}} = \sqrt{\frac{A_1}{b}}\frac{\sqrt{\tilde{R}^{2b/a} - \overline{R}^{2b/a}}}{\overline{R}^{b/a}} \tag{23}$$

Letting

$$\mu = \frac{|A_0|}{A_1} = \frac{|-\sigma_0 - \frac{7}{3}\ln(\alpha)Y_t|}{\frac{7}{3}\ln(\alpha)Y_t} \tag{24}$$

which is roughly the ratio of the impact pressure to the strength of the target, a solution for the plastic crater radius is

$$\tilde{R}^{2b/a} = (1+\mu)\overline{R}^{2b/a} - \mu R_0^{2b/a} \tag{25}$$

In order to estimate the displacement $\overline{R}$ in this equation, we presume that the fraction of the theoretical 1-D depth of penetration that results in the plastic crater expansion is controlled by how much of the wave train in the target is released. An estimate of this fraction is given by the time it takes the wave to travel the axial distance αL, divided by the time it takes the relief wave to travel from the corner of the projectile to the same location. Thus,

$$\overline{R} - R_0 = \frac{\alpha L}{\sqrt{(\alpha L)^2 + (D/2)^2}} P_e = \cos(\theta) P_e \tag{26}$$

The elastic one-dimensional part of the penetration is $(1-\cos(\theta))P_e$, and the total depth of penetration is then

$$\begin{aligned} \frac{P}{L} &= \left(\frac{P}{L}\right)_{1-D} + \left(\frac{P}{L}\right)_{2-D} \\ &= \frac{(1-\cos(\theta))P_e}{L} + \left(\frac{\tilde{R}}{L} - \frac{R_0}{L}\right) \\ &= (1-\cos(\theta))\frac{P_e}{L} + \left\{(1+\mu)\left(\frac{R_0}{L} + \cos(\theta)\frac{P_e}{L}\right)^{2b/a} - \mu\left(\frac{R_0}{L}\right)^{2b/a}\right\}^{a/2b} - \frac{R_0}{L} \end{aligned} \tag{27}$$

The low L/D limit is what is expected,

$$\lim_{L/D \to 0} \frac{P}{L} = \frac{P_e}{L} \tag{28}$$

P/L versus L/D is plotted for the tungsten into steel impacts at velocities v = 1.5, 2.0, 3.0, and 5.0 km/s in Fig. 8 (with α = 10). Equation (27) was used, with σ_0 obtained from the equation of state used in the CTH calculations and P_e from one-dimensional CTH calculations rather than the elastic small displacement constant impedance approximations of Eqs. (2) and (5). The values used are shown in Table 1. Also on the graph are P/L values for the CTH calculations for 1.5, 3.0, and 5.0 km/s, as well as experimental data for 2.0 km/s [8].

The agreement between the model and the hydrocode and experimental results is very good. The depth of penetration equation displays the increase in penetration as the aspect ratio decreases, as is seen in tests and large scale numerical simulations. The decrease in depth of penetration for even smaller aspect ratio is controlled in the model by the assumption in Eq. (26) regarding how much of the penetration is one-dimensional versus multidimensional. This assumption in the modeling deserves more examination, but the current approach yields good results.

Table 1. Values used in P/L calculation (*from linear interpolation)

Impact Velocity (km/s)	Impact Stress (GPa)	1-D P/L (from CTH) (-)
1.5	-44.5	0.58
2.0	-65.6*	0.70*
3.0	-107.8	0.95
5.0	-221.1	1.28

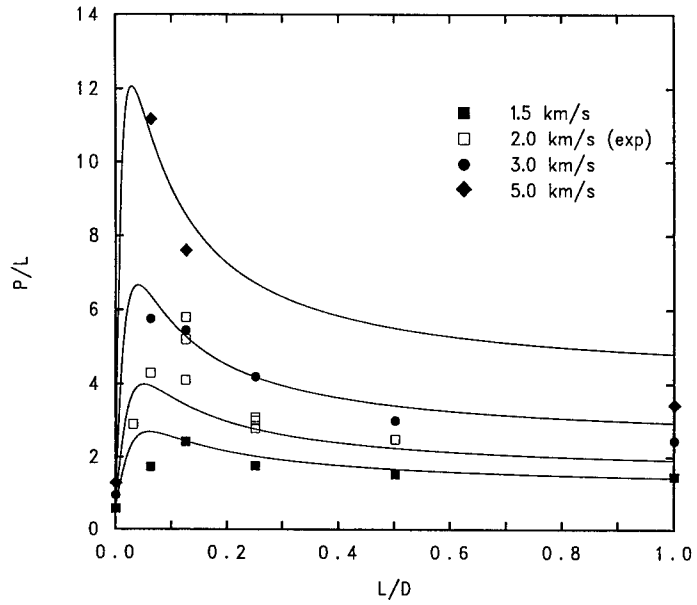

Fig. 8. Model versus computational and experimental results.

CONCLUSIONS

A model for the penetration of low L/D projectiles has been developed. The model divides the penetration into two phases: first a flyer plate type impact, and second, a crater growth phase. Calculations provided insight into the physical mechanism involved in a low L/D impact event. Shortly after impact, the projectile enters a long period of constant velocity penetration. A large crater grows in the target, and the projectile travels into a debris filled crater as a free body. The velocity is "frozen" in when release waves arrive from the free surface. The crater in the target is analyzed by assuming plastic constitutive response, with the motion caused by an impulsive load due to the impact. The final depth of penetration is obtained by combining a 1-D depth of penetration and this plastic target cratering response. The model compares well with both large scale numerical simulations and experimental data.

Acknowledgements—The assistance of Charles E. Anderson, Jr., Dennis Orphal, Roland Franzen, and Phil Schneidewind is greatly appreciated.

REFERENCES

1. J. D. Walker and C. E. Anderson, Jr., "A Time-Dependent Model for Long-Rod Penetration," *Int. J. Impact Engng*, **16**(1), 19-48 (1995).
2. J. D. Walker and Charles E. Anderson, Jr., "An Analytic Penetration Model for A Drucker-Prager Yield Surface with Cutoff," *Shock Compression of Condensed Matter-1997* Ed. S.C. Schmidt, D. P. Dandekar, and J. W. Forbes, pp. 897-900 (1997).
3. J. D. Walker and C. E. Anderson, Jr., "An Analytic Model for Ceramic-Faced Light Armors," *Proc. 16th International Symposium on Ballistics*, Vol. 3, pp. 289-298, San Francisco, CA (1996).
4. D. L. Orphal, C. E. Anderson, Jr., R. R. Franzen, J. D. Walker, P. N. Schneidewind, and M. E. Majerus, "Impact and Penetration by L/D ≤ 1 Projectiles," *Int. J. Impact Engng*, **14**, 551-560 (1993).
5. R. R. Franzen, J. D. Walker, D. L. Orphal, and C. E. Anderson, Jr., "An Upper Limit for the Penetration Performance of Segmented Rods with Segment-L/D ≤ 1," *Int. J. Impact Engng*, **15**(5), 661-668 (1994).
6. J. M. McGlaun, S. L. Thompson, M. G. Elrick, "CTH: A Three-Dimensional Shock Wave Physics Code," *Int. J. Impact Engng*, **10**, 351-360 (1990).
7. G. R. Johnson, "Material Characterization for Warhead Computations," in *Tactical Missile Warheads*, Ed. Joseph Carleone, AIAA Press, Washington, D.C. (1993).
8. T. W. Bjerke, J. A. Zukas, and K. D. Kimsey, "Penetration Performance of Tungsten Alloy Penetrators with L/D Ratios of 1 to 1/32," Ballistics Research Laboratory Technical Report BRL-TR-3246, Aberdeen Proving Ground, Maryland (June 1991).

PERGAMON International Journal of Impact Engineering 23 (1999) 967–980

INTERNATIONAL JOURNAL OF IMPACT ENGINEERING

www.elsevier.com/locate/ijimpeng

TRANSVERSE LOADING AND RESPONSE OF LONG ROD PENETRATORS DURING HIGH VELOCITY PLATE PERFORATION

JEROME D. YATTEAU, GUNNAR W. RECHT, and KARL T. EDQUIST

Applied Research Associates, Inc., 5491 S. Middlefield Road, Suite 100, Littleton, Colorado 80123, USA

Summary—This paper describes the development of mechanically coupled engineering models to predict transverse loading and response of long rod penetrators associated with high velocity perforation of thin to moderately thick plates. Test results for L/D = 20 tungsten alloy rods are presented to illustrate the distinct effects of impact yaw and obliquity on terminal ballistic transverse loading and response of rod penetrators. The yaw effects loading model considers the plate cutting contact force that travels down the side of the rod when yaw is sufficient for contact with the edge of the breaching hole. The obliquity effects model addresses transverse loading due to asymmetric pressure relief as the rod approaches the rear surface and exits the plate. In both cases, the loading is presumed to be impulsive and three-dimensional vector relationships are used to account for the complex encounter geometries associated with arbitrary combinations of impact yaw and obliquity. The response model includes predictions of rod deformation and fracture and post-perforation linear and angular velocity vectors of the residual rod. Model predictions are compared with test results for titanium and tungsten alloy rods. © 1999 Elsevier Science Ltd. All rights reserved.

INTRODUCTION

Long rod penetrators are being considered for use in anti-air missile warheads. The targets and encounter conditions of interest require that the rods perforate multiple spaced target elements with impact obliquities up to 85° and at speeds up to 4 km/sec. The rods will normally be yawed to some extent upon impact depending on deployment orientation and the direction of the relative impact velocity vector. Combinations of impact yaw and obliquity result in penetration force components normal to the rod axis which can produce trajectory deflections, post-impact rod tumbling, and rod deformation and fracture. Axial loading penetration models are well developed and provide accurate mass and velocity loss predictions for unyawed rods and normal impact obliquities. However, penetration predictions for spaced target elements that do not also account for transverse loading effects will generally produce overly optimistic predictions of rod lethality. This paper describes the development of new engineering models to quantify transverse loading and response of rod penetrators for application to spaced plate penetration problems involving any combination of impact obliquity and impact yaw. The new models have been installed in the FATEPEN penetration computer code as part of an effort to extend its applications to long rod penetrators (Yatteau, *et al.* [1]). The current work extends an earlier modeling effort to predict post-impact tumbling behavior for long titanium rods perforating aluminum plates (Zernow [2], and Yatteau [3]).

0734-743X/99/$ - see front matter © 1999 Elsevier Science Ltd. All rights reserved.
PII: S0734-743X(99)00139-6

TERMINAL BALLISTIC TRANSVERSE LOADING AND RESPONSE CHARACTERISTICS FOR LONG ROD PENETRATORS

Impact Yaw Effects

Figure 1 contains multiple exposure radiographs illustrating the effects of increasing impact yaw on terminal ballistic response for tungsten alloy rods perforating steel plates at normal impact obliquity. The yaw angle entries below each set of images in Fig. 1 provide the measured yaw angle projections in the elevation and plan view orthogonal x-rays for each test (only one view is shown for each test). A positive elevation yaw angle corresponds to the nose down orientation and a positive plan view yaw angle corresponds to the nose up. Photographs of the target plate perforations for each test, as viewed normal to the impact face, are included in Fig. 1 to the right of the radiographs. The diameter, D_T, of the round breaching hole in the plates is indicated below the plate images. The darker rod images overlaying the radiographs in Fig. 1 correspond to FATEPEN model predictions for the measured impact conditions and are discussed below after presentation of the transverse loading and response models.

The rods in Fig. 1 punched circular holes in the plates 2.4 times larger than the rod diameter and lost 11% of their length at the nose to axial erosion and extrusion-shear mass loss mechanisms. The rod in the top set of images impacted with a total yaw of only 1.8° which was just sufficient for the tail of the rod to graze the edge of the 10.5 mm hole during passage through the plate (the computed initial contact force location and direction on the rods are indicated by the normal contact force vector, Fc, on the predicted rod images). The tail contact is evident by the slight indent in the edge of the hole in the plate at the 10 o'clock position. There is no noticeable trajectory deflection and only a small post-impact tumble rate is apparent in the post-impact radiographs. The rod in the middle set of radiographs in Fig. 1 impacted with a larger total yaw angle of 3.9° which, together with the measured hole size, indicates that the side of the rod first contacted the edge of the hole at about mid-length. The portion of the rod aft of this point then cut a slot in the steel plate as it passed through the plate. The slot length indicates that rod orientation did not change significantly during passage through the plate. The post-impact trajectory deflection, tumble direction, and rod deformation are all consistent with the slot cutting force tracking along the rear half of the rod, normal to the rod axis, in the yaw plane and directed along the length of the slot toward the axis of the rod. The test in the lower radiographs in Fig. 1 involved an impact yaw of 6° which causes an earlier first contact with the edge of the hole as indicated. The slot length in the target is correspondingly longer and the trajectory deflection, post-impact tumble rate, and rod deformation are all more severe as a result of the larger cutting force component normal to the rod axis.

In general, for normal impact obliquity, the impacting end of a rod penetrator will produce an enlarged circular hole in the plate. The degree of hole enlargement over the diameter of the rod is a critical factor affecting transverse loading and depends on the plate material and increases with increasing plate thickness and impact speed (Yatteau [4]). Depending on the amount of hole enlargement, the rod L/D, and the impact yaw, the side of the rod may contact the edge of the hole at a point behind the nose during passage through the plate. When this "delayed contact" occurs, the rod will cut a slot in the plate and the cutting force will track down the remaining length of the rod giving rise to a trajectory deflection, post-impact tumbling, and possibly deformation and fracture of the rod.

Impact Obliquity Effects

The photographs in Fig. 2 illustrate rod response and plate damage for nearly unyawed tungsten alloy rods perforating steel plates at increasing impact obliquity. At the 45° impact obliquity, the rod lost approximately 20% of its length to axial loading erosion and extrusion-

shear mechanisms and the transverse loading produced a noticeable bend in the rod. There is very little post-impact tumbling of the rod in the elevation view radiograph. At the 75° impact obliquity, the rod lost approximately 40% of its length and was bent more severely by the transverse loads. In both sets of radiographs, rod deformation appears to continue between the two images behind the targets. Part (but not all) of the apparent deformation for the 75° impact obliquity is due to a slight post-impact rotation (roll) of the curved rod about the shotline. Also in this case, the rod appears to have pitched in the counter-clockwise direction contrary to expectations. The unexpected rotation direction is most likely a reaction to contact between the rear of the rod and the edge of the hole due to rotation in the plate.

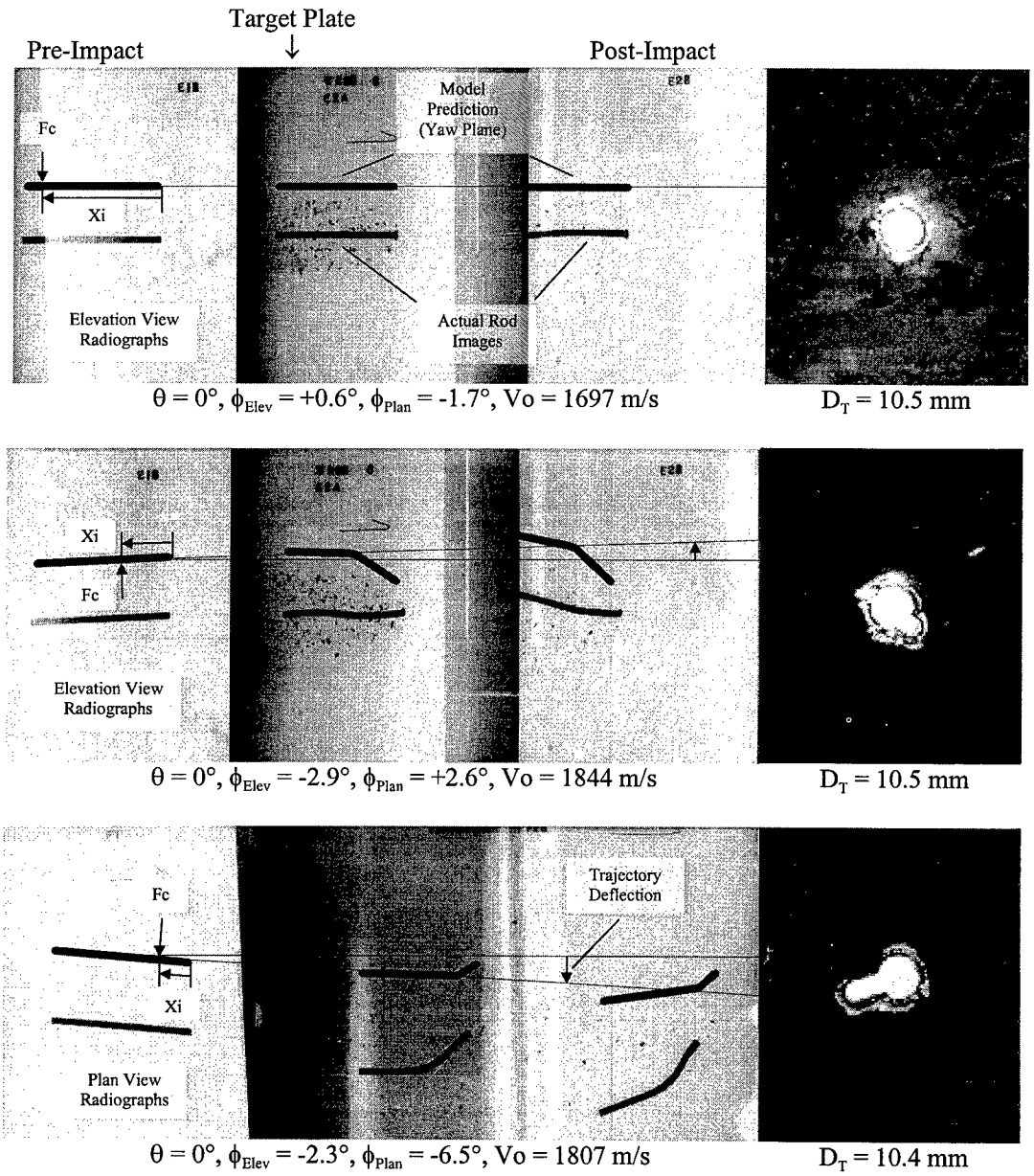

Fig. 1. Effects of increasing impact yaw on rod deformation, trajectory deflection, and post-impact tumble rate. Tungsten alloy rods (R_c30, D = 4.75 mm, L/D = 20) vs. 1018 CR steel plates (BHN 90 - 110, T/D = 2) normal impacts.

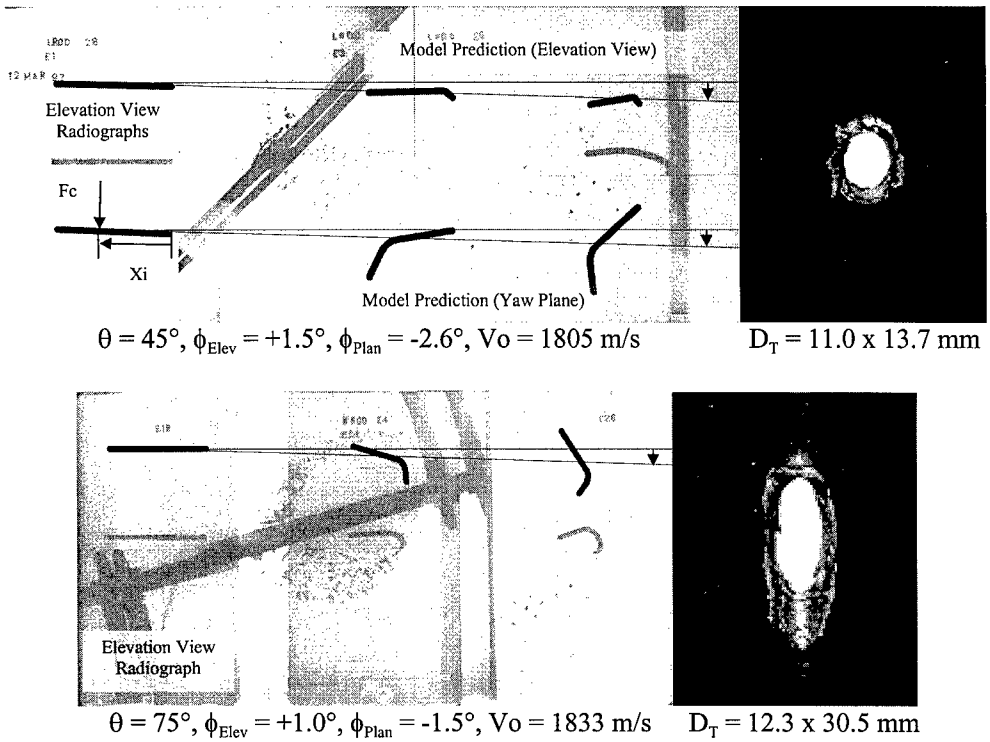

Fig. 2. Effects of increasing impact obliquity on rod deformation, trajectory deflection, and post-impact tumble rate. Tungsten alloy rods (R_c30, D = 4.75 mm, L/D = 20) vs. 1018 CR steel plates (BHN 90 - 110, T/D = 2).

Figure 3 contains rod and plate penetration pressure contours for an L/D = 10 tungsten alloy rod perforating a T/D = 2 steel plate at 45° impact obliquity. The CTH code predictions confirm that pressure relief from the rear surface of oblique plates produces an asymmetric pressure distribution and transverse force component on the nose of the residual penetrator as it emerges from the rear surface. The impulse of the resultant transverse force component is the source of post-impact trajectory deflections, tumbling, and deformations observed in unyawed penetrators during oblique plate perforation. Finally, the obliquity plane cross section of the hole in Fig. 3 reveals an offset between the centerline of the rod and the center of the hole when projected onto the plane normal to the velocity vector (projection plane). The direction of the offset is given by the projection of entry side, outward, plate normal on the projection plane. The hole offset for oblique impacts introduces a dependence of the delayed contact location for yawed rod impacts on the location of the yaw plane relative to the obliquity plane.

Comparisons of the trajectory deflections for normal and oblique impacts reveals that the transverse impulse on the rod due to the yaw effect slot cutting, when it occurs, generally dominates the obliquity effect with regard to trajectory deflection and post-impact tumbling. However, as will be seen in what follows, the obliquity effect becomes significant at speeds near the ballistic limit velocity.

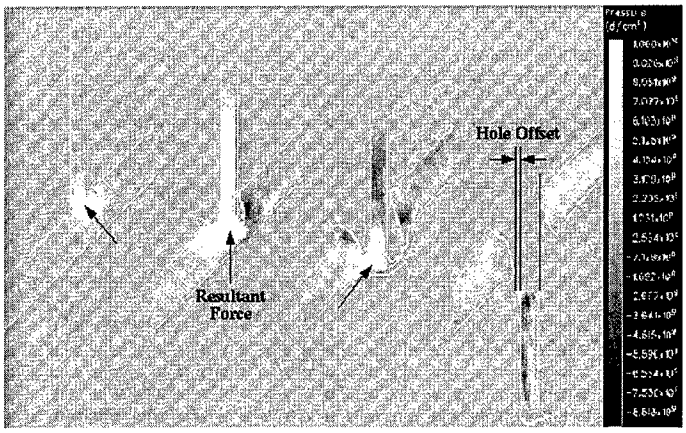

Fig. 3. Three-dimensional CTH simulation results illustrating effects of impact obliquity on penetration pressure distribution and offset between hole center and rod axis. Tungsten alloy rod (R_c30, L/D = 10) vs. mild steel plate (θ=45°, T/D = 2), V = 1524 m/s.

TRANSVERSE LOADING MODEL

The transverse loading and response models are based on the linear and angular impulse - momentum principles with empirical elements introduced to account for unknown material response characteristics. An underlying assumption in the model development is that the loading is impulsive. That is, the passage of the rod through the plate is recognized in the loading geometry but the orientation of the rod is presumed not to change during the penetration.

Impact Yaw Effects

The sketch in Fig. 4 illustrates the delayed contact loading model for a yawed rod penetrator perforating a thin plate. The nose of the rod breaches the plate creating a hole with diameter, D_t, which is larger than the diameter, D_c, of the rod. In the process, the rod length has been reduced from L to L_r and the velocity and angular momentum vectors have been changed from $\bar{V}$ to $\bar{V}_r$ and $\bar{L}$ to $\bar{L}_r$. The pre-impact yaw angle, ϕ, causes the side of the rod to initially contact the edge of the hole a distance X_i from the nose of the residual rod. As the rod continues through the plate, the rear of rod cuts a slot in the plate, and the cutting force, $\bar{F}_c$, tracks down the side of the rod.

The principal elements of the yaw effects loading model include the diameter, D_t, of the breaching hole, the magnitude and direction of the cutting force, $\bar{F}_c$, the initial delayed contact location, X_i, the cutting force tracking speed, $\dot{X}$, down the side of the rod, and the cutting speed, C_s, in the plate. The hole diameter, D_t, is provided by the existing FATEPEN hole size model as a function of target material and thickness and the impact velocity (Yatteau [4]). The cutting force vector is computed to be the product of a modified hydrodynamic flow pressure and the bearing area, A_c, between the rod and target plate.

$$\bar{F}c = \left[\sigma_{ct} + \tfrac{1}{2}\rho_t C_d (V \sin\phi)^2\right] A_c \bar{e}_f \tag{1}$$

where σ_{ct} is the effective target material flow stress for slot cutting, ρ_t is the target density, C_d, is the drag coefficient for flow about the side of a cylinder (C_d = 0.5), and V is the rod velocity.

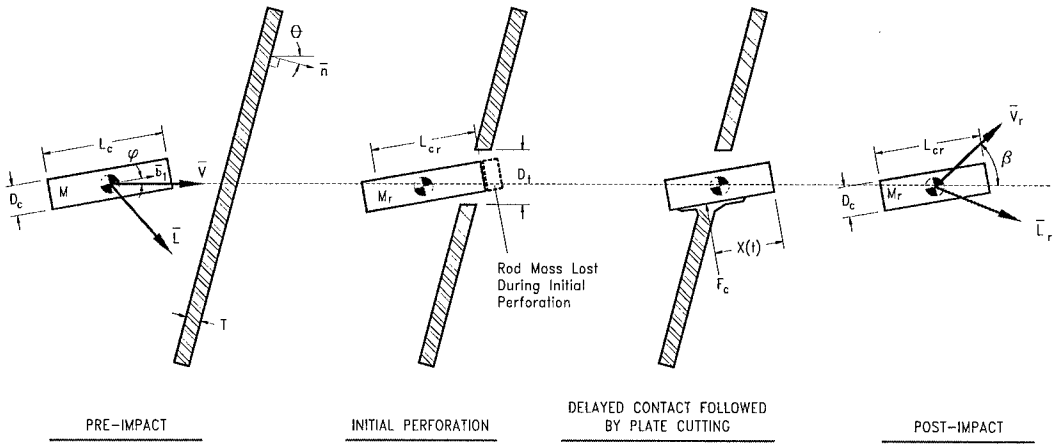

Fig. 4. Transverse loading due to impact yaw (delayed contact).

Friction forces between the rod and plate are neglected in computing the dynamic pressure in Eqn. (1) and thus only the normal component of the relative flow velocity is used.

The cutting force bearing area, A_c, is given by

$$A_c = T_c D \tag{2}$$

where T_c is the width of the plate in contact with the rod

$$T_c = \frac{T}{\bar{b}_l \bullet \bar{n}} \tag{3}$$

where (•) denotes the scalar product, and T is the normal plate thickness.

The effective flow stress, σ_{ct}, is assigned a value between the dynamic yield strength for uniaxial stress, σ_{yt}, and the modified hydrodynamic penetration theory flow stress for confined penetration of semi-infinite plates, R_t. The assignment is determined by interpolation between σ_{yt} and R_t based on T_c/D. The cutting force acts in the yaw plane normal to the rod axis. The unit vector defining the direction of the cutting force on the rod is given by the vector products

$$\bar{e}_f = (\bar{e}_v \text{ x } \bar{b}_l) \text{ x } \bar{b}_l \tag{4}$$

where (x) denotes the vector product, $\bar{e}_v$ is a unit vector along the velocity vector and $\bar{b}_l$ is the unit vector along the rod axis.

Details of the rod/plate encounter geometry are illustrated in Fig. 5 for a yawed rod penetrating an oblique plate with arbitrary orientations for the yaw and obliquity planes. The location of the initial contact point on the side of the rod, X_i, for any impact yaw and obliquity, can be reduced to

$$S_c = \left[\sqrt{\left(\frac{D_t}{2}\right)^2 - (S_h \text{Sin}\alpha)^2} + S_h \text{Cos}\alpha - \left(\frac{D}{2}\right)\text{Cos}\alpha \right] \tag{5}$$

$$X_i = \frac{S_c}{\text{Sin}\phi} \tag{6}$$

where α is the angle between the intersections of the yaw and obliquity planes with the projection plane (Fig. 5) and S_h is the hole offset due to the impact obliquity (Fig. 3) given by

$$S_h = \frac{(D_t - D)}{2} \mathrm{Sin}\theta \tag{7}$$

which provides the maximum offset at the theoretical obliquity of 90° and no offset at normal impact obliquity. The cutting force tracking speed down the rod is

$$\dot{X} = V \frac{\mathrm{Sin}(\phi + \delta)}{\mathrm{Sin}\delta} \tag{8}$$

and the speed of cutting in the plate is

$$C_s = V \frac{\mathrm{Sin}\phi}{\mathrm{Sin}\delta} \tag{9}$$

where δ is the acute angle in the yaw plane between the rod axis and the plane of the plate.

As the rod approaches parallelism with the plate (δ approaches zero), the cutting speed increases without bound. When the cutting speed in the plate exceeds the hole growth rate there can be no delay in contact with the plate. In the absence of a hole expansion rate formula, it is assumed that a lower bound for the hole growth rate is provided by the target material plastic wave speed for uniaxial stress, U_{PT}, and an upper bound is provided by the target Hugoniot wave speed, U_{HT}. A cosine function interpolation formula, with C_s/U_{HT} as the independent variable, is used to reduce the initial delayed contact location, X_i, to zero as C_s increases between U_{PT} and U_{HT}. Thus, when $C_s \geq U_{HT}$, X_i is zero which corresponds to continuous contact between the rod and plate. If $Cs \leq U_{PT}$ the delayed contact location is given by the maximum value from Eqn. (6).

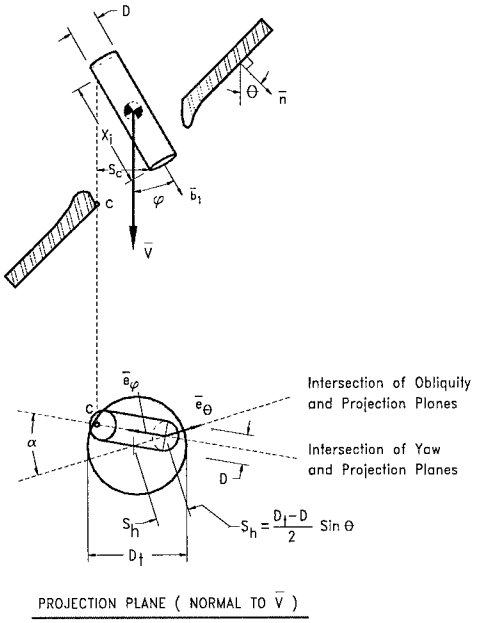

Fig. 5. Delayed contact rod/plate encounter geometry.

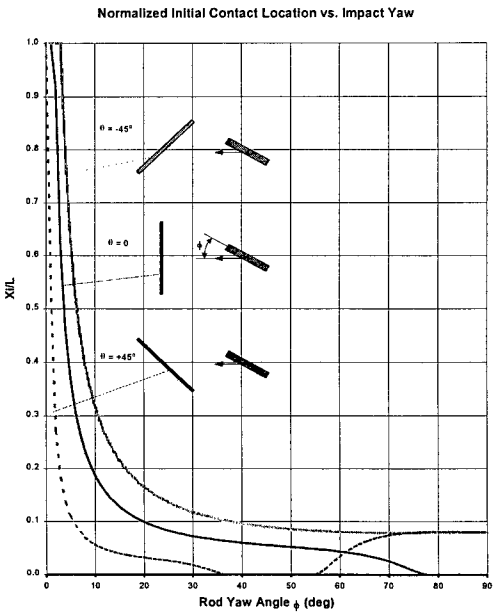

Fig. 6. Normalized initial contact distance vs. impact yaw , L/D = 16 titanium rods vs. aluminum plates, T/D = 1.16, V = 1525 m/s, D_T/D = 1.84.

Typical variations in X_i (normalized by the rod length, L) with impact yaw and obliquity are plotted in Fig. 6. In this example, the yaw and obliquity planes are coincident. In all three cases the rod nose is pitched up relative to the velocity vector. The three curves reveal how quickly the initial contact point shifts towards the nose (and continuous contact) with increasing yaw and also illustrate the effects of the impact obliquity hole offset and cutting speed on the variation in X_i. For the normal obliquity, the rod approaches parallelism with the plate as the yaw angle nears 90° and X_i falls to zero (continuous contact) at a yaw angle near 75° due to the cutting speed effect. For the negative obliquity angle (top of plate tilted up-range), the rod contacts the near edge of the offset hole at nearly zero yaw. Also in this case the rod approaches parallelism with the plate surface when the yaw angle approaches 45° and the cutting speed effect reduces X_i to zero for yaw angles between 35° and 55°. Finally, for the +45° obliquity, the side of rod contacts the far edge of the offset hole at a larger yaw angle near 3° and the rod does not approach parallelism with the plate in the 90° yaw range in Fig. 6.

Impact Obliquity Effects

Transverse penetration force components associated with impact obliquity arise from the shift in the penetration pressure resultant from alignment along the rod axis toward alignment with the rear face of the plate as illustrated in Fig. 3. In the current development, we have not attempted to explicitly model the obliquity effect transverse loading from the complex and time-dependent local flow fields in the penetrator and target as the rod approaches the rear surface. Instead, we have adapted a previously developed correlation for obliquity effects trajectory deflection in terms of the impact velocity normalized by the ballistic limit velocity as shown in Fig. 7 (Recht [5]). Figure 7 contains trajectory deflection angle data for compact steel cylinders (L/D = 1) perforating relatively thin (T/D = 0.25-0.29) mild steel and aluminum plates. Because of their short length and most likely small or zero impact yaw angles (the cylinders were probably spin-stabilized fragment simulating projectiles) the trajectory deflection data in Fig. 7 are presumed to be uncomplicated by any delayed contact yaw effects loading. The correlation for the obliquity effect trajectory deflection angle, β_θ, in terms of V/V_{50} derives from application of the impulse-momentum principle to the ideal plate-plugging geometry sketched in Fig. 7 together with the assumption that the penetration forces on the cylinder due to plate strength effects are rate independent. The formula for β_θ in Fig. 7 has been found to provide reasonably good predictions for unyawed rod penetrator trajectory deflections and is utilized in FATEPEN to estimate the obliquity effect transverse loading contribution to the overall rod linear and angular momentum changes and rod deformation as described below. Note that when the penetrator impacts at just above the ballistic limit velocity (X=1), $\beta_\theta = \theta$ corresponding the largest obliquity effect transverse loading impulse.

RESPONSE MODEL

Trajectory Deflection

In determining the overall trajectory deflection angle, β, it is assumed the obliquity effects loading on the nose of the rod occurs prior to the delayed contact loading due to yaw. The vector change in rod velocity due to the obliquity effect is given by

$$\overline{\Delta V}_\theta = V_{r(\phi=0)}\bar{e}_{vr'} - V\bar{e}_v \tag{10}$$

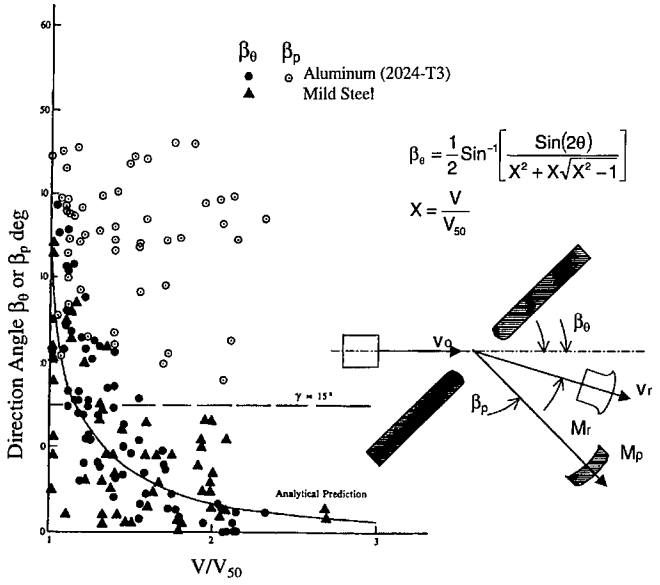

Fig. 7. Obliquity effect penetrator and plate plug trajectory deflections for compact steel cylinders perforating steel and aluminum plates. Impact obliquity = 45° (Ref. [5]).

where $V_{r(\phi=0)}$ is the magnitude of the residual velocity for the unyawed rod as computed using the axial loading models resident in FATEPEN, V is the impact velocity, $\bar{e}_{vr'}$, is a unit vector along the deflected trajectory after the obliquity effect loading , and $\bar{e}_v$ is the unit vector along the impact velocity vector. The $\bar{e}_{vr'}$, unit vector is presumed to lie in the obliquity plane ($\bar{e}_v$- $\bar{n}$ plane) rotated by the angle, β_θ (Fig. 7), from $\bar{e}_v$ toward the plate normal.

The trajectory deflection, β_ϕ, due to yaw effects defines the deflection of the residual velocity vector from $\bar{e}_{vr'}$ to its final orientation along $\bar{e}_{vr}$. The change in velocity due to the slot cutting force, $\bar{F}_c$, tracking down the side of the rod is determined by

$$X_{ir} = X_i - (L - L_r) \tag{11}$$

$$\overline{\Delta V_\phi} = \left(\frac{L_r - X_{ir}}{\dot{X}_r}\right)\frac{\bar{F}c}{Mr} \tag{12}$$

where X_{ir} is the position of the initial contact on the side of the residual rod of length L_r as determined by the axial loading residual mass model, $\dot{X}r = \dot{X}\cdot(V_{r(\phi=0)}/V)$ is the adjusted force tracking speed, and M_r is the rod residual mass. The force, $\bar{F}_c$ (Eqs. 1-4) is also computed after accounting for the obliquity effect on the rod velocity. The change in velocity, ΔV_ϕ, is limited to the component of the initial impact velocity normal to the rod axis to reflect that the cutting force drops to zero when the rod lifts off the bottom of the slot. The residual velocity vector after combined obliquity and yaw effects loading and the overall trajectory deflection, β (and β_ϕ), are obtained by simple vector addition of $\bar{V}$, $\bar{\Delta V}_\theta$ and $\bar{\Delta V}_{\phi'}$.

Post-Impact Tumbling

FATEPEN computes changes in penetrator orientation between impacts from the penetrator residual angular momentum vector , $\bar{L}_r$. The change in angular momentum due to the yaw effect is given by the angular impulse of the cutting force on the residual rod (see Fig. 4)

$$\overline{\Delta L}_\phi = \int_{x_i}^{L_r} \left[\frac{L_r}{2} - x(t) \right] \bar{b}_1 x \bar{F}_c \frac{dx}{\dot{x}} \tag{13}$$

which, after integration reduces to

$$\overline{\Delta L}_\phi = \left(\frac{-x_{ir}}{2} \right) \bar{b}_1 x M_r \overline{\Delta V}_\phi \tag{14}$$

The change in rod angular momentum due to the impact obliquity effect is computed by assuming the effective moment arm of the transverse force component in this case is confined to the deformed nose and specifically the mid-point of the leading caliber of the residual rod length. The corresponding moment of the change in linear momentum can be written

$$\overline{\Delta L}_\theta = \left(\frac{L_r - D}{2} \right) \bar{b}_1 x M_r \left[\overline{\Delta V}_\theta - (\overline{\Delta V}_\theta \bullet \bar{e}_v) \bar{e}_v \right] \tag{15}$$

where the term in brackets reflects the assumption that the component of ΔV_θ (for an unyawed rod, Eqn. (10)) in the direction of the impact velocity vector does not contribute a net angular impulse to the rod (i.e, the associated forces act along the axis of the rod and any associated mass loss is expelled symmetrically about the axis of the rod). The residual angular momentum and angular velocity after the combined yaw and obliquity are obtained from the vector addition of $\bar{L}$, $\overline{\Delta L}_\phi$, and $\overline{\Delta L}_\theta$.

Rod Deformation and Fracture

Rod deformations and fracture are estimated using a modified version of the plastic shear wave propagation model developed by Recht [6] to estimate deflection profiles in plates impacted by cylinders at speeds below the ballistic limit velocity. Adaptation of Recht's model to rod deformation due the impact obliquity effect is illustrated by deforming rod sketches in Fig. 8. The nose mass, M_n , is presumed to be impulsively loaded by the obliquity effect force and achieves an initial velocity, V_n, normal to the axis of the rod given by

$$V_n = \frac{M_r}{M_n} \Delta V_\theta \tag{16}$$

The relative motion of the nose is accommodated by rod deformations associated with the propagation of a plastic transverse or shear deformation wave moving at speed U_τ relative to the undeformed rod. Displacements due to elastic waves (tensile and shear) moving ahead of the plastic wave are neglected. The plastic wave speed, U_τ, is presumed to be constant which is consistent with an assumed bilinear, elastic-plastic, true stress- true strain curve for the rod material. The rod material ahead of the plastic wave is acted upon by a shear stress equal to the dynamic shear strength (bending moment effects are currently neglected in the model). Conservation of momentum dictates that the velocity of the deformed material behind the plastic shear wave decreases. As a result, the shear strain just behind the wave also decreases continuously and the rod material deforms only once on passage of the shear wave. Thus at any given time, all the deformed material and the nose mass have the same velocity V. The impulse-momentum principle applied to the deforming rod provides

$$M_n V_n = (M + M_n)\ V + \int_o^t \frac{\pi D^2}{4} \tau_y dt \tag{17}$$

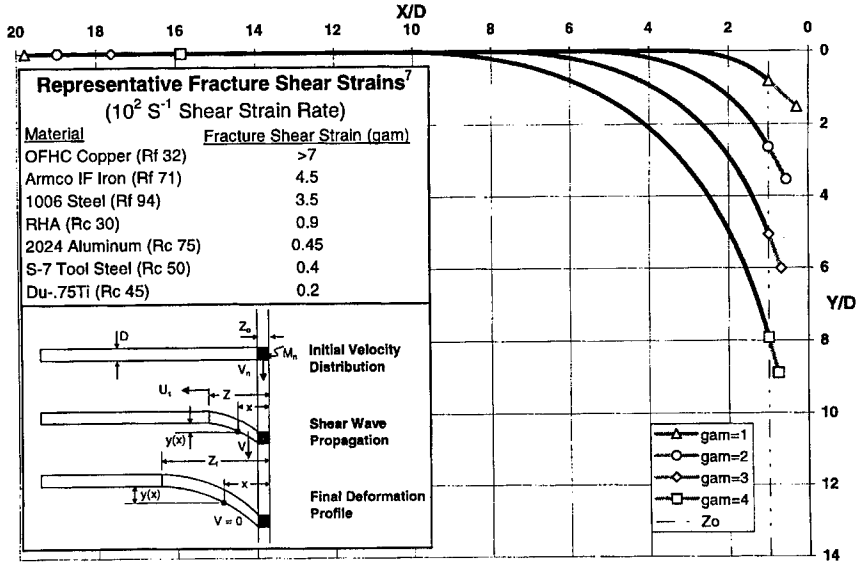

Fig. 8. Shear deformation profiles for L/D = 20 rods corresponding to assumed initial shear strains of 1 - 4.

where we have neglected accelerations in the undeformed portion of the rod due to elastic shear wave reflections between the tail of the rod and the plastic shear wave front, and where M is the mass of the deformed rod between the wave front and the nose mass given by

$$Z=U_\tau t, \quad M=\frac{\pi D^3}{4}\rho\left(\frac{Z}{D}-\frac{Z_o}{D}\right) \tag{18}$$

A change of variables from t to Z in Eqn. (17) followed by double integration leads to the deformation profile of the rod as a function of the wave position, Z. Plastic deformation ceases when the velocity, V, of the deforming material falls to zero. The final deformed profile of the rod is given by

$$j=\frac{M_n}{\frac{1}{4}\rho\pi D^3}, \gamma_\theta=\frac{V_n}{U_\tau}, k=\frac{\tau_y}{\rho U_\tau^2}, i=\frac{\gamma_\theta}{k}, x'=\frac{x-Zo}{D}, \frac{Z_f}{D}=\frac{Z_o}{D}+ij \tag{19}$$

$$\frac{y(x')}{D}=k\left\{j(1+i)\ln\left[\frac{j(1+i)}{j+x'}\right]-ij+x'\right\} \tag{20}$$

where j is the ratio of the nose mass to the mass of one caliber of rod length, γ_θ is the initial (maximum) shear strain adjacent to the nose, Z_f is the deformed length of the rod, x′ is the normalized position of a point on the rod relative to the nose, and y (x′) is the corresponding vertical shear deformation.

Figure 8 includes plastic deformation profiles for L/D = 20 tungsten alloy rods corresponding to a normalized deformed nose mass, j = 1.56, and initial shear strains, γ_θ, of 1 through 4. In plotting the profiles, it is assumed that the one caliber rigid nose piece assumes the slope, γ_θ, of the deformed rod adjacent to the nose and the tail positions for each strain profile are located to preserve the original length of the rod. Within the assumptions of this model, the maximum shear strain occurs adjacent to the nose at the beginning of the deformation. Fracture should

therefore occur at this location when the initial shear strain, γ_θ (Eqn. (19)), exceeds the dynamic fracture shear strain, γ_f (the value for γ_f may actually reflect a tensile failure in some materials). Figure 8 includes a tabulation of measured dynamic fracture shear strains from Ref [7] for a range of more and less ductile materials corresponding to strain rates on the order of 10^2 Sec^{-1}.

Rod deformations and fracture corresponding to the yaw effects plate cutting force are also estimated using the shear deformation model described above. In this case, the cutting force, Fc, tracks down the rod with speed, $\dot{X}$, imparting a transverse velocity, V_T, to the contacted rod segment between X_{ir} and L_r relative to the non-contacted portion. The velocity, V_T, is computed from the impulse-momentum principle assuming impulsive acceleration is resisted by the dynamic shear strength, τ_y. The applied shear stress, τ_c, the initial relative transverse rod velocity, V_T, and the associated shear strain, γ_ϕ, are given by

$$\tau_c = \frac{Fc}{\frac{\pi D^2}{4}}, \quad V_T = \frac{\tau_c - 2\tau_y}{\rho \dot{x} U_\tau}, \quad \gamma_\phi = \frac{V_T}{U_\tau} \tag{21}$$

Failure occurs at the initial contact location if the initial strain exceeds the failure strain, γ_f. If failure does not occur on initial contact, rod deformation is determined by applying the model sketched in Fig. 8 with the effective nose mass, M_n, defined by the smaller of X_i or L_r-X_i and the initial relative velocity, V_T as determined above.

COMPARISONS WITH TEST RESULTS

Model predictions from Eqs 1-15 are compared with measured post-impact trajectory deflections and tumble rates from Ref. [2] in Fig. 9 for titanium rods perforating aluminum plates at normal impact obliquity. The model predicts the increase in trajectory deflections with increasing yaw fairly well and predicts very little difference in trajectory deflections between the L/D = 16 and L/D = 32 rods which is also consistent with the test results. The higher model predictions for the lowest impact speed (1200 m/s) reflect the sensitivity of the transverse loading model to the rod impact speed. That is, the difference between the two sets of curves reflect the counteracting effects of increased impact speed increasing the magnitude of the cutting force while decreasing the duration of the force and the simple geometric decrease in β associated with increasing residual velocity with the same transverse change in velocity. The model properly predicts the steep rise and fall in post-impact tumble rates for both length rods with small increasing impact yaw angles and the lower tumble rates for the longer rod due to its larger transverse moment of inertia. The drop in tumble rates with increasing yaw is due to the decrease in X_{ir} with increasing yaw(Fig. 6). The cutting force effectively tracks along the entire residual rod length for impact yaws greater than about 40° for the shorter rods and 30° for the longer rods.

The FATEPEN code was also exercised to obtain predicted rod responses for comparison with the images in the radiographs in Figs. 1 and 2 (the actual rods were not recovered on these tests). The effective dynamic shear strength and transverse plastic shear wave speed for the tungsten alloy material were determined from Taylor anvil tests and a new transverse wire impact test technique, respectively. The predicted deformed rod profiles were scaled to match the image sizes in the radiographs. The deformed profiles were then overlaid on the radiographs side-by-side with the radiograph images but with the predicted off-shotline excursions and orientations which permits a direct comparison between predicted and observed rod length loss, deformation, trajectory deflection and tumble rate.

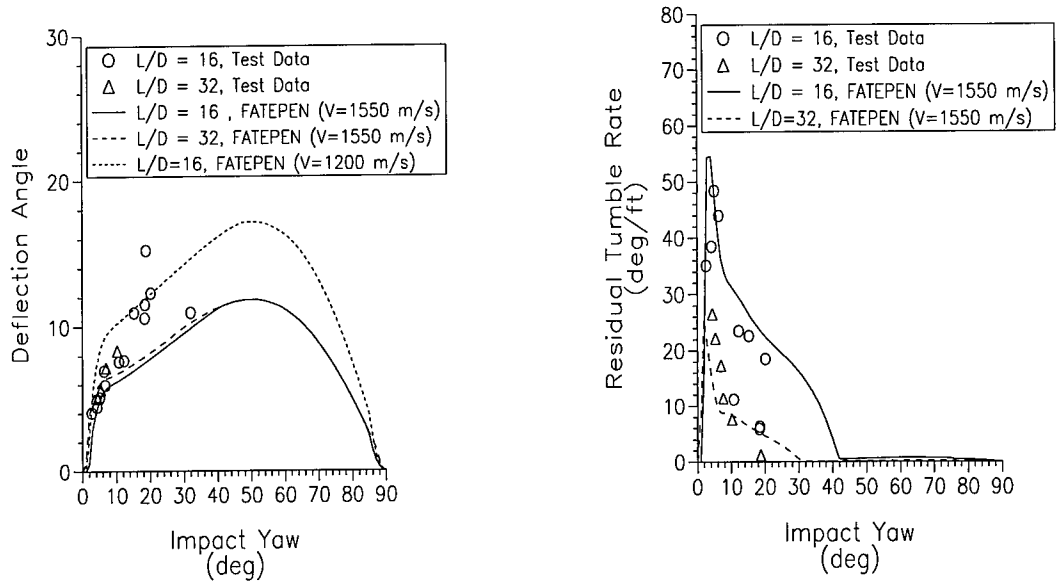

Fig. 9. Post-perforation trajectory deflections and tumble rates for L/D=16 and 32 titanium rods versus 2024-T3 aluminum plates (T/D=1.16), V=1200-1700 m/s, Vavg=1550 m/s, Dt/D=1.84

An overall visual comparison reveals that the model predictions are generally quite realistic The residual rod length and velocity predictions for the normal impacts agreed with the measured values within 2% for residual length and 1% for residual velocity. The effect of increasing yaw on rod deformation, trajectory deflection and tumble rates is also consistent with the radiographs. Note that the predicted images in Fig. 1 correspond to viewing normal to the actual deformation and tumbling plane (i.e., the yaw plane) and thus show slightly more deformation, and rotation then the radiographs which are projections in the vertical or horizontal planes.

The predicted rod images for the 45° impact obliquity correspond to both a predicted obliquity effect (elev. view) and an impact yaw effect delayed contact in the yaw plane. Predicted rod images for the both the obliquity plane and the yaw plane are included and reveal that the tail contact is predicted to cause significant deformation and tumbling in the yaw plane. The predictions could not be confirmed because the post-impact plan view radiographs were not obtained for this test. However, the relatively short predicted elevation view rod image in the second post-impact radiograph indicates the model is over-predicting the yaw plane tumble rate. The model predicts more severe obliquity effect rod deformation and tumbling for the 75° impact obliquity in the lower radiograph of Fig. 2 which is consistent with the radiographs. In this case the tail of the rod is predicted to graze the edge of the hole at a point only 4% from the tail due to the pre-impact yaw. However, this yaw effect is not predicted to cause any deformation and only a 1.5° rotation in the plan view. The actual plan view radiographs confirm no tail deformation but indicate a larger 23° rotation due to the yaw effect. As noted earlier, the apparent counterclockwise rotation in the obliquity plane is attributed to a tail contact due to rod rotation in the plate. The predicted residual length and velocity of the rod in this case agreed with the measurements to within 1% and 3%, respectively.

SUMMARY

New engineering models have been developed to predict rod penetrator transverse loading and response for non-ideal encounter geometries. The models were installed in the FATEPEN penetration code and carefully linked with existing mass and velocity loss models to form a mechanically coupled set of axial and transverse loading and response models for rods penetrating spaced target elements with any combination of impact yaw and obliquity. The combined models predict rod length and velocity losses associated with erosion/extrusion-shear axial loading response mechanisms, and trajectory deflection, post-impact tumbling and rod deformation and fracture due to transverse loading. Comparisons have resulted in good agreement between model predictions and test results for single plate penetration tests involving normal and oblique aluminum and steel plates and titanium and tungsten alloy rods. The improved FATEPEN code should provide more realistic weapons effectiveness assessments resulting in improved rod penetrator warhead designs.

The severity of rod deformation and fracture under a given impulsive transverse loading is determined in large part by the characteristic plastic transverse deformation or shear wave speed, the fracture shear strain, and the dynamic shear strength of the rod material. An improved transverse rod or wire impact test technique was developed as part of the current effort to directly measure these key material parameters from transverse rod deformation profiles versus time recorded by a high speed digital video camera. Planned future work includes additional tests at higher impact speeds to determine critical fracture shear strains and further analyses of the existing deformation profiles to assess the accuracy of the shear wave deformation model presented above

Acknowledgement—The authors acknowledge the important contributions to this paper by Steven R. Ford and David C. Mann of the Denver Research Institute, University of Denver who conducted the tungsten rod penetration tests. The authors also acknowledge their gratitude to Mr. David L. Dickinson and Mr. Thomas L. Wasmund of the Naval Surface Warfare Center (NSWC), Dahlgren Division for their continued support in the development of the FATEPEN penetration model and computer code. The work described herein was funded by NSWC, Dahlgren Division under the technical oversight of Mr. David L. Dickinson.

REFERENCES

1. J.D. Yatteau, G.W. Recht, and K.T. Edquist, FATEPEN Rod Penetration Models- Part II, Applied Research Associates, Inc. for Naval Surface Warfare Center, Dahlgren, Virginia (1998)
2. R.H. Zernow, Penetration methodology assessment for titanium rods. Applied Research Associates, Inc. for Naval Surface Warfare Center, Dahlgren, Virginia (1991).
3. J.D. Yatteau, Preliminary tumbling model for long rod penetrators perforating thin plates. Applied Research Associates, Inc. for Naval Surface Warfare Center, Dahlgren, Virginia (1991).
4. J.D. Yatteau, High velocity multiple plate penetration model. Denver Research Institute, University of Denver, for Naval Surface Weapons Center, Dahlgren, Virginia, NSWC-TR-123 (1982).
5. R.F. Recht, High velocity impact dynamics: analytical modeling and plate penetration dynamics. In *High Velocity Impact Dynamics*, (edited by J.A. Zukas),pp. 452-454, John Wiley and Sons, Inc. (1990).
6. R.F. Recht, Taylor ballistic impact modeling applied to deformation and mass loss determinations. *Int. J. Engng. Sci.*, **16**, 809-827 (1978).
7. G.R. Johnson, J.M. Hoegfeldt, U.S. Lindholm, and A. Nagy, Response of various metals to large torsional strains over a large range of strain rates - part 1: ductile metals, part 2: less ductile metals, *ASME J. Engng Mater. Tech.*,**105**(1), 42-53 (1983).

PERGAMON

International Journal of Impact Engineering 23 (1999) 981–988

INTERNATIONAL JOURNAL OF IMPACT ENGINEERING

www.elsevier.com/locate/ijimpeng

APPLIED RESEARCH OF SHAPED CHARGE TECHNOLOGY

YU CHUAN, TONG YANJIN, YAN CHENGLI, LI FABO, GUI YULIN, ZHANG MING, WANG BINGREN, XIE PANHAI, and LI LIANGZONG

(Laboratory for Shock Wave and Detonation Research ,
Institute of Fluid Physics, CAEP, P.O.Box 523, Chengdu ,610003,CHINA)

Summary—For special requirements of penetrating rock, we have developed a shaped charge jet device, from which a rather uniform and wide jet can be generated. The mass of shaped charge explosive is less than 2.5kg. The profile and velocity of the jet are measured with an X-ray technique. We have simulated the formation and penetration process of the jet with a 2-D HELP code, which provides important reference data in designing the shaped charge. A series of penetration tests into rock at different strengths has been carried out. The penetration tests to the rock with a strength about 600kg/cm^2 show that the average diameter of the hole entrances is 63.5 mm; the average penetration depth of the holes with internal diameters of more than 35 mm is about 1311 mm, the average total penetration depth of the holes is 1531 mm; the coning of the holes are less than 1.4 %. All the results of the tests indicate good penetrating performance.

Additionally, we have designed an explosively formed projectile (EFP) testing device with the explosive of 450g, a liner of 150g and 60mm-diameter. Performance tests and experiments of penetrating multilayer steel plates have been conducted. The EFP penetrates throughout the whole steel target that consists of five layers of 6-mm-thick A3 steel plate spaced in a range of two meters. The diameters of penetrating holes range from 41mm to 46mm. The mass of EFP recovered behind the target is about 98g. © 1999 Elsevier Science Ltd. All rights reserved.

INTRODUCTION

Since World War II, shaped charge technology has been rapidly developed. Generally, the shaped charge has two forms : jet and explosively formed projectile (EFP).

Research in jet technology has been mainly focused on the design of armor penetration warhead for several decades[1,2] As the increasing needs from military engineering and civilian uses, the technology of penetration to non-metal targets (e.g., concrete, rock, etc.) has been widely investigated. For example, jet technology has been used for rapid construction of military protection engineering. Shaped charge warheads have been designed for use against the piers, blockhouses, and strong aboveground fortifications. Additionally, the shaped charge technology has been used to penetrate holes in petroleum prospecting. In 1983, M.J. Murphy, who worked with the Lawrence Livermore National Laboratory (LLNL), investigated jet penetration in concrete[3]

For EFP, applications include semi-armor piercing warheads for anti-ship missiles. Through a design of several liners for the semi-armor piercing warhead, the warhead will explode within the ship to form several EFPs that penetrate multi-separators. This will significantly increase the destroying capability of a warhead. It is now a major trend to apply the EFP technology to warheads of advanced anti-ship missiles. For example, the EFP technology is used in German

0734-743X/99/$ - see front matter © 1999 Elsevier Science Ltd. All rights reserved.
PII: S0734-743X(99)00140-2

Kormoran II anti-ship missile warheads.

JET PENETRATION TO ROCK

The jet must be wider and more uniform to obtain deep penetration depth and a large penetration diameter to meet the requirement of a second explosion within the hole. The slug must be as small as possible to increase the mass of the jet. Additionally, it is essential that the jet have a moderate velocity and velocity gradient so as not to make the jet break out while reaching the target surface.

With an optimum design of the shaped charge and the liner with a curved surface and varying thickness, we have designed the jet devices with two different liners through a numerical simulation with a 2-D HELP code and experimental adjustments. The shaped charge explosive has a density of 1.80g/cm^3 is HMX/TNT (70/30).

Two jet devices was considered. The first one has a liner made up of pure copper. The diameter of the liner is 140mm; the mass of the liner is 1.0kg; the mass of explosive is 2.3kg; and the total mass of this device is about 3.8kg. Figure 1 gives a schematic diagram of the jet device. The second one has a liner made up of aluminum. The diameter of the liner is 141mm, and the mass about 0.62kg; the mass of explosive about 2.5kg; and the total mass of the device is about 3.7kg.

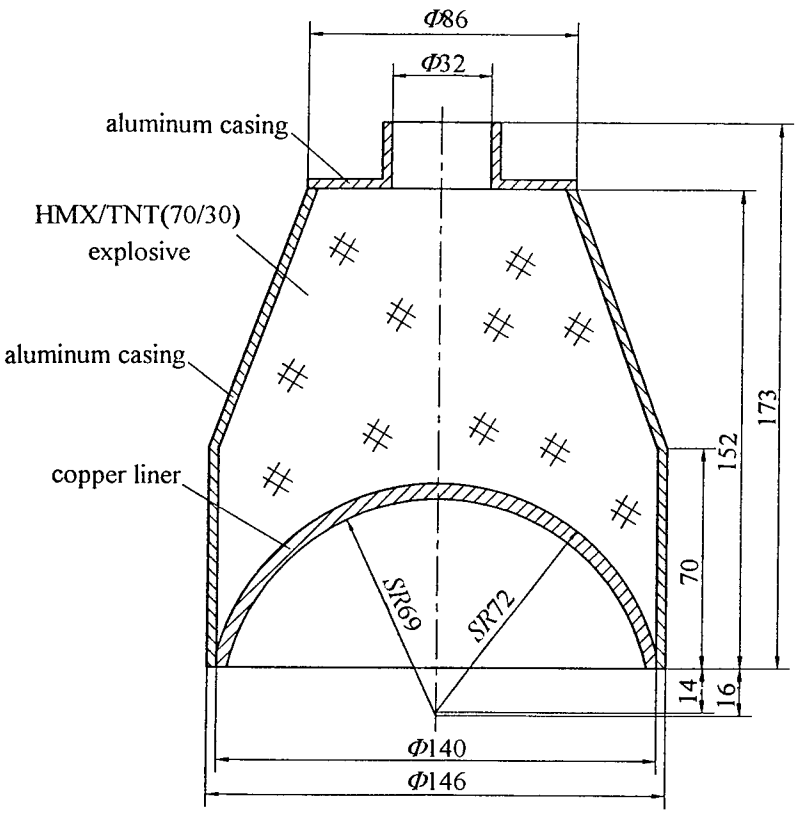

Fig. 1. A schematic diagram of the jet device

Measurement with X-rays

We measured, with X-ray photography, the profile and velocity of the jet generated by the copper liner device (see figure 2).

We can find from Fig.2 that the jet was wide and uniform. Velocity of the head part of the jet is 3.63km/s. At about 261.19μs after the primer detonation, the jet has almost reached the target surface. There is not any fracture except for a small piece in the head part of the jet. The slug is very small. Not considering the slug and the broken piece in the head part of the jet, the length of the jet is 581mm. The diameters of the head and tail parts of the jet are 6.9mm and 21.4mm, respectively.

Rock Penetration Experiments

For the above two jet devices, we have conducted penetration experiments to rocks of different strengths. The industrial primer-8 and a tetryl booster charge (32mm diameter, 11mm length) were used to initiate the charge in these experiments. The experimental setup is shown in Fig.3.

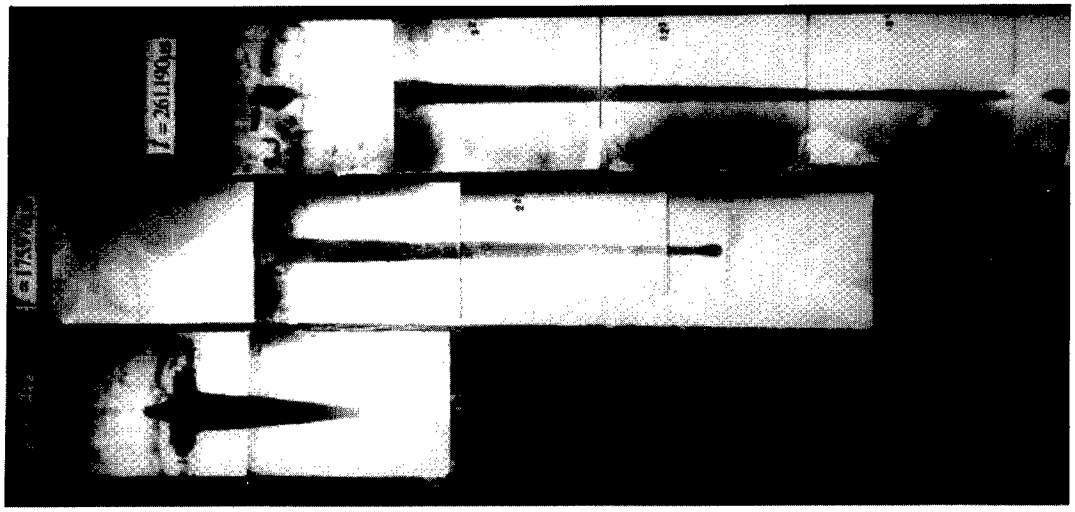

Fig.2. An X-ray photograph of the jet generated by the copper liner device

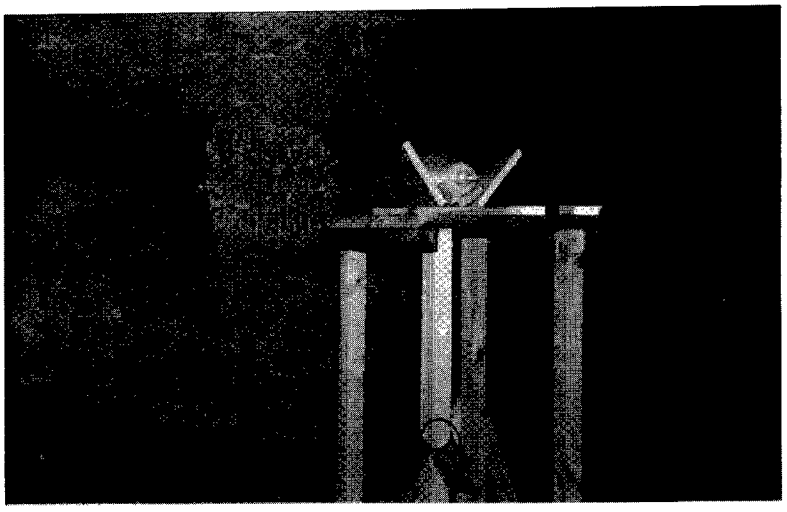

Fig.3. An experimental setup of rock penetration

With copper liner charge, we have carried out eight penetration experiments to three kinds of rocks of different strengths. The typical penetration result is shown in Fig. 4 and a sketch of the pentration channel profile is depicted in Fig.5, from which we can find that there is pit with funnel forms. There is a circular and straight deep hole at the bottom of the pit. The hole is uniform internally with no cracks, dilapidation or blockage.

In order to measure the hole' s coning, we use a cylindrical stick that has diameters (d_2) of 30mm, 35mm, and 40mm respectively to measure the depth (L_2) of diameter larger than d_2 . The hole' s coning can be described as the following,

$$k = \frac{d_3 - d_2}{2(L_2 - L_1)} \tag{1}$$

where, d_3 is the diameter of the hole entrance; L_1 is the total depth of the pit. The test results are listed in Table 1.

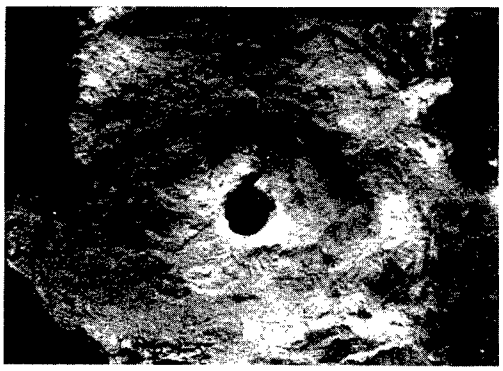

Fig.4. A result of penetration to the rock surface

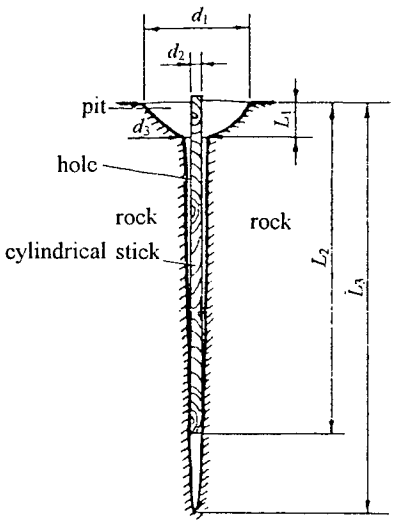

Fig.5. A sketch map of measurement of penetration effects

Table 1. Penetration test results from the copper liner device

No.	σ /(kg/cm^2)	H /mm	D_1 /mm	d_3 /mm	L_1 /mm	L_2 /mm			L_3 /mm	V /cm^3	k /(%)
						d_2=30mm	d_2=35mm	d_2=40mm			
1	1400	1000	300	43	105	530	—	—	605	4782	1.5
2	1400	1100	370	45	145	605	—	—	625	9906	1.6
3	1400	1100	400	40	110	700	—	—	750	8121	0.9
4	1000	1000	260	45	70	515	—	—	1425	2963	1.7
5	600	1080	400	52	135	1510	1230	—	1630	11264	0.8
6	600	1030	420	61	120	1270	1240	—	1275	11227	1.2
7	600	950	250	69	80	1450	1250	—	1540	4835	1.4
8	600	1025	250	72	90	1525	1525	1200	1680	5770	1.3

In Table 1, σ represents the strength of the rock; H is the stand off; d_1 is the diameter of the pit entrance; L_3 is the total penetration depth; and V is the penetration volume.

From Table 1, we can find that, for the three penetration tests to the hard rock with a strength of 1400 kg/cm^2, the average diameter of the hole entrance is 43mm; the average penetration depth for the holes with diameters of more than 30mm is about 612mm; the average penetration depth is 660mm; the average penetration volume is 7603cm^3; and the average coning is about 1.33%. For the hard rock with a strength of 1000 kg/cm^2, these values are respectively 45mm, 515mm, 1425mm, 2963cm^3, and 1.7%.

We have also carried out four tests for the rock with a strength of 600kg/cm^2. Of these tests, the smallest diameter of the hole entrance is 52mm and the average is 63.5mm. The average penetration depth for the hole with diameters of more than 35mm is about 1311mm. The smallest penetration depth is 1275mm, and the average one for the four tests is 1531mm. The average penetration volume of these tests is 8274cm^3. The biggest hole coning of the tests is 1.4%, and the average coning is about 1.2%.

Additionally, for the aluminum liner charge device, we have conducted three penetration tests to the rock with two different strengths. The test results are listed in Table 2.

Table 2. Penetration test results from the aluminum liner device

	σ	H	d_1	d_3	L_1	L_2/mm			L_3	V	k
No.	/(kg/cm^2)	/mm	/mm	/mm	/mm	d_2=30mm	d_2=35mm	d_2=40mm	/mm	/cm^3	/(%)
1	1400	945	900	75	200	430	420	—	430	68310	9.1
2	1400	1200	530	55	140	555	—	—	650	17499	3.0
3	1000	1200	530	68	75	—	1400	875	1500	10999	1.2

From Table 2, for the hard rock with a strength of 1400kg/cm^2, the average diameter of the hole entrance of the two tests is 65mm. The average penetration depth for the holes with diameters of larger than 30mm is about 493mm. The average penetration depth is 540mm; the penetration volume of 42905cm^3; and the hole coning about 6.1%. For the hard rock with strength of 1000kg/cm^2, the diameter of the hole entrance is 68mm. The penetration depths are respectively 1400mm and 875mm for the hole with diameters of larger than 35mm and 40mm. The total penetration depth is 1500mm, the volume of 10999cm^3, and the hole coning about 1.2%.

Numerical Simulation

The jet formation and penetrating process in the rock are numerically simulated with a 2-D Eulerian elastic-plastic hydrodynamic code (HELP). The jets are respectively generated by a pure copper liner charge and an aluminum liner charge[4]. The simulation results of the pure copper liner charge are given in Figure 6 and 7.

From Fig.6, we can find that the results from numerical simulations agree very well with those from X-ray measurements shown in Fig.2. The jet velocity determined from numerical simulation is about 3.87 km/s. At the time of 261μs, the jet length is 866.5mm that is a little more than that from X-ray measurement. The largest penetration depth obtained by numerical simulation is 1560mm; and the average diameter of the hole is about 35mm. Both agree with the experimental results.

EFP PENETRATING A TARGET OF MULTILAYER STEEL PLATES

We have designed a small EFP testing device. TNT/RDX (40/60) explosive with density of 1.70g/cm^3 is used. The mass of the explosive is 450g. The mass of the liner is 150g and its diameter is 60mm. The setup of the testing device is given in Fig.8. The profile and velocity of the EFP are measured by X-rays photography and shown in Fig.9.

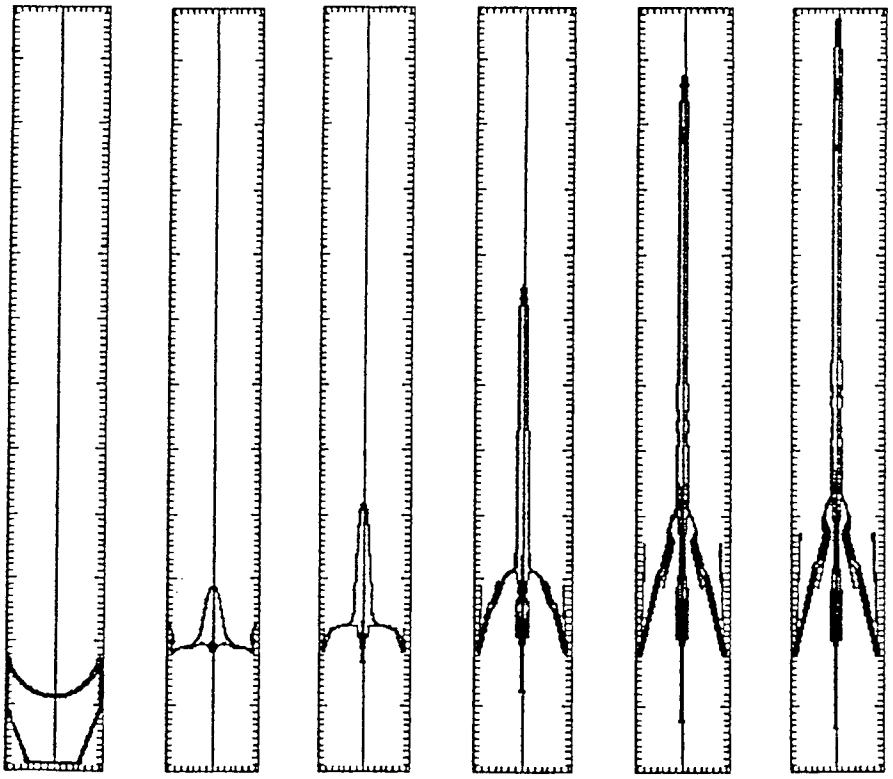

(a) t=0μs; (b) t=60μs; (c) t=91μs; (d) t=175μs; (e) t=261μs; (f) t=281μs

Fig.6. Numerical simulation of the jet formation generated by the pure copper liner charge

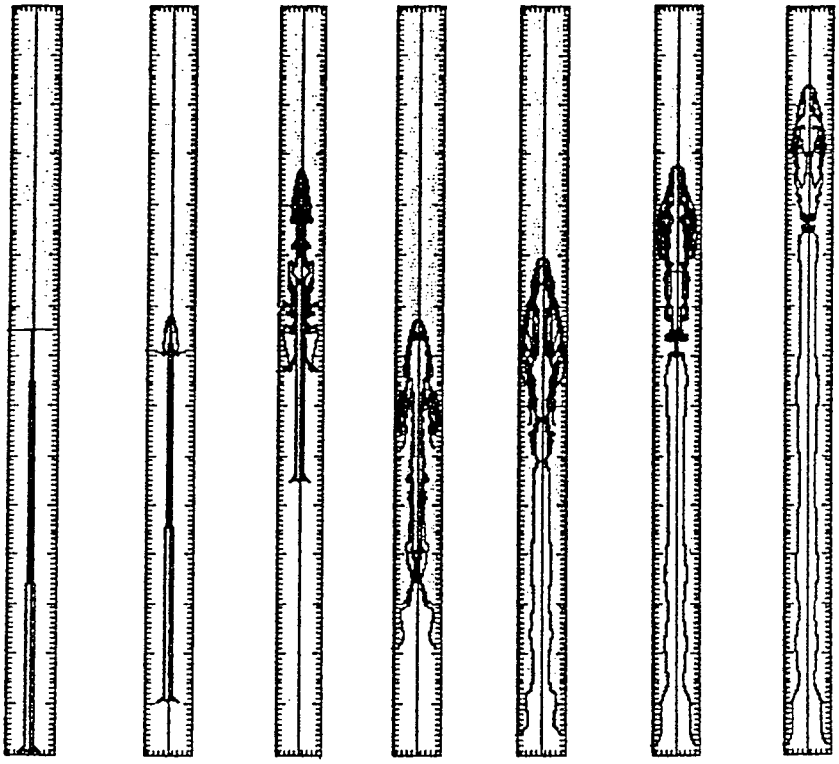

(a) t=0 μs; (b) t=50 μs; (c) t=272 μs; (d) t=472 μs; (e) t=692 μs; (f) t=900 μs; (g) t=1100 μs

Fig.7. Numerical simulation of the jet penetrating process in the rock for pure copper liner charge

We can find from Fig.9 that the EFP has an ideal profile. The ratio of length-to-diameter is 1.32 and the largest diameter is about 32mm. The mass of the EFP is 127g and velocity of 1.52km/s.

Three tests of penetration to a target consisting of multilayer steel plates have been carried out. The plate array consisted of 6-mm-thick A3 steel plate;five plates were used, uniformly spaced over a range of two meters. The EFP testing device is two meters from the first layer of the target. The EFPs penetrate all target elements; the diameters of the penetrating holes range from 41mm to 46mm. A photograph of the hole on the fifth layer of steel plate in the third test is given in Fig.10.

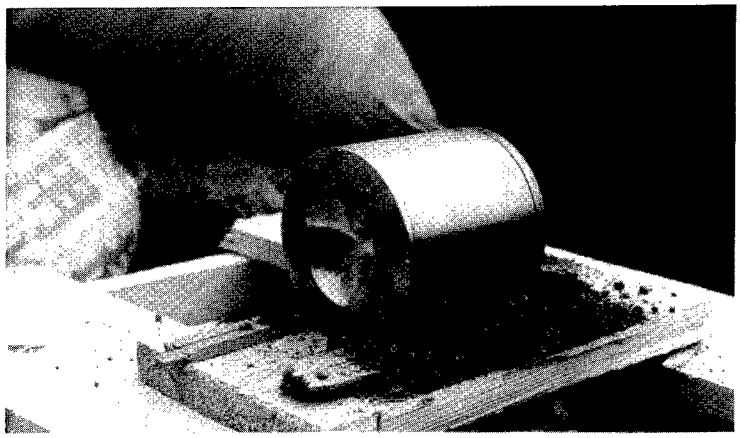

Fig.8. A photograph of EFP testing device

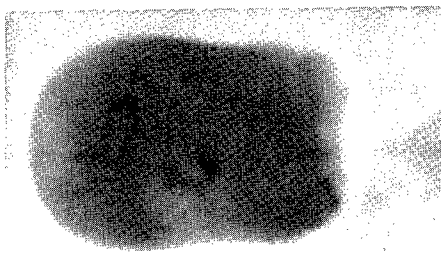

Fig.9. An EFP Profile measured by X-rays

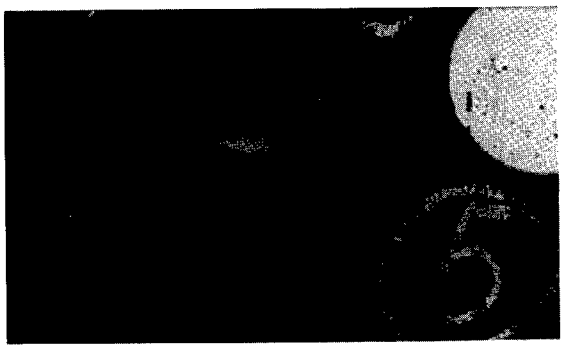

Fig.10. A hole on the fifth layer of steel plate

After penetrating throughout multilayers of steel plate, the EFP does not break into pieces on the whole. An intact EFP of 98g is recovered behind the target.

CONCLUSIONS

1) In designing the liner of the jet device, a technique of curved surface and varying thickness was used. With precise calculations and experiment adjustment, the mass of the jet converted from the liner is increased. The jet is thus uniform and wide that is suitable for penetrating rock. The jet also has a proper velocity distribution.

2) In designing the charge of the jet device, a coning structure of the charge is used, which increases the utilization coefficient of the energy of explosive and decreases the mass of the shaped charge, thus the total mass of the jet device.

3) We have done some work on the fundamental principles of the jet penetration to the rock. Performance of the jet generated from different metal materials and the penetration effects to the rock with different strengths are also investigated. We have fundamentally known well the design of shaped charge that can meet the requirements of both the penetration diameter and depth.

4) The jet and EFP devices we have designed have good penetration effects.

Acknowledgement —The authors thank the following colleagues for their help to the work. They are Zhang Kejian, Sun Chengwei, Liu Guangzou, Jiang Hongzi, Liu Daming, Ding Baoxian, Zang Zentao, Li Yu, Gu Xingrong, Ren Huiqi, Yang Renhua, Mi Zongchueng, Gao Zhenghong, et al.

REFERENCES

1 Kivity Y, Mayseless M, et al. An Efficient Model for Shaped Charge Design. 7th Symp.(Int.) on Ballistics,1983.

2 Xie Panhai, Su Linxiang, et al. Ring Initiation for Improving Shaped Charge Performance. 13th Symp.(Int.) on Ballistics, Sweden, 1992.

3 Murphy M J. Shaped Charge Penetration in Concrete:A Unified Approach. UCRL-53393,1983.

4 Hagcman L J. HELP:A Mult-Matcial Eulerian Program for Compressible Fluid and Elastic-Plastic Flows in Tow Space Dimensions and Time. AD-726459, AD-726460, 1971.

PERGAMON International Journal of Impact Engineering 23 (1999) 989–994

INTERNATIONAL JOURNAL OF IMPACT ENGINEERING

www.elsevier.com/locate/ijimpeng

A SIMPLE ANALYSIS MODEL FOR THE HYPERVELOCITY CRATERING OF SEMI-INFINITE TARGETS BY PROJECTILE

ZHOU NAN

Northwest Institute of Nuclear Technology,
P.O.Box 69-15,Xian,Shaanxi,710024,China

Summary -- In this paper, a simple analysis is developed to describe the hypervelocity cratering characteristics of semi-infinite targets by projectile. The comparison between theoretical and experimental results are made for a spherical projectile with the velocity 2-7km/s. It is found that the results given by the present model are in reasonably good agreement with experiments.
© 1999 Elsevier Science Ltd. All rights reserved.

INTRODUCTION

It is well known that hypervelocity cratering involves complex large multidimensional deformation, and the material response is strongly nonlinear. For this reason, both numerical methods and experimental investigation have been developed to describe hypervelocity penetration. However, numerical solutions can not give directly the dependence of cratering characters on the impact parameters (such as parameters of the projectile and the target material, impact velocity, etc), and are extremely expensive in terms of supercomputer resources.

It is very desirable, then, to have simple analytical or semi-empirical theories to describe the penetration process. In this paper, a simple analysis model that allows for engineering analysis of hypervelocity cratering is developed. Theoretical expressions which are able to predict cratering characters for the hypervelocity impact in semi-infinite targets are derived from the analysis model. Cratering characters include penetration velocity, crater depth and volume, crater diameter and ballistic limit, etc. From theoretical expressions it can be seen that cratering characters not only depend on the density of the projectile and the target material, but also are related to the dynamic yield strength of the target material and the acoustic impedance ratio $\rho_p C_p/(\rho_p C_p + \rho_t C_t)$. The crater approaches a hemispherical shape as the projectile velocity increases. At least for the metal projectile with a length to diameter ratio near unity, it is found that theoretical expressions are in good agreement with experiments of hypervelocity impacts with the velocity 2-7km/s.

THEORETICAL MODEL AND CALCULATION

For an approximate analytic investigation on hypervelocity impact in semi-infinite targets, the velocity of the projectile is divided into the average(or effective) velocity of the projectile mass center and the penetration velocity(i.e. the particle velocity on the impacted surface).We regard the penetration as a continuous compact process, and think that the average velocity u_p and the penetration velocity u satisfy the Hugoniot shock relations. As a good approximation of the

0734-743X/99/$ - see front matter © 1999 Elsevier Science Ltd. All rights reserved.
PII: S0734-743X(99)00141-4

shock Hugoniot relations, we have

$$u \approx \frac{\rho_p c_p}{\rho_p c_p + \rho_t c_t} u_p \tag{1}$$

where ρ, c is the impedance of material, subscript p and t refer to the projectile and target, respectively.

Before further discussion, for the sake of simplicity, we make assumptions and approximations as follows:

(1)The friction between the projectile and target can be neglected.

(2)The compressive force acting on the projectile's nose surface by the target can be neglected.

(3)The effects of both the projectile shape and plastic compressive deformation on resistance of the projectile motion can be partially considered by the projectile shape-factor α.

(4)When the projectile velocity exceeds the plastic limit velocity, u_{ty} ($u_{ty} = (Y_t / \rho_t)^{1/2}$), where Y_t is the dynamic yield stress of the target material), of the target, the crater can continue to expand until the projectile velocity is equal to the plastic limit velocity.

At hypervelocity, the impact stress is much higher than the dynamic yield stress of either target or projectile, and we assume that the stress can be expressed in similar manner as the penetration of a long cylinder:

$$P \approx \frac{1}{2} \rho_t u^2 \tag{2}$$

Penetration Velocity and Energy Decay

Based on the above assumptions and approximations, we apply the method of the exterior ballistics to establish the motion equation of the projectile mass center. From (2) we have

$$m_p \frac{du_p}{dt} = -\alpha \pi R_p^2 p \tag{3}$$

where m_p is the mass of the projectile, R_p is the radius of the projectile cross-section, α is the projectile shape-factor.

Noting that $\frac{d}{dt} = u \frac{d}{dx}$ (where x is the penetration position of the projectile), and combining (1), (2) and (3), we obtain the penetration velocity of the projectile as follows:

$$u = \frac{\rho_p c_p u_{0p}}{\rho_p c_p + \rho_t c_t} \exp\left(-\frac{\alpha \pi R_p^2 \rho_t}{2 m_p} \frac{\rho_p c_p}{\rho_p c_p + \rho_t c_t} x\right) \tag{4}$$

where u_{op} is the initial impact velocity of the projectile.

For a spherical projectile, we have

$$u = \frac{\rho_p c_p u_{0p}}{\rho_p c_p + \rho_t c_t} \exp\left(-\frac{3}{8 R_p} \frac{\alpha \rho_t c_p x}{\rho_p c_p + \rho_t c_t}\right) \tag{5}$$

For a cylindrical projectile, we have

$$u = \frac{\rho_p c_p u_{0p}}{\rho_p c_p + \rho_t c_t} \exp\left(-\frac{1}{2l} \frac{a\ \rho_t\ c_p x}{\rho_p c_p + \rho_t c_t}\right) \tag{6}$$

where l is the undeformed projectile length.

The decay of the kinetic energy, E, with the penetration position x can be written as

$$E = E_0 \exp\left(-\frac{a\ \ \pi\ \ R_p^2 \rho_t}{m_p} \frac{\rho_p c_p}{\rho_p c_p + \rho_t c_t} x\right) \tag{7}$$

where E_0 is the original kinetic energy of the projectile.

From (5), we can obtain the energy consumption portion, ε, of the projectile with the penetration position x as follows:

$$\varepsilon = \frac{E\text{-}E_0}{E_0} = 1 - \exp\left(-\frac{a\ \pi R_p^2 \rho_t}{m_p} \frac{\rho_p c_p}{\rho_p c_p + \rho_t c_t} x\right) \tag{8}$$

For a spherical projectile, we get the energy consumption portion as shown in Fig.1.

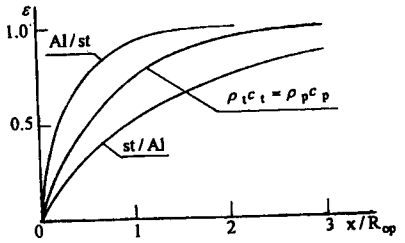

Fig.1. The energy consumption portion

Penetration Depth

By using the condition (4), the penetration depth, $x_{\max}$, is expressed as

$$x_{\max} = \frac{2m_p}{a\ \pi R_p^2 \rho_t} \frac{\rho_p c_p + \rho_t c_t}{\rho_p c_p} \ln \frac{u_{0p}}{u_{ty}} \tag{9}$$

For a spherical projectile, we have

$$x_{\max} = \frac{4d_p}{3a\ \rho_t c_p} \left(\rho_p c_p + \rho_t c_t\right) \ln \frac{u_{0p}}{u_{ty}} \tag{10}$$

where d_p is the diameter of the projectile.

For a cylindrical projectile, we have

$$x_{\max} = \frac{2l}{a\ \rho_t c_p} \left(\rho_p c_p + \rho_t c_t\right) \ln \frac{u_{0p}}{u_{ty}} \tag{11}$$

We note that the expression (10) is in good agreement with the following scaling law for

hypervelocity impact:

$$\frac{x_{\max}}{d_p} = K\left(\sqrt{\frac{\rho_p u_{0p}^2}{Y_t}}\right)^{2/3}\left(\frac{\rho_p}{\rho_t}\right)^{2/3} \tag{12}$$

$$K \approx 0.29 - 0.35 \quad (u_{0p}=2\text{-}7km/s) \tag{13}$$

We systematically calculated the cratering of metal target such as steel, yellow brass(Cu*), Cu and Al, and make a comparison with experiments[1]. In the experiments, the shape of projectile is spherical, the ball diameter d_p is 0.5cm and the projectile velocity ranges from 2km/s to 7km/s.

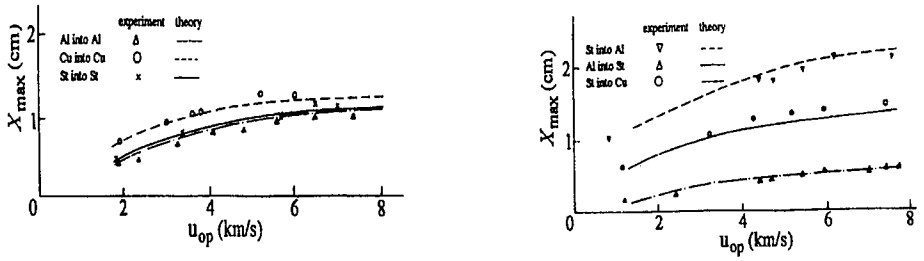

Fig.2. Crater depth at various projectile velocity

Fig.2 shows comparisons between calculated results and the experimental data. It is shown that the results given by the present model are in reasonably good agreement with experiments.

Ballistic Limit

Usually, the ballistic limit is defined as minimum velocity u_{min} of the projectile at which the target of thickness δ is fully penetrated. From (4), we get

$$u_{min} = \left(\frac{Y_t}{\rho_t}\right)^{1/2} \exp\left(-\frac{a\ \pi R_p^2 \rho_t}{2m_p}\frac{\rho_p c_p}{\rho_p c_p + \rho_t c_t}\delta\right) \tag{14}$$

Crater Volume and Radius

A number of experimental studies indicate that the shock crater has the following two characteristics as long as the scale of the projectile in three directions which are perpendicular to each other is approximately equal or the length to diameter ratio is near unity:

(1) The crater shape approaches a hemispherical one;

(2) The volume of the crater is approximately proportional to the kinetic energy of the projectile.

It is well known that at hypervelocity impact the material is fractured, or is melted or vaporized. But the melting effect will play a main role in phase transition for the hypervelocity impact(u_{0p} ≈2km/s ~7km/s), while vaporization is not important[2,3]. So it can be supposed that the kinetic energy of the projectile is entirely transmitted to the melting energy of the target material, and an approximate energy conservation relation can be written as

$$\frac{1}{2}m_p u_{0p}^2 = m_t E_t k \tag{15}$$

where m_t is the mass corresponding with the crater, E_t is the average specific melting energy (J/g),

k is the modified coefficient taking the fragmentation and kinetic energy of the target material into account, which depends on the properties of the projectile and the target material and is determined by experiments. When the impact velocity is in the range 2km/s to 7km/s, we have $k \approx 1.0$.

From (15), the crater volume can be expressed as

$$V_t = \frac{m_p u_{0p}^2}{2\rho_t E_t k} \tag{16}$$

In this paper, the crater diameter d_t is defined the diameter of the equivalent hemisphere of the crater volume. From (16), we get

$$d_t = \left(\frac{6 m_p u_{0p}^2}{\pi \rho_t E_t k} \right)^{1/3} \tag{17}$$

For the spherical projectiles, Fig.3 show experimental results[1] d_t together with theoretical one predicted by (17). From the figures we can see that the present model is in good agreement with the experimental results.

The crater depth normalized by the crater diameter is plotted versus the projectile velocity in Fig.4 for several typical examples such as steel, yellow brass (Cu*), Cu and Al, and a comparison with the experimental results is made. It is shown that (1) the crater approaches a hemispherical shape as the projectile velocity increases; (2) the present model is in reasonably good agreement with the experimental results.

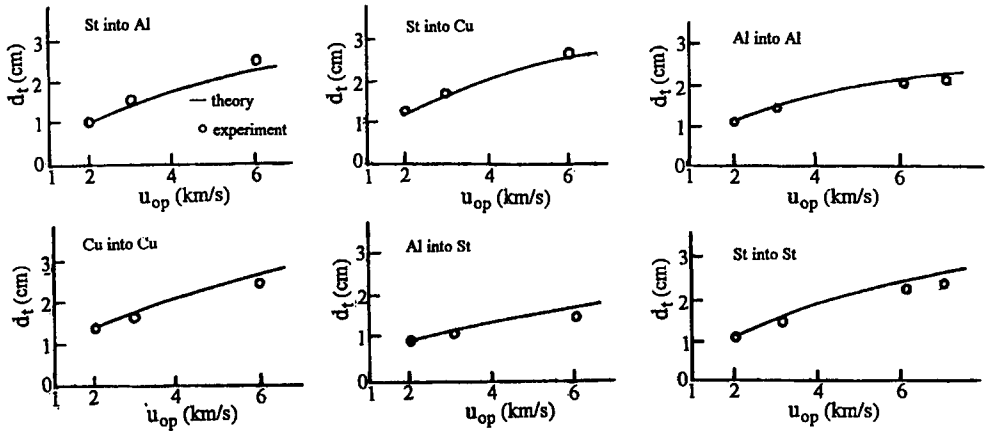

Fig.3. Crater diameter at various projectile velocity

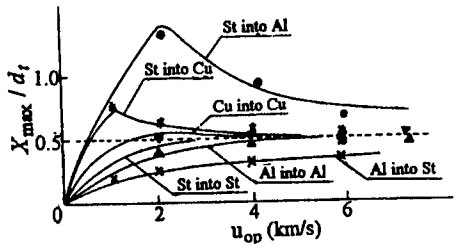

Fig.4. Crater depth to diameter ratio versus impact velocity

CONCLUSIONS

In the present work we have developed a simple analysis model for the engineering analysis of hypervelocity cratering. Applying the model, we have calculated the cratering characteristics for the hypervelocity impact in semi-infinite metal targets such as steel, Cu*(yellow brass), Cu and Al, and made the comparisons with the experimental results. It can be shown that

(1) At least for the metal projectile with a length to diameter ratio near unity, the present analysis model is quite reasonable for predicting the cratering characteristics;

(2) For the hypervelocity impact, the scaling low holds approximately;

(3)In the case of higher impact velocity, the melting may be more important, which will be confirmed by further evidence.

REFERENCES

1. Sun Genchen, Tan Qingming et al., Experimental research of hypervelocity impact cratering for thick plate of metals, *Proc. of 4th National Explosion Mechanics Symposium*, pp.EM4-605/1-8, Hefei, China(1990).
2. J.A. Zucas et al(edited), John Wiley & Sons, N.Y.C(1982).
3. Zhang Deliang, Tan Qingming et al., Experimental investigations of hypervelocity impact onto Aluminum dual-plate structure, *Proc. second Int. Symp. on Intense Dynamic Loading and Its Effects*, pp,629-636, Chengdu, China(1992).

PERGAMON

International Journal of Impact Engineering 23 (1999) 995–1001

INTERNATIONAL JOURNAL OF IMPACT ENGINEERING

www.elsevier.com/locate/ijimpeng

FAILURE WAVE EFFECTS IN HYPERVELOCITY PENETRATION

E. L. ZILBERBRAND,* A. S. VLASOV,* J. U. CAZAMIAS, S. J. BLESS,** and A. A. KOZHUSHKO***

*Science and Technology Centre PHYSIMPEX, 26 Polytechnicheskaya, St. Petersburg 194021, Russia; **The Institute for Advanced Technology, The University of Texas at Austin, 4030-2 W. Braker Ln., Austin, TX 78759, USA

Summary—It has been known for several years that glass is a relatively effective armor against shaped charge jets [1] even though its performance against conventional long-rod projectiles is mediocre. Some of the authors have earlier postulated that this effect is due at least in part to an increase of the R_t value at hypervelocity. This enhancement is due to the fact that in long-rod penetration of brittle materials, a failure wave is generated in front of the penetrator which prematurely damages the material; however, if the penetrator is supersonic relative to this failure velocity, penetration is always occurring in intact material. Consequently, the true strength of a brittle material is only measured in hypervelocity experiments. In order to avoid the uncertainties of analyzing shaped charge penetration data, we have conducted experiments with L/D = 10 W alloy rods (ρ = 17.2 g/cm^3) against glass targets (ρ = 2.5 g/cm^3) to unambiguously search for this effect. In low velocity experiments, the penetration was essentially hydrodynamic, while above 3.9 km/s, the R_t-Y value was on the order of 5.7 to 7.2 GPa. This substantiates the failure wave hypothesis. © 1999 Elsevier Science Ltd. All rights reserved.

INTRODUCTION

Dynamic resistance to penetration, R_t, is conventionally computed from the Alekseevski-Tate equation (see, for example, [2]). It has been noted that whereas R_t for metals is several times the compressive strength, for brittle materials R_t is generally about equal to the compressive strength. R_t values for metals can be derived from cavity expansion analysis assuming elastic-plastic behavior (see, for example, [3]). R_t values for brittle materials can also be computed from cavity expansion analysis, but it is necessary to make some assumptions about the properties of the fractured material ahead of the penetrator (see, for example, [4]).

In order to understand the relationship between R_t and the fundamental strength of brittle materials, two different penetration modes should be distinguished, depending on whether the penetration velocity, U, is below or above the failure wave velocity, V_f, which can be crudely defined as the ultimate rate of propagation of brittle fracture. In general, V_f is assumed to range between the single crack propagation rate (lower limit) and the shear wave speed (upper limit). It should be noted, however, that precise measurements of single crack propagation rates are rare, and that sometimes fracture travels along with the shock front.

Investigations of brittle materials performed at penetration velocities below V_f (impact velocities up to about 2 km/s) show the penetration parameters to depend primarily on the fracture kinetics (for example [2, 4]). These kinetics govern the target strength degradation in a zone ahead of the penetrating projectile and, consequently, the penetration resistance. The fracture kinetics, in turn, depend on the target and projectile geometry, impact pressure, and material properties. For this reason, no direct correlation between the impact behavior of brittle materials and their initial strength properties has been found at $U < V_f$.

0734-743X/99/$ - see front matter © 1999 Elsevier Science Ltd. All rights reserved.
PII: S0734-743X(99)00142-6

For brittle materials at $U > V_f$, the projectile interacts with an intact material, and impact behavior of brittle materials should thus be determined by initial strength properties rather than by the fracture kinetics [5]. This type of penetration is similar to indentation. A study performed at the Ioffe Physico-Technical Institute at $U > V_f$ shows brittle materials to exhibit strength resistance to penetration comparable to their microhardness, i.e., about one order of magnitude higher than most hard metals and alloys [6].

The data in [5] for $U > V_f$ were obtained in experiments using shaped charge jets. The jets exhibit a velocity gradient along the axis which is difficult to account for in calculations. As a rule, R_t is estimated with an error of about 15-20%. One should also keep in mind a possible interaction of the jet with crater walls resulting in a reduction of the jet's effective length which is considered by some authors to be responsible for the high ballistic performance of brittle materials against shaped charge jets.

To obtain more reliable data of R_t and demonstrate unambiguously the high-strength state of brittle materials at $U > V_f$, experiments using tungsten long-rod projectiles were performed against glass. Glass is a common armor material, and it is also often treated as a prototypical brittle solid. More importantly, sound speeds in glass are about half of those in ceramics allowing easier access to the supersonic penetration regime. Two sets of experiments were conducted:

1. Penetration at velocities $U < V_f$ to demonstrate the degradation of the strength of a brittle target when the target material is comminuted ahead of the penetrator.

2. Penetration at velocities $U > V_f$ to determine the true strength of the glass. It should be noted that eventually the target material ahead of the projectile undergoes failure due to the reflection of stress waves from side and rear surfaces.

EXPERIMENTAL DESCRIPTION

Experiments were performed at the Ioffe Physico-Technical Institute (IPTI) and the Institute for Advanced Technology (IAT).

IPTI Techniques

Ordnance velocity experiments were performed with a 15.5-mm diameter smooth-barrel powder gun. The targets were 50 x 50 x 100 mm soda-lime glass ($\rho_o = 2.5$ g/cm^3) blocks. The projectiles were 4 mm diameter, 40 mm long flat-ended cylinders machined from extruded tungsten alloy (W-Ni-Fe) with a density of 17.2 g/cm^3. The projectiles were launched in a polyethylene sabot with its rear tightly pressed into an Al alloy holder. The sabot and the holder strike the target much later then the projectile tip and, thereby, cannot affect the penetration parameters of interest. For this reason, no stripper was used to separate the sabot fragments and the holder from the projectile.

The velocimeter for this gun works without any mechanical contact with the projectile. A hollow cylindrical nozzle with an inside diameter equal to the launch tube caliber is attached to the muzzle. The nozzle is made from high-strength nonmagnetic austenite steel and has two narrow half-spherical grooves spaced 50 mm apart embedded with inductive coils of 10-Ω resistance. The low resistance of the coils and their grounded housing make the circuit very resistant to noise. Both coils are surrounded with magnetic fields generated by two separate permanent magnets to localize the fields around the coils. Passage of a metallic projectile inside the nozzle causes the generation of two electric signals due to the distortion of the magnetic field by the ferromagnet as well as by eddy currents in the nonmagnetic metals. The time of passage of the projectile between the coils is measured by a digital counter with an error of 0.1 μs. Starting and stopping times are determined when the sign of a bipolar pulse changes. The error in the measured projectile velocity is less than 2% within the 0.1-2.0 km/s velocity range.

The second coil of the velocimeter triggers four 400-kV flash X rays that image the projectile inside the target. The trigger pulse is applied to the trigger circuits of all four tubes simultaneously, but the firing of each tube is delayed by a different preset time. Also, the interframe times are independently verified with an oscilloscope using an electron-optic converter. As an example, Fig. 1 shows a set of flash X-ray pictures from Test 1441.

In addition, comparison experiments of penetration of Al projectiles into Al and glass targets were performed at hypervelocity. The study was performed at the Plasma-Gas Dynamics Laboratory using a 30/13-mm two-stage light gas gun. The projectiles were 2 mm diameter, 23 mm long flat ended cylinders (mass of 0.23 g) machined from soft (HB = 0.97 GPa) Al alloy. The projectiles were launched in polyethylene sabots against two kinds of targets: a) 15.5 mm thick Al alloy plate backed with 25 mm thick block of the same material; and b) 15.5 mm thick glass plate (lateral dimensions: 85 x 85 mm) backed with 25 mm thick Al alloy block. The backups served as witness targets in both cases.

IAT Techniques

Hypervelocity experiments with W-alloy projectiles were performed using the IAT light gas gun range, consisting of a 115/38-mm two-stage light gas gun, laser and X-ray projectile velocity measurements, and orthogonal 2-frame 450-kvV X rays of the target. The projectiles were of the same geometry and material as those used in experiments at ordnance velocities. The projectiles were launched in discarded sabots designed and manufactured by the IAT. The sabots were essentially friction-grip aluminum cones pushed by nylatron obturators.

The targets were the same glass blocks used at IPTI. At the face side of the target a mylar make screen was set for triggering X-ray flashes. The gage was covered by a 3 mm thick Lexan plate. The time after impact was recorded from screen shorting ("zero time point").

At the rear side of the target, tungsten carbide prisms were glued. The prisms allowed precise definitions of the target rear face in the flash X-ray photographs. It is the target rear side that serves as a reference in analyzing the photographs. The target was mounted so that the rear face laid in the plane of the X-ray tubes. X-ray trigger times were measured by an oscilloscope; however, unlike the IPTI tests, flash times were not independently verified.

As an example, Fig. 2 shows one of the flash X-ray pictures from Shot 286. Note that the prisms are not shown.

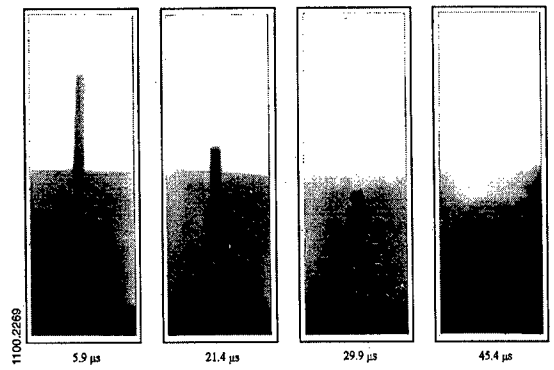

Fig. 1. Typical radiographs obtained at IPTI for penetration into glass. Test 1441.

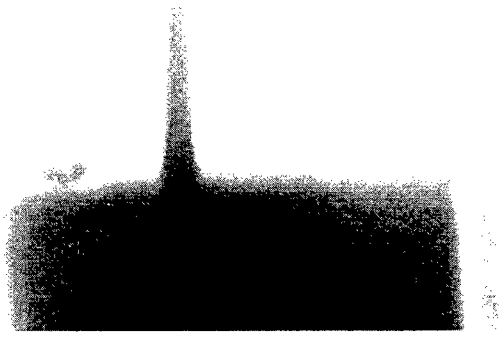

Fig. 2. Radiograph obtained at IAT from shot 286 showing eroding rod in glass.

THEORY

The starting data obtained in the present study consist mainly of a relatively small number of measurements of the projectile position (projectile nose and tail coordinates) at various times after impact. In the present study, physical models for the penetration of brittle bodies by eroded projectiles and projectile deceleration were fit to the data. Briefly, the concepts may be reduced to the following:

1) As a first approximation, the penetration process may be described in terms of a modified hydrodynamic theory using the Alekseevsky-Tate equation

$$\rho_t U^2/2 + R_t = \rho_p (U - V)^2/2 + Y_p, \tag{1}$$

where Y_p is the yield strength of the projectile material. Although this equation was developed for steady penetration into a plastic target, it is also useful for describing penetration into brittle targets. R_t values derived from this equation can show a variation of the strength with the interaction time (see, for example, [8]).

2) The projectile deceleration may be described using the Taylor equation

$$\rho_p L\, dV/dt = - Y_p, \tag{2}$$

where L is the projectile length at a given time, t. However, for V > 3 km/s, it follows that the rod velocity decreases only by several tens of m/s, and consequently, the velocity of the projectile, in particular the velocity of the projectile tail, may be represented by a constant V with good accuracy.

3) There is also the kinematic equation for an eroding projectile

$$\Delta L/\Delta P = (V - U)/U \tag{3}$$

where ΔL is the projectile shortening and ΔP is the penetration depth increment. Then, the U/V ratio may be calculated from

$$U/V = 1/(1 + \Delta L/\Delta P). \tag{4}$$

4) It is assumed that U is initially given by the solution to the shock Hugoniot equations for W striking glass.

RESULTS

Ordnance Velocity Experiments at IPTI

Eight tests were conducted at approximately 1.5 km/s. Fig. 3 shows calculated projectile nose and tail position versus time curves overlaid with data from three experiments. Fig. 4 shows calculated penetration and projectile tail velocities versus time curves. Variation of the penetration resistance, $R_t - Y_p$, with time after impact is presented in Fig. 5.

In the U(t) curve, different portions may be distinguished. The first descending branch represents a transition from the particle velocity, determined by shock adiabats of interacting bodies, to the penetration velocity, i.e., a transition from shock displacement of the interface to real penetration. During this time interval, steady projectile flow is being established. A minimum penetration velocity is then observed. The penetration velocity then increases with time up to a nearly constant value, and it is reasonable to assume that the increase of the penetration velocity is related to growing failure of the target with time that causes a progressive degradation of R_t. This last portion of

the U(t) curve corresponds to steady-state penetration into a medium with negligible strength. In this way, a high-velocity penetration into a brittle target may be represented as a two-stage process: (a) low-velocity penetration with an increasing penetration velocity, and (b) penetration with a nearly constant velocity.

The R_t-Y_p versus time curve is shown for the times >3 μs; before transition, the penetration resistance may not be computed using generally accepted analytical expressions. R_t falls off monotonically with time and remains effectively constant after a specific point of time. The lowest strength resistance is observed at the second (quasi-steady) penetration stage. It should be noted that R_t does not drop down to zero, and this may be accounted for by friction between the particles of the comminuted glass. The highest R_t is calculated, as expected, during the first (low-velocity) penetration stage. It is reasonable to assume that it is this stage that plays a leading part in the high ballistic performance of ceramics at ordnance velocities.

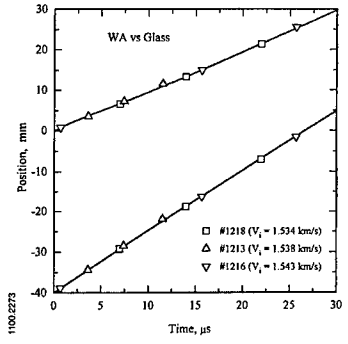

Fig. 3. Position-time curves of the nose and tail of the projectile from three of the eight IPTI shots.

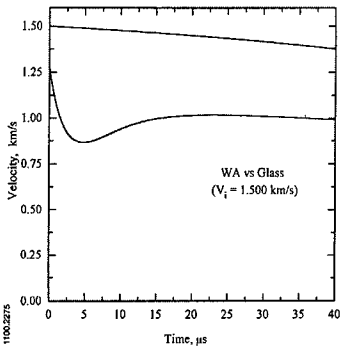

Fig. 4. Fitted velocity-time curves of the penetration front and projectile tail for IPTI experiments.

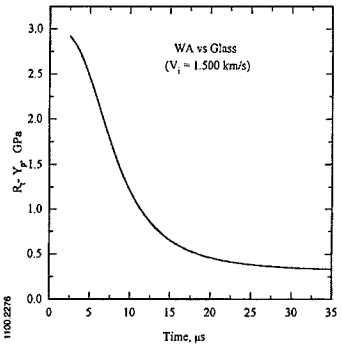

Fig. 5. Variation of target strength versus time as derived from the IPTI experiments.

Hypervelocity Experiments at IPTI

Four shots of Al projectiles into Al and glass targets were performed at 4.2 km/s. Under these conditions, an Al target will undergo hydrodynamic penetration, i.e., no strength effects with $U = V_i/2 = 2.1$ km/s. Taking into account the nearly identical densities of glass and Al, it can be assumed that the penetration depth in witness targets will be markedly less after piercing the glass plate if the glass exhibits a high R_t.

In the experiments, penetration depth in Al alloy witness targets was measured after piercing glass and Al alloy plates of the same thickness. The penetration depths in the backups after piercing Al plates were 10.8 and 10.5 mm (average total penetration = 26.2 mm). The penetration depths in the backups after piercing glass plates were 11.5 and 11.1 mm (average total penetration = 26.8 mm). The similar penetration depths found for Al alloy and glass target are strong evidence that impact behavior of both materials is the same under the test conditions. Assuming that Al alloy behaves hydrodynamically at $V_i = 4.2$ km/s, a conclusion may be made that the glass shows no high strength resistance to penetration and that $V_f > 2.1$ km/s which is consistent with observations of failure waves in glass bars [9].

Hypervelocity Experiments at IAT

Four successful shots were conducted, listed in Table 1. Starting data derived from the flash X-ray study are the penetration depth and the instantaneous projectile length at corresponding points of time. Since the times of the flash X-ray pulses were not recorded independently, it was decided not to use the X-ray time data from the IAT experiment. Instead, the position of the rear of the projectile was taken as a time mark.

For hydrodynamic penetration, U/V = 0.72. As can be seen from Table 1 for shots #281 and 282, the difference of the experimental and calculated U/V ratios does not exceed 2%, i.e., it is within the limits of experimental error. This result is evidence that the penetration resistance is of purely inertial nature, i.e., the projectile interacts with comminuted glass showing no measurable strength. It means that the failure wave in glass propagates with a velocity exceeding the penetration velocity.

On the other hand, the U/V ratios for shots #286 and 349 are substantially less than that for purely hydrodynamic penetration. These give R_t values of about 7.7 to 9.2 GPa (taking $Y_p \cong 2$ GPa) that are commensurate with the inertial penetration resistances, $1/2\rho_t U^2$, of 8.6 to 9.4 GPa. It is reasonable to assume that the projectile travels ahead of the failure wave and interacts with intact glass resulting in a high R_t. Thus, the data confirm existence of a penetration velocity above which brittle solids become more resistant to penetration due to high strength. In addition, the data are helpful to assess velocity of the failure wave in brittle solids under high velocity impact.

Table 1: Hypervelocity Tests at IAT

Parameter	*Shot #281*	*Shot #282*	*Shot #286*	*Shot #349*
Vi, km/s	3.29	3.12	4.13	3.91
$\Delta t=\Delta P/U$, μs	3.20	5.28	4.75	3.74
$\Delta t=\Delta L/(V-U)$, μs	3.18	5.29	4.74	3.72
$\Delta t=\Delta P_{tail}/V$, μs	3.19	5.41	4.75	3.73
U, km/s	2.37	2.22	2.74	2.62
U/V	0.71	0.72	0.66	0.67

DATA SUMMARY

Experimental data for penetration into glass may be classified into two groups.

1) *Data obtained at penetration velocities below 2.4 km/s.* The observations that the projectile consumption rate in Al and glass is the same, and that the ratio of U/V for WA projectiles penetrating glass targets corresponds to the hydrodynamic prediction, are indicative of purely hydrodynamic phenomena in the glass. In other words, the penetration resistance is of an inertial nature and high-velocity strength effects may be neglected. Physically, it means that the projectile penetrates into comminuted glass since the failure wave travels ahead of the projectile-target interface.

2) *Data obtained at penetration velocities above 2.6 km/s.* In this regime, U/V ≅ 0.66 which is markedly less than the hydrodynamic U/V ratio. This gives an R_t for the glass on the order of 8 to 9 GPa. This agrees with that found in experiments with shaped charge jets [5].

The gap between these two regimes allows an estimate of the failure wave velocity on the order of 2.4 to 2.6 km/s for soda-lime glass. This estimate is in line with data obtained in [9].

CONCLUSIONS

Normal penetration may be represented as a two-stage process. The first stage involves penetration with a low velocity that increases as the target material is being fractured. The resistance of brittle materials to penetration decreases with time and is determined by the fracture kinetics. The second stage consists of quasi-steady penetration into comminuted material of very little strength, and the penetration is essentially hydrodynamic. A high value of the penetration resistance, R_t = 5 GPa, exceeding inertial resistance, is observed during the first stage. It is this stage that is

responsible for the high ballistic performance of ceramics as armor materials. For glass, this normal penetration sequence is observed at penetration velocities up to 2.4 km/s.

At a higher impact velocity providing a penetration velocity over 2.6 km/s, a significant deviation of penetration parameters from the hydrodynamic predictions has been found. Under these conditions, the glass shows even greater resistance to penetration, R_t, of about 8 to 9 GPa. This value is in good agreement with data obtained in experiments with shaped charge jets at Ioffe Institute [6]. The above result indicates that a projectile travels ahead of the failure wave in the target and interacts with intact material. Under these conditions, the strength resistance to penetration is determined by fundamental strength properties of the intact target material rather than by the fracture kinetics.

The available data also enables an estimate of the failure wave velocity in soda-lime glass. It lies in the range 2.4 to 2.6 km/s.

Acknowledgment—This work was supported by the U.S. Army Research Laboratory (ARL) under contracts DAAA21-93-C-0101 and DAAL01-96-P-1192.

REFERENCES

1. R. J. Eichelberger, R. Heine-Geldern, "Protection Against Shaped Charges," OSRD 6384 (Final Report), February 1946.
2. A. S. Vlasov, Yu. A. Emelyanov, E. L. Zilberbrand, A. A. Kozhushko, A. I. Kozachuk, G. S. Pugachev and A. B.Sinani, "Some features of the kinetics of high-speed penetration in brittle media," Tech. Phys. Lett, **2** (2), 117- 119 (1997).
3. S. Chocron, C. E. Anderson, Jr. and J. D. Walker, "Long-rod penetration: cylindrical vs. spherical cavity expansion for extent of plastic flow," 17th Int'l Symp. Ballistics, Midrand, South Africa, 23-27 March (1998).
4. S. Satapathy and S. Bless, "Cavity expansion analysis of brittle materials," *Metallurgical and Materials Applications of Shock-Wave and High-Strain-Rate Phenomena*, pp. 187-194, ed. L. E. Murr, K. P. Staudhammer, M. A. Meyers, Elsevier (1995).
5. V. B. Lazarev, A. S. Balankin, A. D. Izotov and A. A. Kozhusbko, "Structure stability and dynamic strength of inorganic materials," M. Nauka, in Russian (1993).
6. A. A. Kozhushko, I. I. Rykova and A. B. Sinani, "Resistance of ceramics to penetration at impact velocities above 5 km/s," *J. de Physique*. IV., Colloque C3, Suppl JPIII, **1** (8), 117-122 (1991).
7. E. L. Zilberbrand, N. A. Zlatin, A. A. Kozhushko, V. I. Polozenko, G. S. Pugachev and A. B. Sinani, "Mechanism of interaction of a plastic striker with a brittle solids," *Sov Phys Tech. Phys.*, **34** (10), 1123-1125 (1989).
8. G. Hauver, "Variation of target resistance during long rod penetration into ceramics," 13th Int'l Symp. Ballistics, Stockholm Sweden, 1-3 June (1992).
9. S. J. Bless, N. S. Brar, G. Kanel and Z. Rosenberg, "Failure waves in glass," *J. Amer. Ceram. Soc.*, **75** (4), 1002-1004 (1992).

PERGAMON International Journal of Impact Engineering 23 (1999) 1003–1007

INTERNATIONAL JOURNAL OF IMPACT ENGINEERING

www.elsevier.com/locate/ijimpeng

ATTENDEES—HVIS SYMPOSIUM

Akahoshi, Yasuhiro	Kyushu Institute of Technology
Altmayer, Claude	ETBS
Anderson, Jeffrey	NASA/Marshall Space Flight Center
Anderson, Jr., Charles E.	Southwest Research Institute
Arnold, Werner	TDW
Asay, James	Sandia National Laboratories
Backofen, Joseph	Briggs, Co.
Barker, Antony	Defence Evaluation & Research Agency
Barnouin-Jha, Olivier	Johns Hopkins University/APL
Baum, Dennis	Lawrence Livermore National Lab.
Baumung, Kurt	Forschungszentrum Karlsruhe
Bell, Lanny	Sverdrup Technology Inc./AEDC Group
Belov, G.V.	Russian Federal Nuclear Center
Bergeret, Nicolas	Commissariat A P'Enagie Atomique
Berry, Don Travis	Institute for Advanced Technology
Best, Steve	Auburn University/Space Power Inst.
Billingsley, James P.	US Army Aviation & Missile Command
Blanks, James	Sverdrup Technology Inc./AEDC Group
Bless, Stephen	Institute for Advanced Technology
Bowden, Katharine	University College London
Buchwald, Peter	European Space Agency
Calcaterra, Jeffrey	US Air Force Research Laboratory—WPAFB
Campbell, James	Cranfield University
Campbell, Mark	US Air Force Research Laboratory—Kirtland
Carroll, Daniel	Sandia National Laboratories
Cauble, Robert	Lawrence Livermore National Lab.
Cazamias, James	Institute for Advanced Technology
Chanteret, Pierre	ISL French German Research Institute
Cheret, Roger	CEA
Chhabildas, Lalit	Sandia National Laboratories
Christiansen, Eric	NASA/Johnson Space Center
Clark, Steven	Mevatec Corp.
Cline, Carl Franklin	Advanced Materials Technology Int.
Coates, Randolph S.	US Army Research Laboratory
Cour-Palais, Burton	Southwest Research Institute
Crawford, David	Sandia National Laboratories
Crews, Jeanne Lee	NASA/Johnson Space Center
Crimmel, William	University of Denver Research Institute
Cullis, Ian G	Defence Evaluation & Research Agency
Curren, Donald R.	SRI International
Davidson, James S.	University of Alabama—Birmingham
Davison, David	Shock Transients Inc.

0734-743X/99/$ - see front matter © 1999 Elsevier Science Ltd. All rights reserved.

Day, Douglas John	AWE PLC
Denigan, Michael H.	
DeRosset, William S.	US Army Research Laboratory
Destefanis, Roberto	Alenia Aerospazio
Dolgoborodov, A.	Russian Academy of Science
Dorsch, Heinrich G.	IABG
Drennov, Oleg	Sarov Nizhni
Dvorak, Bruce D.	Boeing Aerospace
Eberle, Bill	Lockheed Martin Missiles and Space
Espejo, Richard	Mirror Electronics Co.
Espinoza, Nancy	Rice University
Evans, Hilary	Sverdrup Technology/Huntsville
Fahrenthold, Eric	University of Texas at Austin
Fair, Harry D.	Institute for Advanced Technology
Faux, Douglas R.	Lawrence Livermore National Lab.
Forrestal, Michael J.	Sandia National Laboratories
Frank, Konrad	US Army Research Laboratory
Furnish, Michael	Sandia National Laboratories
Galanov, Borys	Inst. for Problems of Material Science
Garcia, Richard	Los Alamos National Laboratory
Gee, David	Institute for Advanced Technology
Geille, Alain R.	Atomic Energy Commission
Gerber, Bence	Century Dynamics
Gillich, William J.	US Army Research Laboratory
Glenn, Lewis	Lawrence Livermore National Lab.
Goldstein, Selma	The Aerospace Corp.
Gooch, William	US Army Research Laboratory
Grace, Fred	US Army Research Laboratory
Grady, Dennis	Applied Research Associates
Grant, John	NASA
Gualco, Mary	Lawrence Livermore National Lab.
Hackbarth, David	US Army Research Laboratory
Hall, Clint	Sandia National Laboratories
Hancock, Steven	Consultant, Primex Technologies
Harrison, Wayne	AWE PLC
Havel, Thomas	US Army Research Laboratory
Hayami, Richard	University of Alabama in Huntsville
Hayhurst, Colin	Century Dynamics Limited
Held, Manfred	Consultant, TDW
Herbert, Mark	University of Kent at Canterbury
Hertel, Eugene	Sandia National Laboratories
Herwig, Stephen	ITT Systems and Sciences Corp.
Hiermaier, Stefan	Fraunhofer Institut fur Kurzzeitdynamik—EMI
Hill, Scott	U. S. Army Aviation & Missile Command
Hiltl, Michael	Lawrence Livermore National Lab.
Hohler, Volker	Fraunhofer Institut fur Kurzzeitdynamik—EMI
Holmquist, Timothy	Network Computing Services Inc.

Hooser, Clinton	846th Test Squadron—Holloman AFB
Hough, Gary	Southwest Research Institute
Howell, Michael	ITT Systems and Sciences Corp.
Huehn, Reiner	Fraunhofer Institut fur Kurzzeitdynamik—EMI
Hunter, David	Nichols Research Corp.
Igenbergs, Eduard	Tuml Raufahrttechnik
James, Brynley	Defence Evaluation & Research Agency
Jolly, William	ITT Systems and Sciences Corp.
Kalantar, Daniel	Lawrence Livermore National Lab.
Kanel, G.	Russian Academy of Science
Karlsson, Svante	FOA Defence Research Establishment
Karmali, Muraol	Cooke Corporation
Karpiuk, Cindi	Lockheed Martin Missiles and Space
Kartuzov, Egor	Institute for Problems in Material Science
Kartuzov, Valery	Institute for Problems in Material Science
Katayama, Masahide	CRC Research Institute—Structural Engng. Dept.
Kennedy, Edward	US Army Research Laboratory
Kerr, Justin	NASA/Johnson Space Center
Kesby, Andrew	Defence Evaluation & Research Agency
Khautouleva, Tatiana	St Petersburg State University
Kielsmeier, Darin	U. S. Army Aviation & Missile Command
Kim, Vadim	Tomsk State University
Kleponis, Davis	US Army Research Laboratory
Kosel, Frank	Drs. Hadland Inc.
Kozhushko, Anatoly	IOFFE Phys Tech Institute
Krivtsov, A.M	St. Petersburg State Tech University
Kruse, Greg	Nichols Research Corp.
Kryukov, Pavel	Ballistic Technologie Scientific Venture
Lach, Erhardt	ISL French German Research Institute
Lambert, David	US Air Force Research Laboratory—Eglin AFB
Lambert, Michel	European Space Agency/ESRTC
Lamontagne, Chantal	University of Toronto Instit.for Aerospace Sci.
Legendre, Jean Francois	ISL French German Research Institute
Lehr, Hartmuth	ISL French German Research Institute
Leiber, Veronique	University of Strasbourg
Lilly, Gerry	Cooke Corp
Lindner, Christelle	ITT Industries systems Division
Littlefield, David	Institute for Advanced Technology
Liu, Cangli	California Institute of Technology
Luu, Kim	US Air Force Research Laboratory—Kirtland
Lynch, Nicolas	Defence Evaluation & Research Agency
Martinez, Eugene	CEA Dam Dif Dcre Bp N 12
Matheson, Erik R.	Lockheed Martin Missiles and Space
Mayo, David	US Army Aviation & Missile Command
Mayseless, Meir	Rafael

McDonnell, Tony	University of Kent at Canterbury
McHenry, Michael	Lockheed Martin Missiles and Space
Medina, David	US Air Force Research Laboratory—Kirtland
Meschevyakov, Yuri I.	St. Petersburg VO
Meyer Jr., Hubert	US Army Research Laboratory
Milman, Yuly	Inst for Problems of Material Science
Moatamedi, Mojtaba	University of Sheffield
Morrison, Walter	US Army Research Laboratory
Motta, Alexandre	University of Texas at Austin
Mullin, Scott	Southwest Research Institute
Naumann, Walter	Technical University of Munich
Nebolsine, Peter	Physical Science Inc.
Nemtchinov, Ivan	Inst for Dynamics of Geospheres RAS
Normandia, Michael	Institute for Advanced Technology
Olsen, Gregory	NASA/Marshall Space Flight Center
Olsson, Lars-Gunnar	FOA Defence Research Establishment
Orphal, Dennis	International Research Associates
Osborn, John	Orlando Technology, Inc.
Palmieri, David	University of Rome
Partom, Yehuda	Rafael
Peskes, Bert	TNO Prins Maurits Laboratorium
Piekutowski, Andrew	University of Dayton Research Institute
Pomykal, Glenn	Lawrence Livermore National Lab.
Poormon, Kevin	University of Dayton Research Institute
Prakash, Anand	US Army Research Laboratory
Radchenko, Andrey	Tomsk Branch—Inst. for Structural Macrokinetics
Raftenberg, Martin	US Army Research Laboratory
Reaugh, John	Lawrence Livermore National Lab.
Recht, Gunnar	Applied Research Associates
Reedal, Donna	Naval Surface Warfare Center
Reinhart, William	Sandia National Laboratories
Riddle, Sherry	Teledyne Brown Engineering
Robinson, Jennifer	NASA/Marshall Space Flight Center
Romanczuk, Glenn	University of Alabama in Huntsville
Rucker, Michelle	NASA/Johnson Space Center
Rumbaugh, Todd	Drs. Hadland Inc.
Rush, John	ITT Systems and Sciences Corp.
Satapathy, Sikhanda	Institute for Advanced Technology
Schafer, Frank	Fraunhofer Institut fur Kurzzeitdynamik—EMI
Schneider, Eberhard	Fraunhofer Institut fur Kurzzeitdynamik—EMI
Schonberg, William	University of Alabama in Huntsville
Sellers, Timothy	
Shi, Hong Hui	Nagoya Institute of Technology
Shin, Young	Naval Postgraduate School
Shivarama, Ravishankar	University of Texas at Austin

Shuvalov, Valery	Institute for Dynamics of Geospheres Ras
Silvestrov, V.	Russian Academy of Science
Sinex, Jeff	
Smalley, Larry	University of Alabama in Huntsville
Smith, Mark	Sverdrup Technology Inc./AEDC Group
Sommers, William	Nichols Research Corp.
Stallworth, Roderick	NASA/Marshall Space Flight Center
Stanley, Michael	New Mexico Inst. of Mining & Tech.
Starritt, Larry Wayne	Allied Signal
Stephanov, Glennin	Institute for Problems in Material Science
Stilp, Alois	Consultant
Strom, Randall	APT Research Inc
Sundberg, Jan	Scandiflash AB
Swaim, Eve Walker	ITT Systems and Sciences Corp.
Swift, Hallock	Physics Applications, Inc.
Szczepanski, Richard	
Tan, Geoffrey	DSO National Laboratories
Taylor, Emma	European Space Agency
Telitchev, Igor	Smara State Aerospace University
Teterev, Alexander	Belarus State University
Thoma, Klaus	Fraunhofer Institut fur Kurzzeitdynamik—EMI
Thompson, Peter	AWE Hunting BRAE
Tipton, John	US Corps of Engineers
Tokheim, Robert	SRI International
Turner, Paul	U. S. Army Aviation & Missile Command
Urtiew, Paul	Lawrence Livermore National Lab.
Vaughan, Bryan	University of Kent at Canterbury
Vedernikov, Yuri I.	Institute of Mathematic SB RAS
Vignjevic, Rade	Cranfield University
Waggner, Samuel	Naval Surface Warfare Center
Walker, James	Southwest Research Institute
Wilbeck, James	ITT Systems and Sciences Corp.
Williams, Kimberly	US Army Aviation & Missile Command
Williamsen, Joel	University of Denver Research Institute
Wilson, Leonard	Naval Surface Warfare Center
Yatteau, Jerome	Applied Research Associates
Zernow, Louis	Zernow Technical Services, Inc.
Zhupanska, Olesya	Ukraine State Univ. of Food Tech
Zwiener, Mark	University of Alabama in Huntsville

PERGAMON International Journal of Impact Engineering 23 (1999) 1009–1011

INTERNATIONAL JOURNAL OF IMPACT ENGINEERING

www.elsevier.com/locate/ijimpeng

AUTHOR INDEX

Ahrens, T. J.	401
Anderson, A. T.	933
Anderson, Jr., C. E.	1, 699
Arnold, W.	13
Artemieva, N. A.	651, 847
Asay, J. R.	27, 421
Baird, J. K.	39
Baker, J. R.	639
Barnouin-Jha, O. S.	51
Baumung, K.	421
Beauchamp, J. L.	401
Belov, G. V.	63
Best, S. R.	67
Bless, S. J.	77, 547, 995
Bluhm, H.	421
Bohmann, A.	509
Brazhnikov, M. A.	283
Burchell, M. J.	895
Burnham, A. K.	933
Campbell, E. M.	87
Campbell, J.	945
Cauble, R.	27, 87
Cazamias, J. U.	995
Chandler, E. A.	409
Chandler, G. A.	27
Chhabildas, L. C.	27, 101, 261, 341, 421
Choo, Y.	621
Christiansen, E. L.	113, 125
Chugunova, S. I.	629
Clegg, R. A.	365
Colvin, J. D.	409
Cooper, T.	933
Cour-Palais, B. G.	113, 137
Crawford, D. A.	169
Cunningham, B. J.	771
Curran, D. R.	933
De La Fuente, H. H.	125
Dekel, E.	795
Destefanis, R.	181, 249
Dickinson, D. L.	193
Dolgoborodov, A. Y.	283
Drennov, O. B.	205
Duggins, B. D.	101
Dvorak, B. D.	215
Dyakin, E. P.	63
Eagleton, R. T.	803
Ebrahim, A. R.	823
Edquist, K. T.	967
Elder, J. S.	1
Evans, A. M.	803
Evans, H. J.	225
Fahrenthold, E. P.	237, 735
Faraud, M.	181, 249
Fleming, K. J.	27
Foord, M.	27
Forrestal, M. J.	723
Fortov, V. E.	421, 745
Franzen, R. R.	467
Friesen, L. J.	113
Furnish, M. D.	261
Galanov, B. A.	431
Garcia, R. M.	547
Geille, A.	271
Genussov, R.	585
Giraud, M.	533
Goel, B.	421
Gogulya, M. F.	283
Gold, D. M.	409
Grace, F. I.	295
Grady, D.	307
Grady, M. M.	319
Graham, G. A.	319
Grant, J. A.	331
Gui, Y.	981
Gupta, S. C.	401
Hall, C. A.	27, 341
Hancock, S. L.	353
Harmon, N. F.	639
Hauer, A. A.	27, 409
Hayami, R. A.	561
Hayhurst, C. J.	365, 895
Henner, M.	533
Herbert, M. K.	319, 377, 883
Hiermaier, S. J.	365, 391

0734-743X/99/$ - see front matter © 1999 Elsevier Science Ltd. All rights reserved.
PII: S0734-743X(99)00144-X

Holland, K. G. 27
Holt, A. C. 771
Hoppé, P. 421
Horban, B. A. 237
Hord, B. L. 771
Humer, N. D. 639

Ivanov, S. M. 431

Jyoti, G. 401

Kalantar, D. H. 409
Kanel, G. I. 421, 745
Kartuzov, V. V. 431
Katayama, M. 443
Kay, L. 895
Kearsley, A. T. 319
Kerr, J. H. 125
Khorev, I. E. 745
Kibe, S. 443
King, T. R. 39, 455
Kobenko, S. V. 745
Koerber, G. 509
Konrad, C. H. 27, 101
Kosarev, I. B. 651, 847
Kossakovski, D. 401
Kozhushko, A. A. 467, 995
Krause, C. D. 757
Krivtsov, A. M. 477
Kruse, G. R. 489
Kryukov, P. V. 501
Kusubov, A. S. 771

Lach, E. 509
Lambert, M. 365, 905
Lamontagne, C. G 519
Latkowski, J. 933
Lee, M. 675
Legendre, J-F. 533
Li, F. 981
Li, L. 981
Liquornik, D. J. 561
Littlefield, D. L. 547
Lynch, N. J. 573

Manuelpillai, G. N. 519
Marchetti, M. 249
Marzenyuk, I. N. 745
Mayo, D. V. 489
Mayseless, M. 585
McDonnell, J. A. M. 319, 597, 883
McHenry, M. R. 621
Mehlhorn, T. A. 27, 421
Mendes, W. R. 489
Meyers, M. A. 409
Mikaelian, K. O. 409
Milman, Y. V. 629
Mohamed, E. 835
Mosher, D. A. 101

Nash, K. D. 489
Nebolsine, P. E. 639
Nemtchinov, I. V. 651
Normandia, M. J. 77, 663, 675

Orphal, D. L. 467, 621, 687, 699

Pai, V. V. 859
Palmieri, D. 249
Pearson, L. B. 803
Peery, J. S. 101
Petrushin, A. V. 63
Piekutowski, A. J. 711, 723
Plastinin, A. V. 859
Poorman, K. L. 723
Protasov, S. A. 63

Rabb, R. J. 735
Radchenko, A. V. 745
Raftenberg, M. N. 757
Razorenov, S. V. 421
Reaugh, J. E. 771
Recht, G. W. 967
Reinhart, W. D. 101, 261, 341
Remington, B. A. 87, 409
Riedel, W. 365
Robinson, J. H. 783
Rose, M. F. 67
Rosenberg, Z. 795
Rothman, S. D. 803
Roybal, R. 811
Rusch, D. 421

Satapathy, S. 77
Schäfer, F. K. 13, 391, 905
Scharf, M. 509
Schirmann, D. 933
Schneider, E. E. 905
Schneider, W. C. 125
Schonberg, W. P. 823, 835
Schultz, P. H. 51, 169
Scott, J. M. 933

Seaman, L. 933
Shively, J. 455
Shuvalov, V. V. 651, 847, 859
Sinani, A. B. 467
Smalley, L. L. 869
Smirnov, G. S. 63
Sommers, W. J. 489
Stein, C. 811
Stokes, H. 811
Summers, R. M. 101

Takeba, A. 443
Taylor, E. A. 519, 883, 895
Telitchev, I. Y. 905
Tennyson, R. C. 519
Teterev, A. V. 921
Tlomak, P. 811
Toda, S. 443
Tokheim, R. E. 933
Tong, Y. 981
Trott, W. M. 27
Trubetskaya, I. A. 651
Trucano, T. G. 27, 101
Trucchi, M. 181
Tsembelis, K. 895

Utkin, A. V. 421

Vaughan, B. A. M. 883
Vesey, R. 27
Vignjevic, R. 945
Vlasov, A. S. 995

Walker, J. D. 957
Wang, B. 981
Wark, J. S. 409
Warren, T. L. 723
Weber, S. V. 409
Weed, R. A. 489
Wilbeck, J. S. 1
Wiley, L. G. 409
Wilkins, M. L. 771
Williamsen, J. 225
Wilson, L. T. 193
Woosley, J. K. 869
Wright, I. P. 319

Xie, P. 981

Yakovlev, I. V. 859
Yan, C. 981
Yang, F. W. 561
Yatteau, J. D. 967
Yu, C. 981

Zhang, M. 981
Zhou, N. 989
Zilberbrand, E. L. 995
Zwiener, M. C. 561

PERGAMON International Journal of Impact Engineering 23 (1999) 1013–1024

INTERNATIONAL JOURNAL OF IMPACT ENGINEERING

www.elsevier.com/locate/ijimpeng

SUBJECT INDEX

ablation, 27, 421, 847
  debris cloud, 391
ablation cloud, 13
accelerator
  plasma drag, 67
adiabatic shear bands, 509, 757
  hardness, 757
after-flow, 621
ALE, 101
Alekseevskii
  see analytical modeling
  see Tate model
analytical modeling
  ablation mass, 651
  Alekseevskii, 431, 467, 995
  aspect ratio, 621
  Baker equation, 639
  ballistic limit, 125, 137, 181, 215, 295, 597, 989
  breakout phase, 639
  breakup model, 353
  brittle materials, 431
  bumper shield, 823
  cavity expansion, 77, 431, 723
  ceramics, 629
  characteristic time, 651
  circulation, 51
  collision zone, 205
  cone cracks, 377
  contact boundary, 205
  crack length, 835
  crack propagation, 835
  crater depth, 137
  crater diameter, 621
  crater volume, 989
  cratering, 51, 933, 989
  critical diameter, 215, 225
  damage, 377, 431, 933
  debris cloud, 823, 835
  diameter effects, 663
  double transmitted wave mechanism, 823
  drag, 51
  ejecta, 51
  ejecta entrainment, 51
  electromagnetic emissions, 169
  equilibrium/non-equilibrium, 869
  erosion, 663, 869
  explosive welding, 205
  FATEPEN, 967
  fracture, 431, 967
  fragmentation, 933
  glass, 137
  hole diameter, 137, 225, 353, 711, 783
  hole growth, 597
  hydrodynamic, 699
  hydrodynamic instability, 409
  jet-tip velocity, 585
  KIDD, 489
  L/D, 621
  material state, 431
  maximum entropy method, 869
  modified Bernoulli equation, 1
  nonequilibrium effects, 651
  obliquity, 1, 823
  optimum target density, 585
  penetration, 295, 989
  penetration degradation, 663
  penetration depth, 137
  penetration efficiency, 621, 663
  penetration path, 663
  penetration velocity, 431, 663, 957
  perforation, 295
  petalling, 835
  porous material, 651
  pressure wall deformation, 835
  pressure wall loading, 835
  radiative flux, 651
  reaction jet attitude control, 561
  release isentrope, 823
  ricochet, 823
  rod deformation, 967
  rod erosion, 639
  rotation, 77
  shaped-charge jet, 353
  shaped-charge jet penetration, 585
  shock wave, 823
  single transmitted wave mechanism, 823
  slot-cutting, 77

0734-743X/99/$ - see front matter © 1999 Elsevier Science Ltd. All rights reserved.
PII: S0734-743X(99)00145-1

analtyical modeling (cont'd)
SLOTPEN, 77
small L/D, 957
specific energy release, 651
stand-off, 585
statistical analysis, 639
steady state, 639
streamline reversal, 699
strength, 1
stress, 431
t/d ratio, 295, 639
Tate, 1, 77, 431, 467, 621, 629, 663, 995
trajectory deflection, 967
transverse loading, 77, 967
tumbling, 967
uncertainty analysis, 225
vortex ring, 51
yaw, 663
angle of attack, 561
aspect ratio, 663
atmosphere
planetary, 51
attenuation, 283
attitude control, 561

back wall
see damage, backwall
ballistic limit, 125, 137, 181, 215, 295, 377, 597, 735, 883, 989
impact energy, 883
obliquity, 883
ballistic limit equation, 225
critical diameter, 113
critical energy, 113
extravehicular mobility unit, 113
obliquity, 113
velocity, 113
behind armor blast, 13
behind armor debris, 573
also see fragmentation
blast impulse, 13
BUMPER, 113, 125, 225
bumper shield, 249, 271, 365, 823, 835, 859, 883
damage pattern, 859
strength effect, 859

Cassini spacecraft, 401
cavity expansion, 431
ceramics, 629
charge carriers, 169
chemical analysis, 401
collision zone, 205
comet, 597
compression test, 365
concrete, 341
constitutive modeling
aluminum, 261, 443
aluminum—1100-0, 621
aluminum—5754, 905
anisotropic, 365, 745
armor steel, 509
bulking, 895
ceramics, 573
cloth, 365
concrete, 341
crack softening, 895
damage, 431
dilation pressure, 895
dynamic, 509
failure modeling, 895
fracture, 193, 431
Hugoniot stress, 261
indentation, 629
index of refraction, 261
Johnson-Holmquist model, 573, 895
Johnson-Cook, 443, 621
Kevlar-epoxy, 365
Mohr-Coulomb, 771, 895
Nextel, 365
orthotropic, 745
porosity, 365
RHA, 675
shear stress, 261
soda-lime glass, 895
steel, 443
steel—4340, 771
Steinberg, 409
stress-strain, 509
stress-strain—AD995, 629
stress-strain—SiC-B, 629
stress-strain—TiB2, 629
stress-strain—WC, 629
tensile failure, 895
transtropic, 745
tungsten alloy, 193
tungsten carbide, 307
contact boundary, 205
cosmic dust, 401
crack propagation, 835
fracture toughness, 905
crater depth, 137, 859

crater diameter, 621, 675, 989
  also see hole diameter
crater distribution, 859
crater efficiency, 675
crater shape, 675
cratering, 51, 63, 67, 137, 319, 331, 377, 443, 597, 811, 859, 895, 921, 933, 989
  chemical analysis, 319
  classification, 377
  debris retention, 319
  degradation, 331
  depth of penetration, 895
  diameter, 519
  entry crater, 519
  Hubble telescope, 319
  impact velocity, 895
  Lonar Crater, 331
  low earth orbit, 319
  Mars, 331
  Meteor Crater, 331
  microdebris, 489
  Millochau Crater, 331
  morphology, 319, 377
  planetary, 331
  projectile density, 895
  projectile diameter, 895
  residual material, 319
  Roter Kamm Crater, 331
  shape effects, 443
  Talemzane Crater, 331
critical diameter, 125, 215
crystal structure, 629
current, 169, 597

damage, 181, 193, 215, 271, 377, 431, 519, 745, 883, 895, 933
  also see failure
  also see fracture
  adiabatic shear bands, 509, 757
  anisotropic, 745
  backwall, 125, 181, 215
  ballistic limit, 883
  bladder, 113
  blast damage area, 883
  brittle cleavage, 757
  conchoidal diameter, 895
  cone cracks, 377
  crack length, 835
  crack propagation, 905
  crack softening, 895
  cracks, 757, 811
  debris shield, 933
  delamination, 519
  diameter, 519
  energy dispersive spectrum, 811
  evolution, 237
  failure, 905
  fracture toughness, 905
  glass, 811
  hole diameter, 783
  impact energy, 883
  Johnson, 271
  Johnson-Cook, 193
  micrographs, 757
  morphology, 883, 895
  pressure wall, 835
  rupture, 835, 905
  spallation, 803
  transmission spectra, 811
  Tuler-Butcher, 803
debris cloud, 13, 181, 249, 365, 391, 519, 823, 835, 883, 905
  ablation, 391
  aerodynamic drag, 391
  damage zones, 519
  debris cone, 883
  dispersion, 519
  effect of pressure, 905
  expansion velocity, 307
  fragmentation, 307
  mass density, 181
  mass distribution, 687
  obliquity, 687
  pressurized vessel, 391
  radial extension, 391
  residual kinetic energy, 687
  residual mass, 687
  residual momentum, 687
  shock wave, 391
  spray angle, 181
  trajectory, 823
  velocity, 181, 391
  velocity distribution, 687
debris shield, 933
debris velocity, 699
deformation, 193, 629
delamination, 519
dentrite, 757
depth of penetration
  see penetration depth
detector
  charge sensitive amplifier, 401

detector (cont'd)
  multi-channel plate, 401
  spectrometer, 401
detector response, 39
detonation waves, 283
diagnostics, 261
  number of particles, 67
  optical flash, 67
  velocity, 67
diamond synthesis, 501
dispersion, 477
displacement law, 39
disruption, 795
drag, 51

ejecta, 51, 811
  charge, 169
  current, 169
  curtain, 51
  density, 651
  electromagnetic emissions, 169
  entrainment capacity, 51
  entrainment flow speed, 51
  height, 51
  plasma, 169, 651
  temperature, 651
elastic deformation, 629
elastic precursor, 431
electromagnetic effects, 169, 651
electromagnetic emissions, 169
EM gun
  see launchers
energy deposition, 933
equation of state, 27, 87, 261, 409, 421, 621, 803, 847
  also see Hugoniot
  aluminum, 443
  JWL, 443
  Octol, 443
  steel, 443
  Tillotson, 443
erosion, 467, 699, 795, 869
erosion rate, 1
experiment
  armor targets, 573
  depth of penetration, 1, 699
  erosion, 1, 699
  erosion rate, 467
  fragmentation, 687
  obliquity, 687
  penetration performance, 573
  penetration velocity, 467
  residual fragments, 687
  reverse ballistics, 467, 699
explosive welding, 205

explosives, 283
  pressure, 283
  temperature, 283
extravehicular mobility unit, 113

failure, 193, 307, 467, 895, 995
  also see fracture
  also see fragmentation
  pressure vessel, 905
  target resistance, 467
failure waves, 467, 995
flux, 597
flyer plate, 341, 365
fracture, 193, 431, 687, 967
  also see failure
  brittle cleavage, 757
  cracks, 757
  shear band bifurcation, 757
fragmentation, 181, 271, 307, 687, 757, 869, 933
  adiabatic shear banding, 757
  behind armor debris, 573
  debris, 933
  debris cloud, 307, 687
  distribution, 271
  droplet size, 933
  fragment size, 687
  Grady-Kipp, 307, 573
  mass distribution, 573, 687
  maximum entropy method, 869
  number distribution, 933
  number of particles, 869
  obliquity, 573
  particle size, 933
  residual kinetic energy, 687
  residual mass, 687
  residual momentum, 687
  shaped-charge jet, 353
  shrapnel, 933
  size distribution, 271
  size of particles, 869
  spatial distribution, 573
  velocity distribution, 687
fusion, 87

gasdynamics, 905

Giotto spacecraft, 597

Halley's comet, 597
hardness, 509, 629
hohlraum, 27, 87, 409, 803, 933
hole diameter, 13, 137, 181, 365, 377, 519, 547, 711, 783, 835, 981
  also see crater diameter
  analytical modeling, 711
  hole morphology, 711
  scaling, 711
hole growth, 77
  analytical modeling, 597
  slot cutting, 77, 967
honeycomb, 883
Hubble Space Telescope
  solar array, 597
Hugoniot, 261, 455
  also see equation of state
  aluminum, 27, 39, 409, 455
  aluminum—6061-T6, 261
  argon—liquid, 455
  beryllium, 87
  concrete, 341
  copper, 39, 409, 455, 803
  deuterium, 87
  gold, 39
  iron, 39, 455
  PMMA, 421
  polyethylene, 421
  polystyrene, 87
  titanium—Ti-6Al-4V, 261
  tungsten carbide, 307
Hugoniot elastic limit, 629
hydrodynamic instability
  growth factor, 409
  Kelvin-Helmholtz, 87, 205, 847
  Rayleigh-Taylor, 87, 409, 847
  Richtmyer-Meshkov, 87
  supernovae remnant, 87
hydrodynamic limit, 699

impact flash, 39, 169, 651
impact inclination
  see yaw
impact ionization, 169, 401
impact plasma
  ionization charge, 597
  ionization current, 597
indentation, 629
index of refraction, 261
inertial confinement fusion, 87
instability
  see hydrodynamic instability
  SPH, 945

interatomic potential
  Buckingham 6-Exp, 455
  Hugoniot, 455
  Lennard-Jones, 455, 477
  Morse, 455
  Rose, 455
  spall, 455
ion beam, 421
ionization charge, 597
isentropic loading, 261, 409
isentropic release, 261, 421
  aluminum, 27

Johnson-Holmquist model, 895
  also see constitutive modeling
  dilation pressure, 895
JWL
  see equation of state

KALIF, 421
Kelvin-Helmholtz, 87, 205, 847
Kevlar-epoxy, 365
KIDD, 489

laser, 811, 933
  HELEN, 803
  National Ignition Facility, 87, 933
  NOVA, 409, 933
  PHEBUS, 933
  profile, 811
  pulsed, 87, 401
  simulated impact, 87, 401, 409
  X-ray, 409
launcher
  ablation, 421
  combustion mixture, 533
  electrostatic, 597
  gascumulative accelerator, 501
  gasdynamic expansion, 501
  graded impactor, 261
  HYPER, 67
  attitude control, 561
  ion beam—simulated impact, 421
  laser—simulated impact, 87, 401, 409
  mass performance, 597
  performance, 533

launcher (cont'd)
plasma drag, 67, 597
powder gun, 533
RAM-accelerator, 501, 533
shaped-charge jet, 443
simulated impact, 421
two-stage light-gas gun, 561
three-stage, 261
TsNIIMASH, 501
two-stage light-gas gun, 597
velocity performance, 533, 597
Z-pinch, 27
LDEF, 597
Leonid meteors, 169
limit areal density, 771
luminous efficiencies, 651

martensite, 757
mass absorption coefficients, 651
mass spectrometer, 401
melting
see phase transition
metal-insulation transition, 87
metallurgy, 757
dentritic, 757
martensitic, 757
micrographs, 757
Meteor Crater, 331
meteor storm, 169
meteoroid, 597
meteoroid environment, 137
cummulative flux, 597
low Earth, 597
meteors
electromagnetic emissions, 169, 651
Leonide, 169
microdebris, 489
environment, 489
microstrain, 101
microstructure, 509
modeling
see analytical modeling
see numerical simulations
Mohr-Coulomb model, 895
also see constitutive modeling
molecular dynamics, 477
momentum, 597
MSCSurv, 225

National Ignition Facility, 87, 933
Nextel, 365
NOVA, 409, 933
numerical simulations
2-D & 3-D, 101
accuracy, 945
ALEGRA, 27, 101
alignment, 547
anisotropic, 745
asymmetry, 101
AUTODYN, 249, 365, 391, 443, 675, 895
ballistic limit, 735
brittle materials, 895
bumper shield, 271, 365
cometary impact, 847
contact algorithm, 945
contact boundaries, 945
coupled particle-finite element, 237, 735
crater diameter, 573
cratering, 921
CTH, 1, 193, 547, 621, 699, 957
damage, 249, 271, 745
damage evolution, 237
debris cloud, 365
debris cloud expansion, 249
debris velocity, 699
depth of penetration, 553, 771
discrete particles, 921
dispersion, 477
disruption, 795
DYNA3D, 77, 945
ejecta plume, 651
energy deposition, 847
erosion rate, 1
fragmentation, 271
free surface velocity, 101
gasdynamic, 651
GLO, 771
GRIM, 573
GRIM3D, 573
Hamiltonian method, 237
HELP, 981
HESIONE, 271
hole diameter, 547
HYADES, 933
hybrid particle-finite element, 237, 735
inhibited shaped charge, 443
instability, 945
interatomic potential, 455
interatomic potential, 477
Johnson-Holmquist model, 573

numerical simulations (cont'd)
L2D, 933
Lagrangian step, 847
LASNEX, 409
long rod, 1, 237
luminous efficiency, 651
mesh size, 391
mesoparticle velocity, 477
microstrain, 101
Mohr-Coulomb, 771
molecular dynamics, 477
nose and tail velocities, 1, 699
obliquity, 1, 573, 735
PAM-SHOCK 3D, 249
parametric studies, 795
penetration channel, 547
penetration depth, 573, 771
penetration efficiency, 547
penetration mechanics, 1, 699
penetration velocity, 1, 699, 771, 957
PISCES 2DELK, 795
planetary impact, 921
plate damage, 249
PUFF, 933
radiation hydrodynamics, 27
radiation transfer, 921
reactive armor, 795
rear wall, 735
remap step, 847
residual projectile length, 573
residual projectile velocity, 573
segmented rod, 547, 675, 957
sensitivity studies, 249
shape effects, 443
shaped-charge jet, 443
shock pressure, 249
shock profile, 307
small L/D, 675, 957
SOVA, 847
spall, 271, 477
spall velocity, 477
SPH, 249, 365, 391, 945
stress oscillations, 945
tail velocity, 771
three dimensional, 735
transverse loading, 77
validation, 101, 249
viscosity, 237
Whipple bumper, 237, 249, 735
WONDY, 261, 307
yaw, 547
yield strength, 101
zero energy mode, 945
zone resolution, 1, 193

obliquity, 1, 77, 113, 181, 215, 377, 519, 573, 663, 687, 735, 745, 823, 883, 967
ballistic limit, 883
debris cloud, 687
interaction thickness, 1
line-of-sight thickness, 1
metal contact, 205
modified line-of-sight thickness, 1
plate impact, 205
residual kinetic energy, 687
residual mass, 687
residual momentum, 687
ricochet, 687
rotation, 1
t/d ratio, 687
trajectory deflection, 967
translation, 1
optical pyrometry, 283
orbit debris environment, 225
orbital debris, 597
cummulative flux, 597

particle flux
distribution, 377, 597
particle velocity, 27, 101, 261, 341, 365, 803
particle-finite element technique, 237
penetration, 621, 989
after-flow, 621
debris velocity, 699
embedment, 77
erosion, 723
hydrodynamic limit, 699
lateral, 77
mass efficiency, 573
nose and tail velocities, 1, 699
penetration path, 723
penetration velocity, 995
primary, 77, 621
rigid body, 723
rock, 981
rod deformation, 77
rod loss, 699
secondary, 621
shaped-charge jet, 585
stages of interaction, 77

penetration (cont'd)
tail velocity, 995
target resistance, 995
terminal, 77
total, 621
trajectory deflection, 967
transients, 77
transition from rigid body to erosion, 723
transverse loading, 77, 967
yaw, 723
penetration channel, 63, 547, 981
penetration depth, 1, 137, 467, 573, 771, 995
penetration efficiency, 63, 137, 547, 621, 663, 675, 771, 957
L/D effects, 675, 957
penetration equation
critical diameter, 113
penetration mechanics, 957
debris velocity, 699
line-of-sight thickness, 1
numerical simulations, 1
obliquity, 1
segmented penetrator, 547, 675, 957
penetration performance, 573
penetration phases, 675
penetration velocity, 1, 467, 699, 995
penetrator
see projectile
perforation
tumbling, 967
phase transformation, 137, 933
also see phase transition
phase transition, 13, 87, 261, 409, 421
window, 283
photomultiplier, 39
pitch, 561
also see yaw
plasma, 169
plastic deformation, 629
plasticity
isochoric finite strain, 237
porosity, 271
pressure vessel, 835, 905
burst pressure, 905
debris cloud, 905
rupture, 905
pressurized mating adapter, 215
projectile
aluminum, 13, 51, 125, 137, 181, 215, 261, 271, 391, 443, 699, 735, 883, 905, 989
aluminum—1100-O, 783
aluminum—2017, 519, 895
aluminum—2017-T4, 113, 711
aluminum—2024-T3, 967
aluminum—2024-T351, 365
aluminum—2024-T86, 639
aluminum—6061-T6, 101, 237
aluminum oxide, 113
asteroid, 169, 921
cellulose acetate, 895
chrome steel—AISI 52100, 895
comet, 847, 921
compact cylinder, 967
copper, 467, 585, 989
cylinder, 547, 883
debris, 933
debris cloud, 835
design, 533
discus, 501
DU, 237, 639
erosion, 1
explosively formed, 63, 981
fins, 533
flyer plate, 261, 271, 341, 477
fracture, 723, 967
glass, 137, 895
iron, 39
laser, 803, 811
long rod, 1, 77, 193, 237, 295, 431, 467, 509, 573, 639, 663, 967
low L/D, 621, 675, 957
magnesium alloy, 13
meteor, 169, 331, 651
meteoroid, 137, 651
microdebris, 489
micrometeoroids, 319, 377
microparticles, 67, 319, 377
mild steel, 967
multiple, 895
nickel, 639
nylon, 113, 137, 377, 883, 895
olivine, 67
orbital debris, 225
phosphor bronze, 895
RAMAC, 533
rod deformation, 967
rotation, 1
sabot, 533
segment rod, 547
segmented penetrator, 957
segmented rod, 675

projectile (cont'd)
shaped-charge jet, 13, 125, 353, 443, 467, 585, 757, 795, 981
shrapnel, 933
small L/D, 621, 675, 957
soda-lime glass, 319, 377
space debris, 319, 377
sphere, 13, 39, 63, 101, 113, 125, 137, 181, 215, 237, 249, 307, 319, 365, 391, 443, 519, 735, 783, 823, 835, 859, 883, 895, 905, 989
sphere—stainless steel, 687
stainless steel, 319, 377
stainless steel—AISI 304, 895
stainless steel—AISI 316, 895
steel, 63, 113, 295, 699, 745, 859, 883, 989
steel—4340, 639, 723
steel—AerMet 100, 723
tantalum, 261
titanium, 261, 639, 883, 895, 967
tool steel, 639
translation, 1
tube, 443
tungsten, 467, 639, 699
tungsten alloy, 1, 77, 193, 295, 431, 509, 547, 573, 639, 663, 675, 771, 957, 967, 995
tungsten carbide, 307
uranium, 237, 639
propulsion, 533
pulsed power, 27, 87, 421, 803

radiation, 27, 39, 87, 409, 651
radiation hydrodynamics, 27
radiation transfer, 921
railgun
see launchers
RAMAC, 533
Rayleigh-Taylor, 87, 409, 847
reaction jet attitude control, 561
rear incident flux, 377
rear wall, 735
see damage, backwall
release
see isentropic release
release isentrope, 341, 823
release wave, 261
reverse ballistics, 699
Reynolds number, 533
Richtmyer-Meshkov, 87
ricochet, 823
trajectory, 823
rod deformation, 77
rotation, 77
Roter Kamm Crater, 331

sabot, 533
scaling, 489
hole diameter, 137, 711
kinetic energy, 573
segmented penetrator, 547, 675, 957
shaped-charge jet, 13, 353, 443, 585, 757, 981
aluminum liner, 981
blast impulse, 13
copper liner, 981
disruption, 795
formation, 443
fragmentation, 353
inhibited, 443
jet breakup, 353
jet radius, 353
liner angle, 13
liner material, 13
mass, 443
mass distribution function, 353
particulation, 353
penetration history, 353
performance, 13
temperature, 13
velocity, 981
shear banding, 757
also see adiabatic shear bands
half width, 757
quenching, 757
temperature, 757
shielding, 125, 137
ballistic limit, 883
bumper, 125
honeycomb, 883
multi-shock, 137
obliquity, 883
shielding
see bumper shield
shock heating, 39
shock velocity, 455, 803
shock velocity - particle velocity, 307, 455
shock wave, 823
attenuation, 283
gasdynamics, 905
obliquity, 823

shock wave (cont'd)
reflection, 905
shock wave experiments, 27
shock wave ignition, 283
shock wave velocity, 283
shock waves, 283
Shoemaker-Levy 9, 847
slot cutting, 77
smooth particle hydrodynamics
see SPH
solar array, 597
sound speed, 341
sound velocity
compressed material, 283
space debris, 783
also see meteoroids
also see orbital debris
space debris morphology, 319
space environment, 597
Space Station, 125, 181, 215
spacecraft
Giotto, 597
spall, 271, 307, 377, 477, 519
crack width, 477
mesoparticle velocity, 477
tungsten carbide, 307
spallation, 137, 803
Tuler-Butcher, 803
spectrometer, 401
SPH, 237, 249, 365, 391, 945
statistical analysis, 639
strength, 409
aluminum, 261
projectile, 1
spall, 477
substrate, 771
supernovae, 87

target, 237, 547
also see bumper shield
also see witness plate
advanced reusable surface insulation, 783
Aerojel, 67
alumina-enhanced thermal barrier, 783
aluminum, 13, 27, 39, 77, 101, 271, 283, 421, 443, 455, 585, 735, 803, 967, 989
aluminum alloy, 401
aluminum foil, 409
aluminum honeycomb, 883
aluminum matrix w/ceramic inclusions, 859
aluminum nitride, 771
aluminum oxide, 283, 431, 573
aluminum oxide—AD85, 771
aluminum oxide—AD96, 771
aluminum oxide—AD995, 629
aluminum powder, 651
aluminum—1100-O, 621, 711
aluminum—1100F, 639
aluminum—2024-T3, 137, 639, 711
aluminum—2219-T851, 215, 249
aluminum—5754, 905
aluminum—6061-T6, 237, 249, 261, 639, 711, 723
aluminum—7075-T6, 137, 215
anisotropic, 745
Apollo, 137
argon—liquid, 455
armor steel, 295, 509
atmosphere, 51
austenitic steel, 509
beryllium, 87
boron carbide, 283, 771
bumper shield, 125, 137, 181, 215, 249, 271, 365, 735, 823, 883
carbon fiber reinforced plastic, 883
carbon fibre/PEEK composite, 519
cast iron, 501
ceramic cloth, 125
ceramics, 869
chemical submunition, 1
cold rolled steel, 639
composite,125, 519
concrete, 341
confined explosives, 795
copper, 39, 67, 283, 341, 455, 639, 803, 989
copper foil, 409
coverglass laminate, 811
crater growth, 957
cryotank, 783
cylindrical can, 101
debris shield, 933
deuterium, 87
double wall, 137
duralumin alloy, 859
Earth, 331
explosive—confined, 795
explosive—HMX/Al, 283
explosive—liquid, 283

target (cont'd)
extravehicular mobility unit, 113
finite thickness, 573
flexible reusable surface insulation, 783
fused-silica, 307, 933
glass, 137, 811, 995
glassplastic, 745
gloves, 113
gold, 39
graphite powder, 651
hard upper torso (HUT), 113
heat shield, 137, 783
helmet, 113
hole diameter, 711
honeycomb, 783, 883
Hubble telescope, 319, 377
iron, 39, 455
Jupiter, 847
kamacite, 401
Kevlar, 125, 783
Kevlar-epoxy, 181, 365
Lexan, 699
lithium floride, 261
low density, 585
lunar surface, 651
magnesium, 639
magnesium powder, 651
metal composite, 859
micro-spheres, 51
mild steel, 585
multi-plate shield, 735
multi-shock shield, 365
multi-wall system, 835
Nextel, 125, 181, 365, 783
organoplastic, 745
orthotropic, 745
paraffin, 283
phenolic refrasil, 639
planetary surface, 169, 921
PMMA, 307, 421
polycarbonate, 699
polyethylene, 421, 585
polystyrene, 87
polyurethane foam, 125
porous, 651
porous aluminum, 283
portable life support system, 113
potassium iodide, 283
pressure vessel, 391, 835, 905
pressurized mating adapter, 215
Pyrex, 771
reactive armor, 795
regolith layer, 651
reusable launch vehicle, 783
RHA, 13, 295, 547, 573, 585, 663, 675, 757
rock, 981
sand (coarse), 51
satellite, 169
semi-infinite, 509, 573, 621, 989
silica phenolic/2024-T4 aluminum, 687
silicon carbide, 283, 467, 629, 771
Skylab, 137
slot cutting, 77, 967
soda-lime glass, 895, 995
solar cells, 67, 319, 377, 811
Space Station, 125, 181, 215, 225, 835
space suit, 113
spaced plates, 193, 639
stainless steel, 401
steel, 1, 63, 77, 295, 443, 967, 981, 989
steel—1018 CR plate, 967
steel—1020, 639
steel—4140,193
steel—4340, 237, 547, 639, 771, 957
steel—armor, 295, 509
tantalum, 261, 341
thermal protection system, 783
tied-wire fabric, 63
titanium, 271, 421, 639
titanium diboride, 629, 771
titanium—Ti-6Al-4V, 261
toughened solar cell, 811
tungsten carbide, 629
uranium, 639
water, 1, 585
weld, 215
windows, 137
yellow brass, 989
zinc, 639
target resistance, 467, 699, 995
failure, 467
penetration velocity, 467
Tate model, 1, 467, 699
also see Alekseevskii
also see analytical modeling
ceramics, 629
target resistance, 629
temperature, 39, 409
thermally choked, 533
time of flight spectra, 401
tumbling, 967

two-stage light-gas gun
  see launcher

uncertainty analysis, 225

validation, 101, 249
vaporization, 651, 699
  also see phase transition
velocity profiles, 341
VISAR, 27, 261
  lithium floride window, 261
vortex ring, 51
vulnerability analysis, 113, 225

wave speed, 341
Wein displacement law, 39
welding, 205
Whipple bumper, 137, 735
  also see bumper shield
window
  lithium floride, 261
  transparency, 261, 283
witness plate, 13, 125, 137, 181, 215, 365, 489, 519, 783, 859, 883

yaw, 77, 193, 547, 561, 663, 723, 967
  segmented rod, 675
  transverse loading, 77, 967
yield stress, 629
  ceramics, 629
  crystal structure, 629
  hardness, 629
  indentation, 629

Z-pinch, 27

Short Course Announcement

STRUCTURAL IMPACT

19 - 21 January 2000

Presented by Professor Norman Jones from the University of Liverpool

at

Ashurst Lodge, Southampton, UK

Organised by
Wessex Institute
of Technology, UK

Centre of Excellence
in Engineering
Research and Training

The objective of this course is to provide participants with an introduction to the response of structures subjected to dynamic loads which produce large inelastic strains. This information is relevant to a broad range of engineering problems for which safety calculations and hazard assessments are required. The topics are relevant to various kinds of dynamic loadings which occur in energy absorbing systems and structural crashworthiness problems as well as the safety and damage of industrial plant under extreme conditions. The topics include a general introduction to the major simplifications and assumptions, dynamic material properties, geometrically similar scaling of experiments and other subjects to provide a sound introduction to the topic.

COURSE OUTLINE

- Dynamic ductile behaviour of beams
- Dynamic ductile behaviour of plates and shells
- Influence of transverse shear and rotary inertia
- Influence of large deflections
- Elementary failure criteria
- Material strain rate sensitivity coefficients.
- Quasi-static behaviour
- Introduction to structural crashworthiness
- Dynamic axial crushing of tubes
- Similitude
- Comments and conclusions

For Further Information on this Course

CONTACT

Clare Bridle
Course Secretariat
STRUCTURAL IMPACT (1490)
Wessex Institute of
Technology (WIT),
Ashurst Lodge, Ashurst
Southampton,
SO40 7AA, UK

Tel: 44 (0) 238 029 3223
Fax: 44 (0) 238 029 2853
EMail: cbridle@wessex.ac.uk

BOOK NOW
LIMITED PLACES

VISIT OUR WEBSITE AT: www.wessex.ac.uk

WESSEX INSTITUTE OF TECHNOLOGY
Centre of Excellence in Engineering Research and Training

FROM ELSEVIER SCIENCE...
SCIENCE PUBLISHER TO THE WORLD

CONTENTS DIRECT

A FREE alerting service by E-mail for Elsevier Science journals

ContentsDirect allows you unrivalled access to the Tables of Contents pages of Elsevier Science journals in the following subject areas:

- Chemistry and Chemical Engineering
- Clinical Medicine
- Computer Science
- Earth and Planetary Sciences
- Economics, Business and Management Science
- Engineering, Energy and Technology
- Environmental Science and Technology
- Life Sciences
- Materials Science
- Mathematics
- Physics and Astronomy
- Social Sciences
- Multidiscipline

What does ContentsDirect provide?

- Journal title
- Volume and issue number
- Title of paper
- Names of authors
- Page details
- Anticipated publication date
- News and offers

Why register to ContentsDirect?

- Provides via E-mail advance notice of forthcoming papers, allowing you to reserve the issue at your library.
- Provides an invaluable information resource to scientists and researchers requiring the very latest information on soon-to-be published papers.
- Keeps you at the forefront of current research.
- Enables you to create a personal archive of key journal contents in your field of interest.

How to register for ContentsDirect:

- The quickest way to register for **ContentsDirect** is via Elsevier Science home page on the world wide web.
- Registration is simple and the selection of titles is provided by access to drop down menus of all subject classifications plus a complete listing of all titles available.
- If you wish to select new titles or amend your existing selection - simply re-visit the web site and personally make your changes.

ContentsDirect

Register now! **ContentsDirect**

www.elsevier.com/locate/ContentsDirect
www.elsevier.nl/locate/ContentsDirect
www.elsevier.co.jp/locate/ContentsDirect

NB If you can't access the web - please note that you can still register by sending an E-mail to **cdsubs@elsevier.co.uk**

8Z-MPD/2

Did you know contributors to Elsevier Science books or journals are entitled to

30% discount

on all our books*?

*(except multi-volume reference works)

Contact your nearest Elsevier Science office in order to obtain a subject catalogue

Regional Sales Offices

For customers in Europe, Middle East and Africa
Elsevier Science, Regional Sales Office, Customer Support Department, P.O. Box 211, 1000 AE Amsterdam, The Netherlands
Tel: (+31) 20 485 3757, Fax: (+31) 20 485 3432, E-mail: nlinfo-f@elsevier.nl

For customers in the United States & Canada
Elsevier Science, Regional Sales Office, Customer Support Department, P.O. Box 945, New York, N.Y. 10159-0945, U.S.A.
Tel: (+1) 212 633 3730, Toll Free number for North-American customers: 1-888-4ES-INFO (437-4636), Fax: (+1) 212 633 3680
E-mail: usinfo-f@elsevier.com

For customers in Japan
Elsevier Science, Regional Sales Office, Customer Support Department, 9-15 Higashi-Azabu, 1-chome, Minato-ku, Tokyo, 106-0044 Japan
Tel: (+81) 3 5561 5033, Fax: (+81) 3 5561 5047, E-mail: info@elsevier.co.jp

For customers in Asia and Australasia
Elsevier Science, Regional Sales Office, Customer Support Department, No. 1 Temasek Avenue, #17-01 Millenia Tower, Singapore 039192
Tel: (+65) 434 3727, Fax: (+65) 337 2230, E-mail: asiainfo@elsevier.com.sg

For customers in Latin America
Elsevier Science, Regional Sales Office, Rua Sete de Setembro 111/16 Andar, 20050-002 Centro, Rio de Janeiro - RJ, Brazil
Tel: (+55) 21 509 5340, Fax: (+55) 21 507 1991, E-mail: elsevier@campus.com.br

ELSEVIER | PERGAMON | NORTH HOLLAND | EXCERPTA MEDICA

CO815/P2

BACK ISSUES OF THIS JOURNAL

Back issues of this and all other Elsevier Science journals are available in hard copy. New subscribers to a journal may purchase back issues of that publication in hard copy edition at 25% discount off the standard price. Elsevier Science maintains stocks of back issues and orders may be placed with confidence at your nearest Elsevier Science office. Should any issue of a volume be temporarily out of stock at the time of ordering, a high quality photoduplicated copy will be supplied at no extra charge to complete your order.

SAVE UP TO 25% BY PURCHASING COMPLETE SETS

Customers wishing to purchase complete sets can do so at a saving of 25% off the individual volume price.

MICROFORM EDITIONS

Back issues in microform of Elsevier Science research journals are also available. For further information please apply to your nearest Elsevier Science office.

BACK ISSUES PRICE LIST

Full details of the rates of back issues of all Elsevier Science journals can be found in our Back Issues Price List. Please contact your nearest Elsevier Science office for a copy.

Regional Sales Offices

For customers in Europe, Middle East and Africa
Elsevier Science, Regional Sales Office, Customer Support Department, P.O. Box 211, 1000 AE Amsterdam, The Netherlands
Tel: (+31) 20 485 3757, Fax: (+31) 20 485 3432, E-mail: nlinfo-f@elsevier.nl

For customers in the United States & Canada
Elsevier Science, Regional Sales Office, Customer Support Department, P.O. Box 945, New York, N.Y. 10159-0945, U.S.A.
Tel: (+1) 212 633 3730, Toll Free number for North-American customers: 1-888-4ES-INFO (437-4636), Fax: (+1) 212 633 3680
E-mail: usinfo-f@elsevier.com

For customers in Japan
Elsevier Science, Regional Sales Office, Customer Support Department, 9-15 Higashi-Azabu, 1-chome, Minato-ku, Tokyo, 106-0044 Japan
Tel: (+81) 3 5561 5033, Fax: (+81) 3 5561 5047, E-mail: info@elsevier.co.jp

For customers in Asia and Australasia
Elsevier Science, Regional Sales Office, Customer Support Department, No. 1 Temasek Avenue, #17-01 Millenia Tower, Singapore 039192
Tel: (+65) 434 3727, Fax: (+65) 337 2230, E-mail: asiainfo@elsevier.com.sg

For customers in Latin America
Elsevier Science, Regional Sales Office, Rua Sete de Setembro 111/16 Andar, 20050-002 Centro, Rio de Janeiro - RJ, Brazil
Tel: (+55) 21 509 5340, Fax: (+55) 21 507 1991, E-mail: elsevier@campus.com.br

CO815/P3

Receive Regular News of Elsevier's Publications

Elsevier Science mails information on new and existing publications regularly. If you would like to be added to the mailing list please send us your name and full mailing address, indicating your fields of interest:

a subject areas

- ⊞ Chemistry and Chemical Engineering
- ⊞ Clinical Medicine
- ⊞ Computer Science
- ⊞ Earth and Planetary Sciences
- ⊞ Economics, Business and Management Science
- ⊞ Engineering, Energy and Technology
- ⊞ Environmental Science and Technology
- ⊞ Life Sciences
- ⊞ Materials Science
- ⊞ Mathematics
- ⊞ Physics and Astronomy
- ⊞ Social Sciences

ELSEVIER

PERGAMON

NORTH HOLLAND

EXCERPTA MEDICA

Regional Sales Offices

For customers in Europe, Middle East and Africa
Elsevier Science
Regional Sales Office
Customer Support Department
P.O. Box 211
1000 AE Amsterdam
The Netherlands
Tel: (+31) 20 485 3757
Fax: (+31) 20 485 3432
E-mail: nlinfo-f@elsevier.nl

For customers in the United States & Canada
Elsevier Science
Regional Sales Office
Customer Support Department
P.O. Box 945
New York, N.Y. 10159-0945
U.S.A.
Tel: (+1) 212 633 3730
Toll Free number for North-American customers: 1-888-4ES-INFO (437-4636)
Fax: (+1) 212 633 3680
E-mail: usinfo-f@elsevier.com

For customers in Japan
Elsevier Science
Regional Sales Office
Customer Support Department
9-15 Higashi-Azabu
1-chome
Minato-ku
Tokyo
106-0044 Japan
Tel: (+81) 3 5561 5033
Fax: (+81) 3 5561 5047
E-mail: info@elsevier.co.jp

For customers in Asia and Australasia
Elsevier Science
Regional Sales Office
Customer Support Department
No. 1 Temasek Avenue
#17-01 Millenia Tower
Singapore 039192
Tel: (+65) 434 3727
Fax: (+65) 337 2230
E-mail: asiainfo@elsevier.com.sg

For customers in Latin America
Elsevier Science
Regional Sales Office
Rua Sete de Setembro 111/16
Andar
20050-002 Centro
Rio de Janeiro - RJ
Brazil
Tel: (+55) 21 509 5340
Fax: (+55) 21 507 1991
E-mail: elsevier@campus.com.br

CO815/P5

AVAILABLE AT YOUR FINGERTIPS...

THE ELSEVIER SCIENCE CATALOGUE ON THE INTERNET

Features include:

ELSEVIER SCIENCE

Catalogue on INTERNET

- ORDER YOUR **FREE** SAMPLE COPY OF *JOURNAL/ BOOK TITLE* TODAY BY CHECKING ITS CATALOGUE ENTRY

Other features include:-

- All the journals, with complete information about journal editors and editorial boards
- Listings of special issues and volumes
- Listings of recently published papers for many journals
- Complete descriptions and contents lists of book titles
- Clippings of independent reviews of published books
- Book series, dictionaries, reference works
- Electronic and CD-ROM products
- Full text search facilities
- Ordering facilities
- Print options
- Hypertext links
- Alerting facility for new & forthcoming publications
- Updated monthly

TRY IT TODAY!

http://www.elsevier.nl/

For further queries please contact:-

Customer Support Department
Tel: +1 (212) 633 3730
Fax: +1 (212) 633 3680
E-mail: usinfo-f@elsevier.com

Customer Support Department
Tel: +31 (20) 485 3757
Fax: +31 (20) 485 3432
E-mail: nlinfo-f@elsevier.nl

ELSEVIER SCIENCE

Catalogue on INTERNET

CO815/P6

ELSEVIER | PERGAMON | NORTH HOLLAND | EXCERPTA MEDICA

FROM ELSEVIER SCIENCE...
SCIENCE PUBLISHER TO THE WORLD

CONTENTS DIRECT

A FREE alerting service by E-mail for Elsevier Science journals

ContentsDirect allows you unrivalled access to the Tables of Contents pages of Elsevier Science journals in the following subject areas:

- Chemistry and Chemical Engineering
- Clinical Medicine
- Computer Science
- Earth and Planetary Sciences
- Economics, Business and Management Science
- Engineering, Energy and Technology
- Environmental Science and Technology
- Life Sciences
- Materials Science
- Mathematics
- Physics and Astronomy
- Social Sciences
- Multidiscipline

What does ContentsDirect provide?

- Journal title
- Volume and issue number
- Title of paper
- Names of authors
- Page details
- Anticipated publication date
- News and offers

Why register to ContentsDirect?

- Provides via E-mail advance notice of forthcoming papers, allowing you to reserve the issue at your library.
- Provides an invaluable information resource to scientists and researchers requiring the very latest information on soon-to-be published papers.
- Keeps you at the forefront of current research.
- Enables you to create a personal archive of key journal contents in your field of interest.

How to register for ContentsDirect:

- The quickest way to register for **ContentsDirect** is via Elsevier Science home page on the world wide web.
- Registration is simple and the selection of titles is provided by access to drop down menus of all subject classifications plus a complete listing of all titles available.
- If you wish to select new titles or amend your existing selection - simply re-visit the web site and personally make your changes.

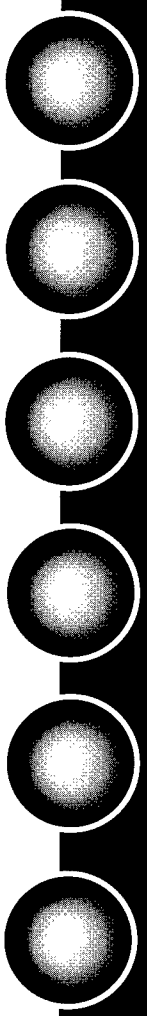

ContentsDirect

Register now!

ContentsDirect

www.elsevier.com/locate/ContentsDirect

www.elsevier.nl/locate/ContentsDirect

www.elsevier.co.jp/locate/ContentsDirect

NB If you can't access the web - please note that you can still register by sending an E-mail to **cdsubs@elsevier.co.uk**

8Z-MPD/2

INTERNATIONAL JOURNAL OF IMPACT ENGINEERING

AIMS AND SCOPE

The *International Journal of Impact Engineering* exists for the publication of original research work concerned with the response of structures and bodies to dynamic loads arising from exposure to blast collision or other impact events. The topics encompassed by the journal include the elastic and plastic response of structures and bodies to impact and blast loading, terminal ballistics, vehicle crashworthiness, containment and other processes and phenomena in which effects due to impact predominate, such as explosive welding. In addition, related matters such as research into fire hazards in association with impact loads will be included. Every paper accepted for publication is strictly refereed and assessed for its contribution to the understanding of impact phenomena or the insight gained for engineering design in areas of high rate loading.

Papers whose concerns are only in the fields of mathematics, materials science or computation are not requested. Similarly, papers whose contents are purely descriptive will not be accepted.

This journal should be of interest to engineers, designers and research workers in the fields of structural crashworthiness, energy-absorbing systems, structural failure, hazard assessments and safety calculations which involve impact loadings. Thus, papers in this journal will be of interest to aeronautical engineers, civil engineers, mechanical engineers, naval architects, nuclear engineers, ocean engineers, offshore engineers, transportation engineers and workers in other branches of engineering and science who are involved in impact loading of various kinds.

INSTRUCTIONS TO AUTHORS

1. The journal is devoted to original papers of high standard which contribute to the understanding of impact in various branches of engineering, and papers offered for publication are refereed and assessed by reference to these aims.

2. The language of the journal is English; however, contributions from all parts of the world are encouraged. Authors are solely responsible for the factual accuracy of their papers.

3. Two copies of the manuscript and figures, etc. of any paper which is offered for publication should be sent to the Editor-in-Chief:

Professor Norman Jones
Department of Engineering
(Mechanical Engineering)
The University of Liverpool
Brownlow Hill
Liverpool L69 3GH, U.K.

4. Only papers not previously published will be accepted and authors must agree not to publish elsewhere a paper submitted to, and accepted by, the journal.

5. Papers of a length exceeding thirty A4 pages (manuscript and figures) will not be acceptable unless a prior arrangement has been made with the Editor.

Authors should examine previous issues of the journal as a general guide to the preparation of papers.

Printed by Polestar AUP Aberdeen Ltd.